Materials Science and Technologies Series

Titanium Alloys

Preparation, Properties and Applications

Pedro N. Sanchez
Editor

Titanium Alloys: Preparation, Properties and Applications : Preparation, Properties and Applications, Nova Science Publishers, Incorporated, 2010.

MATERIALS SCIENCE AND TECHNOLOGIES

TITANIUM ALLOYS: PREPARATION, PROPERTIES AND APPLICATIONS

MATERIALS SCIENCE AND TECHNOLOGIES

Magnetic Properties of Solids
Kenneth B. Tamayo (Editor)
2009. ISBN: 978-1-60741-550-3

Mesoporous Materials: Properties, Preparation and Applications
Lynn T. Burness (Editor)
2009. ISBN: 978-1-60741-051-5

Physical Aging of Glasses: The VFT Approach
Jacques Rault
2009. ISBN: 978-1-60741-316-5

Physical Aging of Glasses: The VFT Approach
Jacques Rault
2009. ISBN: 978-1-61668-002-2 (E-book)

Graphene and Graphite Materials
H. E. Chan (Editor)
2009. ISBN: 978-1-60692-666-6

Dielectric Materials: Introduction, Research and Applications
Ram Naresh Prasad Choudhary and Sunanda Kumari Patri
2009. ISBN: 978-1-60741-039-3

Handbook of Zeolites: Structure, Properties and Applications
T. W. Wong
2009. ISBN: 978-1-60741-046-1

Strength of Materials
Gustavo Mendes and Bruno Lago (Editors)
2009. ISBN: 978-1-60741-500-8

Photoionization of Polyvalent Ions
Doris Möncke and Doris Ehrt
2009. ISBN: 978-1-60741-071-3

Building Materials: Properties, Performance and Applications
Donald N. Cornejo and Jason L. Haro (Editors)
2009. ISBN: 978-1-60741-082-9

Concrete Materials: Properties, Performance and Applications
Jeffrey Thomas Sentowski (Editor)
2009. ISBN: 978-1-60741-250-2

Corrosion Protection: Processes, Management and Technologies
Teodors Kalniņš and Vilhems Gulbis (Editors)
2009. ISBN: 978-1-60741-837-5

Corrosion Protection: Processes, Management and Technologies
Teodors Kalniņš and Vilhems Gulbis (Editors)
2009. ISBN: 978-1-61668-226-2 (E-book)

Handbook on Borates: Chemistry, Production and Applications
M.P. Chung (Editor)
2009. ISBN: 978-1-60741-822-1

Handbook of Photocatalysts: Preparation, Structure and Applications
Geri K. Castello (Editor)
2009. ISBN: 978-1-60876-210-1

Smart Polymer Materials for Biomedical Applications
Songjun Li , Ashutosh Tiwari, Mani Prabaharan and Santosh Aryal (Editors)
2010. ISBN: 978-1-60876-192-0

Definition of Constants for Piezoceramic Materials
Vladimir A. Akopyan, Arkady Soloviev, Ivan A. Parinov and Sergey N. Shevtsov
2010. ISBN: 978-1-60876-350-4

Organometallic Compounds: Preparation, Structure and Properties
H.F. Chin (Editor)
2010. ISBN: 978-1-60741-917-4

Surface Modified Biomedical Titanium Alloys
Aravind Vadiraj, M . Kamaraj
2010. ISBN: 978-1-60876-581-2

Composite Laminates: Properties, Performance and Applications
Anders Doughett and Peder Asnarez (Editors)
2010. ISBN: 978-1-60741-620-3

Shape Memory Alloys: Manufacture, Properties and Applications
H. R. Chen (Editor)
2010. ISBN: 978-1-60741-789-7

Piezoelectric Materials: Structure, Properties and Applications
Wesley G. Nelson (Editor)
2010. ISBN: 978-1-60876-272-9

Titanium Alloys: Preparation, Properties and Applications
Pedro N. Sanchez (Editor)
2010. ISBN: 978-1-60876-151-7

Organosilanes: Properties, Performance and Applications
Elias B. Wyman and Mathis C. Skief (Editors)
2010. ISBN: 978-1-60876-452-5

Piezoceramic Materials and Devices
Ivan A. Parinov (Editor)
2010. ISBN: 978-1-60876-459-4

High Performance Coatings for Automotive and Aerospace Industries
Abdel Salam Hamdy Makhlouf (Editor)
2010. ISBN: 978-1-60876-579-9

Fundamentals and Engineering of Severe Plastic Deformation
Vladimir M. Segal, Irene J. Beyerlein, Carlos N. Tome, Vladimir N. Chuvildeev and Vladimir I. Kopylov
2010. ISBN: 978-1-61668-190-6

Fundamentals and Engineering of Severe Plastic Deformation
Vladimir M. Segal, Irene J. Beyerlein, Carlos N. Tome, Vladimir N. Chuvildeev and Vladimir I. Kopylov
2010. ISBN: 978-1-61668-458-7 (E-book)

Amines Grafted Cellulose Materials
Nadege Follain
2010. ISBN: 978-1-61668-196-8

Amines Grafted Cellulose Materials
Nadege Follain
2010. ISBN: 978-1-61668-494-5 (E-book)

Lanthanide–Doped Lead Borate Glasses for Optical Applications
Joanna Pisarska and Wojciech A. Pisarski
2010. ISBN: 978-1-61668-292-7

Lanthanide–Doped Lead Borate Glasses for Optical Applications
Joanna Pisarska and Wojciech A. Pisarski
2010. ISBN: 978-1-61668-736-6 (E-book)

Piezoelectric Ceramic Materials: Processing, Properties, Characterization, and Applications
Xinhua Zhu
2010. ISBN: 978-1-61668-418-1

Piezoelectric Ceramic Materials: Processing, Properties, Characterization, and Applications
Xinhua Zhu
2010. ISBN: 978-1-61668-814-1 (E-book)

New Developments in Materials Science
Ekaterine Chikoidze and Tamar Tchelidze (Editors)
2010. ISBN: 978-1-61668-852-3

New Developments in Materials Science
Ekaterine Chikoidze and Tamar Tchelidze (Editors)
2010. ISBN: 978-1-61668-907-0 (E-book)

Handbook of Material Science Research
Charles René and Eugene Turcotte (Editors)
2010. ISBN: 978-1-60741-798-9

Innovative Materials for Automotive Industry
Akira Okada
2010. ISBN: 978-1-61668-237-8

Post-Impact Fatigue Behavior of Composite Laminates: Current and Novel Technologies for Enhanced Damage Tolernace
Alkis Paipetis and Dionysios T. G. Katerelos
2010. ISBN: 978-1-61668-672-7

Post-Impact Fatigue Behavior of Composite Laminates: Current and Novel Technologies for Enhanced Damage Tolernace
Alkis Paipetis and Dionysios T. G. Katerelos
2010. ISBN: 978-1-61728-090-0 (E-book)

Recent Advances in Non-Destructive Inspection
Carosena Meola (Editor)
2010. ISBN: 978-1-61668-550-8

Recent Advances in Non-Destructive Inspection
Carosena Meola (Editor)
2010. ISBN: 978-1-61728-082-5 (E-book)

MATERIALS SCIENCE AND TECHNOLOGIES

TITANIUM ALLOYS: PREPARATION, PROPERTIES AND APPLICATIONS

PEDRO N. SANCHEZ
EDITOR

Nova Science Publishers, Inc.
New York

For permission to use material from this book please contact us:
Telephone 631-231-7269; Fax 631-231-8175
Web Site: http://www.novapublishers.com

LIBRARY OF CONGRESS CATALOGING-IN-PUBLICATION DATA

Titanium alloys : preparation, properties, and applications / [edited by] Pedro N. Sanchez.
p. cm.
Includes index.
ISBN 978-1-61122-323-1 (eBook)
1. Titanium alloys. I. Sanchez, Pedro N.
TN693.T5T495 2009
620.1'89322--dc22

2009039827

Published by Nova Science Publishers, Inc. ✣ New York

CONTENTS

PREFACE

Titanium alloys are metallic materials which contain a mixture of titanium and other chemical elements. Such alloys have very high tensile strength and toughness (even at extreme temperatures), light weight, extraordinary corrosion resistance, and ability to withstand extreme temperatures. However, the high cost of both raw materials and processing limit their use to military applications, aircraft, spacecraft, medical devices, connecting rods on expensive sports cars and some premium sports equipment and consumer electronics. This book reviews the recent work on the synthesis of multiphase composites in titanium base alloys to develop high strength and light weight materials with metastable phases. In vitro and in vivo experiments reporting biological performance of Ti-based materials modified by light are also reviewed. Other chapters focus on ultrasonic machining of titanium and its alloys, biomedical applications of laser induced surface modification of titanium alloys, fatigue studies of biomedical titanium alloys, bioactive titanium surfaces, and titanium-base nano-ultrafine eutectic and composites.

Essentials prior to any surface treatment of materials by lasers are consideration and appreciation of: (i)- unique properties of lasers and their effects especially in relation to surface treatment, (ii)- fundamentals of laser-material interaction process and (iii)- correct adjustment and selecting optimized optical parameters from (i) and (ii) for performing a corresponding relevant application. Titanium and its alloys application like any other biomaterials involve the creation of at least one interface between the material and biological tissues. Biocompatibility and bioactivity of biomaterials rely on interactions that take place between the interface of the biomaterial and biological system. The surface morphology, as well as manipulation with the physical state and chemical composition of implant surface may be significant for bone- implant integration.

So, the tissue response to an implant involves physical factors depending on implant design, surface topography, surface charge density, surface free energy and chemical factors associated with the composition of the materials. It is therefore, the intension of Chapter 1, after covering the sections (i) and (ii) to discuss and evaluate the effect of surface morphology produced by Nd:YAG laser radiation and silicone carbide paper as a comparison on surface physico- chemical changes, surface wettability, corrosion resistance, microhardness and osteoblast cells adhesivity on Ti-6Al-4V alloy with respect to possible laser surgery.

The research work in Chapter 2 was aimed at developing a novel noncontacting thermoelectric method for nondestructive detection of material imperfections in metals. The method is based on magnetic sensing of local thermoelectric currents around imperfections

when a temperature gradient is established throughout a conducting specimen by external heating and cooling. The surrounding intact material serves as the reference electrode therefore the detection sensitivity could be very high if a sufficiently sensitive magnetometer is used in the measurements. This self-referencing, noncontacting, nondestructive inspection technique offers the following distinct advantages over conventional methods: high sensitivity to subtle variations in material properties, unique insensitivity to the size, shape, and other geometrical features of the specimen, noncontacting nature with a substantial stand-off distance, and the ability to probe relatively deep into the material.

The authors have successfully adapted the noncontacting thermoelectric method to a series of nondestructive materials characterization applications that are currently not accessible by any other known inspection method. In particular, the authors studied experimentally the effect of the background signature produced by the intrinsic anisotropy and inhomogeneity in a titanium alloy by comparing an analytical model capable of quantitatively predicting the resulting thermoelectric signature. In addition, the authors studied the feasibility of nondestructive detection and characterization of the level of plastic deformation in Ti-6Al-4V by thermoelectric potential (TEP) measurements that have undergone thermo-mechanical process such as cold working. Building on the extensive and very promising results of this research work, it will be possible to develop numerous new NDT techniques that will find application in energy production (nuclear, oil, and gas industries, power generators, etc.), material manufacturing (aluminum, steel, titanium, nickel-base super-alloys, etc.), and in the transportation industry (aerospace, automobile, etc.).

Load bearing implants such as hip joints, knee joints and bone plates etc. are prone to failure from the synergistic effect of fretting wear and fatigue during physical bodily movement. Fretting wear or fretting fatigue is a form of adhesive wear phenomenon wherein a small tangential oscillatory motion under high contact pressure gradually erodes the surface and initiates crack within the contact leading to ultimate failure of the material under fatigue loading condition. Modular junctions of hip implants consist of ball on a tapered shaft experiencing fretting wear during body movements.

Titanium alloys, Stainless steels and Co-Cr-Mo alloys are the most commonly used alloys for medical grade devices. Titanium alloys has high strength to weight ratio, superior biocompatibility and corrosion resistance compare to other materials. Surface modified titanium alloys have better tribological properties. In Chapter 3, the substrate materials used are Ti-6Al-4V and Ti-6Al-7Nb. PVD TiN coating, plasma nitriding, nitrogen ion implantation, laser nitriding favors formation of TiN and Ti_2N of different thickness according to the process. Thermal oxidation process favors formation of hard and brittle oxide layer.

Fretting wear tests were conducted to study the quality of the coatings and modified layers. Laser nitriding and PVD TiN coating has shown better performance than other coatings due to high hardness of the layers. Friction coefficient for PVD TiN coating is around 0.2 throughout the test. Wear volume for PVD TiN coated and laser nitrided samples were almost 10 and 50 times lesser than other coatings respectively.

Fretting fatigue life of surface modified titanium alloys has considerably improved compared to unmodified materials. Plasma nitrided pairs have shown the best performance over all the coatings. The average fretting fatigue lives of unmodified pairs were 15 to 18% of plasma nitrided pairs, 45 to 50% of the PVD TiN coated pairs and about 60% of ion implanted pairs. Fretting of unmodified alloy pairs have shown high friction and oxidation at

the contact due to metallurgical compatibility of the pairs. Fretting of PVD TiN pairs have shown delamination and subsequent oxidation. The damage and friction generated within the contact is a complex interaction between third body particulates, oxide debris and ringer solution. Fretting fatigue life is more for plasma nitride pairs compared to all other modification processes. The damage of ion implanted pairs is similar to unmodified alloys with little improvement in fretting fatigue life. Laser nitrided pairs and thermally oxidation pairs have shown poor fretting fatigue life due to high case thickness and inhomogenities of the layers formed. Friction generated is low compared to al other process, but the specimens experienced premature failure at higher loads.

As discussed in Chapter 4, titanium alloys have excellent mechanical properties and low density. These properties make titanium alloys very attractive structural materials for wide application in industry (aeronautics, aerospace and automotive industry, energy systems, marine, machinery industry, medicine…). A very important concern in all sectors of industry is the need to reduce weight and costs. One of the most interesting developments in aeronautics is to replace much heavier nickel-base superalloys at 550–700°C or conventional disc/blade structure with blinks. Approximately one third the structural weight of modern turbine engines is made up of titanium (e.g. fan blades, compressor components). Besides nickel-base superalloys, titanium alloys are the standard engine materials [1,2]. The elevated temperature near-α titanium alloys are used for rotating components, especially in the hotter compressor stages where the temperature and pressure are higher. Less critical non-rotating components such as compressor cases are also made of titanium alloys. In the case when temperatures are below 300°C, the two phase (α+β) Ti-6Al-4V alloy can be used [3].

Titanium and its alloys are the most widespread materials employed in orthopaedic and dental surgery, because of their good mechanical properties and biocompatibility. In fact titanium has a good fatigue resistance and, at the same time, its elastic modulus is the lowest between metals, so it avoids stress shielding of implants. Moreover titanium surface is naturally covered by an oxide layer preventing corrosion and it is almost inert in contact with biological fluids. Inertness avoids adverse reactions of the body, but at the same time it hampers tissue integration. Several solutions have been proposed, in order to improve titanium bioactivity: bioactive coatings based on hydroxyapatite and calcium phosphates, inorganic surface modifications (alkaline treatments, acid etchings or electrochemical oxidation) and biomolecular surface grafting. A brief commentary of recent research on these topics will be presented.

Moreover an innovative treatment will be described in Chapter 5. It is focused on inducing a bioactive behaviour on Ti6Al4V. The process includes two steps: the first one is an inorganic modification, inducing inorganic bioactivity on the surface (hydroxyapatite precipitation), while the second one is an organic treatment, promoting a biological response. In particular the first step includes an acid etching, in order to remove the natural oxide layer, and a controlled oxidation in hydrogen peroxide. The second step is the covalent surface grafting of a biomolecule (enzyme alkaline phosphatase (ALP) for instance), in order to stimulate cell response.

Results show that the inorganic treatment induces hydroxyapatite precipitation on the titanium surface (it was tested in-vitro by soaking in simulated body fluid (SBF) for two weeks). The oxide layer shows a porous surface texture on a nanoscale and it is quite rich in hydroxyls groups. A thermal treatment could improve the mechanical resistance of this modified layer to the substrate, without altering its bioactive behaviour. The fatigue

performances of the material are not modified by the treatment. ALP has been successfully grafted to the modified titanium surface, maintaining its activity. The results of cellular tests will be reported in order to evaluate the biological behaviour of treated samples. Finally it has been observed that there is a synergic mechanism between inorganic and biological bioactivity, one improving the other one.

Ultrasonic machining (USM) is a mechanical material removal process used to erode holes and cavities in hard or brittle work pieces by using shaped tools, high frequency mechanical motion, and an abrasive slurry. Unlike other non-traditional processes such as laser beam, and electrical discharge machining, ultrasonic machining does not thermally damage the work piece or appear to introduce significant levels of residual stress, which is important for the survival of materials in service. The fundamental principles of stationary ultrasonic machining, the material removal mechanisms involved and the effect of operating parameters on material removal rate, tool wear rate, and work piece surface finish of titanium and its alloys are reviewed in Chapter 6, for application in manufacturing industry.

In Chapter 7, fracture behaviors of titanium alloy TC6 under thermal/mechanical loading in the in-plane shear case are investigated and compared with steel and aluminum materials. A macroscopic crack would be diathermanous for heat. The heat flow would partly or completely pass the crack surface. The crack is then called as the uninsulating crack. An insulating crack implies that the heat flow cannot pass the crack surface completely. The proposed crack model includes both insulating and uninsulating crack cases. The problem of a line crack under the combination of remote uniform heat flow and mechanical shear loading is analytically solved by the complex function method. Obtained are the analytical solutions including the temperature distribution, thermal stress intensity factor, total stress field and strain energy density function. It is found that if the temperature gradient perpendicular to the crack line on the upper and lower crack surfaces remains constant, the mode II thermal stress intensity factor prevails while the mode I thermal stress intensity factor vanishes. It is a typical mode II crack problem. Moreover, the mode II thermal stress intensity factor only depends on the temperature gradient component perpendicular to the crack. The temperature gradient component parallel to the crack line has no influence on the thermal stresses. The diathermanous feature of the crack would affect the thermal stress field. Three materials, say titanium alloy TC6, steel alloy 38Cr2Mo2VA and aluminum alloy LY12, are selected to perform the numerical calculations. Their fracture behaviors under thermal and mechanical loading are discussed and compared by application of strain energy density theory. It is found that for an insulating crack, the positive temperature gradient would partly kill the mechanical loading that would impede the crack growth. However, the uninsulating crack behaves quite different. For the uninsulating crack, the positive temperature gradient would enhance the mechanical loading or the crack growth. The temperature boundary condition plays an important role in the material failure behaviors. The results are useful for the safety assessment of structural members, especially in the pressurized vessels and pipes and nuclear power plants.

In Chapter 8, casting of Ti-Mo alloys having different Mo content (4 to 20 wt%) was performed by arc-melting of pure metals. These alloys present interesting features for potential biomedical applications, e.g., in artificial proteases, owing the favorable characteristics of Ti alloys: apart from mechanical properties and good osseointegration, the strong corrosion resistance in biological environment and the low toxicity of their corrosion products.

The corrosion and anodic behavior of the different alloys was investigated in different electrolytes, including neutral, acidic and chloride-containing solutions. A strong tendency to passivation was observed, caused by the oxygen affinity of the metallic material. However, partial Mo dissolution is likely to occur at very low pH.

Composition and solid-state properties of the passive films were studied by ex-situ XPS, in-situ photoelectrochemical and impedance experiments. Films were found to consist of a mixed oxide phase, mainly containing TiO_2 and bearing small concentrations of MoO_3. The latter depends on starting alloy composition and film thickness.

As a result, also the behavior of the passive films depends on these two factors. In fact thin films or films grown on alloys bearing a small Mo content display n-type semiconducting behavior, analogous to what reported for pure TiO_2. On the contrary, films grown on alloys with higher Mo content are more resistive and change their behavior from semiconducting to insulating with increasing thickness.

As explained in Chapter 9, the successful application of the Ti-6Al-4V alloy relies heavily on the availability of welding process producing superior quality joints. Fusion welding technologies, which are conventionally used to join titanium alloys, generally enable to produce high-quality welds with a relatively high productivity. However, the fusion welding is usually associated with solidification problems which may significantly deteriorate service properties of the titanium weldments.

In this regard, friction stir welding, being an innovative "solid-state" joining technology, may potentially be attractive for Ti-6Al-4V. Basically, FSW involves plunging a specially designed tool rotating at high speeds into abutted edges of sheet workpieces to be welded and then translating the tool along the weld seam. The rotating tool produces frictional heat which softens the material so it can be readily extruded around the tool to fill the cavity to the rear of the tool and to form a joint in a solid state. As a solid-state process, FSW avoids (or limits) solidification problems and thus provides defect-free welds having excellent mechanical properties.

In order to improve the basic physical understanding of FSW of Ti-6Al-4V, the present contribution is focused on microstructural evolution during the welding process. The microstructural development is found to be a complex process involving α-to-β phase transformation during heating stage, deformation in the high-temperature β-phase field during stirring stage and β-to-α phase transformation upon cooling stage of FSW. The α-to-β phase transformation is shown to be governed by epitaxial growth of the pre-existing β phase consuming the α phase. Reconstruction of the β-grain structure and orientation measurements in the retained β phase have demonstrated that microstructural evolution in the high-temperature β phase field is a complex process involving grain growth, geometrical effects of strain, transverse grain subdivision and discontinuous recrystallization stimulated by local grain boundary migration; material flow may be described in the term of simple shear deformation arising from {110}<111> slip. The β-to-α phase transformation after FSW is established to be governed by Burgers orientation relationship which dictated the final weld crystallography.

The effects of preheat and pouring temperatures, as well as annealing temperatures and cooling rates, on microstructure and mechanical properties of γ-TiAl and Ti-6Al-4V (wt.%) investment castings have been studied performing X-ray diffraction (XRD) analysis, light microscopy (LM) and scanning electron microscopy (SEM), quantitative metallography,

hardness and room temperature tensile tests. Annealing of Ti-6Al-4V above and below the β phase transus temperature produces different combinations of strength and elongation, but a compromise may be achieved applying temperature just below the β phase transus of Ti-6Al-4V alloy. Higher values of tensile strength together with lower ductility than reported in the literature cannot be only ascribed to the presence of α' martensite in the microstructure of Ti-6Al-4V alloy. Yttria coating of graphite crucible must be considered as insufficient in preventing the chemical reaction between aggressive titanium melt and carbon. The processing technology of a "self-supporting" ceramic shell mold was successfully verified during precision casting of both tensile-test samples of Ti-6Al-4V and the prototype of the turbocharger wheel made of γ-TiAl. According to experimental results, a processing window for investment casting of the prototype of a turbocharger wheel was established. The results of Chapter 10 also show that besides annealing treatment parameters, melting and casting practice together with ceramic mold technology strongly influence the properties Ti-6Al-4V and γ-TiAl castings.

Due to the shift of market trends and increasing awareness of the need to be environmentally friendly, the most important task facing manufacturers is to reduce the part weight significantly without impinging on its function. Use of the light-weight alloys is becoming important in the material selection stage. One of the most common light alloys is titanium alloys. The applications of titanium alloy are not widespread, however, owing to its high cost. To minimize the weight and cost of products and maximize the efficiency and functions of the material usage, tailor-welded blank technology can be combined with the light-weight alloy and applied during the production stage. However, the forming capability of a light-weight alloy and its tailor-welded blanks are relatively limited. In order to counter these disadvantages, one solution is to use temperature as the process parameters during the forming operation. This can increase the ductility significantly and reduce the yield strengths, forces and pressures during the forming process. Chapter 11 will give an overview of he research activities examination titanium tailor-welded blanks under thermal forming condition.

In Chapter 12, fracture behaviors of titanium alloy TC6 under thermal/mechanical and mode I condition are discussed and compared with steel and aluminum materials. Considered is a line crack in an infinite plate subjected to the combined mechanical and thermal loading. The problem is solved in the framework of thermoelastic theory by integrating with the complex function method. An analytical solution is obtained under the boundary condition that the constant temperature is retained on the crack surfaces while the remote uniform heat flow is imposed. In this case, thermal loading only induces the mode I stress intensity factor and at the same time the mode II thermal stress intensity factor vanishes. Moreover, the heat flow component along the normal direction to the crack line has no influence on the thermal stress intensity factor which only depends on the heat flow component parallel to the crack line. The problem is a typical mode I crack problem. Fracture behaviors of three materials, say TC6 titanium, 38Cr2Mo2VA steel and LY12 aluminum alloys, are analyzed under the combination of mechanical and thermal loading by application of strain energy density factor theory. The applied failure stresses at different scales are numerically calculated. By comparison, the fracture resistances of three materials are different. It is found that the thermal loading would enhance the crack propagation. If the direction of heat flow is changed

to an opposite direction, the thermal effect would impede the crack growth. That is the thermal effect has the positive or negative effect which depends on the direction of heat flow.

Chapter 13 reviews the recent work on the synthesis of multiphase composites in titanium base alloys to develop high strength and light weight materials with metastable phases. The strategies for alloy development, processing methods, evolution of different phase in the microstructure, elastic-plastic behavior are discussed for Ti-Fe-base eutectic and near-eutectic alloy compositions. It is revealed that modification of the eutectic microstructure by 'a non-uniform grain size distribution' $i \triangleright e \triangleright^{c}$ by introducing relatively larger grains in a eutectic matrix, or using multiple phases, is an effective way for improving the plasticity of nanostructured alloys. The influence of alloy compositions, intrinsic structure of the nano-/ultrafine phases and their elastic properties are crucial for developing nano-heterostructured composites.

In: Titanium Alloys: Preparation, Properties and Applications ISBN: 978-1-60876-151-7
Editor: Pedro N. Sanchez, pp. 1-99

Chapter 1

FUNDAMENTALS OF BIOMEDICAL APPLICATIONS OF LASER INDUCED SURFACE MODIFICATION OF TITANIUM ALLOYS

Mohammad Etrati Khosroshahi* and ***Mahboobeh Mahmoodi*****
Amirkabir University of Technology, Faculty of Biomed. Eng., Biomaterial Group, Laser and Biophotonic Lab., Tehran-Iran

Abstract

Essentials prior to any surface treatment of materials by lasers are consideration and appreciation of: (i)- unique properties of lasers and their effects especially in relation to surface treatment, (ii)- fundamentals of laser-material interaction process and (iii)- correct adjustment and selecting optimized optical parameters from (i) and (ii) for performing a corresponding relevant application. Titanium and its alloys application like any other biomaterials involve the creation of at least one interface between the material and biological tissues. Biocompatibility and bioactivity of biomaterials rely on interactions that take place between the interface of the biomaterial and biological system. The surface morphology, as well as manipulation with the physical state and chemical composition of implant surface may be significant for bone- implant integration.

So, the tissue response to an implant involves physical factors depending on implant design, surface topography, surface charge density, surface free energy and chemical factors associated with the composition of the materials. It is therefore, the intension of this chapter, after covering the sections (i) and (ii) to discuss and evaluate the effect of surface morphology produced by Nd:YAG laser radiation and silicone carbide paper as a comparison on surface physico- chemical changes, surface wettability, corrosion resistance, microhardness and osteoblast cells adhesivity on Ti-6Al-4V alloy with respect to possible laser surgery.

*E-mail address: khosro@aut.ac.ir
**E-mail address: m.mahmoodi@aut.ac.ir

1.1. Introduction to the Lasers

An atomic system is characterized by discrete energy states, and usually the atoms exist in the lowest energy state, which is normally referred to as the ground state. An atom in a lower energy state may be excited to a higher energy state through a variety of processes. One of the important processes of excitation is through collisions with other particles. The excitation can also occur through the absorption of electromagnetic radiation of proper frequencies; such a process is known as stimulated absorption or simply as absorption. On the other hand, when the atom is in the excited state, it can make a transition to a lower energy state through the emission of electromagnetic radiation; however, in contrast to the absorption process, the emission process can occur in two different ways.

(i) The first is referred to as spontaneous emission in which an atom in the excited state emits radiation even in the absence of any incident radiation. It is thus not stimulated by any incident signal but occurs spontaneously. Further, the rate of spontaneous emissions is proportional to the number of atoms in the excited state.
(ii) The second is referred to as stimulated emission, in which an incident signal of appropriate frequency triggers an atom in an excited state to emit radiation. The rate of stimulated emission (or absorption) depends both on the intensity of the external field and also on the number of atoms in the upper state. The net stimulated transition (stimulated absorption and stimulated emission) depends on the difference in the number of atoms in the excited and the lower states, unlike the case of spontaneous emission, which depends only on the population of the excited state.

The fact that there should be two kinds of emissions–namely, spontaneous and simulated–was first predicated by Einstein in 1917. The consideration which led to this predication was the description of thermodynamic equilibrium atoms and the radiation field. Einstein (1917) showed that both spontaneous and stimulated emissions are necessary to obtain Planck's radiation low. The phenomenon of stimulated emission was first used by Townes in 1954 in the construction of a microwave amplifier device called the maser, which is an acronym for Microwave Amplification by Stimulated Emission of Radiation. At about the same time a similar device was also proposed by Prokhorov and Basov. The maser principle was later extended to the optical frequencies by Schawlow and Townes in 1958, which led to the device now known as the laser. In fact "laser" is an acronym for light amplification by stimulated emission of radiation. The first successful operation of a laser device was demonstrated by Maiman in 1960 using ruby crystal. Within a few months of operation of the device, Javan and his associates constructed the first gas laser, namely, the He-Ne laser. Since then, laser action has been obtained in a larger variety of materials including liquids, ionized gases, dyes, semiconductors etc.

1.1.1. Nature of Light

The description of the nature of light provided here is at the very basic level. It serves to review the concepts that most readers already may be familiar with. Light is an

electromagnetic field consisting of oscillating electric and magnetic disturbances that can propagate as a wave through a vacuum as well as through a medium.

Young was able to explain phenomena such as the formation of colours in soap films of thin films of oil on wet surfaces in terms of a wave theory by associating different colours of light can come about only because light has a transverse wave nature. By this we mean that the vibrations of the light waves are perpendicular to the direction of travel, unlike the situation with sound traveling through fluids, where the waves are longitudinal with the vibrations along the direction of travel. In a plane polarized beam of light all of the waves have their vibrations coplanar as opposed to the random orientation of the planes of vibration of unpolarized light – the situation is illustrated in Fig 1.1.

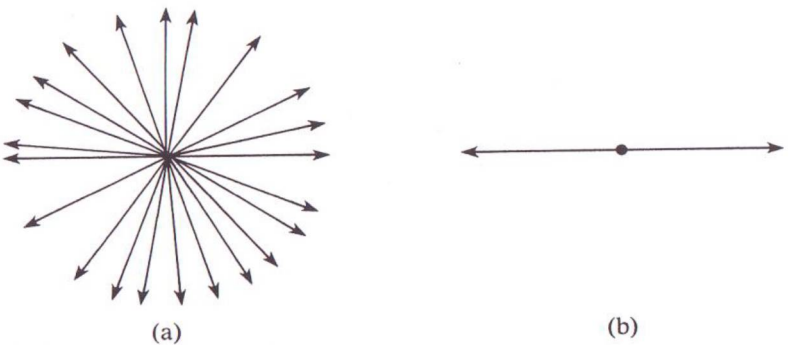

Figure 1.1. (a) shows the random orientations of the electric fields of the waves comprising an unpolarized beam of light traveling normal to the plane of the paper. (b) shows the electric field directions of a horizontally plane–polarized beam of light. where μ_0 is the magnetic permeability of free space and ε_0 is the electric permittivity of free space.

Additional evidence in favor of a wave theory was provided by Fresnel's quantitative explanation of diffraction in terms of light waves, while a major advance in understanding the nature of light was made by Maxwell in 1864. Maxwell combined the experimental work of Faraday, Oersted and Henry on electricity and magnetism into a set of equations from which he deduced the existence of a transverse wave whose speed c in free space was given by:

$$c = \left(\frac{1}{\varepsilon_0 \mu_0} \right)^{1/2} \tag{1.1}$$

Fig 1.1 (a) shows the random orientations of the electric fields of the waves comprising an unpolarized beam of light traveling normal to the plane of the paper. (b) shows the electric field directions of a horizontally plane–polarized beam of light. where μ_0 is the magnetic permeability of free space and ε_0 is the electric permittivity of free space. The extraordinary property of this wave was that its speed c, obtained by substituting measured values of μ_0 and ε_0, agreed almost exactly with the speed of light as measured by Fizeau. Maxwell

therefore proposed that light is an example of an electromagnetic wave having a speed of about 3×10^{8} ms^{-1}, a frequency of about 5×10^{14} Hz and a wavelength of about 5×10^{-7} m. We now accept that this is indeed the case and in its plane polarized form we think of a light wave as consisting of an electric and a magnetic component vibrating at right angles to each other and to the direction of propagation as illustrated in Fig. 1.2.

In 1887 Hertz succeeded in generating nonvisible electromagnetic waves and started the search for other waves of different wavelengths so that we now talk of the electromagnetic spectrum extending from frequencies of 3×10^{10} Hz to frequencies of 3×10^{20} Hz as shown in Table 1.1. The spectrum is somewhat arbitrarily divided into different regions, with no definite boundary between them. We often talk of the optical region which includes the visible together with the near I.R. and U.V. region, say from frequencies of 3×10^{13} to 3×10^{16}Hz; it is within the optical region that we generally find most of laser wavelengths. All of the waves in the spectrum have a simple relationship between frequency ν and wavelength λ, namely $c=\nu\lambda=2.9979\times10^{8}\ ms^{-1}$ in vacuo.

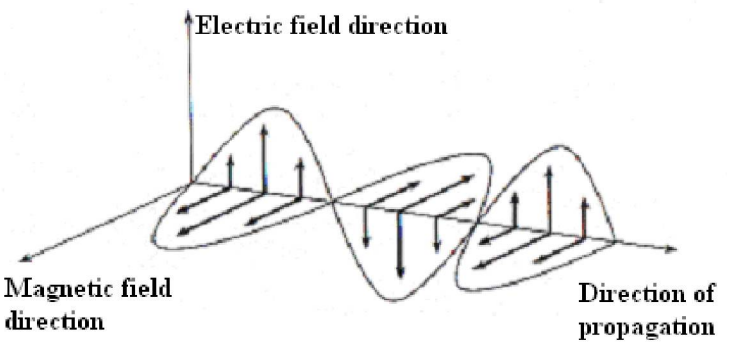

Figure 1.2. Electric and magnetic fields in a plane electromagnetic wave.

Table 1.1. The electromagnetic spectrum.

Type of radiation	Wavelength	Frequency (Hz)	Quantum energy (eV)
Radio waves	100 km	3×10^{3}	1.2×10^{-11}
Microwaves	300 mm	10^{9}	4×10^{-6}
Infrared	0.3 mm	10^{12}	4×10^{-3}
Visible	0.7 μm	4.3×10^{14}	1.8
Ultraviolet	0.4 μm	7.5×10^{14}	3.1
X rays	0.03 μm	10^{16}	40
γ rays	0.1 nm	3×10^{18}	1.2×10^{4}
	1.0 pm	3×10^{20}	1.2×10^{6}

Note: The divisions into the various regions are for illustration only; there is no firm dividing line between one region and the next.

Most of the interactions between light and molecules of biological interest are electrical in nature. Therefore, the description of a light wave focuses on the nature of the oscillating electric field E, which has both a direction and an amplitude (the value corresponding to maxima and minima of the wave). The direction of the electric field, E, for a plane wave traveling in one direction is always perpendicular both to the direction of propagation and to the oscillating magnetic field, B. However, it can be linearly polarized, when the electric field each point is in the same direction. When the electric field is distributed equally in a plane perpendicular to the direction of propagation, it is called circularly polarized. The propagation of light in the z direction with its oscillating electric field E(z,t) is described mathematically as:

$$E(z,t) = E_0 \cos(\omega t - kz) \tag{1.2}$$

$$k^2 = \frac{\varepsilon \omega^2}{c^2} \tag{1.3}$$

and with E_0 defining the initial electric field amplitude of the field, ω is the angular frequency of light given as $2\pi v$ and k, called the propagation vector, is defined as:

$$k = \frac{2\pi}{\lambda} \tag{1.4}$$

It characterizes the phase of the optical wave with respect to a reference point (z =0); thus, kz describes the relative phase shift with respect to the reference point. The Term ε in equation (1.3) is called the dielectric constant, which for optical waves is n^2, with n being the refractive index of the medium. The speed of an optical wave (light) is described by the propagation of waves in a medium. This propagation is characterized by two velocities: phase velocity which describes the travel of phase front and group velocity which describes the travel of wave packet. However, modern theory, quantum mechanics, also imparts a particle–like description of light as energy packets called photons or quanta. This dual–character description of light, which is also shared by matter, is represented in Table 1.2. In a medium such as a glass or a biological material, the speed of an electromagnetic wave, often labeled as *v*, is different. The ratio of the two speeds c and *v* is called the refractive index, n, of the medium. In other words,

$$\frac{c}{v} = \frac{speed\ of\ light\ in\ a\ vacuum}{speed\ of\ light\ in\ a\ medium} = n \quad or \quad v = \frac{c}{n} \tag{1.5}$$

Therefore, n can be viewed as the resistance offered by the medium towards the propagation of light. The higher the refractive index has the lower the speed.

Table 1.2. Dual Character of Light.

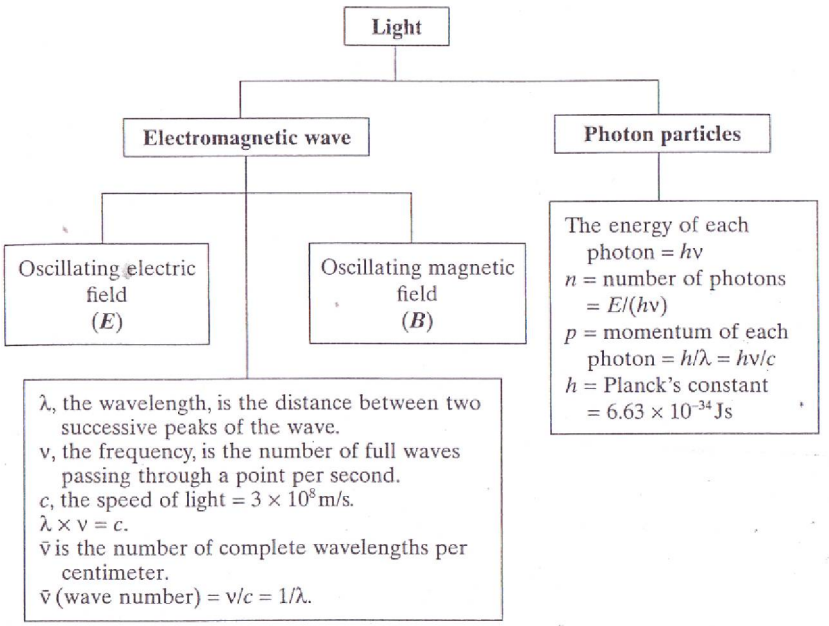

1.1.2. Basic Laser Principles

Let us assume for simplicity a two–level system. Since a large number of photons are involved and we are interested in processes that are stimulated by a classical radiation field it is hence well justified to describe the change of photon number n inside the resonator by a classical rate equation as will be considered shortly. Basically, the energy of the emitted photon during a natural decay is given by the difference between the higher (E_2) and the lower (E_1) energy levels (is $\Delta E = E_2 - E_1$). This energy determines the wavelength of light, which in fact is its colour. When many atoms in a medium undergo spontaneous (natural) orbital decay, the process is known as spontaneous emission defined by Einstein coefficient A_{21}, Fig 1.3a. If, however we imagine that the atoms are initially at the ground state and are required to be excited in such a way to achieve a coherent output, it is done via stimulated absorption defined by Einstein coefficient B_{12}, Fig 1.3b. Clearly, following the atomic transition at this stage it leads to corresponding emission of coherent photons. This process is referred to as stimulated emission defined by Einstein coefficient B_{21}, Fig 1.3c.

Unlike atoms emitting radiation by spontaneouse emission transitions, which occur randomly in time, atoms undergoing stimulated emission radiate their quanta of energy in phase with the stimulating radiation. This means that if an atom is stimulated to emit light energy by a propagating wave, the additional quantum of energy liberated in the process adds to that wave on a constructive basis, increasing its amplitude. It is as though one of the hypothetical secondary sources of Huygens'principle were augmented by a true source of radiation emitting in phase with the original wave.

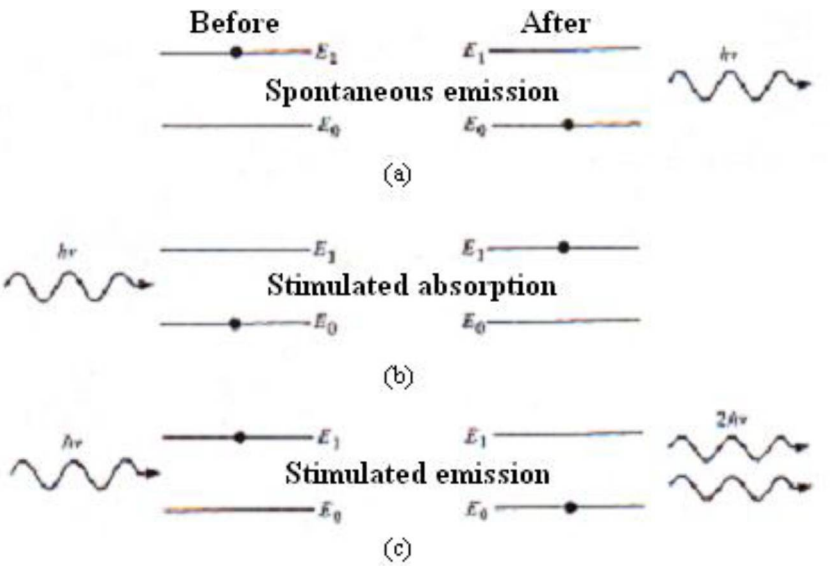

Figure 1.3. Energy-state-transition diagram differentiating between stimulated absorption, spontaneous emission, and stimulated emission. A black dot indicates the state of the atom before and after the transition takes place. In the stimulated emission process, energy is added to the stimulating wave during the transition; in the absorptionprocess, energy is extracted from the wave.

Einstein Relations

The three transition processes–stimulated spontaneous, absorption emission, and stimulated emission–all occur in a collection of atoms. In 1917, Albert Einstein showed that the rates of these processes are related mathematically. The average fractional rate at which atoms in energy state E_1 spontaneously drop to the lower energy state E_0 is designated by a constant, A_{12}, the Einstein coefficient of spontaneous emission. The reciprocal of A_{12} is the time for the $(2 \rightarrow 1)$ transition to occur and therefore is the transition lifetime of the state we referred to earlier $(\tau_{12} = 1/A_{12})$. If there are N_1 atoms in the collection with energy E_1, the number of atoms per second that undergo spontaneous emission is given by the expression

$$\text{Spontaneous emission transition rate} = N_1 A_{12} \tag{1.6}$$

The value of A_{12} , and hence the total rate, depends upon the kind of atom and upon the particular transition involved. For stimulated absorption and stimulated emission to take place, there must be radiation energy present. Einstein postulated that the number of atoms undergoing absorption transitions each second is proportional to the number of atoms in the lower energy state, N_o, and to the spectral density of radiation energy, ρ_v (joule–sec/m^3), at the transition frequency, v_{21}.

$$\text{Stimulated absorption transition rate} = N_0 \rho_v B_{12} \tag{1.7}$$

where the constant of proportionality, B_{12}, is the Einstein coefficient of stimulated absorption. Similarly, the rate at which the stimulated emission process takes place, measured in transitions per second, is given by the number of atoms in the excited state times the spectral radiation density times the Einstein coefficient of stimulated emission, B_{21}.

$$\text{Stimulated emission transition rate} = N_1 \rho_v B_{21} \tag{1.8}$$

The effective spectral radiation energy density associated with the light beam is related to the spectral irradiance of the beam by $\rho_v = I_v / c$. In rewriting Equations (1.7) and (1.8) in terms of the spectral irradiance of the light beam, we thus obtain

$$\text{Stimulated absorption transition rate} = N_0 \frac{I_v}{c} B_{12} \tag{1.9}$$

and

$$\text{Stimulate emission transition rate} = N_1 \frac{I_v}{c} B_{21} \tag{1.10}$$

If conditions of thermal equilibrium are assumed, the coefficients of stimulated absorption and stimulated emission can be shown to be equal,

$$B_{12}=B_{21} \tag{1.11}$$

and the coefficient of spontaneous emission can be shown to be related to the coefficient of stimulated emission by the formula

$$A_{12} = \frac{8\pi h v_{21}^3}{C^3} B_{21} \tag{1.12}$$

Equations (1.11) and (1.12) are known as the Einstein relations. Although obtained under conditions of thermal equilibrium, the equations can be assumed to hold for steady–state (i.e., non–time– varying) conditions, even when true thermal, or blackbody, equilibrium is not established. The second Einstein relation states that the ratio of the probability of spontaneous emission to the probability of stimulated emission for a given pair of energy levels is proportional to the cube of the frequency of the transition radiation. This cubic dependency on v accounts for the principal difficulty in achieving laser action at x-ray wavelengths, where v is of the order of 10^{16} Hz. At this frequency, spontaneous emission occurs so rapidly for a high–energy transition that light amplification by the stimulated emission process is not easily achieved. Fortunately, this difficulty is not great for most lasers at visible wavelengths.

How a Laser Works

The three main components of any laser device are the active medium, the pumping source, and the optical resonator. The active medium consists of a collection of atoms,

molecules, or ions (in solid, liquid, or gaseous form), which acts as an amplifier for light waves. For amplification, the medium has to be kept in a state of population inversion, i.e., in a state in which the number of atoms in the upper energy level is greater than the number of atoms in the lower energy level. The pumping mechanism provides for obtaining such a state of population inversion between a pair of energy levels of the atomic system. When the active medium is placed inside an optical resonator, the system acts as an oscillator.

As such, it is analogous to electrical positive feedback oscillators where a certain amount of the output is fed back in phase with the input, resulting in oscillation at some frequency characteristic of the circuit. In effect, the oscillator selects a frequency component from the noise always present from biasing, amplifies it, and oscillated at that frequency. The laser does essentially the same thing except that an optical oscillator can operate in many allowed modes (natural resonator frequencies).

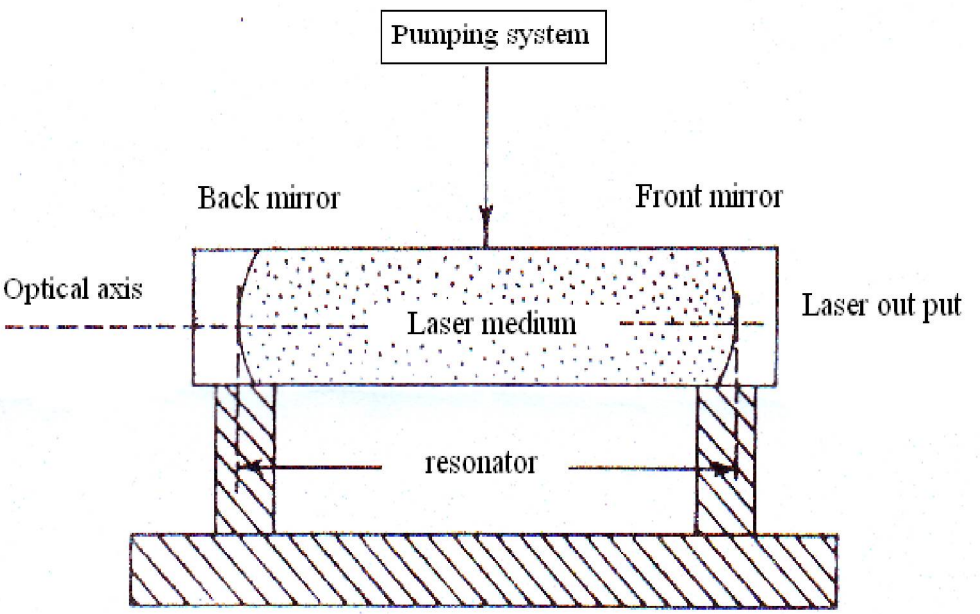

Figure 1.4. Basic arrangement of a typical laser.

All laser action begins with the establishment of a population inversion by the excitation process. Photons are spontaneously emitted in all directions. Photons traveling through the active medium can stimulate exited atoms or molecules to undergo radiative transitions when the photons pass near the atoms or molecules. This factor in itself is unimportant except that the stimulated and stimulating photons are in phase, travel in the same direction, and have the same polarization. This phenomenon provides for the possibility of gain or amplification. Only those photons traveling nearly parallel to the axis of the resonator will pass through a substantial portion of the active medium. A percentage of these photons will be fed back (reflected) into the active region, thus ensuring a large buildup of stimulated radiation, much more than the spontaneous radiation at the same frequency. Lasing will continue as long as the population inversion is maintained above some threshold level.

The optical resonator, because of its geometrical configuration, provides for a highly unidirectional output and at the same time, through the feedback process, for sufficient stimulated radiation in the laser to ensure that most transitions are stimulated. The phenomenon of stimulated emission, in turn, produces a highly monochromatic, highly coherent output. The combined action of the resonator and stimulated emission produces an extremely bright light source even for lasers of relatively low power output.

A schematic diagram of a flashlamp driving circuit normally is used in solid state lasers such as Nd:YAG laser is shown in Fig 1.5. The falshlamps are fired by energizing the bank to a voltage that is less than the breakdown voltage of the flashlamps, and ten applying a trigger pulse to the primary of a transformer. The secondary of the trigger transformer is in series with the lamps. The high–voltage pulse (20 kV) ionizes the gas inside the flashlamp tube and provides a high- current conducting path to discharge the energy bank.

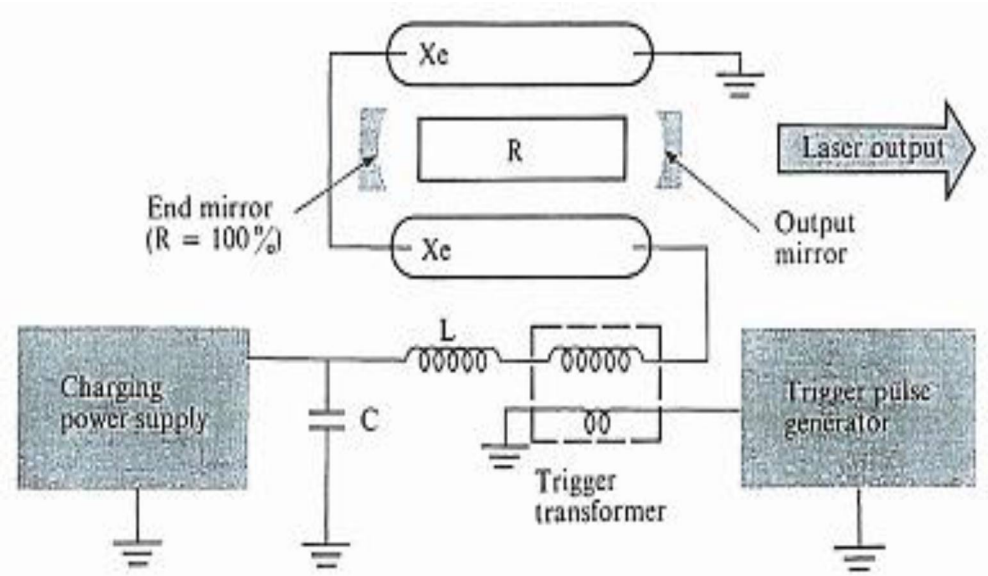

Figure 1.5. Schematic of a simple flashlamp- pumped laser. The trigger pulse generator and transformer provide a high–voltage pulse sufficient to cause the xenon-gas in the lamps (Xe) to discharge. The ionized gas provides a low- resistance discharge path to the storage capacitor (C). The inductor (L) shapes the current pulse, aintaining the discharge. The discharge of the lamps optically pumps the laser rod (R) [113].

Normally a countdown procedure is employed before each firing of a doped insulator laser system, and users shield their eyes. From the standpoint of safety, the flashlamp power supplies are probably as dangerous as the laser output itself. Although the supply may not appear to be a threat, a lager capacitor bank of several millifarad capacitance charged to a potential of several thousand volts can deliver a lethal shock. For this reason, a well-designed power supply contains interlock mechanisms that automatically discharge the capacitor banks when the power supply is opened for inspection. A well– grounded probe with an insulating handle is frequently attached to the door of the power supply to drain off any residual charge on the capacitor bank. Some of laser with their specifications for particular industrial and biomedical applications are listed in tables (1.4) and (1.5).

Table 1.4. Some laser systems.

Laser type	Wavelength	Typical pulse duration
Argon ion	488/514 nm	CW
Krypton ion	531/568/647 nm	CW
He – Ne	633 nm	CW
CO_2	10.6 μs	CW or pulsed
Dye laser	450-900 nm	CW or pulsed
Diode laser	670-900 nm	CW or pulsed
Ruby	694 nm	1-250 μs
Nd: YLF	1053 nm	100 ns-250 μs
Nd: YAG	1064 nm	100 ns-250 μs
Ho: YAG	2120 nm	100 ns-250 μs
Er : YSGG	2780 nm	100 ns-250 μs
Er : YAG	2940 nm	100 ns-250 μs
Alexandrite	720-800 nm	50 ns-100 μs
XeCl	308 nm	20-300ns
XeF	351 nm	10-20 ns
KrF	248 nm	10-20 ns
ArF	193 nm	10-20 ns
Nd: YLF	1053 nm	30-100 ps
Nd : YAG	1064 nm	30-100 ps
Free electron laser	800-6000 nm	2-10 ps
Ti : Sapphire	700-1000 nm	10 fs-100 ps

Table 1.5. Wavelengths and photon energies of selected laser systems.

Laser type	Wavelength (nm)	Photon energy (eV)
ArF	193	6.4
KrF	248	5.0
Nd: YLF (4ω)	263	4.7
XeCl	308	4.0
XeF	351	3.5
Argon ion	514	2.4
Nd : YLF (2ω)	526.5	2.4
He-Ne	633	2.0
Diode	800	1.6
Nd : YLF	1053	1.2
Nd : YAG	1064	1.2
Ho : YAG	2120	0.6
Er : YAG	2940	0.4
CO_2	10600	0.1

1.1.3. Properties of Laser Light

Lasers are characterized by a number of key optical properties most of which play an important role in the interaction with materials. Their five major optical properties are: monochromaticity, coherence, directionality and high intensity and brightness, which are inter– related. For instance, coherence length is inversely proportional to the number of cavity modes excited, and thus to the effective bandwidth of the laser, so that a perfectly monochromatic laser should have an infinite coherence length.

Monochromaticity

Light from sources other than lasers covers a range of frequencies. True single-frequency operation of a gas laser can be achieved by careful design. Although it is more difficult, such a laser can be constructed to have a frequency stability at constant temperature better than one part in 10^{10}. Multimode operation of course reduces the monochromaticity of laser. A small helium-neon laser generally has three or four longitudinal modes excited with a spacing of a few hundred megahertz, depending on the cavity length. This still gives a bandwidth of a few parts in 10^6. Solid state lasers tend to have rather larger frequency spreads.

Coherence

One of the characteristics of stimulated emission is that the stimulated wave is in phase with the stimulating wave; that is, the spatial and temporal variation of the electric field of the two waves is the same. Thus in a 'perfect' laser we would expect the electric field to vary with time in an identical fashion for every point on the beam cross section. Such a beam would have perfect spatial coherence. Another related property is the temporal coherence, which refers to the relative phase relationship of the electric field at the same place as a function of time. If the phase changes uniformly with time then the beam is said to show perfect temporal coherence.

Coherence is often specified in terms of the mutual coherence function $\gamma_{12}(\tau)$. This quantity, which is in fact a complex number, is a measure of the correlation between the light wave at two points p_1 and p_2 at different times t and $t+\tau$. It has an absolute value between 0 and 1. When it has the value zero the light is completely incoherent, while a value of unity implies complete coherence. Although these extreme values are never achieved in practice, the light from a gas laser operating in a single transverse mode has a value quite close to unity. Two useful quantities that are related to temporal coherence are the coherence time and the coherence length. An approximate expression for the distance traveled by a light ray before it loses coherence, known as the coherence length, is given by

$$\begin{aligned} L_{coh} &= c/\delta v \\ &= \lambda^2/\delta\lambda \end{aligned} \tag{1.13}$$

where λ is the wavelength and $\delta\lambda$ and δv are the spread in wavelength and frequency.

Thus for a filament lamp where $\delta\lambda$ is of the order of λ, the coherence length is very small–of the order of the wavelength. For nominally monochromatic sources such as sodium vapour lamps, the coherence length is of the order of a millimeter. However, for a single–mode laser with a frequency spread of one in 10^{10}, the coherence length must be of the order of 10^{10} wavelengths, i.e. 6 km. a multimode helium–neon laser with a frequency spread of the order of 3 in 10^6 will have a coherence length of 20 cm. One important difference between a multimode gas laser and a conventional 'monochromatic' light source is that the pattern of coherence and incoherence is repeated with the periodicity of the round – trip laser cavity length (L_c). Thus the light from a multimode laser with a mirror separation of 30 cm will regain coherence around 60, 120, 180 cm, etc.

In reality of course, the wavetrains are not all the same length but are distributed in some way about a mean value. The conclusion that the irradiance fluctuations will gradually reduce, however, still remains valid. Similarly the exact definition of coherence length is somewhat more involved, but we may still take it to be the path difference at which the irradiance fluctuations die out. The coherence time t_c may then be defined as the time taken for the source to emit a wavetrain of length L_c. Thus:

$$t_c = L_c/c \tag{1.14}$$

Where c is the velocity of light. In fact it can be shown that the coherence time is related to the linewidth of the emission $(\Delta\nu)$ via the equation

$$t_c = \frac{1}{\Delta\nu} \tag{1.15}$$

Although we started the discussion of coherence by considering spontaneous emission, the ideas of coherence length and coherence time apply equally well to laser radiation. Coherence lengths of some typical laser are given in table 1.6.

Table 1.6. Summary of coherence lengths of some common lasers.

Laser	Typical coherence length
HeNe single transverse, single longitudinal mode	Up to 1000 m
He – Ne multimode	0.1 to 0.2 m
Argon multimode	0.02 m
Nd : YAG	10^{-2} m
Nd : glass	2×10^{-4} m
GaAs	1×10^{-3} m
Ruby	10^{-2} m

Divergence

One of the important features of most lasers is that the output is in the form of an almost parallel beam. This is a very useful feature for a number of applications since it means that it

is very easy to collect the emitted radiation and focus it onto a small area using a fairly simple lens system. By contrast conventional sources emit radiation nearly isotropically over a solid angle of 4π sr or so, and only a small fraction of it can be collected and focused. However, even a laser beam is not perfectly parallel. This is not because of some fault in the laser design but is due to diffraction caused by the wave nature of light. It is possible to reduce the amount of divergence, but only at the expense of an ever increasing beam width.

Consider a monochromatic beam of light of 'infinite' extent which passes through a circular aperture of diameter D. The beam will now diverge by an amount dependent on the size of D. To visualize the result more easily we may imagine the emergent beam to be focused onto a screen as illustrated in Fig.1.6. The resulting irradiance distribution on the screen consists of a bright area surrounded by concentric alternate dark and bright rings. The Pattern is formed by the interference of the wavefronts coming from different parts of the aperture. Most of the light energy (~80%) is contained within the central spot, which is known as the Airy disk. A measure of the amount of diffraction is given by the angle θ, where 2θ is the angle subtended by the disk diameter. It may be shown that

$$\sin\ \theta = 1.22\lambda / D \tag{1.16}$$

Where λ is the wavelength of the light. Thus most of the diffracted radiation is contained within a cone of semi angle $\theta = \sin^{-1}(1.22\lambda / D)$. Similar results are obtained when differently shaped apertures are used, and in general an aperture of dimension d gives rise to an angular divergence given by

$$\theta = \sin^{-1}(K\lambda / d) \tag{1.17}$$

where K is a number of order unity.

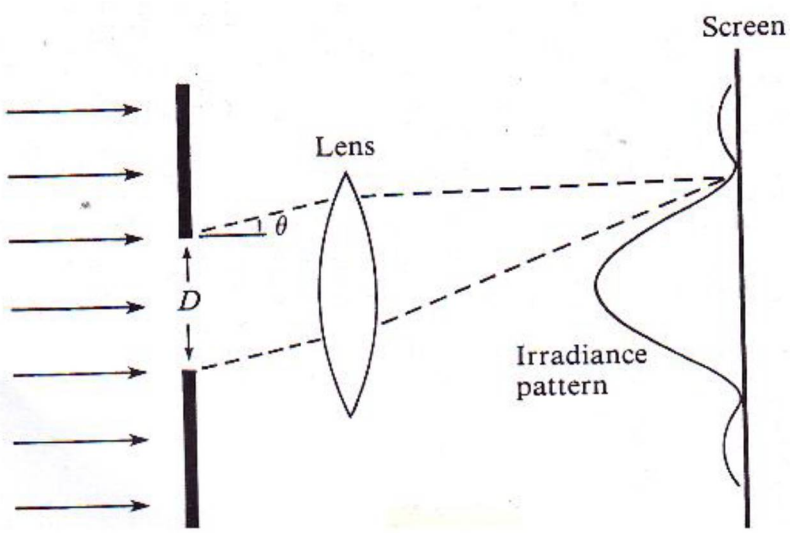

Figure 1.6. Beam divergence from a circular aperture.

High Intensity

This is perhaps the property for which lasers are best known outside the field of optics. Although the optical power output from a small helium- neon laser may only be say 2mW, a beam diameter of 0.5 mm leads to a power density of about 1 W cm^{-2}. Such a beam can readily be focused by a simple lens to spot of diameter 0.05 mm because it is monochromatic and coherent. The incident power density is then 100Wcm^{-2}. High- power carbon dioxide laser can be obtained which deliver a substantial fraction of 1kWcm^{-2} without focusing. Focusing optics produces a beam of sufficient intensity to melt, cut or weld structural materials. Most work to date has been carried out with helium– neon laser of power in the range 1-10 mW. Some studies have been carried out with argon ion lasers whose power typically extends to several watts, but increased power frequently brings the penalty of additional noise and multimode interference. Plasma and ablation require incident power densities in excess of 10 MWcm^{-2}. Such high-power densities are impossible to attain by conventional light sources. Pulsed lasers which incorporate a Q switch routinely produce beam of these intensities and higher for periods of a few tens of nanoseconds. By way of example, neodymium:YAG lasers (wavelength 1.06 μm) are commonly sold to deliver 0.1 J per 15 ns pulse in a beam of diameter 5 mm. A simple calculation shows that the unfocused beam has an approximate peak power of 6 MW and thus a power density in excess of 10^7 Wcm^{-2}. The limiting factor is not the power that is available from commercial lasers, but rather the threshold for damage in the irradiated sample. Indeed, many pulsed lasers are too powerful and must be used at reduced power if the lasers are to be used appropriately for material processing and modification.

Brightness

Brightness is defined as the power emitted per unit area per unit solid angle (the SI units of brightness are thus $Wm^{-2}sr^{-1}$). Sometimes the term specific brightness is used and this is the brightness per unit wavelength range. The divergence of laser beams is generally very small when compared to more conventional sources. Thus although similar amounts of optical power may be involved the small solid angle into which the laser beam is emitted ensures a correspondingly high brightness.

High brightness is essential for the delivery of high power per unit area to a target. In this context the size of the spot to which the beam can be focused is also important. It is interesting, from safety point of view, to note that the sun has a brightness of 1.5×10^5 lumens/cm^2– sterad. The average spectral brightness of the sun is its luminance divided by its bandwidth which is about 300 nm. Thus, the average brightness is $\frac{1.5\times10^5}{300nm} \approx 500$ lumens/cm^2-st-nm. On the other hand 1mW He-Ne laser with 0.2 nm bandwidth gives a brightness of $\frac{2\times10^7}{0.2nm} \approx 10^8$ lumens/cm^2-st-nm. This enormous spectral brightness presents to those who use lasers. Therefore, one must consider the safety condition such as using suitable goggles during laser operation.

1.2. Laser – Matter Interaction

The main goal of this section is to provide an appropriate background for the following section (1.3), concerning with surface modification of materials. However, to do this one ought to consider and appreciate two points: i- the roles played by the nature of light and matter structure at atomic or molecular levels, ii- all the things which we may call then "phenomena" and taking place during the light-matter interaction. Hence, an optical behaviour of light during the interaction with any material surface is one point and how to employ a relevant modern technique to study these phenomena or interaction mechanisms is another. Here, we will focus and discuss the former. It is indeed emphasized to appreciate that a material only reveals its behaviour as its characteristic response with respect to our input (thinking in terms of electromagnetic spectrum) and the limit we define ie., are we interested at micro, meso, nano or even finer structure level? and not mentioning the effects added by the material state. This point becomes even more complicated as well as interesting when one deals with biomaterials such as organic tissue. The reader should be familiar with some manifestations of the fundamental forces that drive the interactions between matter, such as electrostatic, gravity and magnetism. However, nature has used a subtle mixture of these forces and different structure levels in combination with geometric and dynamic effects to determine the interactions of biological molecules. In short, the nature of materials and their behaviour (organic and inorganic) are certainly not fixed parameters and can depend on variables (eg. as a function of time, space, temperature,…) and that our understanding goes as far as the curtains are pulled a side as required or better say asked for.

1.2.1. The Structure and Properties of Matter

By studying the properties of matter, forces and energy and their various interactions one can understand the behaviour of solids, liquids and gases– the three possible phases of matter– physicists regard substances in terms of their basic constituents. Then by studying the behaviour and properties of these most simple components, they hope to gain knowledge of the larger system.

There can, however, be conceptual difficulties in explaining physics at this sub-microscopic level. Usually the minute particles that make up matter can be "seen" only by the effects they have on visible things, or by the gross phenomena that result, when millions of them act together. For the present, a microscopic analysis of physical phenomena remains one of the best ways of understanding physics, and one of the keys to this approach is the molecular nature of matter.

Molecules: The Basic Components of Matter

Experimental evidence supports the idea that matter in all three phases is composed of tiny particles called molecules which are continuously in motion. For any given single substance, the molecules are identical in mass, structure and other properties. They range in size from 10^{-10} macross to about 10^{-6}m. All molecules in a substance exert a force on each other. That is why it is difficult to crush a solid (which involves pushing its molecules together against the intermolecular forces), and it is also difficult to stretch a solid (which

involves separating its molecules against the force). There is therefore both an attractive and a repulsive component of the intermolecular force.

It has been found that both components are basically electrostatic in nature. Molecules consists of groups of atoms, which themselves consists of electrons and unclei. As molecules are forced together, the electrons belonging to the various atoms making up the molecules interact, repelling each other. This repulsion is a very short – range force, and predominates when the distance between the molecules is only about 10^{-10} m. The attraction between molecules is of longer range, and is called the Van der Waals force. Its origin is complicated, but again depends on the electrical interaction between molecules.

In solids and liquids, the molecules move relatively slowly (have relatively low kinetic energies) and they therefore interact fairly strongly. But in the study of gases, the molecular force can often be neglected because the molecules are, on average, widely separated and they interact relatively briefly. For this reason, a simple analysis of the behaviour of gases is much easier than of solids and liquids.

Atoms: The Building Blocks of Molecules

Just as substances can be broken down into molecules, molecules can themselves be broken down into atoms. Atoms in molecules are bound together in various ways, although all of these interatomic forces arise basically from interactions between electrons in the atoms. In some molecules, for example, loosely- bound atomic electrons are shared between adjacent atoms.

An atom is the smallest particle that can represent a particular chemical element. In size, atoms have been photographed with the aid of advanced microscopes. There are three types of particles that can, in a simple description, be considered as making up a typical atom. The central nucleus, with a diameter 10,000 times smaller that of the whole atom, is comprised of neutrons and protons. (The hydrogen nucleus is unique in having no neutron, only a single proton.) The neutron is a particle with no electrical charge, whereas the proton has a single positive charge. Both have roughly the same mass. Circulating about this central region, held in orbit under the influence of the protons positive charge, are the electrons. These are subatomic particles, each with a single negative charge and an extremely small mass: 1/ 1836 that of a proton.

Each chemical element is characterized– and identified – by its atomic number, z, which is the number of protons in the nucleus. Since an electrically neutral atom must contain an equal number of protons and electrons, Z also equals the number of electrons orbiting the nucleus. The mass number A of an atom is the sum of the number of protons and neutrons in the nucleus (thus A – Z is the number of neutrons). As an example, consider the element helium, which has an atomic number (Z) of 2 and a mass number (A) of 4, written ${}_{2}^{4}He$. It has two protons (and hence two electrons) and two neutrons. At the other end of the scale, the fissile isotope of uranium is ${}_{92}^{235}\mathrm{U}$ (with 92 protons, 143 neutrons, and 92 electrons.

Finally, electrons play a major role in determining the properties of the various elements. At the turn of the century physicists spent much effort in trying to derive all the observed phenomena relating to elements from a mathematical model of the atom. One key phenomenon was the spectral lines produces by atoms on being heated: each element has its own unique atomic spectrum. In trying to explain the generation and appearance of atomic

spectra, physicists found that they had to introduce one of the basic concepts of modern physics: the quantum.

Atomic Structure and Quantum Theory

In a simple quantum-based visualization of the atom, the electrons orbit the central nucleus under the electrostatic attraction of the opposing proton charges, like planets in Bohr's miniature solar system, however, more realistically it is more elliptical. The electrons can move only in certain orbits about the nucleus. But by receiving energy they can become "excited" and move into orbits farther out from the nucleus. By giving up that energy, they drop back into the original lower orbits (called the ground state). With each energy change, radiation of a particular frequency is absorbed of emitted.

From this analysis, the origin of atomic spectra can be explained. The individual spectral lines (of certain frequencies) represent electrons falling from high – energy excited states back to their low energy ground states. As they do so, they emit quanta of radiation (photons) of a frequency corresponding to the energy difference. The electrons in an atom can orbit only in paths in which their orbital angular momentum has a fixed value (actually a multiple n of Planck's constant divided by 2π). The sizes of the various allowable orbits - each labeled by the principal quantum number n, beginning at 1 for the innermost orbit-can therefore be calculated. The observed spectral wavelengths result from electron "jumps" between orbits of different quantum number, and the calculations for the simplest atom, hydrogen, agree fairly well with observation. Discrepancies do occur, however, in the more complicated aspect of the spectra of hydrogen and other elements, and more complicated quantum theory is needed for a more complete description.

The Nature of the Electron

So far, electrons have been considered simply as point electric charges. Sometime, however, electrons appear to behave like hard spheres (in collisions with other particles, for example), whereas in other respects – such as electron diffraction – they behave as if they were waves. This wave-particles duality of electrons is recognized in de Broglie's relationship ($\lambda = h/mv$), which assigns a wavelength to any particle of known mass and velocity. It lies at the heart of the more sophisticated theory of the atom known as wave mechanics. According to the theory of wave mechanics, electrons orbiting a nucleus are not particles moving in orbits, but standing waves that can be represented mathematically by what is called a wave function (which measures the probability of an electron being at a particular point in space). Peak values of this function can be taken to represent the orbits of the electrons. There is only a high probability – not a certainty – that the electrons will be found on the orbits; the certainty of the old theory has been replaced be a statistical probability measured by the wave function.

According to Heisenberg's uncertainty principle ($\Delta x \Delta p \geq h$), which arises from wave-particle duality, it is impossible to measure simultaneously both the position and momentum of a particle within certain limits. It can also be shown that it is similarly impossible to measure the total energy and life time of a particle simultaneously and with limitless accuracy. Although the seemingly totally accurate and certain theories of classical physics

have been replaced by the probability arguments and uncertainties of the quantum theory, it turns out that such concepts as Heisenberg's uncertainty principle predict new, hitherto unexpected phenomena. It is theoretically possible to create energy – and indeed particles – out of nowhere. They must quickly disappear, however, to ensure that the law of conservation of energy remains inviolate. Such particles are called vacuum particles, and their fleeting presence has been demonstrated experimentally.

Structure of Crystalline Solids

Essentially a crystalline solid is one in which the constituent atoms are arranged in an ordered array such as in a metal or a semiconductor, as opposed to a disordered array as in a glass, as shown in Figure 1.7. In the ideal crystalline solid, every atom is in its place and there is long – range ordering; in glass (which is essentially a frozen liquid) there is some short – range ordering, but no long range order. Although in recent times a great deal of interest has been shown in glassy material, particularly in amorphous semiconductors, it is crystalline solids that are or primary interest to us.

Several questions now arise: How are the atoms arranged in a given crystalline solid? What is the nature of the forces holding the atoms together? How do real solids compare with our 'ideal' models of solids? What experimental evidence is there to support any models that are developed?

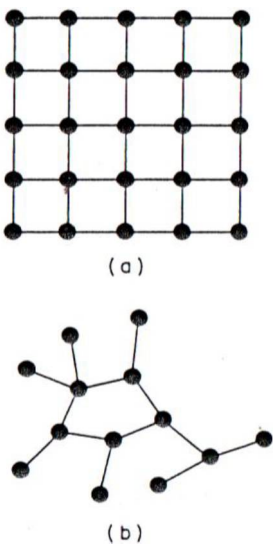

Figure 1.7. (a) an ordered array. (b) a disordered array.

Let us suppose initially that the atoms are like hard sticky spheres which, when placed in contact, stick firmly together without too much deformation. If, on the whole, the atoms remain in the positions in which they are initially placed, then the result is a solid, as opposed to a liquid or a gas, where the atoms are able to move freely through the whole region available to them. If a large number of atoms are placed close together, then fairly obviously they can be arranged in an infinite number of disordered arrays. In fact, they might appear like a jar full of sticky spheres having no ordered arrangement but simply stuck together with

gaps and voids between them. However, the minimum energy state corresponding to equilibrium requires that the atoms are in an ordered array in the solid state. In other words, to comply with physical law, the spheres should be arranged neatly in rows, the rows put together to form planes, and then the planes stacked to form an ordered three- dimensional shape as shown in Figure1.8.

There is evidence in nature that atoms are indeed neatly arranged in this way. Many solids exist that are obviously crystalline (that is they have a regular appearance with definite crystal faces, corresponding pairs of faces having the same angle between them) such as rock salt and calcite. In fact, many solids which appear non-crystalline to the naked eye are seen to be definitely crystalline when viewed through an optical microscope. These solids consist of masses of small crystals randomly orientated with respect to each other and are termed polycrystalline. It would be reasonable to assume that the regular outward appearance of crystals is but a manifestation of a regular internal arrangement of the atoms. This assumption has been demonstrated to be true by the methods of X-ray diffraction.

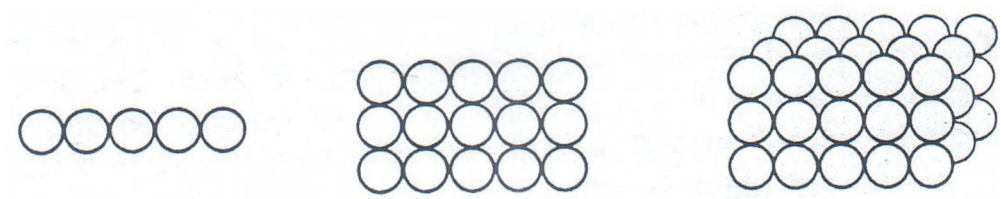

Figure 1.8. Diagram showing the ordered arrangement of atoms in solids.

Crystal Unit Cell Structures

Cubic unit cells are shown in Figures 1.9. The usual convention has been followed in that the unit cell corners are located at the centers of atoms, though this is by no means essential. The diagrams show an 'exploded view' of the structures, in which the atoms are separated from each other and are joined by lines which give an idea of the bonding forces.

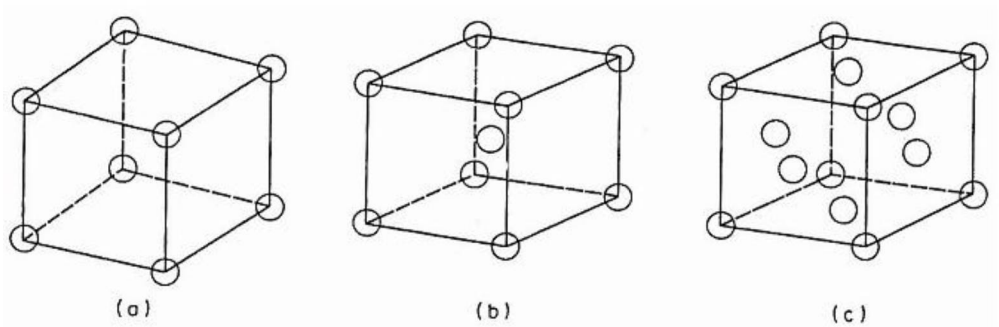

Figure 1.9. Cubic unit cells: (a) simple cubic cell; (b) body centred cubic cell; (c) face centred cubic cell.

A more accurate type of diagram is one in which atoms touch along their nearest neighbour distance, denoted by the letter 'd'. The lattice constant, which is the side length of the unit cell, is denoted by the letter 'a'. Half the nearest neighbour distance is defined as the

atomic radius, R. This is illustrated for a (100) face of the simple and face centred cubic lattices In Figure 1.10.

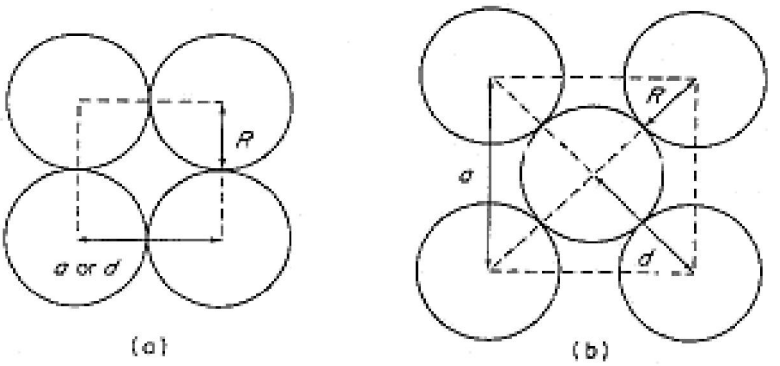

Figure 1.10. Cubic crystal face: (a) simple cubic; (b) face centred cubic.

Cubic Structures

Although only one element crystallizes in the simple cubic form (polonium) it is easy to visualize and is therefore often used as a basic example in discussing crystal structures. As can be seen from Figure 1.9 (a), the unit cell contains one atom, since each corner is shared with seven other unit cells. The fraction of the volume occupied by atoms in a unit cell is called the packing density, which for the simple cubic unit cell is given by the volume occupied by one atom divided by the volume of the cell, which is readily shown to be $\pi/6$. The coordination number, that is the number of nearest neighbours is six. The reason that atoms do not tend to arrange themselves in a simple cubic structure is that it is a very open structure with many empty spaces. As a rule atoms tend to pack together more closely, which we can see, from figures 1.9 (b) and (c), is the situation in the body centred and face centred cubic structures, where some of the more obvious open spaces are occupied.

In the body centred cubic structure (for example Fe, K, Na, W) there are two atoms per unit cell $(8\times\frac{1}{8}+1)$ and the coordination number is eight. For the face centred structure (e.g. Cu, Ag, Au, Al) the number of atoms per unit cell is four $(8\times\frac{1}{8}+6\times\frac{1}{2})$ while the coordination number is twelve. Table 1.7 gives a summary of the more important parameters relating to the cubic systems.

Table 1.7. Summary of the more important parameters.

Parameter	Simple cubic	Body centred cubic	Face centred cubic
Coordination number	6	8	12
Atomic radius	$a/2$	$a\sqrt{3}/4$	$a\sqrt{2}/4$
Packing density	$\pi\sqrt{6}$	$\pi\sqrt{3}/8$	$\pi\sqrt{2}/6$
Atoms per cell	1	2	4

Hexagonal Structure

We can envisage the hexagonal structure as being built up from layers of balls packed in triangular arrays; two such layers, one placed directly above the other, produce the hexagonal structure that has three atoms per unit cell and a coordination number of six. Figure 1.11 shows the relationship of the unit cell to the hexagonal Bravais lattice.

The most important variation of this lattice is the hexagonal close packed (h.c.p.) structure (for example Cd, Mg, Ti, Zn). The atom positions of the h.c.p. structure do not themselves form a Bravais space lattice; rather the structure can be thought of as a simple hexagonal space lattice with two atoms at each lattice point, one located at a reference origin 000 and the other at $(2/3a\ 1/3a\ 1/2c)$ (this is equivalent to two interpenetrating simple hexagonal lattices). The h.c.p. unit cell contains six atoms and the coordination number is twelve, with each atom next to six atoms in its own layer and three in the layers above and below. This structure, together with the face centred cubic, corresponds to the most dense packing of atoms in space. Both structures can be visualized by packing equal spheres together in close packed layers in which each atom is in contact with six others. Such layers can then be stacked in sequence.

A second layer may be packed on the first so that each sphere in the second layer occupies a depression between three spheres in the first layer. There are, however, two ways of adding the third layer. The spheres in the third layer may be placed so that they are directly above those in the first, giving the ABABA... sequence of the h.c.p. structure, or they are placed above depressions in the first layer not occupied by second layer spheres. The spheres of the fourth layer then lie above those of the first in the ABCABCA... sequence of the face centred cubic structure (this layering sequence is seen in the layers of spheres normal to the direction of the body diagonal).

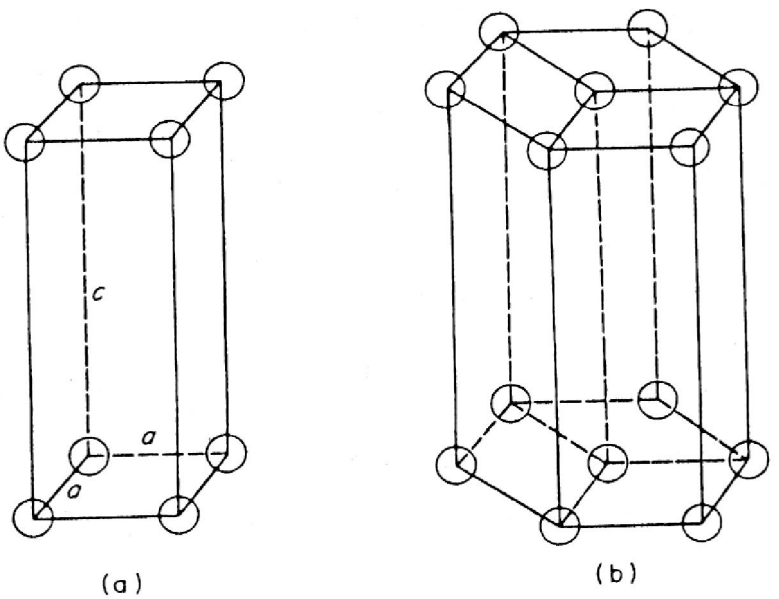

Figure 1.11. The hexagonal Bravais lattice (a) showing its relationship to a hexagonal unit cell (b).

Example

Calculate the packing density for a hexagonal close packed lattice.

Solution. For an h.c.p. lattice, $c/a = \sqrt{8/3}$ *and* $R = a/2$

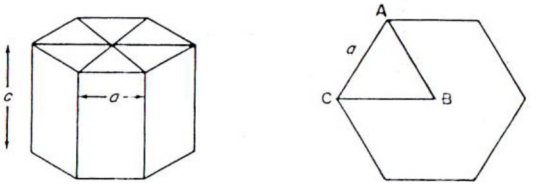

Volume of one atom $(4/3)\pi R^3 = (4/3)\pi(a/2)^3 = \pi a^3/6$

Volume of 6 atom= πa^3

Volume of unit cell= 6 × (area of triangle ABC)×height

Volume of unit cell= $6 \times \frac{1}{2}(\sqrt{3/2})a \times c = \frac{(3\sqrt{3})}{2}a^2 c$

Therefore the packing fraction = volume of unit cell/ volume of crystal

$$= \pi a^3 / \frac{1}{2}(3\sqrt{3})a^2 c$$

$$= \frac{2}{3}\pi / \sqrt{3}a/c$$

But $c/a = \sqrt{8/3}$ so, packing density = $\frac{\sqrt{2}\pi}{6}$

Other crystal structures and their unit cells will be considered in relation to the bonding of the atoms discussed below.

Atomic Bonds

It is said that the atoms in crystalline solids are arranged in neat ordered structures, but the nature of the forces which hold the atoms together has not yet been described. The various ways atoms are bound together will now be discussed. Although the bonding of small groups of atoms can be classified under different types, this is not possible for solids because there are no solids in which the bonding is of one type only. However, as each type of atomic bond is described, consideration will also be given to a typical crystal in which the bonding is predominantly of that type.

Consider, first, the general situation of two identical atoms in their ground states being brought together from an infinite separation. The points of interest are the natures of the forces which come into play, whether these forces are attractive of repulsive and the energy of interaction of the atoms.

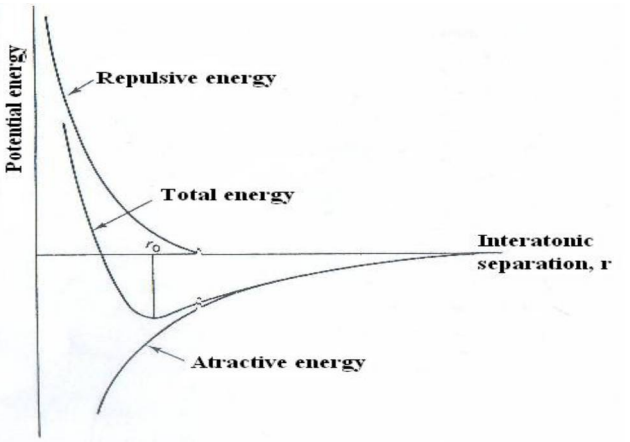

Figure 1.12. The interaction of two atoms as a function of their separation.

Initially, the energy of their interaction is zero. As the atoms approach, the attractive forces increase and the energy increases in a negative sense (the energy of attraction is negative sine the atoms do the work, while that of repulsion is positive as work has to be done on the atoms to force them closer together). At a separation of a few atomic radii, repulsive forces begin to assert themselves, and the atoms reach an equilibrium separation r_0 at which the repulsive and attractive forces are equal and the mutual potential energy is a minimum. The situation is shown in figure 1.12. The repulsive forces have a much shorter range than the attractive forces and are due partly to electrostatic repulsion of like charges and partly to the non-violation of the Pauli exclusion principle. As the atoms come closer together the Pauli principle would be violated unless some of the electrons move to higher energy states; the system therefore gains energy, a situation that is equivalent to the action of an interelectron repulsive force.

In general, the total potential energy can be written as

$$E(r) = -E_{att} + E_{rep} \tag{1.18}$$

where E_{att} can be written as a small index power law

$$E_{att} = \frac{-A}{r^n} \tag{1.19}$$

and E_{rep} as a high index power law or an exponential

$$E_{rep} = B/r^m \quad or \quad B\exp\left(\frac{-r}{\rho}\right) \tag{1.20}$$

where ρ is a characteristic length that governs the rate at which the repulsive energy falls of with distance. The values of the constants A and B, the indices n and m and the characteristic length ρ are governed by the actual nature of the bonding between the atoms, which is

related to the charge distributions in the atoms making up the solid. However, in all cases the interaction provides the cohesive energy that brings the atoms of the solid together, which can be thought of as the difference between the atomic energy in the crystal and the energy of the free atoms.

Example

In a certain solid in which the equilibrium atomic spacing is 0.15 nm, the binding energy is 10% less than would be given for the attractive part alone. What is the characteristic length ρ in the equation

$$E(r) = -A/r^6 + B\exp(-r/\rho)$$

Solution. In equilibrium

$$dE/dr = 0 \; and \; r = r_0$$

therefore

$$\frac{6A}{r_0^7} = \frac{B}{\rho}\exp(-r_0/\rho) \tag{1.21}$$

and hence

$$\begin{aligned} E(r_0) &= -A/r_0^6 + B\exp(-r_0/\rho) \\ &= -A/r_0^6 \times 0.9 \end{aligned}$$

that is

$$B\exp(-r_0/\rho) = 0.1A/r_0^6 \tag{1.22}$$

Combining equations (1.21) and (1.22)

$$\begin{aligned} 60\rho = \mathrm{r}_0 &= 0.15nm \\ \rho &= 0.0025\mathrm{nm} \end{aligned}$$

Ionic Bond

The simplest interatomic force is the ionic bond, which results from the mutual electrostatic attraction of positive and negative charges. If an atom gains or loses one or more electrons it is said to be ionized and obviously it becomes lose or gain electrons very easily because in doing so they acquire a completely filled outer electron shell which is a configuration of great stability. Thus sodium (Na) which has only one electron in its outer occupied shell (the 3s shell) will readily lose this electron to become a singly charged positive

ion (Na^+). Similarly, calcium (Ca) will readily lose the two electrons in its outer occupied 4s shell to become the double charged calcium ion (Ca^{2+}).

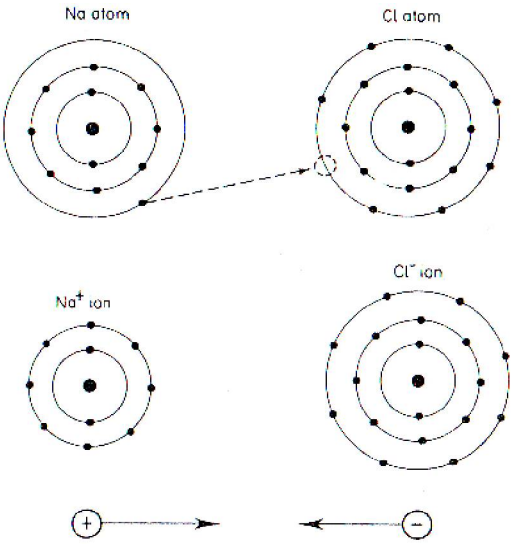

Figure 1.13. The ionic bond in the sodium chloride molecule.

Atoms such as those of chlorine, which have an almost completely full outer shell, readily accept additional electrons to fill the outer shell and thus become negative ions. Thus the building up of a sodium chloride molecule might be visualized as shown in figure 1.13. However, it is incorrect to expect that Na^+ ions and Cl^- ions would link up in pairs as shown, because then there would be strong attractive forces within the paired ions of a sodium chloride crystal but negligible attraction between the pairs. As a result, solid sodium chloride would not exist.

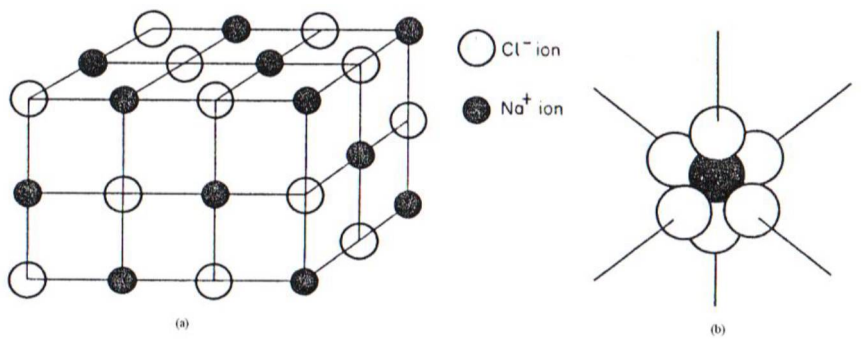

Figure 1.14. Formation of a typical ionic crystal (sodium chloride): (a) a face centred cubic structure of Na^+ ions interpenetrates a similar structure of Cl^- ions; (b) a more realistic representation of Cl^- ions grouped about a Na^+ ion.

Actually, a negative charge possesses an attraction for all positive charges in the neighbourhood, and vice versa. Consequently, Na^+ ions will surround themselves with Cl^- ions and Cl^- ions with Na^+ ions in the crystal in such a way that the attraction between

neighbouring unlike charges exceeds the repulsion due to like charges. The resulting sodium chloride structure is shown in figure 1.14, which shows that there are two interpenetrating face centred cubic structures, one formed from sodium ions and the other from chlorine ions.

In general, the ionic bond is quite strong, as evidenced by the fact that many ionic solids are hard and have quite high melting points (for example lithium fluoride and sodium chloride which have melting points of 845 and 801°C respectively).

$$E(r) = \frac{-e^2}{4\pi\varepsilon_0 r} + B\ \exp\left(\frac{-r}{\rho}\right) \tag{1.23}$$

If the total number of molecules in the crystal is N and n number of nearest neighbours of a given ion, the total interaction energy is

$$E_T = N\left[nB\ \exp\left(\frac{-r}{\rho}\right) - \frac{\alpha e^2}{4\pi\varepsilon_0 r}\right] \tag{1.24}$$

where α is a geometrical factor called the Madelung constant. It can be calculated by summing the individual Coulombic attractions with successive shells of nearest neighbours, and this varies from structure to structure. For NaCl, α is 1.748. Clearly the value of the equilibrium separation r_0 can be found by minimizing this expression. For NaCl, r_0 is 0.28 nm.

Covalent Bond

Another way in which the outer electron shell of atoms can be effectively filled to achieve a stable configuration is by the sharing of electrons – this gives rise to the covalent bond. For example, chlorine requires one electron to complete the outer shell. This can be accomplished if two chlorine atoms join together and share their outer electrons. Figure 1.15 shows the resulting bond which enables the chlorine molecule to be formed.

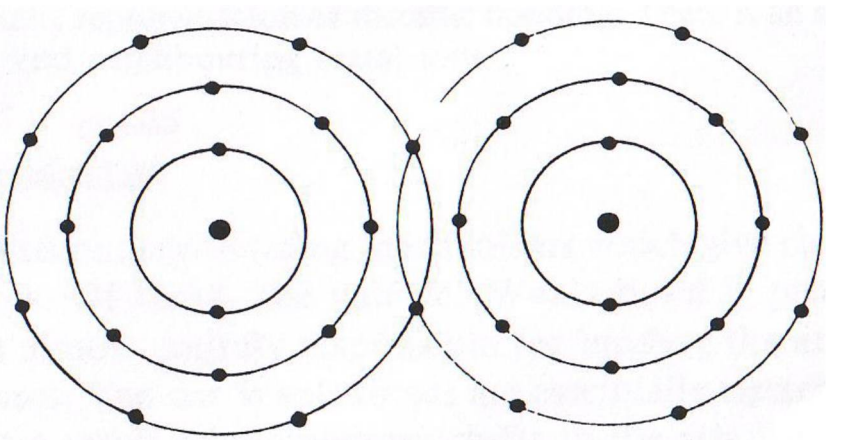

Figure 1.15. The chlorine molecule. By sharing electrons, both atoms effectively fill their outer electron shells.

The atoms taking part in convalent bonding need not necessarily be alike. For example, hydrogen and chlorine may combine as follow:

$$H:H + Cl:Cl = 2H:Cl$$

where the dots represent shared electrons in the outer orbit. The most significant crystal structure resulting from covalent bonding is the diamond structure. The carbon atom has four electrons in its outer shell (n=2) which can accommodate a total of eight electrons. In the diamond structure each carbon atoms can be considered to be at the centre of a regular tetrahedron with its nearest neighbours at the corners of the tetrahedron, as shown in figure 1.16(a). Each of the four corner atoms shares one of its outer electrons with the central atom, thereby effectively making up a closed shell of eight electrons. The central atom, of course, shares each of its four outer electrons with one of the corner atoms, thereby contributing to their closed shells. Each corner atom in turn can be regarded as being at the centre of a tetrahedron so that the structure consists of a system of linked tetrahedral as shown in figure 1.16(c).

The covalent bond is usually very strong so that covalent crystals are usually hard and have a high melting point. Indeed, diamond is the hardest material and it has the highest known melting point at more than 3550°C.

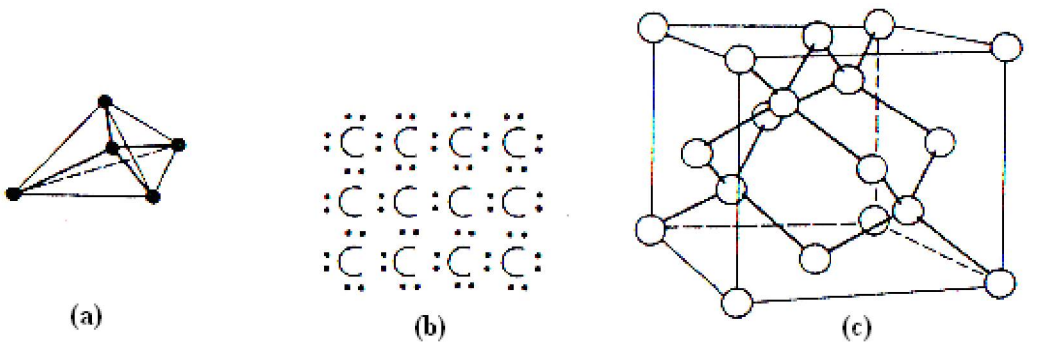

Figure 1.16. The structure of diamond: (a) the tetrahedral bonds; (b) schematic representation showing the bonding electrons; (c) the crystal structure.

Metallic Bond

In contrast to ionic and covalent bonds, the properties of the metallic bond cannot be inferred from the nature of bonding in isolated molecules and a model or bonding in metals is not easy to construct. In some respects, however, it may be regarded as intermediate in character between that of ionic and covalent bonds.

The metal atoms readily lose their valence electrons (thereby acquiring the stable closed shell electron configuration of the inert gases) to form positive ions. The valence electrons may then be regarded as being shared by all of the ions in the crystal. In other words the freed valence electrons form an electron 'gas' which may be regarded as permeating the whole crystal, as shown in figure 1.17. The bonding is then essentially an electrostatic interaction between the array of positive ion cores and the electron gas. The free electrons of this model

explain the high electrical and thermal conductivities of metals together with their high ductility.

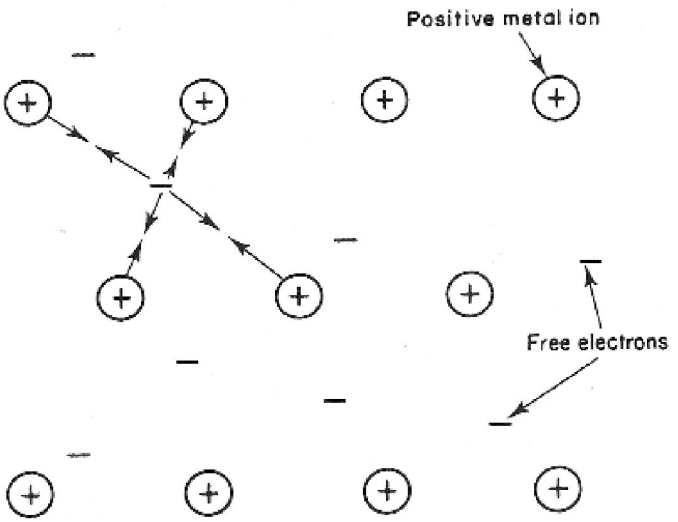

Figure 1.17. Schematic representation of metallic bonding. There is an attraction between each free electron and neighbouring metal ions.

Other Bonds

There are several secondary bonding mechanisms which give rise to rather weak interatomic forces. Of these, the van der Waals bond is probably the most important and is almost entirely responsible for binding the atoms together in solidified inert gases. Van der Waals forces are essentially electrostatic in nature, and they arise as a result of momentary shifts in the relative position of the nucleus and electrons of an atom. As a result, the atom forms an electric dipole which in turn induces dipoles in neighbouring atoms. The attraction between charges of opposite sign in the dipoles thus gives rise to the attractive forces.

Van Der Waals Forces

Van der Waals forces exist between all atoms and molecules whatever other forces may also be involved. We may divide Van der Waals forces into 3 groups.

a) *Dipole – dipole forces.* If we consider a substance such as HCl, where the bonding is largely ionic, the individual molecule will consist of a positive and a negative charge separated by a small distance of the order of 0.1 nm, so that it constitutes a minute electric dipole. This will interact with a neighbouring HCl molecule and produce a net attractive force. The force (see (c) below) will be proportional to x^{-7}, where x is the distance between the molecules.

b) *Dipole-induced dipole forces.* Consider the interaction between say an HCl molecule and a neon atom. The latter has no natural dipole. However, the HCl dipole will induce a dipole in the neon atom and there will then be an attractive force between them again proportional to x^{-7}.

c) *Dispersion forces.* The most 'mysterious' type of force is that which exists between two non-polar atoms such as neon. We know that these atoms must attract one another, for otherwise we could never obtain liquid or solid neon simply by cooling the material and so reducing the thermal energy of the atoms below some critical level. The explanation is as follows. Although the neon atom has a symmetrical distribution of electrons around the nucleus so that the atom has no dipole, this statement is true only as a time average. At any instant there may be some asymmetry in the distribution of the electrons asymmetry in the distribution of the electrons around the nucleus. The neon atom at this instant, therefore, behave as an electric dipole. This produces a field which distorts the electron distribution in a neighbouring atom (polarizes it) so that the neighbouring atom itself acquires a dipole. The two dipoles will attract. This is the basis of the 'dispersion' van der Waals force.

We can easily derive the law of force in the following way. Suppose that at a given moment the first atom has a dipole moment μ (figure 1.18). At a distance x along the axis of the dipole the electrostatic field E is given by

$$E = \frac{2\mu}{x^3}\frac{1}{4\pi\varepsilon_0} \tag{1.25}$$

Where ε_0 is the permittivity of space. (This equation is only valid if x is reasonably large compared with the length of the dipole in figure 4. For closer approach, a more complicated equation would be needed.) If there is another dipole at this point it will be polarized and acquire a dipole μ'. The dipole produced by a field is approximately proportional to the strength of the field. We write

$$\mu' = \alpha E \tag{1.26}$$

where α is termed the atomic polarizability of the atom.

Now a dipole μ' in a field V has a potential energy V given by

$$\begin{aligned} V &= -\mu' E \\ &= -\alpha E^2 = \frac{-4\alpha\mu^2}{x^6}\left(\frac{1}{4\pi\varepsilon_0}\right)^2 \end{aligned} \tag{1.27}$$

This implies a force between the atoms of magnitude

$$F = -\frac{\partial V}{\partial x} = \text{constant/x}^7 \tag{1.28}$$

We see that the force is always attractive and falls off as x^{-7}. We may take this two stages further. For simplicity let us consider the attraction between two hydrogen atoms, where only one electron can be involved in each atom. If the effective radius of the atomic orbital is *r*, the maximum value of the instantaneous dipole is *re*. Substituting in equation (1.27) we have

$$V = -\frac{4\alpha r^2 e^2}{x^6}\left(\frac{1}{4\pi\varepsilon_0}\right)^2 \tag{1.29}$$

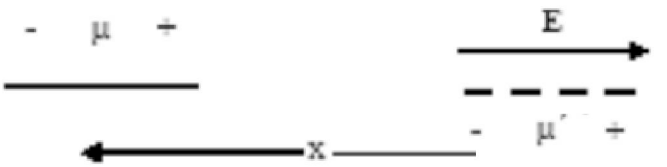

Figure 1.18. A dipole produces an electric field at a distance x a along its axis of amount $E = (2\mu / x^3)(1/4\pi\varepsilon_0)$. This field can polarize another molecule such that mutual attraction occurs.

For a simple atom, or for a small molecule which is virtually spherically symmetrical, the polarizability is given by

$$\alpha = r^3(4\pi\varepsilon_0) \tag{1.30}$$

where *r* is the radius of the atoms or molecule. For reasons which will soon become apparent we select from this relation the value of r^2

$$r^2 = \frac{\alpha}{r}\frac{1}{4\pi\varepsilon_0} \tag{1.31}$$

Insertion in equation (1.29) gives

$$V = \frac{-4\alpha}{x^6}\frac{\alpha}{(4\pi\varepsilon_0)^2}\frac{e^2}{r(4\pi\varepsilon_0)} \tag{1.32}$$

We see that the last term on the right is the quantized energy level hν of the electron when its frequency is ν. We are left with

$$V = \frac{-4\alpha}{x^6} h\nu\left(\frac{1}{4\pi\varepsilon_0}\right)^2 \tag{1.33}$$

This derivation is, of course, rather crude since it assumes that the dipoles are always oriented end – on and we have ignored the fact that the second atom must itself influence the polarization of the first. However, it contains all the essential features of the van der Waals

interaction: the polarizability α, the separation x and the frequency v of the polarized orbital. The rigorous derivation by F. London, in 1930, considered the perturbation produced in the solution of the Schrödinger equation. His result is

$$V = -\frac{3}{4}\frac{\alpha^2}{x^6} hv \left(\frac{1}{4\pi\varepsilon_0}\right)^2 \tag{1.34}$$

and is exactly the same as our simple derivation except for the numerical factor. The frequency v is the same as that which accounts for the dependence of refractive index on the frequency of the incident light, i.e. it is the frequency involved in optical dispersion. For this reason those van der Waals forces which arise by mutual polarization of the atoms or molecules are referred to as dispersion forces. Van der Waals forces are much weaker than ionic and covalent forces. They are central and, like ionic forces, they are unsaturated: also to a first approximation they are additive (see below).

Retardation Effects in Van Der Waals Forces

The derivation of the London relation is valid only if the atoms are less than a few hundred angstroms, i.e. a few tens of nm, apart for the following reason. For large separations the electric field from one atom takes an appreciable time to reach its neighbour: by the time it has done so and polarized it, it itself will have acquired a different electron configuration. There is a lag in the interaction and this leads to what is known as retarded van der Waals forces. In different words we may say that when the atoms are close together the electron fluctuations between neighbours are in close correlation: when they are far apart this correlation gets poorer and poorer, and the potential now falls of as $1/x^7$. We can form some estimate of the distance at which non-retarded forces go over to retarded forces by noting that an orbiting Bohr electron takes about 3×10^{-16} s to rotate about the nucleus so that an electric field, traveling at the velocity of light (3×10^8 ms^{-1}) will cover a distance of about 10^{-7} m or 100 nm in this time. Thus when atoms are more than this distance apart we should expect the correlation to be lost and the interaction to be almost completely retarded. Experiments described below show that, in fact, the transition from non- retarded to retarded forces occurs at a separation of the order of 10 to 50 nm.

There is no simple derivation of retarded van der Waals forces but the following argument provides some insight into its origin. The first point to the emphasize is that retarded Van der Waals forces are not basically a new type of interaction. All that really happens is that the atoms select from the fluctuations in the electron distribution those which occur at a low enough frequency to give good correlation between neighbouring atoms. We replace v in equation (1.34) by c/λ, and specify that if λ is of the same order as the separation x (or greater) fluctuations of this wavelength in one atom will be in good correlation with fluctuations in another atom at distance x. All shorted wavelengths (i.e. higher frequencies) will give such poor correlation that their contributions to the interaction energy can be neglected. We thus convert equation (1.34) into $U = -\frac{3}{4}\frac{\alpha^2}{x^6}\frac{hc}{\lambda}\left(\frac{1}{4\pi\varepsilon_0}\right)^2$ where λ is of order x. This gives as a final result

$$U \approx -\frac{3}{4}\frac{\alpha^2}{x^7} hc \left(\frac{1}{4\pi\varepsilon_0}\right)^2 \tag{1.35}$$

so that attractive force now falls off as $1/x^8$. Equation (1.35) is very close to the correct answer obtained by extremely difficult theory (Casimir gives $23/8\,\pi^2$ instead of $\frac{3}{4}$ in equation (1.35).

van der Waals forces exert their influence in the behaviour of individual atoms or molecules in the gaseous state. The magnitude of these forces can then be deduced by comparing the behaviour of a real gas where these forces operate with that of an ideal gas where intermolecular forces are negligible. A more direct way of determining the magnitude of these forces is by measuring the forces between macroscopic bodies. We assume that the forces are roughly additive and carry out a pair –wise addition for each atom in one body with every atom in the other body. Additivity is not strictly true but is a reasonable good first approximation. For a sphere of radius R at a distance x of nearest distance to a flat surface (or for crossed cylinders each of radius R) the force is

$$F_{non\text{-}retarded} = AR/6x^2 \tag{1.36}$$

$$F_{retarded} = 2\pi BR/3x^3 \tag{1.37}$$

where A and B are known as the Hamaker constants for non-retarded and retarded forces respectively. Experimental results for crossed cylinders of mica are shown in figure 1.19. It is seen that the power law of x changes from 2 to 3 over the range of 10 to about 1.3×10^{-19} J and B a value of about 10^{-28} J m. Retarded forces are not of great importance since they are small and play little part in most physical processes. By contrast the non-retarded forces can be relatively large, particularly if the bodies com into atomic contact. Values of A range from about 10^{-19} J for inorganic solids to about 3×10^{-19} J for metals. If the bodies are immersed in a liquid the value of A is less, often by about an order of magnitude.

For extended parallel surfaces the forces are naturally proportional to the area of the surfaces. The force *f* per unit area has the value

$$f_{non\text{-}retarded} = \frac{A}{6\pi x^3} \tag{1.37a}$$

and

$$f_{retarded} = \frac{B}{x^4} \tag{1.37b}$$

Consider two smooth polished surface placed in contact and kept apart by a few asperities or a few dust particles so that the separation is of the order 1 μm. Then, assuming retarded forces and a value of $B \approx 10^{-28}$ J m, the force *f* is of order 10^{-4} Nm^{-2}, i.e. an attractive force per square meter about equal to the weight of a fly. If, however, the separation were reduced

to atomic dimensions, say 0.2 nm, and if the surfaces were molecularly smooth, the non-retarded force would be of order $10^9 Nm^{-2}$,i.e.100 kg mm^{-2}: this approaches the strength of real solids. These simple calculations show that the range of action of surface forces is small: in theory these forces extend to infinity but their magnitude is appreciable only for separation of the order of a few atomic diameters.

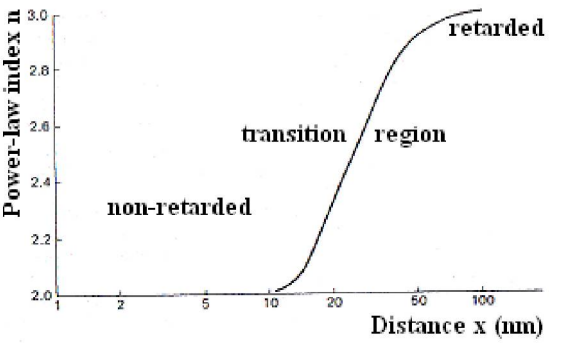

Figure 1.19. Variation of power – law indeed n of the van der Waals law of force between crossed mica cylinders with distance of separation x. Below 10nm the forces are non- retarded and the law of force is $F=AR/6x^n$ with n=2, where R is the radius of the cylinders. Above 50 nm the forces are retarded and the law of force is $F = 2\pi BR/3x^2$, where n =3.

The consequences of this may at once be seen. Even in the absence of ionic or valency forces, surfaces will stick together strongly if they can come into close contact (within a few angstroms) of one another. Again gases will generally be absorbed strongly for the first monolayer but the attraction falls off so rapidly with distance that second and third layers are far less likely. Roughly speaking the formation of absorbed layers depends on whether the potential energy drops by a greater amount than the mean thermal energy. For a molecule, the latter is the order of kT, where k is the Boltzmann constant and T the absolute temperature. This is not the whole story since, of course, the latent heat of condensation is also a factor encouraging further adsorption, whilst the entropy decrease associated with an 'ordered' adsorbed film tends to oppose adsorption. The net result is that polymolecular adsorption is unlikely unless the gas or vapour is very near saturation.

With large particles, such as those in colloidal systems or Brownian suspensions, the position is different. The thermal energy of the individual particle is still given by kT but the van der Waals energy must be integrated for the millions of atoms in the particles. In such systems the van der Waals forces can in fact play a basic part in determining whether particles will stick together or not.

Repulsion Forces

If atoms were subjected only to attractive forces all atoms would coalesce. Thus it is clear that for very short distances of separation some type of repulsive force must operate. In ionic systems the attractive force arises from the electrostatic charge and the repulsive force from the electron shells, which act as a sort of tough elastic sphere resisting further compression. The repulsion may be described as arising from two effects.

First, the penetration of one electron shell by the other, which means that the nuclear charges are no longer completely screened and therefore tend to repel one another. The other effect arises from the Pauli exclusion principle which states that two electrons of the same energy cannot occupy the same element of space. For them to be in the same space (overlapping) the energy of one must be increased – this is equivalent to a force of repulsion.

With covalent and van der Waals forces the repulsion and attraction are all part of a single mechanism and it is not correct to consider them as arising from separate mechanisms; however, for the purpose of simple calculation it is very convenient to do so. We therefore describe the long- range attraction by a term of the form

$$F = \frac{A}{x^m} \tag{1.38}$$

where A and m are suitable constants, and the repulsion by a relation of the form

$$F = \frac{B}{x^n} \tag{1.39}$$

where B is a constant and n has a value of the order 8-10. In fact the power– law relation is not very good and there are theoretical reasons for preferring a relation for the repulsive force of the form $Be^{-x/s}$ where B and s are suitable constants. In the following calculation we shall for simplicity retain the power law for both attraction and repulsion forces. The resultant force is then

$$F = \frac{A}{x^m} - \frac{B}{x^n} \tag{1.40}$$

and this is plotted in figure 1.20. The equilibrium separation x_0 occurs when F=0. This gives $B = Ax_0^{n-m}$.

Hence equation (1.40) becomes

$$F = A\left(\frac{1}{x^m} - \frac{x_0^{n-m}}{x^n}\right) \tag{1.41}$$

We may at once note that for small displacements from the equilibrium position the restoring force is

$$dF = A\left(\frac{n-m}{x_0^{m+1}}\right)dx \tag{1.42}$$

Since the force is proportional to the displacement, the motion of the displaced particle will be simple harmonic. This conclusion is or course not restricted to power- law relations. Any relation of the form F=f(x) will lead to a similar conclusion.

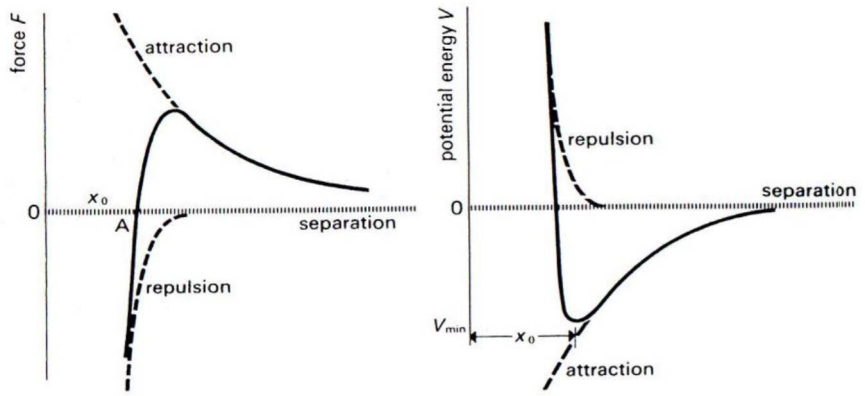

Figure 1.20. (a) Force and (b) potential energy curves for two atoms (or molecules) as a function of separation. There is a long- range attractive force and a short–range repulsive force which operates only when the molecules come close together. The equilibrium separation occurs when the net force is zero (at *A*) or when the potential energy is a minimum.

Potential Energy

The potential energy *V* involved in bringing one atom from infinity to a distance x from another atom is given by

$$V = \int (external \ \ force)dx = -\int (external \ \ force)dx = \int Fdx \qquad (1.43)$$

Since *F* acts in the opposite direction to dx.

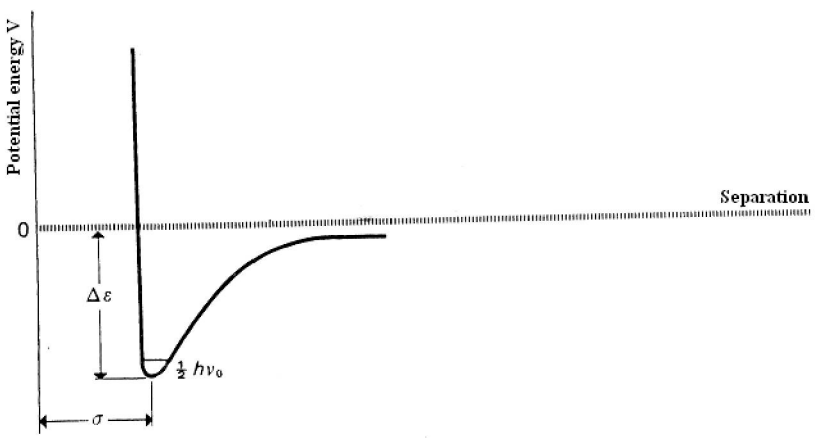

Figure 1.21. Potential energy curve of one molecular in relation to a single neighbour emphasizing the depth of the potential energy trough $\Delta\varepsilon$, the extremely steep repulsive part of the curve, and the effective diameter σ of the molecule. The zero- point energy, $1/2hv_0$, where v_0 is the fundamental frequency of the pair, is very small compared with $\Delta\varepsilon$ and will be neglected in the rest of this treatment.

From equation (1.41) this gives

$$V = A\left(-\frac{1}{m-1}\frac{1}{x^{m-1}} + \frac{1}{n-1}\frac{x_0^{n-m}}{x^{n-1}}\right) \tag{1.44}$$

A potential energy equation of this form was first proposed by Mie in 1903. Note that the attractive term gives a negative potential energy, the repulsive term a positive potential energy.

At the equilibrium position, where $x=x_0$, the potential energy has a minimum value

$$V_{\min} = -A\frac{1}{x_0^{m-1}}\left(\frac{1}{m-1} - \frac{1}{n-1}\right) \tag{1.45}$$

The interatomic forces are summarized in Table 1.8.

Table 1.8. Interatomic forces.

Type	Nature	*A*	*m*	Energy to separate 2 atoms or ions
Ionic	Central unsaturated	Very large	2	$Na^+ F^-$; 10^{-18}J
Covalent	Directed saturated	Very large	a	H-H; 7×10^{-19}J
Van der Waals	Central untreated	Small to very small	7	Ne:Ne; 5×10^{-22}J

[a] The attractive force between two hydrogen atoms in the hydrogen molecule is roughly proportional to $1/x^3$. This only applies for small displacements; it cannot be applied over large displacements nor can it be considered as being valid for covalent forces in general.

Intermolecular Forces

Intermolecular forces are of the same nature as those occurring between atoms. For ionic crystals such as rock- salt one cannot distinguish individual molecules of NaCl, as the crystal is an array of positive (Na^+) and negative (Cl^-) ions held together by coulombic forces. In covalent solids such as diamond the individual carbon atoms are joined, by valency bonds, to form a strongly–linked crystal. In a solid such as paraffin wax, or solid hydrogen, the molecules are held together by weak van der Waals forces. However, in a polymer these may be augmented by the attraction between polar groups or by chemical bonds. There is an additional type of bond which occurs only in the aggregate; this is the metallic bond. Individual metal atoms exist as such in the vapour phase, where a small number of diatomic molecules may occur, but there little tendency for the outermost valency electrons to join forces and produce polyatomic molecules in the vapour phase. There is, however, strong bonding in the condensed solid state. The atoms become ionized and exist as positive ions in a sea of free valency electrons; they are held together by the strong attraction between the ions and the electrons. In effect, energy has to be provided to ionize the metal atoms, but this is more than compensated for by the binding energy between the ions and the electron sea.

The simplest measure of the intermolecular forces is the heat of sublimation, which is the amount of energy needed to separate all the molecules from all their nighbours. This is highest for ionic and covalent solids, high for metals and least for Van der Waals solids. We may make this more quantitative in the following way. If the heat of sublimation E_s is given in calories per mole, we multiply it by 4.2 to convert to Joules and divide by 6×10^{23} to obtain the energy in Joules per single molecule. This conversion factor is 7×10^{-24}. The result is the energy E_s required to break bonds between one molecule and all it neighbours. If, therefore, the coordination number (number of nearest nighbours) is n and only nearest-neighbour interaction is involved, we may write for the binding energy ε between one molecule and one neighbour

$$E_s = \frac{1}{2} n\varepsilon \tag{1.46}$$

The $\frac{1}{2}$ is introduced since otherwise every bond would be counted twice.

We then have

$$E_s \times 7\times10^{-24} = \frac{n}{2}\varepsilon \qquad or \qquad \varepsilon = \frac{14\times10^{-24}}{n} E_s$$

As an example we quote the simplest type of solid–solid neon, which forms a close – packed f.c.c. structure of the van der Waals type. The latent heat of sublimation is found by experiment to be approximately 450 calories per mole. The number of nearest nighbours, n, is 12. Hence

$$\varepsilon \approx 5\times10^{-22} J$$

This agrees well with the theoretical interaction energy between one neon atom and its neighbour. Another example, which is less direct, is worth quoting because it provides a check on our deduced value of ε by a completely different method. In sodium fluoride the energy to convert 1 mole of NaF to Na^+ and F^- free ions is 213000 cal. This is approximately 15×10^{-19} J per molecule of NaF or 7.5×10^{-19} J per ion of Na^+ or F^-. In the crystal lattice each ion is surrounded by 6 ions of opposite sign (i.e. n=6). The energy per unit bond (it is of course negative) is therefore

$$\varepsilon = \frac{7.5\times10^{-19}}{3} = 2.5\times10^{-19} J$$

We may now consider the ionic interaction between a Na^+ and a F^- as they are separated from their equilibrium position in the lattice (separation x_0= 0.231 nm) to infinity. Ignoring the repulsion term, we have

$$\varepsilon = -\frac{1}{4\pi\varepsilon_0}\int_{x_0}^{\infty} \frac{e^2}{x^2} dx = -\frac{1}{4\pi\varepsilon_0}\frac{e^2}{x_0} = -10^{-18} J$$

This assumes only nearest–neighbour interaction. There is, in fact, a very large interaction between the next nearest neighbours. For example the potential energy due to the

attraction between one positive ion and the negative ions surrounding it is greatly reduced by the coulombic repulsion between the positive ion and the nearest positive ions. These are only a little further away than the nearest negative charges and as coulombic potentials fall off only as 1/x, the resultant potential energy is greatly reduces. Detailed calculations show that the energy is reduced from $-(4\pi\varepsilon_0)^{-1}e^2/x_0$ to 0.2905 times.

Table 1.9. Intermolecular forces.

Type	Nature	Example	Mode of Separation	Energy per bond J×10^{21}
Ionic	Indentical Interatomic forces	NaF Crystal	Break up into Na^+ and F^- ions	300
Covalent	Giant molecule held by covalent forces	Diamond	Break up into C atoms	600
Van der Waals	As for atoms	Solid methane CH_4	Break up into CH_4 gas	3
Metal	Metal ions in sea of free valency electrons	K	Vaporize to metal ions +electrons	500

1.2.2. Interaction of Light with Matter

A typical situation where light can act on matter is shown in Fig. 1.22 where in principle, four effects exist which may interfere with its undisturbed propagation. Reflection and refraction are strongly related by Fresnel's law.

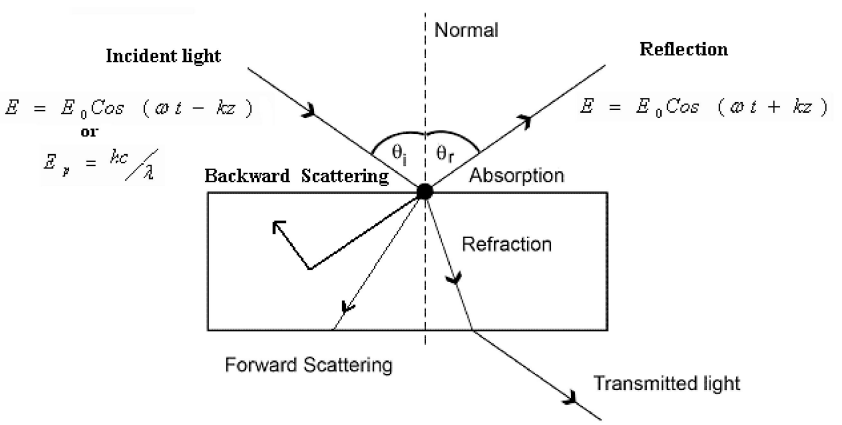

Figure 1.22. Geometry of light interaction with a substrate.

Normally, in light – material interaction process one many use the wave theory to study the energy propagation in a medium and the particle theory for interaction studies of photons with material. When electromagnetic radiation strikes a surface it travels as shown in figure 1.22. Some radiation is reflected, some absorbed and some transmitted. As it passes through the new medium it will be absorbed according to some law such as Beer Lambert's law,

$I = I_0 e^{-\alpha z}$. The absorption coefficient, $\alpha(cm^{-1})$ depends on the medium, wavelength of the radiation and intensity. The manner in which this radiation is absorbed is considered to be as follows. When it passes over a small elastically bound charged particle, the particle will be set in motion by the electric force from the electric field, E.

Provided that the frequency of the radiation does not correspond to a natural resonance frequency of the particle, then fluorescence or absorption will not occur but a forced vibration would be initiated. The force induced by the electric field, E, is very small and is incapable of vibrating an atomic nucleus. We are therefore discussing photons interacting with electrons which are either free or bound. This process of photon being absorbed by electrons is known as the "inverse bremsstrahlung effect". (The bremsstrahlung effect is the emission of photons from excited electrons.) As the electron vibrates so it will either re-radiate in all directions or be restrained by the lattice phonons (the bonding energy within a sold or liquid structure). In this latter case the phonons will cause the structure to vibrate and this vibration will be transmitted through the structure by the normal diffusion type processes due to the linking of the molecules of the structure. The vibrations in the structure we detect as heat. The flow of heat is described by Fourier's laws on heat conduction – a flux equation ($q/A = -kdT/dx$). If sufficient energy is absorbed then the vibration become so intense that the molecular bonding is stretched so far that it is no longer capable of exhibiting mechanical strength and the material is said to have melted. On further heating the bonding is further loosened due to the strong molecular vibrations and the material is said to have evaporated. The vapour is still capable of absorbing the radiation but only slightly since it will only have bound electrons; the exception occurs if the gas is sufficiently hot that electrons are shaken free and the gas is then said to be a plasma.

If the laser radiation is incident on a non- reflecting, absorbing material, then if is progressively attenuated as it penetrates into the sample. Assuming plane waves propagating in the z direction, if the fraction absorbed, δI, in any infinitesimal element is proportional both to the intensity I and the thickness of the element, δz, i.e.

$$\delta I = \alpha I \delta z \tag{1.47}$$

then by integration

$$I(z) = I_0 e^{-\alpha z} \tag{1.48}$$

giving the well known exponential form of absorption.

If, however, the radiation is incident at the surface of a conductor, some of the energy will be reflected, so that

$$I = I' + I'' \tag{1.49}$$

where I' is the absorbed intensity, and I" the reflected intensity. Thus, if R is the reflectivity,

$$R = I''/I \tag{1.50}$$

electromagnetic radiation interacts with the surface of a conductor causing electric currents to flow in the conduction – band electrons. Some of the energy is absorbed by resistive losses

(e.g. electron – phonon scattering processes), while the remainder is reflected. The conduction electrons at the surface screen the interior of the metal from the radiation so that the absorption and reflection take place within a surface layer or 'skin'. A 'skin depth' can be defined (denoted by δ), such that the amplitude of the wave falls to 1/e of its initial value over a distance δ.

At longer wavelengths (e.g. in the infrared) classical physics can be used to calculate the skin depth. If σ and μ_r are the conductivity and relative permeability of the metal respectively, $\mu_0 = 4\pi \times 10^{-7} H\,m^{-1}$ the permeability to free space, and v the frequency of the radiation, then

$$\delta = (\pi \sigma \mu_r \mu_0 v)^{-1/2} \tag{1.51}$$

This formula cannot be used at higher frequencies (e.g. in the visible and ultraviolet) where a quantum mechanical calculation must be made. Substituting $\sigma = 4 \times 10^7 (\Omega m)^{-1}$ and $\mu_r \approx 1$ for aluminum, the skin depth for Nd:YAG radiation at 1.06 μm is approximately 5 nm. We note that the skin conductivity or permeability.

The absorbed energy mostly takes the form of heat so that, in the case of a metal, laser irradiation induces a temperature rise at the surface, while in the case of an insulator, depending upon the nature and magnitude of the absorption processes, it raises the temperature in the bulk of the sample also. In both cases, however, thermal conductivity ensures that the heat eventually becomes distributed throughout the sample. The temperature gradients induced set up stress and strain fields by thermal expansion. These in turn generate elastic waves in solids, which may be of low (sonic) frequency of high (ultrasonic) frequency. The rise in temperature may also, under certain circumstances, cause melting, vaporization, or combustion of the surface material. The stresses set up may be sufficient to damage the material plastically or by crack formation.

Which of these processes occur, and which are significant, depend on the characteristics of the incident radiation (such as average incident power, peak power, whether continuous (with perhaps periodic modulation) of pulsed), and the properties of the material. For instance, for low continuous incident power at a solid surface of ~ 1 W cm^{-2}, the only effect is a steady rise in temperature. If, however, the optical power is modulated thermal 'waves' can be generated. These waves are the solution of the equation for thermal conduction for a periodic heat source.

Interaction Mechanisms

Basically, there are five important mechanisms, Fig.1.23, which can take place during laser- material interaction. Thus, whole process will depend firstly on the material type and its physicochemical parameters and secondly on the laser type and its optical parameters. The processes which dominate ablation depend primarily on the laser power density and wavelength and at a moderate range of fluences the interaction in controlled by pulse duration which infact represents the interaction life time. However, In the light power densities (>

$1GW/cm^2$) both metals and insulators behave similarly and that free electron plasma $\approx 100\mu m$ above the surface controls the ablation.

1) Photochemical: This mechanism is based on the use of a suitable laser wavelength and drug as photo sensitizer such as HPD at very low power densities typically about $1Wcm^{-2}$. This process is known as photodynamic therapy (PDT).
2) Photothermal: This type of ablation basically operates on the absorption of IR laser wavelength by liquid content of material, hence causing vaporization and consequently the removal of material. The mechanism is summarized schematically in Figure 1.24.

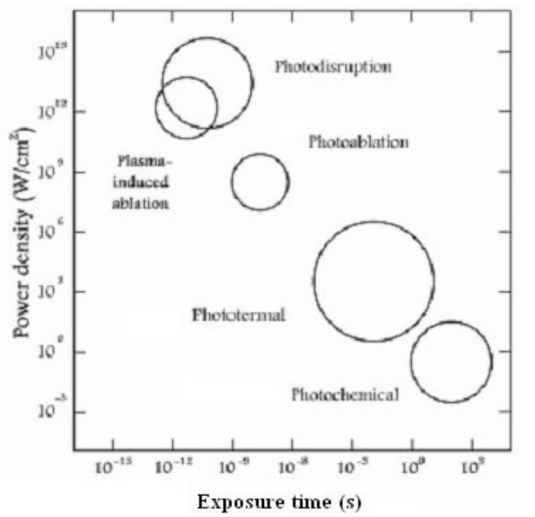

Figure 1.23. Laser – material interaction mechanisms.

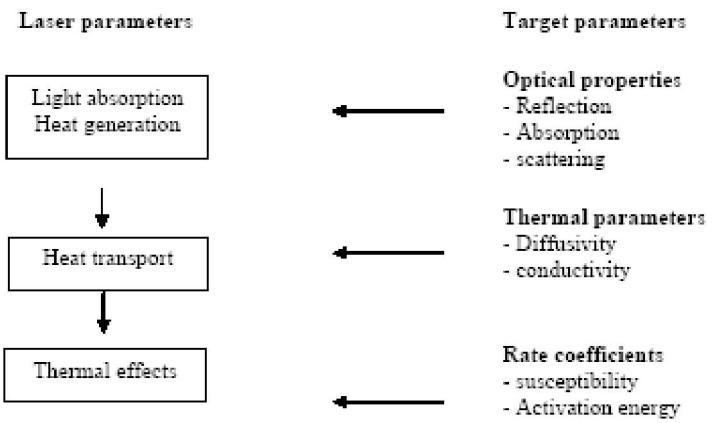

Figure 1.24. Model of photothermal interaction mechanism.

Heat Transport

Once photons are absorbed and heat is produced within a non-scattering material $(\beta = 0)$ ie. $Q = \alpha I(r,z) Wcm^{-3}$ where I is light intensity expressed in terms of radical distance from the interaction point, r, depth or material thickness, z, and time t, then two cases can be considered for heat produced :

1) Adiabatic case where heat is confined within the interaction region, and two conditions must be satisfied:
   a) optical depth (or photon penetration) must be greater than thermal depth ie. $d_0 \geq d_t$, where $d_0 \approx \alpha^{-1}(\mu m)$ and $d_t = (4k\tau_p)^{1/2}$ with k being the material diffusivity (cm^2s^{-1}) which can also be defined in terms of thermal conductivity, K ($Wcm^{-1}\,°C^{-1}$) as $k = \frac{K}{\rho C}$.
   b) pulse duration must be smaller than material thermal relaxation time, ie. $\tau_p << \tau_r$, thermal relaxation time is defined as $\tau_r = \frac{d_\circ^{\,2}}{4k}$.
2) Non-adiabatic (diffuse) case, where unlike the first case heat is not confined within the interaction region. Now the question is how the heat is conducted away and how the temperature field can be described? Which will be discussed shortly in section 1.3.4.
3) Photoablation: This is a process where by a material in photochemically decomposed ie. Photoablative decomposition (PAD) viz direct molecular bond breaking when irradiated by an intense UV laser pulse.
4) Plasma – induced ablation: when a material is exposed to a power density of 10^{11} Wcm^{-2}, it experiences an electric field of 10^7 Vcm^{-1}. This field is much larger than the average coulombic attraction between electrons and the nuclei and causes a dielectric breakdown of material creating a free electron density (plasma) in the focal point of the laser beam in a very short time. This type of ablation is considered for pulses shorter than nanosecond and is spatially confined.
5) Photodisruption: This effect occurs in soft material containing some liquid, such as soft tissue or fluids, under light intensity irradiation and leads to plasma formation. Photodisruption which takes place at nanosecond pulses involves shock waves and cavitations (bubble formation) hence causes material structure damage by a mechanical impact.

1.3. Biomedical Applications of Nd:YAG Laser Surface Modification of Titanium Implants

1.3.1. Introductory Biological Concepts

Biological surface science is broadly defined as interdisciplinary area where properties and processes at interfaces between synthetic material and biological environments are

investigated and bifunctional surfaces are fabricated. Surfaces play a vital role in biology and medicine with most reactions occurring at surfaces and interfaces. In the 19th century, the first observation was made that surfaces control biological reactions. The advancement in surface science instrumentation that has occurred in the past quarter of a century has significantly increased our ability to characterize the surface composition and molecular structure of biomaterials. Similar advancement has been shown in material science and molecular biology. The combinations of these subjects have allowed us to obtain a detailed understanding of how the surface properties of a material can control the biological reactivity of a cell interacting with that surface. Main examples include: medical implants in human body, biosensors and biochips for diagnosis, tissue engineering, bioelectronics and biomagnetics materials, artificial photo synthesis.

Light–matter interaction, which is the basis for optically probing structure and function at cellular and tissue levels as well for the light–activated photodynamic therapy of cancer and other diseases; benefits from a molecular understanding of cellular and tissue structures and functions. This section starts with the description of a cell. It describes the various structural components of the cell and their functions. An important part of a living organism is the diversity of cells that are present in various organs to produce different functions. A Microscopical structure of an animal cell is shown in figure 1.25.

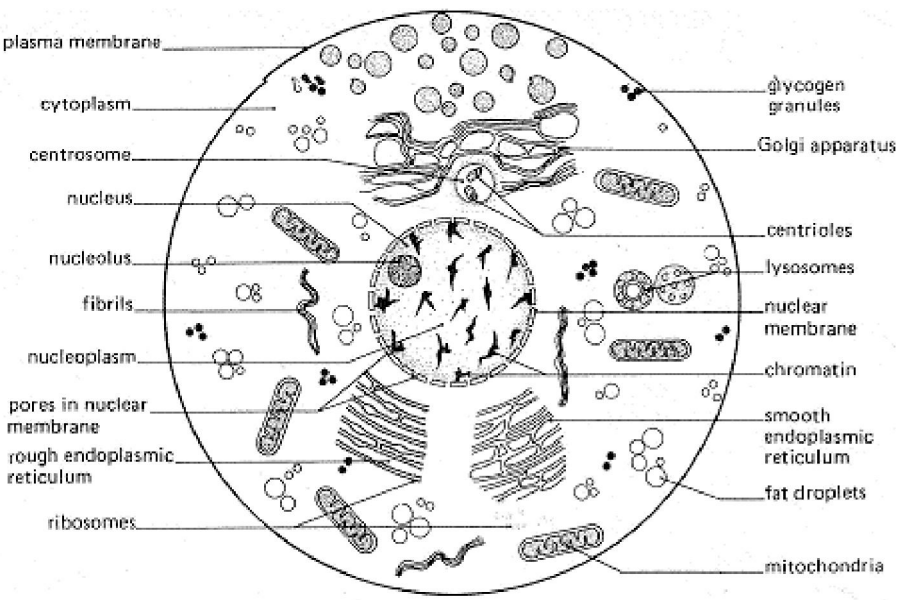

Figure 1.25. An animal cell.

Biological systems are essentially an assembly of molecules where water, amino acids, carbohydrates (sugar), fatty acids, and ions account for 75-80% of the matter in cells. The remainder of the cell mass is accounted for by macromolecules, also called polymers (or biopolymers in the present case), which include peptides/ proteins (formed from sugars), DNA (deoxyribonucleic acid, formed from nucleotide bases and dioxyribose sugar), RNA (ribonucleic acid, formed from nucleotide bases and ribose sugar), and phospholipids (formed

from fatty acids). These macromolecular polymers organize to form cells. The main structural components of a cell are:

- Plasma Membrane: This forms a semipermeable outer boundary of both prokaryotic and eukaryotic cells. This outer membrane, about 4-5nm thick, is a continuous sheet of a doubly layer (bilayer) of long–chain molecules called phospholipids. A phospholipid molecule has a long tail of alkyl chain, which carries a charge (and is thus ionic). Phospholipid molecules spontaneously orient (or self- organize) to form a bilayer in which the hydrophobic tails are pointed inwards. The hydrophilic, ionic head groups are in the exterior and are thus in contact which the surrounding aqueous environment. The plasma membrane controls the transport of food, water, nutrients, and ions such as Na^{+}, K^{+}, and Ca^{2+} (through so-called ion channels) to and from the cell as well as signals (cell signaling) necessary for proper cell function.
- Cytoplasm: Cytoplasm represents everything enclosed by the plasma membrane, with the exclusion of the nucleus. It is present in all cells where metabolic reactions occur. It consists mainly of viscous fluid medium that included salts, lipids, vitamins, nucleotides, amino acids, RNA, and proteins which contain the protein filaments, actin microfilaments, microtubules, and intermediate filaments. These filaments function in animal and plant cells to provide structural stability and contribute to cell movement. Many of the functions for cell growth, metabolism, and replication are carried out within the cytoplasm. The cytoplasm performs the functions of energy production through metabolic reactions, biosynthetic processes, and photosyn- thesis in plants.
- Cytoskeleton: The cytoskeleton structure, located just under the membrane, is a network of fibers composed of proteins, called protein filaments. This structure is connected to other organelles. In anima cells, it is often organized form an area near the nucleus. These arrays of protein filaments perform a variety of functions:

  - Establish the cell shape
  - Provide mechanical strength to the cell
  - Perform muscle contraction
  - Control changes in cell shape and thus produce locomotion
  - Facilitate intracellular transport of organelles

- Nucleus: The nucleus is often called the control of the cell. It is the largest organelle in the cell, usually spherical with a diameter of 4-10 μm, and is separated from the cytoplasm by an envelope consisting of an inner and an outer membrane. All eukaryotic cells have a nucleus. The nucleus contains DNA distributed among structures called chromosomes, which determine the genetic makeup of the organism. The chromosomal DNA is packaged into chromatin fibers by association with an equal mass of histone proteins. The nucleus contains openings (100 nm) in its envelope called nuclear pores, which allow the nuclear contents to communicate with the cytosol.

The inside of nucleus also contains another organelle called a nucleolus, which is a crescent–shaped structure that produces ribosomes by forming RNA and packaging it with ribosomal protein. The nucleus is the site of replication of DNA and transcription into RNA. In a eukaryotic cell, the nucleus and the ribosomes work together to synthesize proteins.

- Mitochondrial: Mitochondrial are large organelles, globular in shape (almost like fat sausages), which are 0.5-10.5 μm wide and 3-10 μm long. They occupy about 20% of the cytoplasmic volume. They contain an outer and an inner membrane, which differ in lipid composition and in enzymatic activity. The inner membrane, which surrounds the matrix base, has many infoldings, called cristae, which provide a large surface area for attachment of enzymes involved in respiration. The matrix space enclosed by the inner membrane is rich in enzymes and contains the mitochondrial DNA. Mitochondria serve as the engine of a cell. They are self- replicating energy factories that harness energy found in chemical bonds through a process known as respiration, where oxygen is consumed in the production of this energy. This energy is then stored in phosphate bonds. In plants, the counterpart of mitochondria is the chloroplast, which utilizes a different mechanism photosynthesis, to harness energy for the synthesis of high – energy phosphate bonds.
- Endoplasmic Reticulum: The endoplasmic reticulum consists of flattened sheets, sacs, and tubes of membranes that extend throughout the cytoplasm of eukaryotic cells and enclose a large intracellular space called lumen. There is a continuum of the lumen between membranes of the nuclear envelope. The rough endoplastic reticulum (rough ER) is close to the nucleus, and is the site of attachment of the ribosomes. Ribosomes are small and dense structures 20 nm in diameter, that are present in great numbers in the cell.
- Golgi Apparatus: It consists of stacked, flattened membrane sacs or vesicles, which are like shipping and receiving departments because they are involved in modifying, sorting, and packaging proteins for secretion of delivery to other organelles or for secretion outside of the cell. There are numerous membrane- bound vesicles (<50 nm) around the Golgi apparatus, which are thought to carry materials between the Golgi apparatus and different compartments of the cell.
- Lysosomes: There are vesicles of hydrolytic enzymes that are 0.2-0.5 μm in diameter and are single–membrane bound. They have an acidic interior and contain about 40 hydrolytic enzymes involved in intracellular digestions.
- Chromatin: The material of a cell nucleus that stains with basic dyes and consists of DNA and proteins.

Various Types of Cells

Cells come in many shapes, and compositions. The human body is made up of over 200 different types of cells, some of which are living cells. The human body also consists of nonliving matter such as hair, fingernails, and hard parts of bone and teeth, which are also made of cells. These cell variations are produced by cell differentiation. Also, different types of cells assemble together to form multicultural tissues or organisms.

- Epithelial Cells: Epithelial cells form sheets, called epithelia, which line the inner and outer surfaces of the body. Some of the specialized types of cells are (i) absorptive cells, which have numerous hair–like microvilli projecting form their surface to increase the absorption area, (ii) ciliated cells, which move substances such as mucus over the epithelial sheet, (iii) secretory cells, which form exocrine glands that secrete tears, mucus, and gastric juices, (iv) endocrine glands, which secrete hormones into the blood, and (v) mucosal cells, which protect tissues from invasive microorganisms, dirt, and debris.
- Blood Cells: These cells are contained in blood, in fact, is a heterogeneous fluid consisting of a number of different types of cells. These cells comprise about 45% of the blood's volume and are suspended in a blood plasma, which is a colloidal (small, suspendable particle) suspended in of proteins in an electrolyte solution containing mainly NaCl. The three different types of blood cells are (i) erythrocytes (commonly known as red blood cells; often abbreviated ad RBC), (ii) leucocytes (commonly known a white blood cells), and (iii) thrombocytes (also known as platelets). Erythrocytes or red blood cells are very small cells, 7-9 μm in diameter, with a biconcave, discotic shape. They usually have no nucleus. One cubic centimeter of blood contains about 5 billion erythrocytes, the actual number depending on a number of factors such as age, gender, and health. They contain an oxygen–binding protein called hemoglobin and thus perform the important function of transporting O_2 and CO_2.
- Muscle Cells: These specialized cells form muscle tissues such as skeletal muscles to move joints, cardiac muscles to produce heartbeat, and smooth muscle tissues found around the internal organs and large blood vessels. Muscle cells produce mechanical force by their contraction and relaxation.
- Nerve Cells or Neurons: Neurons are cells specializing in communication. The brain and spinal cord, for example, are composed of a network of neurons that extend out from the spinal cord into the body.
- Germ Cells: Germ cells are haploids (cells containing one member or a copy of each pair of chromosome). The two types of germ cells specialized for sexual fusion, also called gametes, are (i) a larger, nonmotile (nonmoving) cell called the egg (or ovum) from a female and (ii) a small, motile cell referred to as sperm (or spermatozoon) from a male. A sperm fuses with an egg to form a new diploid organism (containing both chromosomes). Bacteria are another example of haploid cells.
- Stem Cells: Another type of cell that has received considerable attention during recent years is the stem cell. Stem cells can be thought of as blank cells that have yet to become specialized (differentiated), giving them the characteristics of a particular type of cell such as the ones described above. Stem cells thus have the ability to become any type of cell to form any type of tissue (bone, muscle, never, etc). The three different types of stem cells are (i) embryonic stem cells, which come from embryos, (ii) embryonic germ cells, which come from testes, and (iii) adult stem cells, which come form bond marrow. Embryonic stem cells are classified as pluripotent because they can become any type of cell. Adult stem cells, on the other hand, are multipotent in that they are already somewhat specialized.

All living creatures are made up of cells. They exist in a wide variety of forms, from single cell in free-living organisms to those in complex biological organisms. Despite the great diversity exhibited by living systems, all biological systems, amazingly, are composed of the same types of chemical molecules and utilize similar principles in replication, metabolism, and, in higher organisms, the ability to organize at the cell levels. Even at the most elemental cellular level, microorganisms exhibit a large range of length scale, from viruses measuring 20-200nm to a eukaryotic cell measuring 10-100 μm. An important feature of the eukaryotic cell is its ability to differentiate and produce a variety of cells, each carrying out a specialized function. Schematic 1.26 shows structure of biological systems and evolution of a living organism.

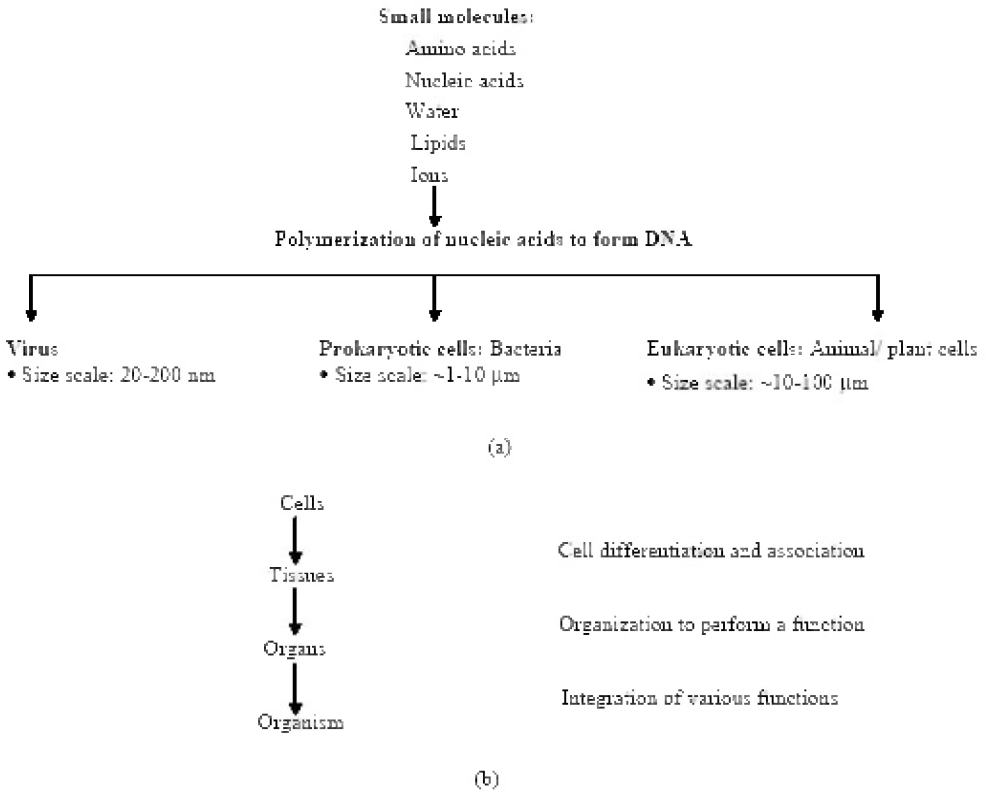

Schematic 1.26. Structure of biological systems (a) and evolution of living organism (b).

Cellular Processes

A living cell is a highly dynamic system in all its functions, from replication, to operation, to communication between cells. The processes involve both physical and chemical changes. Furthermore, the chemical changes can be permanent (such as protein synthesis, DNA replication) of cyclic (such as conversion of ATP into ADP and back). The chemical changes occurring are highly complex, often catalyzed by enzymes (reaction–specific proteins) and coenzymes (small molecules such NADH). The various dynamic processes occurring in a cell are illustrated in schematic 1.27.

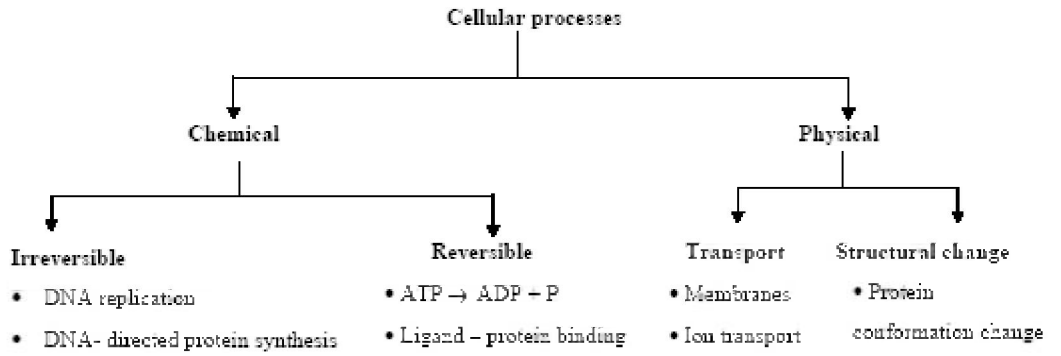

Schematic 1.27. Cellular processes based on their chemical and physical nature.

Proteins

Types of Proteins: Proteins are very diverse in their structure and function and thus can be classified into various groups. Based on structure and shape, proteins can be divided into the following classes:

- Fibrous Proteins, which are the main components of supporting and connective tissues such as skin, bone, and teeth. An example is a collagen, which is the most abundant protein in the body; it is a triple helix formed by three extended chains arranged in parallel.
- Globular Proteins, which consist of polypeptides tightly folded into the shape of a ball. Most globular proteins are soluble in water. Examples are albumin and gamma globulins of the blood. Haemoglobin is another important proteins belonging to this class. However, it is also an example of a proteins group, often classified separately as conjugated proteins, which carry conjugated group for their function. In the case of haemoglobin, this conjugated group is a heterocyclic ring called heme, which binds and releases molecular oxygen.

Protein Function: Proteins provide a wide variety of functions. Many function involve binding with specific molecules called ligands or substrates that produce catalytic chemical reactions as well as them to work as switches and machines. Some of these functions are described here.

- Enzymes, which act as catalysts for a specific biological reaction.
- Structural proteins, such as collagen, which form major connective tissue and bone.
- Contractile proteins, such as action and myosin, which are found in muscles and allow for stretching of contraction.
- Transport proteins, like haemoglobin, which carry small molecules like oxygen through the bloodstream. Other proteins transport lipids and iron.
- Hormones, which consist of proteins and peptide molecules. These are secreted from the endocrine glands to regulate chemical processes. An example is insulin, which controls the use of glucose.

- Storage proteins, which act as reservoirs for essential chemical substances. An example is ferritin, which stores iron for making hemoglobin.
- Protective proteins, which provide protection to various cells and tissues. Antibodies are globular Proteins that provide protection against a foreign protein called antigens. Others are fibrinogen and thrombin, which are involved in blood clotting. Interferons are small proteins that provide protection against viral infection.

Tissue Constituents

A tissue is a multicultural bioassembly in which cells specialized to perform a particular task contact tightly and interact specifically with each other. The functions of many types of cells within tissues are coordinated, which collectively allows an organisms to perform a very diverse set of functions such as its ability to move, metabolize, reproduce, and conduct other essential functions. The various constituents forming tissue are:

1) Cells: normally organized in a defined form.
2) Cell–adhesion molecules (CAM): Different integrad membrane proteins that act as glues on the cell surfaces to bind cells to each other. Adhesion between cells of the same type known as "homophilic" and between different types as "hetrophilic". Most CAMs are uniformly distributed within plasma membranes that contact other cells. The five principal classes of CAMs are: cadherins, immunoglobulins (Ig), selection, mucins, and integrins.
3) Extracellular matrix (ECM): a network of proteins and carbohydrate polymers in the spaces between calls. The matrix helps bind the cells and acts as a reservoir for hormones controlling cell growth and differentiation, also provides a lattice through which cells can move. Connective tissues, which largely consist of the extracellular matrix, form the architectural framework of an organism. A diversity of tissues forms (skin, bone, spinal cord, etc.) is derived from a variation in the relative amount of the different types of matrix macromolecules and the manner in which they organize in the extracellular matrix. Connective tissues consist of cells sparsely distributed in the extracellular matrix, which is rich in fibrous polymers such as collagen. The cells are attached to the components of the extracellular matrix. In contrast, epithelial tissues consist of cells that are tightly bound together into sheets called epithelial. The extracellular matrix consists of three major proteins: (i) highly viscous proteoglycans providing cushions for cells, (ii) insoluble collagen fibers, which provide strength and resilience, and (iii) multiadhesive matrix proteins, which are soluble and bind to receptors on the cell surface. Collagen is the single most abundant protein in all living species.
4) Cell Junctions: Cell junctions occur at many points of cell-cell and cell-matrix contact in all tissues. There are four major classes of junctions:

    - Tight junctions, which connect epithelial cells that line the intestine and prevent the passage of fluids, through the cell layers
    - Gap junctions, which are distributed along the lateral surfaces of adjacent cells and allow the cells to exchange small molecules for metabolic coupling among adjacent cells

- Cell- cell junctions which perform the primary function of holding cells into a tissue
- Cell- matrix junctions, which also perform the primary function of holding cells into a tissue

Types of Tissues

- Epithelial Tissues: Epithelial tissues form the surface of the skin and line all the cavities, tubes, and free surfaces of the body. They function as the boundaries between cells and a cavity or space. Their function is to protect the underlying tissues, as in the case of skin.
- Muscle Tissues: The three kinds of muscle tissues are

  - Skeletal muscles, which are made of long fibers that contract to provide the locomotion force
  - Smooth muscle lines of the intestines, blood vessels, and so on
  - The cardiac muscle of the heart

- Connective Tissues: The cells of connective tissues are embedded in the extracellular materials. Examples of supporting connective tissues are cartilage and bone. Example of binding connective tissues are tendons and ligaments. Another type is fibrous connective tissues, which are distributed throughout the body and serve as a packing and binding material for most of the organs.
- Nerve Tissues: These tissues are composed primarily of nerve cells (neurons). They specialize in the conduction of nerve impulses.

Tissues provide coordinated functions of the constituent cells. The functions of the tissues, however, are not just those provided by the constituent cells, but are also derived from intercellular communications and from the extracellular matrix (ECM) components. ECM acts as a reservoir for many hormones that control cell growth and differentiation. In addition, cells can move through ECM during the early stages of differentiation. ECM also communicates with the extracelular pathways, directing a cell to carry out specific functions.

1.3.2. Cell – Implant Interaction

Introduction

The overall reaction of the living system body to a foreign material implant is governed by a number of factors that determine whether the implant is accepted or rejected. Biocompatibility and biosafety are considered to imply that the clinical application of a biomaterial should neither cause any adverse reaction nor endanger the life of a patient. Generally, parameters determining the biocompatibility are: i- tissue as a host and ii- implant as a guest. Animal testing is an inherent component of biocompatibility testing. The use of in vitro methods can reduce the extend of animal testing and significantly reduce time and cost of testing. Knowledge of basic mechanisms of cell–material interaction and better

understanding of ongoing processes at the cellular level during interaction of anchorage dependent cells can aid in the development of new biomaterials.

Factors affecting the tissue–implant interface from biocompatibility point of view include: general health, immunity factors, roughness, surface porosity, chemical reactions, corrosion and cytotoxicity. Thus, the surface characterization of biomaterials is particularly important if the biocompatibility of implants is to be understood. Possible mechanisms through which a biomaterial can interact with a metallic implant is illustrated in figure 1.28.

A variety of surface properties are believed to be responsible for the favorable performance of titanium implants, in particular the presence of a chemically very stable oxide film protecting the underlying metal from corrosion, the moderate charge of he surface under biological conditions, the very low concentration of charged species within the dissolution products and a dielectric constant ε for titanium oxide close to that of water (ε =78). The result is that the titanium surface does not lead to excessively strong interaction (and denaturation) with proteins in the extra cellular matrix; rather the surface is in some way water like, interacting gently with the hydrophilic outer surface of the protein molecules.

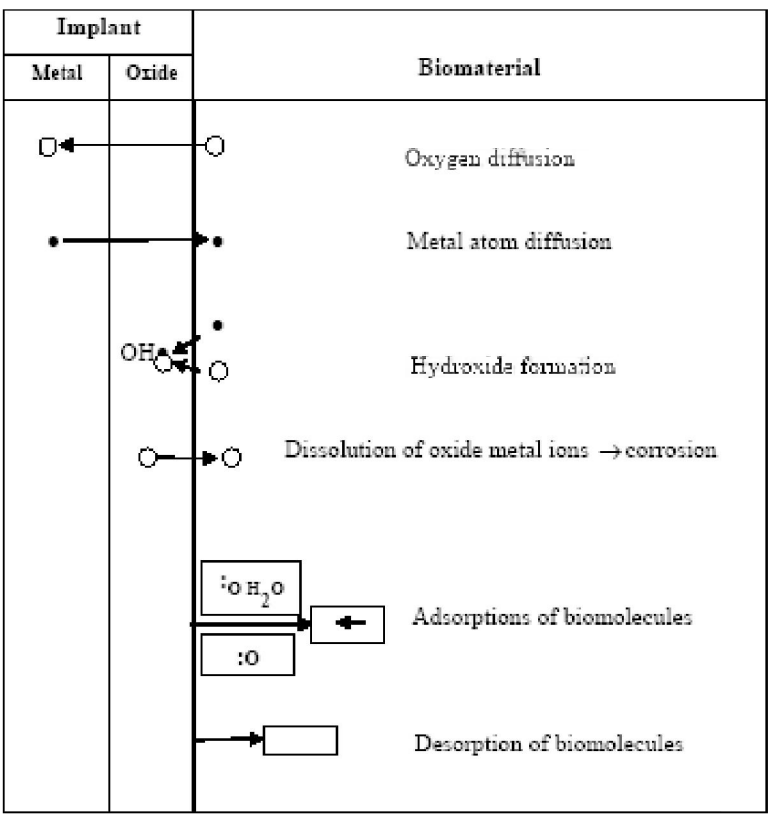

Figure 1.28. Mechanisms of biomaterial interaction with implant–oxide surface.

Nature of interaction between osteoblast cells and their substrate can influence the ability of these cells to produce an osteoid matrix around an implant which in turn will determine the fate of the implant. Attachment of anchorage dependent cells is the first step in the process of

cell surface interactions which in turn can affect subsequent cellular and tissue responses. Cells attach to substrates through contact sites which are classified as focal contacts. It is important to understand the nature of contact of cells interacting with biomaterials. Changes in cell morphology can be studied using different microscopic techniques like phase contrast and electron microscopy. In case of implants intended for orthopaedic application where close apposition with bone cells is required for better osteointegration, cell attachment and adhesivity play an important role.

Protein Adsorption

Titanium implants were first introduced by Branemark in the early 1970s [1] and have been widely used in the medical and dental fields with excellent clinical results. In addition, bone appears to bond with the titanium oxide layer following implantation, a phenomenon termed osseointergation. However, little is known about the specificity of this process and still less is known about the proteins that adsorb on the titania surfaces. In terms of the host tissue- biomaterial interaction the role of adsorbed proteins is likely to be an important one because subsequent events may depend on the composition and conformation of this protein layer and its tendency to change over time. The final protein film may trigger the activation of complementary are coagulation cascades and other inflammatory response [2,3].

Macromolecules adsorption is a complicated process but for simplicity it can be summarized as follow:

1) The encounter of soluble molecules with surface which is determined by diffusion constants of concentration of different species.
2) A reversible binding of molecules to surface which means that bound molecules may be detached in a very short time.
3) Constant modification of the composition of adsorbed layers ie. some species may be replaced by more adhesive ones. This is the basis of Vroman effect.
4) Progressive conformation changes of adsorbed proteins hence strengthening adhesion.
5) Possibility of continues adsorption with formation of multiple protein layers.

As it is seen in figure 1.29 there are various forces such as Vander walls, bipolar, hydrogen, ionic and covalent that can play an important role in adsorption of protein molecules.

The kinetics of adsorption of proteins to solid surfaces generally consist of a very rapid initial phase that is diffusion limited, followed by a slower phase upon approach to the steady-state value. In the initial phase, the proteins typically adsorb a quickly as they arrive at the relatively empty surface. In the later, slower phase, it is presumably more difficult for the arriving proteins to find and fit into an empty spot on the surface. In as short a time as can be measured after implantation in a living system (<l sec), proteins are already observed on biomaterial surfaces. In seconds to minutes, a monolayer of protein adsorbs to most surfaces. The protein adsorption event occurs well before cells arrive at the surface. Therefore, cells see primarily a protein layer, rather than the actual surface of the biomaterial.

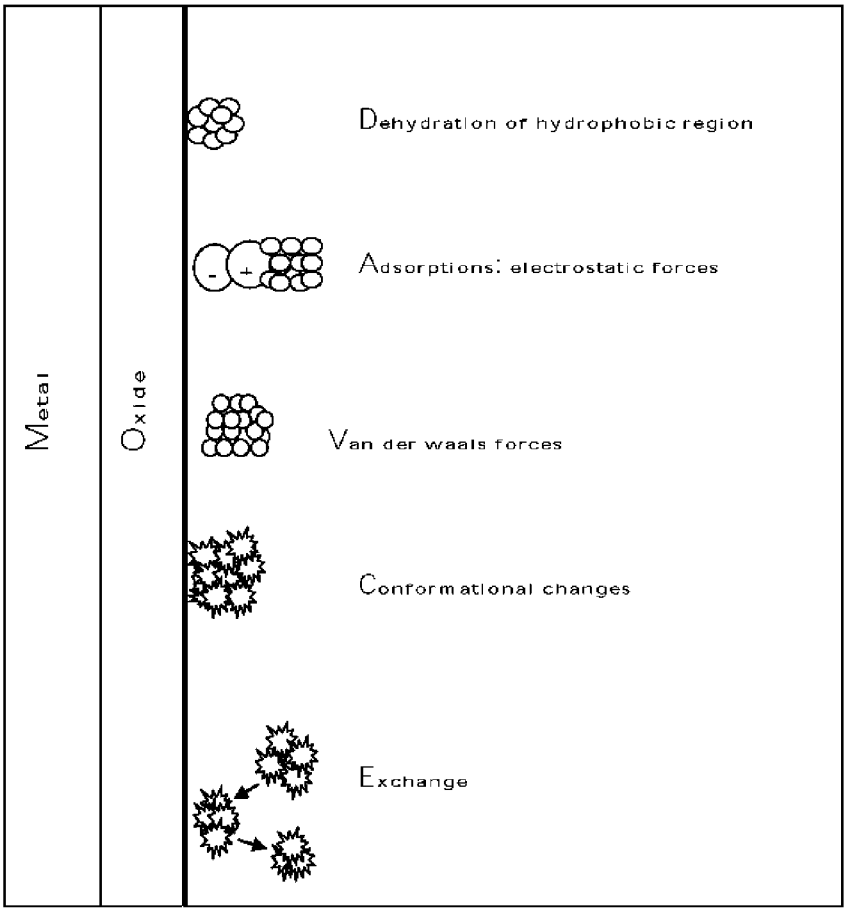

Figure 1.29. Routes of protein adsorption to implant surface.

It is thought that the particular properties of surfaces, as well as the specific properties of individual proteins, together determine the organization of the adsorbed protein layer, and that the nature of this layer in turn determines the cellular response to the adsorbed surfaces. The soluble proteins differ from the insoluble proteins is many ways, including the fact that they are less regular in their amino acid composition and three dimensional structure. The soluble proteins are therefore difficult to describe, this diversity originates in the linear sequence of amino acid that uniquely characterizes each protein.

It is important to note the particular structure assumed by a protein which in fact is a unique arrangement of the amino acid sequence in three – dimensional space exists for each protein. Furthermore, the spatial arrangement results in the hydrophobic residues preferentially located "inside" the protein where they are shielded from water, while the ionized and polar residues are usually on the outside of the proteins and in contact with the aqueous phase.

This spatial arrangement of the amino acids in proteins has a direct bearing on the interaction of proteins with surfaces because it means that the many residues "buried" inside the proteins may not be able to participate in bond formation with the surface. The folded proteins structures have densities of about 1.4 g/cm^3 in comparison with water's density of

1.0, or the density of most synthetic polymers of about 1.1, this basic fact about proteins reflects their tightly folded structure. Therefore, depending on the two major driving forces for adsorption, namely, the relative bulk concentration of each protein and its intrinsic surface activity, the outcome of the competitive process of adsorption is an adsorbed layer that is richer in some proteins than others; the surface composition differ from the bulk composition.

The thermodynamics of protein adsorption are not easily characterized because the process appears to be essentially irreversible. Because adsorption is irreversible, the calculation of an equilibrium binding constant from a plot of adsorption versus bulk concentration, and its conversion to a free energy value in the usual way, is not a valid method to obtain thermodynamic information. The enthalpy of the adsorption process has been observed to vary a great deal. The observation of positive enthalpies upon spontaneous adsorption to certain surface must mean that the process is entropically driven in these cases. The net negative free energy characteristic of a spontaneous process means that $T\Delta S$ is greater than the positive ΔH term in the formula $\Delta G = \Delta H - T\Delta S$. More generally, all protein adsorption processes are thought to be strongly driven by entropic changes. The important of entropic factors in this process can easily be envisaged to arise from changes in water binding to the surface and the protein as well as limited unfolding of the protein on the surface.

The orientation of proteins in the adsorbed phase must also be considered because the proteins are not uniform in properties or structure across their surface. As far as is known, proteins are not very free to rotate once adsorbed, owing to multiple bonding is exposed to the bulk phase. The reactions of proteins in the adsorbed phase may be broadly classed into noncovalent reactions represented by structural transitions, and covalent reactions, such as those that occur with proteins complements.

Cell – Adhesion

There is no need to emphasize the potential interest of controlling or even predicting the outcome of encounters between cells and artificial surfaces. Indeed, such knowledge would greatly facilitate the production and use of biomaterial. Three sequential steps of cell surface interaction are considered as:1-protein adsorption , 2-formation of adhesive ligand–receptor bonds, 3-triggering specific cell function such as apoptosis, proliferation, migration (locomotion), differentiation or activation.

Cell adhesion is a well – studied mechanism of cell communication. Adhesion is a form of mechanical linkage, of cells to cells and cells to the ECM, and is critically involved in cellular signaling events that control proliferation, survival, apoptosis, shape, polarity, motility, and differentiation. Adhesion is mediated by transmembrane proteins, which connect the interior of the cell to its extra cellular environment (Fig.1.30a). One major feature biological adhesion that is different from non- biological adhesion such as with household and industrial adhesives is that the former is mediated by chemical signals that often positively or negatively feedback to adhesion and subsequent cell behavior. In other words, cell adhesion is more than a simple glue to hold cells and tissues together; it is also a critical signaling platform. Integrins and cadherins are two principal classes of molecules mediating primarily cell-ECM and cell-cell adhesion respectively.

Integrins are the best–understood class of adhesion receptors [4]. They mediate both cell - ECM and cell-cell adhesion, differing based on the cell type and the type of receptor used in the interaction. Integrins, composed of $\alpha - \beta$ subunit heterodimer, assemble into 24 distinct integrins and bind to proteins in the ECM such as fibronectin, collagen and laminin [4]. The binding of integrins initiates clustering of integrins to form structures and the recruitment of a host of signaling and adaptor proteins as well as the actin cytoskeleton [5]. These focal adhesions are involved in the signaling events that lead to proliferation, motility, cytoskeletal organization, and cell survival [5].

Cadherins mediate adhesive contact between cells in structures called adherens junctions, and play a vital role in morphogenec events during development . The best studied of these are the classical cadherins, which mediate adhesion between adjacent cells by forming homotypic junctions at sites called adherens junctions, and are linked intracellularly to the actin cytoskeleton through beta-catenin and alpha-actinin (Fig. 1.30b). Similar to integrins, cadherins too have a mechanical and signaling role. Along with the mechanical that adhesion plays in tissue cohesion, cadherins, like integrins, transmit specific signals to the cell interior through proteins at the adhesion site [6,7]. Both integrin and cadherin adhesions are biochemically regulated and are both dynamic and reversible. Normal cell processes such as the rounding of spread cells during mitosis, cell sorting and migration during embryogenesis, or disease processes such as cancer cell metastasis involve active changes in adhesion strength between cell-ECM and cell-cell contacts. Also, adhesive signals regulate many of the same cell function that soluble growth factors do. Adhesion and growth factor pathways are cooperative: for example, anchorage dependent cells do not grow in the absence of adhesion when they are placed in suspension even in the presence of saturating amounts of growth factors, neither do they grow in the absence of growth factors even when adherent. It is only when both adhesive and growth factor signals are present that growth pathways are optimally activated in cells [8].

However, the effects observed for a given protein have been found to vary substantially depending on the nature of the underlying substrate and the method of immobilization [9,10]. Because cells interact with ECM proteins through receptors that bind to localized regions within their proteins ligands, the biological activity of proteins on the surface will depend upon whether specific active peptide sequence in specific proteins are accessible to the arriving cells [11]. Many of the ECM proteins, like fibronectin, laminin vitronectin, von Willebrand factor, carry a sequence of amino acid, arginine-glycin- aspartic acid (RGD) to which cells can bind using specific surface receptors called integrins [12,13]. Integrin-mediated binding of cells is the foundation for cell growth and differentiation and is the dominant mechanism by which cells communicated with noncellular surroundings [14].

In brief, cell adhesion is involved in various natural phenomena such as embryogenesis, maintenance of tissue structure, wound healing, immune response, metastasis as well as tissue integration of biomaterial. Surface characteristics of materials, whether their topography, chemistry of surface energy, play an essential part in osteoblast adhesion on biomaterials. Thus attachment, adhesion and spreading belong to the first phase of cell/material interactions and the quality of this first phase will influence the cells' capacity to proliferate and to differentiate itself on contact with the implant.

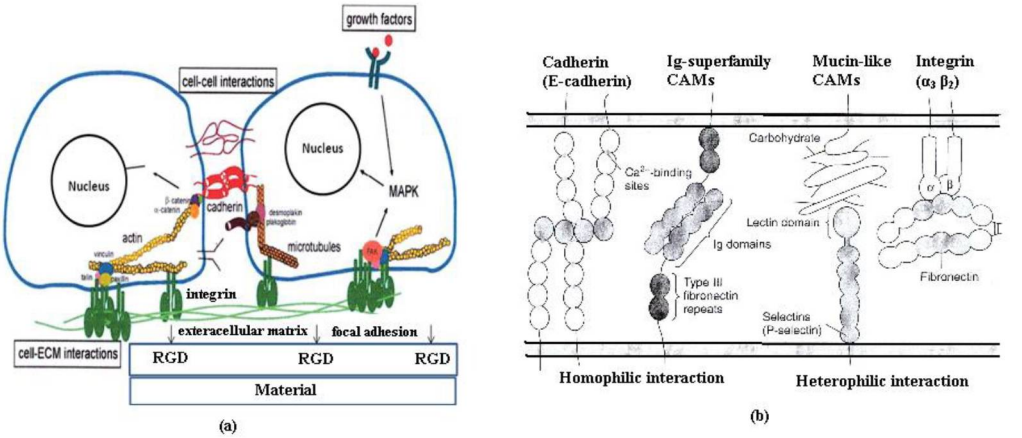

Figure 1.30. Representation of the cell–biomaterial surface interaction (a), and major families of cell–adhesion molecules (b).

Cell spreading is a combined process of continuing adhesion and cytoplasm contractile meshwork activity. Cell adhesion and spreading are influenced by the physicochemical characteristics of the underlaying solid surface. Other important parameters involved in cell-adhesion are: 1- surface charge, 2- topography, 3- porosity, 4- grooves, 5- mechanicl forces, 6- texture and 7- cellular locomotion.

The high ionic strength of the physiological environment and the rapid establishment of ionic equilibrium indicate that surface electrical properties do not significantly influence the formation of initially adsorbing protein layers or adhering cells. The surface topograghy of a biomaterial can be classified according to roughness, texture, and porosity. Porosity is used on a large scale to promote anchorage of biomaterials to surrounding tissue.

Grooved substrata were found to induce a certain amount of cellular orientation and locomotion in the direction of the grooves. Applying grooved substrata will therefore induce cell contact guidance. Mechanical forces around an implant, especially in combination with a rough surface, induce abundant formation of fibrous tissue, owing to the constant irritation of the cells. The texture of an implant surface and its morphology can be adapted to the clinical purpose of the biomaterial by such approaches as changing the fabrication process (e.g., woven, knitted, fibrous, grooved, veloured, smooth). Cellular locomotion can be directed by various gradients in the cell environment. For example, after implantation of a biomaterial, granulocytes are attracted by a negative oxygen gradient. Fibroblasts are attracted by agents produced by macrophages.

1.3.3. Osteoblasts Adhesion to Orthopaedic Implants

Bone Composition

The bones are classified according to their shape into long, short, flat and irregular bones. The long bones are found in arm, fore arm, thigh and leg. Short bones have no shaft but consist of smaller masses of spongy bone surrounded by a shell or compact bone. Long bones

consist of two major regions: compact or cortical bone and cancellous or trabecular bone. The location of these bone types in a femur is illustrated in figure 1.31. Cortical or compact bone is a dense material with a specific gravity of about 2. The external surface of bone is generally smooth and is called the periosteum. The interior surface is called endosteal surface, which is roughened.

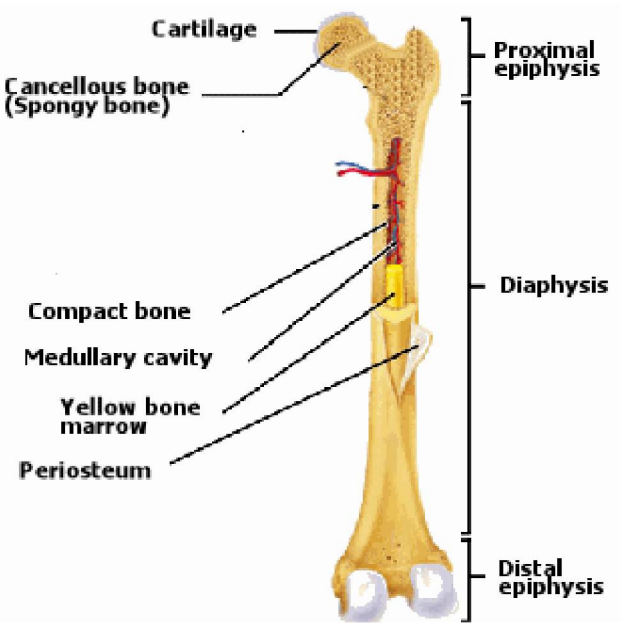

Figure 1.31. Organization of a typical bones.

From a microscopic viewpoint there are three types of cortical bones: woven, laminar and haversian. Woven bone is found typically in both cortical and cancellous regions of young, growing animals. In laminar and haversian bone, minerals and collagen are closely related, whereas woven bone is hyper-mineralized

Osteoblasts and osteoclasts are found within bone marrow and on bone surfaces. Osteoblasts are basophilic, cubical cells responsible for synthesizing bone matrix and regulating bone mineralization. These cells are involved in the synthetic production of type 1 collagen, glycosaminoglycans, alkaline phosphatase, and phosphoprotein (osteonectin). Bone development and bone mass are controlled by close interactions between bone formation by osteoclasts and bone resorption by osteoclasts which are regulated by both systemic and local mechanisms. Osteoclasts produce the specific collagen fibers and closely control their direction and mineralization. At the same time they attach to specific sites on the collagen molecule. The composition of bone tissue is mainly made of minerals, water and collagenous matrix. Wet cortical bone is composed of organic matrix (22-w/o of which 90-96 w/o is collagen) and the rest is mineral (69 w/o) and water (9 w/o).

The major mineral consists of submicroscopic crystals of calcium apatite [Ca_{10} $(PO_4)_6$ $(OH)_2$]. Besides phosphate, there are other minor negative ions such as citrate, carbonate, fluoride and hydroxyl ions. The apatite crystals are formed as slender needles 20-40 nm in length and 1.5-3 nm in thickness in the collagen fiber matrix. These mineral containing fibrils are arranged into lamellar sheets (3-7 μm thick) which run helically with respect to the long

axis of the cylindrical osteons (sometimes called haversian systems). It is interesting to note that the mineral phase is not a discrete aggregation of the calcium phosphate crystals. Rather it is made of a continuous phase as evident from the fact that after complete removal of the organic phase, the bone still retains good strength.

Orthopaedic Implants

Biomaterials are inorganic or organic natural or synthetic materials placed in the body. Biomaterials are expected to be biocompatible, i.e. they should not cause inflammation or rejection. Orthopaedic biomaterials can be implanted into or near a bone fracture to facilitate healing or to compensate for a lack or loss of bone tissue. Since the principal function of the long bones of the lower body is to act as load–bearing members, it was reasonable that the initial materials introduced to replaces joints, such as artificial hips, were metals. Both stainless steel, such as 316L and Co-Cr alloys became the early materials of choice, because of their relatively good corrosion resistance and reasonable fatigue life within the human body. Of course, their stiffness rigidity, strength, exceeded those of bone considerably.

Numbers of properties of the implant materials are important when selecting suitable candidates for joint replacements in current use. In addition to the 316L and Co- Cr alloys mentioned above, titanium and the so–called aviation alloy Ti- 6A1-4V are now also used for the femoral portion of hip prostheses. Chronology of metal alloys in orthopaedic applications is given in table 1.10. Figure 1.32 illustrates interdependence of engineering factors affecting the success of joint replacement.

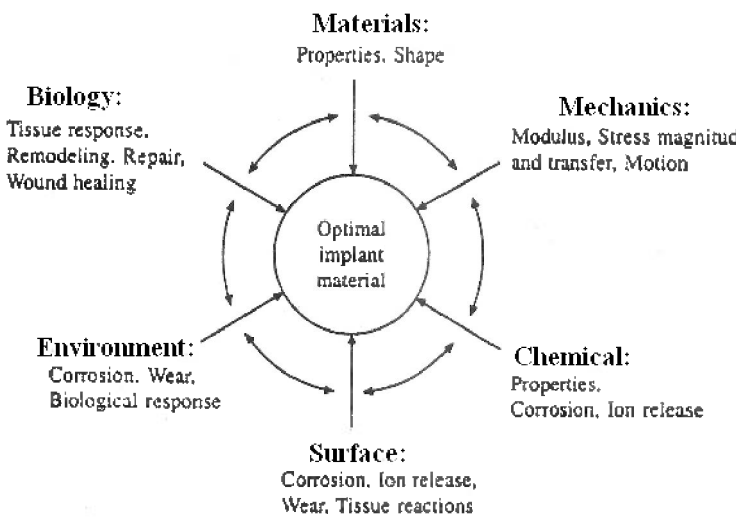

Figure 1.32. Schematic of interdependence engineering factors affecting the success of joint replacements.

Titanium is a transition metal with an incomplete shell in its electronic structure enables it to from solid solutions with most substitution elements having a size factor within $\pm 20\%$. In its elemental form titanium has a high melting point (1678^0c) exhibiting a hexagonal close packed crystal structure (hcp)α up to the beta transus (882.5^0C), transforming to a body

centered cubic structure (bcc) β above this temperature. Titanium alloys may be classified as either α, *near* α, $\alpha+\beta$ metastable β or stable β depending upon their room temperature microstructure. In this regard alloying elements for titanium fall into three categories: α - stabilizers, such as Al, O, N, C, β - stabilizers, such as Mo, V, Nb, Ta, (isomorphous), Fe, W, Cr, Si, Ni, Co, Mn, H (eutectoid), and neutral, such as Zr, α and *near-*α titanium alloys exhibit superior corrosion resistance whit their utility as biomedical materials being principally limited by their low ambient temperature strength. In contrast, $\alpha+\beta$ alloys exhibit higher strength due to the presence of both α and β phases.

Table 1.10. Chronology of metal alloys in orthopaedic applications.

Alloy	Year	Application	Performance issues
Vanadium steel	1912	Bone plates	Corrosion problems
Cast Co-Cr-Mo	1937	Dental devices	Well accepted
Cast Co-Cr-Mo	1938	Orthopaedic implants	Well tolerated, adequate strength
302 stainless steel	1938	Bone plates /screws	corrosions resistance
316 stainless steel	1946	Trauma implants	Better corrosions resistance and strength
Titanium	1965	Hip implants (England)	Corrosion resistance, tissue acceptance
316LVM stainless steel	1968	Trauma implants	Further improvements in corrosion
MP35N	1972	European hip prostheses	High strength
Ti-6Al-4V	1974	Trauma implants	High strength, biocompatibility
Ti-6Al-4V	1976	Hip prostheses	High strength, low modulus
Forged Co-Cr-Mo	1978	Hip prostheses	Highest fatigue strength
22-13-5 stainless steel	1981	Hip implants, trauma	High strength, forgeability
Ti-6A1-7Nb	1982	Hip implants	High strength, biocompatibility
Cold-forged 316LVM	1983	Compression hip screw	High strength
Zirconium 2.5 Nb (zirconia cated)	1994	Joint prostheses	Improved wear resistance, Biocompatibility

Titanium and titanium alloys are largely used as implant materials because of their high in vitro and in vivo biocompatibility and load bearing. It is well established that oseteointegration is an important property of titanium implant surfaces and that the current success rate is satisfactory [15-17]. Osseointegration is a term introduced by Branemark et al. [18] to describe a loaded, stable implant in direct contact with bone. Osseointegrated implants differ from ingrown ones that are dependent upon bone growth into surface macroscopic features or irregularities. By contrast, osseointegration is dependent on tissue ingrowth into minute surface features, such as the fundamental asperities of a smooth surface or as postulated for surfaces of various crystalline calcium phosphates (such as calcium hydroxyapatite) or amorphous, bioactive glasses, on direct chemical bonding between tissue and implant. Nevertheless, some concern remains as to the effects of vanadium and aluminum which are known to be cytotoxic [19,20].

Bone – Cell Adhesion

The attachment phase occurs rapidly and involves short-tem events like physicochemical linkages between cells and materials involving ionic forces Van der Waal forces, etc and the

adhesion phase occurs in the longer term and involving various biological molecules: extra cellular matrix proteins, cell membrane proteins, and cytoskeleton proteins which interact together to induce signal transduction, promoting the action of transcription factors and consequently regulating gene expression. Proteins involved in osteoblast cells adhesion are:

1) Extra cellular matrix proteins The extracellular matrix of bone is composed of 90% collagenic proteins (type I collagen 97% and type V collagen 3%) and of 10% non-collagenic proteins (NCP) (osteocalcin 20% osteonectin 20%, bone sialoproteins 12%, proteoglycans 10% osteopontin, fibronectin, growth factors, bone morphogenetic protein, etc). All these proteins are synthesized by osteoblasts and most are involved in adhesion. Some of the bone proteins have chemotacitc or adhesive properties, notably because they contain an Arg-Gly-Asp (RGD) sequence which is specific to the fixation of cell membrane receptors like integrin (fibronectin, osteopotin, bone sialoprotein, thrombospondin, type I collagen, vitronectin) [21 , 22].
2) Cytoskeleton proteins The sites of adhesion between tissue cultured cells and substrate surfaces are called focal contact or adhesion plaques. Focal contacts are closed junctions where the distance between the substrate surface and the cell membrane is between 10-15 nm. The external faces of focal contacts present specific receptor proteins such as integrings. On the internal face, some proteins like talin, paxillin, vinculin, tensin are known mediating interactions between actin filaments and membrane receptor proteins. Many proteins: integrin, cytoskeletal proteins, proteases, protein kinases and phophatases, signaling molecules, etc are involved in signal transduction. The architecture of the actin cytoskeleton is essential to the maintenance of cell shape and cell adhesion.
3) Adhesion molecules Molecules are characterized by their capacity to interact with a specific ligand. These liangnds may be situated on the membrane of nieghbouring cells or may be extracellular matrix proteins. Adhesion molecules belong to different families of: selectins, immunoglobulin superfamily, cadherins and integrins.

1.3.4. Surface Heat Treatment Processes

Surfaces can be described in terms of chemical composition, crystallography and mechanical stresses present in the surface. Topography, roughness and the degree of ripple as well as surface defects like pores, cracks or grease layers are the major geometrical aspects apart from layer thickness and layer sequence. The microstructure can be characterized by the type, size and distribution of phases and defects.

The motivation for surface treatments in general is the generation of components with either an improved durability or with enhanced tribological properties or with better corrosion behavior. Engineers have modified the surface by means of mechanical, thermal and chemical treatments to help components to withstand surrounding conditions. However, through the development of new physical and chemical technologies, electroheat, PVD and CVD as well as plasma and beam technologies have been the driving forces in surface engineering as interdisciplinary technology. The principle of laser surface treatment (LST) is the modification of a surface as a result of the interaction between a beam of coherent light and

the surface within a specified atmosphere. LST offers a wide range of possibilities to achieve desired surface properties. Whether LST is the best or cheapest way to complete the required task can only be decided depending on the individual component, its size, number and base material. For all three treatments, thermal, chemical and mechanical processes are known to alter the base material leading to a profile of properties that fit better the requirements in service.

Practical uses of laser heat treatment include:

- hardness increase
- strength increase
- reduced friction
- wear reduction
- increase in fatigue life
- increase of corrosion resistance
- surface carbide creation

Common advantages of laser surface compared to alternative processes are:

- chemical cleanliness
- controlled thermal penetration and therefore distortion
- controlled thermal profile and therefore shape and location of heat affected region
- remote non-contract processing is usually possible
- relatively easy to automate

Depending on the intensity and the material parameters. Five processing areas may be distinguished:

Low Intensity 10^4-10^5 W/Cm^2

1) Heating: heat treatment of materials, hardening, oxidation. The material is only heated by the laser radiation. The melting temperature is not yet reached.

Medium Intensity 10^5-10^7 W/Cm^2

2) Melting: soldering, spot-welding, marking, scribing, crystal growing, melt cutting, surface treatment. At the material surface the melting temperature is reached very rapidly. The intensity is then held such that the melt remains liquid until the required volume is melted.

High Intensity 10^6-10^7 W/Cm^2

3) Vaporization: drilling, sublimation cutting, scribing, trimming, penetration welding, carving, shock hardening. With high intensity, mostly in the pulsed operation, the material is vaporized rapidly.

High Intensity 10^8-10^9 W/Cm^2

4) Plasma shielding: At further increase of the intensity a plasma is produced by the vaporized material that shields the laser beam from the material.

Highest Intensity 10^{10}-10^{12} W/Cm^2

5) Gas breakdown: The high laser intensity immediately induces a gas breakdown in the atmosphere.

Material Parameters

Only intrinsic and unalterable properties of the material are considered:

- 1-R - the spectral and intensity – dependent absorption for a given surface
- k - the thermal diffusivity (cm^2s^{-1})
- C - the specific heat capacity ($J\ g^{-1}\ ^oc^{-1}$)
- P - the density (gcm^{-3})
- T_m - the melting temperature (^{o}c)
- T_v - the vaporization temperature (^{o}c)
- Q_m -the melting heat
- Q_v -the vaporization heat

For a defined volume V the minimal energies for melting of vaporization can be determined. The melting energy consists of the energy to heat the volume to the melting point, and the melting heat for the phase transition.

$$E_m = \rho(c(T_m - T_0) + Q_m), \qquad melting\ \ energy\ \ per\ \ volume \tag{1.52}$$

$$E_v = \rho(c(T_v - T_0) + Q_m + Q_v), \qquad evaporation\ \ energy\ \ per\ \ volume \tag{1.53}$$

Laser Parameters

The beam parameters of the laser at the processing position are:

λ - wavelength	F_o- focal length
f- frequency	τ - irradiation time
E- energy	τ_p -pulse duration
P- power	N_p- pulse number
F- fluence	ϕ_b - beam diameter
I- irradiance	ω - beam radius
P_a- average power	ω_o - beam waist radius in the focus
P_p- peak power	θ_d - beam divergence

Applied Relations

$$P = \frac{E}{\tau}(W) \quad I = \frac{E}{\tau_p . A} \quad (Wcm^{-2})$$

$$P_p = \frac{E}{\tau_p}(W) \quad F = \frac{E}{A} \quad (Jcm^{-2})$$

$$P_a = E.F(W) \quad \theta_d = \frac{\omega}{F_o} = \frac{\lambda}{\pi\omega_o} \quad (mrad)$$

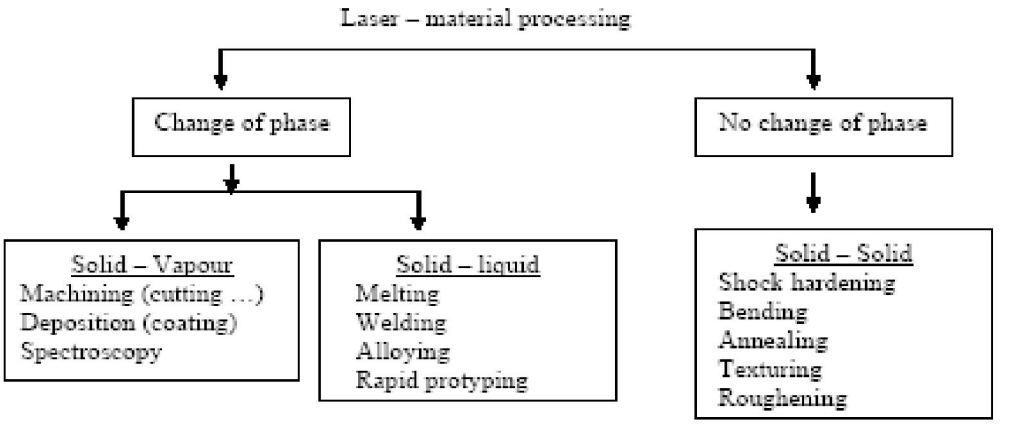

Figure 1.33. Important application of laser – material processing.

The laser has some unique properties for surface heating. The electromagnetic radiation of a laser beam is absorbed within the first atomic layer for opaque materials, such as metals. In fact the applied energy can be placed precisely on the surface only where it is needed. Thus it is a true surface heater and a unique tool for surface engineering. The applications of the laser in material processing are based mainly on the local conversion of the radiation energy into heat. If the primary relaxation process proceeds via the generation of heat, then the release of the heat flow Q/A might proceed via materials diffusion, radiation, convection of heat transfer.

Important application of laser material processing are shown in figure 1.33 and depending on the intended application, laser surface treatments can either improve wear behavior, enhance fatigue properties or increase corrosion resistance.

Heat Transfer via Conduction

In most cases this is primary energy transfer mechanism. The heat flux is proportional to the temperature gradient $\frac{\partial T}{\partial t}$, which is normal to the plane along which the flux proceeds and is directed form high to low temperature i.e. equation 1.59 which is known as Fourier's law. The thermal conductivity K in general depends on the temperature of the substrate. Below the

Debye temperature Θ_{Debye} it is determined for metals by electron transport. Metals with a low number of defects and at low temperatures will show better conductivity since the resistance by lattice vibrations becomes smaller. Above the Debye temperature K stays approximately constant since thermal and electrical conductivity depend directly on each other (Wiedemann – Franz law):

$$K(T) = const.\sigma(T).T \tag{1.54}$$

and the electrical conductivity σ is proportional to Θ_{Debye}/T. The proportionality constant is about $3(k_B/e)^2$. For a thorough calculation of heat flow through the material on energy rate equation has to be constructed which determines the distribution of temperatures within the investigated area as a function of time and space. For a known distribution of temperatures the temperature gradients might be evaluated which determine the rate of heat transfer. Let us assume that the incident power is sufficiently low that the only effect of the incident laser pulse is to raise the surface temperature of the metallic sample. The laser is thus acting simply as a transient heat source. Let us further assume that the optical pulse is short, so that thermal conductivity into the bulk of the sample can be neglected, that the laser uniformly irradiated an area A and that absorption takes place uniformly throughout a depth equal to the skin depth δ. Then the temperature rise in the irradiated material is uniform and is given by:

$$\delta T = \delta F / C\rho A\delta \tag{1.55}$$

i.e. the temperature rise δT is proportional to the absorbed energy density. Let us now consider the effect of non-uniform irradiation but still with absorption within a depth δ. If the incident irradiance and reflectivity are respectively I(x,t) and R then, considering a small element of area dx, the absorbed energy is given by:

$$(1-R)\int_t I(x,t)dx\,dt = C\rho\delta\,dx\;\delta T(x) \tag{1.56}$$

Therefore

$$\delta T(x) = \frac{1-R}{C\rho\delta}\int_t I(x,t)dt \tag{1.57}$$

Thus the temperature distribution across the surface is the same as the fluence distribution in the optical pulse. The beam profile of a pure laser mode is generally Gaussian. Multi- mode beam however, often give rise to hot spots, where I(x,t) is a maximum. Reflectance, R, is the ratio of the power reflected from a surface to the power incident on it. For normal incidence, is related to the refractive index by:

$$R = \left(\frac{n_1 - n_2}{n_1 + n_2}\right)^2 \tag{1.58}$$

Where n_2 and n_1 are the refractive indices of the substrate material and incident medium, respectively. For conducting or absorbing dielectric materials, n_2 is a complex number and the square in equation (1.58) is an absolute square. The magnitude of the refractive index for good conductors (metals) is proportional to $\sqrt{\sigma / 2\pi\mu f}$, where σ is electrical conductivity, μ is magnetic permeability, and f is the frequency of the light. Consequently, metals like copper and silver have high reflectances that increase with decreasing frequency (increasing wavelength). It is found that the reflectance of metals substantially decreases as the temperature nears the melting point.

Thermal conductivity K is the flow per unit area per unit thermal gradient. In one-dimensional heat conduction equation, it relates rate of heat flow Q to thermal gradient $\frac{\partial T}{\partial t}$,

$$Q = -KA\frac{\partial T}{\partial t} \tag{1.59}$$

Thermal diffusivity k is related to thermal conductivity and volume specific heat by:

$$k = \frac{K}{\rho C_v} \tag{1.60}$$

and is a measure of how much temperature rise will be caused by a pulse of heat applied to the material. It also indicates how rapidly heat will diffuse through the material. We now calculate the temperature distribution resulting from the absorption of a laser pulse at the surface of a metal without phase change. We assume that the thermal properties of the metal are independent of temperature that a local thermal equilibrium is established during the pulse, and that negligible energy is lost from the surface by radiation. The differential equation for heat flow in semi-infinite slab (half- space) with a boundary plane at the surface (z=0) is given by:

$$\nabla^2 T - \frac{1}{k}\frac{\partial T}{\partial t} = -\frac{Q_L}{K} \tag{1.61}$$

Where T(x, y, z, t) is the temperature distribution Q_L(x, y, z, t) is the heat produced by laser per unit volume per unit time. The boundary conditions are that T(x, y, z, 0) = 0, and $T \to 0$ as $z \to \infty$, and no heat flux crosses the z=0 plane. By substituting equation (1.60) in (1.61) we get the fundamental differential equation of parabolic Fourier heat conduction equation.

$$\rho c\left(\frac{\partial T}{\partial t}\right) = K\nabla^2 T + Q_L \tag{1.62}$$

The equation (1.62) assumes an instantaneous conversion of pulse energy in to heat upon absorption and its conduction in to the material. In this case, the temperature rise at the

surface (ie. z=0) before ablation and for thermal diffusion depth, $d_t << \alpha^{-1}$, is given by equation (1.63).

$$\Delta T = \frac{(1-R)F\alpha}{\rho c} \tag{1.63}$$

and for z>0 and $d_t \rangle\rangle \alpha^{-1}$ with a Gaussian beam profile we have:

$$T(r,z) = \frac{\alpha I_0 t}{\rho c} e^{-\alpha z} . e^{-2r^2/\omega^2} \tag{1.64}$$

where r is the radial distance from the interaction point at the surface. However it is well known that not always the heat produced is immediately conducted away within the material, but it takes some time to do it. Thus, the equation (1.62) can be modified to a hyperbolic equation by adding the material thermal relaxation time, τ_r, which gives :

$$\rho c \tau_r \frac{\partial^2 T}{\partial t^2} + \rho c \left(\frac{\partial T}{\partial t} \right) = K \nabla^2 T + Q_L \tag{1.65}$$

1.3.5. Studies of Pulsed Nd:YAG Laser Surface Modification of Ti-6Al-4V Alloy for Orthopaedic Applications

It is possible to change localized areas of metals in order to obtain both compositions and microstructures with improved properties. Titanium and titanium alloys are the most frequently used material for load-bearing orthopaedic implants, due to their specific properties such as high corrosion resistance, surface oxidation layer, high strength and high-temperature resistance [15,23-27]. Titanium and its alloys' application like any other biomaterials involve the creation of at least one interface between the material and biological tissues. Biocompatibility and bioactivity of biomaterials rely on the interactions that take place between the interface of the biomaterials and the biological system [28]. It is generally believed that proteins adsorbed on implant surface can play an important role in cell-surface response. Different proteins such as collagen, fibronectin and vitronectin which are acting as ligands are particularly important in osteoblast interaction with surface. Ligands are the junctions which facilitate adhesion of bone cells to implant surface. In another word, more ligand formation implies a better cell-surface interaction [29,30]. *In vitro* studies can be used to study the influence of surface properties on processes such as cell attachment, cell proliferation and cell differentiation. However, *in vivo* studies must be performed to achieve a complete understanding of the healing process around implants. Previous studies have shown that surface characteristics named above have a significant influence on adhesion, morphology and maturation of cultured osteoblasts [31-34]. Also, it has been demonstrated that for primary bovine osteoblasts, the wettability is one of the key factors [35]. In our studies [19,36-39] it is shown that the wettability of the surface can provide a better spreading

condition for osteoblast cells due to reduced contact angle. Bearing in mind that the adhesion of bone cells to implant surface consists of two stages. In primary stage the cells must get close enough to surface in an appropriate distance known as focal distance over which the cells can easily be spread over it. In this respect, the wettability can be effective in providing a preferred accessability to surface and thus reaching the focal distance. The secondary stage includes cell-cell attachment which obeys the regular biological facts.

Interface reactions between metallic implants and the surrounding tissues play a crucial role in the success of osseointegration. The titanium and its alloys like some other medical grade metals are the materials of choice for long-term implants. The effect of implant surface characteristics on bone reactions has thus attracted much attention and is still considered to be an important issue [40-42].

So far as the surface characteristics of the implants are concerned, two main features that can influence the establishment of the osseointegration are the physico-chemical properties and the surface morphology. Cell adhesion is involved in various phenomena such as embryogenesis, wound healing, immune response and metastasis as well as tissue integration of biomaterial. Thus, attachment, adhesion and spreading will depend on the cell-material interaction and the cell's capacity to proliferate and to differentiate itself on contact with the implant [43,44].

Cell behavior, such as adhesion, morphologic change and functional alteration are greatly influenced by surface properties including texture, roughness, hydrophilicity and morphology. In extensive investigations of tissue response to implant surfaces, it has been shown that surface treatment of implant materials significantly influences the attachment of cells [45-51]. Additionally, these modified surfaces must resist both the mechanical wear and the corrosion [52]. It is therefore important to evaluate systematically the role of different surface properties and to assess the biological performance of different implant materials.

Titanium as a biomaterial implant has an excellent biocompatibility due to the fact that it is highly inert and is not soluble in body fluids and forms a protective oxide layer on the surface [53,54]. However, pure titanium could leave metal debris in the tissue due to the higher tendency to produce wear in fretting conditions. Therefore numerous titanium alloys like Ti6Al4V with improved physical and mechanical properties have been developed.

The surface morphology, as well as manipulation with the physical state and chemical composition of implant surface may be significant for bone-implant integration. Surfaces are treated to facilitate an intimate contact between bone and implant. So, the tissue response to an implant involves physical factors, depending on implant design, surface topography, surface charge density, surface free energy and chemical factors associated with the composition of the materials. These substrate characteristics may directly influence cell adhesion, spreading and signaling, events that regulate a wide variety of biological functions [55-59]. Numerous surface treatments including Ion implantation [18,60,61], coating [62-67], shot blast [68-70], machining [71], plasma spray [72,73], plasma nitrid [74], nitrogen diffusion hardening [75] are some of the relatively older techniques in the field of material processing which can be used to change implant's surface topography. But perhaps the laser-assisted method has recently received more attention and has been successful in meeting the new objectives in this field which is mainly because of its wavelength selectivity, coherency, very low thermal or mechanical damage, high accuracy, control and less pollution during laser treatment process. In fact, optical and kinetics of laser parameters like fluence and pulse number as well as surface physical parameters will affect this process [76-80]. For example,

surface modification of metals by Co_2 [81,82], HF [83,84], Nd:YAG [85-87], and diode lasers [88,89], titanium alloy by Nd:glass [90], KrF [20], XeCl [91], diode lasers [92] and However the recent studies on this subject using short Nd:YAG laser pulses have been performed as *In vitro* with some limited but informative results [93-95]. Thus, the success of uncemented orthopaedic implants depends largely upon the body's ability to synthesize new bone directly onto the surface of the device. This gap allows micromotion of the implant, which loosense the device and ultimately leads to implant failure. Some researchers have attempted to circumvent capsule formation by coating metal implants with the synthetic bone analogue, hydroxyapatite (HA). The synthesis and deposition of new bone onto an implant requires the attachment of osteoblast precursor cells to the implant surface, as well as the subsequent differentiation of these cells. Both of these processes are likely mediated by the integrin family of cell adhesion receptors.

Thus, the main intension of this work is to extend the earlier research by carrying out some detailed *In vitro* and *In vivo* experiments using a long pulse (200μs) Nd:YAG laser radiation and 300 and 800 grit SiC papers on surface physico-chemical changes, surface wettability, corrosion resistance, microhardness and direct osteoblast cells adhesivity of Ti6Al4V with respect to possible orthopaedic applications. Finally, to assess and compare the effects of physico- chemical modifications made on mechanically treated surface (MTS) and laser treated surface (LTS).

Materials and Methods

Sample Preparation

Rectangular–shaped specimens with 20×10 mm dimensions and the thickness of 2 mm, were made from a medical grade Ti6Al4V (ASTM F136, Friadent, Mannheim- Germany-GmbH) with chemical formulation Ti(91.63%) Al(5.12%) V(3.25%). The samples were divided into three groups of untreated (7 samples), laser treated (14 samples) and the last group was gradually wet grounded with 300 and 800 grit SiC paper (14 samples). Prior to treatment, all samples were cleaned with 97% ethanol and subsequently been washed twice by distilled water in an ultrasonic bath (Mattachanna, Barcelona-Spain). A final rinse was done by de-ionized water at a neutral pH to ensure a clean surface is obtained. Finally, an optical microscope with magnification of □20 was used to ensure that no particles were left on the sample surface.

Experimental Setup

Surface treatment was performed by Nd: YAG laser with 1.06μm wavelength, 200μs pulse duration and pulse energy of 50 J. The output beam was suitably imaged on to the target surface in a 500 μm spot diameter where it scanned the surface at a constant velocity using a motorized XYZ translator. All the experiments were carried out in air at pulse repetition frequency of 1Hz. In order to achieve the optimum surface treatment conditions, the melting, evaporation thresholds and variation of etch depth with fluence were evaluated. Etch depth per pulse variation as a function of laser fluence can be calculated from equation 66.

$$X = \alpha^{-1}\ln(F/F_t) \tag{66}$$

Where, X is the etch depth, α is absorption coefficient and F_t is the threshold fluence. Two samples were sterilized by de-ionized water and then they were polished using 300 and 800 grit emery papers.

Surface Roughness

The surface micro roughness (R_a) measurements were carried out using a non-contact laser profilemeter (NCLP) (Messtechnik, Germany) equipped with a micro focus sensor based on an auto focusing system. R_a is the arithmetical mean of the absolute values of the profile deviations from the mean line. Five two-dimensional NCLP profiles were obtained for each surface over a distance of 3.094 mm with a lateral resolution of 1μm using a Gaussian filter and an attenuation factor of 60% at a cut-off wavelength of 0.59 mm . The roughness parameters were calculated with the NCLP software similar to that described by Wieland et al. [*96*].

Surface Hardness

Surface microhardness test was carried out with 50 gram load in 10 seconds by a diamond squared pyramid tip (Celemx CMT, Automatic). Each related test was considered at 5 points and reported as an average. The Vickers diamond pyramid hardness number is the applied load divided by the surface area of the indentation (mm^2) which could be calculated from below equation:

$$VHN = \{2FSin\ (136°/2)\}/d^2 \tag{67}$$

This equation could be re-written approximately as:

$$VHN = 1.854(F/d^2) \tag{68}$$

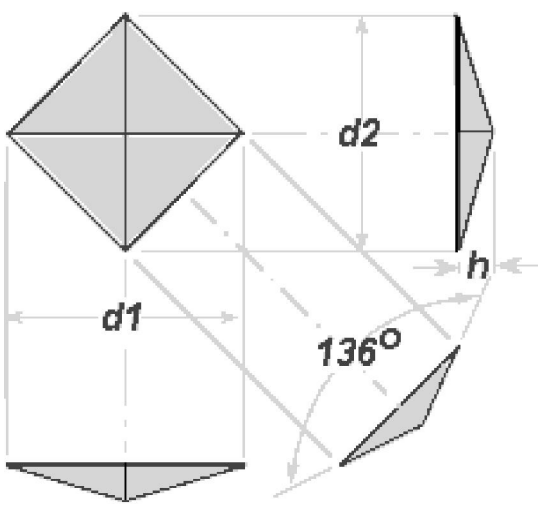

Figure 1.34. Vickers Pyramid Diamond Indenter Indentation.

Where F is load in Newton, d (mm) is the arithmetic mean of the two diagonals, d1 and d2 in mm which is shown in Figure 1.34 and VHN is Vickers hardness. The Vickers diamond pyramid indenter is grounded in the form of a squared pyramid with an angle of 136° between faces. The depth of indentation is about 1/7 of the diagonal length. When calculating the Vickers hardness number, both diagonals of the indentation are measured and the mean of these values is used in the above formula with the load used to determine the value of VHN.

Corrosion Tests

The standard Tafel photodynamic polarization tests (EG&G, PARC 273) were carried out to study the corrosion behavior of specimens in Hank's salt balanced physiological solution at 37°C. The procedure for preparing the Hanks solution is schematically shown in Figure1.35. The metal corrosion behavior was studied by measuring the current and plotting the E-logI (Voltage – Current) diagram. The corrosion rate (milli per year (mpy)) was determined using equation:

$$C.R. = 0.129 \left(M/n \right) \left(I_{corr} / \rho \right) \quad (69)$$

Where M is the molecular weight, n is the charge, I_{corr} is the corrosion current and ρ is the density.

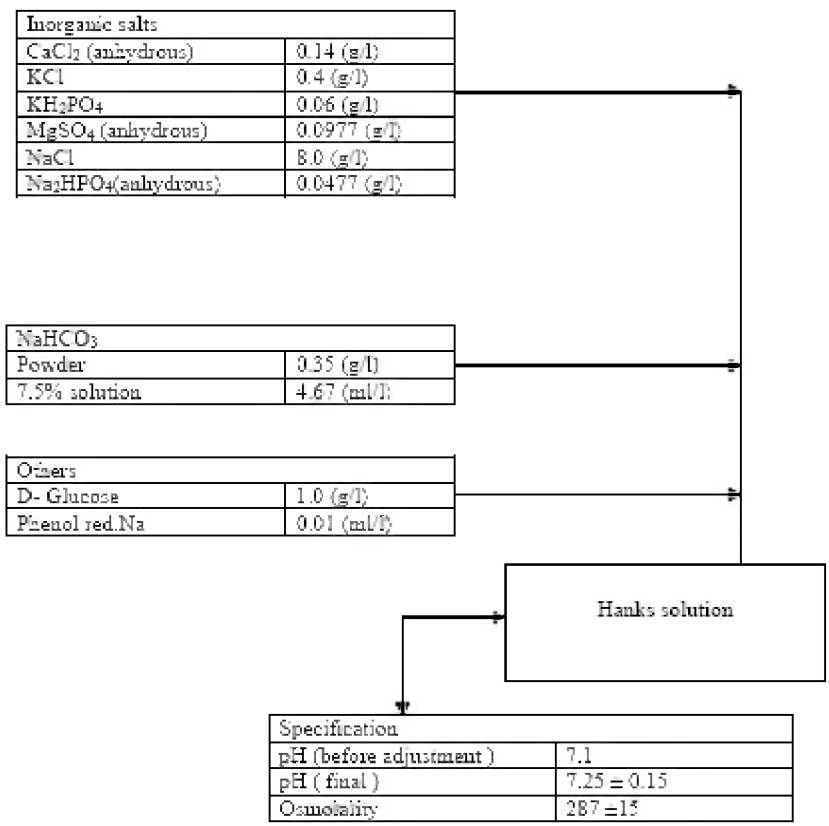

Figure 1.35. Schematic diagram of instructions for preparing the Hanks solution.

Surface Tension

The surface energy of the samples were determined by measuring the contact angle (θ) of test liquids (diiodo-Methane and water; Busscher) on the titanium plates using Kruss-G40-instrument (Germany).The geometric mean equation divides the surface energy in to two components of dispersive and polar and when combined with Young's equation it yields:

$$\gamma_{lv}(1+\cos\theta)=2(\gamma_l^d \cdot \gamma_s^d)^{0.5}+2(\gamma_l^p \cdot \gamma_s^p)^{0.5} \quad (70)$$

Equation (70) can be rearranged as by Ownes-Wendt-Kaeble's equation:

$$\gamma_{lv}(1+\cos\theta)/(\gamma_l^d)^{0.5}=(\gamma_s^p)^{0.5}\ [(\gamma_l^p)^{0.5}/(\gamma_l^d)^{0.5}]+(\gamma_s^d)^{0.5} \quad (71)$$

Where s and l represent solid and liquid surfaces respectively, γ^d stands for the dispersion component of the total surface energy (γ) and γ^p is the polar component.

In Vitro Test

Mice connective tissue fibroblasts (L-929) with 4×10^5 ml were provided and maintained in culture medium (RPMI-1640) consisting of 100U/ml Penicillin, 100U/ml Streptomicine, and 10% fetal calf serum (FCS) .The untreated sample, two LTS and two MTS along with a negative control (ie. fibroblast cells only in the cell culture medium) were then placed inside the culture medium in a polystyrene dish. All the samples were incubated at 37°C in 5% CO_2 atmosphere and 90% humidity for 24h. Then the samples were washed with the de-ionized water and sterilized by water steam for 20 min at 120 °C. Subsequently, the samples were then fixed by using 50%, 65%, 75%, 85%, 96% ethanol and stained by Gimsa. Finally, they were evaluated, without extracting the samples from cell culture dish, with an optical microscope (Nikon TE 2000-U) for cell growth and cytotoxicity. It is worth mentioning that the biocompatibility of the samples was investigated *In vitro* by L-929 fibroblast cell counting on samples through methyl thiazole tetrazolium (MTT) assay. For this purpose an enzymic method ie.1ml of Trypsin/EDTA was used and the cells were then left to trypsinize in the flask at 37° in the incubator for 3 minutes and were monitored by the same optical microscope.

In Vivo Test

Anesthetization

Before depilation of the operation site, the animal was completely anesthetized with midazolam (Dormicum®, Roche, Switzerland) 2.5 mg/Kg intravenously (IV). With any sign of recovery during operation, diluted fluanisone/fentanyl (Hypnorm®, India) was injected slowly until adequate effect was achieved, usually 0.2 ml at a time.

Animal Implantation

One untreated sample, two MTS and two LTS were implanted on femur bone of an eight months male goat weighing 30 Kg. Specimens were steam sterilized before implantation in an

autoclave (Mattachnna, Barcelona-Spain). The steam sterilization was conducted under 132 °C, 2 bar and in 45 minutes. All the specimens were labeled by separate codes for further studies. The operation site was shaved and depilated with soft soap and ethanol before surgery; the site was also disinfected with 70% ethanol and was covered with a sterile blanket. In order to proceed with implantation, cortex bone was scraped by osteotom (Mattachnna, Barcelona-Spain) after cutting the limb from one-third end in lateral side and elevating it by a self – retaining retractor. Copious physiological saline solution irrigation was used during the implantation to prevent from overheating. To ensure a stable passive fixation of implants during the healing period, they were stabilized by size 4 and 8 titanium wires (Atila ortoped®, Tehran-Iran) without any external compression forces (Fig.1.36).

After the operation the animal was protected from infection by proper prescribed uptake of Penicillin for first four days and Gentamicine for second four days. During the eight days of recovery, the goat was administrated with multi-vitamins to help to regain its strength. During this period, the goat was kept in an isolated space under room temperature, ordinary humidity, lightening and air condition, and before it returns to its natural life environment, X-ray radiographs (Fig.1.37) were taken in order to ensure that the implant has not been displaced during the maintenance period. It was observed that calus bone had grown in the vicinity of the implant. After five months the animal was sacrificed and the specimens were removed (Fig. 1.38).

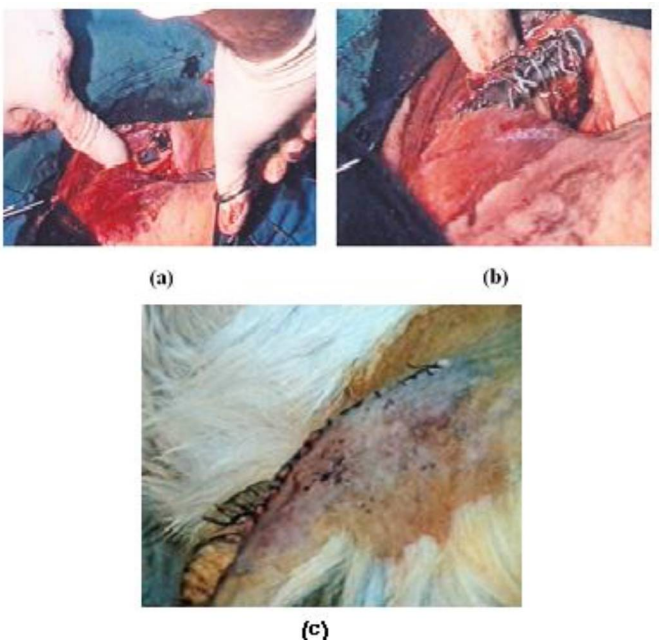

Figure 1.36. Placement of implants in the femur bone of the goat.

The experiments had been approved by the Yazd School of Veterinary Science (Iran) and its animal research authority and conducted in accordance with the Animal Welfare Act of December 20th 1974 and the Regulation on Animal Experimentation of January 15th 1996. The explantation procedure was performed by first cutting the upper and lower section of

femur bone using an electric saw and then the implant together with its surrounding tissues was placed in 4% formalin solution for pathological assessment and SEM.

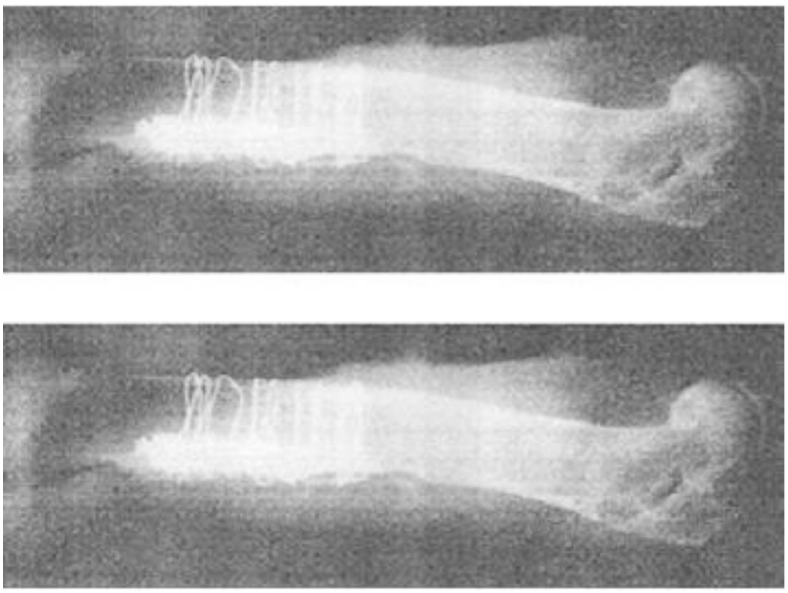

Figure 1.37. The X-ray of implants wired to the bone.

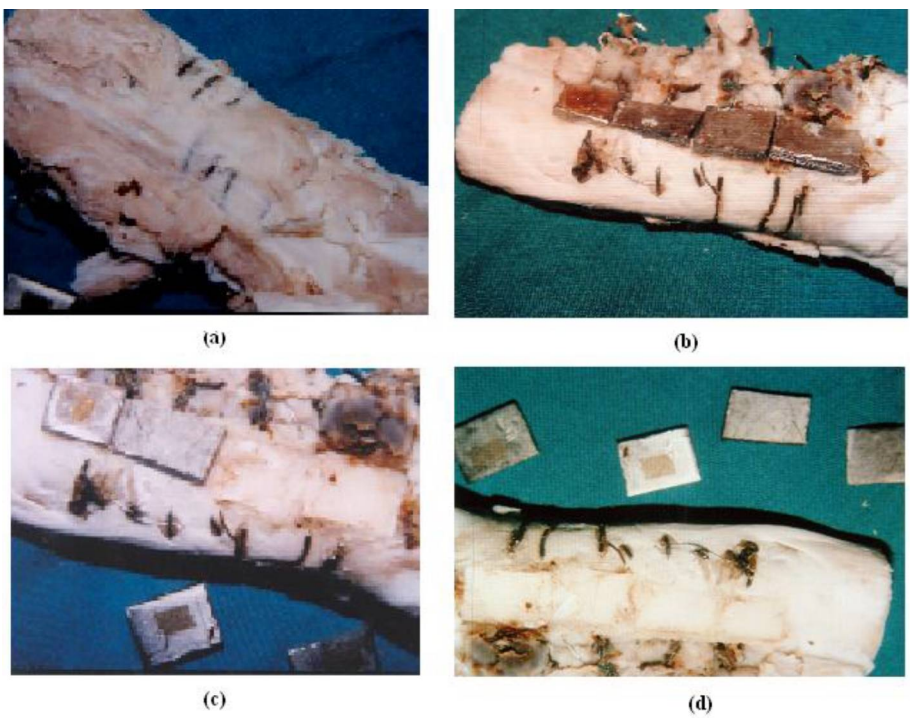

Figure 1.38. Implant removal from the femur bone of the goat: (a) before detachment of the wires, (b) after detachmented (c,d) the foot-print of the implants on the bone.

Cell Analysis

Osteoblast cells spreading (ie.lateral growth) on the six implantes (three samples for imaging and three samples for coulter counter) was analyzed after removal by SEM(stero scan 360-cambridge) and their spreading condition in a specific area was studied using Image J Program software in three separate regions of each specimen at frequency of 10 cells per each region. The number of attached cells in 1 cm^2 area of each specimen was calculated by a coulter counter (Eppendorf, Germany) using enzyme detachment method and Trypsin-EDTA (0.025 V/V) in PBS media at pH = 7.5. The final amount of attached cell can be studied by plotting cell detachment rate versus time.

Histopathology

Surrounding tissues of specimens were retrieved and prepared for histological evaluation. They were fixed in 4% formalin solution (pH = 7.3), dehydrated in a graded series of ethanol (10%, 30%, 50%, 70% and 90%) and embedded in paraffin after decalcification. Then, 10 µm thick slices were prepared per specimen using sawing microtome technique. A qualitative evaluation of macrophage, osteoblast, osteoclast, PMN, giant cells, fibroblast, lymphocyte was carried out by Hematoxylin and Eosin stain and light microscopy (Zeiss, Gottingen-Germany). The light microscopy assessment consisted of a complete morphological description of the tissue response to the implants with different surface topography. Osteoblasts can be in two states; (a) active, forming bone matrix; (b) resting or bone-maintaining. Those make collagen, glycoproteins and proteoglycans of bone the matrix and control the deposition of mineral crystals on the fibrils. Osteoblast becomes an osteocyte by forming a matrix around itself and is buried. Lacunae empty of osteocytes indicate dead bone. Osteoclast, a large and multinucleated cell, with a pale acidophilic cytoplasm lies on the surface of bone, often an eaten-out hollow-Howship,s lacuna. Macrophages, are irregularly shaped cells that participate in phagocytosis.

SEM of Adhered Cells

After implants removal, all three group implants were rinsed twice with phosphate buffer saline (PBS) and then fixed with 2.5% glutaraldehyde for 60 minutes. After a final rinse with PBS, a contrast treatment in 1% osmium tetroxide (merck) was performed for 1 hour, followed by an extensive rinsing in PBS and dehydration through a graded series of ethanol from 30% to 90% as described in histology section. After free air drying, surfaces were thinly sputter coated with gold (CSD 050, with 40 mA about 7 min). Cell growth on implanted specimens and their spreading condition in a specific area was analyzed using Image J Program software in three separate regions of each specimen for 10 cells per each region.

Statistical Analysis

All calculated data were analyzed by using a software program SPSS (SPSS Inc., version 9.0). The results of variance analysis were used to identify the differences between the cells spread area of the treated and cleaned un-treated samples ($p \leq 0.05$).

Results

Characterization of Surface Topography

Optical and Mechanical Effects

Figure 1.39 indicates the variation of etch depth per pulse with the laser fluence where the metal absorption coefficient (α) can be determined from the slope of the curve using the well known beer logarithmic equation (Eq.66). From Equation 66 the values of α and F_t were found $5\times10^3 cm^{-1}$ and 73 Jcm^{-2}, respectively. It is interesting to notice that, in our case, the interaction of laser radiation with metal surface can be divided into four different regions:

In zone I (0-30 Jcm^{-2}) no morphological changes was observed but beyond that where zone II (30-70 Jcm^{-2}) commences, some minor topological alterations such as surface deformations were seen until it reached zone III (70-145 Jcm^{-2}) where the signs of melting were clearly observed and it gradually became stronger. This is consistent with the fact that the power density required for melting (I_m) most metals is in the order of 10^5 Wcm^{-2} which in this case the corresponding range would be between 365-725 $KWcm^{-2}$. It is however, important to notice from metallurgical point of view that melting initially begins due to temperature rise of different elements at the surface. Hence, gradually these island-type molten centers are joined together producing a larger molten pool. Finally, zone IV (145 Jcm^{-2}-above) represents the onset of gradual thermal ablation (vis.vapourization) of Ti6Al4V at $\geq$145 Jcm^{-2} with corresponding temperature of about 3280(°c). Normally this process is accompanied by the presence of plume which basically is defined as ejection of material from the metal surface as gaseous and solid phase particles. Again this behavior is expected to become dominant with vaporization intensity threshold of about 10^6 Wcm^{-2}.It is deduced from 'Figure 1.40 that "Incubation" effect or period can be observed at lower fluences where more laser pulses may be needed in order to reach the ablation threshold.

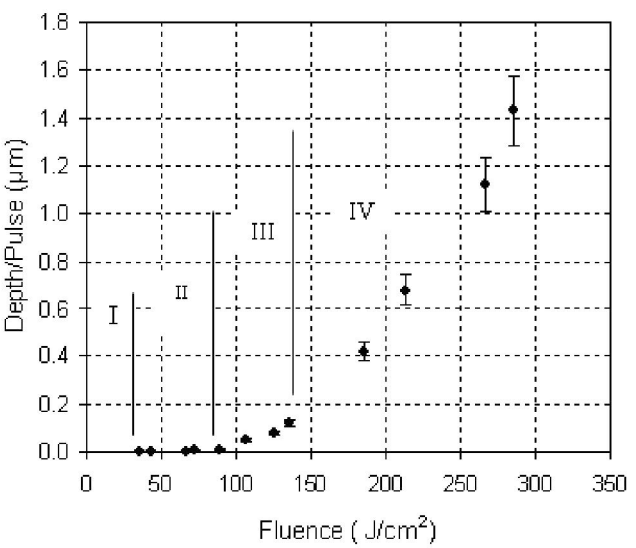

Figure 1.39. Variation of etch depth as a function of fluence.

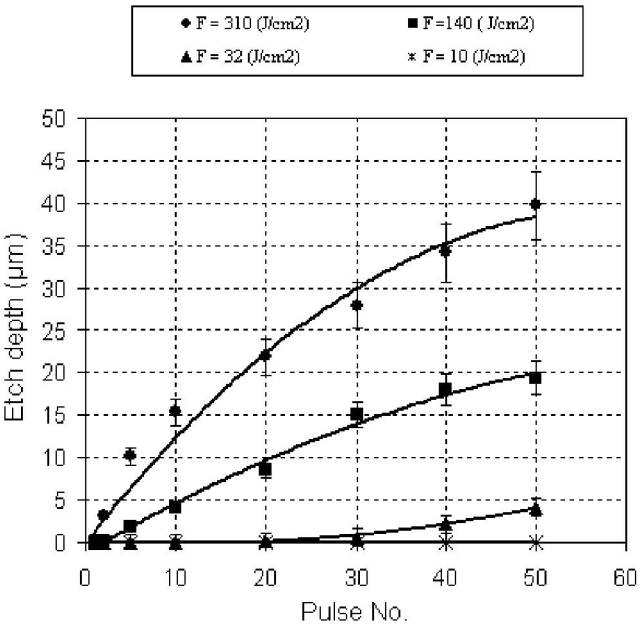

Figure 1.40. Variation of etch depth as a function of laser pulse number at constant laser fluences.

It may be worth while to notice that this effect had also been observed and reported for polymers by other investigators [97,98]. Also to avoid possible errors in assessment and evaluation of interaction process a distinction must be made between the actual physical ablation and surface non-linear roughness (ie. ripples) even occasionally with relatively high amplitudes which in our case this began at about 30 Jcm^{-2}. The etch depth saturation became particularly noticeable at higher fluences, which is mainly thought to be due to an intense interaction between the laser pulse and laser-induced vapor plume, hence causing some effective beam attenuation.

Since in our experiment the pulse duration is much greater than the thermal relaxation time (i.e. $\tau \approx 200\ \mu s \gg \tau_r \approx \alpha^{-2}/4k \approx 140$ ns) and that the optical absorption depth, α^{-1}, is much smaller than thermal diffusion depth, z_t, (i.e.$\alpha^{-1} \approx 2\mu m \ll z_t \approx 2(k\tau_p)^{1/2} \approx 7.5$ mm) thus, the temperature rise at the end of laser pulse on the surface is given by equation 72:

$$T_f - T_i = \frac{(1-R)F}{\rho c (4k\tau_p)^{\frac{1}{2}}} \tag{72}$$

With [99]:

- T_f, T_i = final and initial surface temperature (°c).
- R = surface reflection (0.6)
- C = specific heat capacity ($0.52 Jg^{-1}{}^{\circ}c^{-1}$)
- ρ = density ($4.51 gcm^{-3}$)
- k = diffusivity coefficient ($0.07 cm^2 s^{-1}$)
- τ_p = pulse width (200µs)

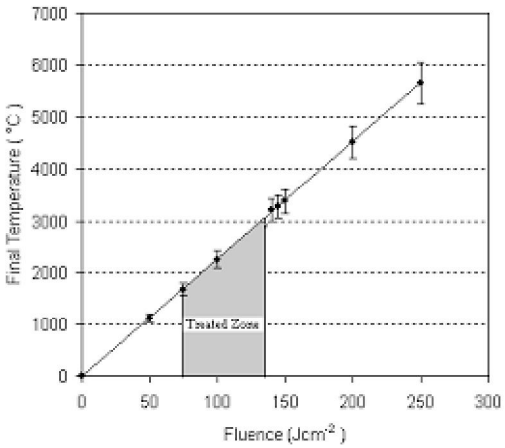

Figure 1.41. Plot of Ti6Al4V surface temperature versus laser fluence.

Figure 1.41 indicates the variation of Ti6Al4V surface temperature as a function of laser fluence. Now by assuming the melting and vaporization points of Ti6Al4V about 1668ºC and 3280ºC respectively and the melting region between (73-145) Jcm^{-2}, using Figure 1.39, then it would be sensible to choose zone III as the treatment area (ie. below ablation).

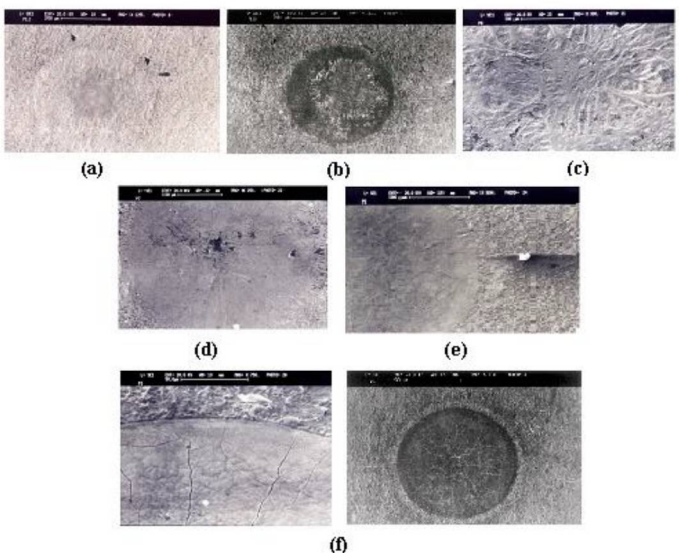

Figure 1.42. Surface morphology of Ti6Al4V treated at a) 30 Jcm^{-2} b) 60 Jcm^{-2} c) 100 Jcm^{-2} d) 140 Jcm^{-2} e) 210 Jcm^{-2} f) Crack formation at Ti6Al4V surface after 10 pulses treated at 270 Jcm^{-2}.

The comparison between morphologically different textures produced by laser at different energy density is shown in Figure 1.42. Figure 1.42a indicates the interaction effect taking place on the sample surface at 30Jcm^{-2} and the pattern of dentritic melted zone at 100Jcm^{-2} is clearly shown in Figure 1.42c. It is known that as the growth rate of solid phase increases with time during solidification process, the morphology of liquid / solid interface changes from planar to dentritic structure.These random fluctuating dentritic features are in turn defined by dentritc tip radius and their spacing between them [100]. When the laser

fluence was increased to 140Jcm^{-2}, the thermal ablation became the dominant mechanism where the irregularities and scratches due to machining and polishing process became smooth after direct laser surface thermal processing, Figure 1.42d. Figure 1.42e indicates the difference between the untreated and treated surface at 210Jcm^{-2} with formation of some grainy structure and cracks in cellular form in the central zone. Finally when the fluence was increased to 270Jcm^{-2} (Fig.1.42f) these cracks became dominant and developed throughout the surface caused by residual mechanical stress originated from steep temperature gradients at the surface during the resolidification process.

Figure 1.43 shows an example of the ablation site at fluence of $\geq$ 250 Jcm^{-2} (i.e. I >1mWcm^{-2}) with 10 pulses which has caused the metal eruption, cracks as well as surface melting. The spectra of colors, mainly blue, are probably because of high temperature plasma roughly defined by $T_e = C.(P\lambda\sqrt{\tau_p})^{1/2}$ where C is a material depending constant, T_e is electrons temperature, P and λ are the laser power and wavelength respectively[101]. Also, other factors like surface composition, solubility degree of alloys and base metal, thermal diffusion and rate of heating-cooling cycle may all have specific roles in crack formation which need a separate attention and analysis.

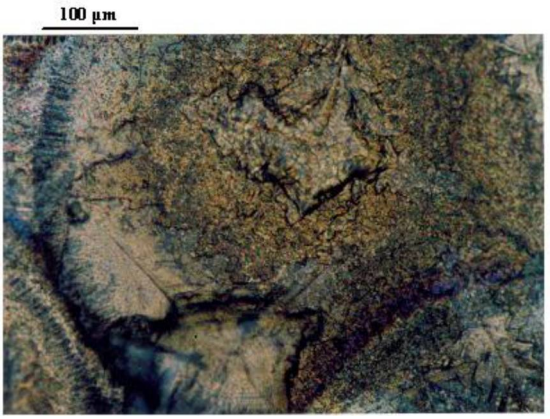

Figure 1.43. Plasma –induced damage of titanium at 250 Jcm^{-2} with 10 pulses.

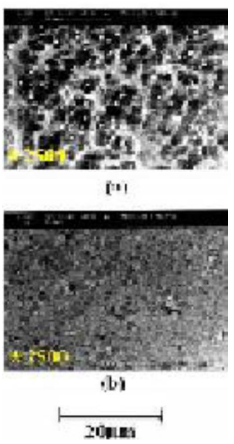

Figure 1.44. Scanning electron micrographs of Ti6Al4V surface morphology for: (a) untreated, (b) laser treated at 140 Jcm^{-2} indicating the disappearing of surface scratches by laser surface melting.

Two morphologically different areas i.e. laser treated and untreated (Fig.1.44) indicate that the inclusions are disappeared and the scratches due to machining and polishing are sealed due to direct laser surface heating. Ti6Al4V alloy is a (α+β) two-phase alloy with around 6wt% aluminum stabilizing the phase and about 4wt% vanadium stabilizing the β phase. At room temperature, the microstructure at equilibrium consists mainly of primary a phase (hcp) with some retained β phase (bcc). It is also well known that in laser surface melting, steep temperature gradient and thermal cycle leads to some micro structural changes in the heat affected zone within very short time. In particular, the α □ β phase transformation during rapid heating and decomposition of the β phase during rapid cooling. The physical and mechanical properties of Ti6Al4V alloy are known to be sensitive to its microstructure. The Ti-β phase has a diffusivity of two orders of magnitude higher than Ti-α phase and flow stress is strongly influenced by the ratio of these phases [102].

Emery Effect

Figure1.45 indicates that SiC treated surfaces have some unevenly distributed microgrooves with occasional scratch and pitting made on it by emery paper. More directionally defined track lines were produced by 800 than 300.

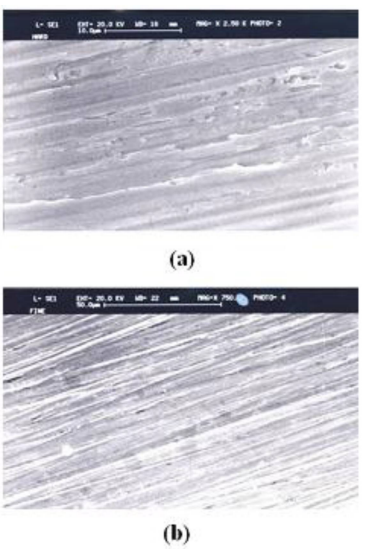

Figure 1.45. Scanning electron micrographs of emery treated surface by: (a) 300 grit, (b) 800grit.

Surface Roughness

In order to obtain a quantitative comparison between the original and treated surface, the arithmetic average of the absolute values of all points of profile (R_a) was calculated for all samples. The values of roughness differed from 21.8 ±0.05 for 300 SiC paper to 7±0.02 for laser treated surface at 140 Jcm^{-2}. Also the R_a values for untreated, laser treated at 100 Jcm^{-2} and 800 SiC paper were 12.3±0.03, 14.2±0.29 and 16.6±0.15, respectively. All the calculations were performed for n=5 and reported as a mean value of standard deviation (SD).

Surface Hardness

The surface hardness measurements presented in Figure 1.46 clearly indicate that micro hardness of the metal increases with laser fluence. Again a non-linear behavior was observed where initially the values of VHN were increased gradually up to about 100 Jcm^{-2}. Afterwards a sharp increase occurred until the point of plateau was reached at 140 Jcm^{-2} which corresponds to roughly 50% improvement of surface hardness. The surface hardness was found to vary from 377 VHN for MTS to 850 VHN for LTS.

The surface hardness results for all the specimens are illustrated in table 1.11.

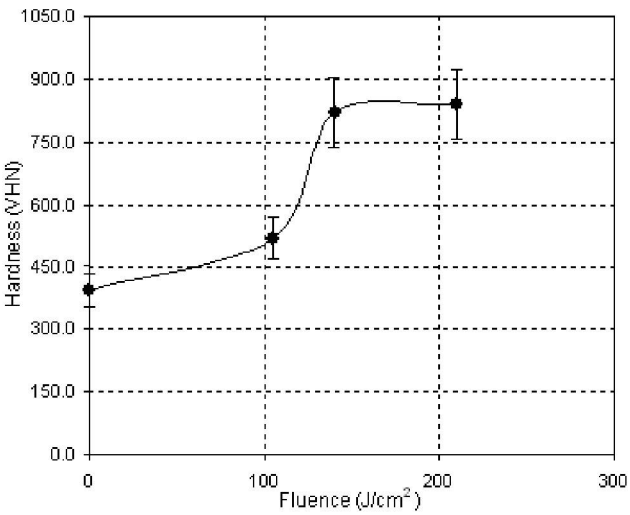

Figure 1.46. Variation of surface hardness with fluence.

Table 1.11. Surface hardness tests before and after treatment.

Sample	Microhardness (HVN)
Untreated	394
Emery 300	377
Emery 800	378
140 Jcm^{-2}	850

EDX Analysis

The experimental results of EDX spectroscopy of the untreated and treated samples in the ambient condition is given in figure 1.47. The analysis exhibited K-α lines for aluminium and titanium for both samples, though it was expected carbon to be detected too. It is seen from figure 1.48 that as the laser fluence was increased, the vanadium percent showed a decreasing trend until it reached to its maximum reduced value at about 145Jcm^{-2} where there onwards it was increased again. Perhaps from biomedical applications point of view a better and safer cell attachment and growth can be expected in above condition since surface toxicity has reduced even further.

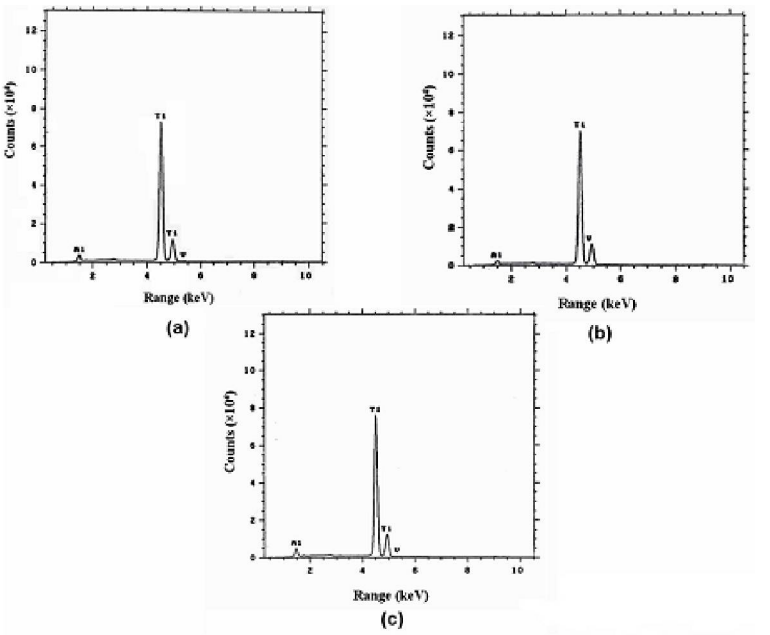

Figure 1.47. EDXA analysis of the implant surface, a) untreated b) treated at 100 Jcm^{-2} c treated at 140 Jcm^{-2}.

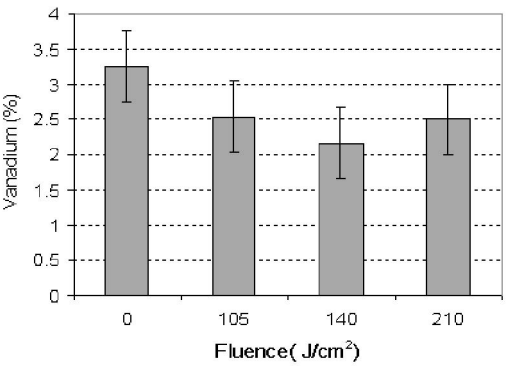

Figure 1.48. Changes of Vanadium at the alloy surface as a function of fluence.

Table 1.12 indicates the differences in surface elements after treating by laser irradiation and SiC paper finishing.

Table 1.12. Surface elements composition before and after treatment.

Element Sample	% Al	%V	%Ti
Untreated	5.15	3.25	91.6
Emery, 300 grit	5.19	3.37	91.4
Emery, 800 grit	6.05	3.35	90.6
140 Jcm^{-2}	3.96	2.54	93.5

Corrosion Test

The comparison of these curves indicates a few important points:1-a value of 1.77×10^{-3} mpy for untreated sample (Fig.1.49a), 2- the corrosion rate for laser treated specimen reduced to 0.46×10^{-3} mpy at 140 Jcm^{-2}(Fig.1.49b), 3- the corresponding corrosion rates for 300 and 800 grit SiC paper were measured as 1.8×10^{-3} and 1.79×10^{-3} mpy respectively (Figs.1.49c,d) 4- E_{corr} varied from -0.51 V to -0.21 V after the treatment at 140 Jcm^{-2} whereas for 300 and 800 grits E_{corr} was changed from -0.36V to -0.38V. This means that the laser treated specimen is placed at a higher position in the cathodic section of the curve hence releasing hydrogen easier and acts as an electron donor to electrolyte. Therefore, by smoothly reaching the passivation region, a more noble metal is expected to be achieved. The corrosion current (I_{corr}) was decreased from 2.54 μAcm^{-2} to 0.66 μAcm^{-2} after surface laser treatment while for 300 and 800 grit SiC treated samples I_{corr} were measured as 2.59 μAcm^{-2} and 2.51 μAcm^{-2} respectively which can imply a better corrosion resistance.

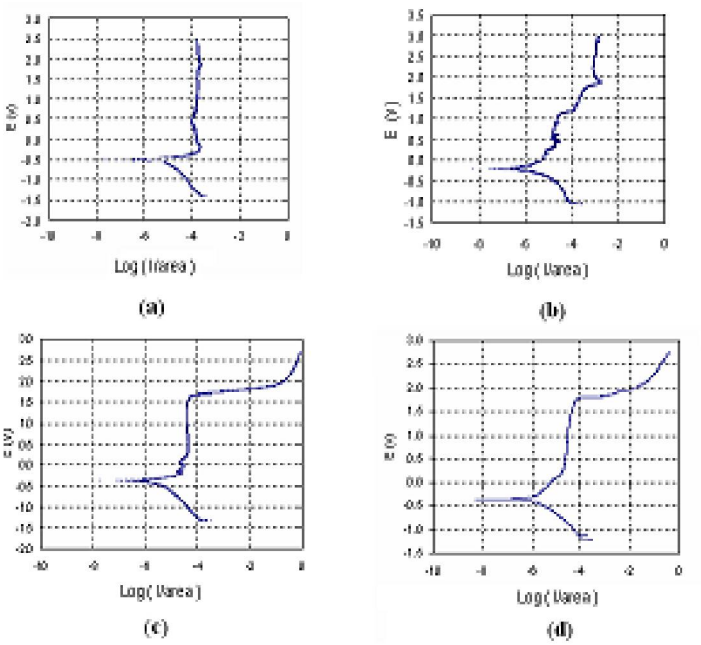

Figure 1.49. Tafel potentiodynamic polarization curves of Ti6Al4V for: (a) untreated, (b) at 140 Jcm^{-2}, (c) 300 grit, (d) 800 grit.

Surface Tension

The change in surface wettability was studied by contact angle measurement for all specimens treated at 100 Jcm^{-2}, 140 Jcm^{-2} and 300, 800 grit emery (Fig.1.50a). A smoother surface was achieved by laser radiation at 140 Jcm^{-2} which means a reduction in contact angle. This effectively implies an increase in degree of wettability of the metal surface. It is, however, important to note that a smoother surface and enhanced oxygen content, which depends on oxide layer thickness, can both help to reduce the contact angle. This is so because the surfaces with higher concentration of oxygen atoms and more incorporation of

oxygen-base polar functionalities of surface exhibit higher wettability (ie. lower contact angle) hence an improvement of biocompatibility, though some believe that, hydrophilicity alone is an inadequate promoter of cell adhesion and retention [103]. As a result, it is emphasized that a better cell adhesion can be obtained for the Specimens with apparently higher surface energy, rather than higher surface roughness.

According to primary melting centers topology, the surface roughness was increased slightly at 100 Jcm^{-2} (R_a =14.2 ± 0.29). Thus an increase of contact angle occurs from 70° to 80° indicating a lower degree of wettability. Following the laser treatment at 140 Jcm^{-2} the contact angle reduced to 37 ° showing still a more acceptable hydrophilic behaviour. Due to fine (800grit) and coarse (300grit) emery effect on the surface, the measured contact angle increased from 45° to 50° respectively.

Also, variation of surface tension for all specimens was calculated by measured contact angle. It is known that as contact angle decreases, the related surface tension will be increased. Therefore, a value of 58mN/m was obtained for γ at 140 Jcm^{-2} which is considerably higher than 39mN/m of the untreated sample. The corresponding values of γ for 100 Jcm^{-2}, 300 and 800 grit were found as 31, 46 and 50mN/m respectively (Fig. 1.50b).

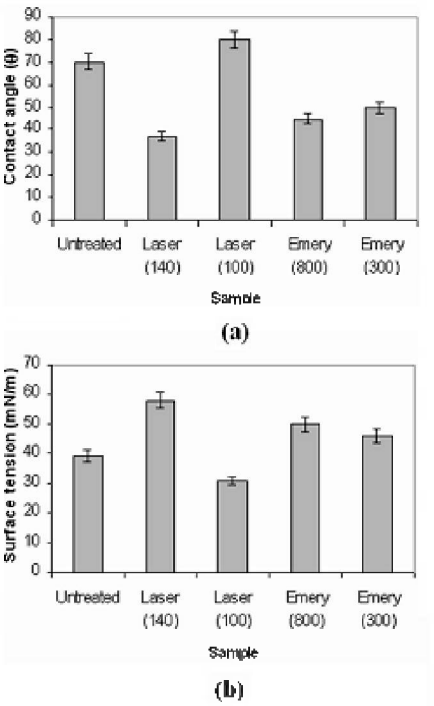

Figure 1.50. Variation of contact angle: (a) and surface tension, (b) with sample surface texture.

In Vitro

Figures 1.51a-c illustrate the morphology and the spreading of cells on the negative control, the untreated and MTS respectively and that for the LTS is shown in figures 1.51d and e. As it is observed in all cases, some of the attached cells spread radially from the centre and developed a filopodia type shape. The surface of cells which are not spread, were

convoluted in to micro ridges and the neighboring cells maintain a physical contact with one another through multiple extensions. Cell spreading is an essential function of cell adhesivity to any surface and it proceeds the proliferation until the surface is fully covered by the cellular network. Overall, the LTS results were very similar to that of the negative control where the cells growth was clearly observed in both cases. The number of cells attached to the surface was evaluated by MTT assay. More cells are attached to the surface (12×10^5) treated at 140 Jcm^{-2} than at 100 Jcm^{-2} (7×10^5). Also, the corresponding values for 300 and 800 grits SiC paper are 9×10^5 and 10×10^5 respectively which still are higher than 8×10^5 for untreated sample (table 1.13).

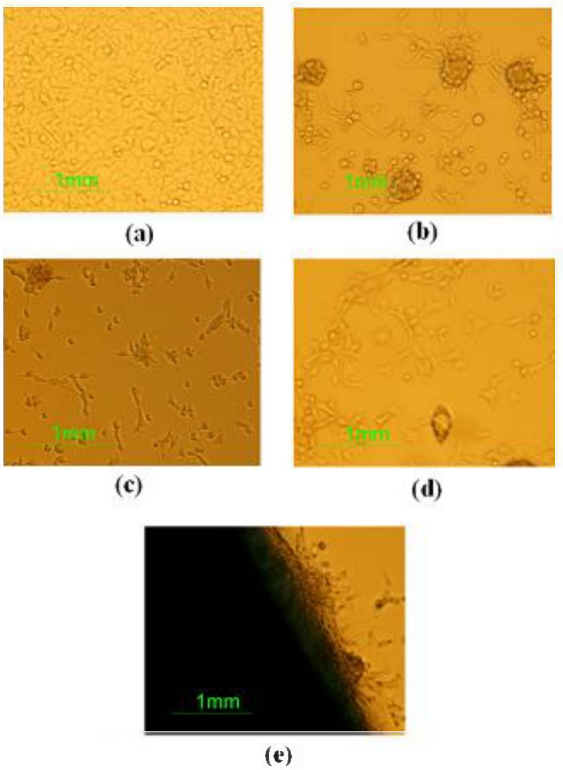

Figure 1.51. Light microscopy of cell culture evaluation (a) negative control, (b) untreated sample, (c) MTS- 800 grit , (d) LTS 140 Jcm^{-2}, (e) Laser treated of the edge at 140 Jcm^{-2}.

Table 1.13. Characterization of the surface before and after treatment.

Sample	Surface tension (mN/m)	Contact angle (θ)	Cell No. (cell/ml)
Untreated	39	70	8×10^5
100 Jcm^{-2}	31	80	7×10^5
140 Jcm^{-2}	58	37	12×10^5
Emery, 300 grit	46	50	9×10^5
Emery, 800 grit	50	45	10×10^5

In Vivo

Cell Spreading Analysis

The experimental results of bone cell growth are given in table 1.14. As it can be seen, cells spreading over the specimen surface is related to laser fluence and surface texture which was measured by Image J program software (IJP). The highest spreading area (488 μm^2) belongs to the LTS at 140 Jcm^{-2}.

Table 1.14. Bone cells spread over the surface of the implanted specimens (average of ten measurements in three separate regions).

Row	Specimens	Spread cell area (μm^2)
1	untreated	352 ± 6
2	Emery, 800 grit	383 ± 5
3	Emery, 300 grit	367± 3
4	100 (Jcm^{-2})	316± 10
5	140 (Jcm^{-2})	488 ± 8

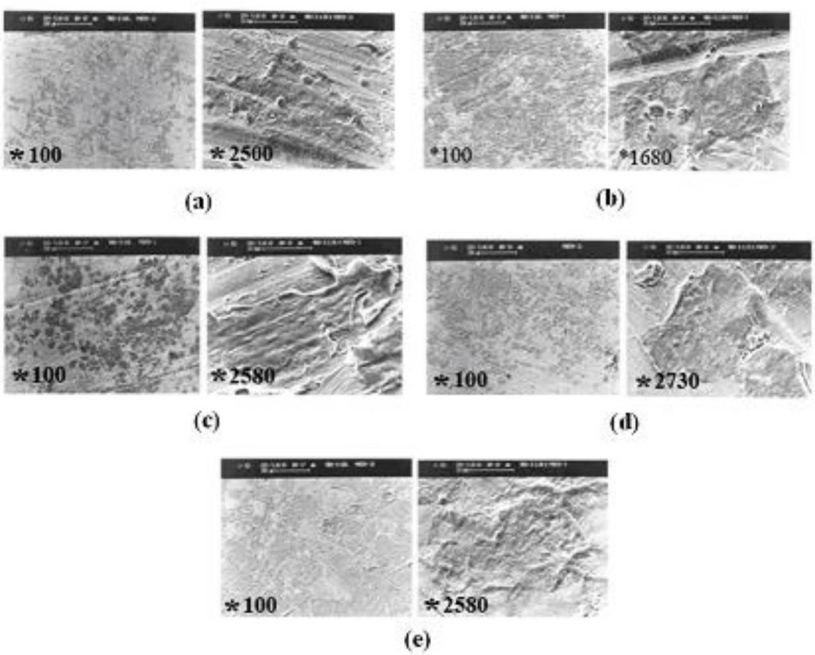

Figure 1.52. Scanning electron micrographs of attached cells on the surface for: (a) untreated, (b) 800 grit,(c) 300 grit , (d) at 100 Jcm^{-2} , (e) at 140 Jcm^{-2}.

The SEM analysis of attached cells morphology (Fig.1.52) indicates that the density of cell network is directly dependent on the laser beam fluence and surface topography. The smooth surface produced at 140 Jcm^{-2} not only caused a dense cell network but also resulted in a wider area covered by a single cell spreading. Density of network is originated from monolayer attachment (cell-surface) change to multilayer (cell-surface & cell-cell). As it is

seen no specific directional spread of attached cells was achieved in laser treated specimens. However, in emery treated surfaces, the orientation of cells was longitudinal and parallel to the lines made by SiC paper. It is observed from figure 1.52 that both the LTS and MTS have more fibroblast cells compared with the untreated sample.

Histopathology

When the implants were retrieved, no inflammatory reaction was observed inside or around the implants. Mineralized matrix deposition and bone cells were observed on the surface of implants which are formed during the five months implantation, see Fig 3a. This deposition was found all around of LTS (Fig.1.53a) and MTS (Fig.1.53b) and bone formation was characterized by the occurrence of osteocyte embedded in the matrix. Also the above samples were surrounded by fibroblast and osteoblast cells and the untreated sample (Fig.1.53c) showed not only less number of fibroblast cells, also contained osteoclast and polymorpho nuclear leukocytes (PMN).

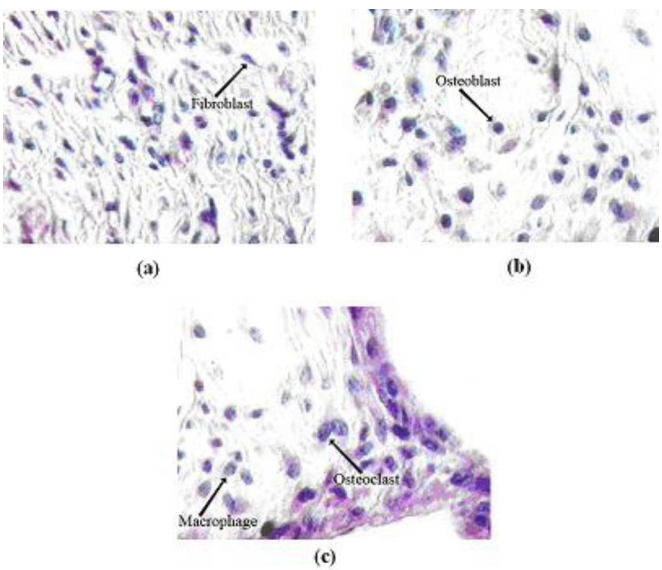

Figure 1.53. Light microscopy evaluation of bone tissue for: (a) samples laser treated at Jcm^{-2}, (b) 800 grit, (c) untreated.

As it is seen from figure1.54 the bone tissue nutrition is carried out through the channel in LTS where as it was not observed in the case of untreated sample. No PMN, giant cells and osteoclast were seen in laser treated samples at 140 Jcm^{-2}. Also tissue healing was better conducted near mentioned implant rather than all the other evaluated specimens. Fibroblast and osteoblast cells were also numerous at 140Jcm^{-2}.

In table 1.15, The symbols indicate the presence of 2-3 cells (+), 3-5 cells (++), more than 5 cells (+++) and lack of cells (-) respectively. No PMN, giant cells and osteoclast were seen in laser treated sample at 140 Jcm^{-2}. Also tissue healing was better conducted near mentioned implant rather than all other evaluated specimens. Fibroblast and osteoblast cells were also numerous in qualitative scales for 140Jcm^{-2} case.

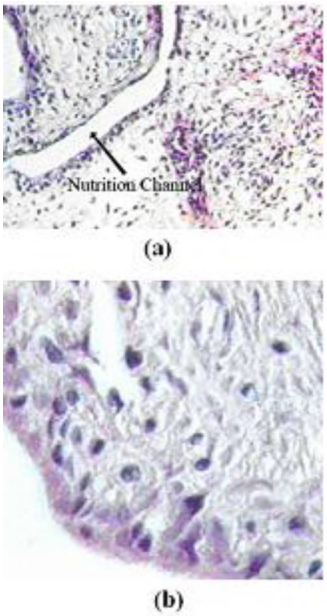

Figure 1.54. (a) Light microscopy evaluation of bone tissue for: (a) laser treated sample at 140 Jcm^{-2}, with a nutrition channel shown, and (b) untreated without the channel.

Table 1.15. Qualitative evaluation of histology results of bone tissue around the implants.

Sample Cell	100 Jcm^{-2}	140 Jcm^{-2}	Emery 800 grit	Emery 300 grit	untreated
Fibroblast	+++	+++	++	++	++
Osteoblast	++	+++	+	+	+
Giant cell	-	-	-	-	-
Osteoclast	-	-	-	-	+
PMN	+	-	-	-	+
Lymphocyte	+++	++	++	++	++
Macrophage	+++	++	+++	+++	++
Healing	+	++	+	+	+

Discussion

The successful incorporation of bone implants strongly depends on a firm longstanding adhesion of the tissue surrounding the implants. The cellular reaction is influenced by the properties of the bulk materials as well as the specifications of the surface, that is, the chemical composition and the topography [104-108]. When one is considering materials for application of orthopaedic implants, it is important to consider a number of factors, such as biocompatibility and surface wettability. The stable oxide layer formed on the implant sample is known to be responsible for the biocompatibility of metal implants. Hence, for a successful laser surface processing of materials some optical and physical parameters must be carefully optimized in order to achieve a desirable surface morphology. It is known that the modification efficiency and the quality is not only the laser fluence dependent but also depend

on the spatial and temporal profile of laser beam. Generally the energy absorbed from the laser is assumed to be converted to thermal energy which causes melting, vaporization of the molten material, dissociation or ionization of vaporized material and shock waves in the vapour and the solid. The interaction process was shown to be dependent on the laser fluence, as well as physico-chemical and optical properties of material. Usually, the deposited energy of laser irradiation is converted in to heat on time scale shorter than the pulse duration or laser interaction time. The resulting temperature profile depends on the deposited energy profile and thermal diffusion rate during laser irradiation. Thermal conductivity, K is related to k,ρ and c as follows:

$$K = k\rho c \tag{73}$$

This gives a value of $16WC^{-1}m^{-1}$ which is much larger than the optical absorption depth (≈2μm). Therefore, the heat source is essentially a surface source. As it was defined earlier the vertical distance (z_t) over which heat diffuses during the τ_p is about 7.5 mm wher z_t determines the temperature profile. The condition $\alpha^{-1} << z_t$ is typically applicable for laser irradiation of metals. In the present study, a non-adiabatic thermal evaporation was considered as the dominant mechanism during the laser-material interaction process.

A numerical simulation is performed based on date given in before section in order to evaluate the variation of the surface temperature of Ti6Al4V during the heating and cooling cycles. The fundamental Fourier heat transform describing the surface temperature T(x,t) is:

$$\rho c \frac{\partial T(x,t)}{\partial t} - k\nabla^2 T - Q(x,t) = 0 \qquad 0<x<\infty \tag{74}$$

where ∇ is laplace transform and Q is the heat source.

During heating ($t<\tau_p$), the solution is

$$T(x,t) = T_h(x,t) = \frac{I_0\alpha}{K}\left[\left(\frac{4kt}{\pi}\right)^{\frac{1}{2}} \exp\left(\frac{x^2}{4kt}\right) - xerfc\frac{x}{(4kt)^{\frac{1}{2}}}\right] + T_0 \tag{75}$$

During cooling the temperature drops for all $t>\tau_p$ and

$$T(x,t) = T_c(x,t) = \frac{I_0\alpha}{K}(4k)^{\frac{1}{2}}\left[\sqrt{t}\times ierfc\frac{x}{(4kt)^{\frac{1}{2}}} - \sqrt{t-\tau_p}\times ierfc\frac{x}{\sqrt{4k(t-\tau_p)}}\right] + T_0 \tag{76}$$

where *i* erf(x) is the integral of the complementary error function defined as

$$ierfc(x) = \int_x^\infty erfc(y)dy = \frac{1}{\sqrt{\pi}}e^{-x^2} - xerfc(x) \tag{77}$$

Equations (75) and (76) have been solven numerically using MATHCAD computer program. Figure 1.55 shows the calculated surface temperature variation with the time for the Ti6Al4V irradiated by the pulsed Nd:YAG laser.

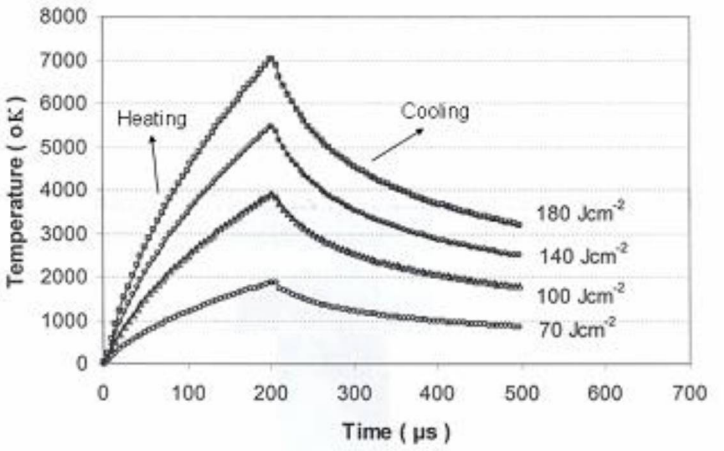

Figure 1.55. The surface temperature variation of Ti6Al4V with time.

The followings results can be calculated from the numerical simultion: (i) increasing the laser fluence, increasing the surface temperature, (ii) the numerical results indicate that the maximum temperature achieved at the end of the laser pulse in higher than experimental values of melting (≈1668°C) and vaporization (3280°C) temperatures, (iii) almost all the pulse energy at 70 Jcm^{-2} is expended to raise the surface temperature to melting point at the end of its duration (i.e., 200 μs). (iv) consequently, at high fluences, a less time is required to reach the melting point and hence the rest of available time is spent for vaporization and some thermal damage. (v) at higher fluences the temperature gradient become steeper and hence the probability of an unstable front leading to dentritics or crack increases during the cooling cycle.

Therefore, selecting a correct energy density for surface treatment has direct influence on the physical properties such as surface microhardness, corrosion resistance, wettability and surface tension of Ti6Al4V. For example, it seems uniformly accepted that any contamination has unfavorable biological effects which may catalyze oxidation, hence it may enhance the dissolution of Ti ions from implant surface. With this view, it is suggested [90] that the surface contamination decreases the surface energy of material which is responsible for the surface adsorption of proteins at molecular level.

This was also shown for surfaces treated by 800 and 300 grits SiC paper where the surface roughness increased due to machining. Secondly, the contact angle decreased by about 50 percent between 100 Jcm^{-2} and 140 Jcm^{-2} when the surface became smoother It is, however important to notice that the NCLP method cannot measure the topographic features smaller than 1μm which are often found on the roughened implant surface due to its resolving power limitation. Also, a superior microhardness value was exhibited by the sample which can be attributed to grain refinement associated with laser melting and rapid solidification.

Generally a change in the corrosion potential (E_{corr}) indicates a microstructural modification in the metal. For this purpose the Tafel potentiodynamic polarization

experiments were performed on Ti6Al4V in Hank's salt balanced physiological solution for untreated, laser treated, 300 and 800 grit SiC paper, see figure 1.49. Also, an increase of corrosion resistance by about 74% which is mainly thought to be due to removal of surface inclusions and surface micro-smoothing during the laser treatment possibly caused by the lateral flow of molten material due to surface tension. Practiclly this means that the laser treated specimen is placed at a higher position in the cathodic section of the curve hence releasing hydrogen easier and acts as an electron donor to electrolyte. Therefore, by smoothly reaching the passivation region, a more noble metal is expected to be achieved which should be more impermeable and resistant to corrosion. This effect was observed within zone III (Fig.1.39), where the surface melting was set at about $70Jcm^{-2}$. Among the possible involved mechanisms controlling the hydrodynamics of the melt region is its displacement resulting from the local pressure applied to the liquid surface as a result of the evaporation process. In this range, surface porosities and irregularities of untreated sample became almost completely sealed, figure 1.42d, and the roughness was reduced. Treatment at fluence of 140 Jcm^{-2} with 10 pulses produced optimum effects on the surface. However, at higher fluences in zone IV, even though melting and vaporization are both at work , the surface roughness mainly defined by grainy structure, meandering , cell boundaries , and the cracks were increased , figure 1.42f. This effect may be resulted from reduced thermal accumulation on the metal surface by blasting off the sealed layer hence, causing the increase of local roughness. The grains, surface cooling rate after laser treatment, heat transfer from lower or lateral metal layer and short time duration between heating and cooling cycle may all cause some changes in remaining β phase shape. In addition to surface morphology, the properties of implant materials affect cellular behavior such as wettability. The wettability of the surface plays an important role with respect to protein adsorption, cell attachment and spreading. It is known that surfaces with high surface free energy are to be more adhesive than those with a low surface free energy. In this study the values for surface free energy showed significant differences between laser treated, untreated sample and the SiC paper modified surface. The surface tension at 140 Jcm^{-2} was greater than 300 and 800 grits SiC paper and the untreated sample.

It is also worth to notice that all the samples were treated in an ambient condition and were steam sterilized which would have a great influence on surface composition of Ti especially in TiO_2 formation. It is proved that the samples irradiated by laser beam during the treatment can cause oxygen diffusion through the molten materials and thus to oxidize the titanium [109]. Also the variation of surface oxidation layer thickness depends on steam sterilization process and the time of exposure to air [110]. As the oxygen content of surface increases, the measured contact angle decreases. This is explained by the fact that surfaces with higher concentration of oxygen atoms and more incorporation of oxygen-base polar functionalities of surface exhibit higher wettability (lower contact angle). The local presence of the alloying elements Al and V within the passive oxide film is likely to influence the adsorption of proteins and their conformation on the surface which in turn is expected to modify cell-surface interaction. If cells are affected by the presence of hydroxides on the surface, then developing an understanding of the mechanisms that control this interaction could lead to the optimization of this parameter in current and future metallic biomaterials [111]. Also, other factors like surface composition, solubility degree of alloys and base metal, thermal diffusion and heating/cooling rate may have a specific role in crack formation which needs a separate attention and analysis.

The interaction of living cells with foreign materials is complicated matter, but fundamental for biology medicine and is a key for understanding the biocompatibility. The initial cellular events which take place at the biomaterials interface mimic to a certain extent the natural adhesive interaction of cells with the extra cellular matrix (ECM). The osteoblasts, which play a principal role in bone formation, readily attach to the material surfaces via adsorbed protein layer consisting or RGD containing ligands like fibronectin, vitronectin or fibrinogen. Family of cell surface receptors that provide trans- membrane links between the ECM and the cytoskeleton. The focal point in laser treated surface at 140 Jcm^{-2} should be approximately 10 nm which is convenient for bone cells to get close enough to be activated and attach to the surface in order to form an extra cellular matrix. In this state, bone cells will spread over the smooth surface much more easily and fluently.

Our study showed that surface micro grooves can affect the orientation guidance of bone cells i.e. the deeper grooves were more effective in guiding the cells as it was evaluated by SEM. However, we did not conduct or evaluate systematically the exact effects of grooves depth and size on cell orientation, but our preliminary results were similar to those reported by Xiong et.al [112].

It seems, however, that laser treated surface did not regulate the cells shape exactly similar to other investigations. The finding of most research works that the osteoblast cells grow slightly better on the rougher surface indicate the fact the surface topography indeed affects the osteoblast cell proliferation. However, our results showed that laser treated samples at 140 Jcm^{-2} produced a smoother and higher wettability characteristics than the mechanically roughend surface. This finding agrees with Hao et.al [80] and Mirhosseini [95] works where they found similar results with Ti6Al4V using diode laser. It is, believed that oxygen content of material surface can contribute to the improvement of the wettability characteristics in laser surface modification. It is also equally important from our point of view to carefully distinguish and discuss the difference between the mechanism of cell attachment on a rough surface and cell adhesivity on a smooth surface and their impacts on biomedical engineering [80,92].

Conclusion

This study was focused on the topographic effects of Ti6Al4V produced by laser radiation on goat bone cell adhesion. The results showed a common feature reported in the previous studies on a variety of cell types and substrates ie, topographic features strongly affects the cell guidance. We found a significant difference when comparing the cells behaviour on unevenly micro grooves and smooth surfaces. This study shows that a smooth surface can exhibit more cell adhesivity compared with micro grooved surface due to its increase of surface tension and reduction of contact angle and probably the presence of oxygen content at the surface. The test confirmed that the highest number of cells are attached to the LTS at 140 Jcm^{-2}. It is also concluded from the SEM, contact angle measurements and preliminary i*n vitro* and *in vivo* tests that Nd:YAG laser can induce a desirable surface modification on Ti6Al4V alloy for cell adhesivity and that a noble and biocompatible Ti alloy with better physico–chemical properties can be obtained under suitably defined optical condition. Finally it is suggested that more detailed experiments are required and would be useful to distinguish and clarify the difference between attachment on the rough surface via

physical anchoring and adhesion on smooth surface by chemical binding. Also, the relation between the grooves size and their orientation must be studied more carefully with respect to cell attachment and their reliability as well as endurance.

References

[1] Branemark, P.I., Hansson, B.O., Adell, R. & et al. (1977). Osseointegrated implants in the treatment of the edentulous *jaw. Scand. J. Plastic recounst. Surg. Suppl.*, **16**, 1-116.

[2] Kazatchkine, M.D. & Carreno, M.P. (1988). Activation of the complement system at the interface between blood and artificial surfaces. *Biomaterials, (Ibid),* **9**, 30-35.

[3] Ziats, N.P., Miller, K.M. & Anderson, J.M. (1988). In vitro and in vivo interactions of cells with biomaterials. *Biomaterials, (Ibid)* ,**9**, 5-13.

[4] Hynes, R.O. (2002). Integrins: bidirectional, allosteric signaling machines. *Cell*, **110**, 673- 687.

[5] Geiger, B. & Bershadsky, A. (2001). Assembly and mechanosensory function of focal contacts. *Curr. Opin. Cell Biol.,* **13**, 584-592.

[6] Shay-Salit, A., Shushy, M., Wolfovitz, E., Yahav, H., Breviatrio, F., Dejana, E. & Resnick, N. (2002). VEGF receptor 2 and the adherencs junction as a mechanical transducer in vascular endothelial cells. *Proc, Natl, Acad, Sci U.S.A.*, **99**, 9462-9467.

[7] Yap, A.S. & Kovacs, E.M. (2003). Direct cadherin – activated cell signaling: a view from the plasma membrane. *J. Cell Biol.,* **160**, 11-16.

[8] Zhu, X. & Assoian, R. K. (1995). Integrin-dependent activation of MAP kinase: a link to shape-dependent cell proliferation. *Mol. Biol. Cell*, **6**, 273-282.

[9] Neff, J.A., Tresco, P.A. & Caldwell, K.D. (1999). Surface modification for controlled studies of cell-ligand interactions. *Biomaterials*, **20**, 2377-2393.

[10] Juliano, D.J., Saaedra, S. S. & Truskey, G.A. (1993). Effect of the conformation orientation of adsorbed fibronectin on endothelial cell spreading and the strength of adhesion. *J. Biomed Mater. Res.*, **27**, 1103-1113.

[11] Yamada, K. (1991). Adhesive recognition sequences. *J. Biol. Chem.*,**266**, 12809-12812.

[12] Pierschbacher, M.D. & Ruoslahi, E. (1984). Cell attachment activity of fibronectin can be duplicated by small synthetic fragments of the molecule. *Nature*, **309**, 30-33.

[13] Ruoslahi, E. & Pierschbacher, M.D. (1987). New perspectives in cell adhesion: RGD and integrins. *Science*, **238**, 491-497.

[14] Ruoslahi, E. (1991). Integrins. *J. Clin Invest*, **87**, 1-5.

[15] Feng, B., Weng, J., Yang, B.C., Qu, S.X. & Zhang, X.D. (2003). Characterization of surface oxide films on titanium and adhesion of osteoblast. *Biomaterials*, **24**, 4663-4670.

[16] Puleo, D.A., Holleran, L.A., Doremus, R.H. & Bizios, R. (1989). Osteoblast responses to orthopaedic implant materials in vivo. *J. Biomed. Mater. Res.*, **25**, 11- 23.

[17] Albrektsson, T., Branemark, P.I., Hansson, B.O. & Lindstrom, J. (1981). Osseointegrated titanium implants. *Acta Orthop. Scand*, **52**, 155-170.

[18] Beraceras, I., Alava, I., Onate, J.I. & Maezto, M.A. (2002). Improved osseointegration in ion implantation-treated dental implants. *Surf. & Coat. Tech.*, 158-159, 28-36.

[19] Khosroshahi, M.E., Mahmoodi, M. & Tavakoli, J. (2007). Characterization of Ti-6Al-4V implant surface treated by Nd:YAG laser and emery paper for orthopaedic applications. *Applied surface science*, **253**, 8772-8781.

[20] Deppe, H. , Warmuth, S., Heinrich, A. & Korner, T. (2005). Laser- assisted three dimensional surface modifications of titanium implants: preliminary data. *Laser in Medical Sc.*, **19**, 229-233.

[21] Malaval, L., Chenu, C. & Delmas, P.D. (1996). *Proteins, de ios. Maladies metaboliques osseuses de iadulte*. Kuntz, D., editors. Paris: Flammarion Medecine Science, 17-35.

[22] Grzesik, W.J. & Robey, P. G.(1994). Bone matrix RGD glycoproteins: Immunolocalization and interaction with human primary osteoblast bone cells in vitro. *J. Bone Miner. Res.*, **9**, 487- 496.

[23] Ducheyne, P. & El-Ghannam, A. (1994). Effect of bioactive glass templates on osteoblast proliferation and in vitro synthesis of bone-like tissue. *J. Cell Biochem.*, **56**, 162-167.

[24] Kelly, R.G., Schully, J.R. & Shoesmith, D.W. (2003*). Electrochemical Techniques in Corrosion Science and Engineering*. New York:Marcel Dekker Inc., 81,240.

[25] Wang, X.X., Yan, W., Hayakawa, S., Tsuru, K. & Osaka, A. (2003). Apatite deposition on thermally and anodically oxidized titanium surfaces in a simulated body fluid. *Biomaterials*, **24**, 4631-4631.

[26] Hsu, R., Yang, C., Huang, C. & Chen, Y. (2004). Electrochemical corrosion properties of Ti-6Al-4V implant alloy in the biological environment. *Mat. Sci. Eng. A*, **380**, 100-109.

[27] Tian, Y.S, Chen, C.Z., Lee, S.T. & Huo, Q.H. (2005). Research progress on laser surface modification of titanium alloys. *Appl. Surf. Sci..*, **242**, 177-184.

[28] Wang, Y.B. & Zheng, Y.F. (2009). Corrosion behaviour and biocompatibility evalution of low modulus Ti-16Nb shape memory alloy as potential biomaterial. *Material Letters*, **63**, 1293-1295.

[29] Tirrell, M., Kokkoli, E. & Biesalski, M. (2002). The role of surface science in bioengineered materials. *Surf. Sci.*, **500**, 61-63.

[30] Anselme, K., Linez, P., Bigeralle, M., Maguer, D.L. Maguer, A.L., Hardouin, P., Hildebrand, H.F., Iost, A. & Leroy, J. M. (2000). The relative influence of the topography and chemistry of Ti-6A1-4V surfaces on osteoblastic cell behavior. *Biomaterials*, **21**, 1567-1577.

[31] Davies, J.E. (1996). In vitro modeling of the bone implant interface. *Anatomical Recorded*, **245**, 426- 445.

[32] Thomas, C.H., McFarland, C.D., Jenkins, M.L. & Rezania, A. (1997). The role of vitronectin in the attachment and spatial distribution of bone-drived cells on materials with patterned surface chemistry. *J. Bomed. Mater. Res.*, **37**, 81- 93.

[33] Cooper, L. F., Masuda, T., Yliheikkila, P.K. & Felton, D. A. (1998). Generolization regarding the process and phenomena of osseointegration, *part II. Int. J. Oral Maxillofac. Implants*, **13**, 163 -174.

[34] Masuda, T., Yliheikkila, P.K., Felton, D.A. & Cooper, L.F.(1998). Generolization regarding the process and phenomena of osseointegration: in vivo studies, *part I. Int. J. Oral Maxillofac. Implants*, **13**, 17- 29.

[35] Meyer, U., Szulezewsli, D.H., Moller, K., Heide, K. & Jones, D.B. (1993). Attachment kinetics and differentiation of osteoblasts on different biomaterial surfaces. *Cells Mater.*, **3**, 129-140.

[36] Khosroshahi, M.E., Tavakoli, J. & Mahmoodi, M. (2007*)*. Analysis of bioadhesivity of osteoblast on titanium by Nd:YAG laser. *J. of Adhesion*, **83**, 151-172.

[37] Khosroshahi, M.E., Mahmoodi, M., Saedinasab, H. & Tahriri, M. (2008). Evaluation of mechanical and electrochemical properties of laser surface modified Ti-6AL-4V for biomedical application: in vitro study. *Surface Engineering*, **24**, 209-218.

[38] Khosroshahi, M.E., Mahmoodi, M. and Tavakoli, J. & Tahriri, M. (2008). Effect of Nd: YAG laser radiation on Ti6AL4V alloy properties for biomedical application. *J. of Laser Applications*, **20**, 209-217.

[39] Khosroshahi, M.E., Mahmoodi, M. & Saedinasab, H. (2009). In vitro and in vivo studies of osteoblast cell response to a Ti6A14V surface modified by Nd:YAG laser and silicon carbide paper. *Laser Med. Sci, Dol* 10001007/s 10103-008-0628-1.

[40] Albrektsson, T. & Johansson, C. (2001*)*. Osteoinduction, osteoconduction and osseointegration. *Eur. Spine. J.,* **10**, 96-101.

[41] Buchter, A., Kleinheinz, J., Wiesman, H.P., Kersken, J., Nienkemper, M., Weyhrother, H., Joos, U. & Meyer, U. (2005). Biological and biomechanical evaluation of bone remodeling and implant stability after using an ostetome technique. *Clin. Oral Implants Res.*, **1**, 1-8.

[42] Buchter, A., Joos, U., Wiessman, H.P., Seper, L. & Meyer, U. (2006). Biological and biomechanical evaluation of interface reaction at conical screw-type implant. *Head and Face Med.,* **2**, 5-18.

[43] Chung, T., Liu, D. & Wang, S. (2003). Enhancement of the growth of human endothelial cells by surface roughness at nanometer scale. *Biomaterials*, **24**, 4655-4661.

[44] Bigerelle, M. & Anselme, K. (2005). Bootstrap analysis of the relation between initial adhesive events and long-term cellular functions of human osteoblasts cultured on biocompatible metallic substrates. *Acta biomaterialia*,**1**, 499-510.

[45] Cheroudi, B., Soorany, E., Black, N. & Weston, L. (1995). Computer-assisted 3D reconstruction of epithelial cells attached to percutaneous implant. *J. Biomed. Mater. Res.*, **29**, 371-379.

[46] Curtis, A.S. & Wilkinson, C.D. (1998). Reaction of cells to topography. *J. Biomat. Sci. Polymer Ed.*, **9**, 1311-1324.

[47] Brunette, D.M. & Cheroudi, B. (1999). The effect of topography of micromachined titanium substrate on cell behavior in vitro and invivo. *J. Biomech. Eng.*, **121**, 49-57.

[48] Lavose-Valereto, I.C., Wolynec, S., Deboni, M.C. & Konig, B.J.R. (2001). In vitro and in vivo biocompatibility testing of Ti-6Al-7Nb alloy with and without plasma- sprayed hydroxyapatite coating. *J. Biomed. Mater. Res.*, **58**, 727-733.

[49] Curtis, A.S. & Clark, P. (2001*). The effect of topographic and mechanical properties of materials on cell behavior. Crit. Rev. Biocompat.* **9**, 1313-1329.

[50] Sowden, D. & Schmitz, J.P. (2002). Self-drilling and self-tapping screws in rat bone: an ultra structural study of the implant interface. *J. Oral Maxillofac Surg.*, **60**, 294-299.

[51] Heinrich, A., Dengler, K., Koerner, T. Haczek, C., Deppe, H. & Stritzker, B. (2008). Laser- modified titanium implants for improved cell adhesion. *Laser in Medical science*, **23**, 5-58.

[52] Sighvi, R. & Wang, D.I. (1998). Review: Effects of substratum morphology on cell physiology. *Biotech. Bioeng.*, **43**, 764-771.

[53] Burser, D. & Schenk, R.K. (1991). Influence of surface characteristics on bone integration of titanium implants. A histomorphometric study in miniature pigs. *J. Biomed. Mat. Res.*, **25**, 889-902.

[54] Breme, H. J. & Helsen, J.A. (1998). *Metals as Biomaterials*, West Sussex:wiley, 30-70.

[55] Sikavitsas, V.I., Temenoff, J.S. & Mikos, A.G. (2001). Biomaterials and bone mechano transduction. *Biomaterials*, **22**, 2581-2593.

[56] Sun, R.L., Mao, J.F. & Yang, D.Z. (2001). Microstructural characterization of NiCr, BSiC, laser clad layer on titanium alloy substrate. *Surf. & Coat. Technol.*,**150**, 199-204.

[57] Ronold, H.J. & Ellingsen, J.E. (2002). Effect of micro-roughness produced by TiO2 blasting-tensile testing of bone attachment by using coin shaped. *Biomaterials*, **23**, 4211-219.

[58] Ronold, H.J. & Ellingsen, J.E. (2002). The use of a coin shaped implant for direct insitu measurment of attachment strenght for osseointegrating biomaterials surface. *Biomaterials*, **23**, 2201- 2209.

[59] Ronold, H.J., Lyngstadaas, S.P. & Ellingsen, J.E. (2003*).* A study on the effect of dual blasting with TiO_2 on titanium implant surfaces on functional attachment in bone. *J. Biomed. Mater. Res.*, **67A**, 524-530.

[60] Tan, L., Dodd, R. & Crane, W. (2003). Corrosion and wear- corrosion behaviour of NiTi modified by plasma source ion implatation. *Biomaterials*, **24**, 3931- 3939.

[61] Assmann, W., Schubert, M., Held, A., Pichler, A., Chill, A., Kiermaier, S.,Schlösser, K., Busch, H., Schenk, K. & Streufert, D. (2007). Biodegradable radioactive implants for glaucoma filtering surgery produced by ion implantation. *Nucl. Inst. & Methods. in phys. Res. Sec.B*, **257**,108-113.

[62] Vercaigne, S., Wolk, J. & Jansen, J. (1998). The effect of titanium plasma-sprayed implants on trabecular bone healing in the goat. *Biomaterials*, **19**, 1093-1099.

[63] Ong, J.L., Raikar, G.N. & Smoot, T.M. (1997). Properties of calcium phosphate coating before and after exposure to simulated biological fluid. *Biomaterials*, **18**, 1271-1275.

[64] Toth, C., Szobo, G., Kovacs, L., Vargha, K., Barabas, J. & Nemeth, Z. (2002). Titanium implants with oxidized surfaces: the background and long–term results. *Smart Mater. Stru.*, **11**, 813-818.

[65] Morra, M., Cassinelli, C., Cascardo, G., Cahalan, P., Cahalan, L., Fini, M. & Giardion, R. (2003). Surface engineering of titanium by collagen immobilization. Surface characterization and in vitro and in vivo studies. *Biomaterials*, **24**, 4639- 4654.

[66] Tian, Y.S., Chen, C.Z., Yue, T.M. & Wang, Z.L. (2004). Study on microstructures and mechanical properties of in-situ formed multiphase coating by laser cladding of titanium alloy with silicon and graphite powder. *Chin. J. Laser*, **31**, 1-12.

[67] Eisenbarth, E., Velten, D. & Breme, J.(2007). Biomimetic implant coatings. *Biomolecul. Eng.*, **24**, 27-32.

[68] Darvell, B.W., Samman, N & Luk, W.K. (1995). Contamination of titanium casting by aluminium oxid blasting. *J. Detistry*, **23**, 319-322.

[69] Kawaura, H., Kawahara, H.O., Nishino, K. & Saito, T. (2002). New surface treatment using shot blast for improving oxidation resistance of Ti-6Al-4V base alloys. *Mate. Sci. & Eng. A,* 329-331, 589-595.

[70] Aparicio, C., Javier, F., Fonceca, C., Barbosa, M. & planell, J. A. (2003). Corrosion behavior of commercially pure titanium shot blasted with different material and sizes of shot particles for dental implant applications. *Biomaterials*, **24**, 263-273.

[71] Sahin, Y. & Sur, G. (2004). The effect of Al_2O_3 ,TiN and Ti (C,N) based CVD coating on tool wear in maching metal. Surface & Coating, **179**, 349-355.

[72] Khor, K.A., Vreeling, A., Dong, Z.L. & Cheang, P. (1999). Laser treatment of plasma sprayed HA coatings. *Mater. Sci. Eng. A*, **266**, 1-8.

[73] Yang, Y.C. & Change, E. (2001). Influence of residual stress on bonding strength and fracture of plasma–sprayed hydroxyapatite coatings on Ti-6AL-4V substrate. *Biomaterials*, **22**, 1827-1836.

[74] Galvanetto, E. Galliano, F.P., Fassati, A. & Borgioli, F. (2002). Corrosion resistance properties of plasma nitrided Ti-6AL-4V alloy in hydrochloric acid *solutions. Corrosion science*, **44**, 1593-1606.

[75] Venugopalan, R., Weimer, J.J., George, M.A. & Lucas, L. C. (2000*).* The effect of nitrogen diffusion hardening on the surface chemistry and scratch resistance of Ti-6AL-4V alloy. *Biomaterials*, **21**, 1669-1677.

[76] Gaggl, A., Schultes, G., Muller, W.D. & Karcher, H. (2000). Scaning electron mircroscopical analysis of laser–treated titanium implant surfaces–acomparative study. *Biomaterials*, **21**, 1067-1073.

[77] Wang, J. T., Weng, C. & Chang, J.G. (2000). The influence of temperature and surface conditions on surface absorptivity in laser surface treatment. *J. of Appl physics*, **87**, 3245-3253.

[78] Fancsaly, A. J., Divinyi, T. , Fazekas, A., Daroczi, C.S. & karacs, A. (2002). Pulsed laser–induced micro and nanosized morphology and composition of titanium dental implants. *Smart Mater. Struct.*, **11**, 819-824.

[79] Hollander, D., Walter, M., Wirtz, T., Paar, O. & Eril, H. (2005). Structural mechanical and in vitro characterization of individually structured Ti-6Al-4V produced by direct laser forming. *Biomaterials*, **27**, 955-963.

[80] Hao, L., Lawerence, J. & Li, L. (2005). The wettability modification of bio-grade stainless steel in contact with simulated physiological liquids by the means of laser irradiation. *Appl. Sur. Sci.,* **247**, 453-457.

[81] Tritca, S., Gakovic, M., Nenadovic, M. & Mitrovic, M. (2001) Surface modification of stainless steel by TEA CO_2 laser. *Appl. Sur. Sci.*, **177**, 48-57.

[82] Ghoo, B.Y., Keum, Y.T. & Kim, Y.S. (2001). Evaluation of the mechanical properties of welded metal in tailored steel sheet welded by CO_2 laser. *J. Mater. Proce. Tech.*, **113**, 692-698.

[83] Deka, B., Dyer, P.E. & Sayers, J. (1980). *Investigation of laser supported detonation waves and thermal coupling 2.8 μm laser irradiated metal targets. J. De Physique*, **41**, C9-75.

[84] Khosroshahi, M.E., Valanejad, A. & Tavakoli, J. (2004). Evaluation of mid-IR laser radiation effect on 316L stainless steel corrosion resistance in physiological solution. *Amirkabir J. of Sci. & Tech.*,**15**, 107-115.

[85] Peyer, P., Scherpereel, X., Berthe, L., Carboni, C., Fabbro, R. & Lemaitre, C. (2000). Surface modification induced in 316L steel by laser peening and shot- peening: Influence of pitting corrosion. *Mat. Sci. Eng.*, **280**, 294-302.

[86] Yang, J., Lian, J., Dong, Q. & Guo, Z. (2004). Nano structured films formed on the AlSi 329 stainless steel by Nd:YAG pulsed laser irradiation. *Appl. Surf. Sci*. **229**, 2-8.

[87] Trtica, M.S., Radak, B.B. Gakovic, B. M., Milovanovic, D.S., Batani, D. & Desai, T. (2009). Surface modifications of Ti6A14V by a picosecond Nd:YAG Laser. *Laser and particle Beams*, **27**, 85-90.

[88] Slocombe, A., Taufik, A. & Li, L. (2000). Diod laser ablation machining of 316L stainless steel powder/polymer composite material: effect of powder geometery. *Appl. Surf. Sci.*, **168**, 17-20.

[89] Majumdar, J.D., Pinkerton, A., Liu, Z. & Manna, I. (2005). Microstructure characterisation and process optimization of laser assisted rapid fabrication of 316L stainless steel. *Appl. Surf. Sci.*, **247**, 320- 373.

[90] Joob-Fancsaly, A., Divinyi, T., Fazekas, A., Daroczi, C.S., Karacs, A. & Peto, G. (2002). Pulsed laser-induced micro- and nanosized morphology and composition of titanium dental implants. *Smart. Mater. Struct.*, **11**, 819-824.

[91] Tritca, M.S., Tarasenko, V., Gakovic, B. & Fedenev, A. (2005). Surface modification of TiN coating by pulsed TEA CO_2 and XeCl lasers. *Appl. Sur. Sci.*, **252**, 474-482.

[92] Hao, L., Lawerence, J. & Li, L. (2005). Manipulation of the osteoblast response to a Ti-6Al-4V titanium alloy using a high power diode laser. *Appl. Sur. Sci.*, **247**, 602-606.

[93] Arisu, H..D., Turkoz, E. & Bala, O. (2006). Effects of Nd:YAG laser irradiation on osteoblast cell cultures. *Laser in Medical Sci.*, **21**, 175-180.

[94] Turner, M.W., Crouse, P.L. & Li, L.(2007). Comparative interaction mechanisms for different laser systems with selected materials on titanium alloys. *Appl. Sur. Sci.*, **253**, 7992-7997.

[95] Mirhosseini, N., Crouse, P.L., Schmidth, M.J.J. & Garrod, D. (2007). Laser surface micro- texturing of Ti-6Al4V substrates for improved cell integration. *Appl. Sur. Sci.*, **253**, 7738-7743.

[96] Wieland, M., Textor, M., Spencer, N.D. & Brunette, D.M. (2001). Wavelength-roughness: a quantitative approach to characterizing the topography of rough titanium surfaces. *Int J Oral Maxilloface Impl*, **16**(2), 163-181.

[97] Srinivassan, R., Braran, B. & Casey, K. (1990). Nature of "incubation pulse" in the ultraviolet laser ablation of polymethyl methacrylate. *J. Appl. Phys.*, **68**, 1842-1847.

[98] Dyer, P.E. & Karnakis, D. (1994). Analysis of UV radiation transport in polymers exhibiting one-photon incubated absorption. *Appl. Phys. A*, **59**, 275-279.

[99] Ifflander, R. (2001). *Solid State lasers for Materials Processing*. Berlin, Springer series in optical sciences.

[100] Dreyfus, R.W. (1992). *Comparison of the ablation of dielectrics and metals at high and low laser Powers.* In: Fogarassy, E and Lazare, S(eds). Laser Ablation of elrctronic materials. NewYork Elsevier science, 61-68.

[101] Majumdar, J.D. & Manna, I. (2003). Laser processing of materials. *Sadhana J,*. **28**, 495-562.

[102] Fan, Y, Chen, P., Yao, Y.L., Yang, Z & Egland, K. (2005). Effect of phase transformations on laser forming of Ti-6Al-4V alloy. *J. of Appl. Phys.*, **98**, 1-10 .

[103] Baier, R.E, Meyer, A.E., Natiella, J.R., Natiella R.R. & Carter, J.M. (1984). Surface properties determine bioadhesive out comes: methods and results. *J. Biomed. Mater. Res.*, **18**, 337-355.

[104] Birte, G.S., Neubert, A., Hopp, M., Griepentrog, M. & Lange, K.P. (2003). Fibroblast growth on surface modified dental implants: An in vitro study. *J. Biomed. Mater. Res.* **64A**, 591-599.

[105] Sikavitsas, V.I., Dolder, J., Bancroft, G. & Jansen, J. (2003). Influence of the in vitro culture period on the in vivo performance of cell/titanium bone tissue- engineered constructs using a rat cranial size defect model. *J. Biomed. Mater. Res.,* **67A**, 944-951.

[106] Fischer, P., Leber, H., Romano, V., Webber, H.P. & Glardon, R. (2004). Microstructure of near-infrared pulsed laser dintered titanium samples. *Appl. Phys. A,* **A78**, 1219-1227.

[107] Peto, G., Karacs, A., Paszti, Z., Guczi, L., Diviny, T. & Joob, A. (2002). Surface treatment of screw shaped titanium dental implants by high intensity laser pulses. *Appl. Sur. Sci.,* **186**, 7-13.

[108] Gyorgy, E., Mihailesco, I.N., Serra, P. & Morenza, J.L. (2002). Single pulse Nd:YAG laser irradiation of titanium: influence of laser intensity on surface morphology. *Surf. & Coating Tech.* **154**, 63-67.

[109] Perez del Pino, A., Serra, P. & Morenzo, J.L. (2002). Oxidation of titanium through Nd:YAG laser irradiation. *Appl. Sur. Sci.*, **8129**, 1-4.

[110] Sitting, C., Textor, M., Spencer, N.D., Wieland, M. & Vallotton, H. (2000). Surface characterization of implant materials c.pTi, Ti-6Al-4V band Ti-6Al-4V with different pretreatments. *J. of Mater. Sci.,* **10**, 35-46.

[111] Bern, L., English, L., Fogarty, J., Policoro, R., Zsidi, A., Vance, J., Drelich, J., White, C., Dunahu, S. & Rohly, K. (2004). Effect of surface characteristics of metallic biomaterials on interaction with osteoblast cells. *7th World Biomat. Cong.*, 1121-1122.

[112] Xiong, L. & Yang, L. (2003). Quantitative analysis of osteoblast behavior on microgrooved hydroxyapatite and titanium substrata. *J. Biomed. Mater. Res.,* **66A**, 677-687.

[113] *Oshea, D.C., Callen, W.& Rhodes, W. (1968). Intraduction to lasers and their applications. Addision-Wesley publishing.*

In: Titanium Alloys: Preparation, Properties and Applications ISBN: 978-1-60876-151-7
Editor: Pedro N. Sanchez, pp. 101-141

Chapter 2

NONDESTRUCTIVE EVALUATION OF MATERIAL IMPERFECTIONS IN A TITANIUM ALLOY

Hector Carreon
Instituto de Investigaciones Metalúrgicas, Edif."U" Ciudad Universitaria,
Morelia, Mich. México 58000-888

Abstract

This research work was aimed at developing a novel noncontacting thermoelectric method for nondestructive detection of material imperfections in metals. The method is based on magnetic sensing of local thermoelectric currents around imperfections when a temperature gradient is established throughout a conducting specimen by external heating and cooling. The surrounding intact material serves as the reference electrode therefore the detection sensitivity could be very high if a sufficiently sensitive magnetometer is used in the measurements. This self-referencing, noncontacting, nondestructive inspection technique offers the following distinct advantages over conventional methods: high sensitivity to subtle variations in material properties, unique insensitivity to the size, shape, and other geometrical features of the specimen, noncontacting nature with a substantial stand-off distance, and the ability to probe relatively deep into the material.

We have successfully adapted the noncontacting thermoelectric method to a series of nondestructive materials characterization applications that are currently not accessible by any other known inspection method. In particular, we studied experimentally the effect of the background signature produced by the intrinsic anisotropy and inhomogeneity in a titanium alloy by comparing an analytical model capable of quantitatively predicting the resulting thermoelectric signature. In addition, we studied the feasibility of nondestructive detection and characterization of the level of plastic deformation in Ti-6Al-4V by thermoelectric potential (TEP) measurements that have undergone thermo-mechanical process such as cold working. Building on the extensive and very promising results of this research work, it will be possible to develop numerous new NDT techniques that will find application in energy production (nuclear, oil, and gas industries, power generators, etc.), material manufacturing (aluminum, steel, titanium, nickel-base super-alloys, etc.), and in the transportation industry (aerospace, automobile, etc.).

1. Introduction

In general the conventional thermoelectric technique monitoring the thermoelectric power of conductive materials, is sensitive to small changes caused by material imperfections. In order to apply the thermoelectric technique for QNDE material characterization, a conductor with well-defined properties (reference probe) and a known temperature difference along it, is used to evaluate the properties given by changes in the thermoelectric power of a second conductor (test sample). However, several parameters can affect these changes in the thermoelectric power of the test sample. The most important parameters affecting the thermoelectric measurements are those associated with volumetric and contact effects [1]. The volumetric effect is related to the thermoelectricity phenomena by the electrons diffusion kinetics throughout the material. This effect is mainly affected by the chemical composition, heat treatment, anisotropy, hardening, texture, residual stress, and fatigue of the material. The contact effects are related to the non-homogeneous contact between the test sample and the reference probe, amount of pressure applied to the probe, temperature of hot and cold junctions and probe material.

On the other hand, the new noncontacting thermoelectric method uses the surrounding intact material as the reference probe providing perfect interface between the region to be tested and the surrounding material. In the self-referencing thermoelectric method the material imperfections naturally form thermocouples in the specimen itself and, in the presence of an externally induced temperature gradient, these thermocouples produce thermoelectric currents around the imperfections that can be detected bias the magnetic flux density B by magnetic sensors from a significant lift-off distance between the tip of the sensor and the material surface imperfection. This is true even when the material imperfections are rather deep below the surface. It is also well known that the noncontacting thermoelectric technique is very sensitive to the presence of foreign body inclusions, when the thermoelectric power of the affected region is significantly different from that of the surrounding medium [2-6]. Figure 1 shows a schematic diagram of the noncontacting thermoelectric measurements process in the presence of material imperfections commonly used in nondestructive materials characterization.

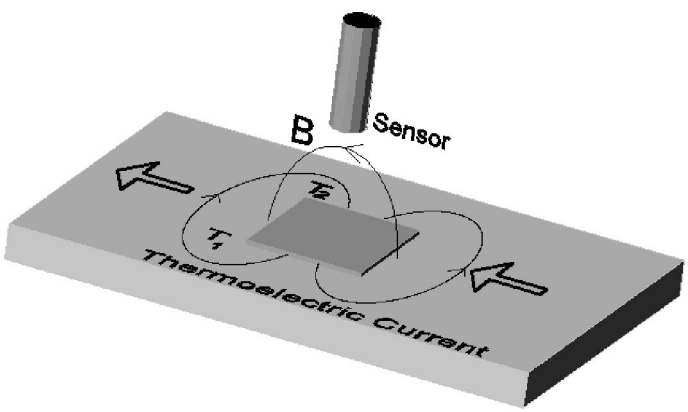

Figure 1. A schematic diagram of noncontacting thermoelectric detection of material imperfections by magnetic monitoring.

In this research work, we have successfully adapted the noncontacting thermoelectric method to a series of nondestructive materials characterization applications that are currently not accessible by any other known inspection method. In particular, we studied experimentally the effect of the background signature produced by the intrinsic anisotropy and inhomogeneity in a titanium alloy by comparing an analytical model capable of quantitatively predicting the resulting thermoelectric signature. In addition, we studied the feasibility of nondestructive detection and characterization of the level of plastic deformation in Ti-6Al-4V by thermoelectric potential (TEP) measurements that have undergone thermo-mechanical process such as cold working

2. Thermoelectric Background Signature Produced by Anisotropic Materials

Recently, Nagy and Nayfeh developed an analytical model to predict the magnetic field produced by thermoelectric currents around surface-breaking and subsurface spherical inclusions in a homogeneous host material under external thermal excitation [7]. These predictions were subsequently experimentally verified using spherical tin inclusions of varying diameter in copper [8,9]. These experiments also revealed that the detectability of small inclusions and subtle imperfections by this novel method is ultimately limited by the intrinsic thermoelectric anisotropy and inhomogeneity of the material to be inspected. The probability of detection (POD) of a given material flaw is determined by the resulting signal-to-noise ratio rather than by the absolute magnitude of the signal itself. With the exceptions of a few special cases, most sensors used in NDE are not limited by temporally incoherent electrical noise but rather by temporally coherent material noise that cannot be eliminated by time-averaging. Strictly speaking, material "noise" is really unwanted background "signal" that is called noise only because it interferes with, and often conceals, the flaw signal to be detected. This material signature is usually produced by macrostructural features, such as heat-affected, work-hardened, strained, and textured regions.

2.1. Fretting Damage

Let us consider an example of how this material signature could limit the detectability of weak imperfections by the thermoelectric method. Let us consider the characterization of weak surface and near-surface imperfections caused by localized plastic deformation that is usually very difficult to detect by conventional NDE methods because they are effectively hidden by the accompanying surface roughness. A good example is the characterization of near-surface material damage on fretted Ti-6A1-4V specimens. Fretting is wear that occurs when cyclic loading, such as vibration, causes two surfaces in intimate contact to undergo small oscillatory motions with respect to each other. During fretting, high points or asperities of the mating surfaces adhere to each other and small particles are pulled out, leaving minute, shallow pits and powdery debris. Fretting can occur in the operation of machinery subject to motion or vibration or both. It can destroy close fits; the debris may clog moving parts; and fatigue failure may be accelerated because stress levels to initiate fatigue in fretted parts are much lower than for undamaged material. In practice, complete elimination of cracks in a

structure is not possible, because cracks can develop in service at low stresses. For example, cracks can develop as a result of repeated rubbing (fretting) between two metallic surfaces. Early initiation occurs in the vicinity of the contact zone where the stress concentration is high and localized. This is a serious problem in the aerospace industry where structural assemblies are often subjected to intense vibration [10]. Several candidate methods for locating and measuring the level of fretting fatigue damage have been identified including eddy currents, surface profilometry, orientation imaging microscopy, X-ray diffraction and ultrasonic crack detection methods [11-14]. Most of these efforts have been hampered to detect some type of damage or change in the material. For example, ultrasonic crack detection method is commonly used to identify fretted components for retirement in the aircraft industry. However, this NDE method is limited by the presence of fretting roughened surfaces particularly for blade disk attachments in turbine engines. So nondestructive evaluation of the contact zone where the stress concentration is high and localized in the shallow subsurface layer is complicated by the adverse effects of the fretting, such as surface roughness and cold work [15].

The Ti-6Al-4V alloy produces a very significant thermoelectric voltage when two pieces of the very same material are rubbed against each other as shown in Fig. 2. This so-called triboelectric signal is entirely due to the fact that the part with the more concentrated fretting damage exhibits a positive thermoelectric voltage with respect to the less damaged counterpart. Figure 2 also illustrates that, after careful removal of the fretted surface layer from the moving part, the sign of the thermoelectric voltage temporally changes until the faster build-up of fretting damage on the moving part reverses it again. Although the tribo-electric method well illustrates the sensitivity of the thermoelectric method in general to fretting damage, this technique cannot be directly adapted to nondestructive inspection of critical engine components because of its poor reproducibility and the inevitable surface damage the inspection itself causes on the part to be inspected. Based on the experimental results reported by author *et al.* [2] in which clearly demonstrated the feasibility of non-destructive evaluation of cold work and residual stress in shot-peened copper and nickel-based superalloys specimens by thermoelectric means.

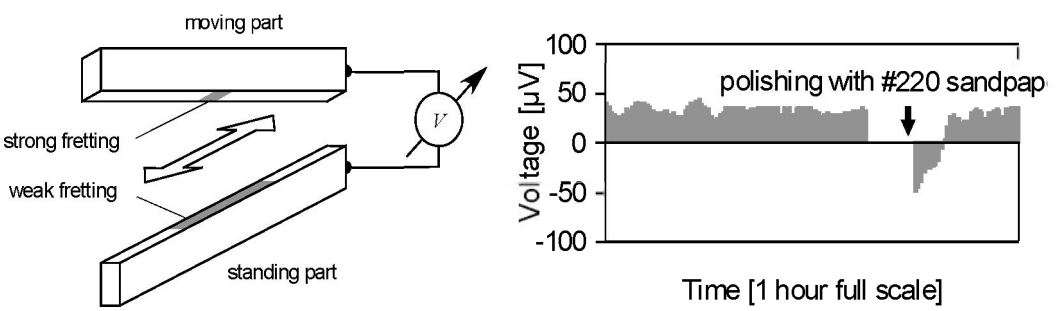

Figure 2. Tribo-electrically generated thermoelectric voltage when two pieces of the very same Ti-6Al-4V material are rubbed against each other.

Fig. 3 shows the magnetic scans of the different fretted Ti-6Al-4V specimens taken at ∇T ≈13.38 °C/cm temperature gradient for two opposite heating directions. The measured peak to peak magnetic flux density is also listed for the experimental results. The measured magnetic

field distributions are very similar in shape to the results published by author in the particular case of hard-alpha inclusions embbeded in a titanium specimen [16].

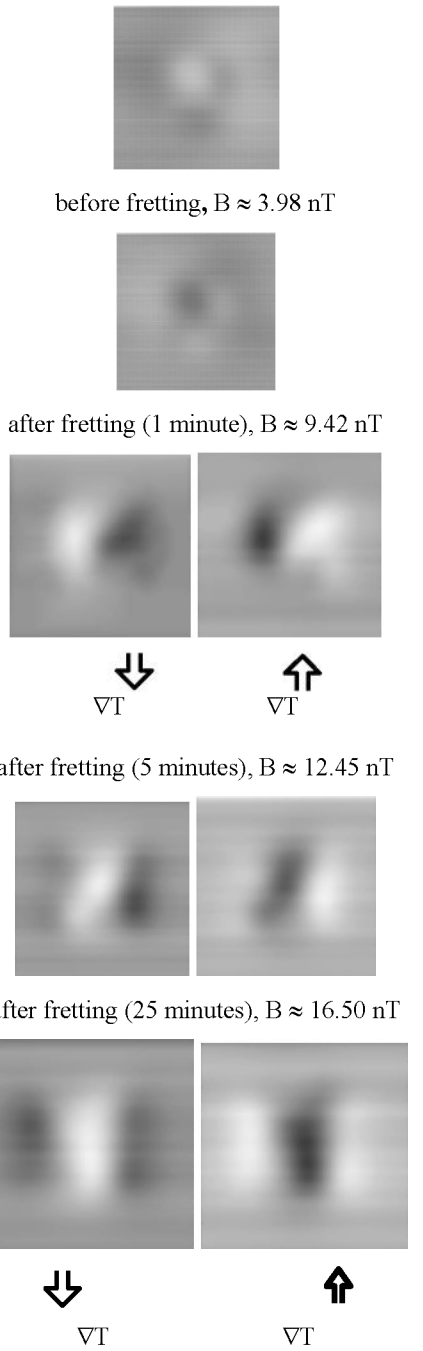

Figure 3. Magnetic images of Ti-6Al-4V before and after fretting damage ($\nabla T \approx 13.38$ °C/cm, 2 mm lift-off distance, 76.2 mm × 76.2 mm scanning dimension). The measured peak magnetic flux density is also listed for comparison.

As we expected, the main lobes (thermoelectric currents) get stronger and the magnitude of the magnetic flux increases as the cold work is more severe and the spatial distribution of the field become well defined (not distortions). The magnetic image recorded from the specimen without fretting damage exhibits a strong background signature due to the manufacturing process used to fabricate stock materials (bar, billet, plate ect.) that tend to induce a preferred crystallographic orientation, leaving the material with a remarkable macroscopic anisotropy. In addition to this morphological anisotropy, due to the dominantly hexagonal grain structure, the Ti-6Al-4V alloy also exhibited a substantial thermoelectric anisotropy [17].

The appearance of the described background signature in no contacting thermoelectric inspection is not surprising at all. It has been known for a long time that pure cold-rolled metals can exhibit a rather significant variation of ~ 1 % in thermoelectric power with respect to the same metal in annealed condition [18]. Texture induced anisotropy can also lead to significant thermoelectric signals between regions of different orientations in the same material [19,20]. Many manufacturing processes produce a textured microstructure that causes a perceivable macroscopic anisotropy in the material properties. The nature of this texture can by crystallographic, e.g., preferred orientation of non-cubic grains in a polycrystalline metal [21], or morphological, e.g., preferred orientation of grain boundaries, dislocations, slip bands, segregations, etc. In addition, the presence of strong residual stresses can also cause weak spurious anisotropy in otherwise isotropic materials via the substantial stress-dependence of the thermoelectric properties. The main goal in this section is to study how thermoelectric anisotropy causes a particular characteristic background signature in metals in order to reliably estimate the POD of certain material flaws. From this point of view, all the above mentioned effects (i.e., hardening, texture, residual stresses) are clearly negative as far as they adversely affect the detectability of flaws. On the other hand, it is also clear that the unique sensitivity of the thermoelectric method to these effects can be readily exploited in the future for the detection and quantitative characterization of these subtle material variations [22].

2.2. Analytical Predictions

Thermoelectricity is a result of intrinsically coupled transport of electricity and heat in metals. The electrical current density $\boldsymbol{j}$ and thermal flux $\boldsymbol{h}$ produced by a given combination of electrochemical potential Φ and temperature T distributions are given by [23]

$$\begin{bmatrix} \boldsymbol{j} \\ \boldsymbol{h} \end{bmatrix} = \begin{bmatrix} \sigma & \varepsilon \\ \overline{\varepsilon} & \kappa \end{bmatrix} \begin{bmatrix} -\nabla\Phi \\ -\nabla T \end{bmatrix}, \tag{1}$$

where σ denotes the electrical conductivity measured at uniform temperature, κ is the thermal conductivity for zero electrical field, and ε and $\overline{\varepsilon}$ are thermoelectric coupling coefficients that can be expressed by the absolute thermoelectric power S of the material as $\varepsilon = \sigma S$ and $\overline{\varepsilon} = \sigma S T$. The thermal conductivity for zero electrical field κ can be easily expressed by the thermal conductivity of the material for zero electrical current, k, which is often easier to determine experimentally, as $\kappa = k + \sigma S^2 T$. The difference between these two thermal conductivities is due to the thermoelectric coupling in the material. It can write

that $\kappa = k(1 + \eta)$, where $\eta = \sigma S^2 T / k$ is a dimensionless factor that provides a measure of the strength of coupling between thermal and electrical transports. For typical metals, the coupling factor is relatively small somewhere between 10^{-3} and 10^{-2}, an important fact that will be exploited in the following calculations.

The total energy flux $\boldsymbol{h}+\Phi\boldsymbol{j}$ includes the thermal flux plus an additional term representing the changing electric potential of the electrons. The rate at which heat is evolved, per unit volume, at any point in the material is $\nabla \cdot \boldsymbol{h}+\nabla\Phi \cdot \boldsymbol{j}$, where it was exploited Maxwell's law that $\nabla \cdot \boldsymbol{j}=0$. If it now assumes the coupling coefficients ε and $\bar{\varepsilon}$ to be small such that their individual squares and products can be neglected, then for thermal loading we can neglect $\nabla\Phi \cdot \boldsymbol{j}$ and, for the steady state, it can concluded that $\nabla \cdot \boldsymbol{h} \approx 0$. Imposing the conditions that the divergences of both the electrical current density and the thermal flux vanish and noting that $\sigma\kappa - \varepsilon\bar{\varepsilon} \neq 0$, Eq. (1) requires that the Laplacians of T and Φ vanish individually, i.e.,

$$\nabla^2 T = 0 \quad \text{and} \quad \nabla^2 \Phi = 0. \tag{2}$$

For a homogeneous isotropic medium, σ, κ, and S are scalar quantities that do not depend directly on the spatial coordinates, though generally they do depend on temperature, that can introduce an indirect spatial variation. For purely thermal excitation in an isotropic medium, the local electrical field $\mathbf{E} = -\nabla\Phi$ is strictly parallel to the temperature gradient ∇T and the electrical current density can be shown to identically vanish everywhere. This means that, regardless of the size, shape, and material properties of a homogeneous isotropic specimen, no thermoelectric current will be generated by any type of heating or cooling. In an anisotropic medium, σ, κ, and S are second-order tensor quantities and the local electrical field is not necessarily parallel to the temperature gradient. Though the divergence of the electrical current density $\nabla \cdot \boldsymbol{j}=0$ is still identically zero everywhere by virtue of Maxwell's theorem, the curl of the electrical current density $\nabla \times \boldsymbol{j} \neq 0$ does not necessarily vanish. Therefore, specimens made of anisotropic materials can produce a nonvanishing thermoelectric current distribution, and an associated nonvanishing magnetic field, even when the material is completely homogeneous. The nonvanishing thermoelectric current distribution in anisotropic media is caused by nonuniform heat flow that can be due to either nonuniform heating and cooling or the irregular shape of the specimen, e.g., a rivet hole that forces the heat flux to go around it.

In the simplest case, the material properties of the anisotropic medium are homogeneous, i.e., they are the same at every point, but they change perceivably with orientation. A significant thermoelectric signature arises only when the direction of the heat flux rapidly changes from point to point due to either nonuniform heating and cooling or the irregular shape of the specimen. The former effect is caused by localized heating and cooling used to introduce the necessary temperature gradient in the specimen. In order to demonstrate how anisotropy can induce a nonvanishing thermoelectric current distribution in a specimen under forced heating and cooling, let us first consider an infinite line source acting in an infinite anisotropic medium. Since all material properties are affected by the same microstructural

symmetry, it will be assumed that the electrical conductivity σ, thermal conductivity κ, and thermoelectric power S tensors all exhibit the same principal directions, though their degree of anisotropy might be very different. In order to further simplify the calculations, it will be assumed that the line source is oriented along one of the principal directions of the medium, that is aligned with the x_3 - axis of a Cartesian (principal material) coordinate system. In this way, the problem becomes essentially two-dimensional with both the heat flux and the thermoelectric current limited to the x_1, x_2 plane of symmetry and exact analytical solutions can be obtained for the thermoelectric current distribution and the induced magnetic field [24]. In order to satisfy our two field equations, $\nabla \cdot \boldsymbol{j}=0$ and $\nabla \cdot \boldsymbol{h}=0$, it will seek solutions in the following forms:

$$T=B\,ln\left[\frac{x_1^2}{\beta_1}+\frac{x_2^2}{\beta_2}\right] \text{ and } \Phi=D\,ln\left[\frac{x_1^2}{\beta_1}+\frac{x_2^2}{\beta_2}\right]. \tag{3}$$

Here, B and D are currently unknown amplitudes that will be later determined from the appropriate boundary conditions and β_1 and β_2 are diffusion coefficients determined by the anisotropic material properties of the medium. The characteristic equation for β_1 and β_2 can be obtained from the field equations and the constitutive relations given in Eq. (1) as follows

$$\begin{bmatrix} \frac{\varepsilon_1}{\beta_1}-\frac{\varepsilon_2}{\beta_2} & \frac{\sigma_1}{\beta_1}-\frac{\sigma_2}{\beta_2} \\ \frac{\kappa_1}{\beta_1}-\frac{\kappa_2}{\beta_2} & \frac{\bar{\varepsilon}_1}{\beta_1}-\frac{\bar{\varepsilon}_2}{\beta_2} \end{bmatrix} \begin{bmatrix} B \\ D \end{bmatrix} = \begin{bmatrix} 0 \\ 0 \end{bmatrix}. \tag{4}$$

Nontrivial solutions are found by first solving the eigenvalue problem and then determining the corresponding eigenvectors. For brevity, it will be introduced the following notation for the ratios of the diffusion coefficients and material properties; $\beta = \beta_1/\beta_2$, $\sigma = \sigma_1/\sigma_2$, $\varepsilon = \varepsilon_1/\varepsilon_2$, $\kappa = \kappa_1/\kappa_2$. Furthermore, $\eta = (\varepsilon_2\bar{\varepsilon}_2)/(\sigma_2\kappa_2) = \sigma_2 S_2^2 T/\kappa_2$ will be used without a subscript to denote the thermoelectric coupling of the material in the second principal direction. The sought characteristic equation for β is obtained by requiring that the determinant of the characteristic matrix in Eq. (4) vanish

$$\eta(\varepsilon-\beta)^2-(\sigma-\beta)(\kappa-\beta)=0. \tag{5}$$

This quadratic equation yields two eigenvalues that are denoted by β_p and β_n

$$\beta_{p,n}=\frac{\sigma+\kappa-2\varepsilon\eta\pm\sqrt{(\sigma-\kappa)^2-4\eta(\sigma-\varepsilon)(\varepsilon-\kappa)}}{2(1-\eta)}, \tag{6}$$

where subscripts p and n correspond to the positive and negative values of the square root in the numerator. Finally, the corresponding eigenvectors can be determined from either rows of Eq. (4) as follows

$$\delta_p = \frac{D_p}{B_p} = -\frac{\varepsilon_2(\varepsilon - \beta_p)}{\sigma_2(\sigma - \beta_p)} \text{ and } \delta_n = \frac{D_n}{B_n} = -\frac{\varepsilon_2(\varepsilon - \beta_n)}{\sigma_2(\sigma - \beta_n)}. \tag{7}$$

Formal solution for the electrical current density and heat flux can be obtained from these temperature and electrical potential distributions by substituting them into the constitutive equation. After some algebraic manipulation, the electrical current density and thermal flux vectors are obtained as

$$\boldsymbol{j} = -2\left(\frac{B_p\gamma_p}{\frac{x_1^2}{\beta_p}+x_2^2} + \frac{B_n\gamma_n}{\frac{x_1^2}{\beta_n}+x_2^2}\right)(x_1\mathbf{e}_1 + x_2\mathbf{e}_2) \tag{8}$$

and

$$\boldsymbol{h} = -2\left(\frac{B_p\nu_p}{\frac{x_1^2}{\beta_p}+x_2^2} + \frac{B_n\nu_n}{\frac{x_1^2}{\beta_n}+x_2^2}\right)(x_1\mathbf{e}_1 + x_2\mathbf{e}_2), \tag{9}$$

where $\mathbf{e}_1$ and $\mathbf{e}_2$ are unit vectors along the x_1 and x_2 coordinate axes, respectively, and

$$\gamma_{p,n} = \varepsilon_2\frac{\sigma - \varepsilon}{\sigma - \beta_{p,n}} \text{ and } \nu_{p,n} = \kappa_2\left(1 - \eta\frac{\varepsilon - \beta_{p,n}}{\sigma - \beta_{p,n}}\right). \tag{10}$$

The temperature and electric potential distributions can be written by extending Eq. (3) as follows

$$T = B_p ln\left[\frac{x_1^2}{\beta_p}+x_2^2\right] + B_n ln\left[\frac{x_1^2}{\beta_n}+x_2^2\right] \tag{11}$$

and

$$\Phi = B_p\,\delta_p\, ln\left[\frac{x_1^2}{\beta_p}+x_2^2\right] + B_n\,\delta_n\, ln\left[\frac{x_1^2}{\beta_n}+x_2^2\right]. \tag{12}$$

Eqs. (8) through (12) are general solutions of the coupled field equations under the assumption that the total heat evolving per unit volume can be approximated by the divergence of the heat flux, i.e., thermoelectric contributions (Peltier and Thomson heat) as well as the Joule heat produced by the weak thermoelectric current are negligible. The only

remaining unknowns, B_p and B_n, can be readily determined from the boundary conditions prevailing around the line source at x_3. By integrating the electrical current density and heat flux, we get

$$-4\pi\gamma_p\sqrt{\beta_p}\,B_p - 4\pi\gamma_n\sqrt{\beta_n}\,B_n = 0 \tag{13}$$

and

$$-4\pi\nu_p\sqrt{\beta_p}\,B_p - 4\pi\nu_n\sqrt{\beta_n}\,B_n = \dot{Q}, \tag{14}$$

respectively, where $\dot{Q}$ denotes the total heat power emanating from a unit length of the line source. These equations can be solved for B_n and B_p as follows

$$B_p = \frac{\dot{Q}}{4\pi\sqrt{\beta_p}\left(\frac{\gamma_p}{\gamma_n}\nu_n - \nu_p\right)} \text{ and } B_n = \frac{\dot{Q}}{4\pi\sqrt{\beta_n}\left(\frac{\gamma_n}{\gamma_p}\nu_p - \nu_n\right)}. \tag{15}$$

Finally, the sought magnetic field can be obtained from Maxwell's equation of $\nabla\times\boldsymbol{H}=\boldsymbol{j}$ by integration. The only nonvanishing component is parallel to the line source

$$H_z = \frac{\dot{Q}}{2\pi}\frac{\tan^{-1}\left(\sqrt{\beta_p}\frac{x_2}{x_1}\right) - \tan^{-1}\left(\sqrt{\beta_n}\frac{x_2}{x_1}\right)}{\frac{\nu_p}{\gamma_p} - \frac{\nu_n}{\gamma_n}}. \tag{16}$$

It is clear that there is no magnetic field along any of the principal directions ($x_1 = 0$ or $x_2 = 0$), i.e., where the material appears to be "quasi-isotropic" in the sense that the corresponding components of the electrical current density and heat flux are parallel to the gradients of the temperature and electrical potential. It should be mentioned that the degree of anisotropy in thermal κ, electrical σ, and thermoelectric ε properties is much smaller than the corresponding degree of anisotropy in mechanical properties. First of all, crystallographic anisotropy is limited to noncubic materials only, which effectively excludes all of the important structural metals such as aluminum, steel, nickel, copper, etc. Even in noncubic metals like titanium, which preferentially crystallizes in hexagonal symmetry, the crystallographic anisotropy is only a few percents. In most cases, anisotropy is caused by relatively weak morphological features of texture, e.g., the evolution of elongated grain shapes in the direction of plastic deformation during cold working. Although, the thermal and electrical properties are perceivably affected by such texturing in the material, the resulting degree of anisotropy is usually rather modest. Therefore, a very useful approximation can be made by assuming that the degree of anisotropy is small ($0.9 < \sigma, \kappa, \varepsilon < 1.1$), so that both β_p and β_n are close to unity and consequently Eq. (16) can be approximated by

$$H_z \approx \frac{\dot{Q}}{2\pi} \frac{\sqrt{\beta_p} - \sqrt{\beta_n}}{\frac{\nu_p}{\gamma_p} - \frac{\nu_n}{\gamma_n}} \frac{x_1 x_2}{x_1^2 + x_2^2} = H_0 F(x_1, x_2) \tag{17}$$

that allows a much clearer separation of the parameters affecting the strength of the magnetic field, H_0, and a simplified universal spatial distribution

$$F(x_1, x_2) = \frac{x_1 x_2}{x_1^2 + x_2^2}. \tag{18}$$

H_0 is a fairly complicated function of the material properties via Eqs. (6) and (10), but it does vanish when the degree of anisotropy diminishes, i.e., when σ, κ, and ε all approach unity. The magnetic field depends only on the angular coordinate of the point of observation with respect to the principal directions but not on the distance from the source. In contrast to the electrical current density and heat flux, which are inversely proportional to the distance from the source, the magnetic field produced by an infinite line source exhibits no loss associated with the spreading of the heat. It should be mentioned again that $F(x_1, x_2)$ vanishes on the principal axes ($x_1 = 0$ or $x_2 = 0$) where there is no skewing between $\nabla\Phi$ and ∇T on one side and $\boldsymbol{j}$ and $\boldsymbol{h}$ on the other side.

2.2.1. Infinite Dipole along a Principal Direction

In order to illustrate the main features of the analytical predictions for the anisotropic thermoelectric effect in the case of simultaneous heating and cooling, let us consider the case of a dipole consisting of a line source and a sink separated by a unit distance $b = 1$ as it is shown in Fig. 4. Because of the cancellation effect between the source and the sink, far away from the dipole the magnetic field decreases as the inverse of the distance from the dipole. Now, the principal directions of the anisotropic material (x_1, x_2) are rotated by an arbitrary angle of θ with respect to the dipole orientation along the $x_3 = \xi_3$ axis. Using superposition, the magnetic field of the dipole can be written in the physical coordinate system (ξ_1, ξ_2, ξ_3) as $H_z = H_0 F_d(\xi_1, \xi_2)$, where

$$F_d(\xi_1, \xi_2) = F_r(\xi_1, \xi_2 + 0.5) - F_r(\xi_1, \xi_2 - 0.5). \tag{19}$$

Here, $F_r(\xi_1, \xi_2)$ denotes the rotated distribution function of a line source, that can be easily calculated from the previously determined approximate spatial distribution function $F(x_1, x_2)$ by rotation from the material coordinate system (x_1, x_2) into the physical coordinate system (ξ_1, ξ_2), i.e., by substituting $x_1 = \xi_1 \cos\theta + \xi_2 \sin\theta$ and $x_2 = -\xi_1 \sin\theta + \xi_2 \cos\theta$. For simplicity, in Eq. (19) it will be normalized all coordinates to the separation distance b between the source and the sink. Figures 5a and 5b show the normalized magnetic field distributions $F_d(\xi_1, \xi_2)$ of the dipole shown in Fig. 4 for $\theta = 0^\circ$

and $\theta = 45^{\circ}$, respectively. When the dipole is aligned with the principal directions of the material ($\theta = 0^{\circ}$), two large asymmetric lobes of opposite signs appear on the two sides of the dipole direction. Since the main heat flux is along the dipole direction from the source towards the sink, this type of material signature is similar to the lobes produced by inclusions. When the dipole is oriented along the bisector between the principal directions of the material ($\theta = 45^{\circ}$), both main lobes split into two twin peaks and the distribution becomes symmetric with respect to the dipole direction. This type of material signature is rather unique and quite different from the typical pattern produced by inclusions. As we mentioned earlier, far away from the dipole the source and the sink increasingly cancel each other and the magnetic field is inversely proportional to distance.

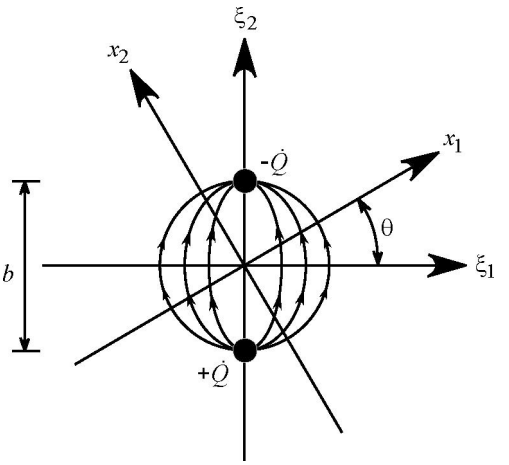

Figure 4. A schematic diagram of a dipole consisting of a line source and a sink separated by a unit distance b =1.

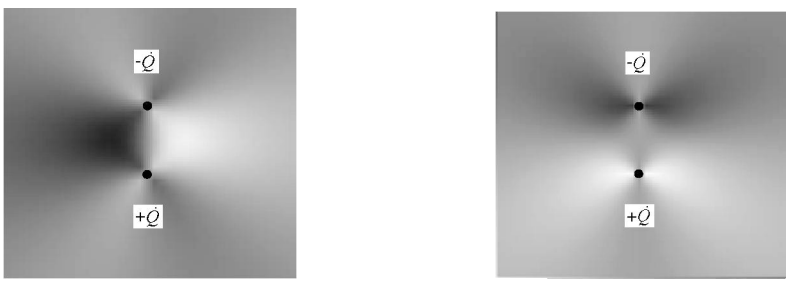

(a) $\theta = 0°$ (b) $\theta = 45°$

Figure 5. Normalized magnetic field distributions of the dipole shown in Fig. 3 in an anisotropic material for (a) $\theta = 0^{\circ}$ and (b) $\theta = 45^{\circ}$.

2.2.2. Experimental Verification in a Titanium Alloy

In order to qualitatively verify the previously described analytical model, it was conducted a series of experiments on a 1.9-mm-thick cold-rolled Ti-6A1-4V plate. First, it was determined the principal material directions in the highly textured plate using an elliptical

eddy current coil of 5:1 aspect ratio at 100 kHz. It was found that the anisotropy of the electrical conductivity, i.e., the relative difference between the principal directions, was approximately 2.3% [25]. It was also measured the degree of thermoelectric anisotropy using an ATS-6044 Alloy ThermoSorter (Walker Scientific, Inc.) which allows directional measurements in a thin plate. First, the equipment was calibrated on reference materials of known absolute thermoelectric power. At each orientation, the thermoelectric power was measured at 200 randomly chosen locations and averaged to get a representative value. Figure 6 shows the measured orientation-dependence of the absolute thermoelectric power in the cold-rolled Ti-6A1-4V specimen (symbols) along with the best fitting sinusoidal curve (solid line). The relative anisotropy of the thermoelectric power was approximately 3.1%, somewhat higher than that of the electrical conductivity. The main goal is simply to qualitatively verify the theoretical model by comparing the rather strange spatial distributions of the analytical predictions and experimental observations, therefore the less easily measurable anisotropy factor of the thermal conductivity was not determined at this point, but it is expected to be close to that of the electrical conductivity.

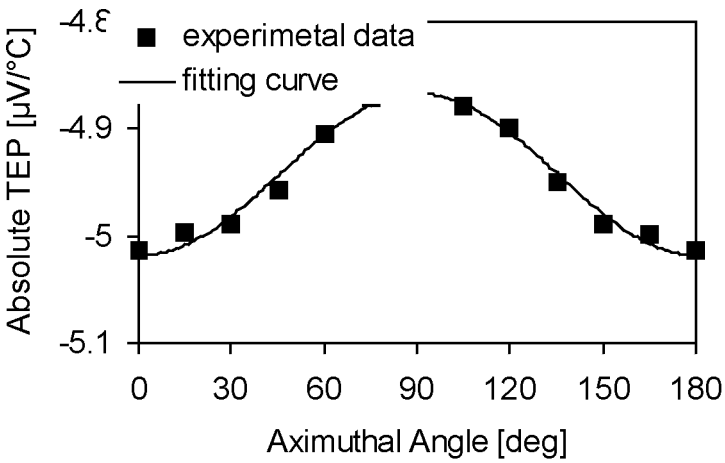

Figure 6. The orientation-dependence of the absolute thermoelectric power in a cold-rolled Ti-6A1-4V plate.

Figure 7 shows a schematic diagram of the experimental arrangement used to map the spatial distribution of the magnetic signature. The experimental data presented here is actually the difference between measurements taken at opposite heating directions and then divided by two. In order to improve heat conduction from the 12-mm-diameter copper conductor rods to the specimen, a heat conducting silicone compound was applied between them. The centers of the heating and cooling spots was 50 mm apart and the temperature there was kept constant at 50 °C and 10 °C, respectively. Because of its particular importance in interpreting the measured data, we should mention that, in order to eliminate the strong magnetic field of the Earth, it was used ac coupling with a high-pass filter of very low cut-off frequency at 0.01 Hz. The pseudo-dynamic magnetic signals required for ac detection were produced by laterally (normal to the main heat flux) scanning the specimen at a speed of ≈ 20 mm/s. In addition to

the relatively fast lateral scanning in the "line" direction, it was also scanned the specimens at a much lower rate in the axial "frame" direction, i.e., parallel to the main heat flux. In this way, a 203 mm × 203 mm scan of 200×200 grid points took about 45 minutes. Whenever the magnetic field is asymmetric to the direction of heating, the resulting bipolar line signal does not exhibit a significant dc component and will be recorded without substantial distortion. However, if the magnetic field is symmetric to the direction of heating, the resulting unipolar line signal looses its dc component and will be significantly distorted.

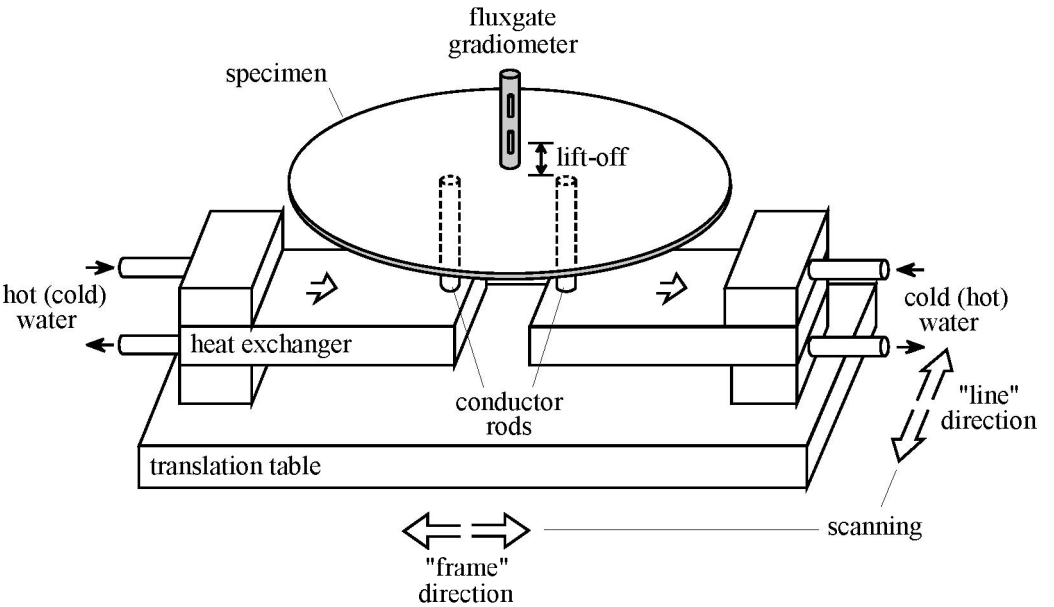

Figure 7. A schematic diagram of the experimental arrangement.

Figure 8 shows the comparison between the theoretical and experimental results for the two-dimensional distribution of the magnetic signature produced by a cold-rolled Ti-6A1-4V titanium-alloy plate at four different orientations. Whenever θ is close to either 0° or 90°, i.e., the principal material directions are aligned with the heating/cooling direction, two large asymmetric lobes of opposite signs appear on the two sides. In this case, the resulting line scans are bipolar in nature and are therefore well reproduced by the experimental data. However, when the dipole is aligned along the bisectors between the principal directions of the material ($\theta = 45^{\circ}$), the main lobes split into twin peaks and the distribution becomes symmetric with respect to the dipole direction. As we mentioned above, these distributions are inherently distorted by the necessity of using ac coupling. This distortion effectively eliminates the average signal in each line scan thereby producing virtual peaks and valleys of opposite sign with respect to the dominating principal features. As a result, the measured distributions exhibit additional secondary bumps not predicted by the theory [26,27].

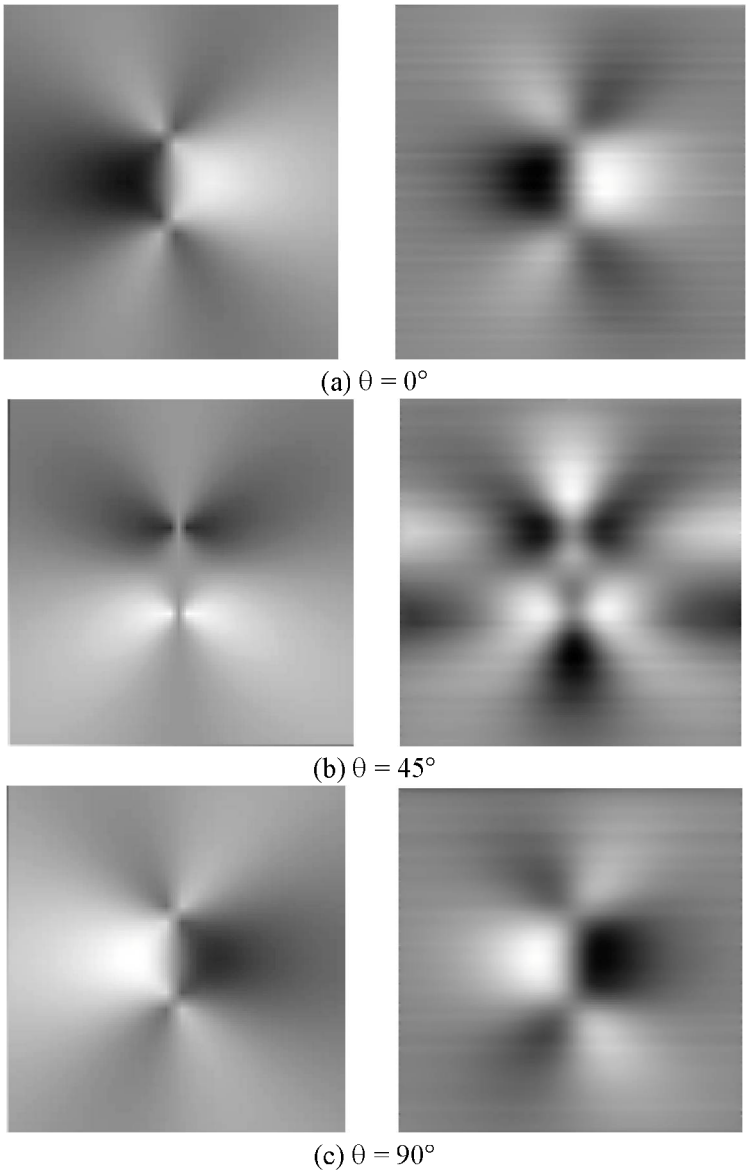

Figure 8. Comparison between the analytical (left) and experimental (right) results for the two-dimensional distribution of the magnetic signature produced by an anisotropic Ti-6Al-4V plate at 12-mm lift-off.

Considering the inherently lower resolution and ac distortion of the experimental images, the agreement with the theoretical predictions is very good, which clearly indicates that the suggested analytical model truthfully captures the main features of the anisotropic magnetic signature of textured materials. These results demonstrate that the earlier observed strange background signatures in textured specimens can be attributed to the thermoelectric anisotropy of the material. In such specimens the best flaw detectability can be achieved by rotating the heating/cooling direction so that the anisotropic effect averages out. The most important feature of the anisotropic material signature is that it changes sign when the

specimen is rotated by 90°, but it always remains the same when the specimen is rotated by 180°. Only noncubic materials such as titanium alloys exhibit crystallographic anisotropy, though a much weaker morphological anisotropy can be also exhibited by textured cubic materials. The results of this study can be used to optimize thermoelectric inspection procedures in textured metals. Furthermore, they also indicate that noncontacting thermoelectric inspection can be used to characterize the macroscopic texture of materials by evaluating their magnetic signatures under external heating and cooling.

3. Thermoelectric Signature Produced by Material Inhomogeneity

The detection probability of small and/or weak imperfections in metals depends on the thermoelectric background signature produced by the intrinsic anisotropy and inhomogeneity of the material [8]. Author *et al.* studied the effect of anisotropic texture in a homogeneous material and developed an analytical model capable of quantitatively predicting the resulting thermoelectric signature for simple inspection geometries [25]. In this section, our goal is to develop and experimentally verify an analytical model capable of predicting the thermoelectric background signature caused by weak material inhomogeneity for the simplest and most common inspection geometry, namely, in the case of an axially heated slender rectangular bar.

Of course, real specimens often exhibit both anisotropy and inhomogeneity, therefore the measured magnetic signature is due to a combination of both effects. Whether the actual signature is dominated by anisotropy or inhomogeneity of the specimen can be established on a case to case basis by comparing the signatures recorded after rotating the specimen around its principal (length, width, and thickness) axes. Since anisotropic properties are invariant for 180°-rotations, the true source of the magnetic signature can be always established by repeated measurements at different orientations of the bar. This technique will be discussed in more details in the experimental part of this section. At this point, it is sufficient to say that in many cases we found that the shape of the background signature essentially remained the same but flipped its sign when the specimen was rotated by 180° around the direction of heat propagation, which clearly indicates that the observed signal cannot originate from the anisotropy of the specimen unless it is also inhomogeneous [28,29]. We will also show that this rotational symmetry can be exploited not only to separate anisotropic effects from those of inhomogeneity, but also to further separate the two principal inhomogeneity components in the thickness- and width-directions from each other.

3.1. Analytical Model

We have already emphasized that, regardless of the size, shape, and material properties of a homogeneous isotropic specimen, no thermoelectric current will be generated by any type of heating or cooling. However, in the presence of material inhomogeneity, the thermoelectric current does not necessarily vanish in the specimen. As an example, Let us consider a slender bar of rectangular cross section with length ℓ much larger than its two other dimensions. The bar is aligned with the z-direction of a Cartesian coordinate system (x,y,z) as illustrated in Fig.

9. In the simplest first-order approximation of inhomogeneity, the spatial dependence of the material properties can be assumed to follow linear profiles

$$\kappa \approx \kappa_0 (1 + a_x x + a_y y + a_z z + \ldots), \tag{20a}$$

$$\sigma \approx \sigma_0 (1 + b_x x + b_y y + b_z z + \ldots), \tag{20b}$$

$$S \approx S_0 (1 + c_x x + c_y y + c_z z + \ldots). \tag{20c}$$

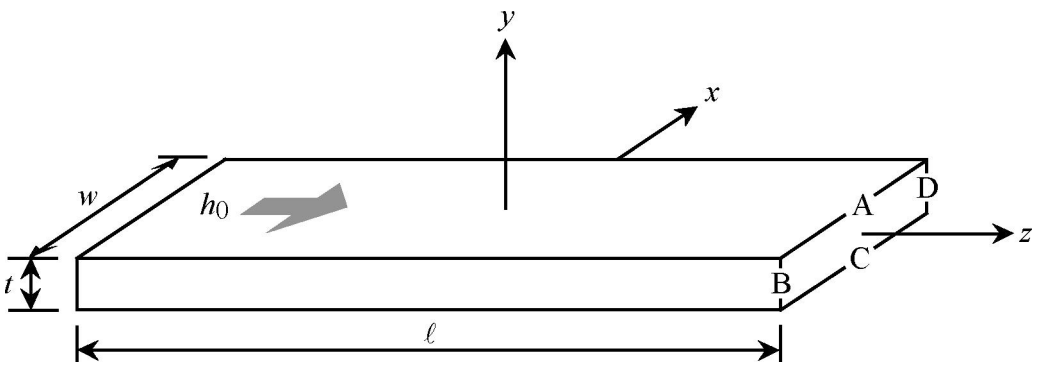

Figure 9. The geometrical arrangement of the rectangular bar and the Cartesian coordinate system used in the analytical calculations.

Here, the subscripts 0 refer to the average values of the material properties, while *a*, *b* and *c* are property gradients characterizing the material inhomogeneity. In the case under consideration, material variations along the length of the bar can be neglected partly because the technological effects responsible for the development of linear inhomogeneity (e.g., cold work, residual stress, etc.) do not cause significant axial variations in the material properties and partly because only material variations normal to the direction of heat propagation cause thermoelectric currents. In order to further simplify our analytical model, it will be assumed property variations along the *y*-direction only

$$\kappa = \kappa_0 (1 + a\, y), \; \sigma = \sigma_0 (1 + b\, y), \; S = S_0 (1 + c\, y), \tag{21}$$

where it was dropped the *y* subscript for brevity. Later, we will present experimental evidence that lateral variations in both thickness- and width-directions of the bar contribute to the observed magnetic signatures. However, this more general two-dimensional inhomogeneity can be easily handled by the one-dimensional model using superposition. The bar is subjected to a uniform axial heat flux h_0 along the *z*-axis while its sides at $x = \pm w/2$ and $y = \pm t/2$ are assumed to be insulated, i.e., it will be assumed that the heat conducted through the metallic bar is much larger than the heat lost by convection and radiation to the surrounding environment. These assumptions reduce the thermoelectric problem into a two-dimensional one in the y, z plane. Imposing the one-dimensional spatial distribution of Eq.

(21) on the field equations given by $\nabla^2 T = 0$ and $\nabla^2 \Phi = 0$ yields the following coupled governing equations

$$\kappa\left[\frac{\partial^2 T}{\partial y^2}+\frac{\partial^2 T}{\partial z^2}\right]+\frac{\partial \kappa}{\partial y}\frac{\partial T}{\partial y}=0 \tag{22a}$$

$$\sigma S\left[\frac{\partial^2 \mathrm{T}}{\partial \mathrm{y}^2}+\frac{\partial^2 \mathrm{T}}{\partial \mathrm{z}^2}\right]+\sigma\left[\frac{\partial^2 \Phi}{\partial \mathrm{y}^2}+\frac{\partial^2 \Phi}{\partial \mathrm{z}^2}\right]+\left[\mathrm{S}\frac{\partial \sigma}{\partial \mathrm{y}}+\sigma\frac{\partial \mathrm{S}}{\partial \mathrm{y}}\right]\frac{\partial \mathrm{T}}{\partial \mathrm{y}}+\frac{\partial \sigma}{\partial \mathrm{y}}\frac{\partial \Phi}{\partial \mathrm{y}}=0, \tag{22b}$$

where it was omitted the contribution of the electric field to the heat flux since it is negligible for the typically very low values of the thermoelectric coupling in metals [10]. The exact analytical solution of these coupled equations for arbitrary boundary conditions is fairly complicated. However, for the slender bar under consideration, the complicated temperature and electrical potential distributions near ends are irrelevant far away from the ends, and T and Φ will be simple linear functions of z only, i.e., $T = T(z) = A z$ and $\Phi = \Phi(z) = A^* z$, where A and A^* are currently unknown constants. Since the sides of the bar are assumed to be insulated, the total heat flux across any cross section normal to the z-axis is conserved and should be equal to the total heat flow $\dot{Q} = h_0 w t$, where h_0 denotes the average heat flux density. Now, far away from the ends $\dot{Q}$ may be estimated as

$$\dot{Q}=-w\frac{dT}{dz}\int_{-t/2}^{t/2}\kappa(y)dy=-twA\kappa_0\ , \tag{23}$$

therefore

$$T = -\frac{h_0}{\kappa_0}z = \nabla T\, z\ . \tag{24}$$

The net electric current through any normal cross section of the bar should be zero

$$\int_{-t/2}^{t/2} j_z(y)dy=-\frac{d\Phi}{dz}\int_{-t/2}^{t/2}\sigma(y)dy-\frac{dT}{dz}\int_{-t/2}^{t/2}\sigma(y)S(y)dy=0\ , \tag{25}$$

which yields

$$\Phi \approx -\nabla T\, S_0\, z\ , \tag{26}$$

where it was exploited that the relative inhomogeneity is low, i.e., $b c t^2 << 1$. Now, we can substitute equations (24) and (26) into the constitutive relations (1) to obtain the electric current density

$$j_z \approx -\sigma_0 S_0 c \nabla T\, y = j_0\, y\ , \tag{27}$$

where j_0 is a constant determined by the material properties and $j_x = j_y = 0$. In Eq. (27), we exploited again that the relative inhomogeneity is low.

Generally, the magnetic field produced by the thermoelectric currents can be calculated using the Biot-Savart law

$$\boldsymbol{H}(\boldsymbol{x}) = \int_{-\ell/2}^{\ell/2}\int_{-t/2}^{t/2}\int_{-w/2}^{w/2} \frac{\boldsymbol{j}(\boldsymbol{X})\times(\boldsymbol{x}-\boldsymbol{X})}{4\pi|\boldsymbol{x}-\boldsymbol{X}|^3} dX\,dY\,dZ \,, \tag{28}$$

where x and X are coordinate vectors of the point of observation and the differential volume of the bar, respectively. Far away from the ends of the long bar neither the electric current density nor the associated magnetic field depends on z, therefore, without loss of generality, we can evaluate the integral at $z = 0$. Performing the cross product in equation (28) and integration along the length of the bar yields

$$H_x(x,y) = -\frac{j_0}{2\pi}\int_{-t/2}^{t/2}\int_{-w/2}^{w/2} \frac{Y(y-Y)}{(x-X)^2+(y-Y)^2} dX\,dY \tag{29a}$$

and

$$H_y(x,y) = \frac{j_0}{2\pi}\int_{-t/2}^{t/2}\int_{-w/2}^{w/2} \frac{Y(x-X)}{(x-X)^2+(y-Y)^2} dX\,dY \,. \tag{29b}$$

Integration with respect to X reduces the integrals to the following one-dimensional forms

$$H_x(x,y) = -\frac{j_0}{2\pi}\int_{-t/2}^{t/2} Y\left\{\tan^{-1}\left[\frac{x+w/2}{y-Y}\right] - \tan^{-1}\left[\frac{x-w/2}{y-Y}\right]\right\} dY \,, \tag{30a}$$

$$H_y(x,y) = \frac{j_0}{4\pi}\int_{-t/2}^{t/2} Y \ln\left[\frac{(x+w/2)^2+(y-Y)^2}{(x-w/2)^2+(y-Y)^2}\right] dY \,. \tag{30b}$$

Finally, the integrals in Eq. (30) can be solved as follows

$$H_x(x,y) = H_0\left[F_x(x+w/2,y,Y)\Big|_{-t/2}^{t/2} - F_x(x-w/2,y,Y)\Big|_{-t/2}^{t/2}\right], \tag{31a}$$

$$H_y(x,y) = H_0\left[F_y(x+w/2,y,Y)\Big|_{-t/2}^{t/2} - F_y(x-w/2,y,Y)\Big|_{-t/2}^{t/2}\right], \tag{31b}$$

where, after some algebraic simplifications,

$$F_x(\xi,y,Y)=\xi y ln[1+(\frac{y-Y}{\xi})^2]+\xi Y+(Y^2-y^2+\xi^2)tan^{-1}[\frac{y-Y}{\xi}], \quad (32a)$$

$$F_y(\xi,y,Y)=\frac{Y^2-y^2+\xi^2}{2} ln[1+(\frac{y-Y}{\xi})^2]-yY-2\xi y tan^{-1}[\frac{y-Y}{\xi}], \quad (32b)$$

and

$$H_0=\frac{j_0}{4\pi}=-\frac{1}{4\pi}\sigma_0 S_0 c\nabla T . \quad (33c)$$

3.2. Experimental Method

In this section, it will describe the experimental setup and procedure it was used to verify that the previously introduced analytical model properly predicts the normal and tangential components of the magnetic field produced by thermoelectric currents induced in an inhomogeneous specimen when it is subjected to an external temperature gradient. A Ti-6Al-4V titanium alloy specimen of length ℓ = 203 mm, width w = 12.7 mm, and thickness t = 6.35 mm was cut from a cold-rolled plate. At an arbitrarily chosen orientation, the top, left, bottom, and right sides of the bar were marked as A, B, C, and D, respectively. Then, any other orientation can be easily identified by the order of the edges progressing in a counter-clockwise direction starting from the top. For example, CBAD, ADCB, and CDAB correspond to 180°-rotations around the x, y, and z axes, respectively.

In order to establish whether the specimen was strongly inhomogeneous and/or anisotropic, it was measured the electrical conductivity and absolute thermoelectric power on the four sides of the specimen. First, it was used a US-450 (UniWest Corp.) eddy current instrument with a 1.5-mm-diameter probe coil at 1 MHz to measure the electrical conductivity. The system was calibrated on reference materials of known electrical conductivity. 100 readings were taken on each side and then averaged to get a representative value. On sides A (0.587 MS) and C (0.590 MS) the electrical conductivity was found to be significantly higher than on sides B (0.572 MS) and D (0.570 MS). The ≈3% difference between sides A&C versus sides B&D was well above the standard deviation (0.003 MS or 0.5%), which indicates the presence of significant anisotropy in electrical conductivity. On the other hand, the small difference between sides A and C or sides B and D was less than the standard deviation, therefore we can conclude that conventional eddy current inspection could not unequivocally verify the presence of a significant inhomogeneity in electrical conductivity. Second, it was measured the thermoelectric power with an ATS-6044 Alloy ThermoSorter (Walker Scientific, Inc.) in an attempt to establish the presence of thermoelectric anisotropy and/or inhomogeneity. Again, the equipment was calibrated on reference materials of known absolute thermoelectric power and 100 readings were taken on each side of the Ti-6Al-4V specimen and then averaged to get a representative value. On sides A (-5.09 μV/°C) and C (-5.11 μV/°C) the thermoelectric power was found to be of significantly higher magnitude than on sides B (-4.69 μV/°C) and D (-4.72 μV/°C). The ≈8% difference between sides A&C versus sides B&D was again above the standard deviation

(0.15 μV/°C or 3%), which indicates the presence of a significant anisotropy in thermoelectric power. As before, the small difference between sides A and C or sides B and D was less than the standard deviation, therefore we can conclude that conventional thermoelectric inspection could not unequivocally verify the presence of significant thermoelectric inhomogeneity in the specimen.

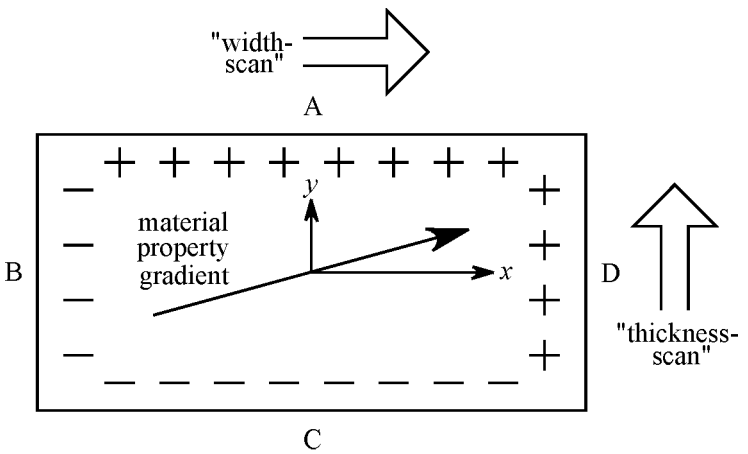

(a) ABCD, reference orientation

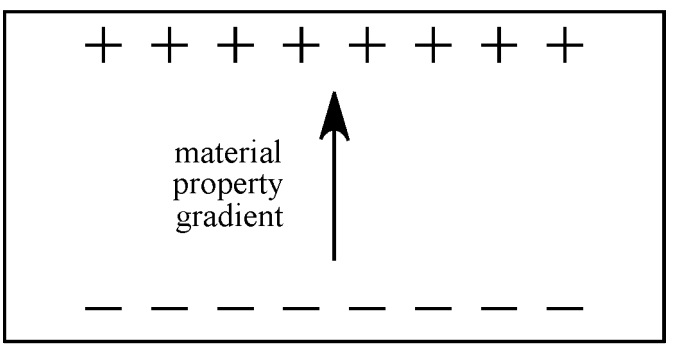

(b) ¼ (ABCD+ADCB-CDAB-CBAD), "thickness-inhomogeneity"

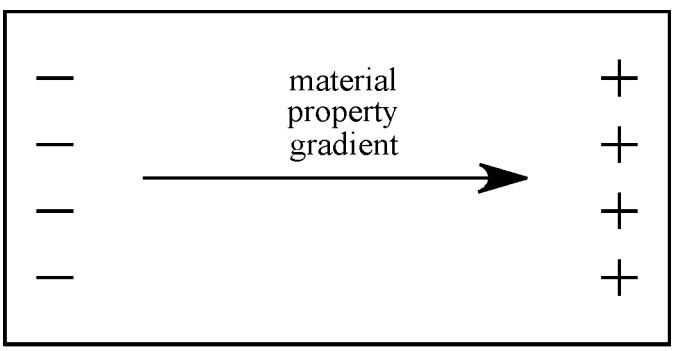

(c) ¼ (ABCD+CBAD-CDAB-ADCB), "width-inhomogeneity"

Figure 10. A schematic drawing of the two-dimensional inhomogeneity of the specimen (a) and how addition and subtraction of different profiles can be used to eliminate either the (b) width- or (c) thickness-component of the inhomogeneity.

In spite of the apparently stronger effect of anisotropy, the thermoelectric background signature of a slender bar could be still dominated by the inhomogeneous contribution because the heat flux is forced to be parallel to the axis of the bar. This could be easily verified by rotating the bar by 180°, upon which the signature should not change at all if it were caused by anisotropy. We found that the signature of the specimen was essentially reversed upon such rotation, therefore it was primarily due to inhomogeneity. We also noticed that the observed change in the signature also depended on how the 180° rotation was executed. The obvious reason for this is that, in contrast with our simple analytical model, the specimen exhibited property gradients in both width- and thickness-directions. Figure 10 illustrates the true two-dimensional inhomogeneity of the specimen (a) and how addition and subtraction of different profiles can be used to eliminate either the (b) width- or (c) thickness-component of the inhomogeneity.

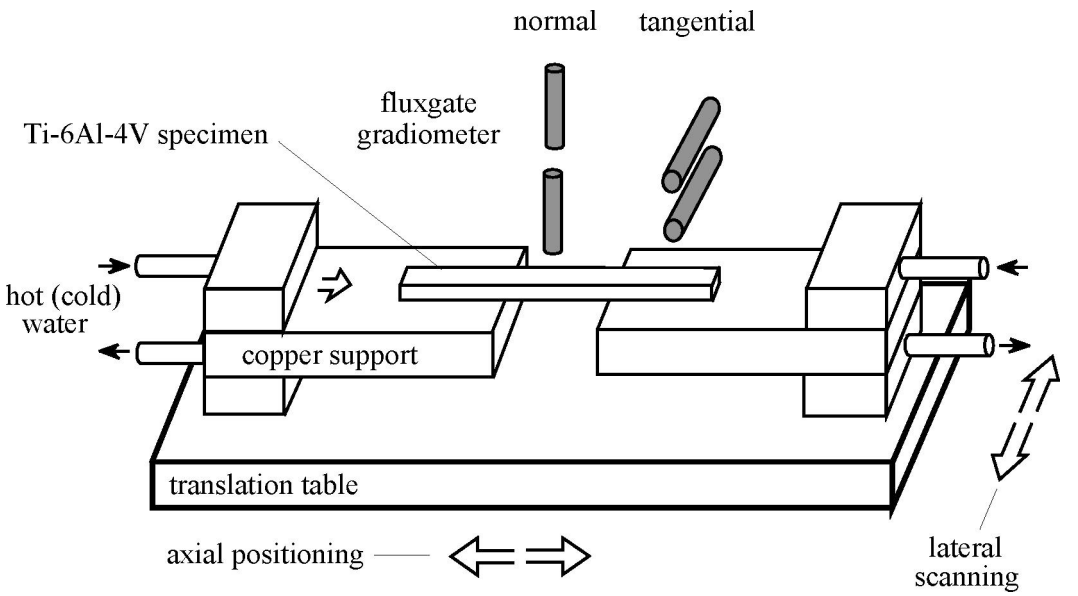

Figure 11. A schematic diagram for the experimental arrangement.

Figure 11 shows a schematic diagram for the experimental arrangement used to study the different thermoelectric signatures produced by the bar. The fluxgate magnetometer can be polarized either tangential or normal to the top surface in order to measure the x and y components of the magnetic field, respectively. The specimen was mounted on two copper supports that also acted as heat exchangers to facilitate efficient heating and cooling and the whole assembly was mounted on a non-magnetic translation table for scanning. In order to improve the heat transfer, a layer of heat conducting silicone grease compound was applied between the specimen and the copper heat exchangers, which were heated and cooled to temperatures of 85 °C and 5 °C, respectively. The actual temperature of the Ti-6Al-4V specimen was monitored by thermocouples at two points and the temperature gradient along the center part of the bar was kept at 4.5 °C/cm in all measurements.

A pair of fluxgate sensors configured in a differential arrangement was used to detect the thermoelectric signals from the specimen. The primary sensor, which is closer to the specimen, measures a stronger signal than the secondary sensor, while the two sensors exhibit essentially the same sensitivity for external sources at larger distances, which are rejected accordingly. In each case the so called lift-off distance, i.e., the gap between the plastic case of the primary sensor and the surface of the specimen was 2 mm. Because of the differential experimental arrangement, the magnetic field must be calculated from the analytical model at the positions of both the primary and the secondary sensors and then subtracted. However, when comparing the experimental results to the model calculations, the actual distance between the probes and the surface of the specimen should be used. The sensing element of the fluxgate is a 15-mm-long ferromagnetic rod of 2 mm diameter inside a 25-mm-long protective case. The specimen was scanned with both normal and tangential sensor polarization. The total distance between the effective center of the sensor and the surface of the specimen were respectively g_{pn} = 13 mm for the primary fluxgate and g_{sn} = 41 mm for the secondary fluxgate at normal polarization and g_{pt} = 6 mm and g_{st} = 14 mm for tangential polarization.

The magnetic signals were detected by horizontally scanning the specimen at the center of the bar in a direction normal to the heat flux. Figure 11 showed how the normal and tangential magnetic signatures can be recorded when scanning in the "width-direction" of the specimen. Since the translation table can move only horizontally, but not vertically, similar scans in the thickness-direction of the specimen were taken by rotating the specimen 90° around its axis and lying it on its thinner side. As it was described above, in order to separate the "width" and "thickness" components of the inhomogeneity, we have to record the magnetic signature at four specimen orientations. Altogether, sixteen independent signatures can be measured using eight specimen orientations and two sensor polarizations. However, all magnetic signatures were recorded with both positive and negative temperature gradient and then subtracted to separate the truly thermoelectric component from spurious contributions of external sources. Therefore, the experimental data to be presented later represents thirty-two measurements. It should be mentioned that numerous additional measures were taken to assure that the magnetic signatures were recorded with minimal distortion and these measures are described in detail in Ref. [30].

3.2.1. Experimental Results in Ti-6A1-4V

In order to compare the measured spatial distribution of the magnetic field due to the assumed inhomogeneity profile, it was used the known geometrical dimensions of the specimen. The relevant physical parameters of Ti-6Al-4V that are needed for substitution into the analytical model are $\sigma_0 = 5.7 \times 10^5$ A/Vm and S_0 = -4.9 μV/°C. Two free parameters, that measure the inhomogeneity in the width c_x and thickness c_y directions, were used to find the best fit between the model predictions and the four experimentally determined signatures in each case. The average of the four best fitting values of c_x can be considered as the best estimates for the actual degree of inhomogeneity in the width-direction, while the same is true for the average of the four best fitting values of c_y and the inhomogeneity in the thickness-direction of the specimen. Though these values cannot be independently verified at this point,

the fact that the four values are reasonably close to each other in both cases lends some confidence to the obtained values.

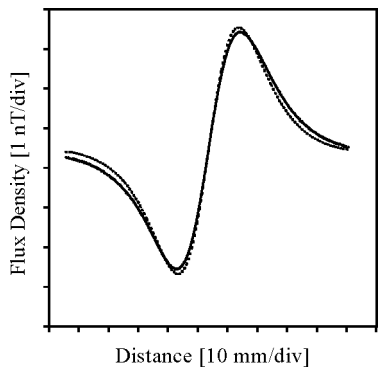

(a) width-scan, normal polarization ($c_y = 22.1\ \mathrm{m}^{-1}$)

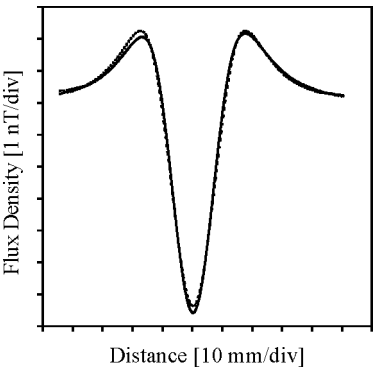

(b) width-scan, tangential polarization ($c_y = 25.8\ \mathrm{m}^{-1}$)

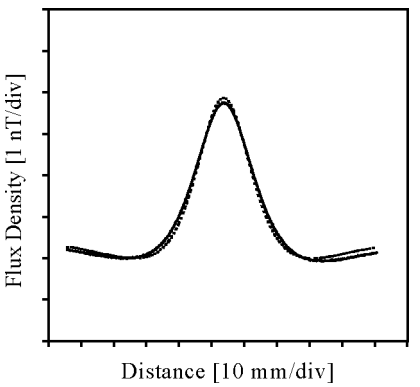

(c) thickness-scan, normal polarization ($c_y = 19.1\ \mathrm{m}^{-1}$)

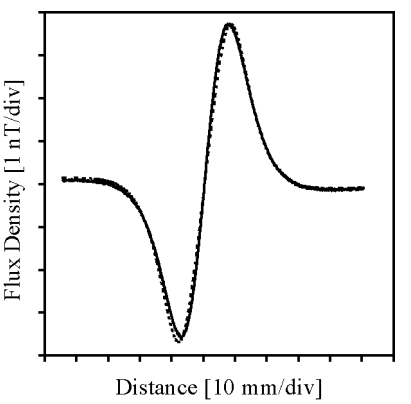

(d) thickness-scan, tangential polarization ($c_y = 21.7\ \mathrm{m}^{-1}$)

Figure 12. Comparison between the experimental and theoretical thermoelectric signatures for thickness-inhomogeneity in the slightly inhomogeneous Ti-6AL-4V specimen (solid line - theory, dotted line - experiment).

Figure 12 shows the comparison between the experimental and theoretical thermoelectric signatures for thickness-inhomogeneity. The width-signature at normal polarization (Fig. 12a) corresponds to $H_y(x, y_{pn}) - H_y(x, y_{sn})$, where $y_{pn} = g_{pn} + t/2$ and $y_{sn} = g_{sn} + t/2$ are the constant distances of the primary and secondary fluxgates from the x-axis at normal polarization. It was noticed that the relatively sharp peaks on the theoretical curves were always somewhat blurred on the experimental results by the finite size of the active element that reduces the spatial resolution of the measurement. Therefore, the theoretical curves were smoothened by averaging over a distance equal to the size of the fluxgate (±7.5 mm for tangential polarization and ±1 mm for normal polarization) in order to simulate the reduced

resolution of the experimental data. With this correction, the agreement between the shapes of the theoretical and experimental signatures is very good. The width-signature at tangential polarization (Fig. 12b) corresponds to $H_x(x, y_{tp}) - H_x(x, y_{ts})$, where $y_{tp} = g_{tp} + t/2$ and $y_{ts} = g_{ts} + t/2$ are the constant distances of the primary and secondary fluxgates from the x-axis at tangential polarization. In a similar way, Figs. 12c and 12d show the comparison between the experimental and theoretical thermoelectric signatures for scanning in the thickness-direction. It should be emphasized that the very good qualitative agreement between the experimental and theoretical data shown is partially due to the fact that each curve was individually best fitted by changing the thickness-inhomogeneity parameter c_y (these values are listed on each figure). The average of the four c_y values was 22.1 m^{-1}, with a standard deviation of 2.7 m^{-1}, which indicates that the accuracy of the thickness-inhomogeneity assessment is $\approx \pm 12\%$.

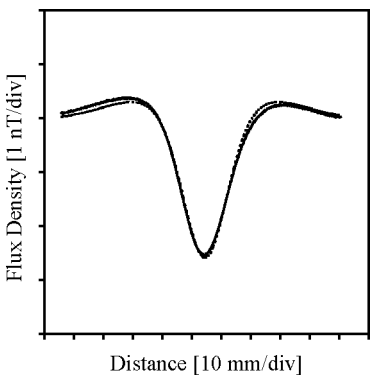

(a) width-scan, normal polarization ($c_x = 2.8$ m^{-1})

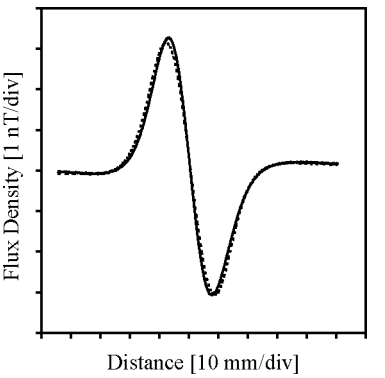

(b) width-scan, tangential polarization ($c_x = 3.5$ m^{-1})

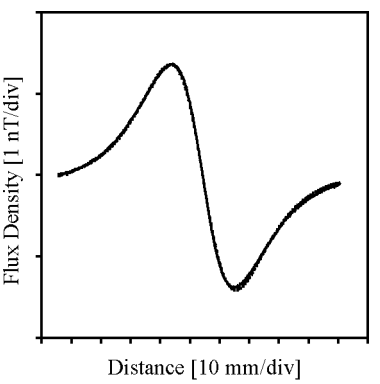

(c) thickness-scan, normal polarization ($c_x = 3.4$ m^{-1})

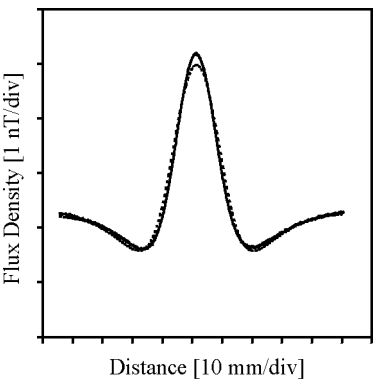

(d) thickness-scan, tangential polarization ($c_x = 3.7$ m^{-1})

Figure 13. Comparison between the experimental and theoretical thermoelectric signatures for width-inhomogeneity in the slightly inhomogeneous Ti-6AL-4V specimen (solid line - theory, dotted line - experiment).

Using the symmetry relationships shown in Fig. 10, the width-inhomogeneity of the specimen can be separately evaluated. Figure 13 shows the comparison between the experimental and theoretical thermoelectric signatures caused by width-inhomogeneity of the specimen. The average value of the four c_x values was 3.4 m^{-1}, with a standard deviation of 0.4 m^{-1}, which indicates that the accuracy of the width-inhomogeneity assessment is also $\approx \pm$ 12%. Considering the rather crude approximations used in the theoretical calculations to account for the finite size of the sensor elements, the fact that the secondary sensor is partially shielded by the primary sensor, and the experimental errors associated with the measurement, the agreement between the experimental and theoretical thermoelectric magnetic signatures is surprisingly good.

These results verify that the observed magnetic signatures are indeed caused by a linear thermoelectric current distribution of the form $j_z = j_{0x}\, x + j_{0y}\, y$ in the slender bar. However, the magnitude of the observed signatures raises serious doubts about the reliability of the previously described contact measurements. The $c_x w \approx 0.043$ and $c_y t \approx 0.14$ products represent our estimates for the total relative variation of the thermoelectric power through the width and thickness of the slender bar, respectively. These numbers are too large to be reconciled with the independent experimental measurements by a conventional thermoelectric alloy sorter. The most probable reason for this lack of consistency is the strong anisotropy of Ti-6Al-4V [31], which preferentially crystallizes in hexagonal symmetry, and its susceptibility to measurement errors by the contact technique [32].

3.2.2. Experimental Results in Artificial Copper/Brass Specimen

In order to independently verify the validity of our analytical model, we prepared an artificial specimen that exhibits a well-defined inhomogeneity that is large enough to be measured not only by the uniquely sensitive noncontacting method but also by the far less sensitive conventional contact method. For this purpose, it was obtained an inhomogeneous sintered specimen made from copper and brass by powder metallurgy. This specimen was w = 7 mm wide, t = 13.5 mm thick, and ℓ = 162 mm long with properties varying only in the thickness (y) direction. The composition of this sintered specimen changes from pure copper on one side to brass (80% copper, 20% zinc) on the other, which blend well at high sintering temperatures. Based on the perceivable change in color from reddish (copper) to yellowish (brass), the transition was fairly smooth and linear. Although we had no means of actually verifying the assumed dependence of the thermoelectric power, the only parameter that is really important in our model, on position throughout the thickness of the specimen, it is reasonable to approximate this variation with a linear function changing from the thermoelectric power of pure copper to that of brass. This seems to work for the electrical conductivity, which can be mapped by scanning the side of the specimen with a small eddy current probe [33]. Figure 14 shows the eddy current image of the conductivity variation in this artificial copper/brass reference specimen, which was obtained by a small 1.25-mm-diameter coil at 85 kHz. Like in the thermoelectric measurements, this processed image was constructed by the above described averaging procedure from four raw images taken from the two sides of the specimen. The electric conductivity changed from σ_{Cu} = 79.5 %IACS on the

copper side to σ_{Br} = 29.3 %IACS on the brass side. In the analytical calculations it was used the average of these two values, i.e., σ_0 = 54.4 %IACS (3.25× 10^7 A/Vm). We have also had two reference pieces made from pure copper and pure brass powder under the same conditions (sintering temperature and time) to measure their respective thermoelectric power and estimated the thermoelectric power of the inhomogeneous specimen by linear regression. The average difference in thermoelectric power between pure copper and brass was found to be S_{Cu} - S_{Br} = ΔS = 0.5 μV/°C. In order to calculate the magnetic signatures predicted by our analytical model, $\Delta S = S_0 \, c \, t$ must be substituted into Eq. (33c).

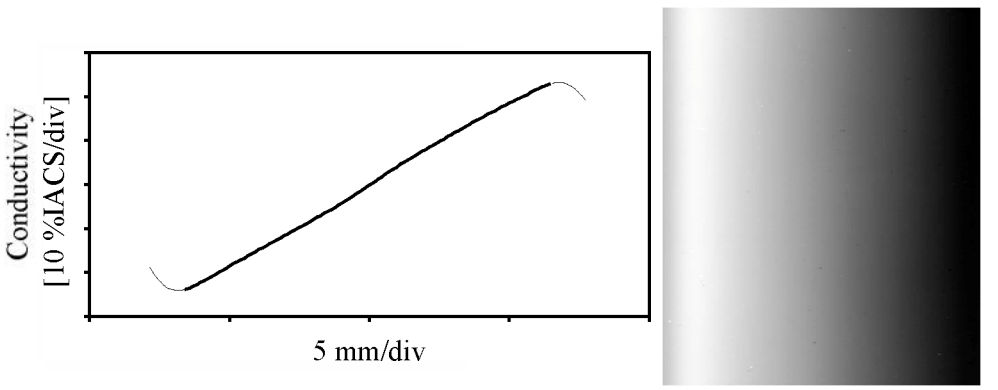

Figure 14. Eddy current image of the conductivity variation in the artificial copper/brass reference specimen.

Needless to say this high-conductivity specimen yielded roughly two orders of magnitude stronger magnetic signals than the typical Ti-6Al-4V bar used in the previous experiment. Figure 15 shows the comparison between the experimental and theoretical thermoelectric signatures for thickness-inhomogeneity. The temperature gradient imposed on the specimen during these measurements was ∇T = 3.6 °C/cm. Again, the four signatures measured for the thickness-inhomogeneity of the specimen were individually best fitted by the predictions of our analytical model and the resulting thermoelectric contrast is listed for each case. Based on these four measurements the average thermoelectric contrast is $\Delta S \approx 0.57$ μV/°C with a standard deviation of 0.08 μV/°C, which is in very good agreement with the $\Delta S \approx 0.5$ μV/°C value independently measured by contact means.

The slight overestimation seems to be mainly caused by the data obtained at tangential polarization when the effect of the sensor size and the shielding effect of the primary sensor on the signal measured by the secondary sensor have a more significant effect on the measured overall signature. Because of these effects, which would be very difficult to include in the analytical model, it appears that all the numbers obtained at tangential polarization are a little higher than those obtained at normal polarization. The measured width-inhomogeneity (not shown) was found to be very small, roughly twenty times lower than the thickness-inhomogeneity. Of course, it should be really zero since the variation is limited to the thickness direction only, but the modest accuracy of the additions/subtractions used to separate these two effects based on their respective symmetry sets a limit on the rejection ratio. In short, our measurements on the artificial reference specimen have verified our

analytical model, though at a level much higher than those encountered in real specimens. Unfortunately, this is unavoidable because the magnetic technique is orders of magnitude more sensitive than the conventional contact thermoelectric testers currently available for the limited purposes of alloys sorting.

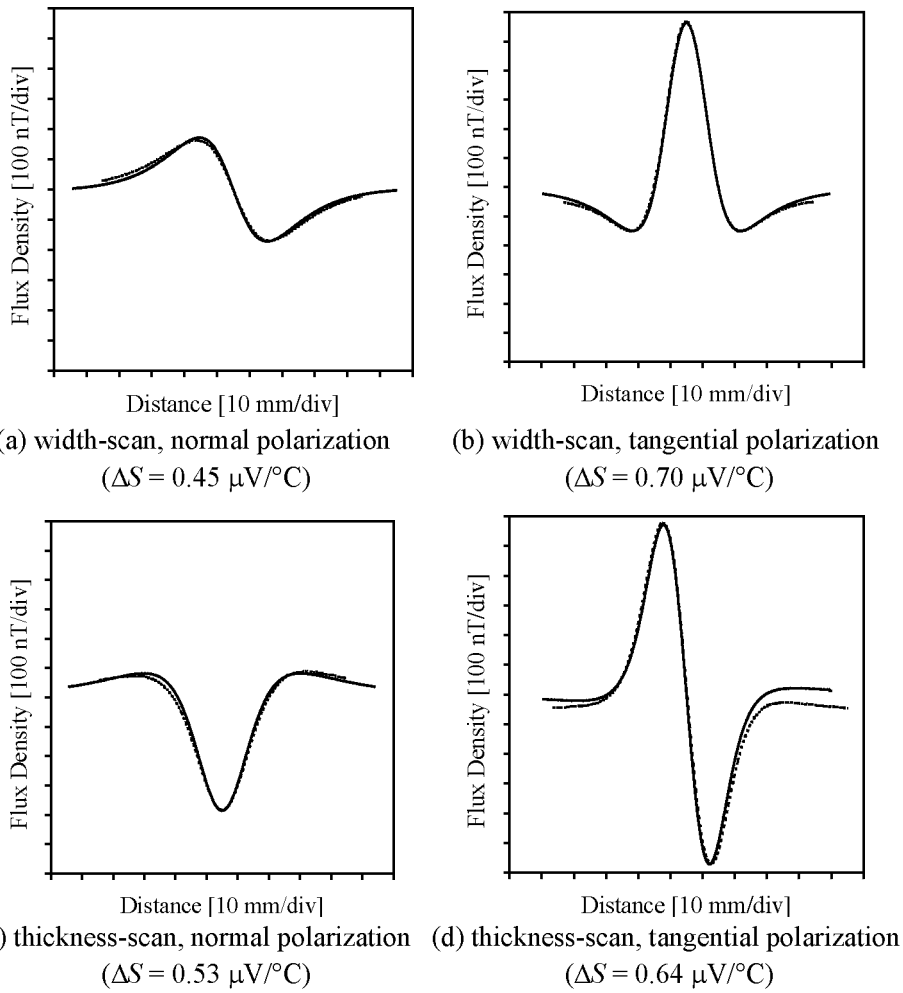

Figure 15. Comparison between the experimental and theoretical thermoelectric signatures for thickness-inhomogeneity in the strongly inhomogeneous sintered copper/brass specimen (solid line - theory, dotted line - experiment).

4. Thermoelectric Power Measurements in Cold-Rolled Ti-6Al-4V Samples

4.1. State of Art

The study of the Seebeck effect in metals and alloys provides valuable information about the microstructure, mechanical properties and thermo-mechanical history of the material,. In

recent years, quantitative assessment of the microstructures and mechanical properties of materials has been carried out through the measurement of thermoelectric power (TEP). Lasseigne et al. [34] measured the TEP to assess the weld-interstitial nitrogen content, which allows for a better correlation between the nitrogen content and the weld-metal microstructure and properties. Hu and Nagy [19] demonstrated an intrinsic sensitivity of the thermoelectric technique to imperfect interfaces that could be exploited for nondestructive evaluation of tightly compressed but metallurgically unbonded interfaces in spot welds, diffusion bonds, and other types of solid-state bonds. Park et al. [35] realized thermoelectric power measurements to evaluate microstructural analysis in HSLA steel weldments and retained austenite volume fraction in TRIP steels. Kawaguchi and Yamanaka [36] showed that the TEP of cast duplex stainless steel increased with aging time and good correlation was found between TEP and toughness. Carabajar *et al.* [37] used the TEP to investigate the evolution of precipitation in a hot-rolled, Ti added, interstitial-free (IF) steel sheet during different annealing treatments. Recently, Carreon [38] investigated the effect of thermoelectric anisotropy on the thermoelectric power measurements in a highly textured Ti-6Al-4V specimen, using a completely nondestructive technique based on the Seebeck effect. The reference research work referenced above clearly demonstrates that the intrinsic sensitivity of the TEP is a very useful tool that could be exploited for quantitative, non-destructive material characterization. Due to its unique set of properties, such as high-temperature, high-strength/density ratio and corrosion resistance, titanium and its alloys are widely used throughout the aerospace industry for many types of structural component including airframes and engine components, in addition to many non-aerospace applications. Titanium and other metals with hexagonal crystallographic structures develop strong deformation textures that lead to a pronounced plastic anisotropy of the polycrystalline sample [39]. Various factors can give rise to anisotropy in metals such as, grain morphology [40], second phase precipitates [41] and substitutional alloying elements [42]. As a consequence, the deformation texture may vary with slight changes of the material composition. Researchers [41,43] agree that crystallographic textures resulting from thermo-mechanical processing such as hot or cold rolling are most directly responsible for anisotropy in metal alloys. Anisotropy of mechanical properties is a concern in the forming of metals into shapes and parts, and the control of texture throughout the process would be very beneficial, particularly for titanium which has a variety of available textures and mixed hexagonal (β) and cubic (α) phases, such as α, near-α and other titanium alloys [44]. Thus, it becomes evident that an understanding on how the thermo-mechanical processing affects the final properties of a semi-finished or finished material is of major significance. The goal of the work presented in this paper is to establish a correlation between TEP measurements with microstructural evolution, in terms of the level of plastic deformation in Ti-6Al-4V, that have undergone thermo-mechanical process such as cold working. Cold working introduces crystallographic texture into the material and produces change in morphology of the grains due to the plastic deformation process. In order to achieve our objective, the thermoelectric technique is applied to highly textured cold-rolled Ti-6Al-4V samples, which have undergone unidirectional rolling at different degrees of reduction in thickness 40% ,60% and 80% respectively.

4.2. Thermoelectric Power

The TEP coefficient is a valuable material property for microstructural assessment. The thermoelectric effect leads to a number of interesting phenomena, some of which can be exploited for nondestructive testing (NDT) and materials characterization. Since microstructure correlates directly to material properties, thermoelectric power provides a rapid and effective way to assess microstructural changes in polycrystalline materials. Figure 16 shows a schematic diagram of the thermoelectric measurements as is typically performed in nondestructive materials characterization. One of the reference electrodes is electrically heated to a preset temperature of T_h, similar to the tip of a temperature-stabilized soldering iron, while the other electrode is left 'cold' at room temperature T_c. The measurement is performed in a few seconds to ensure that the hot reference electrode is not cooled down significantly by the specimen and that the rest of the specimen beyond the close vicinity of the contact point is not warmed up significantly. The measured thermoelectric voltage due to the Seebeck effect is given by

$$V = \int_{T_c}^{T_h} [S_S(T) - S_R(T)]dT = \int_{T_c}^{T_h} S_{SR}(T)dT \tag{34}$$

where T is temperature, and S_S and S_R denote the absolute thermoelectric powers of the specimen and the reference electrode, respectively. Any variation in material properties can affect the measured thermoelectric voltage via $S_{SR} = S_S - S_R$, which is the relative thermoelectric power of the specimen to be tested with respect to the reference electrode. In most cases, the temperature-dependence of the thermoelectric power can be neglected over the range of operation and the thermoelectric voltage can be approximated as $V \approx (T_h - T_c) S_{SR}$. Ideally, regardless of the temperature difference between the junctions, only thermocouples made of different materials, or more precisely, materials of different thermoelectric power, will generate a thermoelectric signal. This unique feature makes the simple thermoelectric testing system one of the most sensitive material discriminators used in nondestructive inspection. Several parameters can affect the changes in the thermoelectric power of the specimen to be inspected. The most important parameters affecting the TEP measurements are those associated with volumetric and contact effects [1]. The volumetric effect is closely related to the thermoelectricity phenomena by the kinetics of the diffusion of electrons throughout the material. The temperature-dependence of the thermoelectric power coefficient, is a function of the electron scattering behaviour, electron concentration and the effective mass of the electrons. Thus the volumetric effect is mainly affected by chemical composition, specific heat treatment, anisotropy, hardening, texture, residual stress and the fatigue of the material. The contact effects are related to the imperfect contact between the test sample and the reference probe, the amount of pressure applied to the probe and the temperature of the hot and cold junctions and the probe material.

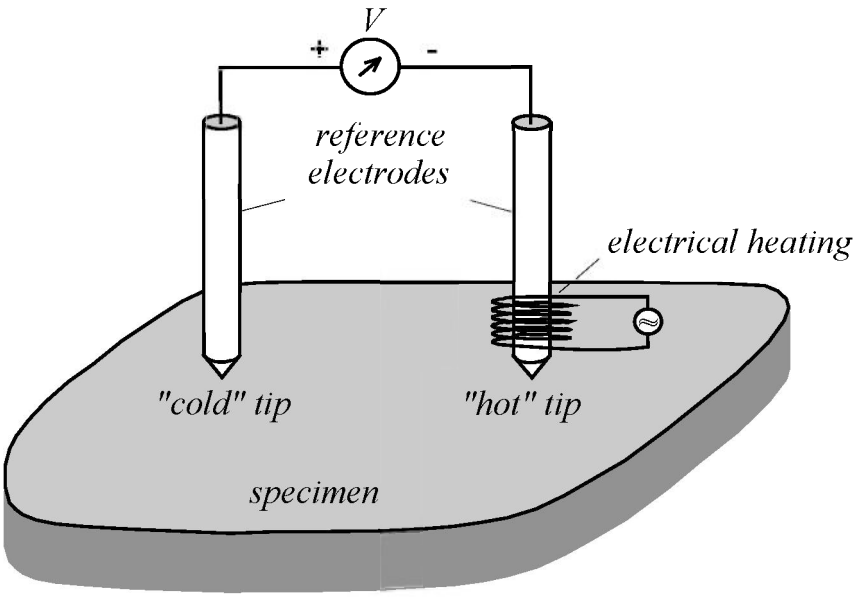

Figure 16. Schematic diagram of the conventional thermoelectric measurements as most often used in nondestructive materials characterization (dual-tipped probe).

4.2.1. TEP vs Cold Work

It is well known that when a material is cold worked by any means (surface treatment, cold rolled, etc), the working process will induce changes in the mechanical and electrical material properties such as increases in hardness and electrical resistivity and a decrease in ductility. All of these changes in material properties depend on the degree of plastic deformation due to cold working, prior processing, material composition and other factors. From this point of view, it is interesting to obtain some information about the relationship between the thermoelectric power and the corresponding change in material properties such as texture, due to the cold working. In the case of copper (cubic crystallographic structure), some information is already available in the scientific literature on the thermoelectric power and the effect of cold work. Kropschot and Blatt [18] measured the thermoelectric voltage produced by a thermocouple made from the same cold-drawn pure copper wire after annealing one leg of the thermocouple to eliminate the existing texture and hardening. Because of the thin diameter of the wire, there cannot be significant residual stresses present even in the cold-drawn wire. Figure 17 shows the thermoelectric voltage as a function of the hot junction temperature when the cold junction was maintained at T_C = -269 °C. For our purposes, the important region is the slope of the curve at room temperature, which is about 0.02 μV/°C and represents roughly 1% relative variation with respect the absolute thermoelectric power of pure copper. This result indicates that extreme levels of cold work found in thin cold-drawn wires could produce variations in the thermoelectric power. In contrast to mechanical properties, thermoelectric properties of cubic materials (aluminum, copper, nickel, steel, etc.) do not exhibit anisotropy.

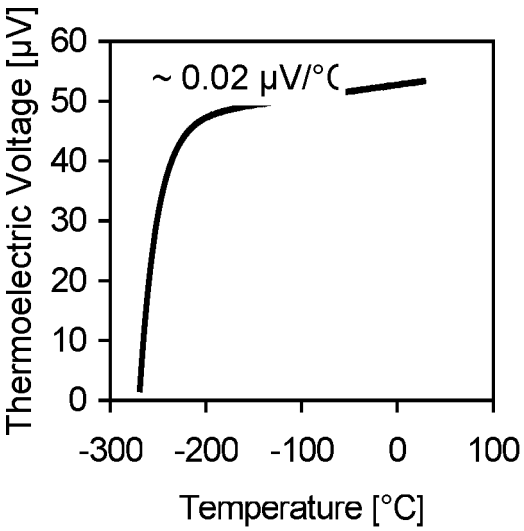

Figure 17. Thermoelectric voltage produced by a thermocouple made of annealed and cold-drawn pure copper wires (the cold junction was kept at Tc = -269 °C).

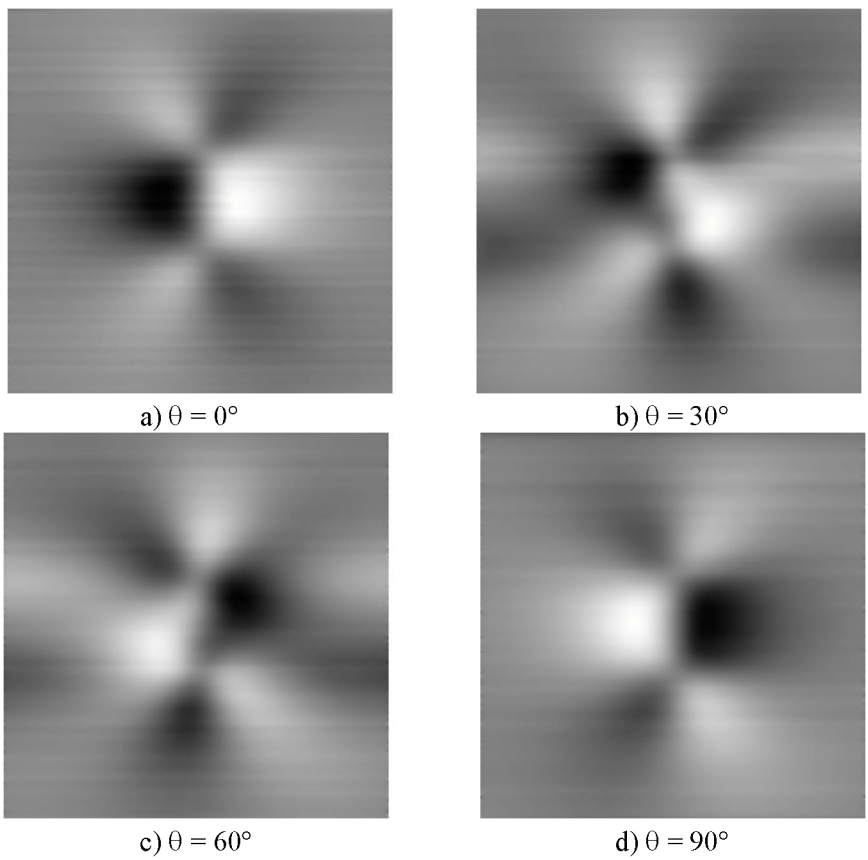

Figure 18. Experimental data for the distribution of the magnetic field produced by thermoelectric currents in an anisotropic Ti-6Al-4V sample.

Titanium and its alloys [45] are structural metals of significant practical importance, that preferentially crystallize in non-cubic (hexagonal) symmetry, which exhibits thermoelectric anisotropy. Nayfeh *et al.* conducted a series of experiments on a cold-rolled titanium-alloy plate, and found that the anisotropy of the electrical conductivity, i.e., the relative difference between the principal directions, was approximately 2.3%. The degree of thermoelectric anisotropy was also measured using the conventional thermoelectric technique which allows directional measurements in a thin plate [25].

Figure 18 shows the orientation-dependence of the magnetic field produced by thermoelectric currents in a highly textured (cold-rolled) titanium-alloy under two-dimensional directional heating and cooling. The results clearly indicate that the observed background signatures in a highly textured specimen can be attributed to the thermoelectric anisotropy of the material. This is due to the high anisotropy of the polycrystalline material arising from the plastic deformation produced by the cold rolling process. Whenever the measurement angle to the rolling direction, θ, is close to either 0° rolling direction (RD) or 90° perpendicular direction (PD), the thermoelectric currents change in sign.

4.3. Experimental Arrangement

Ti-6Al-4V samples were used in this investigation 'as-received', and the material was provided by Titanium Industries, Inc., in the form of sheets (3 pieces) in the 'as-cold rolled' conditions at different degrees of reduction in thickness of 40%, 60% and 80% respectively. The chemical composition of the 40%, 60% and 80% cold-rolled material is shown in Table I. Materials that posses hexagonal crystallites, such as, titanium and zirconium, have a limited number of slip systems and generally developed a strong texture due to the severe plastic deformation it undergoes during cold rolling. Coupon samples were taken out from each of the cold-rolled Ti-6Al-4V material for nondestructive characterization.

Table I. Chemical composition (weight %).

Material	N	C	H	Fe	O	Al	V	Ti
40% cold-rolled	0.006	0.012	0.003	0.17	0.16	6.14	3.85	remainder
60% cold-rolled	0.005	0.009	0.002	0.17	0.15	6.10	3.93	remainder
80% cold-rolled	0.007	0.017	0.006	0.16	0.19	6.22	4.06	remainder

Each of the samples were sectioned into rectangular plates with flat, plane parallel surfaces, such that the angle between the rolling direction (RD) was orientated along the long straight edge of the sample as shown in Figure 19. In order to establish the presence and degree of texture due to plastic deformation of the different cold-rolled Ti-6Al-4V samples, ultrasonic measurements were first taken on each specimen. Ultrasonic measurements of the shear wave velocity provide details on the bulk macroscopic texture of the microstructure as this ultrasonic modes can be polarized either along or orthogonal to the rolling direction [46]. The shear waves polarized in the two orthogonal directions will generally have slightly different propagation velocities, and this is referred to as acoustic birefringence.

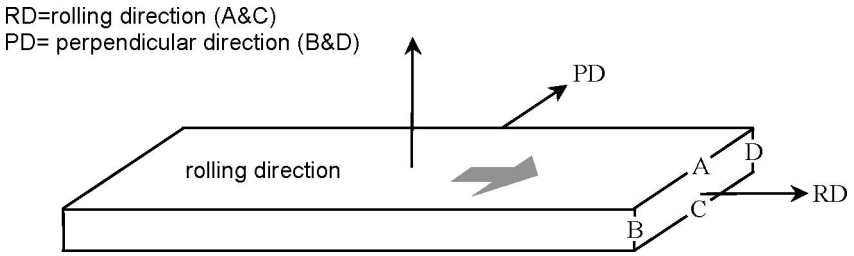

Figure 19. The geometrical arrangement of the Ti-6Al-4V specimen and the Cartesian coordinate system used in the TEP measurements

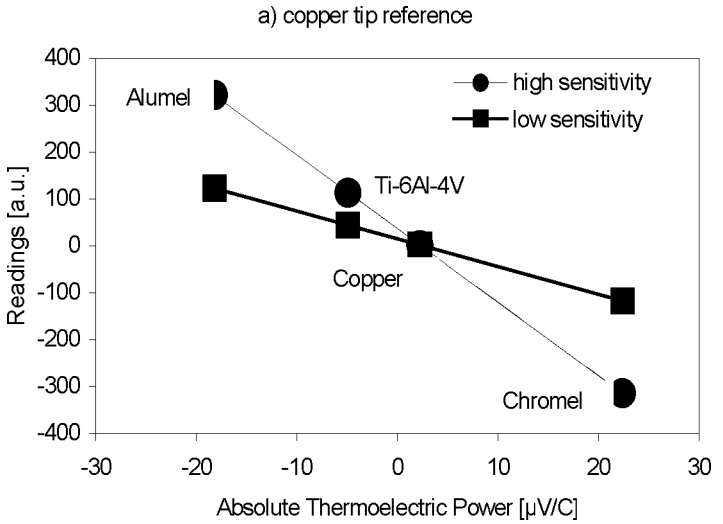

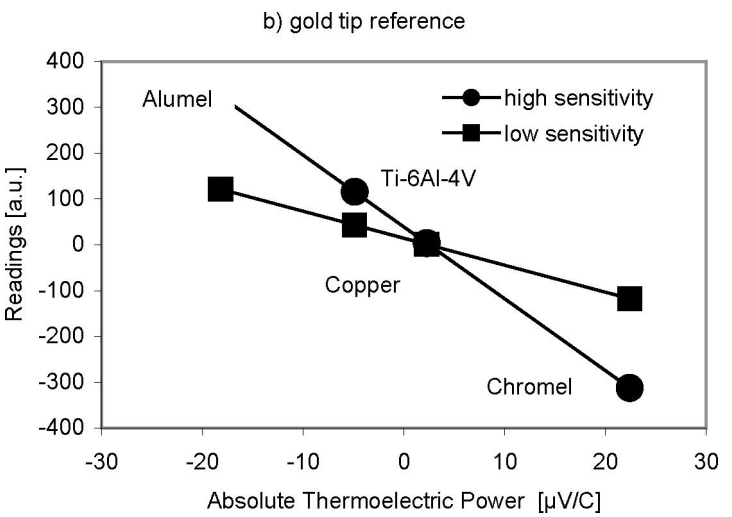

Figure 20. Calibration graphs of the a) copper tip reference and the b) gold tip reference for the absolute thermoelectric power in copper, alumel, chromel and its respective value of the cold-rolled Ti-6Al-4V sample.

A shear wave transducer (20 MHz, 6mm diameter and 7μs delay line) was used to determine the degree of anisotropy in a material by measuring the acoustic birefringence with the transducer polarized along and perpendicular to the rolling direction. Secondly, the absolute thermoelectric power of each Ti-6Al-4V specimen was measured using a calibrated ATS-6044T Alloy ThermoSorter (Walker Scientific, Inc.). This operation of this instrument is based on the well known thermoelectric principle. It is a thermoelectric alloy tester used in NDT, that provides relative readings with arbitrary units. It was firstly calibrated by measuring materials of known absolute thermoelectric power such as copper, with standard thermocouples like Alumel and Chromel. The calibration was realized for the particular case of the copper tip reference and the gold tip reference respectively as shown in Figure 20. The thermoelectric instrument induces the temperature difference in the sample by means of a dual tipped reference probe. One tip is at room temperature and the other is heated to a specific temperature. In our case, a copper hot tip (standard probe), and gold hot tip were used in order to measure the thermoelectric power of the Ti-6Al-4V sample. The dual-tipped probe is placed on the sample, an electric circuit is completed and a signal is generated. This signal is then processed to obtain a peak reading, which is displayed on the microvolts digital display. The variation in this reading with direction on the sample is representative of the anisotropy in the crystalline microstructure of the sample.

4.3.1. Experimental Results

As explained earlier, each of the cold-rolled Ti-6Al-4V samples with different degrees of reduction in thickness 40%, 60% and 80% exhibits a corresponding, varying degree of anisotropy caused by the existence of a preferred crystallographic orientation in the polycrystalline microstructure. In hexagonal close-packed (hcp) metals the low number of easy slip systems, their asymmetric distribution and the strict crystallographic orientation relationships for twinning results in the formation of a strong deformation texture. The deformation mechanism together with the texture is responsible for the strong anisotropy in the material properties. The texture produced by cold working in the Ti-6Al-4V specimens with different degrees of plastic deformation were measured to have acoustic birefringence that differed by 5.8 % at the 80% cold-rolled sample, 4.0% at the 60% cold-rolled sample and 1.8% at the 40% cold-rolled sample. Titanium alloys also exhibited perceivable electrical conductivity anisotropy and were expected to also show substantial thermoelectric anisotropy [18,21]. One hundred TEP measurements were taken on each side (A,B,C & D) of the Ti-6Al-4V samples, which have undergone unidirectional cold rolling at different degrees of reduction (40%, 60% and 80%), and these measurements were then averaged to get a representative value of the thermoelectric power coefficient. Figure 21 shows the results from the thermoelectric assessment of texture using a gold hot tip reference before and after annealing. The measured data of the gold hot tip reference are shown as a histogram of the probability distributions for the rolling direction RD (A&C) and the perpendicular direction PD (B&D) in cold-rolled Ti-6Al-4V samples. Before annealing, the measured data indicates the presence of a strong anisotropy in the thermoelectric power due to the significant difference between RD (A&C) and PD (B&D) measurements. After annealing, the measured data shows that the difference between RD (A&C) and PD (B&D) was reduced considerably, which indicates that the anisotropy in the thermoelectric power has significantly decreased. Figure 21 shows the thermoelectric power coefficient dependence associated with the

different degrees of plastic deformation in the cold- rolled Ti-6Al-4V samples using a gold tip reference before and after annealing.

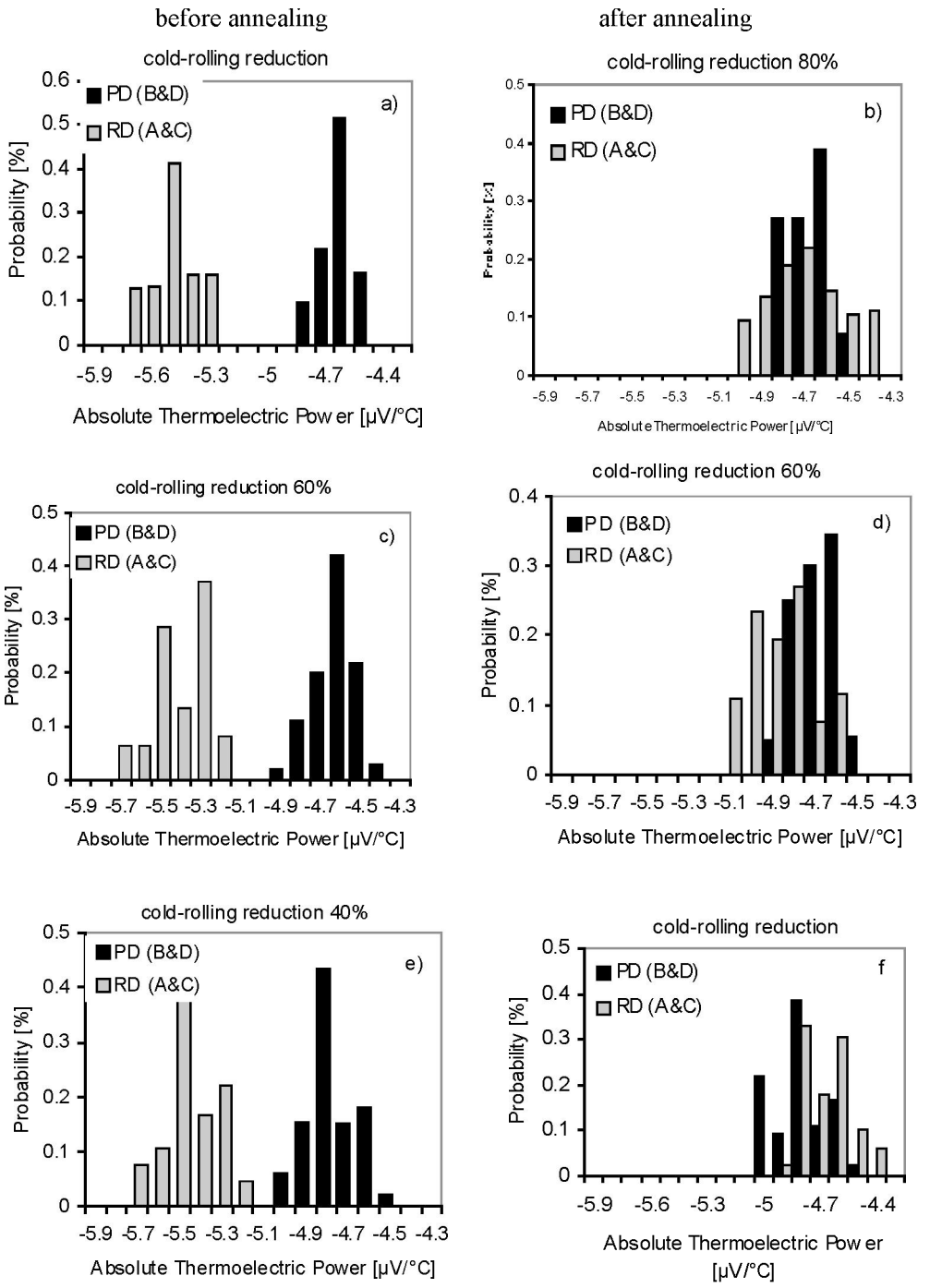

Figure 21. Thermoelectric texture assessment due to the plastic deformation using a gold tip reference in cold-rolled Ti-6Al-4V before and after annealing.

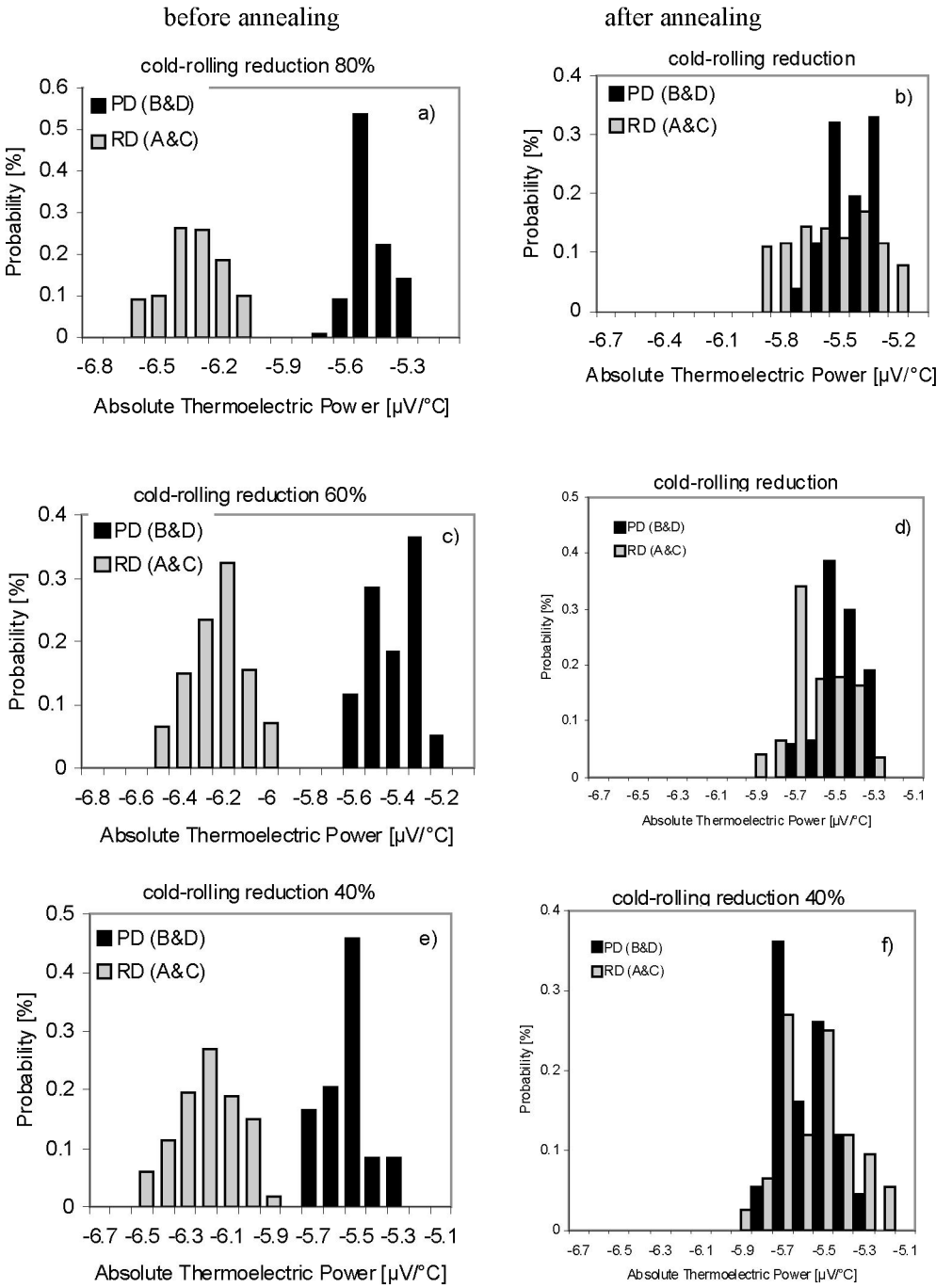

Figure 22. Thermoelectric texture assessment due to the plastic deformation using a copper tip reference in cold-rolled Ti-6Al-4V before and after annealing.

Figure 22 shows the results from the thermoelectric assessment of texture using a copper hot tip reference before and after annealing. The measured data of the copper hot tip reference are shown as a histogram of the probability distributions for the rolling direction RD (A&C)

and the perpendicular direction PD (B&D) in the cold-rolled Ti-6Al-4V samples. Before annealing, the measured data indicates the presence of a strong anisotropy in the thermoelectric power due to the significant difference between RD (A&C) and the PD (B&D) measurements. After annealing, the measured data shows that the difference between RD (A&C) and PD (B&D) was reduced considerably which again indicates that the anisotropy in the thermoelectric power has significantly decreased. Figure 8 shows the thermoelectric power coefficient dependence associated with the different degrees of plastic deformation in the cold- rolled Ti-6Al-4V samples using a copper tip reference before and after annealing. Figures 22 and 23 show that the measurements taken with the gold hot tip reference gave a clearer distinction between the values obtained in rolling direction (RD) and the perpendicular direction (PD) on the TEP when compared to measurements taken using the copper hot tip reference before annealing.

In order to demonstrate that the TEP measurements in the cold-rolled Ti-6Al-4V samples were due to the presence of a strong macroscopic anisotropy produced by the severe plastic deformation, the samples were heated treated (annealed) at 760°C for 2 hours and slowly air-cooled. And example of the microstructure of the 80% cold-rolled sample is shown in Figure 23, in which, the observed metallographic pictures were taken after sectioning, polishing and etching the sample to reveal the microstructure before and after annealing. The microstructure before annealing clearly shows the rolling direction (Fig. 23(a)), in which a preferential orientation of elongated grains is revealed due to the cold rolling process, whereas post annealing (Fig 23(b)) shows a relatively equiaxed and random grain structure with no perceivable preferential orientation and a bimodal grain distribution.

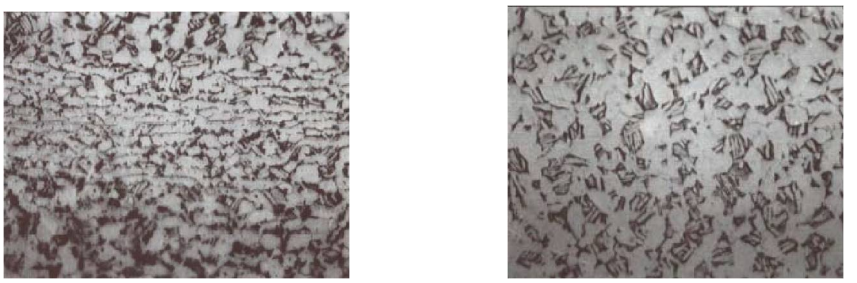

(a) before annealing (b) after annealing

Figure 23. Microstructure of the 80% cold-rolled Ti-6Al-4V sample before and after annealing at 500x. (a) before annealing, it reveals elongated grains with preference orientation (induce anisotropy) due to the rolling process and (b) after annealing, it reveals an equiaxed grain with no preference orientation.

Figure 24 shows the relative difference in the TEP measurements for the rolling direction (RD) and the perpendicular direction (PD) in cold-rolled Ti-6Al-4V samples with the different degrees of reduction in thickness (40%, 60% and 80%) before and after annealing. Before annealing, TEP measurements show an excellent correlation with the different levels of plastic deformation produced by the cold rolling process using gold and a copper tip reference respectively. After annealing, the effects of morphological anisotropic texture caused by the existence of a preferred crystallographic orientation in the polycrystalline microstructure during the manufacturing process (cold work) are greatly reduced. As a result, in all cases the relative difference in the TEP coefficient is not measurable. In addition, the

ultrasonic measurements decreased by as much as ≈1.0% in the relative shear wave birefringence of the different cold-rolled Ti-6Al-4V samples after annealing.

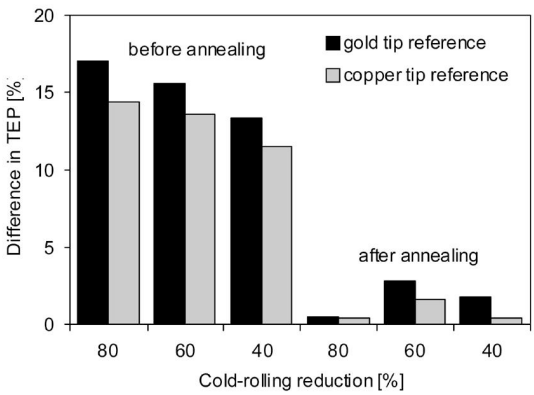

Figure 24. Relative difference in TEP measurements in cold-rolled Ti-6Al-4V with different levels of plastic deformation (cold-rolling reduction) before and after annealing.

5. Conclusion

The research work is organized in the order of the research sequence, i.e., each following section is proposed and developed from the problems encountered in or conclusions derived from the previous sections. Firstly, it was provided an analytical method for calculating the magnetic field produced by thermoelectric currents in anisotropic materials under two-dimensional directional heating and cooling. Experimental results from a textured Ti-6Al-4V titanium-alloy plate are shown to be in very good agreement with the predictions of this model. Since the detectability of small imperfections is ultimately limited by the intrinsic thermoelectric anisotropy and inhomogeneity of the material to be inspected. The described analytical method can be used to optimize thermoelectric inspection procedures and to evaluate the macroscopic texture of metals from their characteristic magnetic signatures. Secondly, it was investigated the spurious magnetic signature produced by the simplest type of macroscopic inhomogeneity when the material properties exhibit a linear spatial variation in the cross-section of a slender bar. An analytical method has been developed for calculating the normal and tangential magnetic fields produced by the resulting thermoelectric currents. Experimental results from a Ti-6Al-4V titanium-alloy bar were shown to be in very good qualitative agreement with the predictions of the analytical model. The results clearly indicate that the observed normal and tangential background signatures on the four sides of the specimen can be attributed to a linear thermoelectric current distribution in the cross-section of the slender bar. However, the larger than predicted magnitude of the observed signatures essentially excludes the possibility that the actual source of these thermoelectric currents is simply a minor inhomogeneity of the isotropic material. Further efforts are needed to better understand the relationship between the strength of the thermoelectric background signature and the microstructural and chemical features of the material. Finally, it has been found that the thermoelectric power coefficient is associated directly with the anisotropy and microstructure in a highly-textured material that presents morphological and crystallographic anisotropy due to plastic deformation produced by the manufacturing process of cold working

in Ti-6Al-4V. The potential applications of the contact and non-contact thermoelectric methods cover a very wide range from detection of inhomogeneities, anisotropy and fretting damage to characterization of hardening, texture, cold work and residual stresses in a titanium alloy.

References

[1] Fulton, J.P., Wincheski, B., Namkung, M. *Nondestructive Evaluation Science Branch*, NASA, 1993; 56.

[2] Carreon, H., Nagy, P. B., Blodgett, M. P. *Res. Nondestr. Eval.* 2002, 14,59.

[3] Carreon, H. *Proc. Vth Int. Adv. Sign. Proces. NDE*, ASNT, CAO, 2006, 5, 163.

[4] Maslov, K., Kinra, V. K. *Mat. Eval.* 2001, 59, 1081.

[5] Tavrin, Y., Krivoy, G. S., Hinken, J. H., Kallmeyer, J. P. *Rev. Prog. Quant. NDE*, AIP, Melville, 2001; 20,1710.

[6] Carreon, H., Nagy, P. B. *Proc. 7th NDE Topical Conf*, ASME, New York, 2001; 20, 209.

[7] Nagy, P. B., Nayfeh, A. H. *J. Appl. Phys.* 2000, 87,7481.

[8] Carreon, H., Nagy, P. B., Nayfeh, A. H. *J. Appl. Phys.* 2000, 88,6495.

[9] Carreon, H. *NDT. & E International*, 2006, 39/1:22.

[10] Shinde, S.R., Hoeppner, D.W. *Wear,* 2006, 261, 426.

[11] Hutson, A.L., Neslen, C., Nicholas, T. Wear, 2003, 36, 13.

[12] Martinez, S.A., Sathish, S., Blodgett, M., Mall, S. Rev. Prog. Quant. NDE, AIP, Melville, 2003; 22, 1531.

[13] Swalla, D.R., Neu, R.W. Tribo. Int. 2006, 39, 1016.

[14] Hutson, A., Sathish, S., Nicholas, T. Tribo. Int. 2006, 39, 1197.

[15] Pyzalla, A., Wang, L., Wild, E., Wroblewski, T. Wear, 2001, 251, 901.

[16] Carreon, H. *J. Alloys & Compounds*, 2007, 427/1-2,183.

[17] Carreon, H. *Proc. Inter. Mech. Eng. Congr. & Exp.* ASME-NDE, Chicago, 2006, 25, 1.

[18] Kropschot, R.H., Blatt, F.J. *Phys. Rev.* 1959, 116, 617.

[19] Hu, J., Nagy, P. B. *Appl. Phys. Lett.* 1998, 73,467.

[20] Rowe, V.A., Schroeder, P.A. *J. Phys. Chem. Sol.* 1970, 31, 1.

[21] Blodgett, M. P., Nagy, P. B. *Appl. Phys. Lett.* 1998, 72, 1045.

[22] Carreon, H. *Wear,* 2008, 465/1-2,255.

[23] Nye, J. F., *Physical Properties of Crystals, Their Representation by Tensors and Matrices,* Clarendon Press, Oxford, 1985; 96.

[24] Carreon, H., Nayfeh, A.H., Nagy, P.B. *Rev. Prog. Quant. NDE*, AIP, Melville, 2002; 21,1455.

[25] Nayfeh, A. H., Carreon, H., Nagy, P. B. *J. Appl. Phys.* 2002, 91,225.

[26] Nayfeh, A. H., Faidi, W. I. *Eur. Phys. J. Appl. Phys.* 2002, 19, 153.

[27] A. H. Nayfeh, W. I. Faidi, M. I. Jaghoub, *Eur. Phys. J. Appl. Phys.* 2003, 22, 103.

[28] Carreon, H., Lakshminarayan, B., Faidi, W. I., Nayfeh, A. H., Nagy, P. B. *NDT. & E International* 2003, 36,339.

[29] Carreon, H., Lakshminarayan, B., Nagy, P. B. *Rev. Prog. Quant. NDE*, AIP, Melville, 2004; 23, 445.

[30] Lakshminarayan, B., Carreon, H., Nagy, P.B. *Rev. Prog. Quant. NDE*, AIP, Melville, 2003; 22, 1523.
[31] Carreon, H., Medina, A. *Nondestruct. Test. Eval.* 2007, 22/4, 299.
[32] Nagy, P. B.,Hu, J. *Rev. Prog. Quant. NDE*, Plenum, New York, 1998; 17, 1573.
[33] Carreon, H. *Nondestruct. Test. Eval.* 2009, 24/1, 233.
[34] Lasseigne, A.N., Olson, D.L., Kleebe, H.J., Boellinghaus, T. *Metal. & Mater. Trans.* 2005, 36A, 3031.
[35] Park, Y.D., Kaydanov, V.I., Mishra, B., Olson, D.L. *Rev. Prog. Quant. NDE*, AIP, Melville, 2005; 24, 1308.
[36] Kawaguchi, H., Yamanaka, S. *J. Nondest. Eval.* 2004, 23, 65.
[37] Carabajar, S., Merlin, J., Massardier, V., Chabanet, S. *Mater. Sci. & Eng. A.* 2000, 281, 132.
[38] Carreon, H. Proc. 136th TMS Annual Meeting, *Characterization of Minerals, Metals, and Materials,* TMS, 2007; 25.
[39] Zaefferer, S. *Mater. Sci. & Eng.* 2003, A344, 20.
[40] Kocks, U.F., Chandra, H. *Acta Metallurgica*, 1982, 30, 695.
[41] Crosby, K.E., Mirshams, R.A., Pang, S.S. *J. Mat. Sci.* 2000, 35,3189.
[42] Philippe, M.J., Serghat, M., Van Houtte, P. *Acta Materiallia,* 1995,43,1619.
[43] Fjeldly, A., Roven, H.J. *Acta Materiallia*, 1996,44,3497.
[44] Zhu, Z.S., Liu, R.Y., Yan, M.G., Cao, C.X. *J. Mat. Sci.* 1997,32,5163.
[45] Carreon, H., Ruiz, A. *Proc. Inter. Mech. Eng. Congr. & Exp.* ASME-NDE, Boston, 2008, 27, 1.
[46] Carreon, H. *NDT. & E International*, 2006, 39/6,433.

In: Titanium Alloys: Preparation, Properties and Applications ISBN: 978-1-60876-151-7
Editor: Pedro N. Sanchez, pp. 143-233

Chapter 3

FRETTING WEAR AND FRETTING FATIGUE STUDIES OF SURFACE MODIFIED BIOMEDICAL TITANIUM ALLOYS

Aravind Vadiraj and M. Kamaraj
Advanced Engineering, Ashok Leyland Technical Center, Vellivoyalchavadi, Chennai, 600 103, Tamilnadu, India, Department of Metallurgical and Materials Engineering Indian Institute of Technology Madras, Chennai, 600 036, Tamilnadu, India

Abstract

Load bearing implants such as hip joints, knee joints and bone plates etc. are prone to failure from the synergistic effect of fretting wear and fatigue during physical bodily movement. Fretting wear or fretting fatigue is a form of adhesive wear phenomenon wherein a small tangential oscillatory motion under high contact pressure gradually erodes the surface and initiates crack within the contact leading to ultimate failure of the material under fatigue loading condition. Modular junctions of hip implants consist of ball on a tapered shaft experiencing fretting wear during body movements.

Titanium alloys, Stainless steels and Co-Cr-Mo alloys are the most commonly used alloys for medical grade devices. Titanium alloys has high strength to weight ratio, superior biocompatibility and corrosion resistance compare to other materials. Surface modified titanium alloys have better tribological properties. In this work, the substrate materials used are Ti-6Al-4V and Ti-6Al-7Nb. PVD TiN coating, plasma nitriding, nitrogen ion implantation, laser nitriding favors formation of TiN and Ti_2N of different thickness according to the process. Thermal oxidation process favors formation of hard and brittle oxide layer.

Fretting wear tests were conducted to study the quality of the coatings and modified layers. Laser nitriding and PVD TiN coating has shown better performance than other coatings due to high hardness of the layers. Friction coefficient for PVD TiN coating is around 0.2 throughout the test. Wear volume for PVD TiN coated and laser nitrided samples were almost 10 and 50 times lesser than other coatings respectively.

Fretting fatigue life of surface modified titanium alloys has considerably improved compared to unmodified materials. Plasma nitrided pairs have shown the best performance over all the coatings. The average fretting fatigue lives of unmodified pairs were 15 to 18% of plasma nitrided pairs, 45 to 50% of the PVD TiN coated pairs and about 60% of ion implanted pairs. Fretting of unmodified alloy pairs have shown high friction and oxidation at the contact

due to metallurgical compatibility of the pairs. Fretting of PVD TiN pairs have shown delamination and subsequent oxidation. The damage and friction generated within the contact is a complex interaction between third body particulates, oxide debris and ringer solution. Fretting fatigue life is more for plasma nitride pairs compared to all other modification processes. The damage of ion implanted pairs is similar to unmodified alloys with little improvement in fretting fatigue life. Laser nitrided pairs and thermally oxidation pairs have shown poor fretting fatigue life due to high case thickness and inhomogenities of the layers formed. Friction generated is low compared to al other process, but the specimens experienced premature failure at higher loads.

1. Introduction

1.1. Materials

Materials used for biomedical implants are medical grade stainless steels (SUS 316 LV), Co-Cr-Mo alloys, and titanium alloys (Sumita et. al., 1994). The elements used in these alloys such as Ni, Cr, Mo and Co are not so compatible to the human system (Mark et. al., 1998, Kamachi Mudali et. al. 2003). Titanium alloys are widely used for various applications such as aerospace, chemical industries and biomedical industries. They are selected for biomedical applications due to superior performance in terms of biocompatibility and corrosion resistance within the human body (Mark et. al., 1998). They also have high specific strength, high hardness, and low stiffness compared to other materials which helps in minimizing bone resorption. The primary drawback of titanium based biomedical alloys is its poor resistance to sliding wear or fretting wear which needs immediate attention for increasing the service life as implants. Leyens and peters (2004) attribute the poor wear resistance of pure titanium and titanium alloys to lower c/a ratio of α phase. The wear damage can be minimized by altering the surface composition, which favors the formation of hard ceramic compounds with better tribological properties.

1.2. Surface Engineering of Biomedical Implants

Surface engineering is one of the emerging areas in the field of material science or tribology aiming towards modification of the surface for improving its life and efficiency while retaining its original bulk properties. It shows improvement in in-service performance, useful working lifetimes, aesthetic appearance or economics of production. The surface modified components not only improve the tribological performance of the parts but also minimize the investment on repair or replacement. Surface engineering of biomaterials has attracted attention for various important reasons. Wear, fretting and corrosion have become the most important concern in designing the various implants. Harder and biocompatible surfaces of implanted materials prolong the life of the device within the harsh human body environment. Human body fluid contains blood, tissue fluids, amino acids and proteins (Sumita et. al., 1994). Lower partial pressure of oxygen within the body accelerates corrosion of metallic implants due to reduced availability of oxygen for repassivation (Kamachi Mudali et. al., 2003). The various forms of surface damage produce unwanted products which invite hostile tissue reactions and also minimize the life of the implant. In biomedical devices, quality overrules the cost of the product. It is extremely necessary to maintain the superior

quality of the device for improved performance in the human body. Therefore surface modification has become an important part of the manufacturing processes for all the bio implants in the recent times.

1.3. Importance of Surface Treatments for Titanium Alloys

Surface modification of titanium alloys are also widely studied to serve the purpose of improved performance within the aggressive body environment. It is observed that surface modified titanium alloys perform much better in terms of both biocompatibility and wear resistance than virgin materials. Elements such a nitrogen, carbon and oxygen are introduced into the surface by various methods thereby altering the chemistry of the surface for superior performance. Nitrogen alloyed titanium is by far the widely studied area for medical applications. It favors formation of hard and chemically resistant titanium nitride/oxides which offers high resistance towards fretting damage. However there is always an optimum level of modified layer thickness beyond which the performance of load bearing components would degrade due to lower ductility and hence strain tolerating capacity of the modified layers.

1.4. Fretting Wear and Fretting Fatigue

Fretting phenomenon is observed when contacting bodies are under vibration induced relative sliding (100 - 200μm) (Mutoh, 1995, Waterhouse, 1972). Fretting wear is due to micro motion between contacting bodies induced by vibration and fretting fatigue is due to micro motion induced by cyclic loading of one of the contact member. Fretting wear induces localized damage at the contact, but fretting fatigue causes catastrophic failure of cyclically loaded member. It is common to observe such a thing in flywheel fitted to shaft fabricated as one assembly under cyclic load. Fretting damage is observed along the circumference of such a joint. Bearings of automobiles and gun mountings in military vehicles have also incurred such problems due to vibration during its motion (Waterhouse, 1972). In some cases fretting is considered beneficial to dampen vibration by absorption of the energy. Fretting can also take place in different temperatures and environments depending upon the application of the material. Depending upon the medium, it can take place in sea water, within the human body, nuclear reactors or heat exchangers. Fretting can also produce deleterious effects in electrical contacts, bio implants, steel ropes, cycle pedals and industrial valves. The damages caused by fretting are classified into pits, debris, scratches, metal transfer, surface plasticity, subsurface cracking, and craters. Dobromirski, 1992 indicates that there are more than fifty parameters that govern fretting phenomenon of the interacting surfaces.

The main principle of fretting wear experiments is described in Fig 1.1. It involves two contacting surface under a definite normal pressure. The contact configuration can be of different types. Ball-on-flat arrangement is most commonly used. Fretting wear is induced with definite slip amplitude and normal force (indicated by arrows). Tangential force is monitored with force transducers butted to a stationary member of the contact pair. Data acquisition systems are used to record the various parameters. Fretting wear results are represented as variation of tangential force with time or fretting cycles, changes in force-

displacement (F-D) loop with time or number of cycles, scar micrographs, roughness profile along the scar and wear volume generated.

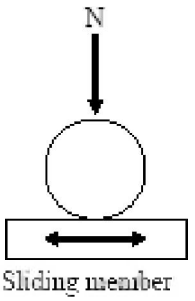

Figure 1.1. Principle of fretting wear.

Fretting fatigue is simulated in the laboratory using tensile specimen and contact pads as shown in Fig 1.2. There are wide varieties of specimens and contact pad configurations that have been used to conduct laboratory scale fretting fatigue experiments. Contact pads are used to apply normal pressure on opposite sides of the tensile specimen subjected to cyclic stress amplitude at certain frequency. The area of contact initially is always less than the real area due to surface irregularity. This is called the apparent area of contact. Crystallographically smooth surface is generally difficult to prepare. Asperities wear down and the area of contact gradually increases with time. When a calibrated normal force (P) is applied on the specimen, tangential force (Q) is generated at the interface during sliding. Extensive localized plastic deformation at the interface area can be observed depending upon the material and magnitude of contact pressure. The relative motion between rubbing interfaces is normally measured as slip amplitude (δ), which is one of the important parameter to predict the life of the components.

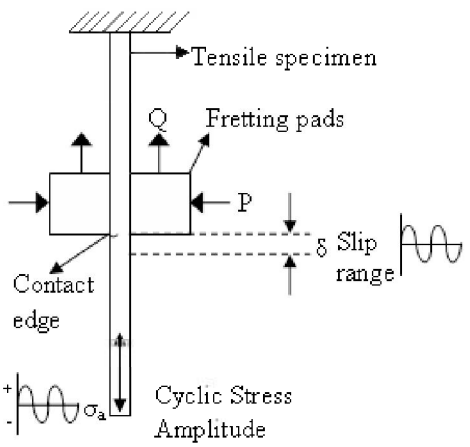

Figure 1.2. Schematic diagram of fretting fatigue phenomena.

Laboratory tests must simulate the original fretting conditions of the contact as closely as possible in order to correlate the results to the original service of the components. Therefore fretting experiments involve large number of independent variables acting synergistically introducing complexity in quantifying and correlating them to the final life of the components. Localized fretting action will also raise the temperature of the mating bodies and causes transformation of the surface material. The transformation product is also influenced by the environment around the components.

1.5. Scope of the Present Work

The present work focuses on investigating the effect of surface coatings/modification on fretting wear and fretting fatigue damage of Ti-6Al-4V and Ti-6Al-7Nb alloys. The surface modification processes used in this work are PVD TiN coating, plasma nitriding, nitrogen ion implantation, laser nitriding and thermal oxidation. Fretting wear is conducted with alumina ball and 1N normal force in air and Ringer fluid for all the coatings. Fretting fatigue is conducted with 40 MPa (600 N) contact pressure and axial stresses in the range of 67 to 500 MPa.

2. Literature Review

2.1. Preface

The following section gives an extensive literature on biomaterials, titanium alloys used for biomedical applications, orthopedic devices, total hip arthroplasty (THA), fatigue and fretting fatigue of biomedical devices, fretting wear and fretting fatigue mechanism and its applications related to engineering materials including biomedical titanium alloys.

2.2. Biomaterials

Biomaterials are a class of biologically compatible materials utilized for restoring the activity of damaged part of the human body, which can perform similar function of a natural system. They are widely used for repair, replacement or augmentation of diseased or damaged parts of musculoskeletal system. According to their period of service, they are classified as implants when they remain for substantial period of time and prostheses when they last until the end of lifetime. Orthopedic implants are normally fixed unto the skeletal system for restoring the lost function of the original part. Figure 2.1 shows some of the biomedical devices used in different parts of the body. It is also necessary for them to function without receiving any adverse tissue reactions or any inappropriate effects. Material suitable for implantation must therefore tolerate the aggressive environment and cyclic stress condition in case of load bearing joints. Orthopedic materials include ceramics, polymers and metallic alloys are commonly used for manufacturing medical devices.

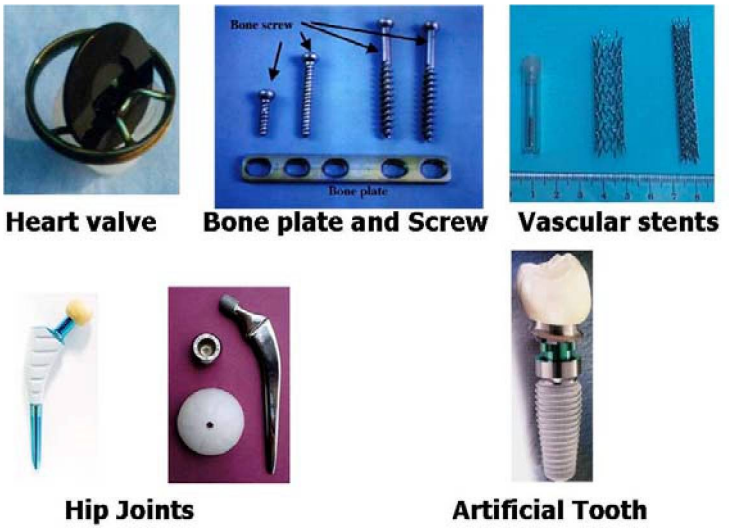

Figure 2.1. Biomedical devices for various applications.

Ceramics are inorganic compounds known for its good chemical stability within the body environment. They are carbon, alumina, zirconia, bioactive glass and calcium phosphate. The limitations of ceramic materials are their low tensile strength and fracture toughness. Polymers are normally used for hip sockets due to its close resemblance to natural tissue components. They are prone to degradation from biochemical and mechanical factors within the body environment resulting in formation of hydroxyl ion finally leading to allergic reactions. Fiber reinforced polymers have also been investigated for femoral components of hip joint arthroplasty and bone cements. They also suffer from degradation under complex states of stresses and low mechanical strength. Metals and alloys have wide range of applications ranging from dental amalgams to total joint replacements. The high strength and ductility of metallic systems makes them more suitable for load bearing implant applications due to reduced susceptibility for permanent dimensional changes in response to cyclic stress conditions. Three common alloys used for orthopedic applications are stainless steel (316 LV), cobalt-chromium alloy and titanium alloys. Amongst all the materials, titanium and its alloys are most commonly used for orthopedic devices (Marc Long et. al., 1998).

2.3. Titanium Alloys for Orthopedic Applications

Titanium alloys are attractive material in the field of orthopedic applications due to its lower modulus, excellent biocompatibility and corrosion resistance compared to other conventional materials previously used such as stainless steels and cobalt based alloys. The composition must be carefully selected to obtain the required properties as well as to avoid any adverse reaction from the release of elements. The metallic alloys used for fabrication of artificial joints undergo corrosion and release metallic ions into the patient's body. High corrosion rates and solubility of the corrosion products by release of metal ions by implants induces detrimental allergic effects. Elements such as V, Ni and Co are found to be highly

toxic (Sumita et. al., 1994). Therefore, stainless steels and cobalt-chromium alloys are not suitable as implants for this reason. Whereas Ta, Nb and Zr are good biocompatible substitutes for these elements. Even Mo, Al and Sn are reported as not fully biocompatible elements (Yoshimitsu et. al., 2005, Marc Long et. al., 1998, Nadim et. al.,, 2003). The most often observed form of this allergy is skin rashes. The frequency of skin sensitivity to metals in patients with artificial joints is substantially higher than that in the general population (Hallab, 2001). The β titanium alloys with lower modulus of elasticity falls into the category of second generation alloys having made from more biocompatible elements such as Ta, Zr and Nb. Geetha et. al., 2003 gives a detail review on corrosion and microstructural aspects of titanium and its alloys. Some of advanced alloys are being tried for vascular stents, catherter guide wires, orthodontic arch wires and cochlear implants. Table 2.1 (Mitsuo Niinomi, 1998) gives the mechanical properties of all the medical grade titanium alloys currently in wide application for medical prosthesis.

Table 2.1. Mechanical properties of biomedical titanium alloys (Mitsuo Niinomi, 1998).

Alloy	Tensile strength (MPa)	Yield strength (MPa)	Elongation (%)	RA (%)	Modulus (GPa)	Type of alloy
Pure Ti Grade 1	240	170	24	30	102.7	α
Pure Ti Grade 2	345	275	20	30	102.7	α
Pure Ti Grade 3	450	380	18	30	103.7	α
Pure Ti Grade 4	550	485	15	25	104.1	α
Ti-6Al-4V ELI (mill annealed)	860-965	795-875	10-15	25-47	101-110	α+β
Ti-6Al-4V (annealed)	895-930	825-869	6-10	20-25	110-114	α+β
Ti-6Al-7Nb	900-1050	880-950	8.1-15	25-45	114	α+β
Ti-5Al-2.5Sn	1020	895	15	35	112	α+β
Ti-5Al-1.5B	900-1080	820-930	15-17	36-45	110	α+β
Ti-15Sn-4Nb-2Ta-0.2Pa (annealed) (aged)	715-919	693 806	28 18	67 72	94 99	α+β
Ti-13Nb-13Zr (aged)	973-1037	836-908	10-16	27-53	79-84	Near β
TMZF (Ti-12Mo-6Zr-2Fe) (annealed)	1060-1100	1000-1060	18-22	64-73	74-85	β
Ti-15Mo (annealed)	874	544	21	82	78	β
Tiadyne 1610 (aged)	851	736	10	-	81	β
Ti-15Mo-5Zr-3Al (ST) (aged)	852 1060-4400	838 1000-1060	25 18-22	48 64-73	80	β
21 RX (annealed) (Ti-15Mo-2.8Nb-0.2Si)	979-999	945-987	16-18	60	83	β
Ti-35.3Nb-5.1Ta-7.1Zr	596.7	547.1	19	68	88	β
Ti-29Nb-13Ta-4.6Zr (aged)	911	864	13.2	-	80	β

2.4. Total Joint Replacement (TJR)

It is generally understood from many years of medical investigation and experience that human joints such as hip, knee or shoulder joints are highly prone to degeneration leading to acute pain and joint stiffness commonly termed as osteoarthritis. Osteoarthritis develops slowly over several years. The symptoms are mainly pain, swelling, and stiffening of the joint. Pain is usually worse after activity, such as walking.

People, who suffer from chronic hip pain or degenerative joint disease of the hip, often have their ailing hip joint replaced with an artificial one. These artificial joints (or hip implants) are made of alloys, such as titanium or stainless steel, and have long stems which penetrate deep into the femur canal (center of the thigh bone) to hold them in place.

2.5. Total Hip Arthroplasty (THA)

In a surgical operation known as Arthroplastic surgery or Primary Total Hip Replacement (PTHR), the surgeon initially anesthetizes the lower part of the body below from the hip, while the blood is continuously supplied from the upper region of the body. The hip area is incised and the surgeon cuts off the natural joint and later drills a hole down the femural canal, and inserts the implant firmly into the hole, sometimes using special cement (PMMA) or a positioning ring (Fig 2.2) to ensure that implant stays tightly fixed in place. The surgery normally takes several hours and complete healing takes several months. Hip prosthesis is made up of a shaft, ball and socket that fit together to form a joint similar to natural joints. The parts of the hip shaft will be explained clearly in the later part of the chapter.

Various types of high-grade surgical metallic alloys used in combination with special metal/plastic/ceramic weight-bearing surfaces are cemented into place, reproducing a smooth articulating joint. An X-Ray negative of the implanted hip prostheses is shown in Fig 2.2 (Sumita et. al., 1994).

Figure 2.2. X-Ray of an implanted hip.

2.6. Fatigue Fracture of Total Hip Prosthesis

All the modern alloys used for manufacturing total hip prosthesis are strong enough to resist fatigue fracture from these repeating stresses in average.

There is a limit to how much repetitive loads the prosthesis will eventually sustain. This limit is specific for every form of the total hip prosthesis and for the metal alloy used for manufacturing the prostheses. Above this limit, the prosthetic shaft will not sustain the fatigue fracture. Closer examination of these cases revealed that the fractures occurred in heavy patients, often after an accident. The examination of the broken shafts sometimes reveals defects on the surface such as scratches and pits (Teoh, 2000). Many manufactures have also developed bulky models of artificial joints for heavyweight patients. Evaluation of fatigue behavior is normally done through fracture mechanics approach and in-vitro fatigue test. Fracture mechanics approach involves investigation of crack growth rate of pre-cracked compact tension specimens in physiological medium. In-vitro test for evaluating of fatigue resistance in physiological medium is more useful due to conjoint effect of corrosion and fatigue.

2.7. Stress Shielding

The prosthetic shaft takes off a part of the stress that walking and other everyday activities put on the upper part of the thighbone holding the prosthesis. The stiffness of the bone (10 - 30 MPa) is almost 7 times less than stainless steels (>200 MPa) and Co-Cr-Mo (230 MPa) alloys. The shielded bone thus loses its strengthening substance and becomes weak due to improper transfer of load from the prostheses. The total hip joint may then fail due to improper anchorage in a weakened femural canal. The remedy is to use a prosthetic shaft manufactured from metal alloys with stiffness similar to bone. Second generation titanium alloys (β grade) have the lowest stiffness among all other orthopedic materials and therefore shafts of cementless total hips are often made from these alloys.

2.8. Fretting Fatigue of Hip Prostheses and Bone Plates

Figure 2.3a shows hip prostheses implanted within the femur canal experiencing compressive cyclic loads due to body weight. Fig 2.3b shows fracture fixation device or bone plate with screws. Fretting areas are clearly indicated in both the figures. Modular joints and stem-bone cement interface are the two possible areas of fretting failures in hip prostheses. Fig 2.4 shows the post implantation failure incidences due to fretting fatigue in hip joints and bone plates. Modular junctions involve male/female tapered junction interlocked together due to friction. Metal-metal or metal-ceramic combinations are widely used as stem and ball heads. The combinations can be same or different in metal on metal couples. Cobalt-chrome heads on titanium stems are commonly used with cobalt-chrome, titanium, alumina or zirconia heads.

Kamachi et. al., 2003 have reported a detailed survey of failures of stainless steel orthopedic implants due to corrosion, fatigue and wear. According to their assessment, 74% of implants failed at the tapered junction of the shaft due to fretting fatigue. Every fretting cycle compounds the damage, generates harmful metal debris and exposes the bare metal surface to

the surrounding corrosive bio environment. It also causes clearance at the contact. Adverse toxic effects have been reported even with 10 ppb of micro-debris particles (Teoh, 2000). Some of the prostheses are provided with metal fixtures to prevent the stem from turning.

In titanium implants, which are considered highly biocompatible compared to other materials, blackening of surrounding tissues have been reported, which is called metallosis (Sumita et. al., 1994). This may arise due to severe fretting conditions such as large variation in contact pressure and cyclic loads.

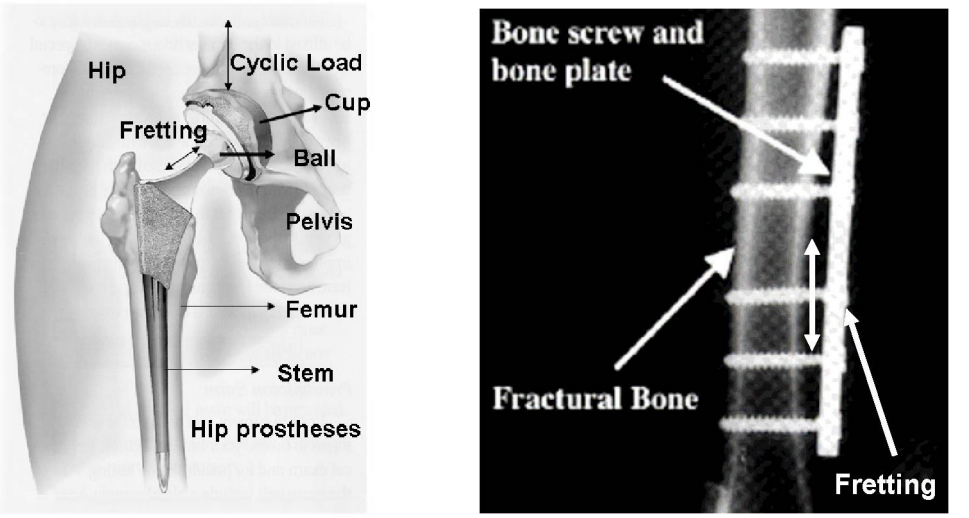

Figure 2.3. Fretting of (a) Hip implant, (b) Bone plate (Sumita et. al., 1994).

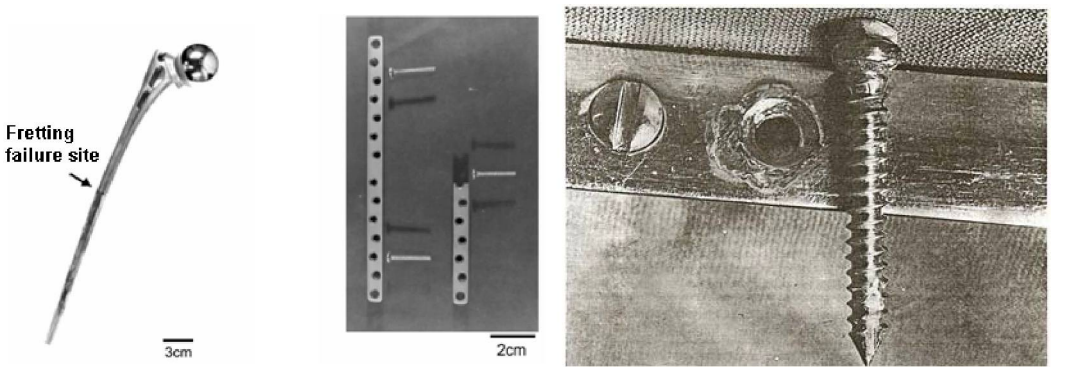

Figure 2.4. Fretting failure incidences of hip joints and bone plates (Sumita et. al., 1994).

Therefore, either fretting action must be completely arrested or damage must be minimized by surface modification. The concentration of each metallic element is obtained from filtering the recovery liquid through certain membrane and analyzing the residue. Fretting motion experience lubricating conditions experiencing more dwell in the gross slip regime. Tangential force will be relatively reduced compared to fretting test in air unless the medium is highly corrosive causing the roughening of the surface. Longer dwell time may also aggravate the corrosion of exposed underlying metal.

From the electrochemical reaction point of view, fretting of surface would lead to fracture of oxide layers and drop in the OCP voltage (Hallab et. al., 2003). Its repassivation would increase the concentration of harmful chloride and hydrogen ions at the surrounding area due to consumption of oxygen. Both the mechanism would reduce the stability of the oxide film. Corrosion of implants will lead to premature failure and immediate tissue reaction. Most in-vivo studies indicate sustained release of metallic elements into the body fluids leading to infection and inflammation from toxic compounds. It is assumed that implant alloys continuously dissolves and reprecipitates on its surface. Repassivation time of the surface depends upon the material and surrounding medium.

Fretting fatigue failures can also be encountered by fretting damage of shaft from filler bone cement within the femur canal. Bone cement is filler material used for fixation of the artificial joints to the bone stock. It is a compound consisting of 90% polymethylmetacrylate (PMMA) and barium sulfate. The bone cement as prepared by the surgeon at the operation table is a material with many drawbacks. (a) It is mechanically weak because it has entrapped impurities such as air and blood, (b) It spawns small particles from its surface containing hard crystals of Barium sulfate, which scratch and damage the fine joint surfaces of the artificial joint. (c) It may also cause allergy and anaphylactic reaction during the operation. So fretting degradation is highly possible in this area.

Fretting studies of titanium alloys is more meaningful in a physiological medium representing the body fluids. Ringer solution, phosphate buffered solution (PBS), hank's balanced salt solution (HBSS) are some of the widely accepted mediums for preliminary biomaterial fretting fatigue studies. Starosvetsky et. al., 2001 have studied the corrosion behavior of 1 μm titanium nitrided coating on Ni-Ti alloy in ringer solution although the protein may influence the surface. Laure Duisabeau et. al., (2004) have conducted fretting wear test for Ti-6Al-4V and AISI 316L stainless steel in ringer solution. They remark that the presence of a solution containing chloride ions activates a localized corrosion phenomenon, which leads to modification of the displacement regime. Wear tests of biomedical alloys are normally conducted with dilute bovine serum in varying concentration. It is also observed that high temperatures generated during fretting will denature the protein and increases the viscosity of the medium. Although the fretting motion is affected by the proteins in the body, the effect of chloride ions is considered in these experiments.

Surface engineering of titanium alloys used for biomedical applications has a promising future from the view of minimizing in-service degradation of biomedical devices due to wear and corrosion. It also greatly improves the biocompatible nature of the materials to suit the surrounding body fluid environment. Some of the widely used processes of surface modification are described below.

2.9. Surface Engineering of Titanium Alloys

2.9.1. Nitriding of Titanium Alloys

Nitriding of titanium alloys has been investigated for many years. Nitrogen is found to significantly strengthen the surface layer due to its higher solubility in α-Ti. It has higher diffusion coefficients in titanium alloys. Introduction of nitrogen into titanium produces compound layers of TiN and Ti_2N with hardness of 3000 and 1500 VHN respectively (Ani

Zhecheva et. al.,, 2004). Harder and biocompatible layers of nitrides are favorable for improving tribological properties of biomedical devices. The formation of compounds also depends upon the process being used to inject nitrogen into the material. It can be introduced by slow diffusion process aided by thermal energy or quickly through ion implantation.

2.9.2. Processes of Surface Modification

Many different processes are available for improving the surface properties of biomedical devices. They are selected based on their quality of improvement of implant surfaces. The following is a brief description of the processes normally used for surface modification of titanium alloys and the processes used for current experiments.

2.9.2.1. Physical Vapor Deposition (PVD)

PVD is a form of vapor deposition wherein a substance is evaporated, and then condensed onto a substrate for the purpose of coating the substrate. This process is generally performed in a vacuum. The basic idea behind physical vapor deposition (PVD) is the physical change of state of the material that is being deposited (target material). There are two main ideas that are used to obtain a vapor state of the material being deposited. There is evaporation of the material either through thermal heating of a filament or through melting the material with an electron beam or laser. The second method that is used is to physically remove the target material atoms with the transfer of momentum from an incident particle such as ions. This type of material removal is called sputtering. The coatings can be from a single element or a compound. Compounds can be produced by mixing the evaporated element with another element usually in the form of gas. This process is widely used for developing titanium nitride (TiN) coating on titanium alloys and has been under investigation since many years for biomedical applications.

Huang nan et. al., 1996 have studied the fatigue behavior of titanium based biomaterial coated with 1.4 μm titanium nitride film by ion beam enhanced deposition. Shenhar et. al., (2000) have characterized residual stresses and fretting wear behavior of 2 μm TiN coating developed on surgical titanium alloys by powder immersion reaction assisted coating method. A major reduction in fretting damage was reported from the coated alloys. In these experiments, an attempt is made to study the fretting wear and fretting fatigue behavior of 2 μm thick PVD TiN coated titanium alloys.

Zenghu Han et. al., 2004 have investigated the effect of coat thickness and substrate (high strength steel and stainless steel) on the mechanical properties of PVD TiN coatings using nano indentation technique. He concluded that hardness and modulus of TiN vary with different substrates and different coating thicknesses. TiN coatings on harder substrates or with higher thicknesses show greater hardness and elastic modulus. These effects can be attributed to the internal stress of TiN. TiN coatings are generally characterized by high abrasion resistance, low coefficient of friction, high temperature stability and high hardness. These properties also make it more biocompatible in the human body. It is observed that TiN with (111) preferred orientation has the highest hardness governed by thickness and residual stresses of the film (Wen-Jun Chou et. al., (2003)). The ultimate interfacial shear stresses between coating and substrate can be evaluated from simple tensile test and measurement of surface cracks (Wen-Jun Chou et. al., 2003, Takahito Ohmura et. al., 2003).

TiN has a NaCl type structure with the active slip system of {110} <110> (Hultman et. al., 1994). Plastic deformation is possible if resolved forces act on this plane. If the external forces are perpendicular to (111) system, then it is difficult for the deformation and hence higher hardness are obtained. At higher temperatures (> 200 °C), the hardness of the substrate decreases and the wear rate rapidly increases (Badisch et. al., 2003). Post heat treatment of coated samples also sometimes improves the hardness of the coating due to structural rearrangement (Wen-Jun Chou et. al., 2003).

2.9.2.2. Plasma Nitriding (PN)

It is a thermochemical treatment by which nitrogen is ionized in vacuum and allowed to diffuse into the substrate maintained at high negative voltage. Plasma nitriding (also known as glow discharge or Ion nitriding) is a low temperature; low distortion surface engineering process. Glow discharge plasma is used to transfer nitrogen ion into the surface of the components undergoing treatment. It requires specialized equipments with high ionizing energies. The components are made the cathode of an electrical circuit whilst the chamber becomes the anode; application of a voltage between the 2 electrodes establishes a current intensive glow discharge. This anomalous glow discharge covers the entire cathode supplying heat to the surface of the parts and a supply of nitrogen. Nitrogen is able to diffuse into the surface where it combines with nitride forming elements to form alloy nitrides. Bekir et. al., 1996 has investigated plasma nitriding of Ti-6Al-4V and found a dramatic improvement in wear and frictional properties from the presence of δ-TiN and ε-Ti_2N.

2.9.2.3. Laser Nitriding (LN)

Laser beam nitriding is also a specialized technique meant for improving the surface of materials apart from cutting, melting and welding applications. Laser nitriding works by melting the surface using a focused beam in nitrogen atmosphere to form hard nitride layers. Nitrogen is fed through nozzle held at 30 degrees into the melt pool. The process parameters such as laser pulse energy, scanning speed and gas flow rate and concentration determines the thickness of surface layer compounds. It requires special equipments and also dependant on the geometry of the process. Man et. al., 2005 have studied laser nitriding on Ti-6A-4V and reported the formation of three dimensional networks of TiN dendrites.

2.9.2.4. Ion Implantation (II)

Ion implantation is a high technology approach for modifying surface properties of materials. Unlike coating process, it does not involve the development of layer on the surface. It was initially developed for use in semiconductor applications and in fact still used extensively in that capacity today. Ion implantation utilizes highly energetic beams of positively charged ions to modify surface structure and chemistry of materials at low temperature (< 180°C). The process does not adversely affect component dimensions or bulk material properties. Early applications of ion beams were removal of material (now called etching) and deposition using non-reactive beams. From the 1980s until today, their use have eventually progressed to reactive processes and property modification. Surface properties improved with Ion Implantation are wear resistance, corrosion resistance, hardness, reduced

friction, fatigue and fretting fatigue resistance, oxidation, adhesion, and decorative finish (Elder et. al., 1989). The process can be applied to virtually any material, including most metals, ceramics and polymers. However, the effects of the process are typically material-specific. Examples of components treated with ion implantation are Ti and Co-Cr orthopedic prostheses, which are made harder and more wear resistant with the process and silicone rubber catheters, which are made less tacky and more water wettable for improved insertion and biological compatibility. Currently the high cost of process has restricted their use in medical implants, nuclear fuels, jet engine parts and expensive tools.

The three hardening mechanisms of ion implanted titanium alloys are: ion induced damage, solid solution hardening, and precipitation hardening. Ion induced lattice damage creates dense network of dislocations similar to cold worked structure. The strain fields make the deformation of the lattice network more difficult thereby improving tribological properties. In solid solution strengthening, the same strain fields are obtained through interstitial or substitutional impurity atoms. In precipitation strengthening, the dislocation movements are hindered by coherent or incoherent precipitates. Precipitates are usually observed for fluence greater than 10^{17} ions/cm^2. Solid solution hardening is achieved by fluence in the range of $10^{16} - 10^{17}$ ions/cm^2. The hardening achieved by surface compressive residual stresses or lattice damage is obtained with the fluence less then $10^{15} - 10^{16}$ ions/cm^2.

2.9.2.5. Thermal Oxidation (TO)

TO is a novel, cost effective and environmentally friendly surface engineering technique for titanium or titanium alloys. It can be conducted in ambient air. It is thermally aided diffusion of oxygen at elevated temperatures. Several investigations have been done on characterization of TO layer in Ti-6Al-4V alloy (Hasan Guleryuz et. al., 2004). TO can provide a titanium surface with dramatically reduced coefficient of friction and galling tendency when in rubbing contact with another engineering material surface, especially under lubricated conditions. Furthermore, the load bearing capacity of the surface is greatly increased. TO process can not only significantly improve the tribological behavior but also the corrosion resistance of titanium and titanium alloys. The surface is chemically inert and biologically compatible with cells and tissues and is ideally suited to use in surgical implants.

The oxygen atoms that diffuse into the metal can occupy both interstitial and substitutional sites, making the material harder, and since the concentration of oxygen at the surface would be much greater than interior, it should be harder near the surface and relatively softer inside. The correlation between the concentration profiles and hardness profiles suggests that microhardness testing can be an effective tool in studying the oxygen diffusivity in titanium.

2.10. Studies on Specific Titanium Alloys

2.10.1. Ti-6Al-4V (ASTM 1472)

It is one of the most popular α+β titanium alloys developed in the early 1950s at Illinois Institute of Technology, USA. It has good balance of mechanical properties and by far the most intensively developed and tested titanium alloys. Aerospace industries are the largest

users of these all alloys. It is also very well suitable for medical applications compared to stainless steels and cobalt-chrome-moly alloys due to low stiffness and excellent biocompatibility, two most important factors for designing medical implants. Although they possess excellent biocompatibility and corrosion resistance, the presence of Al and V are known to cause cytotoxic effects and neurological disorders in its long term applications as virgin implants. Conjoint action of corrosion and wear is studied through fretting corrosion potential measurements of real implants in a simulated body solution. The various oxide films on the surface may also play a significant influence on adhesive wear of mating couple. Surface modified alloys have served far better compared to virgin alloys due to its superior resistance to wear and corrosion. The case depth, hardness and uniformity of the modified layer determine the capacity to resist wear damage. The implants such as hip joints or knee joints have to function for longer periods in younger patients. Surface modified Ti-6Al-4V promise a great future in coming generation of new medical devices.

2.10.2. Ti-6Al-7Nb (ASTM 1295)

This α+β alloy is especially designed for medical implants. Aluminum stabilizes α phase. Niobium is a biocompatible element and stabilizes β phase as discussed earlier. The wear resistance of these alloys is also poor and needs enhancement of surface properties. The biocompatibility of the surface also depends upon the nature of oxides present. Al_2O_3 and Nb_2O_5 are normally found on the surface of these alloys (Sittig et. al., 1999). Ion implantation and plasma nitriding on these alloys has been investigated by several researchers who established the superior quality of the surface in terms of wear and corrosion resistance due to formation of nitrides (Thair et. al., 2002). Alloys for load bearing applications need special consideration in terms of wear and fatigue. Surface modification must not induce defects in the highly stressed parts of the implants. Hard and brittle nitride compounds are prone to initiate failures if the loads exceed critical value.

2.11. Details of Fretting Wear and Fretting Fatigue Mechanisms

Wear mechanism are classified into adhesive wear, abrasive wear, three body wear, fatigue wear and corrosive wear. Two mating bodies exhibit adhesion when the atomic forces occurring between the materials in two surfaces under relative load are stronger than inherent material properties of either surface. It is related to repeated formation and breaking of bond junction between contacting asperities. Fretting is a form of adhesive wear between contacting bodies under normal load and relative motion. Fretting wear tests are normally conducted for the purpose of ranking the wear resistant nature of materials or to understand the underlying damage mechanisms of the wear phenomena. It may also serve the purpose of understanding the wear damage characteristics of alumina and titanium couplings used for hip implants, intramedullary nails etc. The following discussion on fretting wear may serve all the purpose. Fretting fatigue tests is conducted to study the damage mechanism of surface modified titanium alloy couplings. The following section gives some literature details about fretting wear and fretting fatigue failures.

2.11.1. Fretting Wear

Fretting wear damage is predominant in many areas of engineering applications such as power generation industries, electrical contacts as well as biomedical applications. Young Ho Lee et. al, 2005 have studied the fretting of Korean power plant steam generator tubes, which is made of Inconel 690 coupled with ferritic and martensitic steels as supports. Some of the grade of Inconel alloys could resist plastic deformation much better compared to others. SEM observation revealed that fretting condition induced extensive plastic deformation at the local area and generated debris in the form of thin plates and particles causing third body wear mechanism. Microstructural constituents also influence the fretting wear damage mechanism. Jin-Ki Hong et. al., 2005 have studied the effect of microstructure on fretting wear of Inconel 690. Larger grain sizes (60 to 80μm) with coarser carbides along the grain boundaries have good resistance to fretting wear. However, they are also held responsible for formation and propagation of cracks. Sung et. al, 2001 studies the effect of TiN coating in reducing fretting wear damage of Zircaloy-4 tube. It is reported that the main wear damage mechanism of TiN coating was the brittle rupture of the film followed by low slip amplitude fretting and cumulative plastic flow at the contact edge. Adhesive and abrasive damage followed by oxidation was prominent at high slip amplitude.

In the area of biomedical applications, Animesh et. al, 2004 have investigated the tribological behavior of three different titanium based alloys which indicates that the major wear mechanism of titanium alloys is tribomechanical abrasion, transfer layer formation and cracking due to extensive plastic deformation under tribomechanical stress conditions and persistent slip band formation. Chen et. al, 2002 have investigated the fretting wear characteristics of CrN and PVD TiN coating coupled with corundum ball at different relative humidities. It is reported that TiN coating exhibits high friction in dry conditions i.e., at reduced relative humidities compared to high humidities. Contact friction is also very much related to the type of debris. Chen et. al, 2005 indicates that low coefficient of friction coincides with nanocrystalline debris and high coefficient of friction with amorphous debris. Anatase or rutile is commonly formed as debris during fretting of PVD TiN coatings. Tan et al, 2005 have studied the effect of oxygen implantation on wear behavior of NiTi shape memory alloys indicating improvement in wear resistance of the alloy.

Ion implanted materials also shows remarkable improvements in fretting wear resistance with reduced friction (Tan et. al., 2005, Prakash et. al., 2003). The case depth of implanted materials is shallow and easily worn off within few cycles unlike thicker coatings. Improved adhesion of TiN layer can also be obtained when ion implantation is coupled with PVD process (Gunzel et. al., 2001).

Plasma coatings are reported to improve wear, corrosion and fatigue strength of biomedical implants (Hong et. al., 2004, Chu et. al, 2002, Sobiecki et. al, 2001). Plasma nitrided surface gives superior surface textures with no significant geometric distortions (Alves et. al, 2005). The wear debris formed during fretting is predominantly titanium oxides and titanium oxynitrides (Gokul Lakshmi et. al, 2004). The temperature plays more important role than other parameters like treatment time, gas flow ratio etc.(Shengli et. al, 2004, Mishra et. al, 2003). The material removal in saline medium for plasma nitrided titanium alloys in is influenced by both mechanical wear and electrochemical oxidation (Galliano et. al, 2001). More than 50% of the wear volume generated is attributed to electrochemical oxidation during fretting process.

Laser nitriding of titanium alloys involves melting and introduction of nitrogen species within a few micron layers from the surface before resolidification. The hardness profile of the modified layer is very much dependent upon nitrogen concentration gradient and interaction time (Carpene et. al., 2005). Laser nitriding generates 3D network of TiN dendrites (Man et. al., 2005, Mohamad et. al., 2001). The cracking tendency is influenced by the volume fraction of TiN dendrites and preheating the specimens before nitriding can reduce such tendencies and also bring about uniformity in case depth (Hu et al, 1999). Tribological properties of laser nitrided alloys are better compared to unmodified alloys (Ettaqi et. al., 1998). The resistance is mainly offered by the TiN dendrites formed during the process.

Thermal oxidation involves gradual diffusion of oxygen into titanium substrate material producing hard α titanium oxide layer. Even water vapors can be utilized as a source to produce surface titanium oxides (Yves et. al., 1997). The wear, corrosion and galling resistance of titanium alloys can be greatly improved with thermal oxidation process due to reduced tendency for adhesion (Borgioli et. al., 2005, Guleryuz et. al., 2005, Güleryüz et. al., 2004, Dong et al, 2000, Wiklund et. al., 2001). The chemical composition of the oxidized layer depends on the temperature and thickness of the film. Below 200°C the oxidation process produces predominantly TiO_2 and at higher temperatures the presence of Ti_2O_3 was detected from the beginning of the process (Vaquila et. al.,, 2001).

2.11.2. Mechanism of Fretting Wear Damage

Figure 2.5 shows the possible mechanism of damage occurring during fretting wear of unmodified and surface modified alloys. In unmodified condition, fretting motion generates wear particulates according to the mechanism shown in Fig 2.5a.

Multiple cracks starts within the contact area inclined to the surface and later delaminate into chips and flakes of different sizes once these cracks turn parallel to the surface due to tangential force generated during fretting.

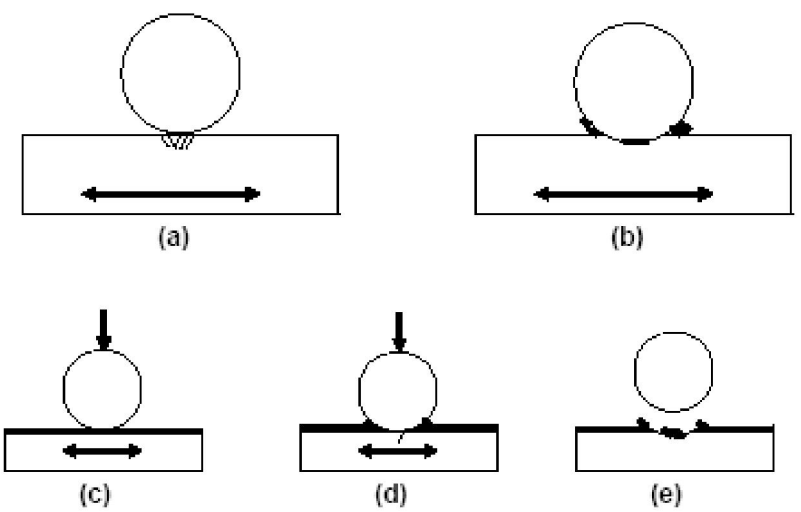

Figure 2.5. Fretting wear damage mechanism.

The generation and interaction of multiple dislocations within the subsurface layers may be responsible for propagation of fine cracks to form debris. Two body wear change to three body wear mode with the particulates in the contact. Continued sliding would further squash and grind them within the contact which is compacted within the cracks or ejected out of the contact area as shown in Fig 2.5b. Finer particles would transform to different oxide products during mechanical attrition. Wear products harder than parent material can also augment the severity of damage. Wear volume depends upon the loading and contact conditions. The generation as well as structure of wear products also depends upon the medium of fretting. The damage is dependent on physical nature of the debris so formed.

In case of surface modified materials, fretting motion initially damages the layer until it reaches the base material as shown in Fig 2.5d. The damage is delayed until the layer is completely worn off. Thicker and harder layers can offer resistance for a long period. The debris generated from the modified layer may or may not influence the fretting behavior. Fretting wear tests with ball contact configuration generates fine crater on the surface after the test as shown in Fig 2.5e.

Electrochemical activity can also influence fretting behavior depending on the medium used. In medical applications, fretting of implants takes place within the body in presence of saline and protein medium. Chloride corrosion is always a problem with some of the medical devices used in the body. Fretting normally enhances the corrosive activity by exposing fresh surface to the surrounding medium.

2.12. Fretting Fatigue Process

The following section gives some details about the fretting fatigue mechanism, fretting maps and the variable that affect the mechanism.

2.12.1. Mechanism of Fretting Fatigue Damage

Plain fatigue and fretting fatigue life is compared and presented in the form of Stress-Number of cycles (S-N) curves. Fretting fatigue lives are normally lower than plain fatigue lives due to premature damage caused by the contacting body as shown in Fig 2.6a. The total fretting fatigue life is divided into fretting and fatigue cycles. Both of them are again influenced by different set of parameters. Fretting cracks usually initiate within few cycles of operation and further growth of these cracks is controlled by axial fatigue load cycles.

In all the cases, initially it is observed that these cracks grow inclined to the tensile axis from the surface of the material and then propagate normal to the tensile load when the effect of tangential force diminishes when the crack reaches the bulk leading to ultimate fracture as shown in Fig 2.6b (Endo et. al.,, 1976). The three modes of crack propagation are also shown in the same Fig 2.6b. For high strength materials such as TiAl, the fatigue lifetimes were suggested to be determined by the cycles needed for initiation of crack rather than propagation (Hansson et. al., 1999). Here the SN curve is flat in contrast to metallic materials.

The growth rate of cracks is governed by microstructure of the base material, and bulk fatigue loads.

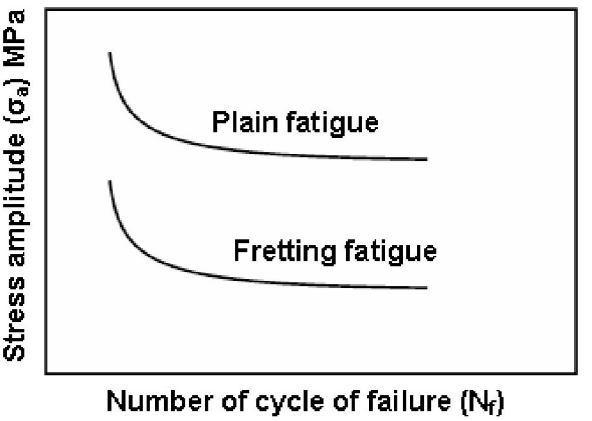

(a)

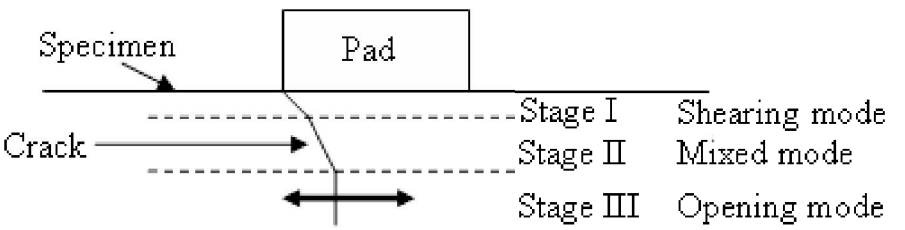

(b)

Figure 2.6. (a) S-N curve for fretting fatigue tests showing decreased lives compared to plain fatigue lives. (b) Modes of crack initiation and propagation during fretting fatigue test (Endo et. al., 1976).

They are observed to initiate along the contact edge as shown in Fig 2.6b and sometimes contain large number of cracks inclined at various angles with compacted debris particles during fretting (Hoeppner, 1994). At higher stress levels the role of fretting in crack nucleation is overridden by persistent slip bands.

However at lower stress levels, the fretting motion has greater influence in reducing life, because the damage at the contact acts as crack nucleation sites. The number of cycles to initiate fretting cracks decreases as the fretting conditions becomes more severe. Fretting process will lead to particle generation and ejection from the contact. Fretting particles would generate from deformation of surface layers and crack assisted delamination. In some cases microscopic observation reveals the compaction of debris within the surface cracks (Antoniou et. al., 1997).

Fretting action can produce various types of surface symptoms distinct from ordinary wear phenomenon by which it can be diagnosed. For example, the rust debris on steel will be much more reddish than ordinary rust or aluminum debris is black instead of white (Waterhouse, 1972). This indicates that the fretting products may result in transformation of the original structure or chemical composition of the parent materials. Since fretting damage is mostly encountered under heavy pressure, it will certainly produce debris of different chemical structure depending upon the environment around the joint (Chan et. al., 2002).

2.12.2. Fretting Maps

Fretting damage phenomena of a particular combination of materials are normally quantified by what is called fretting maps. Vincent et. al., 1992 have given running condition and material response maps for fretting fatigue tests. Running condition fretting maps (RCFM) as shown in Fig 2.7a demarcates stick, partial slip and gross slip regions for a particular contact material and number of cycles. Material response fretting maps (MRFM) demarcates no crack, crack and debris formation regions for the same material as shown in Fig 2.7b. Frequency and roughness also influence the regime of fretting operation.

Gross sliding regime corresponds to dissipative process (large area of Force-Displacement (FD) curve) where the members slide without any obstruction. Area within the FD curves indicates the energy lost by the system. Gross slip is normally characterized by low contact pressure and longer strokes. The sliding tangential force is small enough not to cause any destruction of surface films. For larger slip amplitudes, wear phenomena predominates over fretting. For brittle materials such as ceramics, it normally corresponds to one cycle.

Partial slip or mixed stick-slip region is the most dangerous from the crack initiation point of view due to destruction of surface films and interface adhesion. Tangential force increases due to such adhesion of underlying exposed metal surfaces. Relative motion is frequently checked by micro-welding and rupture of asperity junctions indicated sometimes by squeaking and squealing sound during operation. It is commonly observed during fretting of metallurgically compatible pairs. In combination of the above phenomenon, it is difficult to predict the fretting fatigue lives of the materials. Fracture mechanics approach sometime helps us to understand the process better (Mutoh et. al., 1989). Stick regime is encountered at higher contact pressures as seen from Fig 2.7a. It is characterized by non dissipative elastic accommodation of fretting movement.

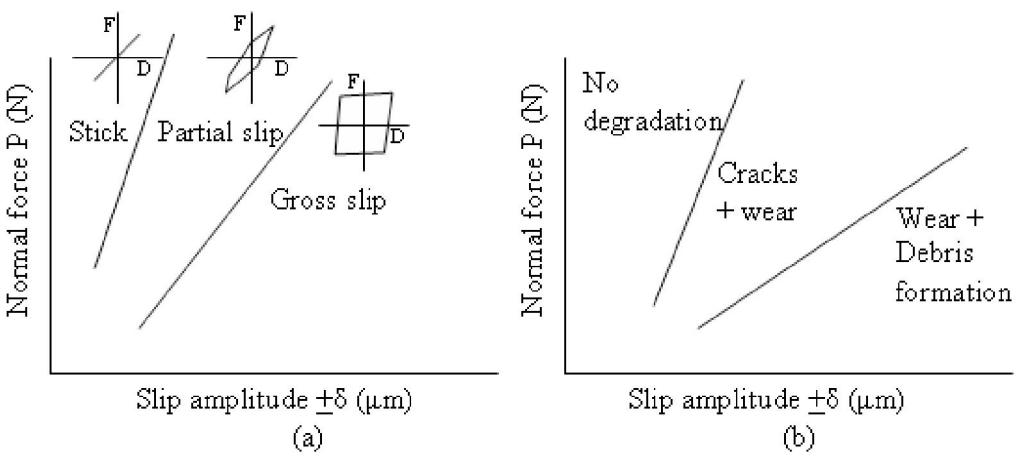

Figure 2.7. Fretting maps (a) Running condition fretting maps (RCFM), (b) Material response fretting maps (MRFM).

Due to reduction of sliding motion, the fretting fatigue life is sometimes increased in this region.

2.12.3. The Effect of Variables on Fretting Process

The following section gives some of the most important variables that affect both fretting wear and fretting fatigue mechanisms. It is a general description and hence applicable to both titanium alloys as well as other materials. All the information contained in the following section pertains both to biomedical area as well as to other engineering applications due to limited availability of literatures in the area of biotribology.

2.12.3.1. Fretting Media

The process of fretting can often be aggravated by the medium of its action depending upon the load and frequency of operation. The nature and volume of debris produced depends upon the aggressiveness of the environment. Oxidation or corrosion of materials can influence the fretting wear. Fretting action alone may provide sufficient driving energy for the atoms on the contact surfaces for the chemical reaction even at low temperatures. Fretting in vacuum or inert atmosphere produces much less damage due to absence of chemical reaction that weakens the surface strength. Fretting of steels in oxygen or air indicates more damage than nitrogen or helium atmosphere (Waterhouse, 1972). Dissolved oxygen in these fluids significantly influences the test results. It must be controlled strictly to represent the body fluid as genuinely as possible. N_2 and O_2 mixture is normally introduced continuously in the solution during the test to control the dissolved oxygen content. Fretting of bio implants made of titanium alloys is of very great concern in the area of orthopedic surgery due to high manufacturing and surgery cost. Fretting debris generated from these implants elicit adverse tissue reaction. It also depends upon the corrosion rate and solubility of the corrosion products. Human body fluid contains blood, tissue fluids, and 0.9% amino acids and proteins. The pH is 7 and body temperature is 37°C at 1atm pressure (Sumita et. al., 1994). Lower partial pressure of oxygen within the body accelerates corrosion of metallic implants due to reduced availability of oxygen for repassivation. There is also an assumption that corrosion is caused by increasing concentration of H^+ and Cl^- ions in the solution. Therefore bioimplants within the body must withstand the corrosive action of these chemicals along with fretting. This is another broad area of study under the name fretting corrosion. Khan et. al., 1999 comments that the wear of titanium alloys increase in the presence of proteins. The study on conjoint action of wear and corrosion on titanium alloys indicates that Ti-13Nb-13Zr alloys perform better than other alloys. Resistance to corrosion action can also be improved by some other specialized processes such as ion implantation (Thair et. al., 2002) and powder immersion reaction assisted coating (PIRAC) (Shenhar et. al., 2000). PIRAC nitriding reduced fretting induced metal dissolution up to 25%.

2.12.3.2. Frequency

Frequency of vibration due to dynamic loading is an important factor in structures that undergo fretting damage. It is reported that damage of mild steel specimens in weight loss are severe at lower frequencies (< 1000 Hz) due to magnified activity of chemical forces acting on the exposed fretted surfaces for longer time (Waterhouse, 1972). Where as, frequency has no effect in non reactive atmosphere (vacuum tests). Papakyriacou et. al., 2001, from their investigation on HCF studies of annealed and cold worked niobium and tantalum and also

commercially pure titanium and Ti-6Al-7Nb alloy, concludes that there is no statistically significant influence of cyclic frequency on the endurance data and the mean fatigue limit. However, the fracture initiation mode changed from ductile transgranular mode at lower frequency to brittle intergranular mode at higher frequency. Rebecca et. al., 1999 indicated that constant amplitude higher frequency fatigue conditions on Ti-6Al-4V alloy produced shorter fatigue lives then those conducted under low-frequency fretting fatigue conditions. The effect of frequency on bioimplants within the simulated body fluid also depends on the severity of media surrounding the implant surface. Test frequency of 1 to 5 Hz is normally selected for bio implant fretting fatigue test (Hallab, 2003). There is a possibility that corrosion rate due to chemical reaction of exposed metal surfaces during low frequency fretting may be higher than the higher frequencies due to longer dwell period of exposed damaged area.

2.12.3.3. Slip Amplitude

Relative slip amplitude measured between the two fretting members is an important parameter because the volume of material removed increases linearly with the amplitude of slip. In some cases, wear loss increases rapidly above certain limit of slip amplitude and the damage is very severe. The slip amplitude depends upon the range of alternating stresses and strains in the fatigue loaded specimen. Variation of slip amplitude with friction coefficient is a useful plot from the design point of view. Vincent et. al.,, 1992 gives running condition and materials response fretting maps for 2091 aluminum alloys clearly demarcating the three regions viz. stick, partial slip and gross slip regions. It is observed that all materials are covered with some form of protective layer that comes in contact with each other during initial stages of fretting. Fretting life is very much influenced by the properties of such layers. Such layers can also be produced using surface engineering techniques to improve the fretting life of materials which will be discussed later. During first few cycles, the friction is low and gross sliding is prominent. In this stage the natural films rub each other until they break away from the surface after certain period and the force displacement plot assumes trapezoidal form. After several cycles, the natural film rupture and the bare metals underneath are exposed to each other. In this partial slip stage friction increases due to adhesion of two bare surfaces. Elastic accommodation of slip is increased here resulting in damage of the surface films. Surface modification with stronger films will increase the period of rupture of the protective coatings thereby delaying the shift of gross slip regime. Apart from the surface films the shift in the fretting regime is also dependent upon the surrounding media. With regard to bio implant, the shift in the regime may be much more delayed due to lubrication effect of the protein serum or may also aggravate due to corrosive nature of the fluid. Therefore the contact behavior is primarily governed by particle detachment and debris ejection from contact area. The initial surface roughness also plays a significant role in controlling slip amplitude during fretting process.

2.12.3.4. Normal Pressure

Normal pressure is the stress applied by the pads perpendicular to the surface of the fatigue specimen during fretting process. The magnitude of normal pressure affects the shift in the region of fretting maps. However the effect of normal pressure is always felt depending

on the material and surface condition of the contacts. If contact pressure is high enough, it may cause premature rupture of surface film due to high friction and expose the underneath bare metal earlier causing adhesion.

Fig 2.8 shows the effect of normal pressure on fretting fatigue life of Ti-6Al-4V (Kozo Nakazawa et. al., 2003). Three normal pressures are selected for 1.65kN maximum cyclic load and one normal pressure is selected for 3.30kN maximum cyclic load. It is evident from Fig 2.8 that increase in normal pressure has reduced the life of hip prostheses under cyclic loading conditions. Higher cyclic load (3.30kN/0.330kN) induces more severe fretting due to increase in relative slip amplitude between the contact pairs.

This has drastically reduced the life of the material for the same contact pressure (41.4 MPa). Hager et. al., 2004 have characterized the mixed and gross slip wear regimes in Ti-6Al-4V to identify the critical normal load and displacement corresponding to these regimes. Their experiments have shown that there is a linear relation between the load and displacement. Galling and cold welding were much evident on the fretted surface at the critical values. At modular joints, it is expected that load would reach two to three times the total body weight and extreme pressures are generated along the contact during fretting action (Kamachi Mudali et al, 2003). It may also vary because the hip joints are available in wide variety of designs and modular area varies for each design. Some of the hip prostheses come as a single piece with the entire model made of single alloys. There are no modular junctions and fretting problems are expected at the stem inside the femur canal where the bone cement or positioning ring is in contact with the shaft.

Even the compacted debris within the contact influences the variation in pressure throughout the test. The contact pressure varies according to the nature of the transformation product. Rutile formation is unavoidable in case of fretting of titanium alloys unless it is perfectly insulated from the ingress of oxygen.

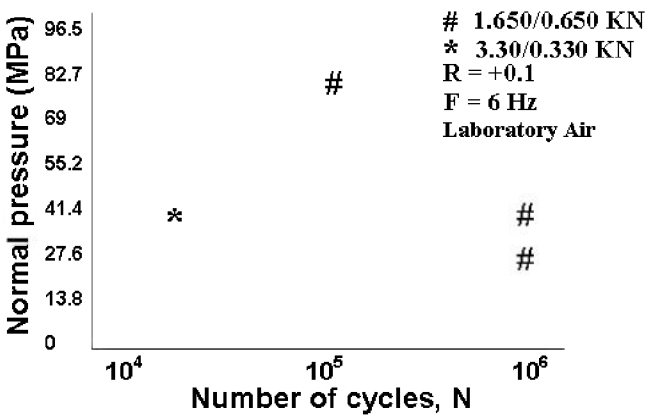

Figure 2.8. Ti-6Al-4V fretting fatigue test with hip prostheses loading conditions, (Kozo Nakazawa et. al., 2003).

In the case of alloys made of similar materials the friction is severe because the contact pairs are metallurgically compatible. The specimen damage is considered more importance because the effect of axial load is more prominent in the specimen than pads which constitute failure.

2.12.3.5. Hardness

With regard to hardness, there should be a balance between increase in the fretting life due to higher hardness of the surface and decrease in the life due to decreased toughness lowering the energy required to initiate fretting fatigue cracks. High surface hardness can effectively prevent fretting wear damage, whereas it can cause premature failure of cyclically loaded member during fretting fatigue. Therefore, there should be a balance between the hardness and thickness of the modified layer.

2.12.3.6. Surface Finish

Surfaces finish play a vital role in the fretting process as described in many sections earlier. Normally even very smooth surface will have defects at the atomic level. The defects are normally sharp projections and asperities of different contours. This causes the unevenness of the surfaces and it is practically difficult to achieve crystallographically flat surfaces in metals and alloys even with high degree of surface finish. The real area of contact between mating surfaces is considerably reduced due to higher roughness and the wear debris can be accommodated with in the asperities. As mentioned earlier the decrease in surface roughness results in increased friction and increase in surface roughness will produce asperity interlocking resulting in decreasing fretting amplitude. Since this process is non-dissipative, elastic accommodation relives the surface from fretting process. The hip implant ball is normally completed to a high degree of surface finish to minimize the wear debris generation. It is further improved by specialized surface modification techniques to improve the hardness and biocompatibility. This will reduce frictional forces between surfaces. For the industrial components lubrication coatings such as MoS_2, DLC or CuNiIn films are used to reduce friction (Yongqing Fu et. al., 1998). Bulatov et. al., 1997 produced fretting resistive surface from "Vibro-rolling" method containing regular roughness pattern. Vibro-rolling involves fine plastic deformation of subsurface layers with hard tool (hardened ball or rounded diamond tip) which is forced into the surface and passed in a regular fashion creating different roughness pattern.

2.12.3.7. Contact Materials and Microstructure

Plain fatigue life will be superior for fine grain than coarse grained material. For c.p. titanium, the endurance limit is increased by 70 MPa when the grain size is reduced 20 times (Leynes and Peters, 2004). The surface microstructure plays an important role in initiating the fretting induced cracks. A reduction in the grain size increases plain fatigue strength and coarse grains reduce the fatigue crack growth rate. Even oxygen content bears influence on crack growth rate. Hyukjae et. al., 2004 investigated the effect of dissimilar pad materials (Aluminum alloy 2024 and Inconel 718) on the fretting fatigue behavior of Ti6Al4V. At lower contact forces, there was no effect on fretting damage. When the contact forces increases, the hardness effects overrode the effect of slip amplitude and coefficient of friction of the mating material. Therefore relative hardness of the contact materials makes the difference. Hoeppner et. al., 2003 also investigated the effect of Al-1100, Cu, 0.40/0.50 steel and Ti-6Al-4V pads on Ti-6Al-4V alloy. Significant reduction in fatigue life was obtained by Ti-6Al-4V in contact with Ti-6Al-4V. Sinha et. al., 2001 investigated the effects of colony

microstructure on fatigue crack growth rate of Ti-6Al-4V. The growth rate reduces with increase in the alpha lathe size and colony size. So fretting fatigue life in such a case would also improve due to delayed fracture of the bulk specimen. Even if fretting action were to initiate cracks in short time, the slower crack growth rate within the bulk will delay ultimate failure of the specimen.

2.12.3.8. Contact Configurations for Fretting Fatigue Tests

Fig 2.9 shows the different types of pads and specimens that can be used in fretting fatigue experiments. Some of the pads makes a point or line contact with the specimen and usually they are used in fretting wear studies. They are called hertizian contact. They conform to the shape of the opposing surface after certain period due to wear. The present experiments on fretting fatigue were carried out in flat on flat mode of contact and many methods, as shown in Fig 2.9, are employed which modify the stress distribution at the contact area.

Ochi et. al., 2003 have investigated the effect of bridge pad geometry (Fig 2.9d) on fretting fatigue behavior. The fretting fatigue strength decreases with decrease in pad height and stick area increases with increase in pad height. The contact pressure seems to be concentrated inside the pad wherever the crack has initiated. This indicates that fretting is more pronounced when the leg height is smaller. Increase in stick implies the minimization of surface damage due to fretting and improvement in life. Bridge type of pads (Fig 2.9d) is normally used for fretting fatigue experiments which normally allows calibrating for friction coefficient.

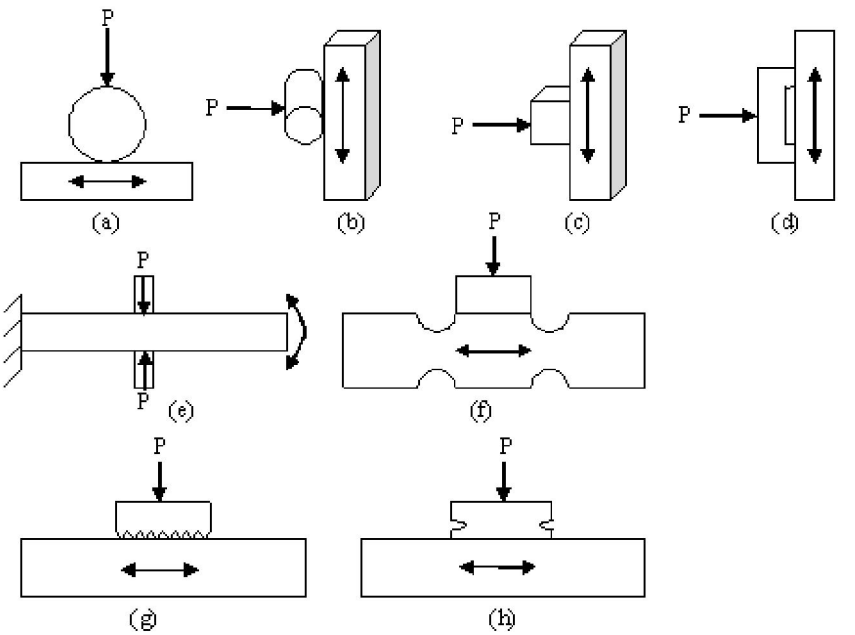

Figure 2.9. Types of specimen- pad configurations for fretting fatigue test (Hattori et. al., 2003, Kozo et. al., 2003).

2.13. Fatigue and Fretting Fatigue Studies on Titanium Alloys

Cyclic loadings are frequently experienced by the joint implants due to body motion resulting in alternating elastic, elastic-plastic or plastic deformation. Fatigue strength evaluation of implants is no doubt a difficult but critical task due to obvious differences in conditions during laboratory test and in-service conditions. The difficulty arises in correlating size, material, loading conditions of the implants. The standard material normally selected for investigation of fatigue and fracture performance of implant material is Ti-6Al-4V. These are high strength alloys used also for gas turbine parts. Its mechanical response is found to be extremely sensitive to grain size and thermo-mechanical processing history.

Widmanstatten structure is found to enhance fracture and fatigue performance. However HCF resistance has shown improvement through shotpeening. Titanium alloys are reported to be highly notch sensitive. Surface treatments such as electropolishing or porous coating for cemented prosthesis may result in reducing fatigue life by initiating cracks within the coating-substrate interface during cyclic loading. Fatigue strength also shows an improvement by the addition of interstitial elements like O, C, N and H with a slight increase in the modulus. Fatigue strength in simulated body environment has indicated varying trends. Oxygen concentration seems to play a role in altering the life of the implant although the importance of stress conditions of fatigue testing methods seems to make a difference. Corrosion resistance of Ti alloys degrades due to rupture of passive oxide films. Corrosion fatigue strength is reduced due to lower oxygen content in the simulated test solution and longer immersion time. Fretting induced corrosion fatigue is more deleterious due to enhanced electrochemical activity of the surface. The fretting motion would repeatedly expose fresh surface to the corrosive environment thereby deepening the surface damage.

Titanium alloys are also highly susceptible for fretting damage from cyclic loading action. Fretting action initiates crack on the surface and the plastic strain produced causes the disruption of surface films and leads to fatigue failure by direct metal to metal contact or third body wear from continuously produced abrasive particles. Contact temperature increases during fretting induced frictional heating generating rutile type of oxide bed within the contact. Therefore surface treatments are absolutely necessary for minimizing such surface defects on the component. Shot-peening, lubrication or surface coatings etc. are some of the most common methods employed for minimizing fretting damage. Surface oxides of titanium alloys are always very thin (in the order of 30 nanometers) and insufficient to prevent fretting failures (Antoniou et. al., 1997). Fretting behavior depends upon the type of contact material chosen. Jin et. al., 2002 has also investigated the effect of independent pad displacement on fretting fatigue behavior of Ti-6Al-4V. Fretting fatigue life which is very much influenced by slip amplitude showed minimum at 50 and 60 micron slip range and later increased with increasing relative slip range. They also remarked that debris particles generated during fretting influenced the evolution of fretting loops.

2.14. Role of Surface on the Wear Mechanism

Surface as well as subsurface characteristics plays very important role in analyzing failures due to friction and wear of interacting surfaces. Metal combination with the introduction of novel surface modification techniques has given best results in terms of

minimizing friction and wear. XRD analysis of debris particles indicates the formation of thick layer of TiO over relatively thin layer of TiO_2 above the Ti matrix (Kamachi Mudali et. al., 2003). Mechanical instability of these oxide layers is quoted as responsible for increasing the friction of the contact surface. High friction on worn surfaces is generally noted by directional scratches, ridges or sharp projection for abrading and causing undue damage to the mating surface. Abrasive wear occurs when such locally rough regions plows through relatively softer surface removing the material from its wear tracks. When such particles become embedded on one of the surfaces, it further aggravates the contact layer. Therefore some amount of resistance to plastic flow of the subsurface layer is necessary to maintain the continuity of the oxide layer. This plastic flow would alter the microstructure and introduces dislocations glide along favorable crystallographic directions. Further increase in plastic strain causes dislocation pileup and cracks below the surface to induce delamination of oxides.

3. Objectives and Scope

3.1. Preface

The following section gives the objectives and scope of the project work on fretting wear and fretting fatigue studies on surface modified biomedical titanium alloys with respect to the current perspective of the need of such studies.

3.2. Objectives of the Project

One of the key objectives of this project in the area of fretting wear and fretting fatigue of implant grade titanium alloys is to understand and compare the influence of surface modified layers in minimizing the surface damage during the process of fretting in a representative physiological medium. The focus of the work is also to determine the fretting damage mechanism of individual surface modified layers under fretting wear and fretting fatigue conditions.

3.3. Scope of the Project

In this project an attempt is made to study the fretting wear and fretting fatigue behavior of surface modified Ti-6Al-4V and Ti-6Al-7Nb alloys. Many published articles and supplementary literatures are on hand regarding general resistance of surface modified titanium alloys towards corrosion and wear under the heading of fretting wear and fretting corrosion. But not much information is available regarding the effect of coatings on fretting behavior or fretting on fatigue behavior of surface modified titanium alloy couple. Studies on fretting behavior of coatings give good information on the quality of the coatings. Fretting fatigue studies also gives the mode of failure of specimens in presence of surface modified layers which is not investigated in depth or interpreted well so far. The same mode of failure is expected in original implants. Such a study will also help us design or modify the existing parameters of various surface modification processes for improving surface layer properties.

These alloys are treated with some of the specialized surface modification techniques such as plasma nitriding, laser nitriding, ion implantation, PVD TiN coating and thermal oxidation for minimizing fretting damage on the surface. An attempt is made to exactly simulate the conditions of load bearing implants such as hip joints and bone plates. The combination of surface modified alloys used in this work for fretting fatigue studies has not been attempted by anyone so far and it would be useful to understand the expected magnitude of friction and damage.

The basic characterization of substrate materials and surface modified layers is done with optical microscope (OM), scanning electron microscope (SEM), energy dispersive spectroscopy (EDS), roughness profilometer, nano indentation, scratch test and X-ray diffraction analysis (XRD).

Fretting wear test is conducted in air and ringer solution to understand the basic fretting response of the all the coatings. The final magnitude of damage shows the general fretting resistance of the layer.

The fretting damage of individual coatings is characterized with optical microscope (OM), scanning electron microscope (SEM), friction coefficient curves, and roughness measurement. Slip between specimen and pads are measure with clip gage. Friction coefficient curves give better understanding of the progression of ongoing fretting damage. Running condition fretting response of the contact is quantified through online monitoring of friction at the contact, which is difficult to model in testing real implants. The damage sequence of individual coatings with the number of cycle can be understood better by this process of experimentation which is normally difficult in testing with original implants. It may involve much more complex sophistication and design of testing systems. Therefore, this is a kind of prototype investigation to establish the kind of coating required for implants in a particular location in the body for a particular loading condition taking into consideration the contact behavior for each coating during the process of fretting. To some extent, it can be correlated with the damage that can be expected during service of surface modified titanium alloy implants. The flow chart of the work is shown below.

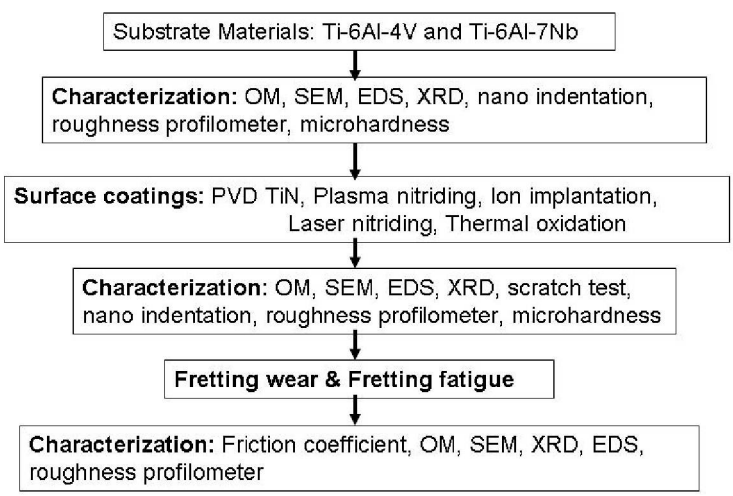

Figure 3.1. Flow chart of the experiments.

4. Experiments

4.1. Preface

The following sections gives details of the materials used, the parameters used for the different surface modification processes, details of fretting wear machine and fretting fatigue fixture assembly and methods used to characterize modified layers and fretting damage.

4.2. Substrate Materials

Hot rolled and annealed Ti-6Al-4V bars of dimension 200mm X 60mm X 10mm and Ti-6Al-7Nb rod of diameter 16mm and length 127mm were procured. Fatigue specimens and fretting pads were profile cut with wire-cut EDM as shown in Fig 4.1 from Ti-6Al-4V from Ti-6Al-7Nb alloys respectively. EDM cutting of alloys leaves a recast layer on the surface which is initially removed by mildly pressing on the belt grinding. The fatigue specimens were later polished with emery sheet mounted in sequence (1 – 4) on a circular shaft connected to a motor. Both the specimens and pads were polished to mirror finish with alumina slurry (3 μm) and diamond paste (0.5 μm) and later ultrasonically cleaned before the application of surface treatments. The chemical composition and mechanical properties of the alloys are shown in Table 4.1 and 4.2 respectively. Ti-6Al-7Nb alloy has more strength and ductility compared to Ti-6Al-4V alloy.

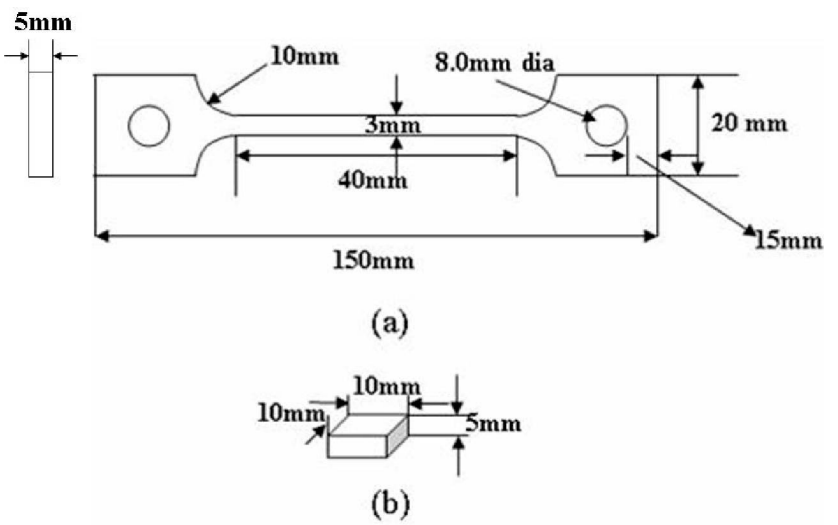

Figure 4.1. Dimensions of (a) Ti-6Al-4V fatigue specimen, (b) Ti-6Al-7Nb pads.

Table 4.1. Chemical composition of Titanium alloys (wt%).

Elements	Al	C	Fe	N	Nb	O	H	V	Ti
Ti-6Al-4V	6.21	0.016	0.05	0.0123	-	0.109	0.0025	4.16	Bal
Ti-6Al-7Nb	6.12	0.003	0.15	0.008	7.08	0.178	0.0012	-	Bal

Table 4.2. Mechanical properties of titanium alloys.

Properties	Ti-6A1-4V	Ti-6A1-7Nb
U.T.S (Mpa)	895	1027
0.2% Y.S (MPa)	825	910
% Elong	10	17
% R.A	20	48
E (GPa)	104	109
Hardness Rc	37	35

4.3. Details of Surface Modification Processes

4.3.1. PVD TiN Coating

The specimens were initially cleaned with alumina slurry blast and later ultrasonically cleaned with acetone. The components were then placed in a vacuum chamber (316 stainless steel chamber) maintained at 10^{-4} torr. For PVD TiN coating, the pads and the specimens was placed in a vacuum chamber maintained at vacuum level of 10^{-4} torr. The samples were initially preheated to 280°C and later bombarded with Ar and H (3:1 mixture) ions to clean the surface prior to deposition. The cathodic arc process evaporates the coating material from the commercially pure (CP) titanium disc target (100 mm diameter). When this material is evaporated, a high percentage of it is ionized. An electrical charge is then applied to the substrate (~250V), which draws the ions to the surface. Nitrogen gas is steadily maintained at the pressure of 15 Pa within the chamber. The evaporated material reacts with nitrogen gas to form TiN. The process is continued until the required coating thickness (2μm) has been obtained. Then the substrate is allowed to cool and later removed from the chamber.

4.3.2. Plasma Nitriding

The specimens were placed in nitriding chamber (stainless steel) which operated within the d.c. bias voltage of 500V. The specimens were initially cleaned by surface sputtering in Ar-H_2 (3:1 ratio) plasma for 50 min prior to nitriding. The nitriding was carried out in an H_2 – N_2 (1:3 ratio) plasma for 4 hours. The pressure within the chamber is around 480 to 520 Pa. The work piece temperature is maintained in the range of 450°C to 500°C.

4.3.3. Laser Nitriding

Laser nitriding was performed with class IV 10 KW industrial CO_2 laser indigenously developed at Raja Ramanna Center for Advanced Technology (RRCAT), Indore. It is a three axis workstation with maximum laser pulse energy of 2 Joules and wavelength of 10.6 μm. The laser scan was optimized to 300mm/min and 0.4 sec interaction time. The current was maintained at 16 – 17 amps and nitrogen gas was passed from the nozzle surrounding the beam at 60 lpm for efficient transmission to the melted zone. The distance from the nozzle tip to the work piece decides the diameter of the spot. This diameter was maintained at 2mm by optimizing the working distance. The indication of nitriding is the appearance of blue plasma

during melting and golden orange tinge at the nitrided area. Laser nitriding induces many surface undulations with brownish ripples since the modified layer is deeper than other process due to melting and resolidification. Therefore, they were grinded with alumina wheel for removing the uneven part.

4.3.4. Ion Implantation

Ion implantation is conducted with TAMSAMES 150 keV particle accelerator machine. Both the pads and the specimens were cleaned with acetone and fixed inside a cylindrical stainless chamber with a circular channel window at the side for sending ion beam towards the target. The specimen area to be implanted is exposed towards the incoming beam. The dose of implantation is fixed to 2 X 10^{16} ions/cm^2 with the energy of 100 keV. The beam current was maintained within 2μA and the sample temperature was below 40 °C. The vacuum was maintained below 10^{-7} torr throughout the test. The time for implantation of single area was more than 5 hours. This makes the process more expensive and time consuming.

4.3.5. Thermal Oxidation

The specimens were thermally oxidized at 650 °C in a tube furnace in ambient atmosphere for 72 hours. The oxidized layer consists of black rutile (about 100 μm) above the hard alpha case (about 20 μm). Rutile was removed meticulously with emery paper without removing the case.

4.4. Fretting Wear Machine Details and Testing Methodology

The basic components of test rig used for fretting wear studies are as shown in Fig 4.2a. The details of the machine are given elsewhere (Ramesh and Gnanamoorthy, 2006). The original mating components undergoing fretting wear damage are prepared into specimens and butted against each other (1 & 2). A reciprocating system based on motor is designed to induce fretting oscillation of desired amplitude (3). Vertical motion along one end of the machine is translated to horizontal motion at the sample holder. Reciprocating rod is butted to sample holder via a force transducer. Frequency is basically decided by the motor speed (r.p.m). Fretting amplitude is manipulated by adjusting the cam connected to the motor. A feedback circuit system senses the relative displacement. Dead weights (4) are normally used to apply the contact pressures. Ball-on-flat (point contact) system was used in the present experiments. The tangential force and sliding amplitude is sensed with calibrated S-beam force transducer and displacement sensors (5 & 6). Displacement sensors usually come with non contact laser pointer system or eddy current sensing system. A laser beam pointer sensor with 1μm accuracy was used to record relative displacement in this machine. Tangential force is continuously monitored and recorded to explain the contact behavior during fretting.

Alumina ball of 10mm diameter was chosen as the counter material on flat specimens (10mm X 10mm). Both the specimen and the ball were cleaned with acetone before making the contact every time. Dead weights were used to apply normal pressure. The normal force applied in all the tests was 1N. Fretting frequency was adjusted to 5Hz at sliding distance of

200 µm. This requires manipulation of motor driven reciprocation system. Tangential force and displacement was continuously recorded through data acquisition system.

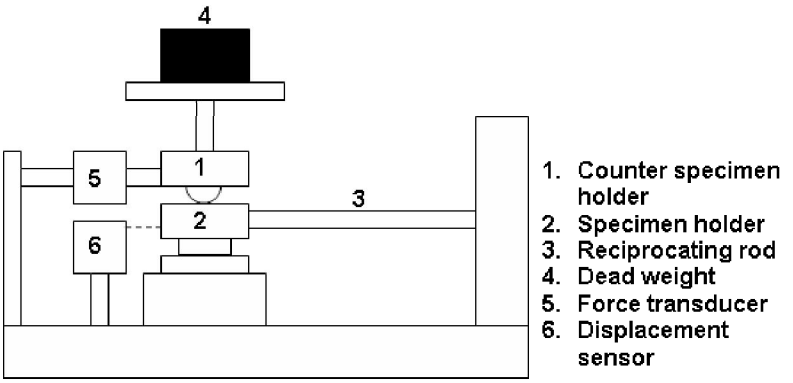

Figure 4.2. Test rig for fretting wear studies (Ramesh et. al., 2006).

The specimen holder is designed to contain ringer solution to conduct fretting experiments within the liquid environment. Ringer solution with the following composition was used for both fretting wear and fretting fatigue experiments: NaCl (6.5 g/l), KCl (0.14 g/l), $CaCl_2$ (0.12 g/l), $NaHCO_3$ (0.2 g/l) and Dextrose (0.4 g/l). All the experiments were conducted both in ambient atmosphere and in ringer solution. The relative humidity (RH) was 85% during the test in air. Humidity level also affects the friction at the contact. Hardened steel balls (10mm diameter) were also used to generate fretting loops for uncoated alloys at different loads. Two tests were conducted for all the conditions to check the consistency of the work.

4.5. Fretting Fatigue Test

4.5.1. Machine Details and Test Rig Design

Fretting fatigue tests were conducted in 100 kN DARTEC servo-hydraulic UTM with 9600 Hydrowin modular. The specimens were held at two ends with cotter-pin self aligning fixtures.

4.5.2. Designing of Proving Ring and Pad Holders

Proving ring was designed to apply the lateral force on the specimen. The ring is made from AISI 4340 (En 24) alloy steel as shown in Fig 4.3. Four strain gages with terminals were pasted at the opposite ends along the circumference to form a full bridge Wheatstone network. Two active gages were provided for sensing the strain and two were dummy gages for completing the network as shown in Fig 4.3a. Circuit wires were appropriately soldered to the terminals.

Two similar pad holders were profile cut with wire-cut EDM form 316 stainless steel as shown in Fig 4.3b. Strain gages were pasted underside of both the pads. The pads were fixed

rigidly with Allen screws after ensuring proper flatness of contact on the specimen. The alignment of pads on fatigue specimen is obtained automatically from butting hardened steel balls on a pit drilled behind the pad holders. Stainless steel fixtures were also deigned to hold the pads rigid during the fretting fatigue test.

Five channel strain amplifier was used to record the pad strains. One full bridge channel is used for proving ring and two half bridge channels for two pad holders. Pad holder strain gages were clubbed in series with a resistor of similar value. This makes the half bridge complete to couple with in-built resistors within the stain amplifier. Strain amplifier output is connected to the computer through RS232 cable and the values were obtained and recorded in hyperterminal.

4.5.3. Calibration of Proving Ring and Fretting Pads

Proving ring was calibrated according the ASTM E-74 – 02 standard, which gives the standard practice for calibrating force measuring instruments and verifying the force indication of testing machines.

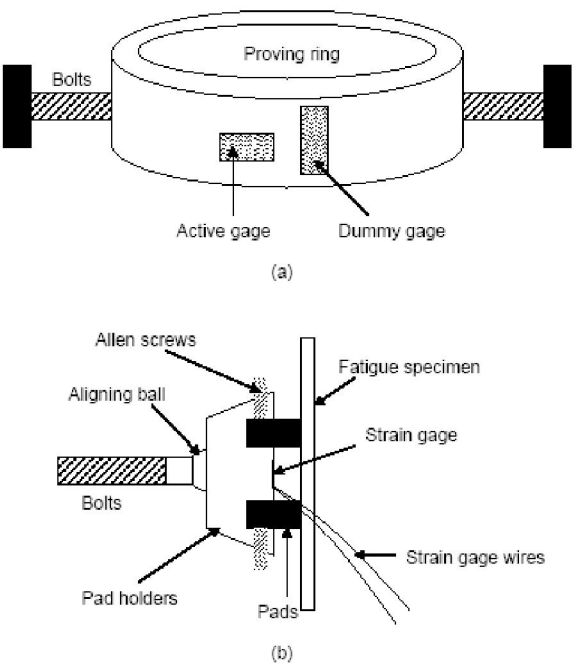

Figure 4.3. Schematic sketch of design of proving ring and pad holder.

The calibration involves applying a known load to the ring and recording the strain values. The strain generated during the circumferential deformation of the ring is proportional to the applied load. The ring was held rigidly in DARTEC universal testing machine along the bolts and a series of tensile load is applied. Then the strain values corresponding to the load is recorded. This procedure was repeated several times to get a steady value. Pad holders were similarly calibrated for each of the surface coatings. Each specimen were cut into two halves and assembled with a small gap between them. The pads and the proof ring were then

assembled. A small sinusoidal displacement is applied to the specimen under stroke mode and the transmitted load is recorded as a function of pad strain. The slope of this graph gives the pad calibration value which enables the conversion of measured fretting pad strain to frictional force.

4.5.4. Fretting Fatigue Test

Contact pressure is applied by tightening the bolts along the circumference of the proving ring (Fig 4.4 a & b) and tangential force is deduced and recorded from strain gages bonded below the pad holders. Modular junction of the hip shafts normally experiences two to three times the weight of the upper portion of body above the hips (200 to 600 kilograms) (Kamachi Mudali et al (2003)). It would roughly correspond to 40 MPa although it varies with design of the prostheses and load excursions, like climbing staircase up or down sometimes causing sudden impact along the taper section of the joints. Therefore, contact pressure of 40 MPa (600N) was applied before testing all the specimens. Cyclic loads of 3 to 7.5 kN at 5 Hz frequency were applied during the test. Stress ratio R was maintained at 0 because the modular junction undergoes tensile force at the contact point while compressive load is applied on the ball.

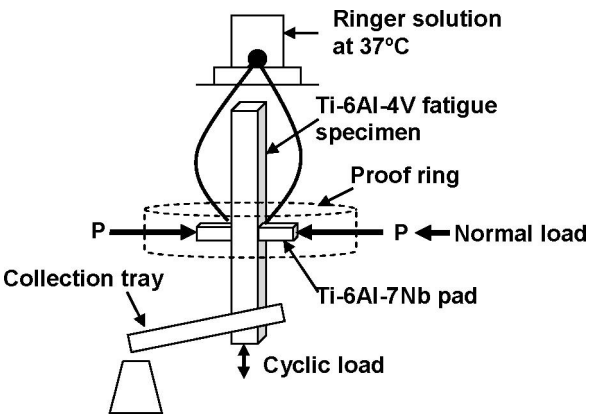

(a)

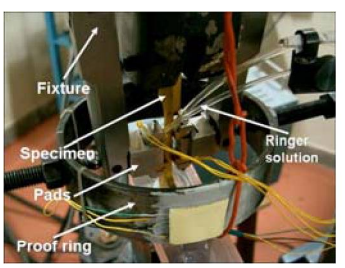

(b)

(c)

Figure 4.4. (a) Experimental setup for fretting fatigue test, (b) Camera view of fretting fatigue setup, (c) Slip amplitude measurement setup with CTOD clip gage.

Slip range between pads and the specimens were measured with CTOD clip gage as shown in Fig 4.4c.

Ringer solution contained in a glass jar maintained at 37°C was continuously streamed on pads with a rubber hose and collected in a container below. This flow is adjusted to obtain complete immersion of contact area similar to fretting action of hip joints surrounded by continuous flow of physiological medium.

4.6. Characterization Techniques

4.6.1. Microscopic Examination

Microstructural examination of substrate materials, surface modified layers and fretting damage areas is carried out with Zeiss MC43 optical microscope and JSM - 840A JEOL Scanning electron microscope (Japan). EDS analysis of the damaged area is done with ISIS link microanalysis, Oxford Instrument – UK. The etchant used is Keller's reagent (6 ml HNO_3, 2 ml HF and 92 ml distilled water).

4.6.2. Microhardness Measurement

Vickers microhardness profile measurement of plasma nitrided and thermal oxidized titanium alloys is done with Leco M-400 microhardness tester. The load level selected ranged from 5gms to 500gms. The hardness was measured for every 2 micron interval from the surface and also the load carrying capability of modified layers is done by measuring hardness with increasing load from 25gms to 2000gms. The test was repeated three times to check consistency.

4.6.3. X-Ray Diffraction (XRD) Analysis

XRD analysis is performed on uncoated as well as coated specimens with Shimadzu XD-D1 (Cu K_α) X-Ray diffractometer. A small piece of substrate and coated samples were always preserved for microstructural as well as XRD tests. The diffraction peaks were indexed with JCPDF software. The same is compared with the other journal publications for confirmation.

4.6.4. Scratch Test

Scratch testing of PVD TiN coating, plasma nitriding and ion implanted alloys is done with custom-built scratch test machine. A Rockwell stylus was fixed normal to the samples. The stylus traverse at the speed of 2mm/sec on the sample fixed to a rigid holder. The sample holder was tilted to one degree which applies progressively increasing normal load with the movement of the stylus. The sudden drop in the normal and traction force indicates the rupture strength and adhesion strength of the coating. Each test was repeated two to three times to check for consistent values.

4.6.5. Nano Indentation

Nano indentation test is performed with Nano X40NM to measure the hardness and reduced elastic modulus of thin coatings. The samples were cleaned with acetone and glued to a small steel disc and placed on a magnetic holder. The indentation area is initially selected after observation with optical microscope. The Berkovich indenter later scans a small part of the surface with higher depth of focus similar to AFM. The indentation area can be selected from the scanned picture. Normal load applied ranged from 100μN for ion-implanted samples to 500 mN for unmodified sample. The force and displacement resolution of the instrument was below 0.04 μN and 0.04 nm respectively. The load-depth curve is plotted from the values recorded during indentation. The hardness and the elastic modulus of the surface layer is calculated from the maximum load and unloading part of the curve respectively. The control software automatically shows the values of hardness and elastic modulus. Test was repeated three times to get consistent values.

4.6.6. Roughness Measurement

The roughness profiles of coatings and fretting damage were measured with M2 stylus profilometer. The travel distance was varied from 1.6 mm to 5.4 mm.

5. Results and Discussion

5.1. Preface

This section is described in four different parts beginning with characterization results of substrate materials and surface modified layers followed by results and discussion on fretting wear and fretting fatigue tests of surface modified alloys. The final section describes some of the important features of fretting fatigue failures commonly observed during the tests. The references to the results described below are very limited since the work is entirely a new approach in the area of biotribology.

5.2. Characterization of Substrate Materials

5.2.1. Microstructural Details of Substrate Titanium Alloys

Fig 5.1 shows the optical micrograph of Ti-6Al-4V and Ti-6Al-7Nb. The volume fractions of primary α in Ti-6Al-4V and Ti-6Al-7Nb alloys are 53% and 91% respectively. The volume percent of α+β colony in Ti-6Al-4V and Ti-6Al-7Nb alloys is 47% and 9% respectively. The lamellar α+β colony of Ti-6Al-4V is more resolved compared to Ti-6Al-7Nb with smaller primary α size. Since the alloy is hot rolled and annealed, it shows bimodal structure with equiaxed primary α within α+β matrix. Microscopic observation along the longitudinal direction (rolled surface) reveals elongated lamellar structure. Bimodal structures are generally known for its high ductility and fatigue strength with well balanced properties due to combined influence of lamellar and equiaxed microstructures. In these alloys, Al stabilizes h.c.p alpha phase and Nb and V stabilizes b.c.c beta phases in these alloys. Fig 5.2

shows the XRD analysis pattern of the base materials indicating the presence of α phase. The surface of Ti-6Al-4V and Ti-6Al-7Nb will be dominated with semicrystalline TiO_2 layer (~30 nm) along with oxides of Al, V and Nb respectively (Sitting et. al., 1999). Fatigue lives are generally governed by the volume fraction of the phases present. The presence of finer phases on the surface of unmodified materials is favorable for increasing fretting fatigue crack initiation life.

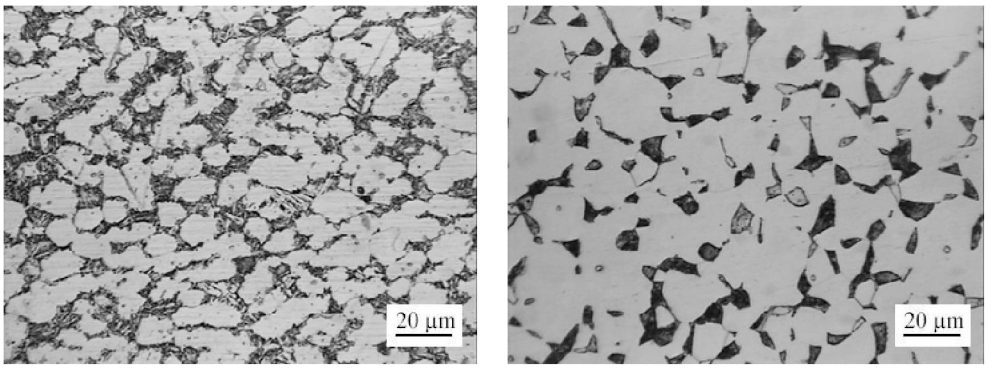

Figure 5.1. Optical micrographs of (a) Ti-6Al-4V, (b) Ti-6Al-7Nb.

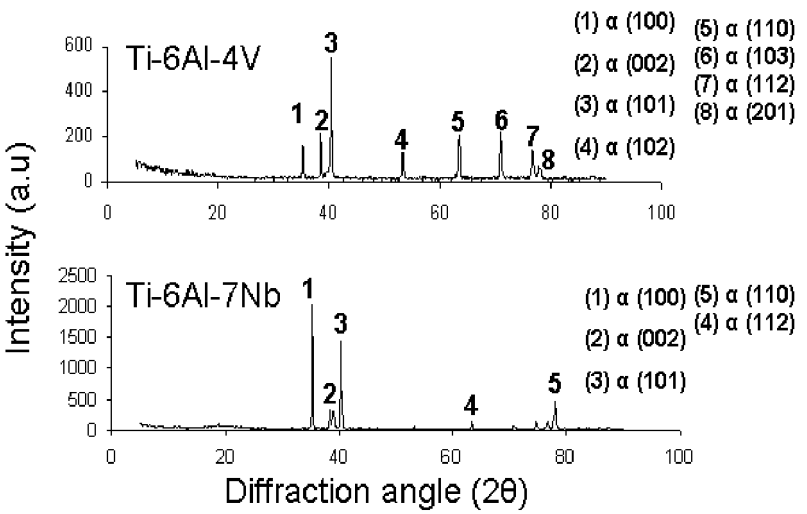

Figure 5.2. X-Ray Diffraction pattern of substrate titanium alloys showing α phase.

5.2.3. Nano Indentation Test

Fig 5.3 shows the load-depth nano indentation plot of Ti-6Al-4V substrate. Nano indentation is suitable for studying the properties of thin films or modified layers. It can be used for all possible materials in engineering applications. Normal load is applied gradually through a diamond indenter (Berkovich indenter) which will penetrate few tens of nanometers from the surface. The load and depth are continuously recorded as shown in Fig 5.3. For Ti-6Al-4V substrate, maximum normal load of 5 mN was applied and the penetration depth was

below 60nm. The surface layer properties are calculated with constitutive equations and presented in terms of hardness and reduced elastic modulus. The elastic modulus is reduced due to small amount of deformation experienced by the indenter during penetration. The hardness and reduced elastic modulus of the substrate are 4 GPa and 129 GPa respectively. Nano indentation test results of all thin layer coatings are presented in the subsequent sections.

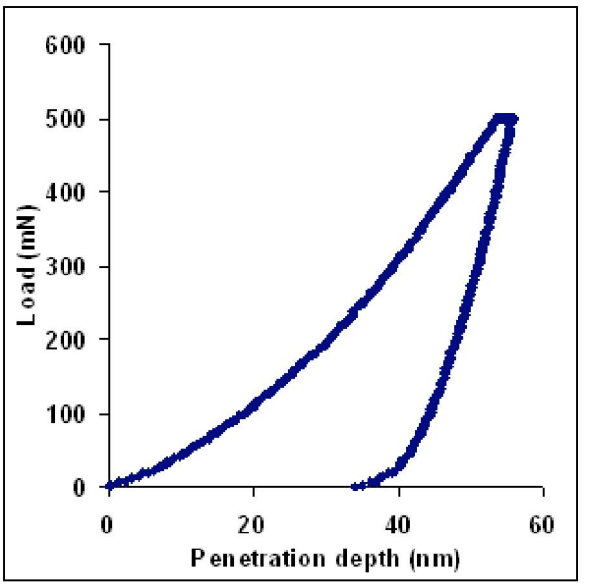

Figure 5.3. Nano indentation profile of Ti-6Al-4V substrate.

5.3. Characterization of Surface Modified Layers

5.3.1. PVD TiN Coating

Fig 5.4a shows coating of TiN on Ti-6Al-7Nb and Fig 5.4b shows the XRD pattern of the TiN layer indicating the pure titanium nitride phase. The growth of TiN layer is normally columnar on the substrate during the PVD process. This feature however was not resolvable in the presented micrograph. The coating introduces bi-axial residual stresses, which scales with the substrate yield stress, and strongly resists the propagation of shear fracture along the columnar boundaries (Bhowmick et. al., 2004). Therefore it appears that the integrity of the TiN columns is mainly due to the compressive residual stresses developed during the deposition. The main deformation mechanism of TiN during indentation is shear fracture ruling out any possibility of dislocation slip effecting gross plastic deformation. The hardness of the layer is 2800 HVN with adhesion strength of 90N. The surface feature and roughness profile (R_a = 0.3 μm) as shown in Fig 5.4c indicates uneven surface of the coating. Lots of debris can be expected during fretting within the contact from the interaction of surface projections. It is also sometimes assumed favorable during fretting because the surface depressions can provide sink for the generated particles thereby minimizing three body wear.

Finally the ability to resist exfoliation of the film from the substrate depends on the adhesion strength, purity and uniformity of the film.

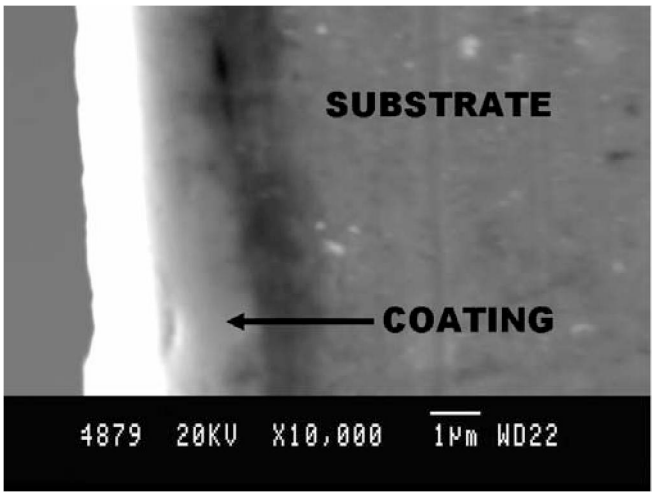

(a)

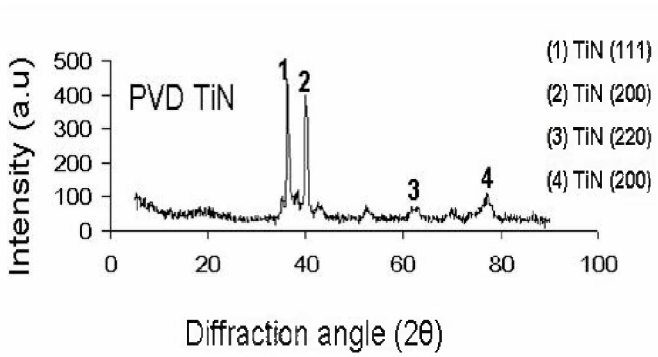

(b)

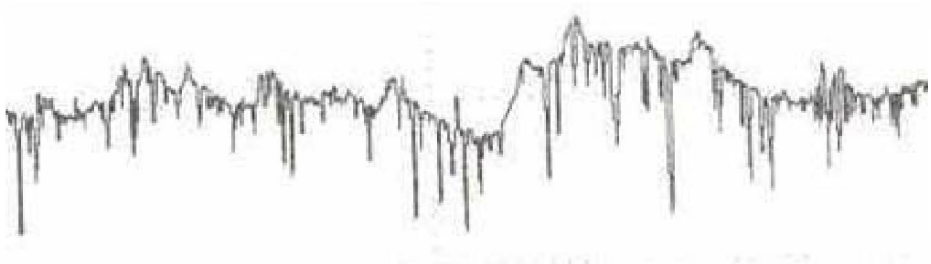

(c)

Figure 5.4. (a) PVD TiN layer on Ti-6Al-7Nb, (b) XRD of TiN layer, (c) Surface roughness profile of PVD TiN coated alloy (R_a = 0.3 µm).

Fig 5.5a shows the nano indentation profile of PVD TiN layer. Maximum load of 2.5mN was applied to get a penetration depth less than 60nm. Elastic recovery is much more compared to unmodified substrate due to high hardness of the layer. It is indicated by the

reduced area of the loop. The hardness and the reduced elastic modulus are reported as 40 GPa and 332 GPa respectively. Fig 5.5b shows the nano indenter scanning probe micrograph of the layer with the indenter impression.

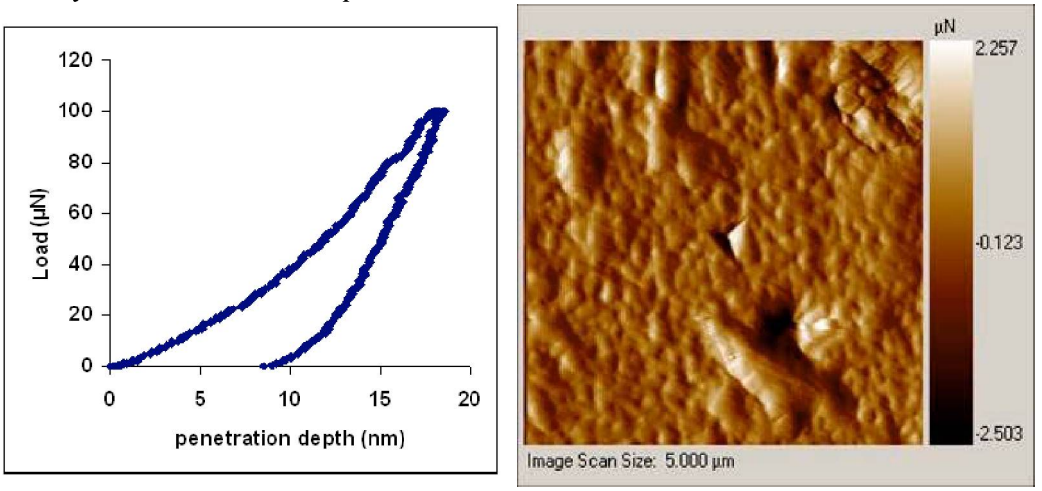

(a) (b)

Figure 5.5. (a) Nano indentation profile of PVD TiN coating, (b) Surface profile.

5.3.2. Plasma Nitriding

Fig 5.6a shows the cross section of plasma nitrided Ti-6Al-4V alloy. Plasma nitriding deals with thermal diffusion of nitrogen under negative pulsed DC biased voltage and temperature. The gradient or diffused layer is more clearly visible in the picture. The case thickness is dependent upon the processing temperature and time. XRD results as shown in Fig 5.6b indicate the formation of two prominent phases TiN and Ti_2N. These phases are not clearly demarcated since the layer must be within the order of nanometer. Plasma nitriding at higher temperatures (700 – 900°C) with higher nitrogen potential produces thicker case with larger volume fractions of TiN and Ti_2N. Thicker and harder modified case is not at all preferable because it always favors reduction in fatigue strength (Ani Zhecheva, 2004). The weight fractions of these phases will normally vary within the nitrided layer. TiN is always found in higher volume towards the surface due to availability of higher amount of nitrogen (Bekir et al, 1996). The layer beneath TiN would be a mixture of Ti_2N and TiN. Solid solution of nitrogen in α is found below the mixed layer. Therefore there is a gradient of hardness below the surface layer. In such case, the gradient layer may serve double purpose of preventing catastrophic failures due to thicker and harder modified case while delaying the fretting induced surface defects. The softer volume of the layer will have more capacity to accommodate the surface and subsurface plastic deformation due to fretting. However, the layer is comparatively stronger than the base substrate. This will ensure higher fretting fatigue strength compared to unmodified alloy.

The plasma nitrided samples are smoother (R_a = 0.035μm) than as polished unmodified alloy (R_a = 0.113μm). Since the layer is chemically inert due to the formation of ceramic nitride compounds, the friction will be minimum compared to unmodified alloys.

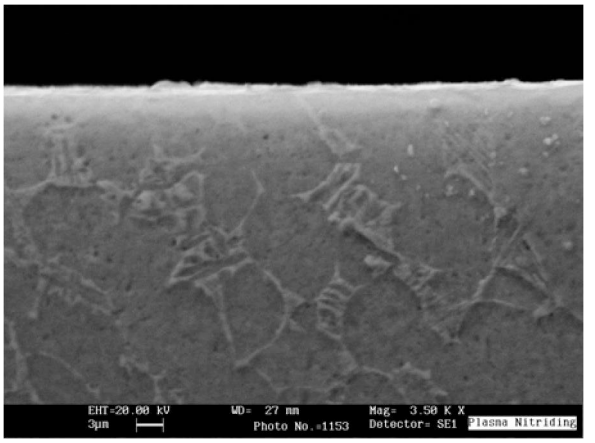

(a)

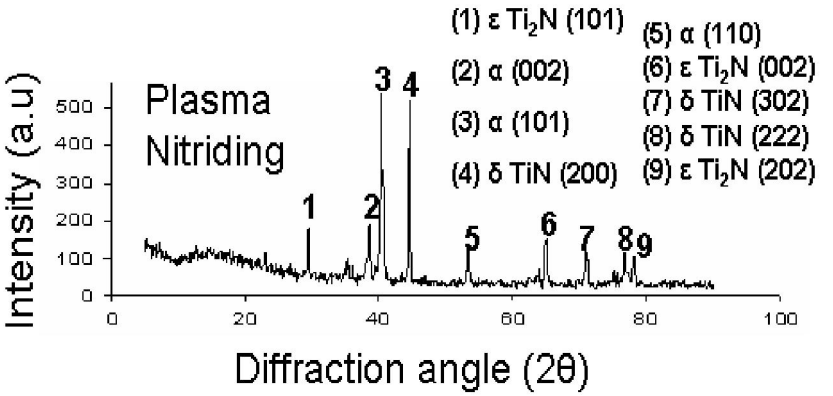

(b)

Figure 5.6. (a) Plasma nitrided layer, (b) XRD pattern of the nitrided layer.

Fig 5.7 (a) and (b) shows the hardness profile of the plasma nitrided Ti-6Al-4V alloy. It shows a decreasing trend from the surface indicating the reduced concentration of nitrogen below the surface. It can be observed that the hardness is below 700 VHN within at a depth of 2 µm. The hardness produced by plasma nitriding process usually crosses 1000 VHN on the surface. This indicates that hardest layer with TiN and Ti_2N is less than 2 µm. This effect can be observed in Fig 5.7b. The hardness drops after certain load when the indenter penetrates the layer giving the composite hardness rather than the film hardness. The gradient layer may be more useful during fretting fatigue because the surface strains developed during fretting can be easily relieved by softer layer than hard coatings like PVD TiN which may experience failure due its inability for accommodating fretting induced tangential strains. This fact is discussed later. Fig 5.8a shows the nano indentation profile of plasma nitrided Ti-6Al-4V alloy with maximum load 1 mN giving penetration depth of about 40nm. The layer is softer compared to PVD TiN layer with hardness and reduced elastic modulus of 23 GPa and 201 GPa respectively. Fig 5.8b shows the nano indenter scan probe micrograph of the surface showing fine scratches.

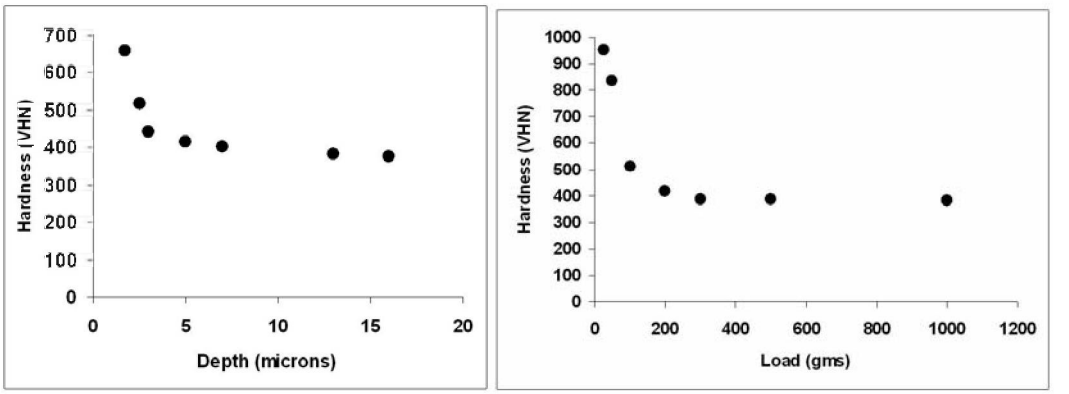

(a) (b)

Figure 5.7. (a) Hardness depth profile and (b) Hardness load profile of plasma nitrided Ti-6Al-4V.

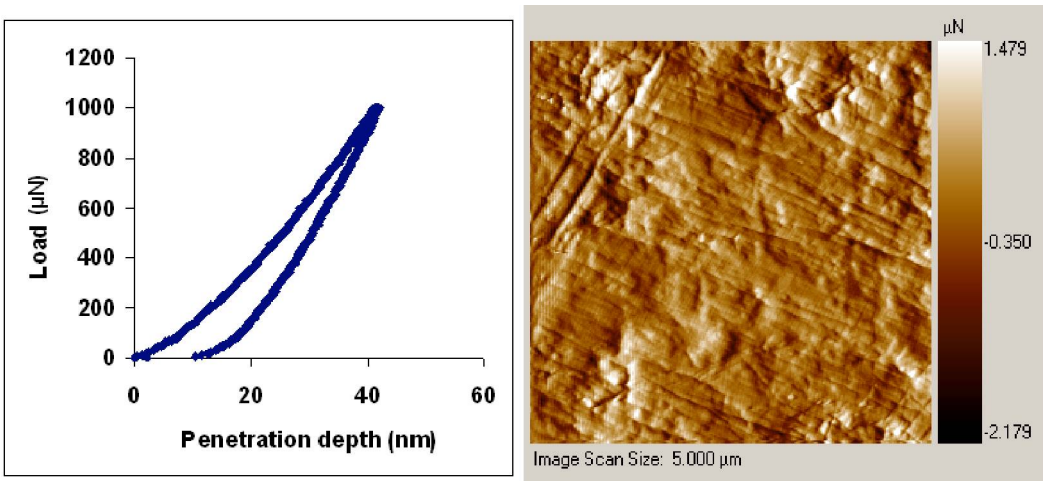

(a) (b)

Figure 5.8. (a) Nano indentation profile of plasma nitrided Ti-6Al-4V, (b) Surface profile.

5.3.3. Nitrogen Ion Implantation

The ion implanted specimens do not generally produce contrasting changes in surface color like thermally oxidized or PVD TiN coated specimens. However, a slightly burnt brownish appearance was visible indicating the implantation. From the TRIM (Transport of Ions in Matter) software, the projected range of nitrogen in this titanium alloy was found to be 170 nm. This is the case because, the ions are forced to diffuse within the layer with the acquired kinetic energy without the aid of any other force. The ions trajectory therefore depends upon the mass and the kinetic energy.

Fig 5.9a shows the nano indenter profile of nitrogen ion implanted titanium alloy. Maximum load of 0.1 mN or 100 µN was applied since the layer is very thin. The penetration depth is below 20 nm, which is well within the surface modified layer of 170 nm. The hardness and the reduced elastic modulus of the layer are reported as 6 GPa and 115 GPa

respectively. Fig 5.9b shows the nano indenter scan probe micrograph of the surface of ion implanted alloy. The indenter mark is also seen at the center.

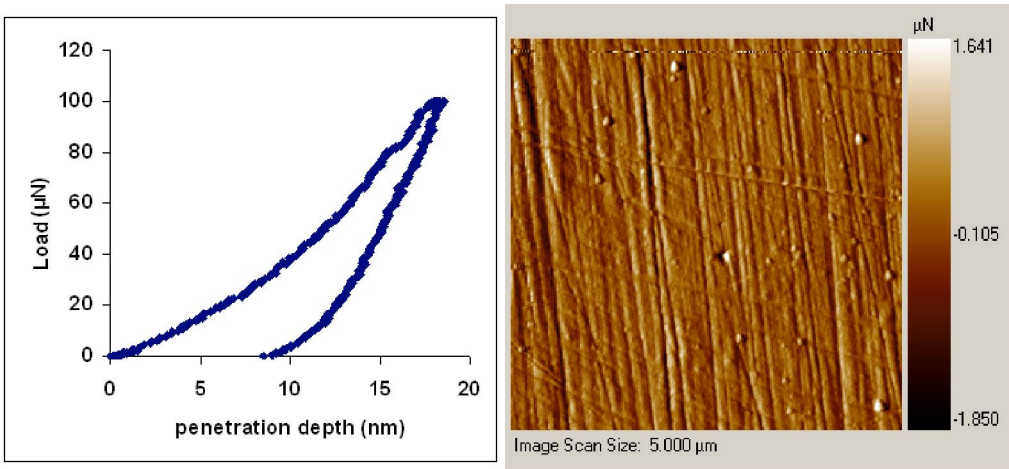

(a) (b)

Figure 5.9. (a) Nano indentation profile of nitrogen ion implanted Ti-6Al-4V (b) Surface profile.

Fig 5.10 shows the comparison of the properties of all the thin layers. This shows that PVD TiN layer has the highest hardness and the elastic modulus among all the thin layers. Ion implanted samples have shown least improvement in the properties.

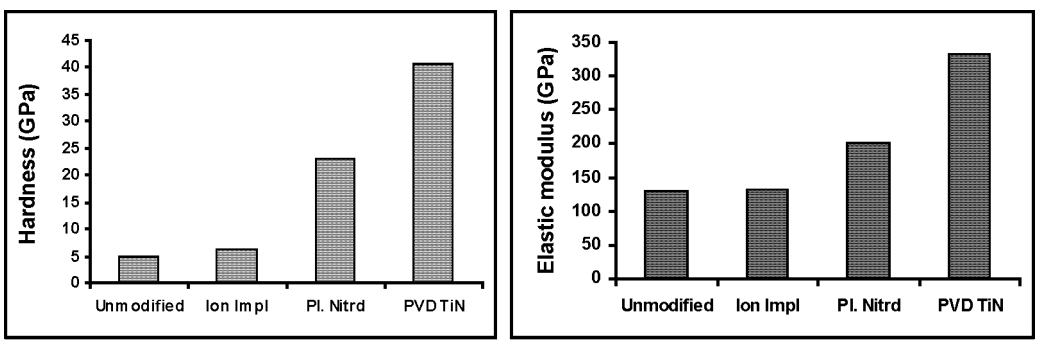

Figure 5.10. Comparison of the properties obtained from the nano indentation test of thin layers.

Figure 5.11 shows scratch test results of PVD TiN coating, plasma nitriding and ion implanted layers. Scratch testing is normally used to obtain adhesion strength of the surface coated layers. It can also indicate the general scratch resistant property of modified layers. PVD TiN has better strength in terms of critical rupture and traction force compared to other layers. Traction force value refers to adhesion strength of the layer to the substrate. Therefore it cannot be strictly compared with other processes since all other processes used are the modification techniques except PVD TiN. Plasma nitrided alloys are softer compared to PVD TiN. Ion implanted alloys have shown least value due to shallow modified layer. Traction force of modified layers indicates the resistance to plowing action of the diamond indenter.

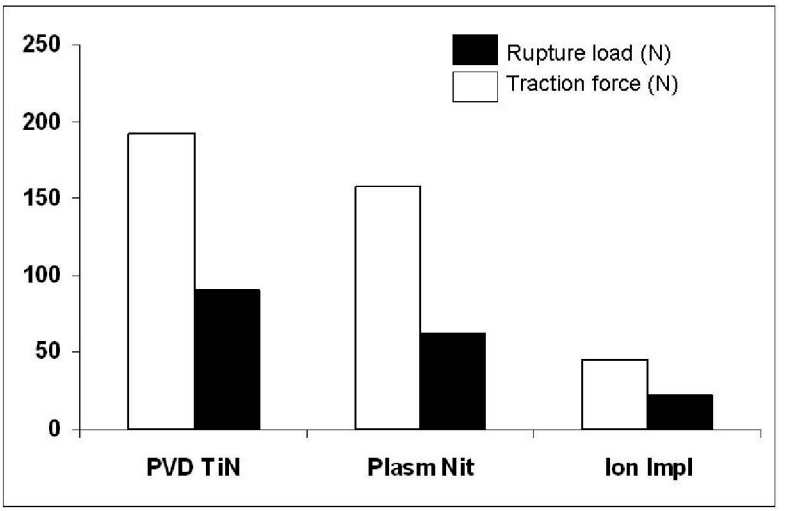

Figure 5.11. Scratch test results of thin layers.

5.3.4. Laser Nitriding

Fig 5.12a shows the gage portion of laser nitrided Ti-6Al-4V fatigue specimen. It appears more like a weld overlay along the load axis of the specimen. The edges have melted due to high power density of the laser. The depth of penetration is as shownin Fig 5.12b, is extremely high compared to all other process used in these experiments. Undercuts and cracks were also observed along either sides of extended overlay portion on the flat grip area of the fatigue specimen. Macroscopic observation reveals golden brownish melt deposit indicating the formation of nitrides. The hardness of TiN deposit ranged from 1450 to 1600 VHN. The scan speed and the power density were optimized with few test coupons to obtain minimum penetration and complete nitridation. The optimized power density should provide minimum penetration and complete dissociation of nitrogen at the melting zone. The appearance of blue plasma during melting is the indication of dissociation of nitrogen. One of the recommended methods offered was to have high power density with minimum interaction time to have complete dissociation of nitrogen as well as minimum penetration. This will also offer the advantage of developing finer microstructural features on the surface. The nitriding can also be made efficient through controlled high purity nitrogen atmosphere around the material. Convection currents in combination with high level of diffusion of nitrogen in the melt ensure complete nitridation. Fig 5.13 shows the boundary between base material and the HAZ. Grain size difference is clearly visible between the substrate and HAZ. HAZ grains are finer and barely distinguishable even after deep etching. Geeta et. al., 2004 indicates that needle like structure just below the melt deposit in Fig 5.14 consists of mixture of $TiN_{0.3}$, TiN and α' - Ti. Dendritic TiN is within the melted zone and hexagonal $TiN_{0.3}$ is also formed close to the melt/HAZ boundary as shown in Fig 5.14. The boundary between brittle melt deposit and HAZ is sharply outlined which can become a potential site for initiating failure because the properties of the layer and the substrate significantly vary.

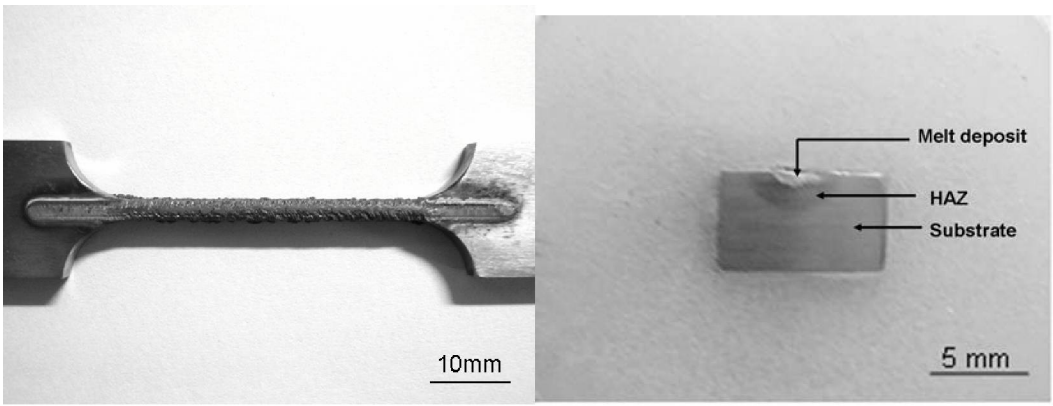

Figure 5.12. Laser nitrided Ti-6Al-4V (a) Fatigue specimen, (b) Sample cross section.

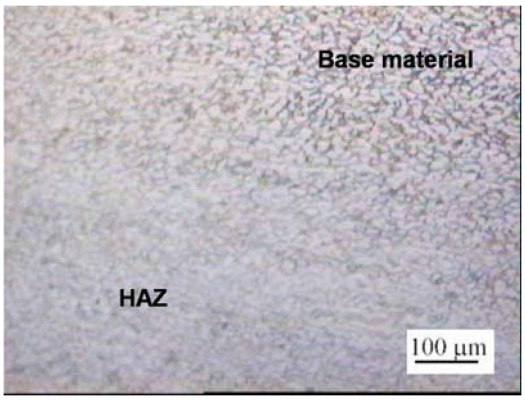

Figure 5.13. HAZ-base material boundary.

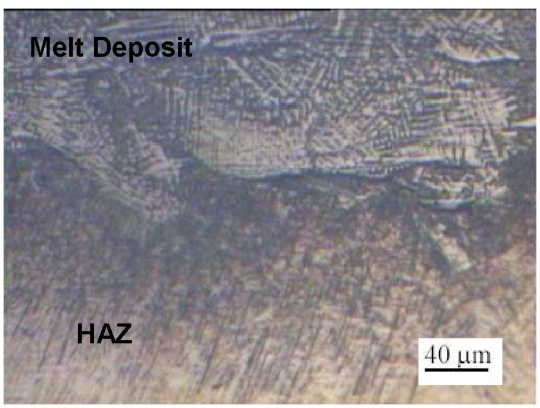

Figure 5.14. Melt deposit - HAZ boundary.

Fig 5.15 shows the microstructural features of laser nitrided Ti-6Al-4V alloy. The melt deposit is almost 0.3 to 0.5 mm thick consisting of randomly oriented TiN dendrites (60 to 70 Vol %) as shown in Fig 5.13a. Dendritic features are expected due to melting of substrate,

alloying and resolidification similar to a mini casting process. Fig 5.16 shows XRD analysis of laser nitrided Ti-6Al-4V confirming the presence of TiN and Ti_2N phase.

The volume of dendrites can also be varied by dilution of nitrogen with inert gases. Fig 5.15b shows the heat affected zone (HAZ) adjacent to melt deposit. This is a typical martensite α' structure due to faster cooling of the region. It is interesting to observe that the growth of needles is perpendicular to each other in certain favorable crystallographic orientation. The average hardness of HAZ is around 432 VHN which is slightly more than the base material.

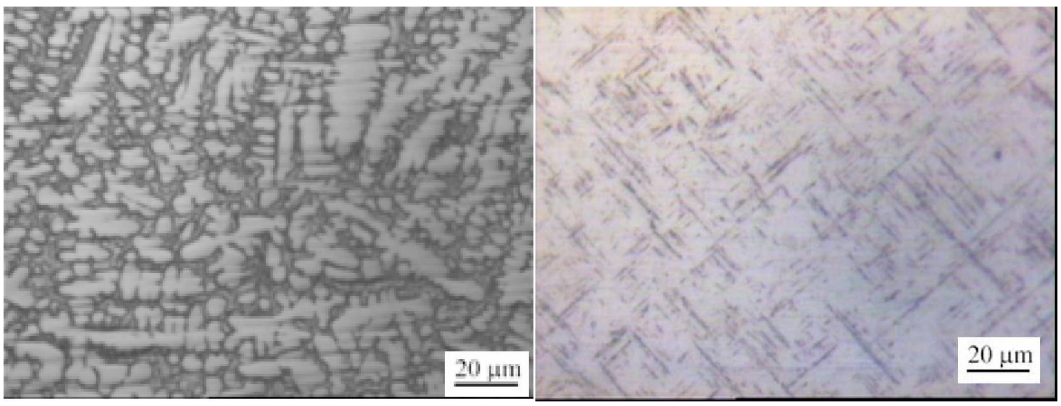

(a) (b)

Figure 5.15. Microstructural features of laser nitrided Ti-6Al-4V (a) Melt deposit, (b) Heat Affected Zone (HAZ).

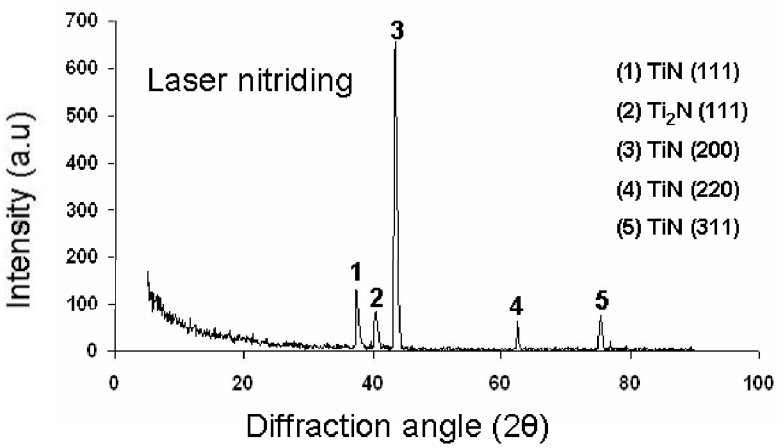

Figure 5.16. Diffraction pattern of laser nitrided Ti-6Al-4V.

5.3.5. Thermal Oxidation (To)

Thermal oxidation of titanium alloys has produced very rough surface with black oxide layer on the top and hard α case (solid solution of oxygen in titanium in high concentration) beneath the oxide layer as shown in Fig 5.17. The interface between black oxide and α case is highly irregular as observed in figure. In such case, removal of oxide layer without disturbing

the case beneath would be a difficult task. Reproducing the necessary roughness will also be a problem. Usually there will be a gradient of hardness across the layer since the oxygen concentration is not uniform through out the layer cross section. XRD analysis shown in Fig 5.18 confirms the rutile phase formation (indicated by R) due to high temperature oxidation. Figs 5.19 (a) and (b) shows the hardness profile of the thermally oxidized layer which shows a decreasing trend from the surface.

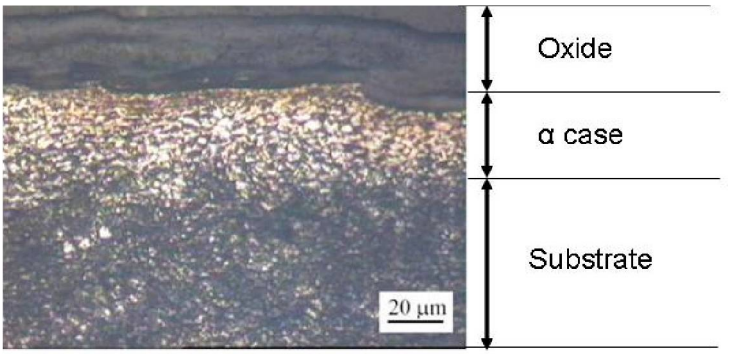

Figure 5.17. Thermally oxidized Ti-6Al-4V showing the oxide layer at the top and α case beneath the oxide layer.

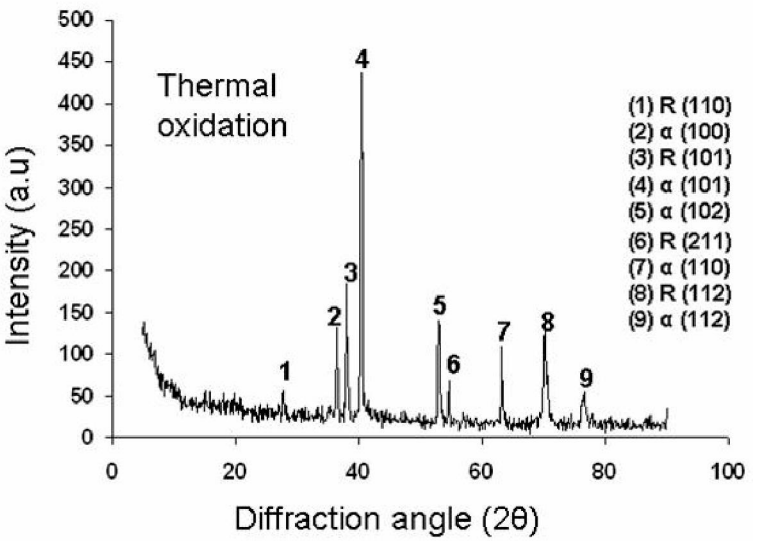

Figure 5.18. X-Ray Diffraction analysis of thermally oxidized Ti-6Al-4V showing rutile and alpha phase.

An oxidized titanium alloy has higher strength and lower ductility on the surface due to stabilization of α phase. It is reported that α case within the surface layer of titanium improves tribocorrosion and galling resistance of titanium alloys (Hasan et. al., 2004). The modified layer here is much thinner compared to laser nitriding, as it is a time dependent thermal diffusion of oxygen. The higher the temperature and time, the higher will be the case depth obtained. Thicker and harder case will degrade the fatigue properties. The case depth can be

controlled with time of oxidation. Controlled oxidizing atmosphere can also be used for thermal oxidation process.

Fig 5.19a shows the load carrying capacity of the layer. At lower loads, the layer offer good indentation resistance and at higher loads, the indenter penetrates the layer. Fig 5.19b shows the hardness profile across the cross section of the sample. Hardness gradient is proportional to concentration gradient across the layer.

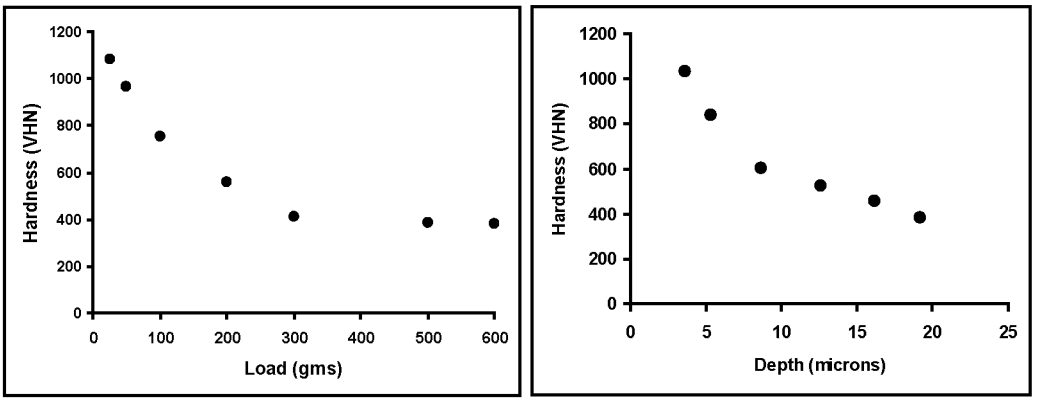

(a) (b)

Figure 5.19. Microhardness profile of thermally oxidized Ti-6Al-4V.

5.4. Fretting Wear Damage Characterization

This section gives fretting wear test results on surface modified titanium alloys compared to unmodified alloy. Fretting wear is a possible damage mechanism in modular junctions of hip shaft models comprising of ceramic heads (alumina or zirconia) with surface modified metallic shafts (titanium alloys). Fretting with alumina balls, as a counter material, has produced a wear scar with different configurations depending upon the parameters. The wear rate has been calculated from the wear scar profile which unavoidably includes compacted oxides in case of tests conducted in air.

5.4.1. Unmodified Alloy

Fig 5.20 (a) and (b), and (c) and (d) shows optical and SEM micrographs of fretting scar on unmodified titanium alloy surface respectively.

Fretting scar is bigger and uniformly circular in ringer solution which is not observed in the fretting scar tested in air. Rutile is commonly formed product during fretting of titanium based alloys. The nature of debris formed very much influences the fretting behavior. In case of fretting in air, the oxides form at the contact and gets compacted within the scar. The transfer of products was also observed on the ball at contact point. Due to the presence of oxides, the abrasive counter body (alumina ball) cannot dig the surface effectively during fretting. The humidity of the atmosphere also influences fretting behavior (Chen et. al., 2002). Therefore the fretting scar width is less compared to that of ringer fluid in Fig 5.20 (b) and (d). The coefficient of friction is quite high compared to all other cases as will be seen later.

In case of fretting in ringer fluid, the oxidized product is ejected out exposing fresh surface to mechanical attrition.

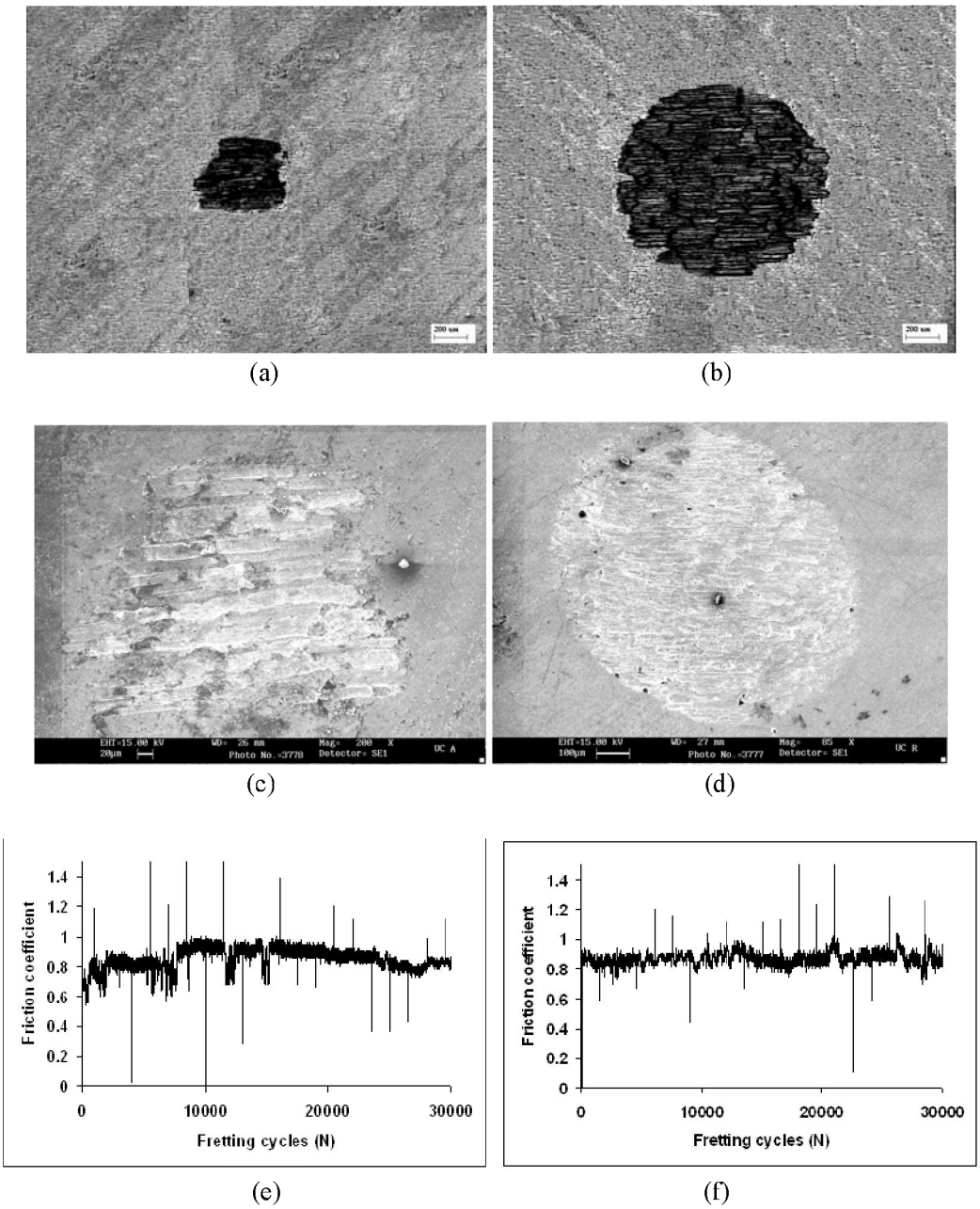

Figure 5.20. (a,c) Fretting scar of unmodified alloy in air, (b,d) Fretting scar in ringer fluid, (e) Friction coefficient curve in air, (f) Friction coefficient curve in ringer fluid.

The compacted oxides are loosened by interaction with the fluid. Black oxides were found scattered around the scar after the test. Increasing in scar width is due to combined effect of mechanical attrition and dominating electrochemical oxidation (Gallino et. al, 2001).

The repeatedly exposed area at every fretting cycle acts anodic to the surrounding undamaged cathodic region for the electrochemical oxidation. The reacted area becomes weaker easily loosing more material during fretting even if the friction is lower. Wear particulates generated during fretting motion at the contact also take part in abrasive action (three body wear) of the layer along with electrochemical activity. Abrasive particulates can generate from both the modified layers as well as alumina ball. Fig 5.20 (e) and (f) shows friction coefficient curves for fretting wear of unmodified alloys in air and ringer fluid. It is observed to be steady within the range of 0.8 to 1.0 in both the cases. Intermittent formation and removal of oxides may be responsible for low friction events during fretting.

5.4.2. PVD TiN Coating

Fig 5.21 (a) and (b) and (c) and (d) shows optical and SEM micrographs of fretting scar on PVD TiN coated titanium alloy. The TiN layer is naturally more resistant to abrasion and electrochemical oxidation process compared to fretting of unmodified alloy. In case of air, fretting mark is little deep compared to ringer fluid. The oxides are also observed during test. Nano crystalline or amorphous rutile or anatase is a possible oxides produced from fretting on TiN layer (Chen et. al., 2005).

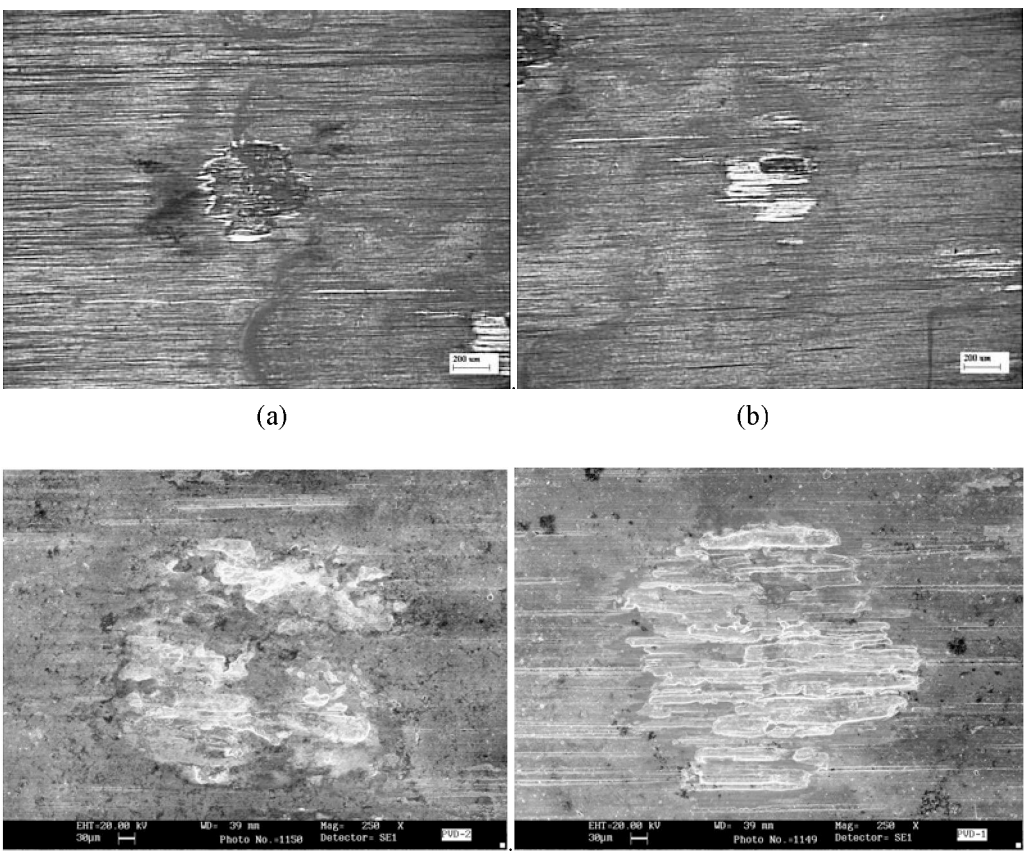

Figure 5.21. Continued on next page.

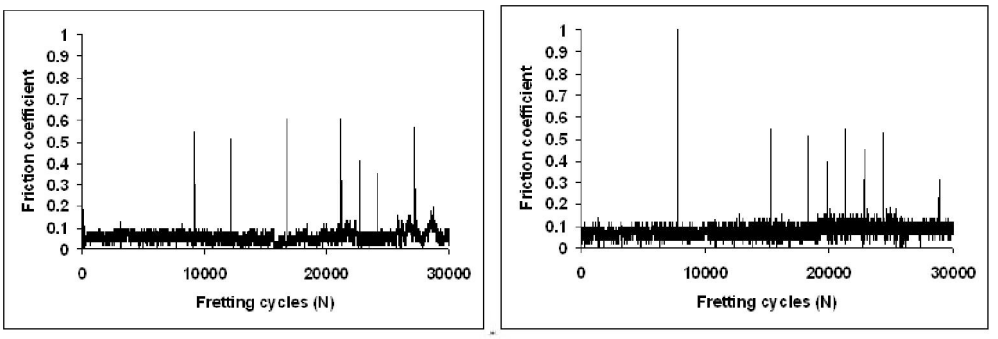

(e) (f)

Figure 5.21. (a,c) Fretting scar of PVD TiN coated alloy in air, (b,d) Fretting scar in ringer fluid, (e) Friction coefficient curve in air, (f) Friction coefficient curve in ringer fluid.

Fig 5.21 (e) and (f) shows friction coefficient curves for PVD TiN coated alloy. It is observed that friction is steady and lies below 0.2 in both air and ringer fluid throughout the test. This shows the superior tribological properties of TiN layer towards fretting wear resistance.

5.4.3. Plasma Nitriding

Fig 5.22 (a) and (b), and (c) and (d) shows optical and SEM micrographs of fretting scar on plasma nitrided titanium alloy surface. A substantial difference in the average wear scar diameter is observed in ringer solution and air. The shows that it is difficult to penetrate the layer in air than ringer fluid. The worn area is also very irregular and rough with debris particulates. The nitride debris appears to dwell in the contact even during fretting. The layer removal is also not very uniform like that of Ringer fluid. The fretting scar profile is similar to unmodified alloys with oxidation in air and electrochemical oxidation phenomena in ringer fluid. Compacted oxides are present after fretting in air and absent in Ringer fluid. The surface roughness also plays a role during fretting. Smoother surface will have higher magnitude of real contact and should normally experience higher friction. Rougher surface will have to initially fret and stabilize the peaks and valleys before it can get the real contact area.

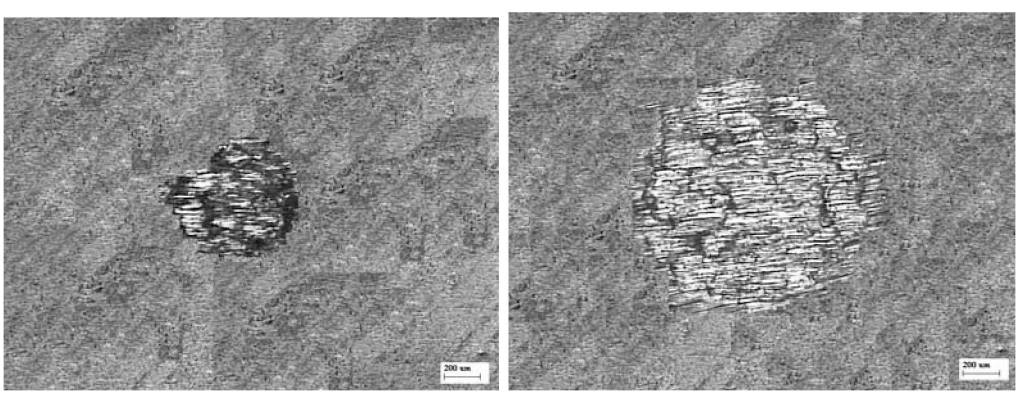

(a) (b)

Figure 5.22. Continued on next page.

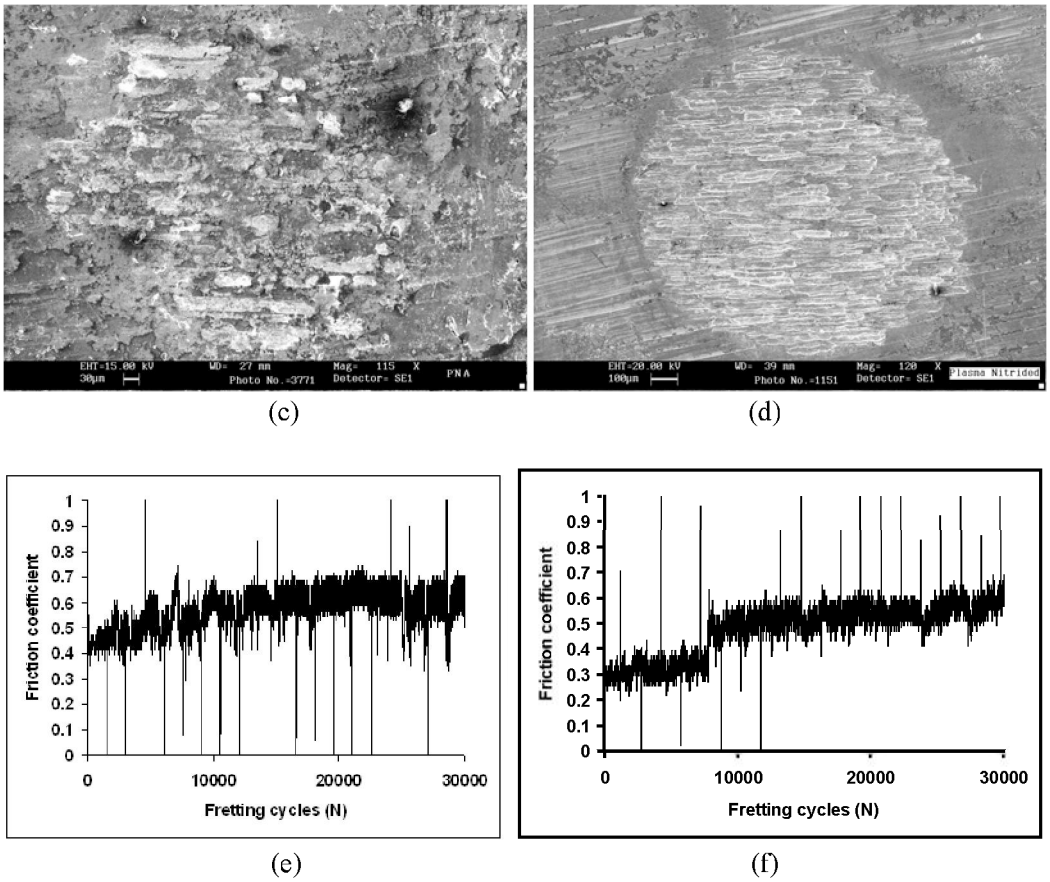

Figure 5.22. (a,c) Fretting scar of plasma nitrided alloy in air, (b,d) Fretting scar in ringer fluid, (e) Friction coefficient curve in air, (f) Friction coefficient curve in ringer fluid.

Fig 5.22 (e) and (f) shows friction coefficient curves in air and ringer fluid. In both the cases steady increase in friction from 0.4 to below 0.7 is observed. However there is an abrupt rise in friction in ringer fluid after 8000 cycles but below 0.6. This is possibly due to fretting on the substrate after the modified layer has eroded away.

5.4.4. Nitrogen Ion Implantation

Fig 5.23 (a) and (b) and (c) and (d) shows Optical and SEM micrographs of fretting scar on nitrogen ion implanted titanium alloy surface. The average wear scar diameter is almost similar in ringer solution as well as in air. However, the scar profile is more irregular in air and regular in Ringer fluid. Fretting scar for specimen tested in Ringer fluid has generated a larger and deeper scar due to fretting induced electrochemical dissolution process similar to unmodified and plasma nitrided alloys. Compacted oxides were observed within the fretting scar for specimen tested in air. Whereas the oxides were found scattered around the contact for specimen tested in Ringer solution. The implanted layer being softer and thinner could not protect the surface for a longer period.

Fig 5.23 (e) and (f) shows friction coefficient curves for fretting studies on ion implanted titanium alloy. It can be observed in Fig 5.23e that film has ruptured after 2500 cycles

increasing the friction coefficient from 0.6 to 0.8 during fretting in air. Whereas in ringer fluid it has steadily maintained between 0.5 and 0.75 although it has penetrated the modified layer.

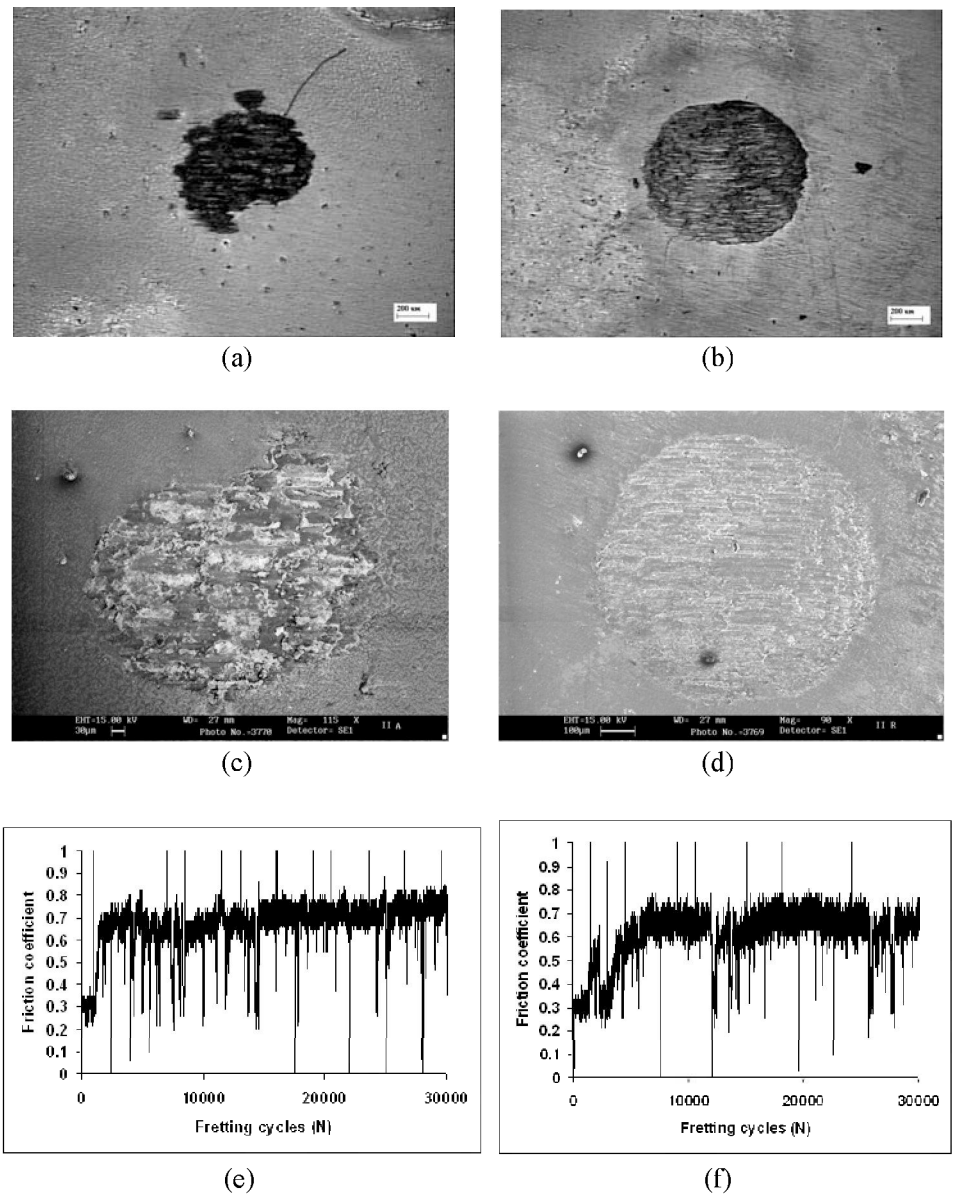

Figure 5.23. (a,c) Fretting scar of nitrogen ion implanted alloy in air, (b,d) Fretting scar in ringer fluid, (e) Friction coefficient curve in air, (f) Friction coefficient curve in ringer fluid.

5.4.5. Laser Nitriding

Fig 5.24 (a) and (b) shows optical micrographs of fretting scar on laser nitrided titanium alloy surface. The scar profile could not be observed in SEM due to shallow area. Average scar diameter in ringer solution is smaller compared to that of air. The damage is minimal in laser nitrided alloys compared to all other cases even though steady state friction coefficient is

reasonably high compared to PVD TiN. It can be readily attributed to the presence of large volume fraction of closely spaced TiN dendrites in the modified volume as well as high roughness. TiN dendrite is harder compared to matrix.

Since it is present in substantially large volume percent, it acts to protect the bulk from higher rate of material loss. Dendritic TiN is highly hard and stable than the matrix surrounding it and high friction could be due to mechanical interlocking of projected dendrites and roughness peaks with the alumina ball surface during fretting.

Fig 5.24 (c) and (d) shows friction coefficient curves for fretting on laser nitrided alloy. It can be observed that in both cases, the friction coefficient is steady. It is almost 0.65 in case of air and 0.35 in case of fretting in ringer fluid with a slight decreasing trend during later stages. Compared to other processes it can be observed that the friction coefficient does not vary in wide range here. It is also noted that the surface damage profile is far less compared to other cases even though friction coefficient is higher than say PVD TiN coating. Therefore, there is a possibility that the material loss may have occurred to the counter body (alumina ball) than to the nitrided layer. The severity of the wear damage always depends upon the relative hardness. The harder material damages the softer one during wear process. Since the TiN dendrites are substantially harder than alumina counterpart is, the damage is less severe to the nitrided surface. The magnitude of friction also depends upon the roughness at the contact.

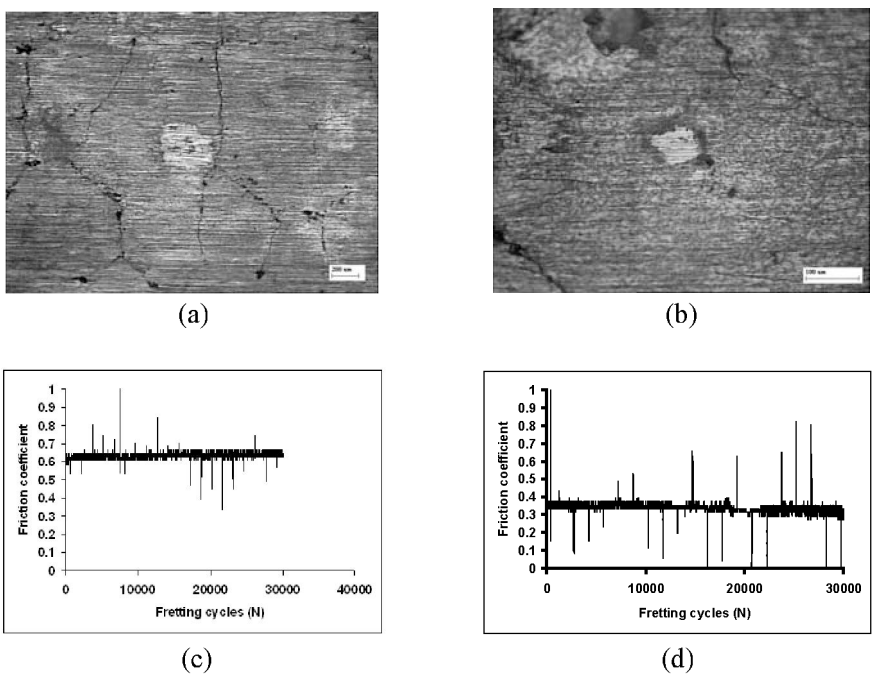

Figure 5.24. (a) Fretting scar of laser nitrided alloy in air, (b) Fretting scar in ringer fluid, (c) Friction coefficient curve in air, (d) Friction coefficient curve in ringer fluid.

5.4.6. Thermal Oxidation

Fig 5.25 (a) and (b) and (c) and (d) shows optical and SEM micrographs of fretting scar of thermally oxidized titanium alloy surface. The surface coating on PVD TiN is uniform all

over the substrate and surface modification through ion implantation is also uniform over the entire implanted surface. Both processes do not allow any post surface preparations and the substrate has to be properly prepared prior to any modification.

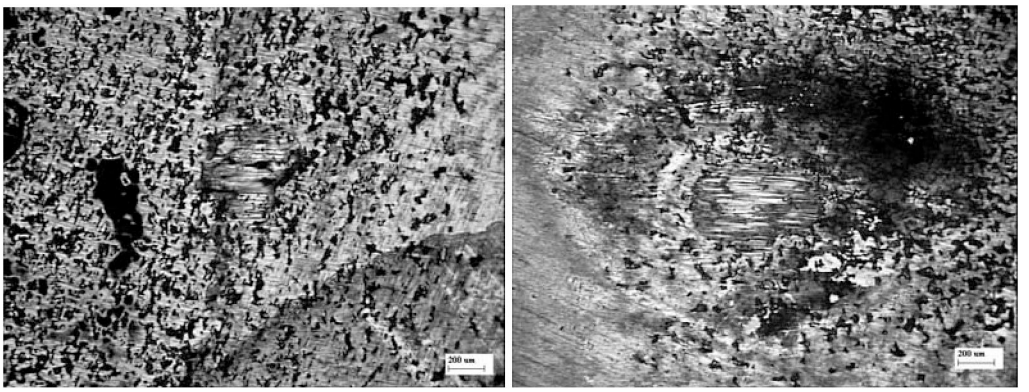

(a) (b)

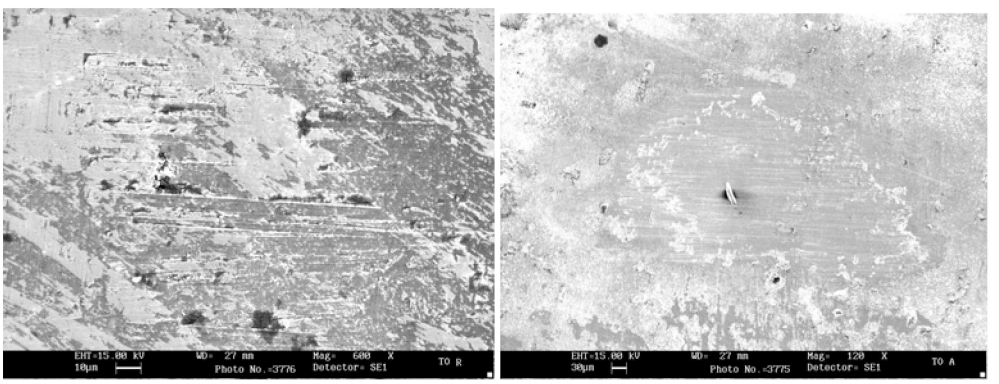

(c) (d)

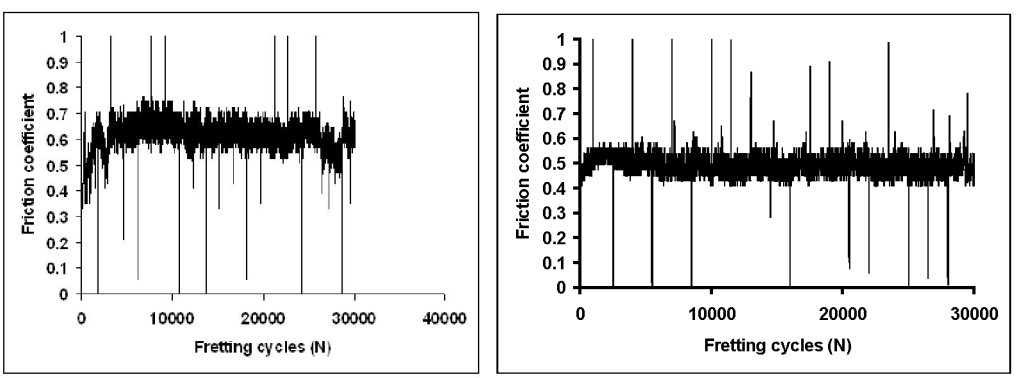

(e) (f)

Figure 5.25. (a,c) Fretting scar of thermally oxidized in air, (b,d) Fretting scar in ringer fluid, (e) Friction coefficient curve in air, (f) Friction coefficient curve in ringer fluid.

However, in case of thermal oxidation, although the surface is uniformly oxidized through out the substrate material, the development of oxidized case is highly non uniform below the black rutile layer. Since the interface between the rutile and oxidized α case is highly irregular or wavy by nature, it poses difficulty in producing smooth surface for fretting tests. The nature of the surface is shown in Fig. 5.25 (a) and (b). Some amount of modified case is also removed during surface preparation through polishing. This indicates that the oxygen diffusion into the alloy is not very uniform during the process of oxidation. Polishing process has removed the case completely in some region leaving the surface with varied distribution of α islands. Fretting test is therefore performed on a selected area where there is a high probability of undisturbed α case. Even though fretting scar width is less both in air and in Ringer fluid, the oxidized alloy has produced high friction coefficient throughout the test due to irregular surface profile.

The average wear scar diameter is smaller in air compared to ringer solution. The scar profile is irregular in both cases. The oxidized case, even though irregular, is thick in addition, hard enough for preventing deeper damage during fretting compared to other processes. The wear tracks are seen aligned along the fretting direction.

Fig 5.25 (e) and (f) shows friction coefficient curves for fretting on thermally oxidized titanium alloy. Here the steady state friction is between 0.6 and 0.7 after gradual increase from 0.4. Whereas in ringer fluid, it ranges from 0.4 to 0.6.

5.4.7. Comparative Study of Steady State Friction Coefficient and Wear Scar Diameters

Figure 5.26(a) shows the comparison bar chart of steady state friction coefficient for all the surface treated alloys tested for fretting wear in air and ringer fluid. Friction coefficient is higher in air than ringer solution for all the cases, except PVD TiN coating which could be due to dominating asperities, oxides and wear debris interaction at the contact. Ringer solution also offers lubricating effect during fretting reducing the friction at the contact in all other cases. PVD TiN coating has shown the lowest friction coefficient (10 – 20%) compared to all other coatings.

Figure 5.26(b) shows comparison of average fretting wear scar diameter for all the cases. The scar profile and friction depends very much on (a) Layer hardness, (b) Layer thickness, (c) Layer microstructure, (d) Fretting medium and (e) Products formed within the scar during fretting. The wear scar generated during fretting is irregular shaped in air and regular circle with definite diameter in ringer fluid in unmodified, plasma nitrided and ion implanted samples. The wear scar diameters in ringer fluid is larger compared to air in all the cases. Large differences in wear scar diameters are observed in case of laser nitrided, unmodified and plasma nitrided alloys. Finally PVD TiN coating and laser nitriding proves to give best performance in terms of minimal fretting damage and PVD TiN gives minimum damage as well as reduced coefficient of friction for 30,000 fretting cycles. Thermal oxidation has given intermediate performance. The wear tracks developed due to fretting is shown at higher magnification SEM micrograph in Fig 5.27. Tracks are all aligned parallel to fretting direction. The same is observed in case of unmodified, plasma nitrided and ion implanted alloys tested in ringer solution. PVD TiN coating showed good fretting resistance both in air as well as ringer fluid.

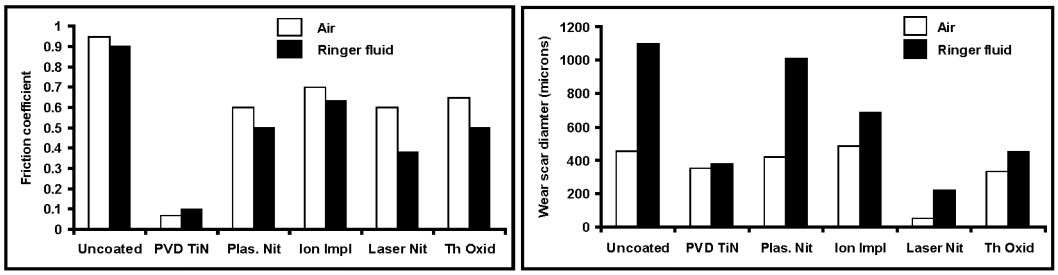

(a) (b)

Figure 5.26. Comparison chart of (a) Steady state friction coefficient, (b) Wear scar diameter for fretting wear tests.

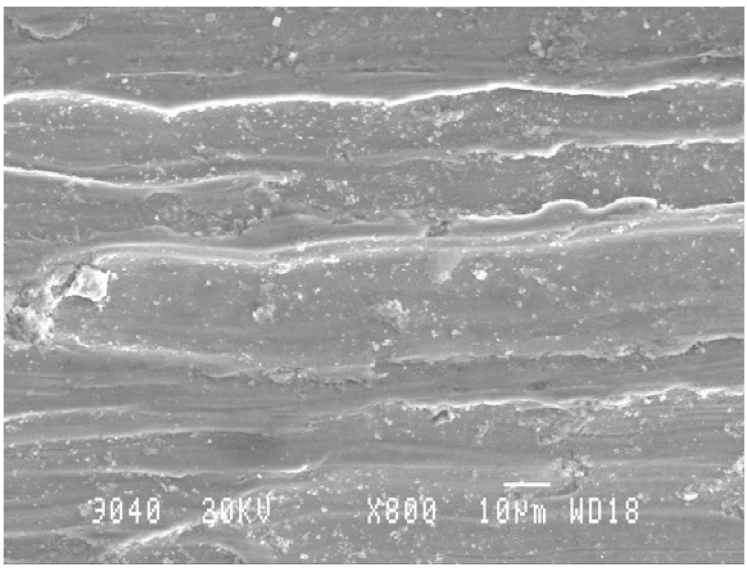

Figure 5.27. Wear tracks within the fretting scar of unmodified alloy.

5.4.8. Fretting Wear Scar Depth and Wear Rate Comparison

Figure 5.28 (a) and (b) shows fretting wear scar depth comparison in air and ringer solution. It is clearly evident that laser nitriding and PVD TiN coatings have shown good performance over all other coatings with minimum surface damage. Laser nitrided coatings have proved superior even to PVD TiN coating. The scar width is the smallest in air for laser nitrided sample as seen earlier and the depth is also very shallow. The scars were difficult to locate even with naked eye in both these cases. The scar is broad and shallow in both cases. The scar depth is higher for softer thin film layers and unmodified samples. The magnitude of scar depth is intermediate for thermally oxidized samples. The depth is irregular in all the cases because of mechanical abrasion in two body and three body wear mode. In ringer fluid it is little more uniform due to influence of electrochemical activity during fretting. It is also observed that depth is more in ringer fluid for unmodified, plasma nitrided and ion implanted alloys than other coatings. This indicates that the base material is very much influenced by the medium during fretting. The influence of corrosion during fretting although not studied here is expected to have occurred favoring easier removal of material.

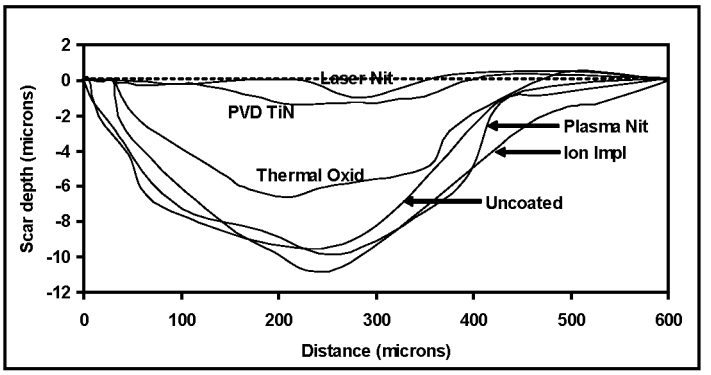

(a)

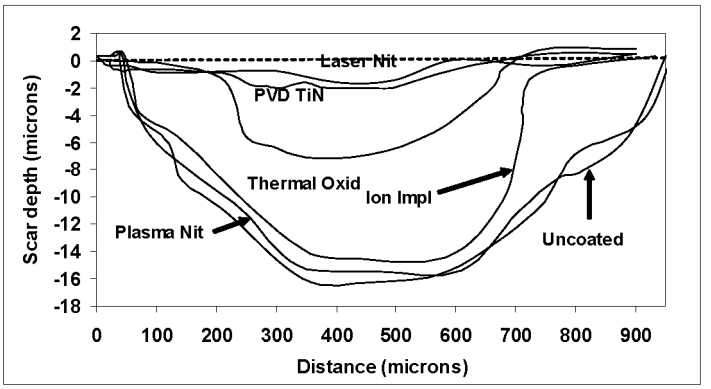

(b)

Figure 5.28. Fretting wear scar depth profiles in (a) Air and (b) Ringer solution.

Fig 5.29 shows comparison chart of wear rate during fretting for all the surface modified layers. It is clearly evident that PVD TiN coatings, laser nitriding and thermal oxidation have shown low wear rates compared to other layers. The wear depth is very shallow for these layers and hence volume of material removed is naturally less compared to others. It can also be inferred that the wear damage is much more reduced for laser nitrided case compared to PVD TiN even though the laser nitrided layer has experienced higher friction coefficient during the fretting wear test.

This indicates that TiN developed through laser nitriding is much more superior compared to PVD process. PVD process develops TiN in columnar structure with high residual stresses between the columns as explained earlier in section 5.3.1. Whereas the laser nitriding process produces TiN in dendritic form during melting and solidification of the substrate. This form of TiN has shown a slightly superior wear resistance compared to PVD TiN layer. It may be related to fretting induced relaxation of residual stresses developed by PVD coating process. This can finally break the TiN columns perpendicular to the growth direction.

Wear rate is higher in ringer fluid than air in all cases. The difference is especially large in case of unmodified, ion implanted and thermally oxidized specimens. The wear rates for laser nitrided, PVD TiN coated and thermally oxidized samples is 0.6, 3 and 12.5% respectively compared to other three layers.

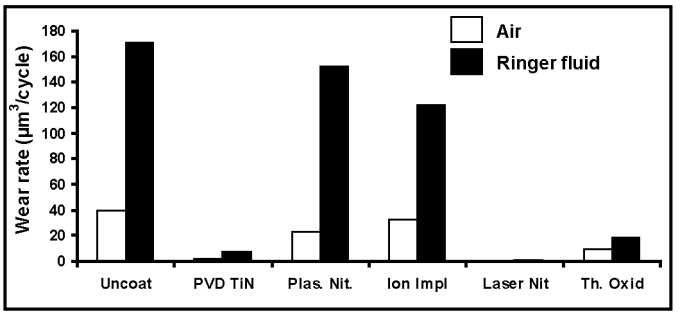

Figure 5.29. Wear rate comparison for fretting tests of all the surface modified alloys.

5.4.9. Comparison of Fretting Loops

Figure 5.30 shows fretting hysteresis loops generated for different coatings after 30,000 fretting cycles in air and ringer fluid for 1N normal load. The area of hysteresis loop generally describes about the frictional energy dissipated during process of fretting.

In general, larger area of the loop indicates more energy dissipation in the form of friction at the contact. In every case there is a difference between loops generated in air and ringer fluid. The loop pattern will be almost similar to a rectangle in the beginning. The changes in contour occurs only when the friction is altered by various parameters such as relative humidity in air, ringer fluid and debris formation.

Oxide debris plays a major role during the process. The contour of the hysteresis loop is almost unaltered in case of unmodified alloys and PVD TiN coated alloys in air and ringer fluid.

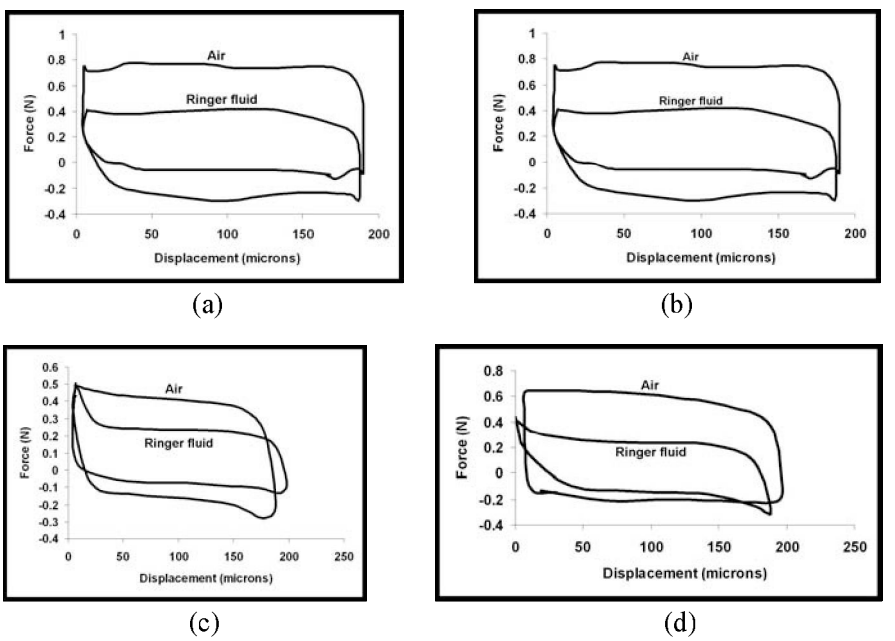

Figure 5.30. Continued on next page.

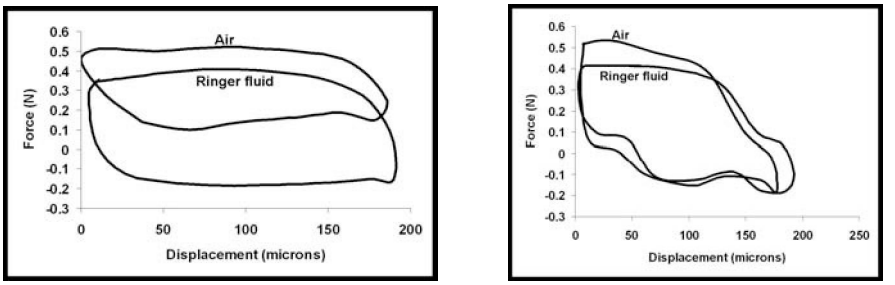

Figure 5.30. Force – displacement (F-D) loops after 30, 000 fretting cycles for 1N normal load in Air and Ringer fluid (a) Unmodified, (b) PVD TiN coated, (c) Plasma nitrided, (d) Nitrogen ion implanted, (e) Laser nitriding, (f) Thermal oxidation.

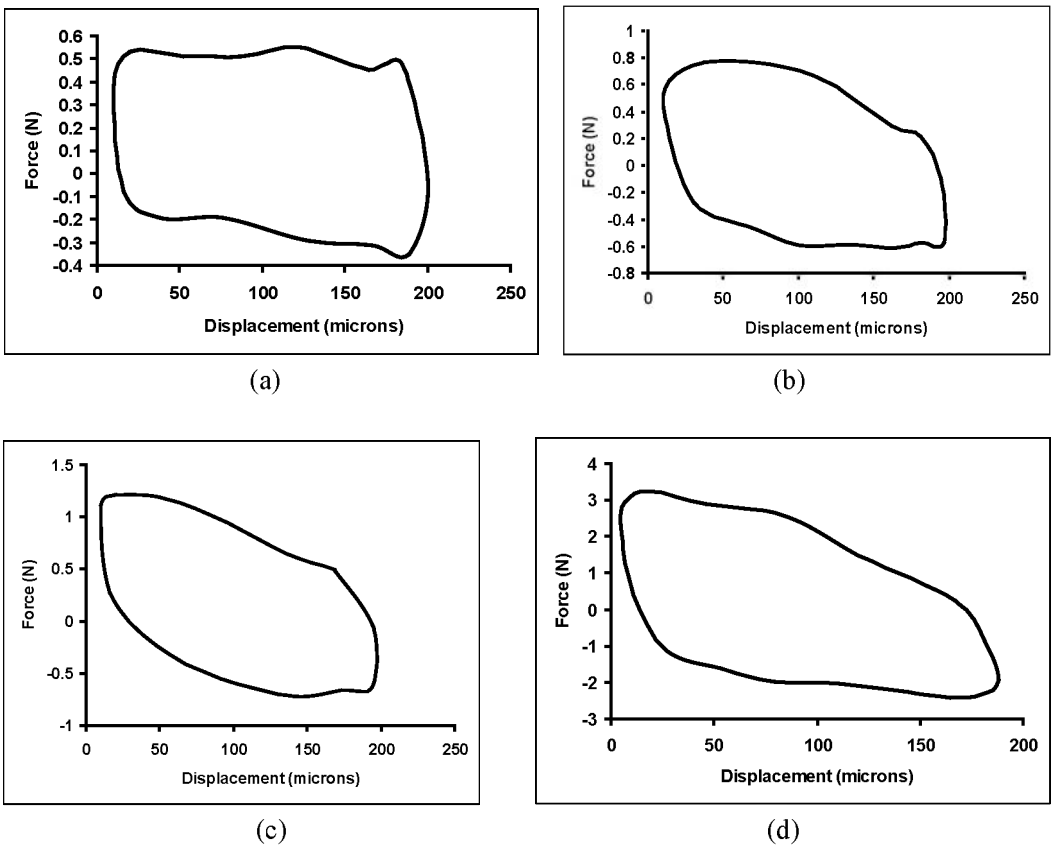

Figure 5.31. Force – displacement (F-D) loops for different normal loads with hardened steel ball on unmodified Ti-6Al-4V alloy. Normal Load: (a) 1N, (b) 5N, (c) 8N, (d) 25N

Figure 5.31 shows force – displacement (F-D) loops for fretting of unmodified Ti-6Al-4V and hardened steel ball configuration at different loads. We can observe that loop pattern changes with increasing normal load. It changes from rectangular shape at lower loads to oval shape at higher loads. This indicates the shift in the fretting regime, i.e. changing from gross slip to partial slip regime. The frictional energy dissipation reduces with the change in fretting

regime. At lower loads, surface asperities plays role in altering the friction. At higher loads, surface and subsurface plastic deformation dominates more than the asperities interactions. Usually friction coefficient reduces with increasing normal load due to plastic flow at the contact as seen from Fig 5.32.

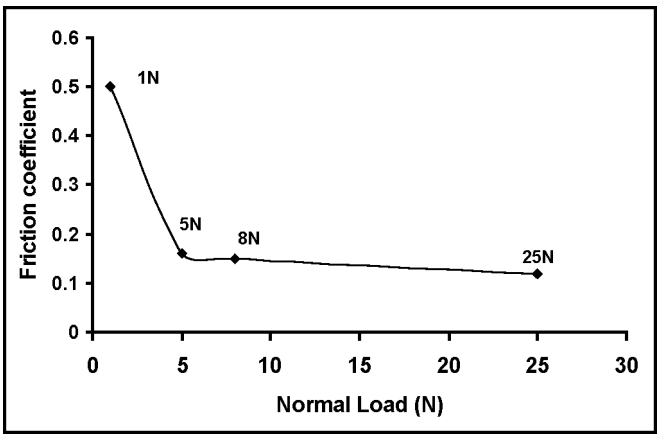

Figure 5.32. Friction coefficient for different normal loads.

5.5. Characterization of Fretting Fatigue Failures

This section describes the comparison of lives of modified specimens under fretting fatigue conditions along with variation in relative slip range between the pads and the specimens. This is followed by detailed analysis of surface damage during fretting fatigue. These results cannot be compared with the fretting wear since the counter body is different. The contact behavior very much depends upon the counter body and the medium around the contact. Fretting wear was conducted with alumina ball on all the surface modified samples. However, fretting fatigue tests are conducted with two similarly modified pairs. Therefore it cannot be correlated with the fretting wear results. In fretting wear tests, the hardness of alumina ball is relatively less compared to unmodified alloy. So the damage is substantially severe. Where as the hardness of PVD TiN film and TiN developed through laser nitriding is relatively higher.

5.5.1. S-N Curve

Figure 5.33 shows the S-N curve for fretting fatigue tests of all the surface modified alloys. It can be compared with the unmodified specimens and plain fatigue tests. The tests for all conditions were conducted until the ultimate failure of the specimen. A drastic reduction in lives of both surface modified and unmodified alloys has been observed compared to plain fatigue lives. The arrow indicates the specimens which did not fail after a million cycles. At 500 MPa cyclic stresses, the fretting fatigue life of unmodified specimen is just 3% of the plain fatigue life as shown in Fig 5.33. This highlights the conspicuous effects of fretting on the life of titanium alloys.

Plasma nitrided pairs have shown the best performance over all the coatings due to gradient modified layer which have high strain accommodation capacity during fretting induced surface and subsurface plastic deformation compared to other layers. For example, the fretting fatigue life of unmodified alloy pair is just 15 to 18% of the life of plasma nitrided pair at 500 MPa cyclic stresses. This shows the effect of modified layer on fretting fatigue strength. Although the final surface damage is similar to unmodified alloys, the layer is more effective during the initial period. PVD coatings failed earlier compared to plasma nitrided pairs possibly due to severe third body wear mode of contact interaction in the later stages of fretting. But life is improved compared to unmodified alloys. For example, the fretting fatigue life of unmodified alloy is 45 to 50% of the PVD TiN coated alloy at 500 MPa cyclic stresses. Whereas the life of PVD TiN coated couple is almost 50% of the plasma nitrided couple at 500 MPa cyclic stresses. The improvement is naturally much larger at lower stresses as seen from the S-N curve. Plain fatigue life of PVD TiN coated alloy crossed one million cycles without failure. It is due to the effect of hard layer on the surface preventing the formation of extrusions and intrusions which acts like micro notches for initiating fatigue cracks.

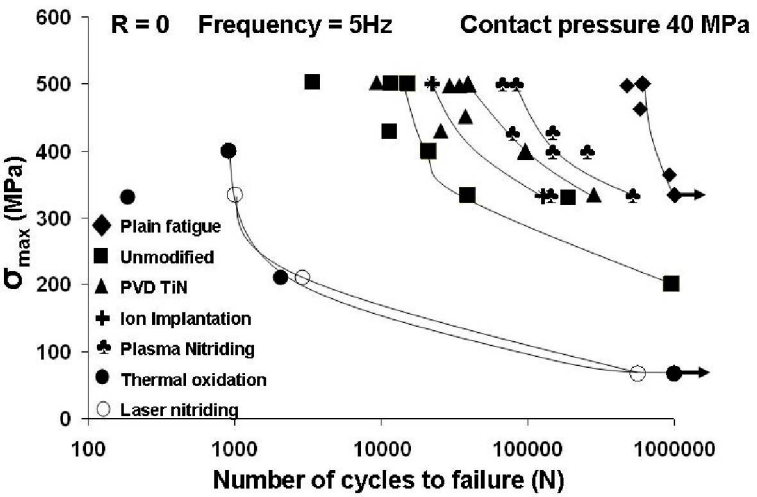

Figure 5.33. S-N curve for titanium alloys under different conditions.

Ion implantation showed slight improvement (20 to 25%) over the unmodified alloys at 500 MPa axial stresses and good improvement at lower axial stress. Due to complexity of the treatment and process constraints, only two specimens were tested with ion implantation. Laser nitriding and thermal oxidation has shown very poor performance. At higher nominal stress levels, they both experienced premature failure and at lower stress, they have shown infinite lives with intangible fretting at the contact. This is possibly from the effect of high case depth in case of laser nitrided samples and irregular surface profile for thermally oxidized specimens. When tensile load exceeds the yield limit of the modified case, the specimen fails earlier. In case of thermally oxidized pairs, the specimen failure is primarily due to irregular case development during the thermal processing as explained earlier. The region between unmodified and oxidized case acts like a potential failure site. This will be explained further during the analysis of the damage profiles for each of the above cases.

The main interest here is only to show the improvement of fretting fatigue lives due to surface modification on titanium alloys and not to identify or optimize any specific parameters. Average life of any specimens under fretting fatigue conditions can only be adjudged after testing many specimens in similar load conditions. Usually it is observed that there would be a lot of scatter in the lives of specimens under plain fatigue conditions itself due to inevitable differences in test specimens.

Recent trend is to obtain the Gaussian distribution of lives for a single cyclic load rather than plotting an S-N curve. Many specimens are tested for same load and a record on distribution of lives would give us an apparent idea of the fatigue life of the material of a particular geometry. In fretting fatigue experiments it is more difficult to get even a rough estimate of life at a particular load history due to more complexity in stresses involved at the contact area. Therefore there are no standards followed in fretting fatigue experiments as of today.

The tendency for crack initiation also depends upon the surface microstructural homogeneity or uniformity, which may vary for different specimens under test. The compacted debris in itself may influence the severity of fretting. Harder transformed products may be severely damaging whereas softer products may lubricate the surface and reduce friction.

Figure 5.34 shows the average roughness at the contact area before and after fretting fatigue test. The damage is severe for unmodified, PVD TiN, plasma nitrided and ion implanted alloys. It is to be expected because all these coatings have endured longer fretting fatigue cycles with gradual increment of damage. The roughness value also includes that of compacted rutile oxides within the damaged area, as it could not be removed. Laser nitrided and thermally oxidized pairs have not shown any marked changes due to premature failure of the samples as seen from the S-N plot.

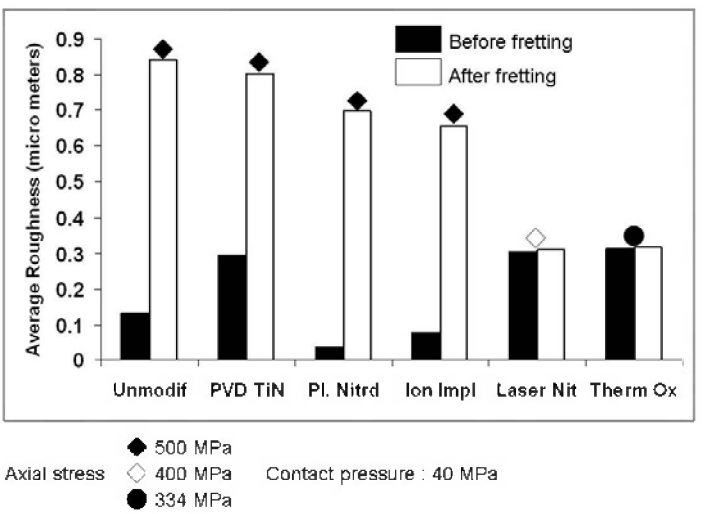

Figure 5.34. Comparison of roughness before and after fretting fatigue tests.

5.5.2. Slip Amplitude

Figures 5.35 (a) and (b) shows the variation in slip range with the applied static axial stress in air and Ringer fluid. It can be observed that slip increases with increase in maximum applied stress in air as well as ringer fluid. Slip experienced by contact pairs in ringer fluid is

slightly higher compared to air due lubricating effect. They appear almost equal at same applied stresses because the asperities interlocking during sliding is released by flow of ringer fluid. The effect of asperities is more observed in air than ringer fluid. Surface modified pairs have shown slightly higher slip compared to unmodified pairs in air as well as fluid. Even unmodified pairs have thin adherent oxide layer which will eventually break during cyclic fretting. When the friction between mating pairs is less, the relative sliding is higher and vice versa.

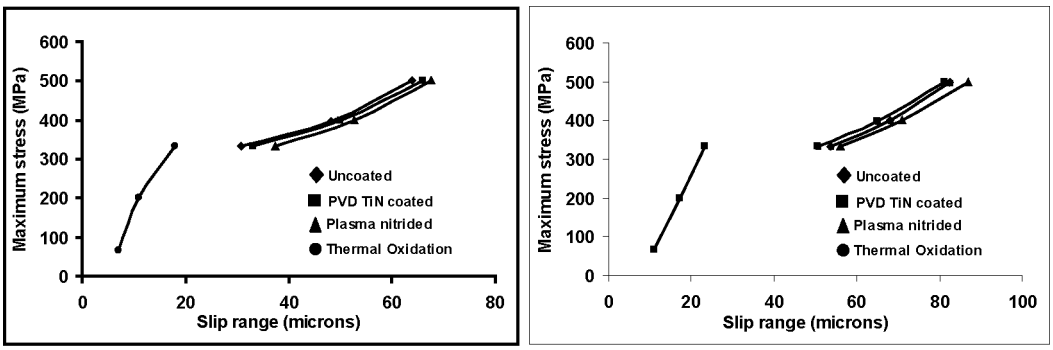

Figure 5.35. Variation in slip range with maximum stresses under static loading conditions in (a) Air, (b) Ringer fluid.

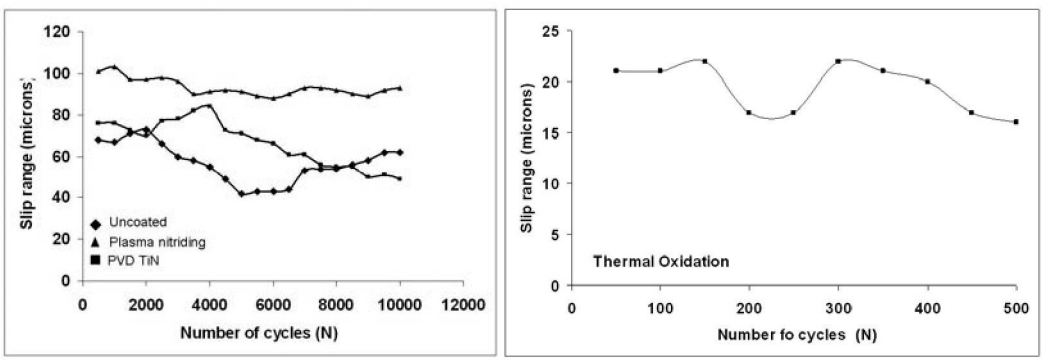

Figure 5.36. Slip range variation during the progression of fretting fatigue.

Figure 5.36 (a) and (b) shows variation in slip range with fretting cycles. The test is conducted only for 10,000 cycles. As shown in Fig 5.36a, larger variation is observed in case of unmodified and PVD TiN coated pairs. Where as the slip range variation is almost consistent with plasma nitrided pairs. Fretting of unmodified pairs shows high metallurgical compatibility as said earlier undergoing frequent adhesion or micro-welding of projected asperities. Adhesion and break away of asperities affects the slip regime during fretting fatigue as observed in the figures. In case of PVD TiN coated alloys, the process of adhesion is delayed for some period and the irregularities in slip amplitude are mainly due to particulate production and entrapment during the course of fretting. However, in both cases, higher slip amplitude indicates low friction between mating pairs and vice versa. The

variation in slip range of thermally oxidized alloy pair is shown in Fig 5.36b. The profile is similar to former case but with reduced slip range values.

5.5.3. Fretting Fatigue Surface Damage Characterization

In this section, the fretting fatigue damage features is explained for each individual case beginning with unmodified pairs. The damage features were almost similar at all the contact points except in some cases. The damage progression during fretting process is explained with friction coefficient curves. It is assumed that friction is also affected by pad geometry apart from fretting during the test. Bridge type pad configuration offers advantage of measuring friction but also has disadvantage of contact gapping normally difficult to observe during test. The friction curve in each case here is the average of two pads on either side of the specimen. Therefore two curves are observed in each case. Surface damage micrographs shown is for 500 MPa axial stresses in case of unmodified, plasma nitrided, PVD TiN coated and ion implanted specimens and 400 MPa and 334 MPa for laser nitrided and thermally oxidized pairs respectively. All other conditions remain same for all the cases. EDS analysis shows the chemical composition at the damage site.

5.5.3.1. Unmodified Alloys

Fretting fatigue surface damage of unmodified alloy at 500 MPa axial loads is as shown in Fig 5.37 (a and b). It is characterized by heavily worn out surface in the form of deep scratches, particle detachment, oxidation and transfer from counter surface. Fig 5.38 is an EDS of the scar showing Nb peak which indicates the transfer of particles from the opposing pad surface. Both the specimen-pad couple, being the same material, exhibit high metallurgical compatibility which is the primary reason for such an extreme form of damage. Higher compatibility induces localized adhesion and mutual dissolution of the contact materials during fretting process. Frequent stick-slip at contact also produces squeaking sound which was intermittently witnessed during the test. The laminates and fine particles with high surface area are more prone to chemical reactions with tissues and protein which may induce allergic response. Fig 5.39 shows the roughness profile of the damaged area indicating extreme unevenness of the surface (R_a = 0.84 µm compared to R_a = 0.11 µm for as polished surface).

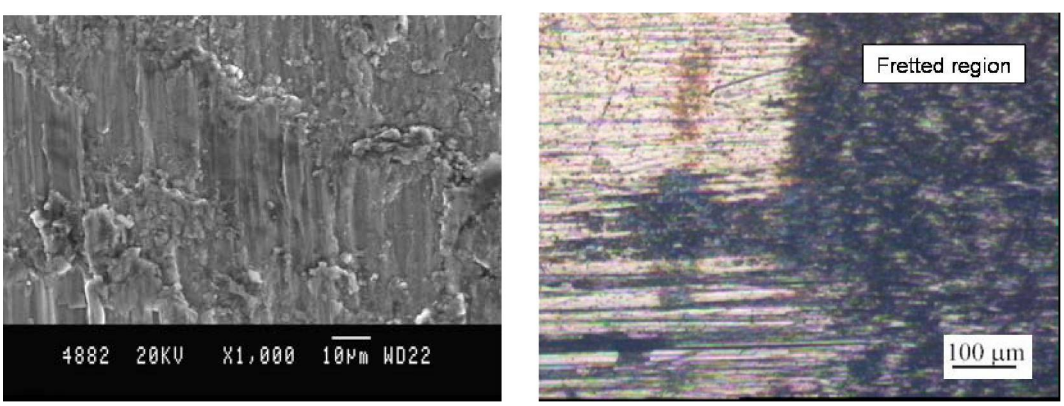

(a) (b)

Figure 5.37. (a) SEM micrograph (b) Optical micrograph of fretting scar of unmodified alloys.

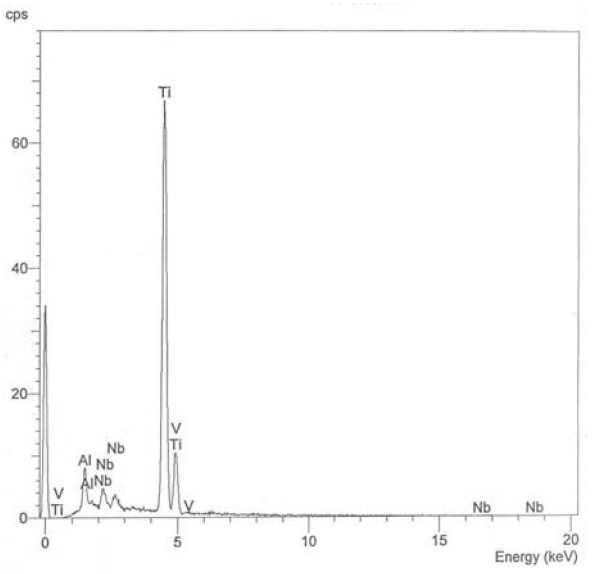

Figure 5.38. EDS of fretting scar of unmodified Ti-6Al-4V.

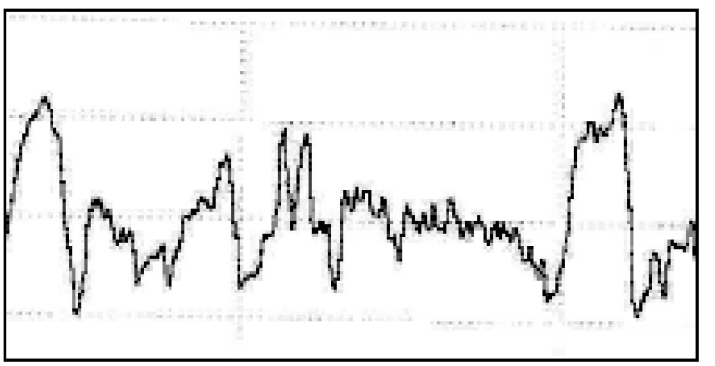

Figure 5.39. Roughness profile of the damaged site of unmodified Ti-6Al-4V.

Fig 5.40 (a) and (b) shows the friction curves for the fretting fatigue tests of unmodified alloys at 500 MPa axial load. It is interesting to note that both the pairs of pads have experienced similar variation of friction during fretting. At higher axial load, this may be possible due to higher sliding amplitude when local surface inhomogenities are overruled. As said earlier, frequent localized-welding and rupture of junctions occurs during fretting of bare surface. When slip amplitude increases with increasing axial load, the rupture of localized welded junctions takes place more rapidly. Friction coefficient for 500 MPa varies from 0.3 to 0.6 and reaches 0.8 just before ultimate failure. It is also observed to steadily glide down after initial few cycles. This can be attributed to the combined lubricating effect of biofluid and oxide bed. The steady formation and ejection of oxides at the contact also minimizes the resistance to sliding motion. The degree of damage gradually compounds from frequent ejection of oxides with the flow of fluid and formation of fresh oxides from exposure of fresh surface. The saline fluid also mixes with the oxides which get compacted within surface cracks causing further dissolution of material at the crack tip. Higher friction values before

ultimate failure indicates severity of damage. As seen earlier from the roughness profile, the pads would plough into the surface resulting in deep scratches and immediate crack initiation and propagation to failure within few cycles.

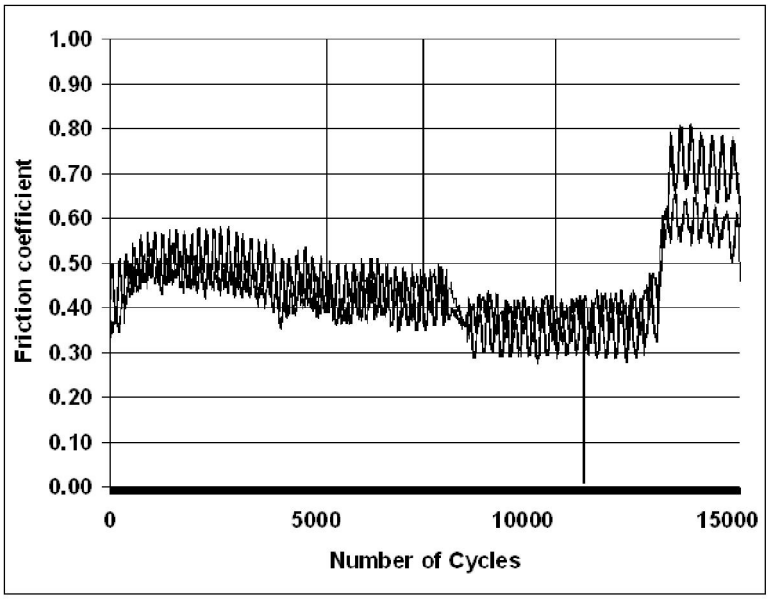

Figure 5.40. Friction coefficient curves of unmodified alloy pairs for cyclic stresses of 500 Mpa.

5.5.3.2. PVD TiN Coating

For all the PVD TiN coated alloys, fretting cracks was observed to nucleate along the contact edge as well as within the contact region. Friction is minimized with TiN coatings due to its excellent tribological properties compared to unmodified alloys. But it could not withstand the fretting process for a long time when compared to unmodified alloys as observed in Fig 5.41(a). The lives of unmodified specimens were almost 45 to 50% of the PVD TiN coated samples. The film ruptured at the later stages of fretting resulting in gradually detachment of hard TiN layers. The ultimate rupture is preceded by the formation of network of cracks within the contact. Even the cracked layers can protect the surface for certain period of time until they are fragmented further. Some of the laminates are found deeply embedded within the underlying substrate material. Fretting motion under contact pressure has disintegrated the coated layer from the substrate and buried them deeper. The adhesion strength of the film depends upon the prior cleaning of the substrate and the purity of the film. Fig 5.41(b) shows the fractured cross sectional features of PVD TiN coated alloy. Fractured surface layer is not distinctly visible although some features of brittle rupture can be observed at the edge.

In these experiments, TiN layer is coated on both the specimen and pads. Since the hardness is the same, reasonable wear rate can be expected during gross sliding. It is also observed that some of the ejected TiN laminates had fretting marks on their surface. Surface projections initially rub against each other and ultimately rupture leaving these marks on the delaminated particulates. Uneven surface are sometimes beneficial in fretting application

because the surface depressions can provide sink for the debris particulates preventing harmful effects.

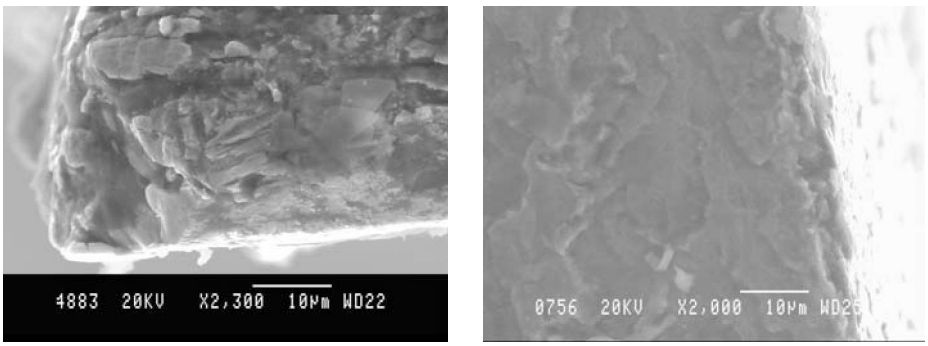

(a) (b)

Figure 5.41. (a) Edge of contact failure area of PVD TiN coated alloy, (b) Cross section of fractured specimen.

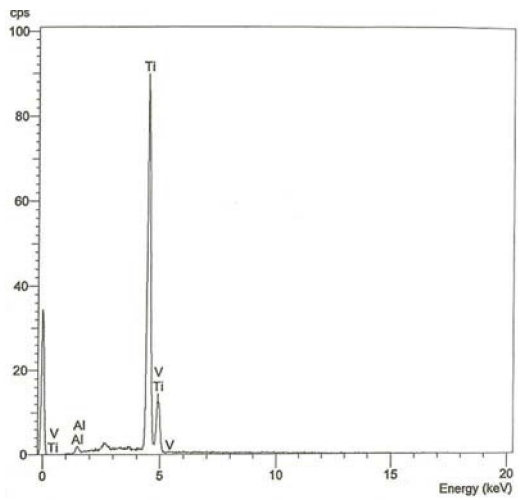

Figure 5.42. EDS of the damaged site of PVD TiN coated alloy indicating Al and V exposed from the substrate.

Fig 5.42 shows EDS of ruptured area indicating Al and V peak from the exposed substrate. As mentioned earlier, these elements (even 10 ppb) are known to cause toxic effect and it is therefore important to maintain the continuity of the film for long term application of prosthetic devices. Delaminated TiN particles acted as potential abrasives for further damage on both the surfaces. Their sizes vary from less than a micron to more than 10 microns. Larger particles with sharp edges can be more harmful as they could easily plow into the surface during fretting. The stiffness of the film usually increases with increase in its thickness due to good packing and almost reaches theoretical density at higher thickness (Takahito Ohmura et al., 2003). When the flexibility is lost, it is easier to break the film by deflection or fretting. Some sort of surface preparation before coating may also help in altering the film properties because the substrate also plays a role in altering the nature of the

film growth. The purity of the film also helps in retaining the continuity during sliding motion. Post coating heat treatment may help us to recover from some of these defects (Wen-Jun Chou et al., 2003).

Fig 5.43 shows a crack on the TiN layer of a specimen perpendicular to the loading axis. Many such cracks are sometimes observed on the surface of the TiN layer especially adjacent to the contact edge. When the load crosses the elastic limit of TiN, such cracks appears distinctly all on surface because the layer cannot accommodate higher levels of surface strains like substrates due to high hardness (~40 GPa) and stiffness (~332 GPa).

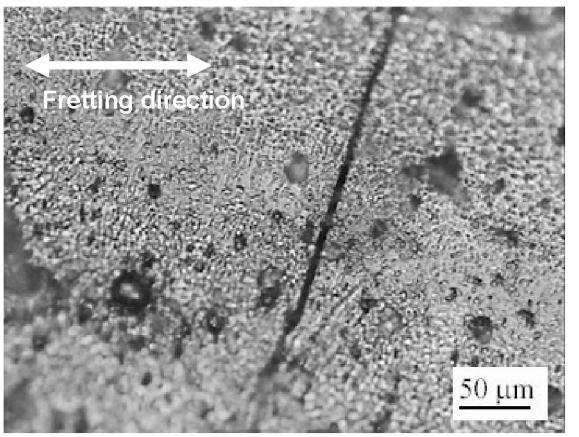

Figure 5.43. Cracks on the surface of PVD TiN coated fatigue specimen.

The substrate hardness is 4.2 GPa and stiffness is 104 GPa. Deformation is in plastic mode for substrate and elastic mode for the TiN layer. The axial load level was within the yield stress for the substrate but beyond the yield strength for the TiN layer. Therefore the TiN layer fails before the specimen. Fig 5.44 shows oxidation within one of the localized damage site. The weaker site on the film will expose the underlying substrate for oxidation when it ruptures.

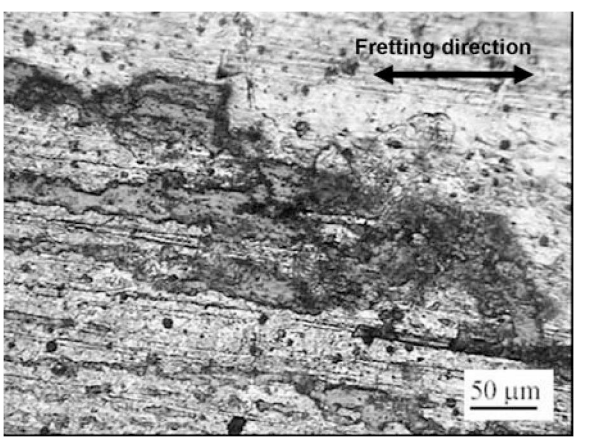

Figure 5.44. Oxide within one of the localized damage site of fretting fatigue damaged specimen.

Fig 5.45(a) shows the friction curve for PVD TiN coated pair for 500 MPa axial loads. Friction coefficient varies from 0.1 to 0.35 throughout the test. Fretting process on TiN layer differ compared to unmodified alloy. So it is observed that friction is maintained within the limits till complete failure.

It is more unsteady compared to fretting of unmodified alloys as evident from the zigzag nature of the curve. Initial increase in friction is due to interaction of roughness peaks and later it goes down due to rupture of these projections. These ruptured particles forms initial debris bed within the contact and cause further release of particles from third body wear mode of contact interaction. After 20,000 cycles it is seen that there is a sudden increase in friction which can be attributed to delamination process and formation of oxide later reduces friction by fluid interaction and ejection of particles.

The formation of oxide always causes gradual or immediate slump in the friction due to smoother accommodation of tangential motion. Finer particles may or may not loose its effect from the compaction within the oxide debris. However it is not always applicable at all points of contact because each point experiences difference in contact behavior. These curves are the average values of two contact pads sliding on either side of the specimen.

Fig 5.45(b) shows the friction curve for 5000 cycles at reduced contact pressure of 20 MPa. The unsteadiness of the curve is still present, but within 0.1. This test was done just to show the effect of contact pressure on friction. Reducing the contact pressure reduces friction significantly. The variation is still present due to interaction of asperities. The reduced normal pressures would allow more gradual wear of the surface. The contact point showed some sort of flat shining area indicating the initial gross sliding regime of fretting contact.

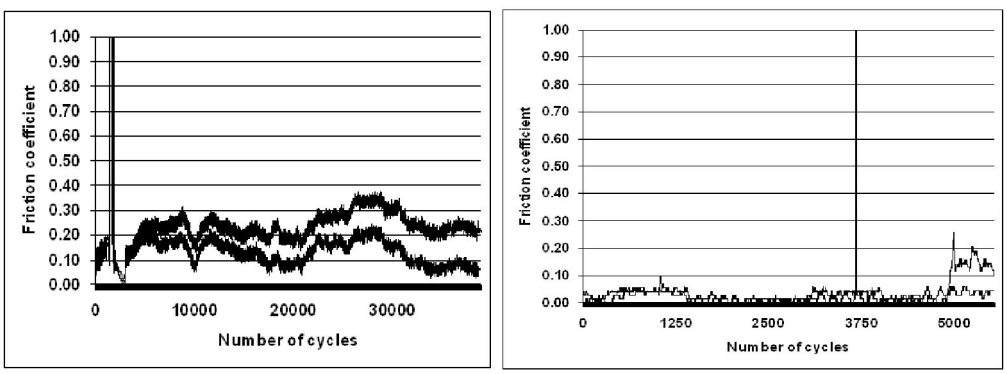

(a) (b)

Figure 5.45. Friction curves for contact pressures of (a) 40 MPa, (b) 20 MPa.

5.5.3.3. Plasma Nitriding

Fig 5.46(a) shows fretting damage site of plasma nitrided specimen. The lives of unmodified specimens were less than 18% compared to plasma nitrided specimens under fretting fatigue conditions. It is observed that the surface is not uniformly covered with oxides which mean that proper contact may not always occur between the mating components during fretting. Nitrided layer being stronger than unmodified alloys does not allow early damage and oxidation. This delayed phenomenon is responsible for longer life of the coated components. The transformation of alloy to oxides can only happen while the debris

particulate dwells within the contact undergoing attrition from the rubbing materials which later gets compacted within the damage location. Both the pads and the specimen almost suffer the same form of damage. Fig 5.46(b) shows another contact area with three body wear phenomena. The surface has been plowed by the release of few hard particles from either of the mating surface. The particle is released from combined influence of tangential force and normal pressure initiating cracks within the composite modified layer. The three different phases present in the layer are TiN, Ti_2N and matrix.

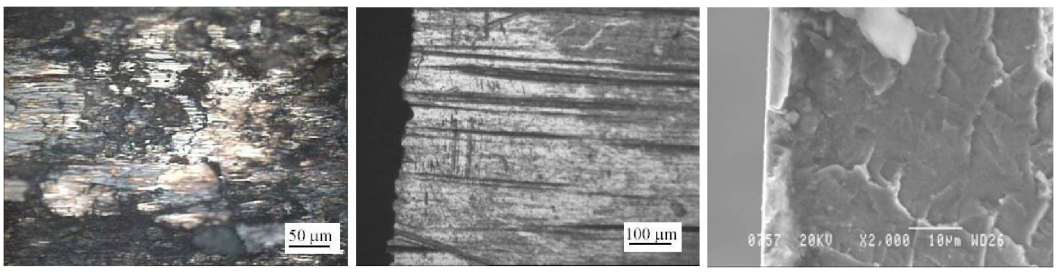

(a) (b) (c)

Figure 5.46. (a) Oxidative fretting damage, (b) Three body wear during fretting by release of particulate from the mating contacts, (c) Fractography of plasma nitrided Ti-6Al-4V at 500 MPa.

It would mostly initiate at the junction of the same phase or different phases which normally have different mechanical properties. All of them have variations in strength and hardness level. The failure was along the edge of contact and increase in pad constraint due to presence of released particle may be responsible for the failure. The surface is still softer compared to PVD TiN layer (Nano indentation results) and hence could accommodate higher strains compared to the former case. The gradient layer can offer higher resistance to final failure than surface coatings with abrupt change of properties along the interface. Oxidation was also observed at some contact points.

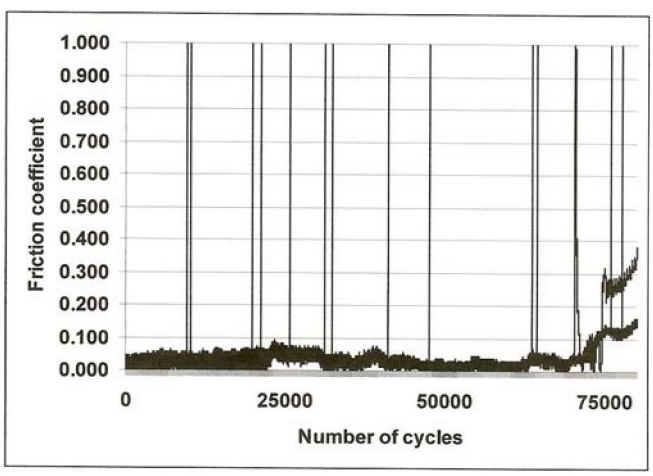

Figure 5.47. Friction curves for plasma nitrided samples.

Fig 5.46(c) shows the cross section of the fractured specimen. The ruptured gradient layer is also visible in the micrograph. Sharp interface cannot be expected due to the nature of the process which involves diffusion of nitrogen within the surface. Faceted feature in the interior of the specimen indicates the plane strain propagation of crack till the ultimate fracture of the specimen. Beach marks and fatigue striations were not observed. Plain fatigue loading will normally initiate subsurface cracks. Fretting induces surface defects deliberately from the surface. Fig 5.47 shows the friction coefficient curve for axial load of 500 MPa. It can be seen that friction coefficient is well within 0.1 throughout the test except at the time of failure.

High friction at the end can be attributed to third body interaction within the contact which may have come into effect after 60,000 cycles with ejection of coarse particles. The failure, as explained earlier, is due to inability of the coating to accommodate the surface strains effecting from increased constraint of pads due to release of nitride particle. The contact area being smoother must normally produce high friction. But the high hardness and chemical inertness combined with lubrication offered by the ringer fluid has reduced adhesion and friction to a low level which is very favorable for implants in minimizing fretting debris generation and surface damage.

5.5.3.4. Ion Implantation

Fig 5.48(a) shows the fretting damage area of ion implanted Ti-6Al-4V at 500 MPa axial stresses. The mode of damage is almost similar to unmodified specimens with lumps of oxides. Thinner implanted layer has worn off within few cycles exposing the bare surface for deeper damage. In this case, we may infer that the dose of 2 X 10^{16} ions/cm^2 can only offer little improvement in fretting fatigue strength. In general, higher dose of implantation produces higher resistance to wear damage from the formation of nitride precipitates. The beam line mode of ion implantation has specific disadvantage of its inability to modify complex geometries and hence it is time consuming and costly.

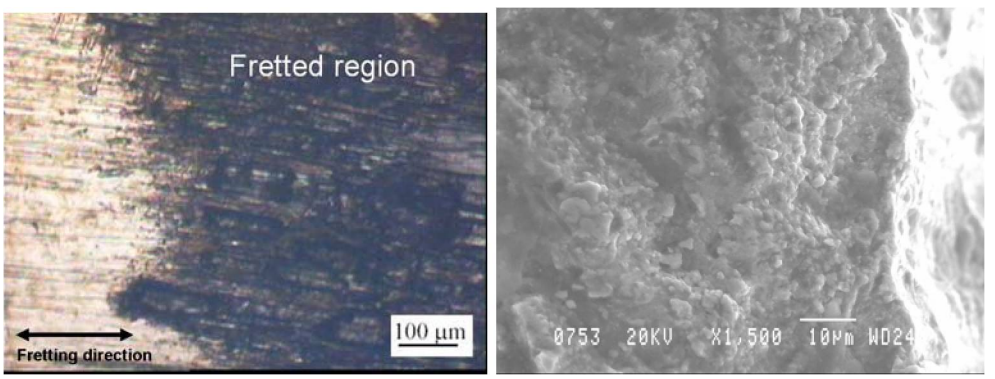

(a) (b)

Figure 5.48. (a) Fretting fatigue damage (b) Fractography of ion implanted Ti-6Al-4V at 500 Mpa.

Fig 5.48(b) shows the cross section of the fractured specimen indicating no sign of surface layer. At the edge it is seen that crack has taken an inclined path in the beginning and later aligned perpendicular to the stress axis which is indicative of typical feature of fretting fatigue crack propagation as mentioned earlier. The modified layer being very thin has not

shown any sign of brittle feature at the surface. Internal surface shows some kind of any oxidized debris formed during gradual crack propagation.

Fig 5.49 shows the friction coefficient curves for fretting fatigue of ion implanted Ti-6Al-4V alloy. Two curves indicate the average friction of the two pairs of pads on either sides of the specimen. It is observed that friction is high during the intermediate period which may be attributed to the contact of bare surfaces. The protection of ion implanted layer may have been before this period when the friction is low. Unlike the friction curve of unmodified specimens which has shown sudden increment to a high value just after few cycles, the ion implanted layer has protected the material to some extent. Ion implanted layer is very thin and easily wears off within few cycles and the exposed bare surface comes in contact affecting the friction in that region. It is almost similar to unmodified alloys where the friction increases to 0.6 and gradually drops to 0.3. Second pad has maintained the same increase and decrease of friction, but within the lower regime of 0.3. The critical damage may have occurred during the intermediate period when the friction is high. The effect of biofluid and oxide bed is also considered in reducing friction similar to fretting of unmodified alloy.

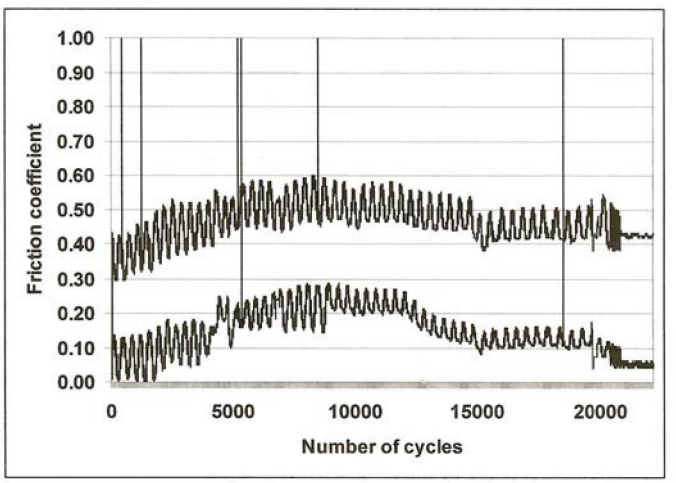

Figure 5.49. Friction curve of Ion Implanted Ti-6Al-4V.

5.5.3.5. Laser Nitriding

Figure 5.50(a) shows fretting fatigue failure edge of laser nitrided Ti-6Al-4V specimen. Cracks have developed perpendicular to the loading axis at the fretting edge. Many such cracks were observed through out the specimen length. The gage thickness of the fatigue specimen is 5 mm and the weld deposit along with HAZ occupies about 1 mm on both the sides. 2 mm out of 5mm thickness constituted hard and brittle phase (TiN dendrites). The axial load applied must have crossed the yield strength of the melt-HAZ composite which will not allow any plastic flow of material.

Fig 5.50(b) shows cross section of the nitrided portion of the failed sample with the faceted features indicating brittle mode of fracture with no gross plastic deformation.

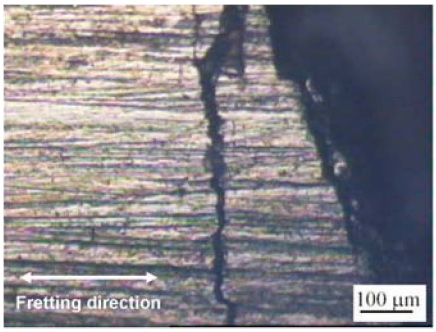

(a)

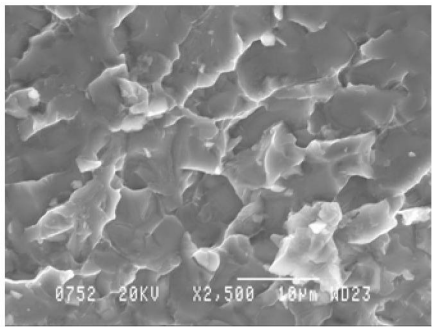

(b)

Figure 5.50. (a) Fretting fatigue failure edge (b) Fractography of laser nitrided Ti-6Al-4V specimen at 334 MPa.

Figure 5.51 shows networks of cracks on the nitrided region of the grip portion of the specimen developed during fretting fatigue. They are almost perpendicular to the loading direction (shown with arrow). It is clearly due to inability of the nitrided portion to accommodate the axial strain during cyclic loading. The same cracks are not observed in the substrate portion above the nitrided region of the specimen because of higher ductility and strain tolerating capacity of the material. The process of laser nitriding requires much improvement before it can be adopted for surface engineering of bioimplants. It may be difficult to obtain efficient nitriding if the melted zone is thin because it has a larger volume of unmelted substrate below the surface for quicker removal of heat. In such cases, thicker nitride case is unavoidable and the results in tensile loading will be the way as shown here.

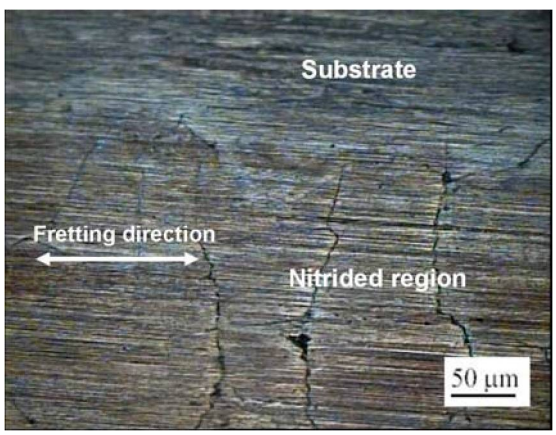

Figure 5.51. Crack networks on the specimen grip portion developed perpendicular to the loading axis (arrow indicates the direction of loading).

Fig 5.52 shows the friction curve for fretting fatigue of laser nitrided titanium alloys. The friction coefficient nearly touches 0.1 and shows a little increment before final fracture. Hard surface asperities have a role to play in inducing friction by interlocking. The case is very hard and chemically inert by nature. It is shown to have low resistance to sliding motion.

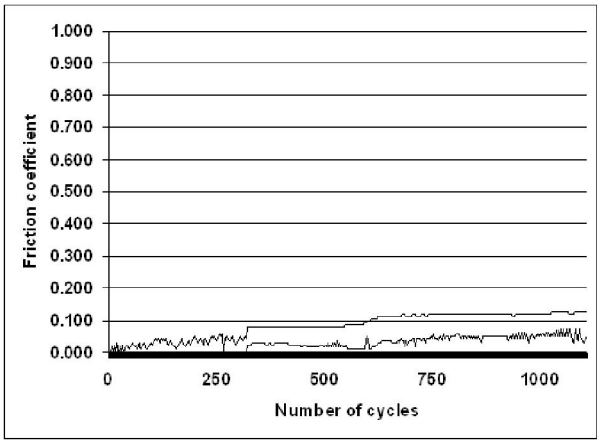

Figure 5.52. Friction curve for fretting fatigue of laser nitrided Ti-6Al-4V alloy.

5.5.3.6. Thermal Oxidation

Fig 5.53(a) shows the fretting fatigue failure edge of the fatigue specimen indicating the brittle failure of the oxidized specimen. Some part of the case has chipped off during fretting oscillation as seen in Fig 5.53(a). As seen from the cross section of the oxidized specimen earlier, the growth of oxide layer is very uneven during the process of thermal oxidation and hence it was difficult to remove the black oxide layer completely. An attempt to remove the layer completely would also damage the case beneath the layer exposing the underlying substrate. Discontinuous film may not be acceptable for load bearing implant applications. The failure must have initiated along such discontinuities. Black oxides were not observed in the failed specimens along any of the contact points. Fig 5.53(b) shows the cross section of the fractured oxidized surface. It is similar to laser nitrided surface which shows faceted features indicative of brittle failure.

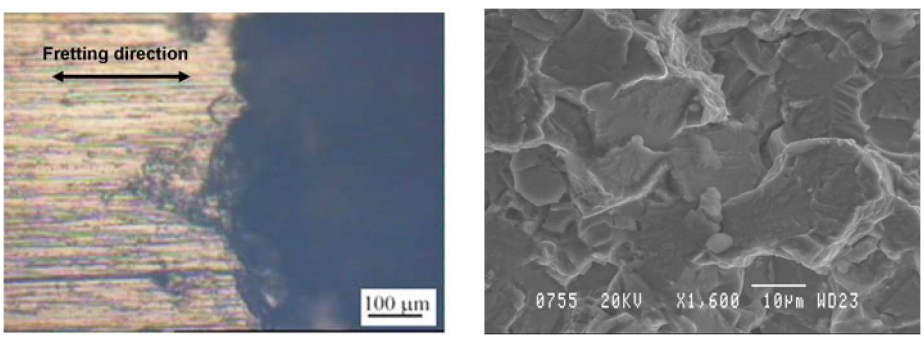

(a) (b)

Figure 5.53. (a) Fretting fatigue failure edge (b) Fractography of thermally oxidized Ti-6Al-4V specimen at 400 MPa.

Fig. 5.54 shows the friction curve for fretting fatigue of thermally oxidized titanium alloy pairs. The specimen fractured in very short time, but the friction experienced by the surface is very low. The value is well below 0.03. No other coatings discussed earlier have experienced

such low friction between the contact pairs. Therefore the failure is mainly due to irregular (wavy) modified case. Since it is difficult to obtain uniform case depth, thicker case was selected, but the purpose is not served due to weakness of the case itself. The specimens cannot be prepared properly without damaging the case as discussed in fretting wear experiments. The process should be carefully controlled to obtain uniform case. Controlled atmospheres can help achieve better uniformity in the case.

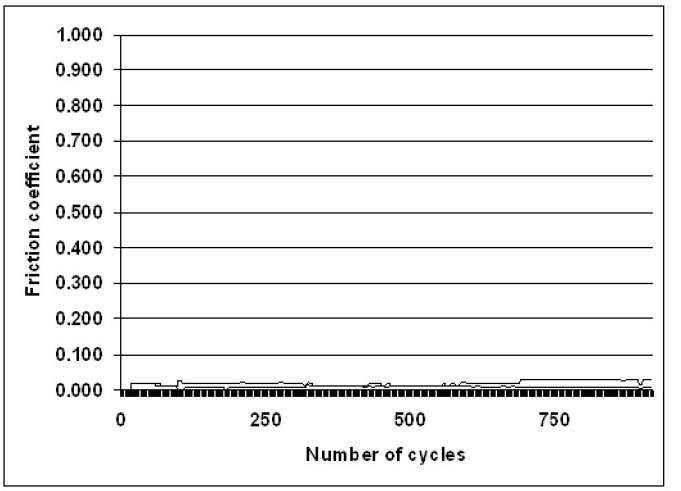

Figure 5.54. Friction curve of thermally oxidized Ti-6AL-4V alloy.

5.6. Some Important Features of Fretting Fatigue Failures

In this section, general features of fretting fatigue failures are explained with some analysis on crack propagation mode during fretting fatigue, the importance of contact configuration following a general model on crack nucleation in unmodified and surface modified pairs.

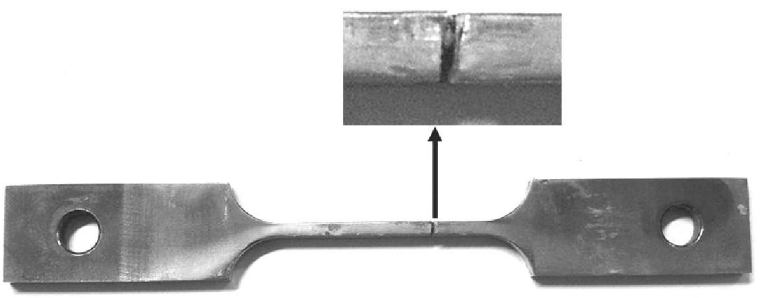

Figure 5.55. Fractured site of a fretting fatigue test specimen.

Fig 5.55 shows the fretting fatigue failure site of a sample. It clearly indicates the fact that fretting failures are always expected at the pad – specimen contact region due to higher stress concentration effecting from severe frictional damage due to fretting oscillation under contact

pressure. The sliding motion has also produced visible tracks on the surface as observed in Fig 5.55 indicated by an arrow. The damage slowly compounds with time and nucleates numerous cracks of varied sizes within the contact area as shown in Fig 5.56. From there on, the axial load takes charge for the critical crack to propagate to final fracture.

The crack usually initiates along the edge of contact (EOC) or in between the stick-slip boundary.

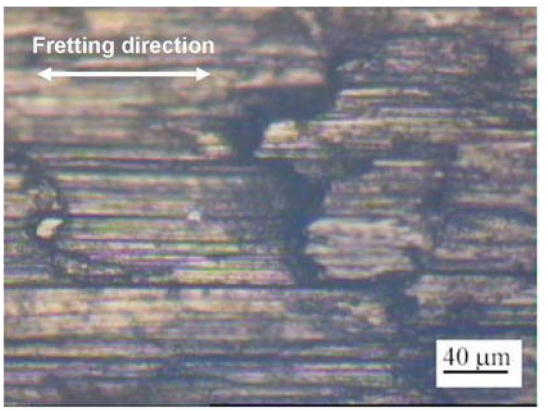

Figure 5.56. Cracks within the fretted region.

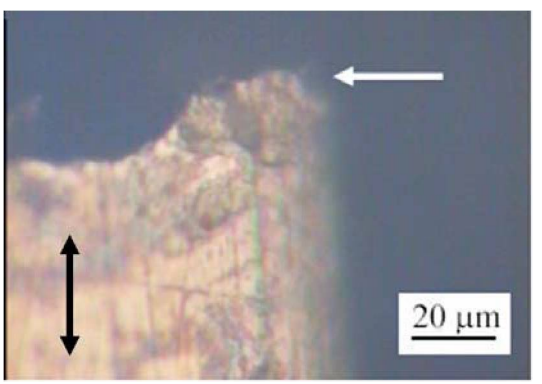

Figure 5.57. Cracks inclined to tensile axis after initiation during fretting fatigue.

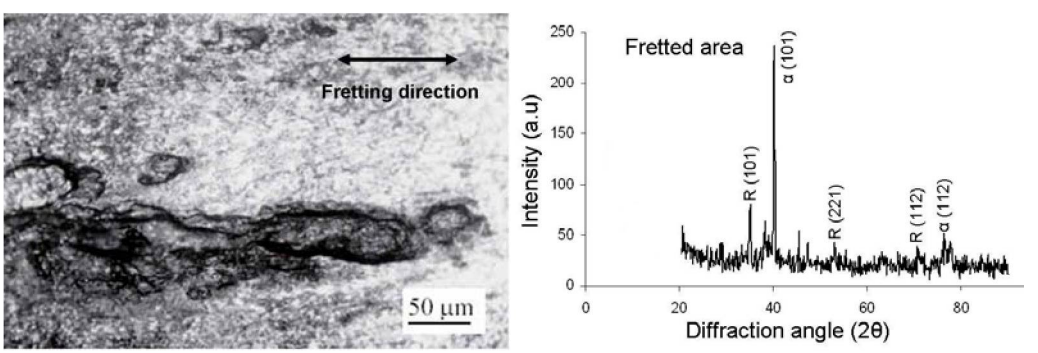

(a) (b)

Figure 5.58. (a) Rutile splotch at the fretted area (500X), (b) XRD of the fretted area.

The cracks will initially propagate inclined to the axial load and later detours perpendicular to the load axis when the effect of tangential force diminish below the surface as seen in Fig 5.57. It is explained that the crack will generally propagate along some weak planes almost 45 degrees to the load axis. This is generally considered due to effect of tangential force on the surface. Some of these primary cracks are also responsible for releasing debris particles which will oxidize during later part of cycle or gets compacted within the oxide bed already present. The microscopic examination of the damage site in fretting fatigue tests often reveals what is called tribologically transformed structures (TTS) (Sauger et. al., 2000), as shown in Fig 5.58(a). The black splotch of rutile (TiO_2) has formed during fretting fatigue test without biofluid as confirmed from the XRD analysis in Fig 5.58(b). It may not form to this extent due to limited availability of oxygen within the body. But the physiological or biological fluid surrounding the contact area may influence different tribo-chemical reactions. It is confirmed that the temperature at the contact area often reaches very high level to cause transformation of structures in contact materials (Antoniou and Radtke, 1997). Rutile formation is often experienced during oxidation tests of titanium alloys. Therefore it can be inferred that the contact area has experienced high temperature during sliding motion.

The tissues may not be able to tolerate the chemical effect of rutile and the damage caused may also introduce favorable sites for stress concentration and early crack initiation and propagation due to fatigue loads in hip joints. The fretting oscillation also depends upon the design of the prostheses or implants. Under severe load excursions, as in the case of climbing staircase etc., it may experience severe deflection in case of hip joints and fretting action is inevitable.

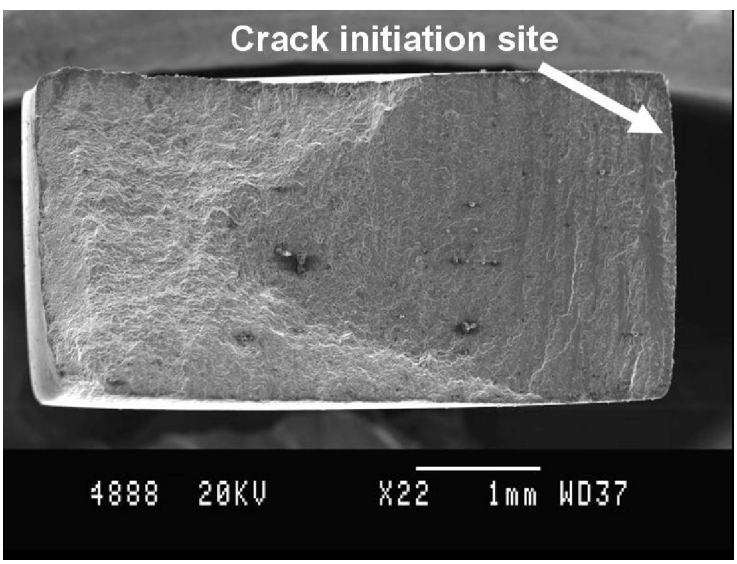

Figure 5.59. Cross section of fractured fretting fatigue test specimen.

The cross section of the fractured specimen is also shown in Fig 5.59. The crack has been initiated from the right side of the specimen cross section as shown in figure and gradually propagated inward (towards left of the specimen). Closer observation in SEM did not reveal any striation marks that are often the notable feature of the fractured cross sectional surfaces

of fatigue samples. Some literatures reports striation marks in case studies of failed implants (Teoh, 2000). The flat area in Fig 5.61 indicates that fatigue crack has propagated in a plain strain condition with repeated pounding of the surface against each other.

When the cross section was no longer able to bear the load, the specimen separated in a ductile manner as observed in left region of the specimen. Closer examination in left area revealed dimpled surface with a network of teared ligaments which is a typical feature of a quasi-cleavage mode of fracture. Higher axial load increase the area with quasi-cleavage features and lower axial load increases the plain strain area. The growth of fatigue crack is slower when the axial load is reduced. EDS analysis in this area also shows sodium and chlorine peak, possibly entered from the saline fluid used in these tests. Corrosive conditions are often aggravated from oxygen depletion and chlorine ion concentration around the damage area.

5.7. Fretting Fatigue Process

This description is a general analysis of mechanism of fretting fatigue damage based on the results obtained from the above tests. When two surface of the solid are bought together as shown in Fig 5.60, the real contact is actually at the projected asperities of both the surface which is only few percent of the actual area of the surface. The actual area is determined by a range of material properties such as compressive yield strength and surface characteristics such as roughness and surface films. The real contact would tend to increase with the sliding motion under the combined action of normal and tangential forces that acts on the surface. During sliding of the bare surface, the junction would microweld to form what is called super junctions. Sliding of chemically inert surface would produce a different effect. High friction is produced during formation of super junctions and breakaway of junction would release the surface and produces surface damages and debris particles. With the growth in junctions, the shear force required to cause sliding will increase with each cycle.

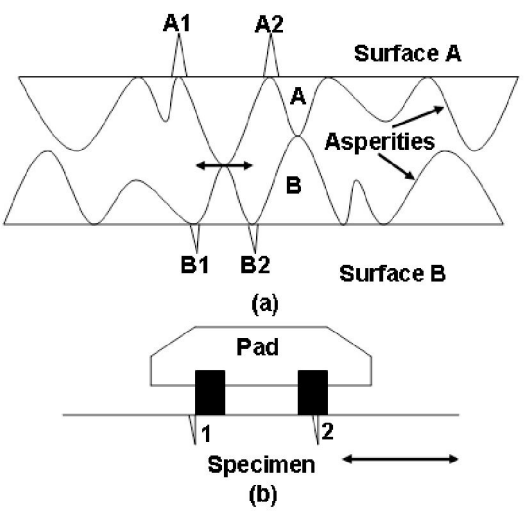

Figure 5.60. Crack nucleation model in fretting fatigue test.

In Fig 5.60(a), when surface A comes in contact with surface B, it may cause shear force to act within the asperities (A or B) and subsequent transfer of ejected particles or cracks may begin develop and grow at points A1 and A2 or B1 or B2 or a combination of both. The crack may increase in length due to action of friction and tensile forces and propagate to failure. Due to large number of such asperities, number of cracks would nucleate at the fretted area and finally link up to a critical crack. The contact of biofluid within the cracks may tend to dissolve fresh, uncontaminated and active surface atoms to form chlorides or some other complex compounds. Corrosion products also tend to affect the stress concentration within the cracks.

Corrosive attack without stress often forms pits on the alloy surface. These pits acts as notches and reduce the general fatigue strength. The effect of fretting is much more deleterious because it aids corrosion more easily by repeated exposure of fresh surface by deformation and delamination.

The propagation of crack is modified due to presence of transformation products. Oxide induced crack closures is the possible mechanism for reducing the effective stress concentration at the crack tip. So the removal of oxides from the fretted area may reveal such cracks. In Fig 5.60(b), crack 1 tends to behave differently from crack 2 because surface frictional forces tend to open type 1 crack. Type 1 is more deleterious than 2 because crack closure mechanism may become active within type 2 cracks to reduce the effective stress concentration. Crack extension become more prominent in type 1.

Fretting fatigue damage sequence of surface modified alloys can be apparently explained as shown in Fig 5.61. Initial sliding motion between hard and chemically inert surfaces will naturally produce low friction if the roughness level is within certain limits. Uneven surface profile will produce high initial tangential force due to interaction from surface asperities until they fracture when the force crosses elastic limit. Then the sliding motion steadily produces wear particles which get crammed within the contact and increases damage severity as shown in Fig 5.61(b). The wear particles along the trailing edge of the pads are ejected out of the contact, but the middle ones are entrapped within the region and further dig into the surface because of high contact pressure. Then the contact pressure may slightly reduce, but the fretting motion has already initiated the crack. Contact experience frequent shift in the fretting regime (gross slip, partial slip and stick) by oxidation and corrosion reaction as shown in Fig 5.61(c).

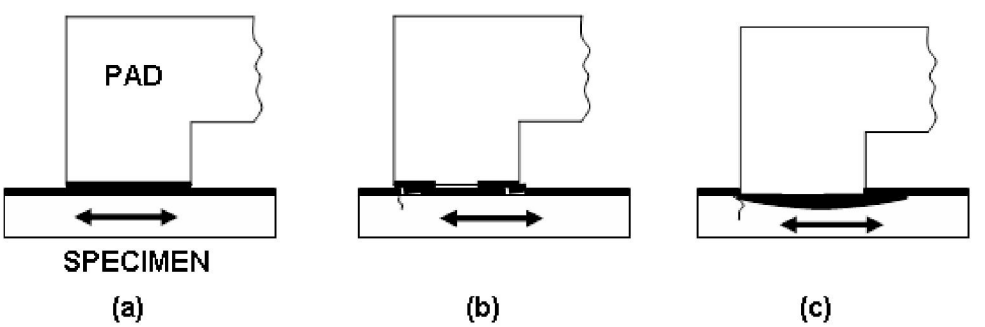

Figure 5.61. Fretting fatigue damage mechanism sequence for surface modified alloys.

The delaminated particles are found squashed within the compacted oxide. Within the body environment, there may be a different tribochemical reaction at the contact leading to formation of different kind of products. In case of unmodified alloys, the initiation of crack usually begins along one of the weak slip planes inclined to the load axis. But for surface modified alloys, it depends upon the physical nature and properties of the layer. Hard ceramic layers do not generally undergo any gross deformations like metallic systems. So when the tangential force crosses the elastic limit of the layer, they tend to rupture. The crack is usually initiated at the edge of contact because of the constraint offered by the pad at that boundary. Variation in contact pressure due to formation of debris could be one of the reason for pads to offer increasing constrain leading to brittle rupture.

Surface modified layers normally offer better resistance to than surface coatings due to absence of interface delamination effecting from stress concentration during fretting action for coatings. Shear deformation at the interface of surface coating depends upon the adhesion strength of the layer on the substrate. Where as the modified layers does not undergo any mechanical detachment like coatings. There is no sharp interface between the substrate and modified layers which shows diffused surface profiles. Therefore modified layers may require higher shear stress to break the particle from the substrate.

Fretting damage is understood to originate from myriad of interacting mechanical and chemical phenomenon like wear, corrosion and fatigue. So the all inclusive model of crack nucleation will lead us to an absurd region. Even in highly controlled experiments it is very difficult to predict the origin and orientation of fretting cracks. Therefore explanation of the fretting phenomenon merely by observation of cracks has deluded many of the researchers. There are many semi-empirical models based on contact-stress field and surface slip amplitude to interpret these observations. Many fretting researchers believe that fretting is a gradual phenomenon with damage gradually accumulating leading to crack nucleation. So it can be termed as crack nucleation instead of initiation.

6. Conclusion

6.1. Preface

Fretting failures of biomedical titanium alloys used for hip prostheses has been an important area in the field of orthopedic surgery. The substrate materials (Ti-6Al-4V and Ti-6Al-7Nb) used for this work represents one of the possible pairs of materials in contact during fretting along modular junction of hip joints or bone plate-screw combination. The surface treatments given are plasma nitriding, PVD TiN coating, ion implantation, laser nitriding and thermal oxidation. Each one of the surface layers are individually characterized with optical and SEM microscopes, X-ray diffraction analysis, roughness profile, microhardness, nano indentation and scratch test. The surface damage during fretting of individual coatings has been presented with both optical and SEM micrographs and the damage sequence have been explained with friction coefficient curves. Fretting wear and fretting fatigue process cannot be compared due to different couplings. Fretting wear behavior is studied with alumina ball on different modified layers, where as fretting fatigue behavior is studied with couplings made of same modified materials. The results of these experiments give some understanding of the

damage behavior of surface modified implants within the body. The following text explains the conclusive remarks of all the tests conducted.

6.2. Characterization of Surface Coatings and Modified Layers

In this work, five different coatings were chosen for the surface modification of titanium alloys. Substrate titanium alloys have the hardness of around 380 VHN (4 GPa).

PVD TiN coating is a mechanically bonded film of 2μm thickness with the hardness and reduced elastic modulus of 40 GPa and 334 GPa respectively. The adhesion strength of the coating is 90N. XRD analysis shows pure TiN phase on the substrate.

Plasma nitriding is a surface modification process with diffusion of nitrogen under the effect of thermal and electrical potential. XRD data shows TiN and Ti_2N phases within the layer (3μm). Gradient hardness profile indicates gradient nitrogen concentration within the layer. Nano indentation test shows the hardness and elastic modulus of the layer is 23 GPa and 201 GPa respectively.

Ion implanted sample is 170 nm thick and shows little improvement in properties over the substrate for the dose of 2 X 10^{16} ions/cm^2. The hardness and elastic modulus is 6 and 115 GPa respectively. It shows no contrasting change in the surface color after implantation.

Laser nitriding of titanium alloys produces super hard TiN dendrites (60 – 70 Vol. %) within the melted region. This has posed difficulty in surface preparation. The modified case is very thick (~0.5mm) with hardness varying between 1450 – 1600 VHN. XRD data shows TiN and Ti_2N in the modified layer.

Thermal oxidation produces black rutile layer above the hard α case (solid solution of oxygen in titanium). It also shows gradient hardness below the surface with the hardness of around 1100 VHN. The case developed by thermal oxidation is highly irregular with deeper and shallow oxidation at different regions.

6.3. Fretting Wear Test Results

The following section gives the test results of fretting wear conducted with alumina ball on flat specimen configuration. In every case, the damage is a localized irregular or regular scar on the surface.

6.3.1. Unmodified Alloys

Unmodified alloys have shown irregular scar in air and circular scar in ringer fluid. The friction coefficient varies in the range of 0.8 to 1.0 in both cases. Rutile oxides are observed in scar tested in air and absent in case of scar tested in ringer fluid. The scar is wider and deeper in ringer fluid than air. This is due to electrochemical influence during fretting ringer fluid.

6.3.2. PVD Tin Coating

The scar pattern for PVD TiN coated alloy is irregular in both air and ringer fluid. The friction coefficient is below 0.2 in air as well as ringer fluid. Oxidation is observed in air, but

not in ringer fluid. The scar width is shallow and irregular in both cases compared to unmodified alloys. This indicates that TiN layer is more resistant to mechanical abrasion as well as electrochemical oxidation.

6.3.3. Plasma Nitriding

Plasma nitrided layer is softer than PVD TiN layer and the scar profile is similar to unmodified alloys after the fretting wear test. Compacted oxides are observed after the test in air and scar width is deeper and wider in ringer fluid without oxides. Friction coefficient ranges from 0.4 to 0.7 in air and 0.2 to 0.6 in ringer fluid.

6.3.4. Ion Implantation

Ion implanted layer is more softer and thinner compared to plasma nitrided and the scar profile is as good as uncoated alloys with compacted oxides in air and deep and wide scar in ringer fluid without oxides. Electrochemical oxidation has influenced during fretting in ringer fluid. Friction coefficient ranges from 0.3 to 0.7 during test in air and 0.2 to 0.4 in ringer fluid.

6.3.5. Laser Nitriding

Laser nitrided layer is very thick and hardest of all the coatings. Fretting scar is shallow and irregular in both air and ringer fluid. It is attributed to the presence of large volume percent of closely spaced TiN dendrites in the layer. Even though damage is minimal, friction coefficient is quite high. It ranges between 0.6 to 0.7 in air and 0.3 to 0.4 in ringer fluid.

6.3.6. Thermal Oxidation

Thermally oxidized layer is also thick, but less hard compared to laser nitriding and PVD TiN coating. The wear scar is irregular in both air and ringer solution. The depth and width of the scar is intermediate between uncoated and laser nitrided alloys. Friction coefficient ranged from 0.4 to 0.7 in air and 0.4 to 0.6 in ringer fluid.

6.3.7. Summary of Fretting Wear Results

In the present study on fretting wear of surface modified titanium alloys, Laser nitrided and PVD TiN coated alloys have shown the best performance due to large volume of hard and higher wear resistant TiN phase. The force-displacement loop area is also less for PVD TiN layer indicating the superior wear resistant nature of the layer. The wear volume generated during fretting is minimal primarily due to TiN. Thermally oxidized alloy has shown intermediate performance and plasma nitrided and ion implanted alloys have shown very poor performance due to softer and thinner layers. In terms of quantitative results, the average wear rates for laser nitrided, PVD TiN coated and thermally oxidized samples is 0.6, 3 and 12.5% respectively compared to ion implanted and plasma nitrided samples having shallow thickness and low hardness. Fretting wear rate is higher in uncoated, ion implanted and thermally oxidized alloys due to fretting assisted electrochemical dissolution process.

6.4. Fretting Fatigue Test Results

The following section describes conclusive remarks on the performance of surface modified alloys under fretting fatigue conditions.

6.4.1. S-N Curve

Fretting fatigue has reduced the life of uncoated specimens compared to surface modified specimens. For example, Fretting fatigue life of uncoated pairs is 15 to 18% of plasma nitrided pairs, 45 to 50% of PVD TiN coated pairs and 60 to 65% of the ion implanted pairs at 500 MPa axial stresses. The difference and scatter in results is more at lower axial stresses. Plasma nitrided pairs have shown the best results over all the coatings due to gradient hardness from the surface. Laser nitrided and thermally oxidized pairs have undergone premature failure due to irregular case thickness.

6.4.2. Slip Amplitude

The slip between pad and specimen increases with increase in the applied stress. The slip is slightly high in ringer fluid due to release in constraint from the flow of ringer fluid. During cyclic loading, large variations are observed due to frequent shift in fretting regime (Gross slip, partial slip and stick).

6.4.3. Surface Damage Characterization

6.4.3.1. Unmodified Alloys

Fretting of unmodified alloys shows intense oxidation and surface damage due to high metallurgical compatibility of materials which induces frequent adhesion and rupture of exposed surface. Formation of rutile along the fretted area is confirmed with XRD analysis. Friction curves indicate the mode of contact behavior during fretting. Friction coefficient has declined gradually due to lubrication effect from biofluid and oxide debris bed within the contact. Specimen will fail when the cross section will no longer endure the axial stress.

6.4.3.2. PVD Tin Coating

PVD TiN coating is characterized by formation of hard TiN layer on the surface with sharply visible interface. XRD analysis confirms the formation of pure TiN phase on the surface. Plain fatigue of TiN coated Ti-6Al-4V did not fail even after million cycles because the surface layer prevented the formation of extrusions and intrusions. Fretting fatigue damage is characterized by delamination and compaction of TiN particles within the oxide bed. The life of all the specimens with TiN layer has improved compared to unmodified alloys indicating the positive effect of coating. Friction coefficient curve indicate the unsteady nature of the contact during fretting. But friction coefficient is below 0.4 throughout the test compared to uncoated alloys. Repeated interaction of surface asperities and rupture during fretting can be understood from the initial part of friction coefficient curve. The uneven nature of the curve can be attributed to complex interaction between roughness peaks, debris particles and lubricating effect of biofluid. So fretting is mostly on the surface of the coating

before delamination. High friction during the later part of the cycle explains the failure of coating. The effect of biofluid and oxide bed in reducing the friction is also confirmed from the last part of the friction curve.

6.4.3.3. Plasma Nitriding

Plasma nitrided surface is smoother than as polished unmodified alloys. XRD analysis confirms the formation TiN and Ti_2N capable of resisting wear damage. Surface modified layers are much better than coatings due to absence of sharp interface between substrate and surface modified layer. However layers of higher thickness will have negative effect on fretting fatigue life. Fretting fatigue damage area of plasma nitrided titanium pairs is also characterized with oxidation and deep scratches effecting from third body wear mode of contact interaction. Friction coefficient remained below 0.1 for most of the cycle. The surface damage is very gradual.

6.4.3.4. Nitrogen Ion Implantation

Nitrogen Ion implanted layer shows no visible changes or features on the surface. Even though it is a surface modified layer, it can perform better only under low normal load due to low thickness. Implanted depth was reported as 170 nm from the TRIM software which can calculate the projected range of ions for a material with particular combination of elements. The properties of the layer can be well characterized with nano indentation. Scratch test can only indicate the presence of hard modified layer. Fretting fatigue induced damage is almost comparable with unmodified alloys having large amount of oxides within the damaged area. Friction curve shows gradual increase and decrease with the number of cycles. Increase in friction during first half of the life is attributed to slow damage of surface layer and adhesion of surface. Decrease in friction during later part of the cycle before failure is attributed to lubricating effect of biofluid and oxide debris.

6.4.3.5. Laser Nitriding

Laser nitrided titanium alloys contain large volume fraction of TiN dendrites within the melt deposit on the surface. The melt deposit itself is almost 0.5mm thick from the surface. All the specimens experienced brittle failure during fretting fatigue test within short cycles due to hard and thick modified layer. Friction coefficient is below 0.1 till final failure. The separation of the specimens was at the contact edge and some of them failed away from the contact area due to thick and brittle modified layer. Oxidation was not observed in any of the specimens. The process of laser nitriding needs improvement for bioimplant applications. It cannot be used for implant with complex geometries and also not usable for mass production. Post operative machining and further surface preparations may be necessary which generally pose difficulties.

6.4.3.6. Thermal Oxidation

Thermally oxidized surface is characterized by hard α case below the layer of rutile. Oxidation of titanium alloys at high temperature allows thermally aided diffusion of oxygen forming non uniform hard case. It is reported to have excellent tribocorrosion and wear

characteristics. But fretting fatigue life is very poor due to non-uniform case thickness. The process of thermal oxidation used in this work is not very suitable for fatigue applications. Like laser nitrided alloys, many specimens also failed within short number of cycles. Friction coefficient was below 0.05 throughout the test for one of the specimen tested at 334 MPa. Fretting damage and oxidation was not observed in any of the specimens tested. There seems to be sharp fatigue limit above which the specimen cannot endure and below which it would never fail. Surface preparation after thermal oxidation is difficult due to uneven nature of oxide growth.

6.4.3.7. Summary Results of Fretting Fatigue Tests

In the present study on fretting fatigue behavior of surface modified titanium alloys, plasma nitriding process has shown the best performance in terms of increasing fretting fatigue life due to shallow gradient layer having higher capacity for accommodating fretting induced surface deformations thereby minimizing the probability of early crack nucleation. Fretting wear performance is therefore poor. PVD TiN coating is slightly inferior due to mechanical adhesion of the super hard layer. Even though fretting wear performance is good, the layer delamination is responsible for failure during fretting fatigue. Ion implanted layer is shallow and soft with fretting fatigue behavior almost similar to uncoated pairs. Laser nitrided and thermally oxidized pairs have undergone premature failure due to irregular case thickness. Fretting fatigue results cannot be correlated with fretting wear results due to different couplings. The results are highly dependent on the relative hardness of the contact pairs as explained earlier.

6.4.4. General Observations of Fretting Fatigue Failures

Fretting fatigue failure is always observed to initiate along the edge of contact between pad and the specimen. Fretting fatigue life is classified into crack initiation life and crack propagation life. Cracks initially traverses inclined and later align perpendicular to the stress axis. This transition occurs when the effect of tangential force gradually diminishes below the surface during crack propagation in proportionate to increase in the effect of axial load. Numerous cracks can be observed within the damaged site filled with fretting debris. Oxidation is inevitable because the contact experiences high temperatures during fretting process. The cross section of the failed specimen usually shows beach marks and features with quasi cleavage mode of fracture.

References

[1] Antoniou R.A., Radtke T.C. (1997), Mechanism of fretting fatigue of Titanium Alloys, *Materials Science and Engineering A,* Vol. 237, 229 – 240.

[2] Alves, Jr. C., Guerra Neto C.L.B., Morais G.H.S., Da Silva C.F. and Hajek V. (2005), Nitriding of titanium disks and industrial dental implants using hollow cathode discharge, *Surface and Coatings Technology*, Vol. 194, Issues 2-3, 196-202.

[3] Ani Zhecheva, Wei Sha, Savko, Adrain Long (2004), Enhancing the microstructure and properties of titanium alloys through nitriding and other surface engineering methods,

Surface and Coatings Technology, Vol. 200, Issue 7, 21 December 2005, Pages 2192-2207.

[4] Animesh Choubey, Bikramjit Basu, R. Balasubramaniam (2004),Tribological behaviour of Ti-based alloys in simulated body fluid solution at fretting contacts, *Materials Science and Engineering A,* Vol. 379, 234–239

[5] Borgioli F., Galvanetto E., Iozzelli F. and Pradelli G. (2005*),* Improvement of wear resistance of Ti–6Al–4V alloy by means of thermal oxidation, *Materials Letters*, Vol. 59, Issue 17, 2159-2162.

[6] Badisch E., Fontalvo G.A., Stoiber M., Mitterer C. (2003), Tribological behavior of PACVD TiN coatings in the temperature range up to 500 °C, *Surface and Coatings Technology*, Vol. 163 –164, 585–590.

[7] Bhowmick S., Jayaram V., Biswas S.K. (2005), Deconvolution of fracture properties of TiN films on steels from nanoindentation load–displacement curves, *Acta Materialia*, Vol. 53, Issue 8, 2459-2467

[8] Bulatov V. P., Krasny V. A., Schneider Y. G. (1997), Basics of Machining methods to yield wear and fretting resistive surfaces having regular roughness pattern, *WEAR*, Vol. 208, 132 – 137.

[9] Bekir S. Yilbas, Ahemt Z. Sahin, Ahmed Z. Al-Garni, Syed A. M, Zaki Ahmed, Abdulaleem B. J., Muhammed Sami (1996), Plasma Nitriding of Ti-6Al-4V alloy to improve some tribological properties, *Surface and Coatings Technology*, Vol. 80, 287 – 292.

[10] Chan P. C. and Thornley J. C. (2002), Common features of fretting fatigue cracking in steels, *Practical Failure Analysis*, Vol. 6, 85 – 90.

[11] Chen H., Wu P. Q., Xu K. W. (2002), Comparison of fretting wear of Cr-rich CrN and TiN coatings in air of different relative humidities, *WEAR*, Vol. 253, 527 – 532.

[12] Carpene E., Shinn M., Schaaf P. (2005), Free-electron laser surface processing of titanium in nitrogen atmosphere, *Applied Surface Science*, Vol. 247, Issues 1-4, 307-312.

[13] Chu P. K., Chen J. Y., Wang L. P., Huang N. (2002), Plasma-surface modification of biomaterials, *Materials Science and Engineering R,* Vol. 36, Issues 5-6, 143-206.

[14] David W. Hoeppner, Amy M. H. Taylor, and Venkatesan Chandrasekaran (2003), Fretting fatigue behavior of Titanium alloys", Fretting Fatigue: Advances in Basic Understanding and Applications, *Standardization of Fretting Fatigue Test Methods and Equipments,* ASTM STP 1425, 291 – 306.

[15] Dobromirski, J.M. (1992) Variables of Fretting Processes: Are There 50 of Them?, Standardization of Fretting Fatigue Test Methods and Equipments, *ASTM STP* 1159, 60 - 66.

[16] Dong H., Bell T. (2000), Enhanced wear resistance of titanium surfaces by a new thermal oxidation treatment, *WEAR*, Vol. 238, Issue 2, 131-137.

[17] Elder J. E., Tahmburaj R., Patnaik P. C. (1989), Optimizing ion implantation conditions for improving wear, fatigue and fretting fatigue of Ti-6Al-4V, *Surface Engineering*, Vol. 5, No.1, 55 – 75.

[18] Endo K and Goto H (1976), Inititation and propagation of fretting fatigue cracks, *WEAR*, Vol. 38, 311 – 324.

[19] Ettaqi S., Hays V., Hantzpergue J.J., Saindrenan G., Remy J.C. (1998), Mechanical, structural and tribological properties of titanium nitrided by a pulsed laser, *Surface and Coatings Technology*, Vol. 100-101, 428-432.

[20] Geetha M., U. Kamachi Mudali, R.Ashokmani and Baladev Raj (2003) Corrosion and Microstructural aspects of titanium and its alloys as orthopedic devices, *Corrosion reviews*. Vol 21, Nov 2-3, 125 – 159.

[21] Geetha M., Kamachi Mudali U., Pandey N. D., Asokamani R., Baldev Raj (2004), Microstructural and corrosion evaluation of laser surface nitrided Ti – 13Nb – 13Zr alloy, *Surface Engineering*, Vol. 20, No. 1, 68 – 75.

[22] Galliano F., Galvanetto E., Mischler S., Landolt D. (2001), Tribocorrosion behavior of plasma nitrided Ti–6Al–4V alloy in neutral NaCl solution, *Surface and Coatings Technology*, Vol. 145, Issues 1-3, 121-131.

[23] Gokul Lakshmi S., Arivuoli D. 2004), Tribological behaviour of plasma nitrided Ti-5Al-2Nb-1Ta alloy against UHMWPE, *Tribology International*, Vol. 37, Issue 8, 627-631.

[24] Günzel R., Shevshenko N., Matz W., Mücklich A., Celis J. P. (2001), Structural investigation and wear resistance of submicron TiN coatings obtained by a hybrid plasma immersion ion implantation process, *Surface and Coatings Technology*, Vol. 142-144, 978-983.

[25] Hager C.H., Jr., Sanders J.H., Sharma S. (2004), Characterization of mixed and gross slip fretting wear regimes in Ti6Al4V interfaces at room temperature, *WEAR* Vol. 257, 167–180.

[26] Hallab. N. (2001), Safety of metallic implants, *Journal of Bone Joint Surgery* Vol. 83 - A, 428 - 436.

[27] Hallab. N and Joshua J. Jacobs (2003) Orthopedic Implant Fretting Corrosion, *Corrosion Review*, Vol. 21, 183 – 214.

[28] Hyukjae Lee and Shankar Mall (2004), Effect of dissimilar mating materials and contact force on fretting fatigue behavior of Ti-6Al-4V, *Tribology International*, Vol. 37, 35 – 44.

[29] Hasan Guleryuz, Huseyin Cimenoglu (2004), Effect of thermal oxidation on corrosion and corrosion-wear behavior of Ti-6Al-4V alloy, *Biomaterials*, Vol. 25 3325 – 3333.

[30] Hasan Guleryuz, Huseyin Cimenoglu (2005), Surface modification of a Ti-6Al-4V alloy by thermal oxidation, *Surface and Coating Technology*, Vol. 192 (2005) 164 – 170.

[31] Hansson T, Kamaraj M, Mutoh Y, Pettersson B, High temperature fretting fatigue behavior of an XD γ-base TiAl, *ASTM STP*, Vol. 1367.

[32] Hattori T., Nakamuram M., and Watanabe, T (2003), Improvement of Fretting Fatigue Strength by Using Stress-Release slits", Fretting Fatigue: Advances in Basic Understanding and Applications, Standardization of Fretting Fatigue Test Methods and Equipments, *ASTM STP* 1425, 159 – 168.

[33] Huang nan, Chen Yuanru, Cai Guangjun, Lin Chenggang, Wang Zhongguang, Yiao Guo, Su Huehe, Liu Xianghuai, Zhen Zhihong (1996), Research on the fatigue behavior of titanium based biomaterial coated with titanium nitride film by ion beam enhanced deposition, *Surface and Coatings Technology*, Vol. 88, 127 – 131.

[34] Hultman L., Shinn M., Mirkarimi P. B., Barnett S. A. (1994), Characterization of misfit dislocations in epitaxial (001)-oriented TiN, NbN, VN, and (Ti,Nb)N film

heterostructures by transmission electron microscopy, *Journal of Crystal Growth*, Vol. 135, 309-317.

[35] Hu C., Baker T. N. (1999), The importance of preheat before laser nitriding a Ti–6Al–4V alloy, *Materials Science and Engineering A*, Vol. 265, Issues 1-2, 268-275.

[36] Hong Liang, Bing Shi, Aaron Fairchild and Timothy Cale (2004), Applications of plasma coatings in artificial joints: an overview, *Vacuum*, Vol. 73, 317-326.

[37] Hoeppner D. W. (1994), *Fretting fatigue, ESIS* Vol. 18, 3 – 19.

[38] Jin O. and Mall S. (2002), Effects of independent pad displacement on fretting fatigue behavior of Ti-6Al-4V, *WEAR*, Vol. 253, 585 – 596.

[39] Jin-Ki Hong, In-Sup Kim, Chi-Yong Park, Eung-Seon Kim (2005), Microstructural effects on the fretting wear of Inconel 690 steam generator tube *WEAR*, Vol. 259, 349-355.

[40] Kamachi Mudali U., Sridhar T. M., Eliaz N., Baladev Raj (2003) Failures of stainless steel orthopedic devices – causes and remedies, *Corrosion Reviews*, Vol 21, Nos 2-3, 231-267.

[41] Kamachi Mudali U., Sridhar T. M., Baladev Raj (2003), Corrosion of bio implants, *Sadhana*, Vol 28, Parts 3 & 4, 601 – 637.

[42] Khan M. A., Williams R. L., Williams D. F. (1999) "Conjoint corrosion and wear in titanium alloys", *Biomaterials*, Vol. 20, 765 – 772.

[43] Kozo Nakazawa, Norio Maruyama, Takao Hanawa (2003), Effect of contact pressure on Fretting Fatigue of 316L Stainless steel, Standardization of Fretting Fatigue Test Methods and Equipments, *ASTM STP* 1425, 169 – 182.

[44] Leyens C., Peters M. (2004) *Titanium and Titanium alloys*", Ch. 5, WILEY-VCH GmbH & Co. KGaA.

[45] Laure Duisabeau, Pierre Combrade, Bernard Forest (2004), Environmental effect on fretting of metallic materials for orthopedic implants, *WEAR*, Vol. 256 805 – 816.

[46] Mutoh Y., Satoh T., Tanaka K., Tsunoda E. (1989), Fretting fatigue at elevated temperatures in two steam turbine steels, *Fatigue & Fracture of Engineering Materials and Structures*, Vol. 12, 409 – 421.

[47] Man H.C., Zhao N.Q., Cui Z.D. (2005), Surface morphology of a laser surface nitrided and etched Ti–6Al–4V alloy, *Surface and Coatings Technology*, Vol. 192, 341-346.

[48] Mohmad Soib Selamat, Baker T. N., Watson L. M. (2001), *Study of the surface layer formed by the laser processing of Ti–6Al–4V alloy in a dilute nitrogen environment*, Journal of Materials Processing Technology, Vol. 113, 509-515.

[49] Mutoh Y. (1995), *Mechanism of fretting fatigue*, JSME Vol. 38, 405 – 414.

[50] Mitsuo Niinomi (1998) Mechanical properties of biomedical titanium alloys, *Materials Science and Engineering A*, Vol. 243, 231 – 236.

[51] Marc Long and Rack H.J. (1998), Review – Titanium alloys in total joint Replacement a material science perspective, *Biomaterials* Vol. 19, 1621 – 1639.

[52] Man H.C., Zaho N.Q., Cui Z.D. (2005), Surface morphology of laser nitrided and etched Ti-6Al-4V alloy, *Surface and Coatings Technology*, Vol. 192, 241 – 346.

[53] Mishra S.C., Nayak B.B., Mohanty B.C., Mills B. (2003), Surface nitriding of titanium in arc plasma, *Journal of Materials Processing Technology*, Vol. 132, 143-148.

[54] Papakyriacou M., Mayer H., Pypen C., Plenk H., Jr., Stanzl-Tschegg S., (2001) Influence of loading frequency on high cycle fatigue properties of b.c.c and h.c.p metals, *Materials Science and Engineering A*, Vol. 308, 143 – 152.

[55] Prakash B., Richter E., Pattyn H., Celis J.P. (2003), *Ti*–B and Ti–B–C coatings deposited by plasma immersion ion implantation and their fretting behavior, *Surface and Coatings Technology*, Vol. 173, 150-160.

[56] Rebecca Cortez, Shankar mall, Jeffrey R. Calcaterra (1999), Investigation of variable amplitude loading on fretting fatigue behavior or Ti-6Al-4V, *International Journal of Fatigue*, Vol. 21, 709 – 717.

[57] Ramesh R., Gnanamoorthy R. (2006), Development of a fretting wear test rig and preliminary studies for understanding the fretting wear properties of steels, *Materials & Design,* Vol. 27, 141-146.

[58] Sumita M., Hanawa T., Ohnishi I., Yoneyama T. (1994) Failure Processes in Biometallic Materials, *Comprehensive Structural Integrity*, Vol. 9, 131–167.

[59] Shenhar A. (2000), Titanium nitride coatings on surgical titanium alloys produced by a powder immersion reaction assisted coating method: residual stresses and fretting behavior, *Surface ad Coatings Technology*, Vol. 126, 210 – 218.

[60] Sinha V., Soboyejo W.O. (2001), An investigation of the effects of colony microstructure on fatigue crack growth rate in Ti-6Al-4V", *Material Science and Engineering A*, Vol. 319 – 321, 607 – 612.

[61] Sittig C, Hahner G., Marti A., Textor M., Spencer N. D. (1999), The Implant Material, Ti6Al7Nb: surface microstructure, composition and properties, *Journal of Materials Science in Medicine*, Vol. 10, 191 – 198.

[62] Starosvetsky D., Gotman I. (2001), Corrosion behavior of titanium nitride coated Ni-Ti shape memory surgical alloy, *Biomaterials*, Vol. 22, 1853-1859.

[63] Shenhar A., Gotman I., Radin S., Ducheyne P., Gutmanas E. Y. (2000), Titanium nitride coatings on surgical titanium alloys produced by a powder immersion reaction assisted coating method: residual stresses and fretting behavior, *Surface and Coatings Technology*, Vol. 126, 210 – 218.

[64] Sung J.H., Kim T.H., Kim S.S. (2001), Fretting damage of TiN coated zircaloy-4 tube, *WEAR*, Vol. 250, 658–664.

[65] Shengli Ma, Kewei Xu, Wanqi Jie (2004), Wear behavior of the surface of Ti–6Al–4V alloy modified by treating with a pulsed d.c. plasma-duplex process, *Surface and Coatings Technology*, Volume 185, Issues 2-3, 22 July 2004, Pages 205-209.

[66] Sobiecki J. R., Wierzcho T., Rudnicki J. (2001), The influence of glow discharge nitriding, oxynitriding and carbonitriding on surface modification of Ti–1Al–1Mn titanium alloy, *Vacuum*, Vol. 64, 41-46.

[67] Sauger E, Fouvry S, Ponsonnet L, Kapsa Ph., Martin J. M, and Vincent L, (2000), *Tribologically transformed structure in fretting*, WEAR, Vol. 245, 39-52.

[68] Teoh S. H. (2000) Fatigue of biomaterials: a review, *International Journal of Fatigue* Vol. 22, 825–837.

[69] Thair L., Kamachi Mudali U., Bhuvaneswaran N., Nair K.G.M., Asokamani R., Baldev Raj (2002) Nitrogen ion implantation and in vitro corrosion behavior of as-cast Ti-6Al-7Nb alloy, *Corrosion Science*, Vol. 44, 2439 – 2457.

[70] Takahito Ohmura, Saburo Matsuoka (2003), Evaluation of mechanical properties of ceramic coatings on a metal substrate, *Surface and Coatings Technology*, Vol. 169 – 170, 728 – 731.

[71] Tan L, Shaw G, Sridharan K, Crone W C (2005), *Effects of oxygen ion implantation on wear behavior of NiTi shape memory alloy, Mechanics of Materials*, Vol. 37, 1059 – 1068.

[72] L. Tan, G. Shaw, K. Sridharan and W.C. Crone (2005), Effects of oxygen ion implantation on wear behavior of NiTi shape memory alloy, *Mechanics of Materials,* Vol. 37, Issue 10, 1059-1068.

[73] Tan L., Crone W.C. (2005), Effects of methane plasma ion implantation on the microstructure and wear resistance of NiTi shape memory alloys, *Thin Solid Films,* Vol. 472, Issues 1-2, 282-290.

[74] Vincent L. Berthier, Y., Godet, M. (1992) Testing Methods in Fretting fatigue: A Critical Appraisal, Standardization of Fretting Fatigue Test Methods and Equipments, *ASTM STP* 1159, 33 - 48.

[75] Vaquila I., Vergara L. I., Passeggi Jr. M.C.G. (1999), R. A. Vidal and J. Ferrón, Chemical reactions at surfaces: titanium oxidation, *Surface and Coatings Technology,* Vol. 122, 67-71.

[76] Wen-Jun Chou, Ge-Peng Yu, Jia-Hong Huang (2002), Mechanical properties of Tin coatings on 304 stainless steel substrates, *Surface and Coatings Technology*, Vol. 149, 7 – 13.

[77] Wen-Jun Chou, Ge-Ping Yu, Jia-Hong Huang (2003), Effect of heat treatment on the structure and properties of ion-plated TiN films, *Surface and Coatings* Technology, Vol. 168, 43–50.

[78] Wiklund U., Hutchings I.M. (2001), Investigation of surface treatments for galling protection of titanium alloys, *WEAR*, Vol. 251, 1034-1041.

[79] Waterhouse R. B (1972), *Fretting Corrosion*, Ch. 7, Pergamon press.

[80] Xuanyong Liu, Paul K. Chu, Chuanxian Ding (2004), Surface modification of titanium, titanium alloys, and related materials for biomedical applications, *Materials Science and Engineering R*, Vol 47, 49 – 121.

[81] Yasuo Ochi, Yohide Kido, Taisuke Akiyama, Takashi Matumura (2003) Effect of Contact Pad Geometry on Fretting Fatigue Behavior of High Strength Steel", Fretting Fatigue: Advances in Basic Understanding and Applications, Standardization of Fretting Fatigue Test Methods and Equipments, *ASTM STP* 1425, 220 – 232.

[82] Yongqing Fu, Nee Lam Loh, Andrew W. Batchelor, Daoxin Liu, Xiaodong Zhu, Jaiwen He, Kewei Xu (1998), Improvement of fretting wear and fatigue resistance of Ti-6Al-4V by application of several surface treatments and coatings, *Surface and Coatings Technology*, Vol. 106, 192 – 197.

[83] Yves Wouters, Alain Galerie and Jean-Pierre Petit (1997), Thermal oxidation of titanium by water vapour, *Solid State Ionics*, Vol. 104, 89-96.

[84] Young-Ho Lee, Hyung-Kyu Kim (2005), Characteristic of slipping behavior in vibratory wear of a supported tube, *WEAR*, Vol. 259, 337-348.

[85] Yoshimitsu Okazakia, Emiko Gotoh (2005), Comparison of metal release from various metallic biomaterials in vitro, *Biomaterials*, Vol. 26, 11-21.

[86] Zenghu Han, Jiawan, Jijun Lao, Geyang Li (2004), Effect of thickness and substrate on the mechanical properties of hard coatings, *Journal of Coating Technology: Research,* Vol 1, No.4, 337 – 341.

In: Titanium Alloys: Preparation, Properties and Applications ISBN: 978-1-60876-151-7
Editor: Pedro N. Sanchez, pp. 235-267

Chapter 4

INFLUENCE OF PROTECTIVE COATINGS ON PROPERTIES OF NEAR-ALPHA TITANIUM ALLOYS

Tomasz Moskalewicz and Aleksandra Czyrska-Filemonowicz
AGH University of Science and Technology, Faculty of Metals Engineering and Industrial Computer Science Al. Mickiewicza 30, PL-30-059 Kraków, Poland

1. Introduction

Titanium alloys have excellent mechanical properties and low density. These properties make titanium alloys very attractive structural materials for wide application in industry (aeronautics, aerospace and automotive industry, energy systems, marine, machinery industry, medicine…). A very important concern in all sectors of industry is the need to reduce weight and costs. One of the most interesting developments in aeronautics is to replace much heavier nickel-base superalloys at 550–700°C or conventional disc/blade structure with blinks. Approximately one third the structural weight of modern turbine engines is made up of titanium (e.g. fan blades, compressor components). Besides nickel-base superalloys, titanium alloys are the standard engine materials [1,2]. The elevated temperature near-α titanium alloys are used for rotating components, especially in the hotter compressor stages where the temperature and pressure are higher. Less critical non-rotating components such as compressor cases are also made of titanium alloys. In the case when temperatures are below 300°C, the two phase (α+β) Ti-6Al-4V alloy can be used [3].

Commercially pure titanium (cp Ti) has a hexagonal close-packed crystal structure at low temperature and is called α-titanium. At high temperature more stable is β-titanium, which has a body-centered cubic crystal structure. The transformation from α to β titanium occurs at a transus temperature. For cp Ti, the β transus temperature is 882±2°C.

Titanium alloys are classified into five categories: α, near-α, two phase (α+β), metastable β and stable β alloys. The near-α titanium alloys are very interesting for elevated temperature applications (550–700°C). They offer moderate strength in combination with good creep resistance and fracture toughness. One of the most recently developed near-α alloy is

TIMETAL 834. This alloy has the highest operating temperature (about 600°C) of any titanium alloys. Major uses for TIMETAL 834 include rings, compressor discs and blades for aeroengines [2].

The current temperature limit of near-α titanium alloys is mainly due to long-term microstructure stability problems (low oxidation resistance above 600°C), though creep strength obviously decreases continuously with increased temperature [3]. The possible approaches to increase the temperature capability of conventional titanium alloys are [4]:

- by addition of rare earth elements,
- by developing protective coatings.

Numerous investigations have been carried out to increase the operating temperature of titanium alloys [5–15]. A very prospective way to improve their oxidation resistance is surface treatment, which promotes the formation of highly protective alumina scales during oxidation. Among coating processes, magnetron sputtering is an excellent method to reproducibly manufacture thin films with complex and homogenous chemical composition as well as uniform morphology and coating thickness [7,9–12]. Another very attractive, simple and low cost method for coating processing is slurry deposition [16,17]. A glass-ceramic based coating processing by slurry provides very promising material for protection of titanium alloys against oxidation at elevated temperature [18].

In order to improve the oxidation resistance of the TIMETAL 834 alloy, different protective coatings were applied in our studies:

- γ-TiAl coatings with Ag or with Si and Ag addition deposited by magnetron sputtering [19,20],
- glass-ceramic coating deposited by slurry dipping method [21].

Analytical scanning and transmission electron microscopy as well as X-ray diffraction were used for detailed analyses of the microstructure and chemical composition of the coatings. The adhesion of the coating to the substrate was tested by scratch-test. Energy-dispersive synchrotron radiation diffraction was applied for stress analysis. Subsequent, oxidation resistance test results and selected micro-mechanical properties characterisation results will be given.

Besides poor oxidation resistance, the application of titanium-based alloys is limited also by their relatively low hardness and poor tribological properties. Its use is largely restricted to non-tribological applications because of its high coefficient of friction and relatively poor wear resistance. These properties can be improved by diffusion surface treatment, which takes advantage of the high reactivity of titanium with respect to carbon, nitrogen or oxygen to produce high hardness coatings well bonded to the tough matrix. Glow-discharge nitridation and oxynitridation are assessed techniques, which allow for a significant improvement of the wear resistance of titanium-based components [22–26].

In order to improve mechanical and tribological properties of titanium alloys, hard coatings formed during nitridation or oxynitridation under glow discharge were applied [27-29]. The microstructure formed during this surface treatment is complicated and phase composition is difficult to identify. As the microstructure and phase composition of coatings play a major role in tailoring the alloy desired properties, the aim of our studies was a

systematic characterization of hard coatings formed on TIMETAL 834 during its nitridation or oxynitridation under glow discharge. The microstructure findings were correlated with layer micro-mechanical and tribological properties.

2. Near-ALPHA Titanium Alloys

Microstructure of near-α titanium alloys consists mainly of α phase (hexagonal close-packed; hcp) and contain a small amount of β phase (body-centred cubic; bcc). These alloys contain elements stabilizing α phase (Al), 1–2% of elements stabilizing β phase (Mo, Nb, Si) and neutral elements (Sn and Zr). Near-α alloys have good creep resistance and fracture toughness combined with moderate mechanical strength, which is retained at elevated temperatures up to about 600ºC. The presence of a small amount of β phase allows for heat treatment and forging in the hot state.

Near-α alloys are ideal to be applied at elevated temperature because they combine the excellent creep behaviour of α alloys with the high strength of α+β alloys [1].

2.1. Development of the Conventional Elevated-Temperature Alloys

The conventional elevated-temperature titanium alloys have been developed mainly for aeronautics and aerospace applications. The operating temperature of titanium alloys has been raised from about 300°C to nearly 600°C over the last 50 years (Fig. 1). Over the years an evolutionary trend in alloy design is observed from the low temperature α+β alloys to the elevated temperature near-α alloys [1]. All near-α alloys used today were developed from two (α+β) phase Ti-6Al-4V alloy. These alloys contain less β phase than Ti-6Al-4V alloy. The α phase has hcp crystal structure and exhibits far lower diffusivities than bcc β phase, therefore it forms a major constituent (more than 95%) in elevated-temperature titanium alloys [30].

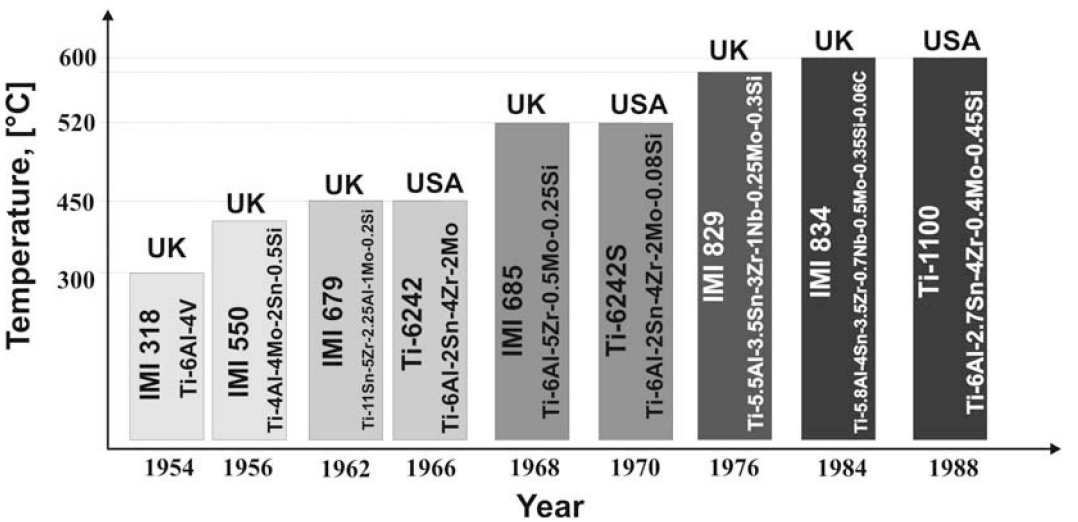

Figure 1. The influence of chemical composition for increase of application temperatures of titanium alloys.

The Ti-6Al-4V alloy is used in aeronautics for manufacture of fan blades and compressor components, such as discs and blades of the low-pressure compressor (first 4 to 5 stages). The maximum operating temperature for this alloy is about 300°C [1, 31]. However, temperature in high-pressure compressor may reach 800°C [32]. Thus, elevated-temperature near-α alloys are used for fabrication of last stages compressor parts in modern gas turbines. Today the temperature limit for application of these alloys is about 600°C. This limit is mainly due to their poor oxidation resistance [1]. These temperature limitations for application of titanium alloys in gas turbines indicate that disc and blades of the last compressor stages, have to be manufactured from Ni-base superalloys at nearly twice the weight. Additional problem is different thermal expansion behavior and the bonding techniques of Ti-base alloys and Ni-base superalloys [1]. The best way to solve these problems is to develop a compressor made completely of titanium alloys. Therefore the increasing of operating temperature of titanium alloys above 600°C is a goal of extensive research.

One of the most recently developed near-α titanium alloys is TIMETAL 834 (chemical composition: Ti-5.8Al-4Sn-3.5Zr-0.7Nb-0.5Mo-0.35Si-0.06C; wt%, TIMET data) [2]. This alloy was developed as IMI 834, jointly in the United Kingdom by IMI Titanium Ltd. and Rolls-Royce in the 1980s. After IMI was acquired by Titanium Metals Corporation (TIMET), this alloy received a trade name TIMETAL 834 [1]. TIMETAL 834 has the highest temperature capability of all conventional titanium-based alloys under dynamically loaded conditions [33]. This alloy offers increased tensile strength and creep resistance up to 600°C, together with improved fatigue strength [2,33], in comparison with creep resistant TIMETAL 6-2-4-2, TIMETAL 829 and TIMETAL 685 titanium alloys. The β transus temperature for this alloy is 1055°C [2].

Presently, this alloy is used as a compressor disc material in the last two stages of the medium-pressure compressor and the first four stages of the high-pressure compressor in variants of the Rolls-Royce Trent series commercial jet engine. A bimodal microstructure with a primary α (volume fraction of 15%) has proven to be a optimum microstructure for this particular application [1].

Microstructure and Properties of Near-α Alloys

Microstructure

The microstructure of titanium alloys is characterised by the size, shape and distribution of α and β phases. The different microstructures of titanium alloys are produced by thermo-mechanical processing (combination of deformation and thermal treatment) and heat treatment. The response of these alloys to heat treatment depends of the alloy chemical composition and the effects of alloying elements on α and β volume fraction. Heat treatments that are generally applicable to all titanium alloys are stress relieving, mill annealing as well as solution treatment and ageing [34].

Stress relieving is a low temperature (from about 480 to 700°C) treatment, followed by air or controlled cooling. This process is applied for relieves internal stresses that occur during deformation. Mill annealing is a high temperature (from about 650 to 815°C) treatment, followed by air cooling. This treatment decrease hardness and increase ductility of the alloy. Solution treatment and ageing is a high-temperature treatment with a rapid cooling, followed by a low temperature ageing treatment. After such treatment the highest tensile

strength and moderate ductility combined with a good fatigue strength, fracture toughness and creep resistance is achieved. Solution treatment and ageing is adequate for two (α+β) phase and β alloys [35].

Two microstructure features are important in commercial titanium alloys:

(i) the β grain size and shape,
(ii) the morphology of the α phase within the β grains.

Control of the β grain size is depended of two factors, recrystallization and subsequent grain growth.

The morphology of the α phase within the β matrix is determined by processing route. Two basic processing may be applied:

- β processing, which is carried out either entirely above the β transus or is completed below the β transus but at a temperature high enough that very little α phase is present,
- α+β processing, carried out below the β transus temperature in the field of presence of α phase.

Subsequent annealing below the transus within about 175°C of the transus temperature results in a distribution of primary α phase. With material generated by β process, a lenticular α morphology is achieved. Thus in α+β processing, the primary α+β becomes globular during subsequent heat treatment [36].

The following various microstructures of titanium alloys are possible:

- equiaxed,
- lamellar,
- bimodal (also referred as duplex).

The equiaxed microstructure is formed during recrystallization at temperatures in two (α+β) phase field. Lamellar microstructure is formed during slow cooling from the β phase field. The lamellae are coarser when the cooling is slower. Bimodal microstructure is formed during solution heat treatment just below the β transus temperature and consists of equiaxed primary α grains in a lamellar α+β matrix (α platelets within β grains). Fast cooling leads to develop narrow, randomly oriented platelets of α phase, referred as a Widmanstatten structure [35].

The examples of different microstructures of elevated temperature near-α titanium alloy – TIMETAL 834 observed by light microscope (LM) are shown on Figure 2. The alloy was slowly cooled following a final forging step low in the α + β phase field. The resultant microstructure consists of a large volume fraction of elongated primary α, in a transformed β matrix (Fig. 2a). Subsequently the material was annealed at the β phase field (temperature range 25-35°C above β transus) and slowly cooled in air. This heat treatment develops a lamellar microstructure (Fig. 2b) and improves the fracture toughness, fatigue crack growth and creep resistance. The changes in cooling rates enable formation of a fine or coarser lamellae.

The bimodal microstructure (consisting of equiaxed primary α grains in a lamellar α+β matrix) of TIMETAL 834 alloy was achieved by recrystallization annealing. This treatment consists of heat treatment at 30°C below the β transus temperature followed by cooling in air (Fig. 2c). Recrystallization annealing improves the fracture toughness and ductility of the alloy.

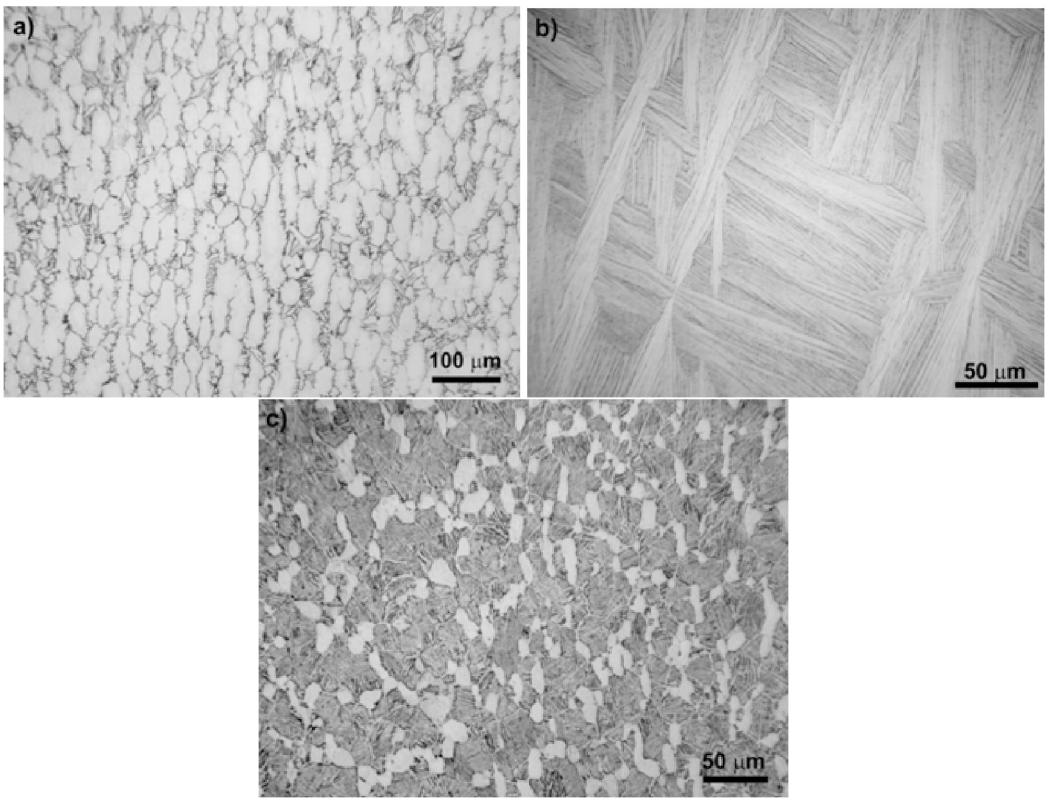

Figure 2. Different microstructure of TIMETAL 834 alloy: a) equiaxed, b) lamellar, c) bimodal, LM.

The investigations of the as hot forged TIMETAL 834 alloy microstructure performed by analytical transmission electron microscopy (TEM) methods allow for detailed phase identification. The typical TEM bright-field (BF) image of the alloy microstructure is shown on Figure 3. The microstructure of the as received (forged) alloy consists mainly of the α phase (hcp) and of a small amount of the β one (bcc). The average size of the α and β grains is in the range of 2–60 μm and 1 μm, respectively. Additionally, precipitates of the Zr_5Si_4 phase (tetragonal primitive, tp) are identified, both in the inside of the grains and on the grain boundaries. It should be mentioned that the phase identification based on electron diffraction patterns in this case was ambiguous. For several diffraction patterns possible solutions for Zr_5Si_4 and ZrSi (orthorhombic) were found, therefore the ZrSi precipitates could not be unequivocally excluded. The precipitates were irregularly shaped. The average size of silicides was estimated as 0.3–0.6 μm. Chemical composition analyses (both, scanning transmission electron microscopy-energy dispersive spectroscopy (STEM-EDS) line analysis and elemental distribution maps) revealed an enrichment of Al and Ti in the α phase, Mo and Nb in the β phase, as well as Si and Zr in the silicides (Fig. 4) [27,28].

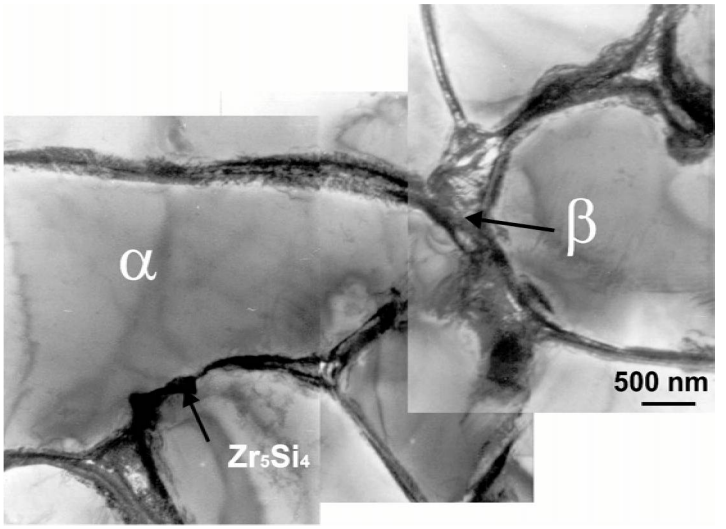

Figure 3. Microstructure of the as hot forged TIMETAL 834 alloy; TEM-BF image [28].

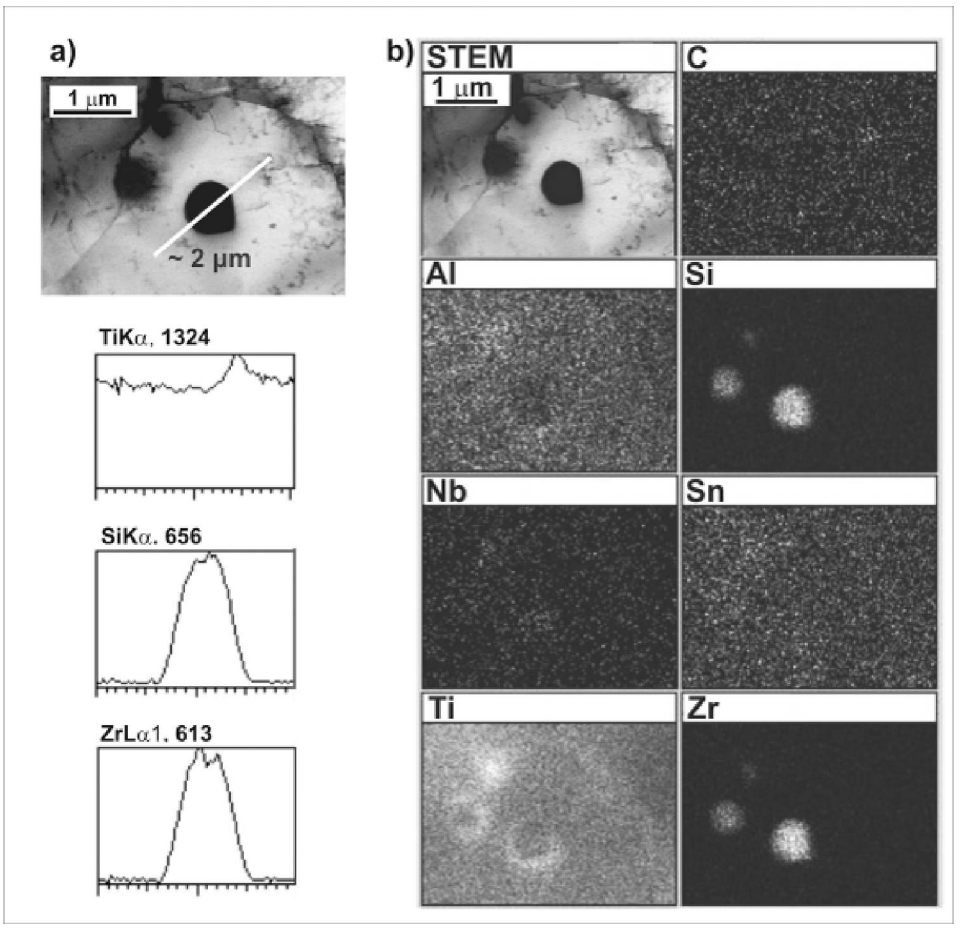

Figure 4. Zr_5Si_4 precipitate inside the α grain of the as hot forged TIMETAL 834 a) STEM-EDS linescane analysis along line marked, b) Elemental distribution maps; STEM-EDS [28].

Properties

Microstructure has an essential influence on the properties of titanium alloys. The important elevated-temperature properties of titanium alloys are: tensile strength, creep, fatigue and fatigue crack propagation resistance, fracture toughness and oxidation resistance. Table 1 shows influence of a microstructure on selected properties of near-α titanium alloys.

Table 1. Effect of microstructure on selected properties of near-α titanium alloys ("↑" - positive influence; "↓" - negative influence).

Property	Microstructure	
	Lamellar	Bimodal
Strength	↑	↓
Ductility	↓	↑
Fatigue crack propagation	↑	↓
Fatigue crack initiation	↓	↑
Creep strength	↑	↓
Fracture toughness	↑	↓

There are generally two ways to improve the physical and mechanical properties of titanium alloys: alloying and processing. Alloying provide a basic for an increase in strength (e.g. solid-solution strengthening, age hardening), allows the generation of ordered structures, determines most of the physical properties (e.g. density, elastic modulus, coefficient of thermal expansion) and largely controls the chemical resistance of the material (corrosion, oxidation). Processing allows the careful balancing of the strength and plastic properties of titanium alloys. Depending of the properties required for the final application, different microstructures (described earlier) can be produced by means of thermo-mechanical treatment [37].

The fatigue properties of near-α alloys are strongly influenced by α grain size, degree of age hardening, oxygen content and also by the morphology and arrangements of the α and β phases. Lamellar, equiaxed and bimodal microstructure can be generated by thermo-mechanical treatment. Important microstructure parameters include prior β grain size, colony size of α lamellae and the width of α lamella in lamellar microstructures. Additional parameters for bimodal (duplex) structure are grain size and volume fraction of the primary α phase [38].

The microstructure has an essential influence on fatigue crack propagation behaviour. For example, according to Wagner [38] for long cracks, fatigue crack propagation behaviour is superior for coarse lamellar structures compared to a fine equiaxed structure; however the behaviour is reversed for small cracks. A reduction of prior β grain size in lamellar structures and a reduction of the primary α volume fraction in duplex structures increase both low-cycle fatigue (LCF) life as well as fatigue strength. The fine grained lamellar microstructure shows superior crack growth behaviour over the coarse grained lamellar structure, while for duplex structures the lower primary α volume fraction is superior to the higher one.

The creep resistance in near-α alloys is increased by the heat treatment above β transus temperature. During cooling, a lamellar α structure is formed. In contrast, the equiaxed α

structure, resulting from both hot working and subsequent heat treatment in the α+β phase field, exhibits lower creep resistance. For β processed titanium alloys, the creep strength depends on the morphology of the α phase, which can be controlled by cooling rate from the β heat treatment temperature. The β heat treated structures also show superior fracture toughness and fatigue crack growth resistance. On the other hand, α+β treated equiaxed structures exhibit higher ductility and LCF properties. In order to optimize both creep and fatigue resistance the near-α alloys are used in α+β heat treated condition with a 5-15% of equiaxed α phase in the structure [4].

The microstructure of titanium alloys influence their microhardness. The changes in a microhardness (Vickers hardness number; VHN) of TIMETAL 834 alloy as a function of different microstructure are shown in Table 2.

Table 2. The influence of different microstructures on microhardness of TIMETAL 834 alloy

Microstructure	VHN [GPa]
equiaxed	3.3±0.05
lamellar	3.6±0.1
bimodal	3.8±0.1

Near-α titanium alloys are usually considered for applications at elevated temperatures (e.g. in gas turbines). Thus, good creep behaviour is important. The microstructure has a strong influence on the alloy creep properties. Bimodal and lamellar microstructures are produced for elevated temperature near-α titanium alloys. Lamellar microstructure usually shows superior creep behaviour due to their coarser structures meaning a lower volume fraction of phase boundaries [37]. Therefore, lamellar microstructures should be preferred. However, these structures show poor fatigue behaviour, particularly under LCF conditions, where microcrack propagation determines alloy life-time. In these cases, a change of phase morphology between the surface and the bulk of a component by means of shot peening and subsequent heat treatment can be advantageous [38]. On the other hand, equiaxed and bimodal microstructures show better fatigue properties due to their fine microstructures [37]. Summarizing, for primary creep-limited elements of gas turbine compressor in modern engines, the titanium alloys with lamellar microstructure are applied, whereas bimodal microstructures are preferred for primary low-cycle fatigue limited elements.

Surface tribological properties of titanium alloys are poor and need a treatment for an efficient use in the wear environment [39-47]. Important are high friction coefficient and relatively poor wear resistance resulting from their low hardness [47]. Friction coefficient of the titanium alloys is in the range of 0.4-0.6. The wear resistance of TIMETAL 834 will be described in next section.

The Role of Alloying Elements in TIMETAL 834

The α phase is solid solution strengthened with stabilizing elements (e.g. Al) and neutral elements (e.g. Zr, Sn). The addition of aluminium increases alloy tensile strength and creep resistance as well as reducing alloy density. However, the maximum solid solution strengthening by Al is limited to 6 wt% Al; above 6 wt% Al promotes formation of a brittle

Ti_3Al phase. Tin is used as a solid solution strengthener and α phase stabilizer. Tin is often used together with Al to achieve the higher strength without embrittlement. Zirconium forms continuous solid solution with titanium and increases strength at low- and intermediate temperatures. The content of zirconium above 5 wt% may reduce ductility and creep resistance [30]. Oxygen strengthened titanium. The oxygen content is usually kept fairly low (0.1-0.5 wt%) in the titanium alloys. Higher oxygen content influences to lower ductility, toughness and long-term elevated temperature stability [30]. Carbon is a stabilizer of α phase.

Molybdenum and niobium are used as the β phase stabilizers. Nb is added to improve the surface stability (oxidation resistance) at elevated temperature. Substituting Nb for some amount of Mo provides β phase strengthening with the least possible lowering of the β transus [4].

Silicon (0.1-0.5 wt%) increases strength at all temperatures and improve creep resistance. Therefore, Si is very important element in elevated-temperature titanium alloys. Si interaction with dislocation (decrease stacking fault energy; SFE) and impedes dislocation motion by restricting cross slip [3,48].

Maximum effective concentration of Si in near-α titanium alloys is governed by its tendency to form a zirconium silicides [3]. Silicides may form during solidification. However, more often, silicides precipitate slowly during ageing or service in elevated-temperature titanium alloys. The precipitation of silicides in titanium alloys have been investigated extensively due to importance of Si addition on the elevated temperature properties of near-α titanium alloys [49-54]. It has been reported that, the solvus temperature of silicides is about 990°C and precipitation of silicides only occurs at temperatures higher than 450°C, which in most cases is lower than the service temperature of near-α titanium alloys [53-54]. Formation of the silicides cause of Si removal from the solid solution, what leads to reduce of ductility [47] and creep resistance [54].

One possible exploitation of positive influence of Si on creep behavior is that at high temperatures Si precipitates as silicides on dislocations, thus hindering dislocation climb, a key deformation mechanism for creep. Although not finally clarified, the positive influence of silicon on the creep behavior was reported [37].

3. Improvement of Wear Resistance and Hardness of TIMETAL 834 by Hard Coatings

Due to their favourable properties as low density, high strength, and good corrosion resistance, titanium-based alloys are used in many fields of applications. However, their use is largely restricted to non-tribological applications because of their high friction and relatively poor wear resistance [50]. From a tribological standpoint, a combination of high hardness with low friction is always desired but seldom achieved in most sliding surfaces. Therefore, the effect of coating on the tribological properties of the titanium alloys is a key aspect for practical applications. The surface hardening of titanium alloys becomes a fundamental requirement in design when the components are subjected to wear [55,56]. Many advanced surface engineering technologies have been developed during the last decade, such as plasma nitriding, laser surface alloying, thin film coatings by CVD and PVD, ion implantation etc. [57-62].

One of the attractive method allows to producing coatings with controlled microstructure is glow discharge, which take advantage of the high reactivity of titanium with respect to carbon, nitrogen, or oxygen to produce hard diffusion coatings with good adhesion to the substrate [22,25,27-29,63,64]. The microstructure formed during its plasma-assisted surface treatment, e.g. during nitridation or oxynitridation, is complicated and phase identification is difficult. The microstructure and phase composition of coatings play a major role in tailoring the alloy desired properties. Therefore, the aim of our studies was a systematic characterization of hard coatings formed on TIMETAL 834 during its nitridation or oxynitridation under glow discharge. The microstructure findings were correlated with micro-mechanical and tribological properties of the coatings [27-29].

The microstructure of the oxynitrided and nitrided coatings produced on TIMETAL 834 by glow discharge, revealed by LM of the cross-section samples, is shown in Fig. 5. The thickness of the oxynitrided coating is up to 40 μm, while the nitrided one is approximately 70–180 μm thick. However, some areas were observed in the nitrided coating, where the effect of nitriding was visible up to 275 μm in depth from the specimen surface. It can be clearly seen that the nitrided coating is consisting of two different zones: outer continuous (about 45 μm thick) and a distinct intermediate zone containing a large grains. The smooth transition between the intermediate zone and the substrate results from nitrogen diffusion into the surface-treated material.

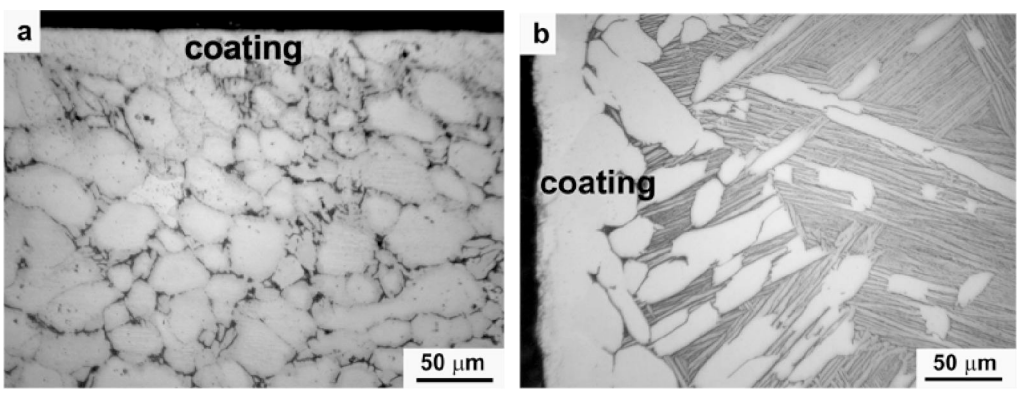

Figure 5. Microstructure of the oxynitrided (a) and nitrided (b) TIMETAL 834; LM-cross section images.

In order to obtain detailed information for the coatings microstructure and phase composition, analytical TEM investigations was performed on the cross-section thin foils. The phase identifications were carried out using selected area electron diffraction (SAED) patterns, energy dispersive X-ray spectroscopy (EDS), electron energy loss spectroscopy (EELS) and energy filtering TEM (EFTEM). These complementary methods allows for very precise and detailed characterisation of the coating microstructure. EELS involves analyzing the energy distributions of initially monoenergetic electrons, after they have interacted with a specimen. EELS can especially determine quantitatively low-atomic-number elements with high sensitivity (e.g. nitrogen in nitrided and oxynitrided coatings). It is important advantage over EDS. EELS can also provide detailed information about the electronic state and chemical bonding of the sample. Fine structure around the ionization edge in the EELS spectrum, which is due to bonding effects, is termed energy-loss near-edge structure

(ELNES). EFTEM is used to record elemental distribution images at nanometer resolution and with short acquisition times (< 50 ms). EFTEM elemental maps can be directly converted into quantitative elemental maps, important for detailed phase distribution within coatings. Uniform thickness of cross-section thin foils prepared by FIB allows for accurate measurements of chemical composition by EELS/EFTEM.

Analytical TEM investigations of the oxynitrided coating show a layered substructure consisting of three sublayers. Figure 6 shows a TEM image of a representative coating microstructure. The outermost sublayer (labelled as "1o"), roughly 0.2–0.4 μm thick, consists of TiO (face-centered cubic; fcc). The following sublayer (labelled as "2o") roughly 3.5 μm thick, consists of ε-Ti_2N (tetragonal primitive; tp). Some precipitates of Zr_5Si_4 (tp; 0.05–0.25 μm in size) were also found. Underneath the ε-Ti_2N sublayer, a nitrogen-rich α (N) solid solution (hcp) and an intermediate layer were formed.

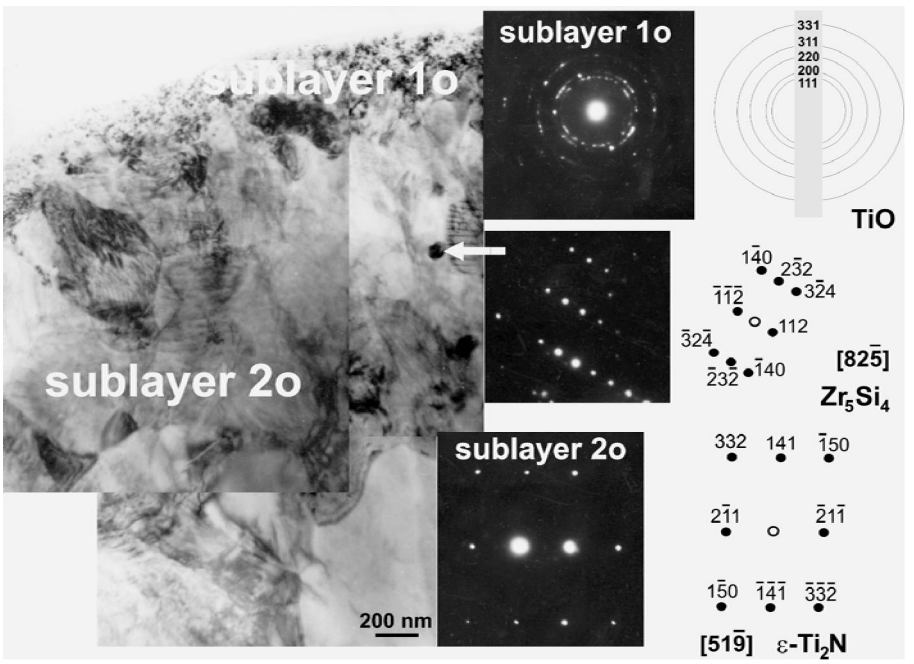

Figure 6. Microstructure of the oxynitrided TIMETAL 834; cross-section TEM BF image of the coating and corresponding SAED patterns taken from particular sublayers [28].

TEM analysis of the nitrided coating performed by SAED and EELS indicated a layered substructure consisting of four main sublayers (Fig. 7). The outermost sublayer (thickness up to 2.3 μm) consists mainly of nanocrystals of δ-TiN (fcc; NaCl like). The crystal size estimated from dark-field (DF) TEM images was about 10-100 nm. The following sublayers consist mainly of δ'-Ti_2N (body-centred tetragonal; bct) and ε-Ti_2N (tp). The δ'-Ti_2N and the ε-Ti_2N sublayers were up to 2.5 μm and up to 3 μm thick, respectively. These sublayers consisted of about 0.2 μm large grains of δ'-Ti_2N and 2.5 μm ε-Ti_2N grains. Electron diffraction analysis of the δ'-Ti_2N sublayer revealed also the presence of other phases, such as Ti_3AlN (cubic primitive; cp) and $TiAlN_2$ (fcc). The presence of Al in the nitrided coating was confirmed by linescane analysis performed by STEM-EDS (Fig. 8). The Zr_5Si_4 precipitates (size up to 1μm) were identified by SAED and STEM-EDS, mainly at the grain boundaries

and sporadically inside the ε-Ti_2N grains (Fig. 8). EDS and EFTEM investigations revealed an enrichment of Si and Zr in the precipitates formed in ε-Ti_2N sublayer. Figure 9 shows a typical EFTEM jump ratio images of Ti, N and Zr taken from the ε-Ti_2N sublayer. Underneath the Ti_2N sublayers, a nitrogen-rich α (N) solid solution was formed.

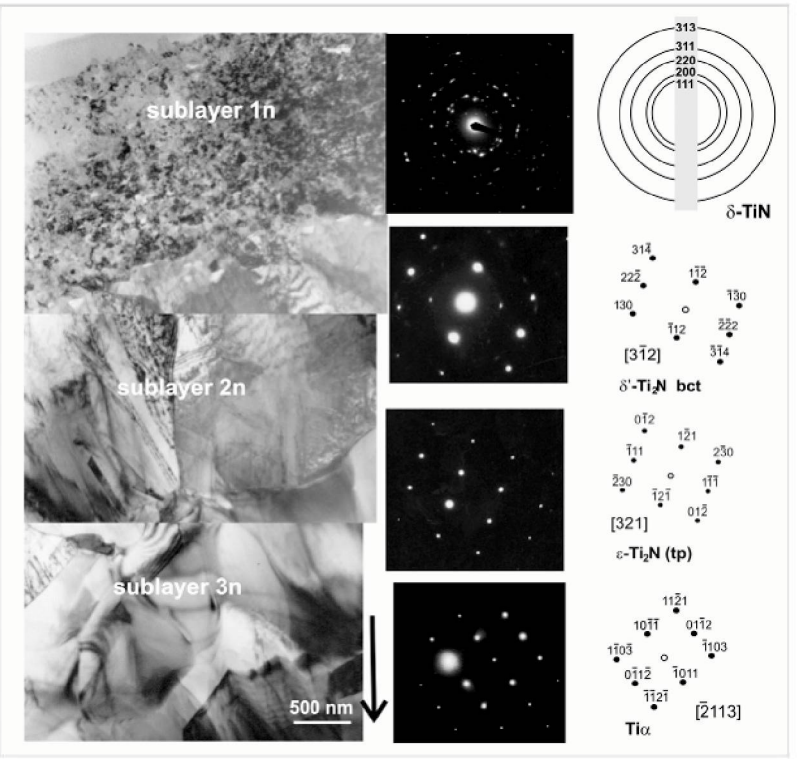

Figure 7. Microstructure of the nitrided TIMETAL 834; cross-section TEM BF image of the coating and corresponding SAED patterns taken from particular sublayers [27, 28].

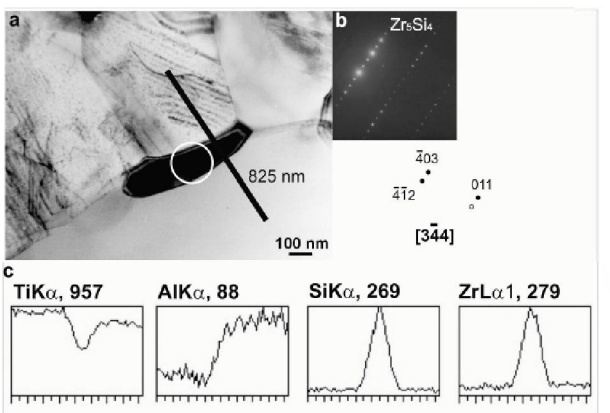

Figure 8. a) Zr_5Si_4 precipitate at the ε-Ti_2N grain boundary; b) corresponding SAED pattern and its identification; c) STEM-EDS linescane analysis along line marked on fig. a – nitrided coating on TIMETAL 834; cross-section thin foil, TEM [27].

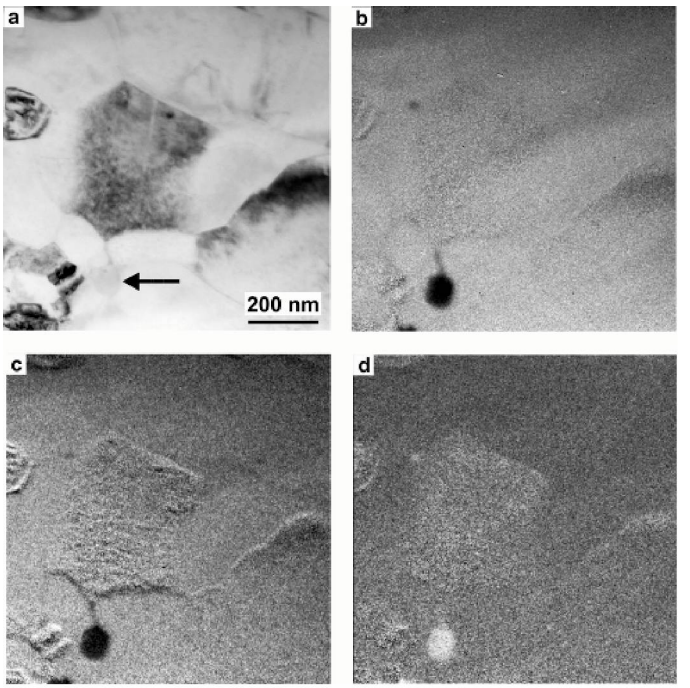

Figure 9. a) TEM BF zero-loss filtered image of the ε-Ti_2N sublayer; b) Ti $L_{2,3}$ jump ratio image; c) N K jump ratio image; d) Zr $M_{4,5}$ jump ratio image; arrow indicates the Zr_5Si_4 precipitate [27].

The intermediate layer, mainly nitrogen-rich α (N) solid solution, is composed of large grains enriched with N penetrating into fine α +β microstructure, which can be clearly seen in the LM image (Fig. 5b). This morphology contributes to a good adhesion of the nitrided coating to the substrate formed by diffusion under glow discharge on the underlaying substrate. Similar microstructure was found in our earlier studies on nitridation of two (α+β) phase Ti-6Al-4V alloy [25].

For a better understanding of the microstructure and the precise measurement of the nitrogen concentration in the nitrided coating, chemical and structural analyses by EELS were performed. It was found that the nitrogen percentage for the nitrided coating region decreases with increasing distance from the surface. Energy loss near-edge structures (ELNES) spectra were compared with experimental spectra of reference compounds. The EELS analysis of the nitrided coating show that the Ti-$L_{2,3}$ ionization edge is similar for all sublayers, whereas the shape of the N-K ionization edge is different for particular sublayers (Fig. 10). These changes in the N-K profiles are in good agreement with those observed by Hofer et. al. [65] in VN and V_2N as well as with calculated N-K spectra via the FEFF8 code for TiN_x as a function of x [66]. As described by Kihn et. al. [67] for values of the atomic concentration ratio $C_{N/Ti}$ between 0.75 and 1, the nitrides have the δ-TiN structure, for values of $C_{N/Ti}$ close to 0.5, the nitrides can be identified as involving the ε-Ti_2N structure. Our investigations show that for the first δ-TiN sublayer $C_{N/Ti}$ = 0.85, for the second and third: δ'-Ti_2N and ε-Ti_2N sublayer $C_{N/Ti}$ = 0.43÷0.56. In the nitrogen-rich α (N) solid solution sublayer $C_{N/Ti}$ = 0.12÷0.16. These EELS results confirm the phase identification in the nitrided coatings performed by SAED, EDS and EFTEM.

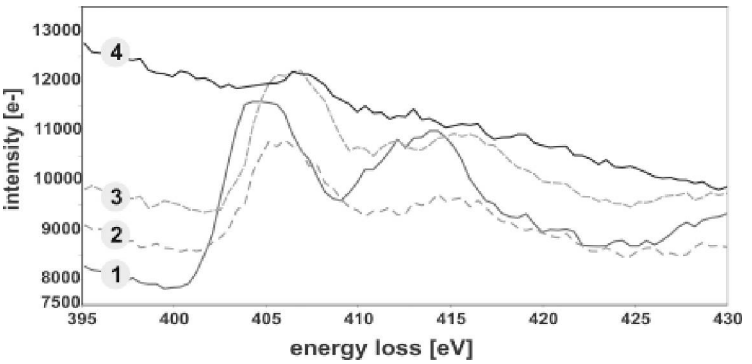

Figure 10. N-K edge profiles taken from different sublayers of the nitrided coating marked as 1- δ-TiN, 2- δ'-Ti_2N, 3- ε-Ti_2N, 4- α(N); TEM-EELS [27].

Micro-mechanical and Tribological Properties

The microhardness of baseline (forged) TIMETAL 834 was measured as 3.2 GPa (320 VHN), whereas the Young's modulus was 120 GPa. Figure 11 shows cross-section microhardness and Young's modulus profiles of the nitrided and oxynitrided coatings. It shows that both coatings exhibited a much higher microhardness than those of the untreated alloy. It should be noted that the nitrided coating shows considerably higher microhardness than the oxynitrided one. The highest microhardness is correlated with a presence of an outermost nanocrystalline δ-TiN sublayer of the nitrided coating. The Young's modulus also followed the same trend, as shown on Fig. 11.

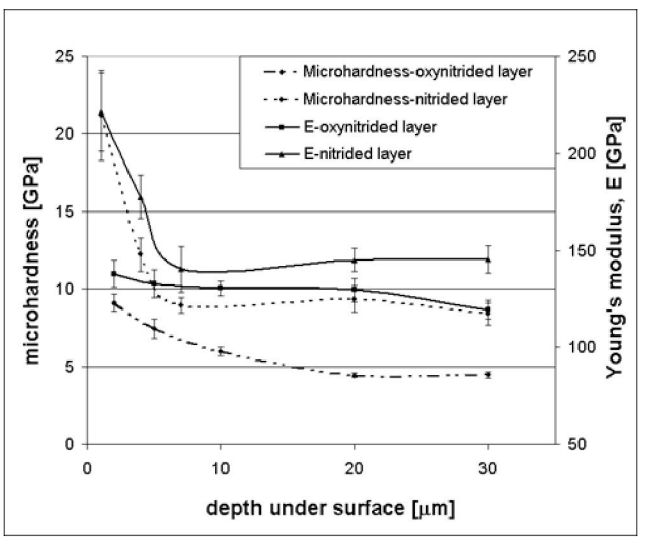

Figure 11. Microhardness and Young's modulus of the TIMETAL 834 alloy nitrided and oxynitrided under glow discharge [28].

The gradient character of the micro-mechanical properties of both nitrided and oxynitrided coatings result from a multicomponent character of these coatings, which are

consisting of different sublayers. It might be attributed to the different composition of the phases present in the sublayers established by analytical TEM investigations. An increase of the microhardness after nitridation is caused by the higher nitrogen concentration and the formation of new phases (δ-TiN, δ'-Ti_2N, and ε-Ti_2N) within the nitrided coating which were formed on the alloy substrate. Therefore, the detailed studies of the phase composition and microstructure after surface treatment were essential to understand the improvement of the mechanical and tribological properties of the alloy.

Friction wear resistant tests were carried out on the as received (untreated) and on the surface-treated samples by means of "ball-on-disc" method using a CSEM tribometer (according to ASTM G99-90 and ISO 20808 standards). Because of the relatively high microhardness of the Al_2O_3 ball used in the test, the wear of the investigated materials exhibited abrasive character. During friction, an accumulation of wear products on both track sides were observed. The track depth was measured as 10.5 μm in the case of the untreated alloy surface, while it was only 0.3 μm for the nitrided alloy and 0.4 μm for the oxynitrided one (Fig. 12). Surface treatment under glow discharge essentially improves the frictional wear resistance of the TIMETAL 834. Both, nitrided and oxynitrided alloys exhibited much better wear resistance than that of the untreated alloy. This is not only due to the much higher microhardness of the coatings, but also because of their different phase composition. The results obtained confirmed the previous findings obtained for other two phase titanium-based alloys [24,25]. The presence of TiN and Ti_2AlN phases contributed to high microhardness, while the Ti_2N phase is known for its excellent wear resistance [25].

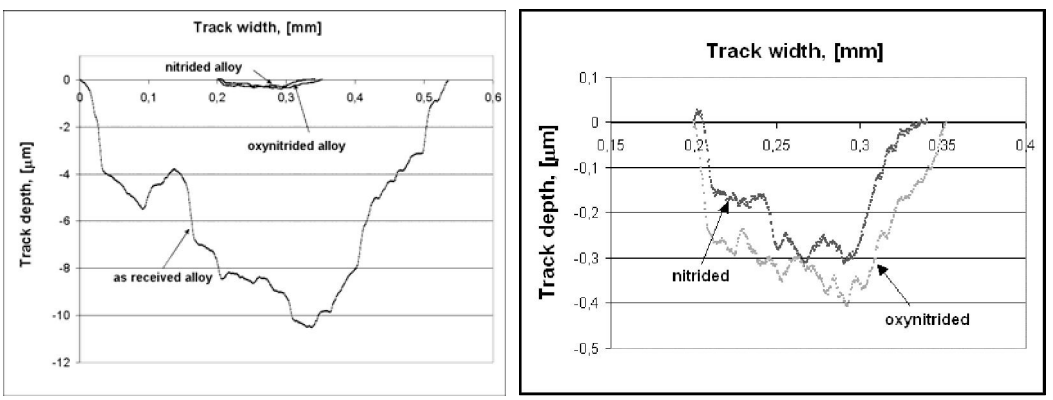

Figure 12. Frictional wear resistance of the TIMETAL 834 nitrided and oxynitrided under glow discharge compared with the wear of the untreated alloy (magnified details on right) [28].

4. Improvement of TIMETAL 834 Oxidation Resistance by Protective Coatings

The maximum service temperature of TIMETAL 834 is about 600°C. This limit is associated with the gradual decrease in creep resistance and reduction in ductility due microstructure instability, mainly silicide precipitation, and a poor oxidation resistance [16]. Numerous investigations have been carried out to improve oxidation resistance of titanium alloys at elevated temperatures (in the range of 600-800°C) [5-15, 19-21, 68-77]. The

oxidation resistance of titanium alloys can be improved by addition of alloying elements and coatings.

Oxidation Kinetics

Formation of an oxide scale on titanium alloys during oxidation at elevated temperatures maight be divided into four steps [5]:

- adsorption of oxygen at the surface,
- oxide nucleation,
- lateral growth of the nuclei,
- formation of a compact oxide scale.

Type and morphology of the oxide scale has an influence on mechanism of mass transport to varying extent:

- gas transport through cracks and voids,
- grain boundary diffusion,
- volume diffusion.

At low temperature, mass transport is predominantly influenced by grain boundary diffusion and by cracks and voids that may provide direct access of oxygen to the metal surface. At elevated temperatures, mass transport can be dominated by volume diffusion.

There are two fundamental effects relevant to the oxidation of titanium alloys, formation of an oxide scale and dissolution of non-metals in the subsurface zone of the alloys. Depending of the alloys, both phenomena may have different effects on the oxidation behavior and the mechanical properties of the alloy [5].

The formation of an oxide scale during oxidation of titanium alloys in elevated temperatures is mainly influenced by thermodynamics. The most important are high growth rate of TiO_2 (tp; rutile) in comparison to α-Al_2O_3 (trigonal primitive; alumina) and similar stabilities of TiO (fcc) and alumina. Rutile scale, rather than TiO one is found in practice, because the titanium monoxide is rapidly oxidized to the dioxide [5].

Oxidation of uncoated titanium alloys at elevated temperatures leads to formation of non-protective rutile scale, whereas oxidation of coated alloys leads to formation of the following scales:

- multilayered scale consists of mixture of alumina and rutile in varying proportions,
- alumina scale.

Sufficient oxidation resistance of titanium alloys can only be achieved by the formation of an alumina scale on the surface of the alloy.

Formation of an oxide scale depends on many parameters, such as alloy chemistry, exposure conditions (temperature, time) and oxidizing atmosphere. Other important parameter influenced on oxidation is alloy microstructure. For example, as described by

Leyens et al. [78], near-α TIMETAL 1100 alloy with a lamellar microstructure has a higher oxidation resistance than that with a bimodal one.

The effect of addition of alloying elements (besides Al, which is the most effective alloying element) is limited to selective formation and stabilization of the alumina scale or reduction of the growth rate of the mixed rutile and alumina scale. Si, Nb, W, Cr can reduce mass increase by oxide scale formation on titanium alloys.

A very prospective and the best way to improve the oxidation resistance of titanium alloys is surface treatment, which promotes the formation of highly protective alumina scale during oxidation.

The most important properties of the protective coatings are:

- oxidation resistance: the coating material must form a protective alumina-based scale,
- compactness and gas tightness: the coating must be free of cracks and pores, which are paths for the fast diffusion of aggressive components from the atmosphere to the substrate.

With regard to practical applications, the following key issues for the oxidation protection of titanium alloys have been identified: adhesion of the coatings to the substrate, long–term stability of the coating and degradation of the mechanical properties of the substrate [5]. The adhesion of a coating is mainly determined by deposition process. Coatings produced by "cold" processes, such as sputtering, often require bond layers or post-deposition heat treatment. Moreover, residual stresses as the consequence of the deposition process influence adhesion of the coatings. Cold process, such as magnetron sputtering may induces high compressive residual stresses in the coatings. The main source of stress in sputtered coatings is the deposition growth process. This type of residual stress is known as an intrinsic residual stress [79]. Its level depends on coating morphology and density, which are controlled by deposition conditions such as gas pressure, substrate bias and deposition temperature. Another source of residual stress is thermal gradient stress resulting from the mismatch in coefficients of thermal expansion (CTE) between the substrate and the coating. The CTE of coating material should be close to that of the substrate alloy. The compressive residual stress may cause coating spallation or lower the fatigue life of coated components. Therefore, the analysis of the residual stress level is especially important for the future in-life service of the protective coatings.

During exposure at elevated temperatures different coefficients of thermal expansion between substrate and coating as well as non-relaxed residual stress in the coating and formation of brittle intermetallic phases at the substrate-coating interface are of the great importance [5].

TiAl-X Intermetalic Coatings

Novel oxidation-resistant coating concepts for protection of titanium alloys are based on coatings from the TiAl-X system (where "X" is additional element as Cr, Hf, Nb, Si, Ag, Ta or W) [5,9-12,14,15]. Various additional elements "X" improve the oxidation resistance of TiAl coatings by increasing the diffusivity of the Al atoms in the coatings, what facilitate preferential nucleation of the protective γ-Al_2O_3 phase on the coating surface [9,10] and

decreasing of the oxidation growth of the non-protective TiO_2 rutile scale. The intermetallic phases of the Ti-Al system have been considered because they offer a good combination of high oxidation resistance and useful mechanical properties at temperatures higher than those possible with conventional titanium alloys [9-11,13]. The TiAl-X coatings are less brittle and have higher ductility than the γ-TiAl coatings. Therefore, in order to improve the oxidation resistance of the TIMETAL 834 alloy we selected for our studies the γ-TiAl coatings with Ag and/or Si addition. The micro/nanostructure characterization of coatings is very complex and best performed by advanced TEM. Advanced TEM provides detailed structural-, phase- and crystallographic data which allows for explanation, quantification and tailoring of the coating micro/nanostructure.

The goal of our investigations [19,20] was a detailed characterisation of micro/nanostructure and chemical composition as well as residual stress analysis of the intermetallic TiAl(Si,Ag) and TiAl-Ag coatings produced on TIMETAL 834 alloy by reactive magnetron sputtering as well as on influence of applied surface treatment on the alloy oxidation resistance. In order to unequivocal microstructure characterisation and detailed identification of phases present in the protective coatings, analytical TEM investigations were performed on the cross-section thin foils prepared by Focused Ion Beam (FIB). The phase identifications were carried out using SAED, EDS and EELS. These complementary methods allow for very precise and detailed characterisation of the coatings microstructure.

Typical microstructure of both investigated intermetallic TiAl-X coatings are shown on Figs 13,14. The SEM and TEM investigations revealed that both coatings are composed of two sublayers with a different microstructure (marked in Figs 13,14 as Sublayers 1A and 2A for TiAl-Ag coating as well as Sublayers 1B and 2B for TiAl(Si,Ag) coating). The total thickness of the TiAl-Ag coating was estimated as 7 μm (Fig. 13), while the TiAl(Si,Ag) coating as 3.5 μm (Fig. 14). Both coatings were dense and very uniform in thickness.

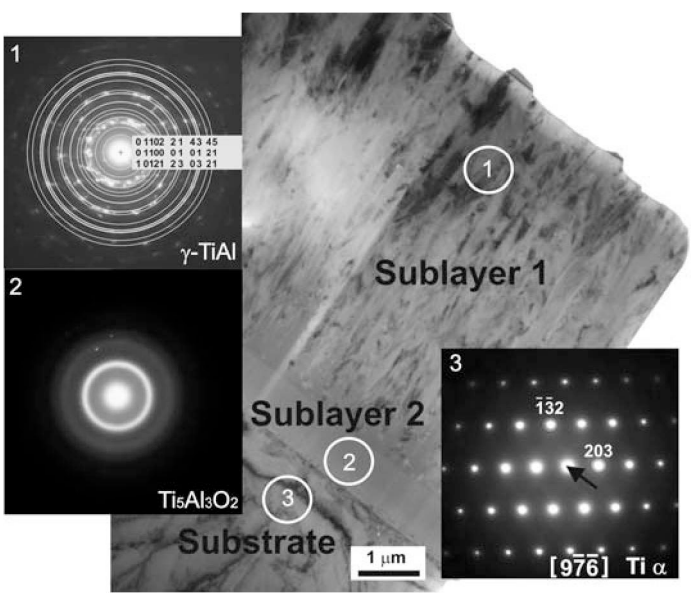

Figure 13. Microstructure of the TiAl-Ag coating on TIMETAL 834 and corresponding SAED patterns taken from the areas marked and their identification; TEM-Bright Field image, cross-section thin foil [19].

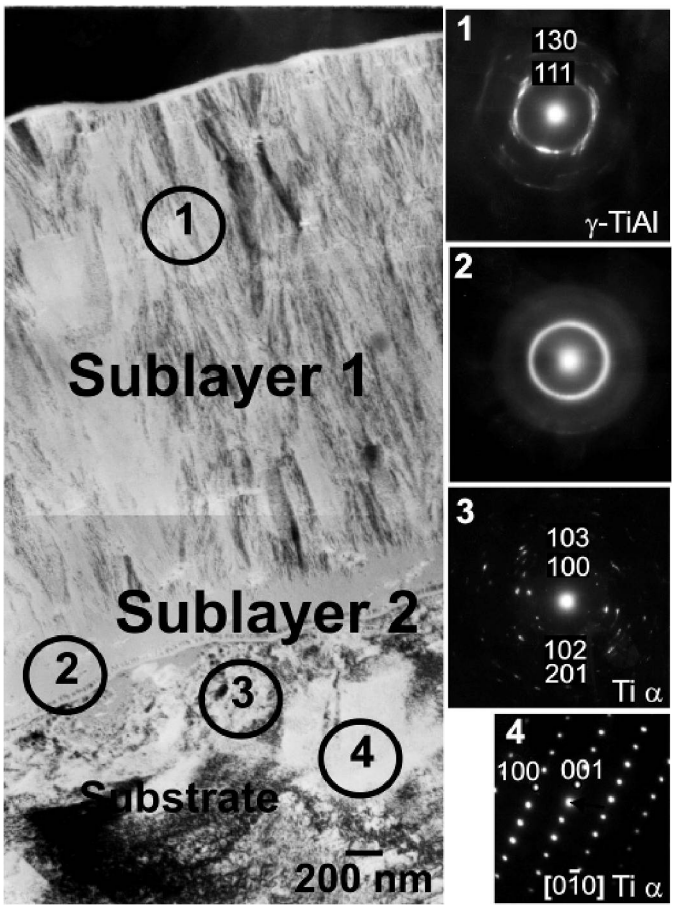

Figure 14. Microstructure of the TiAl(Si,Ag) coating on TIMETAL 834 and corresponding SAED patterns taken from the areas marked as 1–4 (area 1 — Sublayer 1; area 2 — Sublayer 2;areas 3–4 — substrate) and their identification; TEM-BF, cross-section thin foil [20].

Results of SEM-EDS analysis on the TiAl-Ag coating performed on specimens' cross-sections indicated that Sublayer 1A was highly enriched in Ti and Al, containing low concentration of Ag. With the increasing depth under the surface Ti content increased from 37 to 49 at.%, while Al content decreased from 60 to 49 at. %. Ag content was approximately constant within Sublayer 1A and equals 1.7–1.9 at. %. Sublayer 2A was highly enriched in Ti and O and contained only a little amount of Al. Measurements of the chemical composition in the Sublayer 2A performed by TEM-EELS revealed the following chemical composition 51.6 at.% Ti, 29.4 at.% Al and 18.9 at.% O.

Results of SEM-EDS analysis of the TiAl(Si,Ag) coating showed that Ti content increases from 44 to 57.5 at.%, while Al content decreases from 48.2 to 36.4 at.% with the increase depth under the surface. Also Si and Ag content slightly decreased with the increase of the depth under the surface (from 6.3 to 5 at.% for Si and from 1.5 to 1.1 at.% for Ag).

Detailed TEM analyses revealed that the outermost Sublayers 1A and 1B of both coatings identified by electron diffraction as γ-TiAl (tp), show a columnar morphology. In the Sublayer 1A, some $TiAl_2$ (orthorhombic primitive; op) was also found.

These results agree well with findings documented for similar coatings in the literature [9]. The evolution of columnar structure of the TiAl(Si,Ag) and TiAl-Ag coatings can be interpreted in terms of structure zone models (SZM) [80-82]. In this model microstructural features are classified among three different zones (Zones 1-3) and depend on processing parameters as deposition temperature, pressure and ion bombardment. The great importance is the deposition temperature. According to the SZM model when the homologous temperature T_s/T_m (where T_s is the substrate temperature during coating processing and T_m is the melting point of the film material) is in the range between 0.3 and 0.5 the coating consists of columnar grains separated by distinct, dense, intercrystalline boundaries (Zone 2) [80,81]. In our work, the homologous temperature during magnetron sputtering was about 0.21, what is in not good agreement to SZM and indicates also for strong influence of other deposition parameters as pressure and ion bombardment.

Both, the Sublayers 2A and 2B have an amorphous structures [18,19]. The Sublayer 2A is composed mainly of $Ti_5Al_3O_2$ phase (cubic primitive; cp), while the Sublayer 2B is composed of γ-TiAl (tp). The amorphous structure of coatings produced by magnetron sputtering is often described in a literature [10,83,84]. Formation of the amorphous structure in the Sublayer 2 might be explained by gradual stabilizing of deposition parameters (e.g. substrate temperature, power of magnetrons) at the first stage of the coating processing.

The adhesion of the coating to the substrate material is its basic characteristic, which should be taken into account for different applications. If the adhesion is insufficient, premature failures may result from detachment of the coating by interfacial fractures. The adhesion of the TiAl(Si,Ag) coating to TIMETAL 834 substrate was evaluated by a scratch test conducted in accordance to a standard procedure [85]. The applied load, tangential force, penetration depth and acoustic emission were recorded simultaneously. The acoustic emission (AE) from the surface of the sample can be used to obtain information about fracture of the coating under the indenter loading. The smallest value of the load corresponds to first fracture of the coating or delamination, registered as an abrupt increase of the intensity of the AE on the (AE, scratch length) diagram. The corresponding value of the load Lc_1 is an important micro-mechanical parameter of the coating, referred to as Critical Load Lc_1 [85].

Initially during scratch test of the coated TIMETAL 834, under load of 3 N, small area perforation inside scratch truck has been observed. Under load of 9 N first cohesive cracks along the scratch truck borders have appeared (Fig. 15). The scratch test was also performed for coated TIMETAL 834 after oxidation at 800°C for 300 h in air. In this case, cohesive cracks were not observed. The first cracks (shell shaped) on the side surface of the scratch truck were observed under the load of about 16 N.

Measurements of microhardness and Young's modulus have been carried out on cross-section specimens using MCT with Vickers intender. The microhardness of baseline TIMETAL 834 was measured as 3.3 GPa (VHN), while the Young's modulus as 120 GPa. Figure 8 shows microhardness and Young's modulus of the coated TIMETAL 834 as a function of depth from the surface. It shows that the microhardness and Young's modulus of the coated TIMETAL 834 decreased with increase of the distance from the specimen surface. This is due to changes in a microstructure and chemical composition of the coating, composed of two different sublayers.

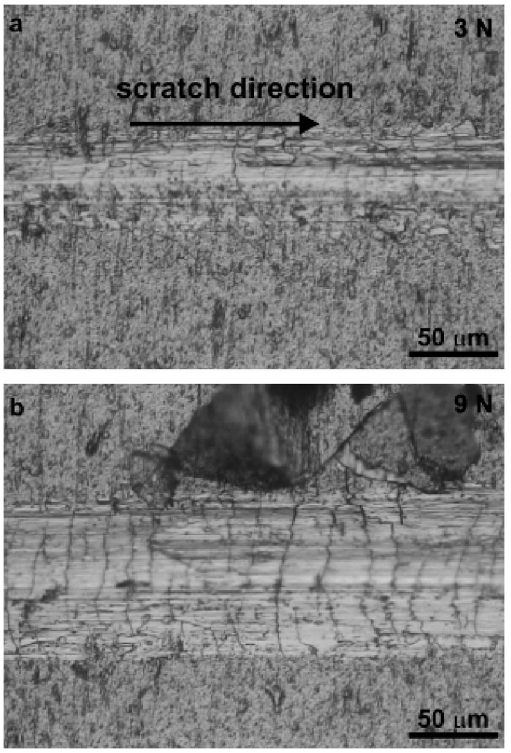

Figure 15. The surface of TiAl(Si,Ag) coating after scratch test with the load of 3 N (a) and 9 N (b); LM [20].

Understanding of basic processes as residual stresses between substrate and coating is a necessary requirement for the development of coatings which guarantee long-life and suitable properties of the whole system. The residual stresses were evaluated for the substrate and for the γ-TiAl sublayer of the coatings by energy dispersive diffraction experiment using white beam synchrotron radiation. Details are given in Refs [19,20]. A compressive stress of -525±20 MPa was obtained for γ-TiAl sublayer of the TiAl(Si,Ag) and – 350±20 MPa for γ-TiAl sublayer of the TiAl-Ag.

Glass-Ceramic Coating

Oxide based glass- and glass-ceramic coatings with excellent chemical inertness, high temperature stability and superior mechanical properties are very promising materials for protection of titanium alloys against oxidation at elevated temperature [18,86-89]. Their processing by a simple and inexpensive slurry method is an excellent method to manufacture reproducibly protective coatings with complex and homogenous chemical composition, uniform morphology and coating thickness [16,17].

The other important advantageous of glass-ceramic based coatings is availability of many glass-ceramic compositions. Thus, it is easy to formulate suitable coating composition that will have similar thermal behavior with that of the substrate, which ultimately minimize a possibility of spallation of the coating during thermal cycling and formation of the coating defects [89]. The SiO_2-Al_2O_3-CaO-Na_2O glass-ceramic was chosen for protection of

TIMETAL 834 against oxidation because has nearly the same CTE as TIMETAL 834 alloy. CTE of glass-ceramic is 10.7×10^{-6} °C^{-1} [16], whereas of TIMETAL 834 is 10.6×10^{-6} °C^{-1} (20-200°C) [2].

The cross-section of the coated TIMETAL 834 as seen by SEM is shown on Fig. 16. SEM observations showed that no changes in the base alloy microstructure were introduced during coating deposition. The coating thickness, evaluated by LM and SEM, was approx. 300 μm (Fig. 16). The microstructure of the glass-ceramic based SiO_2-Al_2O_3-CaO-Na_2O coating is presented on Figure 17. The results of the SEM-EDS analyses of the coating performed on the sample cross-section revealed a presence of two areas with different chemical compositions. In the areas marked as 1 and 2 (Fig. 17), the following chemical compositions (in at. %) were found: 55 O, 25 Si, 11 Ca, 9 (Al + Na) for area 1 and 55 O, 22 Si, 10 Na, 7 Ca, 6 Al for area 2.

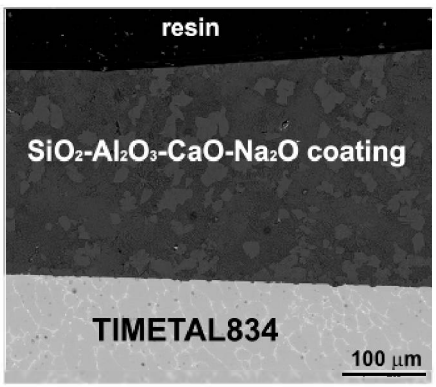

Figure 16. Cross-section of SiO_2-Al_2O_3–CaO-Na_2O coating on TIMETAL 834 substrate, SEM electron back scattered image [21].

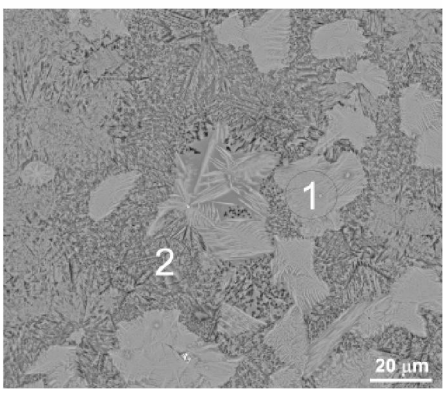

Figure 17. Microstructure of the SiO_2-Al_2O_3–CaO-Na_2O coating, SEM electron back scattered image [21].

Microstructure and phase composition of the coatings were characterised by analytical TEM on cross-section thin foils. Phase identification performed by electron diffraction confirmed XRD analysis and revealed a presence of the following crystalline phases: $CaSiO_3$ (monoclinic primitive; mp), $NaAlSiO_4$ (hcp) and Na_2CaSiO_4 (cp) (Fig. 18). Additionally, the

amorphous phase containing 50 O, 30 Si, 15 Al, 5 (Ca+Na) (in at. %) was found. The electron diffraction pattern taken from amorphous phase is shown in Fig. 18 (up-left corner).

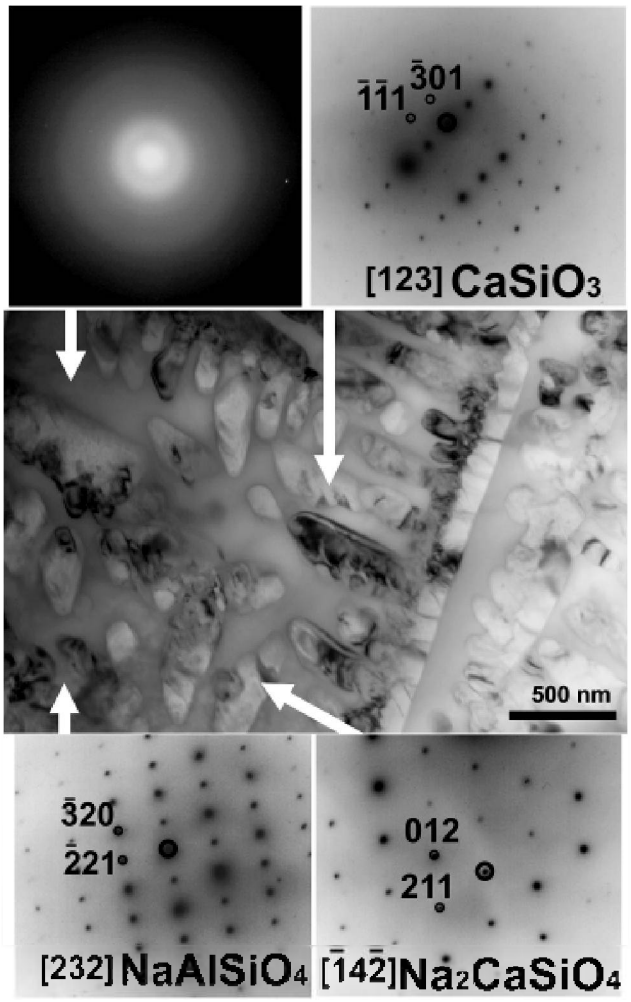

Figure 18. Microstructure of the SiO_2-Al_2O_3–CaO-Na_2O coating on TIMETAL 834 as well as SAED patterns and their identification, TEM, cross-section thin foil [21].

These results are in good agreement with the results of STEM-EDS element distribution investigations. Typical STEM-EDS element distribution images results are presented in Fig. 19. Three distinct phases are distinguished:

(i) a phase containing mainly Ca, Si, O and some Na,
(ii) a phase containing Si, Al and O,
(iii) a phase containing Ca, Si and O.

TEM analysis of the coating close to the substrate (up to 2 μm above the substrate surface) revealed a presence of areas containing mainly an amorphous phase.

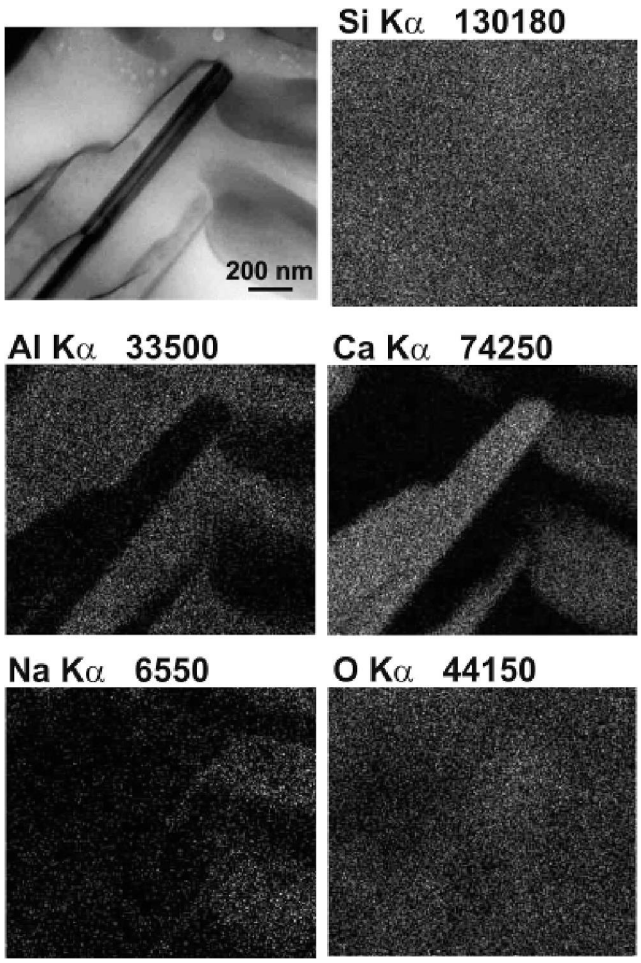

Figure 19. Elemental distribution images in the SiO_2-Al_2O_3–CaO-Na_2O coating on TIMETAL 834; STEM-EDS, cross-section thin foil [21].

The adhesion of the SiO_2-Al_2O_3-CaO-Na_2O glass-ceramic based coating to TIMETAL 834 substrate was evaluated by a scratch test, described earlier. The first cohesive cracks along the scratch track borders have appeared under the intender load of 15 N. Under the load of 23 N, small perforation areas inside the scratch track have been observed. The results of the scratch test showed that neither flaking nor delamination occurred in the SiO_2-Al_2O_3–CaO-Na_2O coating during testing under a load of 30 N, what indicated for a good coating adhesion to the substrate.

In order to determine the effect of the applied surface treatment on the selected mechanical properties, measurements of microhardness and Young's modulus were carried out on cross-section specimens with use of the MCT with Vickers indenter. It has been found that the coating exhibits about 3 times higher microhardness than that of the substrate. The mean microhardness of the coating was measured as 12.7±0.3 GPa (VHN). The Young's modulus of the coating and the substrate were very similar and equal to 122±17 GPa and 121±9 GPa, respectively.

Oxidation Resistance

The main problem for application of TIMETAL 834 alloy at temperature above 600°C is its poor oxidation resistance. Therefore, an oxidation test and detailed characterisation of scale microstructure were applied. The oxidation test was performed at 800°C for 300h in the static air at normal pressure. The microstructure of the baseline (uncoated) and surface treated TIMETAL 834 after oxidation test was investigated by SEM, TEM and XRD. It was found that the very brittle scale (approx. 11 μm thick) formed during oxidation on the uncoated alloy consists of TiO_2 (rutile, tetragonal primitive (Fig. 20a).

It was found during XRD analyses that the scale formed on the coated alloy is composed mainly of α-Al_2O_3 (trigonal primitive) and TiO_2 rutile (tetragonal primitive). Also Ti_3Al (hcp) and α Ti (hcp) were identified.

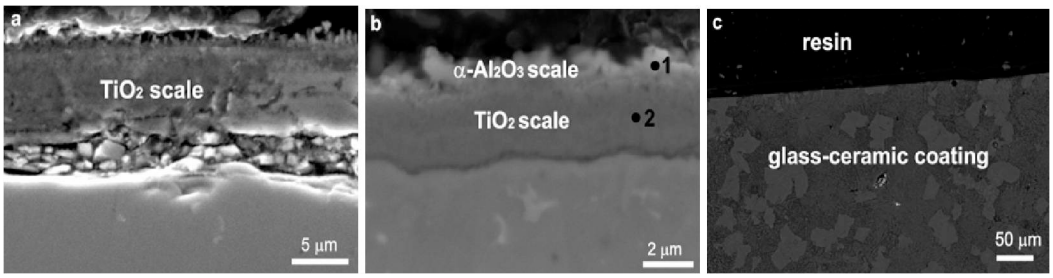

Figure 20. a) Microstructure of the TiO_2 (rutile) scale formed on uncoated TIMETAL 834 [20] b) Microstructure of the scale formed on the TiAl(Si,Ag) coated TIMETAL 834 [20] c) SiO_2-Al_2O_3–CaO-Na_2O coating on TIMETAL 834 after oxidation test, SEM.

Typical microstructure of the coated TIMETAL 834 after oxidation in air at 800°C/300h is shown on Figure 20b (TiAl(Si,Ag) coating) and Figure 20c (glass-ceramic coating). SEM and analytical TEM investigations of the TiAl(Si,Ag) coated alloy showed that the scale (about 3 μm thick) is consisting of two sublayers with different morphology and chemical composition. The results of SEM-EDS revealed following chemical composition:

(i) outer sublayer: 28.2 at. % Al, 64.5 at. % O, 6.9 at. % Ti and small amount (less than 0.25 at. %) of Si, Zr and Ag (point 1 on Figure 20b), what indicates for a presence of mainly Al_2O_3 phase,
(ii) inner sublayer: 62.1 at% O, 33.5 at. % Ti, 2.75 at. % Si, 1 at. % Al and 0.65 at. % Zr (point 2 on Figure 20b), what indicates for TiO_2 phase.

Detailed analytical TEM phase identification performed by SAED and TEM-EDS confirmed that a multilayered scale consists of α-Al_2O_3 (trigonal primitive) on the top of TiO_2 rutile scale. The α-Al_2O_3 (about 0.5 μm thick) consists of grains in the range from 200 to 600 nm, while the TiO_2 (about 2.5 μm thick) has a nanocrystalline structure (Fig. 21). STEM-EDS line analysis also confirmed enrichment of Al and O in the outer sublayer as well as Ti and O enrichment of inner sublayer of the scale. It was found that microstructure of the material under the scale was composed with Ti_3Al (hcp). Directly under the scale, a region of Ti_3Al (up to 2 μm thick) with Zr_5Si_4 (tp) precipitates was observed. The average size of precipitates

was estimated to 40-250 nm. The presence of Zr_5Si_4 precipitates was also confirmed by STEM-EDS line analysis.

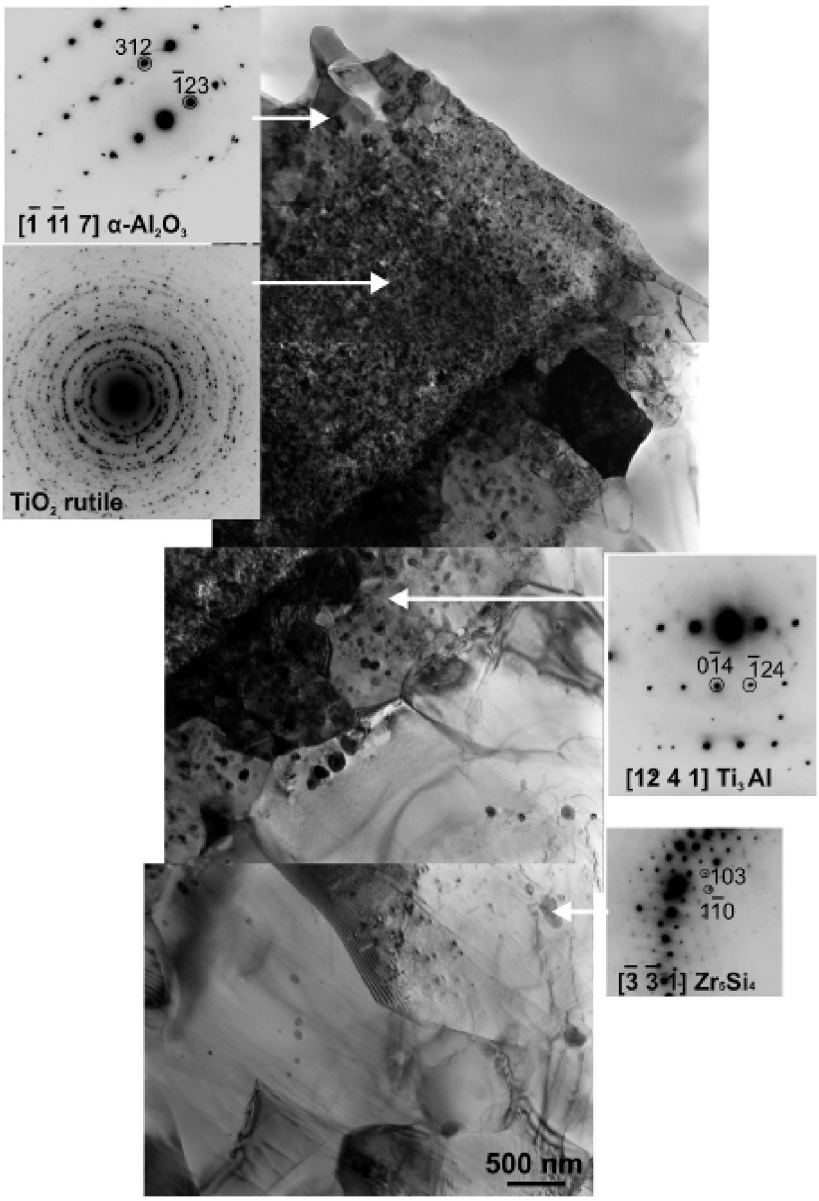

Figure 21. Microstructure of the coated TIMETAL 834 after oxidation at 800 °C during 300 h in air and corresponding SAED patterns taken from the areas indicated by arrows and their identification; TEM-BF, cross-section thin foil [20].

A comparison of the oxidation behaviour of the TiAl(Si,Ag) and glass-ceramic coated specimens of the TIMETAL 834 alloy with that of an uncoated one during oxidation tests in static air at 800°C is shown in Fig. 22. In comparison with the uncoated specimen at a constant temperature, the weight gain was reduced by more than 50% for the TiAl(Si,Ag) coated specimen, while no weight gain was observed for glass-ceramic coated samples.

Moreover, oxide scale spallation occurred for uncoated alloy, while coated alloy did not show any spallation.

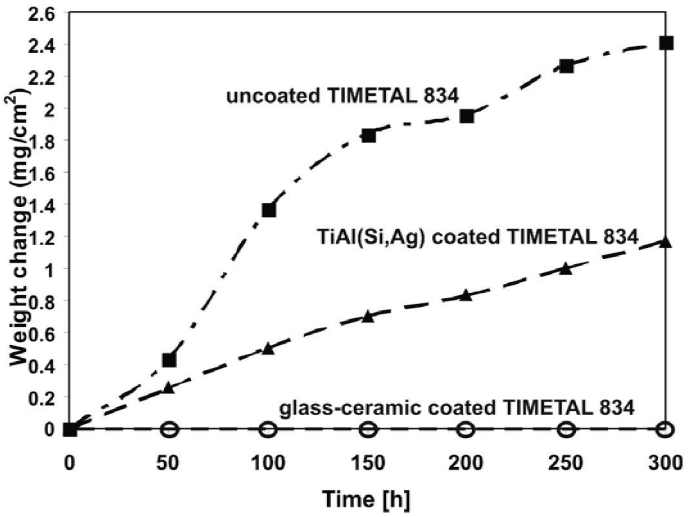

Figure 22. Results of oxidation tests on uncoated, TiAl(Si,Ag) and glass-ceramic coated TIMETAL834, (800°C/air) [20,21].

It was found in numerous earlier studies [5,9,11,15,90] that the magnetron-sputtered microalloyed (Cr or Nb or Ta or Mo or Ag or Si) γ-TiAl coatings are promising for protection of elements made from titanium alloys against oxidation in air (above 600°C). The improvement of oxidation resistance of TiAl(Si,Ag) coated TIMETAL 834 is mainly due to a positive influence of the Si addition on decreasing of the oxidation growth of TiO_2 rutile scale.

From the results of oxidation tests it is very clear that the glass-ceramic coated alloy shows a remarkable improvement in the resistance to oxidation of the TIMETAL 834 alloy in static air at 800°C.

5. Conclusions

Elevated-temperature near-α titanium alloys are used in aeronautics for gas turbine engine components. The high volume fraction of α (hcp) phase, addition of solid solution strengthening elements and silicon allow for using of these alloys up to 600°C. This limit in applications at temperatures above 600°C is associated mainly with the gradual decrease in creep resistance and a poor oxidation resistance. Besides poor oxidation resistance, the application of titanium-based alloys is limited also by their relatively low hardness and poor tribological properties.

In order to improve mechanical, tribological properties and oxidation resistance of near-α TIMETAL 834, protective coatings were deposited. For tribological properties, nitrided and oxynitrided coatings were applied, whereas for improvement of oxidation resistance, the TiAl-Ag, TiAl(Si,Ag) and glass-ceramic SiO_2-Al_2O_3-CaO-Na_2O were deposited.

Tribological coatings. The multilayers formed on the TIMETAL 834 by diffusion under glow discharge revealed a complex microstructure. The nitrided coating consists of four sublayers: δ-TiN, δ'-Ti_2N, ε-Ti_2N, and nitrogen-rich α (N) solid solution. The oxynitrided multilayer consists of three sublayers: TiO, ε-Ti_2N, and α (N). The Zr_5Si_4 precipitates are present in both coatings. EELS investigations show a graded character of the nitrided layers with continuously varying nitrogen content.

The nitrided coating has significantly higher microhardness than the oxynitrided one and revealed a high gradient of microhardness. The highest microhardness is related to the presence of a nanocrystaline δ-TiN sublayer. Surface treatment under glow discharge essentially improves the frictional wear resistance of the TIMETAL 834. Both nitrided and oxynitrided alloys exhibited much better wear resistance than that of the untreated alloy. This is not only due to the much higher microhardness of the coatings, but also because of their different phase composition.

Oxidation resistant coatings. The protective TiAl-Ag and TiAl(Si,Ag) coatings produced on TIMETAL 834 by magnetron sputtering consist of two different sublayers. The outer sublayer contained mainly γ-TiAl and some Ti_3Al or $TiAl_2$, while the inner one contained mainly γ-TiAl (in the case of TiAl(Si,Ag) coating) and $Ti_5Al_3O_2$ (in the case of TiAl-Ag coating). The outer sublayer had a columnar structure, whereas the inner one exhibited an amorphous structure.

Investigated TiAl-X coating has significantly higher microhardness than the baseline alloy. The results of the residual stress analysis showed that tensile residual stresses are present within the TIMETAL 834 substrate, while there are compressive residual stresses within the γ-TiAl sublayer.

The SiO_2-Al_2O_3-CaO-Na_2O glass-ceramic produced by a slurry technique on the TIMETAL 834 alloy is composed of the crystalline phases: $CaSiO_3$, $NaAlSiO_4$, Na_2CaSiO_4 and amorphous phase (containing mainly O, Si and Al). The surface treated alloy has significantly higher microhardness than the virgin alloy, whereas the values of the Young's moduli of the coating and of the substrate are very similar.

Both, TiAl-X and glass-ceramic coatings significantly improve the oxidation resistance of the TIMETAL 834. The glass-ceramic coating is an excellent oxidation protection barrier for the TIMETAL 834 alloy at elevated temperatures (up to 800°C). No weight change of the glass-ceramic coated alloy was observed after 300 hours at 800°C in contrast to an important weight change for the uncoated specimens.

Analytical scanning and transmission electron microscopy methods are excellent tools for a detailed characterisation of a microstructure and phase chemical composition of the protective coatings.

Acknowledgments

This work was supported in part by the EU Network of Excellence project Knowledge-based Multicomponent Materials for Durable and Safe Performance (KMM-NoE) under the contract no. NMP3-CT-2004-502243.

Part of this study concerning microstructure of TIMETAL 834 was supported by the Polish Ministry of Science and Higher Education (MNiSW, project no. N N507 278436).

A part of this study has been performed under bilateral cooperation agreement between the AGH University of Science and Technology and the Politecnico di Torino (MNiSW, no. 183/N-Włochy/2008/0).

The authors appreciate a valuable contribution of Prof. T. Wierzchoń (Warsaw University of Technology), Prof. B. Wendler (Lodz University of Technology), Dr F. Smeacetto (Politecnico di Torino) to coating processing, Prof. W. Ratuszek (AGH-UST) to the XRD investigations, Prof. F. Hofer and Prof. W. Grogger (TUG) to the EELS/EFTEM investigations as well as Prof. W. Rakowski, Dr.M. Kot, and Dr. S. Zimowski (AGH-UST) to mechanical/tribological tests.

References

[1] Peters, M., Kumpfert, J., Ward, C.H., Leyens, C. In : *Titanium and titanium alloys;* Leyens, C., Peters, M.; Ed.; WILEY-VCH Verlag GmbH & Co. KGaA, Weinheim, 2003; pp. 333-350.

[2] *http://www.timet.com.*

[3] Eylon, D., Fujishiro, S., Postans P.J., Froes, F.H. *J. Metals* 1984, 11, 55-62.

[4] Collinge, E.W. In: *Mechanical properties data handbook: Titanium alloys*; Boyer, R., Collings, E.W., Welsch, G.; Ed.; ASM International, Materials Park, OH, USA, 1994; p. 77.

[5] Leyens, C. In *Titanium and titanium alloys*; Leyens, C., Peters, M.; Ed.; WILEY-VCH Verlag GmbH & Co. KGaA, Weinheim, 2003; pp. 187-223.

[6] Trivedi, S.P., Das, D.K. *Intermetallics* 2005, 13, 1122–1133.

[7] Leyens, C., Peters, M., Hovsepian, P.Eh., Lewis, D.B., Luo, Q., Münz, W.-D. *Surf. Coat. Technol.* 2002, 155, 103–111.

[8] Gurrappa, I., Gogia, A.K. *Surf. Coat. Technol.* 2001, 139, 216-221.

[9] Wendler, B.G., Kaczmarek, Ł. *J. Mater. Process. Technol.* 2005, 164–165, 947-953.

[10] Kaczmarek, L., Wendler, B.G., Siniarski, D., Rylski, A., Bieliński, D., Dobrowolski, O., Lipiński, P. *Surf. Coat. Technol.* 2007, 201, 6167-6170.

[11] Leyens, C., Peters, M., Kaysser, W.A. *Mater. Sci. Forum* 1997, 251-254, 769-776.

[12] Tang, Z., Niewolak, L., Shemet, V., Singheiser, L., Quadakkers, W.J., Wang, F., Wu, W., Gil, A. *Mater. Sci. Eng. A* 2002, 328, 297-301.

[13] Romankov, S., Sha, W., Kaloshkin, S.D., Kaevitser, K. *Surf. Coat. Technol.* 2006, 201, 3235-3245.

[14] Fox-Rabinovich, G.S., Wilkinson, D.S., Veldhuis, S.C., Dosbaeva, G.K., Weatherly, G.C. *Intermetallics* 2006, 14, 189-197.

[15] Fröhlich, M., Braun, R., Layens, C. *Surf. Coat. Technol.* 2006, 201, 3911-3917.

[16] Smeacetto, F., Salvo, M., Ferraris, M., Cho, J., Boccaccini, A.R. *J. Eur. Ceram. Soc.* 2007, 28, 61-68.

[17] Góral, M., Moskal, G., Swadzba, L. *J. Achiev. Mater. Manuf. Eng.* 2006, 18, 463-466.

[18] Das, S., Mukhopadhyay, A.K., Datta, S., Das, G.C., Basu D. *J. Eur. Ceram. Soc.* 2008, 28 729-738.

[19] Moskalewicz, T., Schaffer, B., Manescu, A., Rustichelli, F., Czyrska-Filemonowicz, A. *Surf. Coat. Technol.* 2007, 201, 7635–7640.

[20] Moskalewicz, T., Wendler, B., Smeacetto, F., Salvo, M., Manescu, A., Czyrska-Filemonowicz, A. *Surf. Coat. Technol.* 2008, 202, 5876–5881.
[21] Moskalewicz, T., Smeacetto, F., Czyrska-Filemonowicz, A. *Surf. Coat. Technol.* 2009, 203, 2249–2253.
[22] Wierzchoń, T. *Mater. Sci. Forum* 2003, 426-432, 2563-2568.
[23] Sobiecki, J.R., Wierzchoń, T. *Vacuum* 2005, 79, 203-208.
[24] Czyrska-Filemonowicz, A., Łucki, M., Buffat, P.A., Moskalewicz, T., Lekki, J., Wierzchoń, T. *Arch. Mater. Sci.* 2005, 26, 79-88.
[25] Czyrska-Filemonowicz, A., Buffat, P.A., Łucki, M., Moskalewicz, T., Rakowski, W., Lekki, J., Wierzchoń, T. *Acta Mater.* 2005, 53, 4367-4377.
[26] Molinari, A., Straffelini, G., Tesi, B., Bacci, T., Pradelli, G. *Wear*, 1997, 203–204, 447-454.
[27] Moskalewicz, T., Grogger, W., Czyrska-Filemonowicz, A. *J. Microsc.* 2006, 223, 195-199.
[28] Moskalewicz, T., Czyrska-Filemonowicz, A. *Int. J. Mat. Res.* 2006, 97, 1059-1066.
[29] Moskalewicz, T., Zimowski, S., Kitano, Y., Wierzchoń, T., Czyrska-Filemonowicz, A. *Kovove Mat.* 2006, 44, 133-138.
[30] Gogia, A.K. *Def. Sci. J.* 2005, 55, 149-173.
[31] Partridge, A., Li., Y.G., Loretto, M.H., Voice, W., Rugg, D. In: *Proc. 5th International Charles Parsons Turbine Conference*; Strang, A. et al.; Ed.; Cambridge, July 2000; pp. 798-810.
[32] Leyens, C., Liere, J.-W. van, Peters, M., Kaysser, W.A. *Surf. Coat. Technol.* 1998, 108-109, 30-35.
[33] Thomas, M.J., Wynne, B.P., Rainforth, W.M. *Mater. Char.* 2005, 55, 388-394.
[34] Wood, J.R., Russo, P.A. *Industrial heating*, 1997, *April issue*, 51-55.
[35] Freese, H.L., Volas, M.G., Wood, J.R. In: *Titanium in medicine;* Brunette, D.M., Tengvall, P., Textor, M., Thomsen, P.; Ed.; Springer-Verlag Berlin Heidelberg New York, 2001; pp 26-49.
[36] Cahn, R.W., Haasen, P., Kramer, E.J. In: *Materials Science and Technology, A Comprehensive Treatment*; Matucha, K.H.; Ed.; Weinheim, New York, Cambridge, Tokyo, VCH 1996; Vol. 8, pp 403-412.
[37] Peters, M., Hemptenmacher, J., Kumpfert, J., Leyens, C. In: *Titanium and titanium alloys;* Leyens, C., Peters, M.; Ed., WILEY-VCH Verlag GmbH & Co. KGaA, Weinheim, 2003, pp. 1-36.
[38] Wagner, L. In *Titanium and titanium alloys*; Leyens, C., Peters, M.; Ed., WILEY-VCH Verlag GmbH & Co. KGaA, Weinheim, 2003, pp. 153-185.
[39] Yilbas, B.S., Sunar, M., Gasem, Z., Abdul Aleem, B.J. *J. Mater. Sci. Technol.* 2009, 209, 1199–1208.
[40] Wang, Y., Wang, H.M. *App. Surf. Sci.* 2004, 229, 81–86.
[41] Pang, X., Shi, L., Wang, P., Zhang, G., Liu, W. *Surf. Coat. Technol.* 2009, 203, 1537–1543.
[42] Navaneethakrishnan, P., Ganesh Sundara Raman, S., Pathak, S.D., Gnanamoorthy, R., Ravi N. *Surf. Coat. Technol.* 2009, 203, 1205–1212.
[43] Hampshire, J., Kelly, P.J., Teer, D.G. *Th. Sol. Films* 2004, 447 –448, 392–398.

[44] Guo, B., Zhou, J., Zhang, S., Zhou, H., Pu, Y., Chen, J. *Surf. Coat. Technol.* 2008, 202, 4121–4129.
[45] Abdel-Aal, H.A., Nouari, M., Mansori, M. El. *Trib. Int.* 2009, 42, 359–372.
[46] Ouyang, J-H., Sasaki, S., Murakami, T., Zhou, Y., Zhang J. *Wear* 2009, 266, 96–102.
[47] Dong, H., Bell, T. In: *Proceedings of the* 10^{th} *World Conference on Titanium*; Lütjering, G., Albrecht, J.; Eds.; CCH-Congres Center Hamburg, Germany 13-18 July 2003; vol. 1, pp. 867-873.
[48] Sieniawski, J. In: *Progress of materials science and materials engineering*; Hetmańczyk, M.; Ed.; WPŚ, Gliwice, 2002, pp. 231-286 (in Polish).
[49] Wang, X., Jahazi, M., Yue, S. *Mater. Sci. Eng. A* 2008, 492, 450–454.
[50] Ramachandra, C., Singh, A.K., Sarma, G.M.K., *Metall. Trans. A* 1993, 24, 1273–1280.
[51] Thomas, M., Lindley, T., Jackson, M. *Scripta Mater.* 2009, 60, 108–111.
[52] Dudek, H. J., Borath, R., Leucht, R., Kaysser, W. A. *J. Mater. Sci.* 1997, 32, 5355-5362.
[53] Kehoe, M., Broomfield, R.W. In *Titanium Sci. Tech.*; Jaffee, R.I., Burte, H.M.; Ed.; Plenum Press, New York, 1973, pp. 2167–2178.
[54] Winstone, M.R., Rawlings, R.D., West, D.R.F., *J. Less Common Metals* 1975, 39, 205–217.
[55] Dong, H., Bell, T., In: *Ti*-2003 *science and technology;* Lütjering, G., Albrecht, J.; Eds.; Wiley-VCH Verlag, Weinheim, 2004; Vol. 1, pp. 867-874.
[56] Cui, C.D., Zhu, S.L., Man, H.C., Yang, X.J. *Surf. Coat. Technol.* 2005, 190, 309-313.
[57] Bemporad, E., Sebastiani, M., Staia, M.H., Puchi Cabrera E. *Surf. Coat. Technol.* 2008, 203, 566–571.
[58] Cai, F., Zhou, Ch., Wang, N., Gong, S., Xu, H. *Vacuum* 2006, 81, 85–90.
[59] Zhou, Ch., Cai, F., Kong, J., Gong, S., Xu, H. *Surf. Coat. Technol.* 2004, 187, 225–229.
[60] Meng, Q., Geng, L., Ni, D. *Mater. Lett.* 2005, 59, 2774 – 2777.
[61] Vadiraj, A., Kamaraj, M., Gnanamoorthy, R. *Mater. Sci. Eng. A* 2007, 445–446, 446–453.
[62] Wang, Y., Wang, H.M. *App. Surf. Sci.* 2004, 229, 81–86.
[63] Czyrska-Filemonowicz, A., Buffat, P.A., Wierzchoń, T. *Scripta Mater.* 2005, 53, 1439-1442.
[64] Czyrska-Filemonowicz, A., Buffat, P.A. *Micron* 2009, 40, 15–21.
[65] Hofer, F., Warbichler, P., Scott, A., Brydson, R., Galesic, I., Kolbesen, B. *J. Microsc.* 2001, 204, 166-171.
[66] Ankudinov, A.L., Ravel, B., Rehr, J.J., Conradson, S.D. *Phys. Rev. B* 1998, 58, 565-7576.
[67] Kihn, Y., Mirguet, C., Calmels, L. *J. Elect. Spectr.Rel. Phen.* 2005, 143, 117-127.
[68] Fujishiro, S., Eylon, D. *Th. Sol. Films* 1978, 54, 309-315.
[69] Fujishiro, S., Eylon, D. *Met. Trans. A* 1980, 11*A*, 1259-1263.
[70] Das, D.K., Alam, Z. *Surf. Coat. Technol.* 2006, 201, 3406-3414.
[71] Sai Srinadh, K.V., Singh, V. *Bull. Mater. Sci.* 2004, 27, 347–354.
[72] Gurrappa, I. *Oxid. Met.* 2001, 56, 73-87.

[73] Gurrappa, I., Manova, D., Gerlach, J.W., Mändl, S., Rauschenbach, B. *Surf. Coat. Technol.* 2006, 201, 3536- 3546.
[74] Januszewicz, B., Winiarski, D. *Vacuum* 2006, 81, 215–220.
[75] Sarkar, S., Datta, S., Das, S., Basu, D. *Surf. Coat. Technol.* doi.org/10.1016/ j.surfcoat.2008.12.029
[76] Zhou, Ch., Cai, F., Xu, H., Gong, S. *Mater. Sci. Eng.* 2004, *A*386, 362–366.
[77] Gurrappa, I. *J. Alloys Comp.* 2005, 389, 190–197.
[78] Leyens, C., Peters, M., Kaysser, W. *Mater. Sci. Tech.* 1996, *A*12, 213-218.
[79] Spaepen, F. *Acta Mater.* 2000, 48, 31-42.
[80] Thornton, A. *Annu. Rev. Mater. Sci.* 1977, 7, 239-260.
[81] Thornton, J.A. *J. Vac. Sci. Tech. A* 1986, 4, 3059-3065.
[82] Barna, P.B., Adamik, M. *Th. Sol. Films* 1998, 317, 27-33.
[83] Shen, Y.G., Mai, Y.W., McBride, W.E., McKenzie, D.R., Zhang, Q.C. *Appl. Phys. Lett.* 1999, 75, 2211-2213.
[84] Huang, F., Barnard, J.A., Weaver, M.L. *Surf. Coat. Technol.* 2002, 155, 146-151.
[85] Randal, N. (1996). Advances in surface mechanical properties characterization. CSEM Instruments, Applications Bulletin. http://www.csem.ch/instrum
[86] Skowronski, R.P. *J. Am. Ceram. Soc.* 1994, 77, 1098-1100.
[87] Wang, L., Meng, Ch., Liu, Ch., Wang, L. *J. Am. Ceram. Soc.* 2002, 85, 2867-2869.
[88] Datta, S., Das, S. *Bull. Mater. Sci.* 2005, 28, 689-693.
[89] Sarkar, S., Datta, S., Das, S., Basu, D. *Surf. Coat. Technol.* 2009, 203, 1797-1805.
[90] Nickel, H., Niewolak, L., Żurek, J., Quadakkers, W.J. *Microchi. Acta* 2004, 148, 241-249.

In: Titanium Alloys: Preparation, Properties and Applications ISBN: 978-1-60876-151-7
Editor: Pedro N. Sanchez, pp. 269-293

Chapter 5

BIOACTIVE TITANIUM SURFACES

S. Spriano[1], S. Ferraris[1], C.L. Bianchi[2], C. Cassinelli[3], P. Torricelli[4], M. Fini[4], L. Rimondini[5] and R. Giardino[6]

[1]Department of Material Science and Chemical Engineering, Politecnico di Torino, Turin Italy
[2]Physical Chemistry and Electrochemistry Department, University of Milan, Milan, Italy
[3]Nobil Bio Ricerche, Portacomaro, Asti, Italy
[4]Experimental Surgery Department, Research Institute Codivilla Putti, Rizzoli Orthopaedic Institute, Bologna, Italy
[5]Department of Medical Sciences, University of Eastern Piedmont "Amedeo Avogadro", Novara, Italy
[6]Surgical Pathophysiology, University of Bologna, Bologna, Italy

Abstract

Titanium and its alloys are the most widespread materials employed in orthopaedic and dental surgery, because of their good mechanical properties and biocompatibility. In fact titanium has a good fatigue resistance and, at the same time, its elastic modulus is the lowest between metals, so it avoids stress shielding of implants. Moreover titanium surface is naturally covered by an oxide layer preventing corrosion and it is almost inert in contact with biological fluids. Inertness avoids adverse reactions of the body, but at the same time it hampers tissue integration. Several solutions have been proposed, in order to improve titanium bioactivity: bioactive coatings based on hydroxyapatite and calcium phosphates, inorganic surface modifications (alkaline treatments, acid etchings or electrochemical oxidation) and biomolecular surface grafting. A brief commentary of recent research on these topics will be presented.

Moreover an innovative treatment will be described. It is focused on inducing a bioactive behaviour on Ti6Al4V. The process includes two steps: the first one is an inorganic modification, inducing inorganic bioactivity on the surface (hydroxyapatite precipitation), while the second one is an organic treatment, promoting a biological response. In particular the first step includes an acid etching, in order to remove the natural oxide layer, and a controlled oxidation in hydrogen peroxide. The second step is the covalent surface grafting of a biomolecule (enzyme alkaline phosphatase (ALP) for instance), in order to stimulate cell response.

Results show that the inorganic treatment induces hydroxyapatite precipitation on the titanium surface (it was tested in-vitro by soaking in simulated body fluid (SBF) for two weeks). The oxide layer shows a porous surface texture on a nanoscale and it is quite rich in hydroxyls groups. A thermal treatment could improve the mechanical resistance of this modified layer to the substrate, without altering its bioactive behaviour. The fatigue performances of the material are not modified by the treatment. ALP has been successfully grafted to the modified titanium surface, maintaining its activity. The results of cellular tests will be reported in order to evaluate the biological behaviour of treated samples. Finally it has been observed that there is a synergic mechanism between inorganic and biological bioactivity, one improving the other one.

Introduction

The success of an implant, in dental and orthopaedic applications, depends on its rapid and strong anchorage to the surrounding bone, in order to quickly withstand the continuous cyclic loading that occurs during mastication and joint motion. Several factors, such as surgical technique, implant design, surface topography and biochemistry are known to influence the bone in-growth and on-growth. The optimization of the surface properties for inducing a bioactive behaviour has become a key issue. So it is requested that the implant surface will stimulate osseointegration and new bone formation, beyond being biocompatible and mechanically suitable [1]. This bioactive behaviour can be due to a physicochemical interaction of the surface with body fluids and it results in the in-vivo precipitation of apatite on the surface [2] or it can be due to a specific biological response of the cell to the biosurface [3]. A multifunctional bioactive surface, showing both these behaviours, could be of great interest for stimulating the growth of both the biological and inorganic components of new bone. A performant and cost effective technique, devoted to obtaining a bioactive behaviour of titanium, is not developed on an industrial scale nowadays, despite of the wide research performed on these topics in the last ten years

State of the Art

Bioactive Coatings Based on Hydroxiapatite and Calcium Phosphates

Apatite and calcium phosphates are too brittle for use as bulk materials under loaded conditions, which makes that they are frequently applied as coatings onto the surface of metallic implant materials. These coatings are employed in order to conjugate bone bonding ability of the bioactive material with mechanical properties of the metallic one. Hydroxyapatite, carbonate-apatite and calcium phosphates are the most widespread bioactive ceramics employed, because they are close to the natural mineral phase of bone and several literature works underline that they are able to guide bone growth on their surface [4, 5]. The bioactive ceramic layer guides bone growth along the implant surface, and, as a result, bone formation now occurs both from the surrounding tissue and the implant surface. The ceramic coating functions as a physiological transition between the non-physiological titanium surface and the surrounding bone.

The main problem related to ceramic coatings on a metallic substrate is the creation of an interface between two materials with quite dissimilar properties and behaviour. This interface

represents a critical point both during surgical implantation of the coated device and during its physiological loading.

Plasma spray deposition represents the most widespread technique, commercially employed, in order to realize bioactive coatings onto metallic substrates, because it allows coating of large areas with high deposition rates [5,6]. Any material that does not decompose or vaporize during melting is suitable for the deposition. It is possible to maintain the substrate at low temperature, so avoiding phase transitions and grain growth. Plasma spray can be performed in different atmospheres: air (APS), vacuum (VPS) or controlled atmosphere, depending on the characteristics of the deposited material. VPS deposition shows several benefits compared to APS. In particular higher purity of the coating (any reaction between particles and reagents is avoided), major adhesion with the substrate and better cohesion inside the coating (particles have a lower deceleration in a vacuum environment), higher durability (stronger bonding between substrate and hydroxyapatite because the substrate is not oxidized). Finally vacuum environment avoids gas inclusion resulting in denser coatings.

One of the main drawbacks of plasma spray is that coatings must be at least 50 μm thick, in order to completely cover the implant, with the risk of poor adhesion and delamination. Mechanical surface pre-treatment, such as grit-blasting, could improve adhesion by increasing mechanical interlocking. The roughness of the resulting coating is not affected by the initial surface roughness, but mechanical interconnections between weak points of the substrate and the coating can occur with a decrease of the fatigue resistance and coating delamination. Nowadays multilayers are often deposited in order to enhance adhesion. They consist of a first layer of dense VPS titanium (about 50 micron thick), a second layer of porous VPS titanium (about 150-250 micron thick) and a third layer of apatite with high crystallinity (about 50 micron thick). The rationale is that porous titanium can enhance osseointegration ability of the surface, in case of in-vivo apatite resorption. On the other hand dense titanium avoids mechanical interconnections. Moreover plasma spray processes involve high temperatures that influence, in an unpredictable way, chemical and crystallographic phase constitution of the final coating. The heating of hydroxyapatite powders at temperatures higher than 1200°C and their rapid cooling, during deposition, cause the transformation of crystalline hydroxyapatite into amorphous calcium phosphates, which are more soluble in physiological environment [4, 6]. So the final porosity and the crystalline structure of the coating could be tailored only in a limited range, by adjusting process parameters. The possibility to deposit nanostructured granules of hydroxyapatite through plasma spray technique has been investigated [7], but overheating during process results in apatite decomposition and loosing of nanostructure.

As far as clinical applications are concerned plasma spray hydroxyapatite coating have demonstrated a high amount of successful applications in the orthopaedic field while their effectiveness is still debated in the dental one. A possible explanation is that dental surgery is more receptive for innovation, so it has started in using plasma spray coatings earlier than orthopaedic one, when the technique was not optimized. Employed coatings have been too thick to be completely replaced by new bone in case of delamination. Moreover dental implants are percutaneous and consequently more frequently interested by peri-implantitis and subsequent coating rapid resorption. In case of thick coatings this situation leads to implant motion and failure. Finally hydroxyapatite coatings have been often associated to particular implant designs with poor primary fixation. Crystalline fraction of the apatite

coating has to be increased and thicknesses lower than 10 μm have to be obtained in order to realize reliable hydroxyapatite coatings for dental applications.

In order to overcome these problems bioactive glasses have been deposited onto titanium and Ti-alloys surfaces preserving amorphous structure and bioactivity [8,9,10,11]. Moreover Vernè et al. investigated composite coatings (bioactive glass plus Ti particles) prepared by means of vacuum plasma spray [9]. The metallic phase can improve the mechanical properties of the glassy one. It has been observed that composite coatings obtained by plasma spray of pre-sintered composite particles present better properties than in situ plasma spray of glass and titanium particles.

The same research group [10,11] demonstrates that the adhesion strength of bioactive glass or glass ceramic coatings is higher than for hydroxyapatite. They successfully explored also the possibility of surface modifications in order to confer specific properties to the coating (e.g. antibacterial behaviour).

Electrochemical ceramic coatings are based on the electro-deposition of calcium phosphates from electrolytes containing Ca^{2+} and PO_4^{3-} ions. The structure and phase composition of such coatings could be tailored by varying pH, temperature, concentration and agitation of the electrolyte. Some commercial solutions could be cited among these coatings [12, 13, 14, 15]. They were commercialized since 1995 and consist of an electrodeposited bioresorbable CaP coating performed at room temperature on substrates previously covered with porous titanium via plasma spray coating (VPS). The idea is that the ceramic phase is essential in the early phases of bone healing but could become deleterious for long periods, because of coating damage and large particles release. They are constituted mainly of brushite, a precursor f apatite, in the form of 10-25 μm long and plate like crystals which can uniformly cover porous substrates, nearly in vertical alignment, maintaining porosity with a free volume up to 80%. The coating has an average thickness comprised between 10 and 25 μm and could be completely resorbed within 6 -10 weeks. It has been observed that such coating could also improve corrosion resistance of titanium. Cell cultures with osteoblasts show that this resorbable coating improve cells adhesion, metabolism and spreading onto material surface. In vivo test on pig model underline a significantly higher bone apposition for this coating if compared with VPS coated implants. It has been observed that resorption is mainly based on ionic dissolution rather than particle release, or even on an easier phagocytosis mechanism, in fact macrophages and multi-nucleated cells always detected on implant site of plasma spray coating are not observed around these implants.

Other coating techniques, such as RF magnetron sputtering, electrospray, pulsed laser deposition, sol-gel deposition and biomimetic deposition have been studied, but they do not have significant clinical applications at the moment [5].

RF magnetron sputtering [5, 16] enable thin uniform and dense coating with an average thickness comprised between 0.5 and 3 μm, characterized by a strong adhesion. On the other hand it is a time consuming technique characterized by low deposition rates. This process could induce alteration in coating properties (such as chemical composition) like the plasma spray one. Sputtered coatings present amorphous nature or a low degree of crystallinity and a smooth morphology. Subsequent thermal treatment increase both crystallinity and roughness. It has been observed that thermal treatment in presence of water vapour enhances crystallization.

Electrospray deposition [5, 17] is based on the generation of a spray of charged micron-sized droplets on heated substrates by means of a potential difference. This technique allows the control over coating composition and in particular a fine control of the final coating morphology is possible. A three dimensional interconnected pore network has been obtained under certain conditions. The chemical composition of the precursor solutions and mixing characteristics influence droplet size, precipitation kinetics and, as a consequence, coating morphology. Electrosprayed coatings thickness is of at about 0.1 – 5 μm. The process enables even co-deposition of biomolecules. On the other hand so prepared coating coatings present low mechanical strength and the heating of the substrate is a further drawback.

Pulsed laser deposition [5, 18] could be employed for the realization of apatite coatings from an apatite sintered target ablated by a pulsed laser (often ArF excimer laser) in a vacuum chamber filled with water vapour. Thermal treatments are often performed in order to favour coating crystallization. This technique allows the control of coating chemistry and morphology, enables thin coatings (0.05 – 5 μm) with higher adhesion strength than conventional plasma spray coating and good fatigue resistance. On the other hand it is a line of sight technique. It has been observed [19] that coating with 0,2 – 0,5 μm thickness could improve alkaline phosphatase, osteocalcine and mRNA protein production in rat bone marrow cells, but does not affect their proliferation rate.

Sol-gel deposition of hydroxyapatite layers from calcium and phosphorous precursor has been widely investigated [5, 20]. This technique enables coating of complex geometries with small coating thickness (less than 1 μm). Low processing temperature, with a good control of physical and chemical homogeneity of the coating, is allowed. It is possible to change coating structure and properties by varying process parameters, in particular drying temperature. It has been observed [21] that the addition of gelatine in the sol could improve its stability during coating formation. No high vacuum neither complex equipment are necessary for sol-gel coating, but the process requires controlled atmosphere processing and expensive raw materials.

Biomimetic deposition is based on the precipitation of bioactive ceramic coatings (hydroxyapatite or calcium phosphates) from inorganic solutions directly on the substrate before implantation. This process exploits material ability to promote the precipitation, so this technique needs bioactive substrates. A pre-treatment capable of making bioactive the metal surface is necessary in order to apply this method to titanium. In literature thermal [22,23], chemical [24] and electrochemical [22] processes have been proposed and applied in order to realize biomimetic hydroxyapatite coatings. This technique enables coating of complex geometries and even co-deposition of biomolecules, but it is a time consuming technique and it requires close monitoring of pH. These coatings are less then 30 μm in thickness.

Inorganic Surface Modifications

Inorganic surface modifications are an alternative to coatings in order to improve bone bonding ability of metallic implants. These surfaces do not present a ceramic biomimetic coating, but they are able to induce in-vivo apatite precipitation after implantation. This approach could overcome interface critical situation of coatings [25], because they introduce a graded interface between bulk material and surface thin modified layers.

These processes include chemical and electrochemical treatments, but they are not commercially employed so widespread at the moment.

At the end of Nineties T. Kokubo and its research group proposed a new thermo-chemical treatment based on alkaline solutions, in order to confer an in-vivo bioactive behaviour to titanium surfaces [2, 26-29]. The process includes a first chemical modification in alkaline solution (mainly NaOH) at 60°C for 24 hours and a subsequent heat treatment 1 hour at 600°C in air. The thickness of the modified layer is at about 1 μm.

Bioactivity mechanism is explained considering that modified surfaces release into SBF sodium ions, which are replaced by H_3O^+ ions, forming Ti-OH groups on the surface, so the surface gets a negative charge and adsorption of Ca^{++} ions occurs. This is the first step of apatite precipitation. In vivo tests underline a good bone bonding ability of the treated devices. The main drawback of the technique is a significant decrease in fatigue resistance of the modified material, but also a long process treatment and employment of high corrosive solution and high temperatures.

The possibility to modify NaOH treatment introducing a sodium removal passage has recently been investigated [30] in order to avoid interferences with sodium equilibrium of cells. The procedure considers samples soaking in dilute HCl after NaOH treatment, water washing and final thermal treatment. The result is an increase in surface area and roughness, the removal of sodium from surface. On the other hand chlorine traces are introduced. Experimental tests suggest that this procedure improve in vitro bioactivity in SBF and also bone bonding ability in vivo.

A multi-step thermo-chemical treatment have been proposed by Spriano et al. [31,32] in order to improve biological properties of Ti6Al7Nb alloy. The process includes firstly nitric acid passivation (30min in 35%wt HNO_3 at room temperature) followed by alkaline treatment (24h in 5M NaOH at 60°C) and finally thermal treatment at 600°C in air or in vacuum. Modified surfaces are constituted mainly of titanium oxide. Small sodium content has been individuated by means of EDS analyses. Passivation treatment does not induce any significant morphological alteration while NaOH passage results in a microporous layer. Heat treatment induces a densification of the modified layer. The final surface porosity is at about 1,15% for air treated samples and 0,13% for the vacuum treated ones. The treatment induces a significant increment in surface water wettability. Ion release in simulated body fluid (SBF) is reduced thanks to the treatment in HNO_3. Moderate in vitro bioactivity has been observed. Interactions with fibroblast and osteoblast-like cells result in good spreading without cytotoxicity evidence. The main drawback of NaOH treatments is a significant decrease in material fatigue resistance (at about 43%).

Osaka, Tsuru and co-workers explored the possibility to modify commercially pure titanium surfaces with different hydrogen peroxide solutions, in order to obtain a bioactive material [33-41]. They showed that samples treatment in H_2O_2 for less than 1 hour can produce a porous surface (200nm pores) while longer treatments (up to 72 hours) results in a dense surface layer with a more marked bioactivity in simulated body fluid. Treatments longer than 24 hours favours gel crystallization and Ti^{4+} deposition. The same research group investigated the effect of several additives to H_2O_2 solutions such as HCl, TiF_4, and $TaCl_5$. It has been observed that Tantalum favours low temperature crystallization and enhance bioactive behaviour. A final thermal treatment in the range 300-600°C induce gel crystallization in anatase structure without changing in porosity, while heating at temperatures higher that 600°C produces rutile as main phase and surface layer densification. Thermal

treatments up to 600°C induce an enhancement in bioactive behaviour due to anatase presence. A water-aging treatment at 80°C has been proposed to substitute thermal treatment, avoiding damage of mechanical properties and loss in surface hydroxyls.

Electrochemical treatments are widely commercially employed in order to increase corrosion resistance (colour and dark anodizing), but they were also explored for obtaining a bioactive behaviour. Treatments above the breakdown limit (spark anodizing) result in increase in surface roughness and the development of a three-dimensional oxide structure with numerous open pores. This surface shows bioactive behaviour. This process can produce adherent oxide films up to 20μm in thickness. The composition of the oxide layer could be tailored varying the electrolyte composition. Some [42-44] could be enumerated as commercial treatment among anodic spark deposition treatments. The process includes two anodic spark deposition steps: the first one in a solution containing calcium and phosphate ions, the second in a solution containing only calcium ions. The final step is a treatment in concentrated KOH or NaOH at 60°C for 24 hours. Modified surfaces present a dark grey colour. The resulting modified layer is constituted mainly of anatase and shows surface enrichment in oxygen, calcium and phosphorous. The average roughness is 0.29 ±0.03μm. SEM observations reveal a microporous morphology given by the anodic spark deposition and a nano-roughed texture due to final chemical treatment. In vitro bioactivity tests show that this modified surface is able to induce the formation of a compact and thick (at about 10μm) hydroxyapatite layer after 14 days in simulated body fluid (SBF). Human osteoblast like cells (MG63) cultured on modified titanium surface show good proliferation rate flattened morphology and their filopodia are anchored to nanotextured surface. In vivo study in a sheep model shows a significant increase in both affinity index and bone ingrowth for these devices if compared to controls.

Aita et al. [45] recently propose ultraviolet functionalization of titanium in order to improve its bone integration ability. Briefly it has been shown that UV irradiation applied for times from 1 up to 48 hours decreases carbon surface contamination and induces super-hydrophilicity. So modified surfaces show enhanced protein adsorption ability, increase in osteoblast adhesion and proliferation and also higher bone formation in *in vivo* models if compared to traditional machined titanium.

Biomolecular Surface Grafting

Surface grafting of biologically active molecules such as peptides, proteins and growth factors has the aim to produce materials bioactive from the biological point of view (able to stimulate a specific cellular response). In this way it is possible to influence cellular adhesion, proliferation and differentiation with the final aim to reduce healing time and favour a more stable long term integration of implanted materials. Several kinds of biomolecules could be grafted [1, 46] depending on the type of cells and tissues that have to be stimulated. Proteins from the extracellular matrix (ECM proteins), such as integrin, fibronectin, vitronectin, type I collagen, osteopontin and bone sialoproteins, or their peptides (mainly the sequence Arg-Gly-Asp – RGD) could be considered in case of biomaterials intended for bone tissue integration [47]. Bone morphogenetic proteins, growth factors or enzymes could be contemplated as well in order to improve tissue regeneration [48]. As far as ECM proteins and peptides are concerned the aim is to reproduce the natural environment involved in osteoblast cells

adhesion and so improve cell attachment on the artificial substrate; while in case of BMPs, growth factors and enzymes the purpose is to send biological signals able to affect cells behaviour and stimulate a physiological healing on the artificial material.

Biochemical functionalization could be performed by means of three different methods [1, 46]: physical adsorption, inclusion into a resorbable carrier or chemical binding. The first solution is based on physical-chemical interaction between biomolecules and material surface (mainly Van der Waals, hydrophobic or electrostatic forces). This technique is quite simple, but it does not allow controlling biomolecular amount and orientation during grafting. Moreover the adhesion between biomolecule and substrate is quite weak. The second strategy considers biomolecule introduction into a resorbable carrier (often a polymeric coating) that enables its transport and release. Carrier dissolution kinetics must be compatible with the ones desired for molecular release. Moreover coating could alter material surface topography and reactivity, resulting in a material different from the starting one. As far as covalent immobilization is concerned a strong chemical binding is realized between biomolecule and substrate. The binding is supported by reactive groups, characteristic of the material or introduced through proper treatments. This technique allows a stronger and more specific grafting. It is possible to perform covalent grafting either directly through reactive groups (direct grafting) or by the interposition of spacer molecules. Silanization is one of the techniques that could be employed in order to obtain covalent grafting of biomolecules onto titanium surfaces [4]. Different reactive residues of the biomolecules could be employed in order to perform grafting to silanized surfaces, in particular thiol-, amino- and carboxyl-directed immobilization have been widely investigated. Many linking reagents, such as malemides, alkyl-halides, glutaraldehyde or carbodiimide, could be employed in order to carry out a specific biding between the reactive residue of biomolecule and reactive group exposed on silanized surface.

Bagno et al. [49] grafted two different synthetic peptides (a RGD-containing peptide and one mapped on human vitronectin - HVP) on titanium previously sand blasted and oxidized. Silanization with amminopropyltriethoxysilane and glutaraldehyde activation have been employed for both peptides. Functionalized surfaces are able to promote cellular adhesion, in particular RGD one seems to be more effective, but non osteoblast specific while HVP one is less effective, but it is osteoblast specific.

Nanci et al. [50] grafted alkaline phosphatase (ALP) and albumin on cleaned and oxidized commercially pure titanium through aminosilane functionalization, using glutaraldehyde as coupling agent. ALP maintains its activity after covalent binding up to 7 days. Albumin shows a stable binding with antigenicity preservation too.

The main drawback of glutaraldehyde employment is due to its toxicity.

Organic chlorides could be employed in order to obtain a covalent direct grafting of biomolecules onto metallic surfaces. These molecules act as good outgoing groups favouring biomolecular grafting onto activated substrate, without the interposition of any spacer.

Hayakawa et al. [51, 52] use surface activation with pure tresyl-chloride (without any solvent) in order to graft fibronectin and collagen to titanium. XPS and FTIR analysis show an effective and stable binding of both molecules. Cellular experiments underline that collagen immobilized titanium is effective for the enhancement of gingival fibroblast initial adhesion and spreading while fibronectin immobilized one not.

Self-assembled monolayers [4] are widely used in order to prepare ordered and well-defined chemical composition on gold surfaces. Phosphoric and phosphonic acids have been

successfully employed also on TiO_2 with the aim of producing similar situation on oxides surface.

As far as ECM protein immobilization is concerned Morra et al. [53] successfully graft in a covalent way collagen to titanium by a surface modification process based on the deposition of a thin film from hydrocarbon plasma followed by acrylic acid grafting and collagen coupling. They obtained a homogeneous and complete surface coverage with a thickness higher than XPS sampling depth (>40 Å). The coated implants result biocompatible both in cell culture and in animal model (rabbit); in particular in vivo tests underline an increase in bone to implant contact and healing rate. The same research group [54] explored the opportunity to covalently graft hyaluronan (HA) of different molecular weight to aminated titanium surface, with the aim of reducing unspecific cellular adhesion. Two different functionalization techniques have been employed in order to introduce amino groups onto metallic surface: polyethileneinmine (PEI) adsorption and deposition from allylamine plasma. The first solution allows a higher density of functional groups. In both cases HA has been coupled exploiting carbodiimide chemistry. Cellular tests on fibroblast confirm the ability of modified surfaces to resist to cell adhesion.

Photochemical approaches [4] could be applied to biological functionalization in two different ways because the reactive functionalities are inert until they are photolyzed. The first one is the total synthesis of a bioconjugate compound bearing both a bioactive species and a photoactive group. After this molecule is adsorbed onto solid surface the photosensitive group is activated by the application of light or heat in order to realize binding. The second approach is first to covalently attach the photosensitive group to a surface, then to adsorb the biomolecule and finally to activate the non-specific binding reaction by application of light or heat and complete grafting.

Electrospray technique could be successfully employed in order to realize thin biomolecular films on implant surfaces without altering molecular characteristics. As an example De jonge et al. [55] produced an enzyme (alkaline phosphatase) coating onto titanium surface via electrospray. They demonstrate that this method enable the maintenance of ALP activity and increase material bioactivity in cell culture medium. It has been observed [56] that the simple absorption of the same enzyme on plasma sprayed titanium implants could improve bone production in rabbit model.

Innovative Treatment

Considering the state of the art, it can be noted that implantable titanium devices presenting a bioactive surface (different from conventional hydroxyapatite coating) are not present on the market, despite extensive research conduced in recent years. The only exception is to be sporadic cases of dental implants without wide spread. So the problem is still open and new efficient and cost effective techniques must be developed.

Starting from these considerations, an innovative surface modification of titanium alloys was studied. It consists of a thermo-chemical oxidation of the surface, as first. The process parameters were optimized by focusing on inorganic bioactive behaviour (apatite precipitation), suitable roughness and mechanical properties (fatigue and scratch resistance). Moreover the in-vitro biological response of human osteoblasts to the modified Ti surface

was tested. MG63 human osteoblast-like cells were cultured on the modified surface and cell attachment, morphology, viability, activation and differentiation were evaluated.

Materials and Methods

Material Characterization

Discs of Ti-6Al-4V alloy were employed for testing the modification treatment (Ø 10mm, h 1 mm). They were mirror polished by using conventional metallographic techniques. The surface modification was performed by chemical treatment (aqueous solution of H_2O_2), and thermal treatment (600°C) as detailed reported elsewhere [57].

The morphology of the surface was observed by Scanning Electron Microscopy (SEM) and the roughness was measured by using a surface profiling instrument (KLA TENCOR P15).

The inorganic bioactive behaviour was tested by soaking in simulated physiological body fluid (SBF) at 37°C for 15-30 days, followed by EDS-SEM characterization.

Transmission Electron Microscopy (TEM) investigation was performed by using a Philips CM12 electron microscope. Titanium grids were treated according to the previous process and used as samples. TEM camera diffraction constant was assessed by using a pure Al standard reference.

X-ray photoelectron (XPS) spectra were taken in an M-probe apparatus (Surface Science Instruments). The source was monochromatic AlK radiation (1486.6 eV). A spot size of 400x1000μm and pass energy of 150 eV were used for survey spectra, while for the single-region acquisitions a spot size of 200x750 μm and a pass energy of 25 eV were used. Resolutions were 1,39 and 0.74, respectively. The energy scale was calibrated with reference to the $4f_{7/2}$ level of a freshly evaporated gold sample, at 84.00 ± 0.1 eV, and with reference to the $2p_{3/2}$ and 3s levels of copper at 932.47 ± 0.1 and 122.39 ± 0.15 eV, respectively.

The binding energies (BE) were corrected for specimen charging by referencing the C 1s peak to 284.6 eV, and the background was subtracted using Shirley's method.

X-ray diffraction analysis was performed by using an X'Pert Philips Diffractometer and the collected data were analyzed by PANalytical X'Pert HighScore program, based on PCPDFWIN database.

Cell Experiment

Human osteoblast-like cell line MG63 was used for the in vitro tests. Osteoblasts were cultured in DMEM (10% FCS, 100 IU/ml penicillin and 100 μg/ml streptomycin solution), and incubated at 37°C in a humidified 95% air / 5% CO_2 atmosphere. Cells were released before confluence with 0.05% (w/v) trypsin and 0.02% (w/v) EDTA, counted (Coulter Counter Z1, Beckman Coulter Inc., Miami, FL, USA) and used at a concentration of 2×10^4 cells/ml for the experiment.

Disk shaped (Ø 10mm, h 1mm) samples of each material were used for cell experiment. Twelve samples of Ti-6Al-4Valloy modified by the surface innovative treatment (called Ti-treated in the following) and twelve Ti-6Al-4V un-treated polished reference samples (called

Ti-untreated in the following) were placed in 24-well plates and a 50µl osteoblast suspension (2.0×10^4 cells/ml) of MG63 osteoblast-like cell line was directly seeded on every sample. The same amount of cells was plated in the same number of polystyrene wells without materials as Control (CTR). After having allowed cell adhesion, 950µl of medium (DMEM plus 10% FCS, 100 IU/ml penicillin and 100 µg/ml streptomycin solution) were added. Plates were incubated in standard conditions up to 7 days, changing medium every two days. DMEM additioned with β-Glicerophosphate (10^{-8}M) and Ascorbic acid (50 µg/ml) was used to activate osteoblasts. For the production of osteocalcin the culture medium was enriched with 1,25 $(OH)_2D_3$ 48 hours before end of experimental time.

Osteoblast Adhesion

Adhesion of osteoblasts was investigated on the samples surfaces after 24-hour incubation. Samples of Ti-untreated and Ti-treated were washed in PBS and cells were fixed in a solution of 4% formaldehyde in PBS for 15min at 37°C. Then cells were permeabilized in 0.5% Triton X-100 for 15min, washed in PBS, and a FITC-conjugate phalloidin solution (1:100 in PBS) was added for 30min at 37°C. After washing, samples were examined by fluorescence microscope.

Osteoblast Proliferation

Cell Proliferation Reagent WST-1 test was done to assess cell proliferation and viability (3, and 7 days): 100 µl of WST1 solution and 900 µl of medium (final dilution: 1:10) were added to the cell monolayer, and the multi-well plates were incubated at 37°C for a further 4 h. Supernatants were quantified spectrophotometrically at 450 nm with a reference wavelength of 640 nm. Results of WST1 are reported as optical density (OD).

Osteoblast Activity

Finally the supernatant was collected from the wells and centrifuged to remove particulates, if any, at the end of experimental times (3 and 7 days). Aliquots were dispensed in Eppendorf tubes for storage at -70°C and assayed for Type I Collagen (CICP, Prolagen-C enzyme Immunoassay kit, Metra Biosystem, CA, USA), and Interleukin – 6 (IL-6, Elisa immunoassay, R&D Systems, MN, USA).

Alkaline Phosphatase activity (ALP, Immunoassay kit, Metra Biosystem, CA, USA), Lactate Dehydrogenase (LDH, Biosystems S.A., E) and Osteocalcin (OC, Novocalcin enzyme Immunoassay kit, Metra Biosystem, CA, USA), were tested on supernatants immediately after collection. The measured CICP, OC, IL-6 concentration and ALP, LDH activity were normalized by cell number to take into account the differences in cell growth.

Osteoblast Morphology

Samples for each material were processed for Scanning Electron Micrographs (SEM) at the end of experimental times: osteoblasts grown on the materials were fixed in 2.5% glutaraldehyde, in pH 7.4 phosphate buffer 0.01 m for 1 h and dehydrated in a graded ethanol series. After a passage in hexamethyldisilazane, the samples were air dried. The samples were

sputter-coated with gold prior to examination with a Philips XL-20 Scanning Electron Microscope.

Statistical Analysis

Statistical evaluation of data was performed using the software package SPSS/PC$^+$ Statistics ^{TM} 10.1 (SPSS Inc., Chicago, IL USA). The experiment was repeated three times and the results presented are the mean of the triplicate values. Data are reported as mean ± standard deviations (SD) at a significance level of $p<0.05$. A one-way ANOVA was done for comparison between groups after having verified normal distribution and homogeneity of variance. Finally, the Scheffé's post hoc multiple comparison tests were performed to detect significant differences between groups.

Biochemical Functionalization

The opportunity to conjugate inorganic bioactivity, induced by the previous described thermo-chemical treatment, to a more specific biological bioactivity has been considered. The enzyme alkaline phosphatase (ALP) has been covalently grafted to modified Ti6Al4V substrates.

Direct grafting via tresyl chloride activation, as described by Hayakawa et al [51] has been performed. The main difference consists in the application of this method to a modified titanium surface presenting a high density of active OH groups.

Samples modified from the inorganic point of view have been completely covered with tresyl chloride (2,2,2-Trifluoroethanesulfonyl chloride, 99% Aldrich) and stored 48 hours at 37°C.

Samples have been gently washed in anhydrous acetone at the end of soaking and let to dry at ambient temperature.

So activated samples have been put in a 5mg/ml solution of alkaline phosphatase in phosphate buffered saline (PBS) for 24 hours at 4° C in order to covalently graft the enzyme. ALP solution has been prepared dissolving the lyophilized enzyme (Phosphatase Alkaline from bovine intestinal mucosa lyophilized powder, ≥10DEA units/mg solid, Sigma Aldrich) in PBS (Phosphate buffered saline, pH 7.2 25°C, Sigma Aldrich) in a beaker with a magnetic stirrer.

Samples have been gently washed in TRIS-HCl solution, after soaking, in order to remove unbounded enzyme and let dry at ambient temperature. TRIS-HCl solution has been prepared dissolving 2,42g of TRIS (Tris (hydroxymethyl) aminomethane – $(HOCH_2)_3CNH_2$, 99,9+% ultrapure grade, Aldrich) in 100ml of double distilled water, pH has been adjusted to 7.5, at room temperature, by adding 1M HCl.

ALP grafting has been verified by means of XPS analysis in order to detect the presence of the biomolecule on the surface. An enzymatic activity test has been performed in order to verify molecular activity after grafting. As far as this last measure is concerned functionalized samples have been put into a reactive mixture containing equal volumes of $MgCl_2$ 2mM, p-nitrophenilphosphate 2 mM and 2-amino-2-methyl-1-propanol (AMP) 2 mM (all reagents have been purchased from Sigma Aldrich Fluka). The pH value of the reactive mixture is 10,5. The reaction between ALP and p-nitrophenilphosphate produces p-nitrophenol which

has a yellow colouring that can be quantified by means of UV-vis spectroscopy recording absorbance at 405 nm.

Results

Surface Characterization

The morphology of the chemical treated surface was observed by SEM (Figure 1). It shows an increment in roughness respect to the polished untreated surface. The surface presents a roughness on a microscale, due to acid etching, concave areas, smaller than titanium crystallographic grains, divided by ridges (Figure 1a) and a sub-micrometric porosity superimposed on it (Figure 1b), due to the etching in hydrogen peroxide. The subsequent thermal treatment does not affect significantly the morphology of the surface. The roughness of the treated surface is about 600 nm (R_a), while R_z value is about 4 μm.

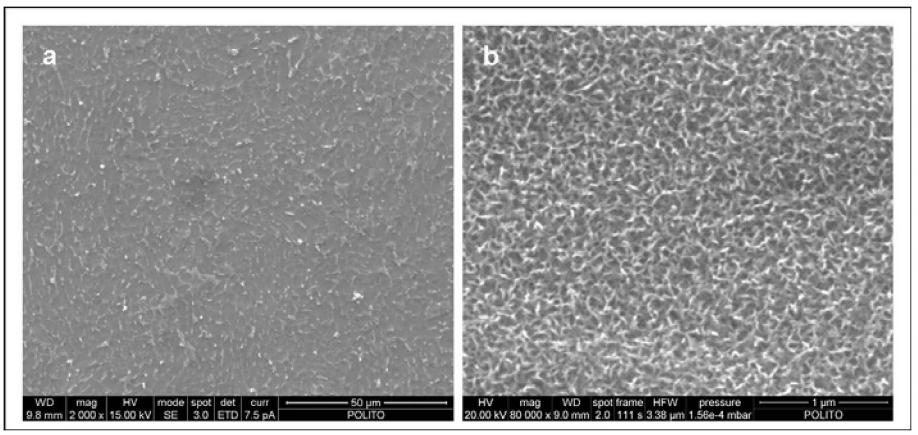

Figure 1. (a-b): SEM microphotographs of chemical treated Ti-6Al-4V alloy.

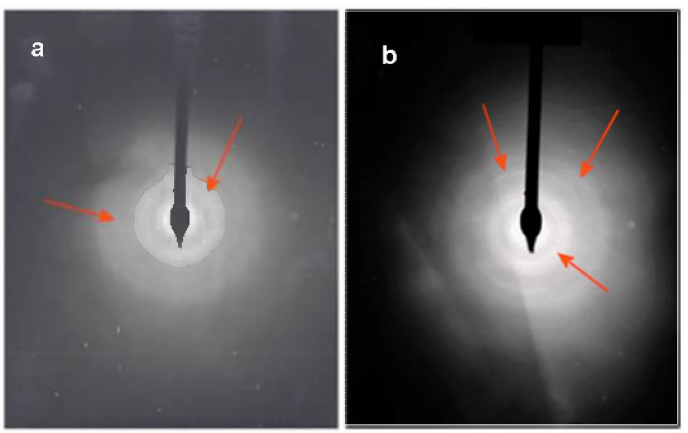

Figure 2. Selected area diffraction patterns (TEM) of chemical (a) and thermo-chemical (b) treated samples.

The crystallographic structure of the surface oxide was analysed by TEM investigation (Figure 2a, 2b). A relevant amorphous component is present both after the chemical and the thermal treatment, as it can be deduced from the presence of a broad halo on the electron diffraction patterns (2.7 Å) and from a typical salt-pepper contrast on the bright field images. It is not easy to assess the structure of the crystalline component of the oxide, due to the close relationships among the different titanium oxides; in any case it seems to be a structure close to anatase or to the nonstoichiometric oxide Ti_3O_5 (d_{hkl} = 1.8Å).

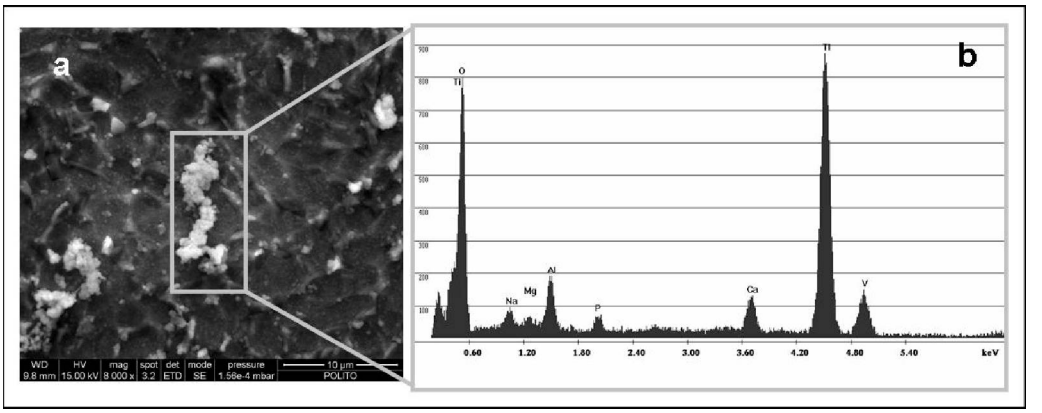

Figure 3. SEM microphotograph of thermo-chemical treated Ti-6Al-4V alloy after soaking in SBF (a) and EDS analysis (b) of the precipitates.

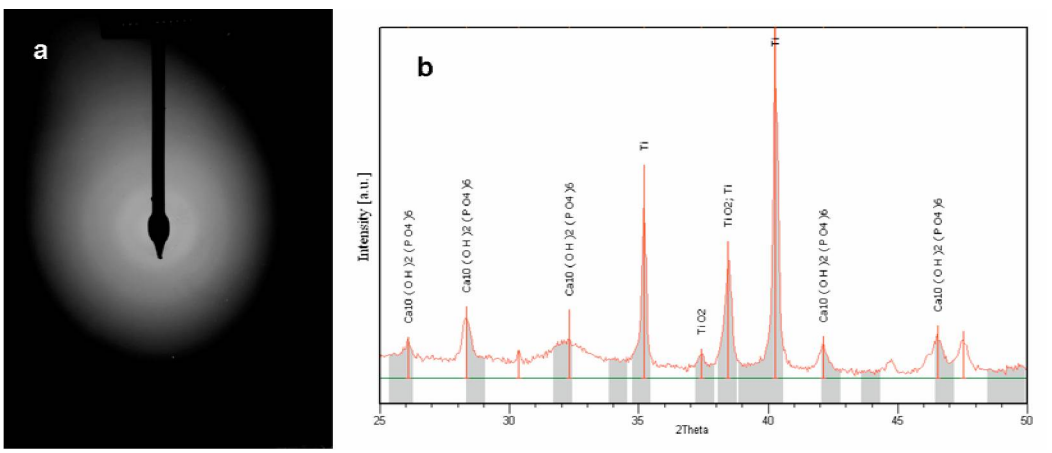

Figure 4. Selected area diffraction patterns (TEM) of a thermo-chemical treated sample after soaking in SBF (a) and XRD pattern of the thermo-chemical treated Ti-6Al-4V alloy after soaking in SBF (b).

The inorganic bioactivity of the treated surface was tested by in-vitro soaking in SBF solution. An adsorbed layer, containing Ca and P, covers the entire titanium surface after soaking and well developed precipitates of different size were randomly detected (Figure 3). The atomic Ca/P ratio is about 0.5 into the adsorbed layer, while it is close to 1.6 inside precipitates. TEM analysis of soaked grits confirmed the interaction between the treated surface and the SBF solution (Figure 4a). The amorphous halo of the electron diffraction patterns is shifted towards higher interplanar spacing (3.18 Å) and a new ring, corresponding

to an interplanar spacing of about 1.8 Å, appears after soaking. This signal can be related to the hydroxyapatite structure, while it is absent in the titanium oxides. Also XRD analysis confirmed the presence of the hydroxyapatite phase on the surface (Figure 4b); it is present in the form of an amorphous phase and crystallites of small dimensions, as can be deduced from the presence of broad diffraction peaks.

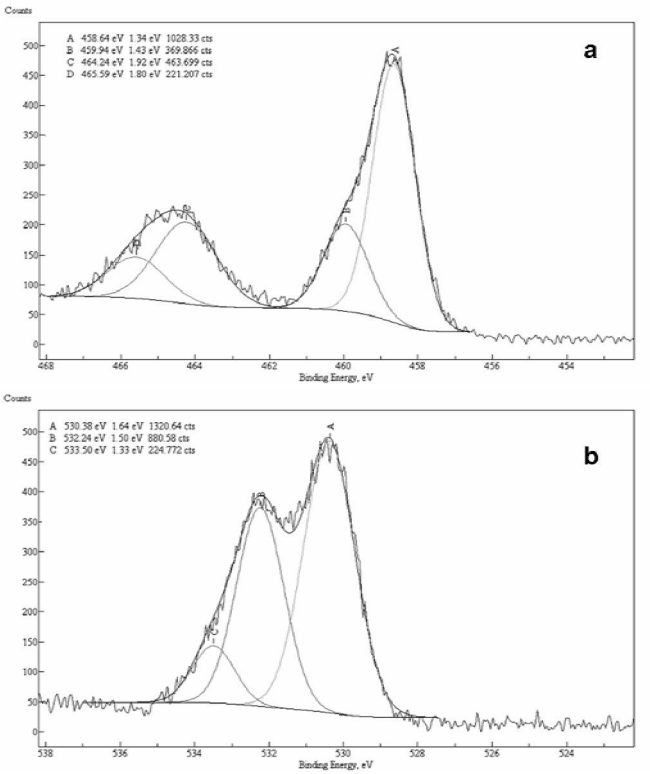

Figure 5. XPS analysis of a thermo-chemical treated Ti-6Al-4V alloy - deconvolution relative to the titanium (Ti_{2p}) and oxygen (O_{1s}) species.

XPS analysis was performed in order to investigate the mechanism of the inorganic bioactive behaviour. The survey spectrum of the chemical and heat treated samples shows the presence of Ti, Al, O and C. The last one is due to the unavoidable surface contaminations. Figure 5 shows the deconvolution relative to the titanium (Ti_{2p}) and oxygen (O_{1s}) species. The peaks labelled as A and C in Figure 5a referred to titanium with an oxidation number of IV, as expected for the TiO_2 oxide, while signals B and D could be due to the presence of a nonstoichiometric oxide [58].The peaks labelled as A, B and C in Figure 5b referred respectively to oxygen into the TiO_2 oxide (530.38 eV) and to two different species of OH groups (532.24-533.5 eV). The hydroxyl groups are classified as acidic if they show a signal around 531 eV, while if they show a higher density of negative charge, they are accounted as basic. So in this case they can be classified as basic. The ratio between the total signal due to hydroxyl groups (B+C) and the A signal is 0.84. So the treated surface appears as negatively charged and it shows a high density of basic hydroxyl groups.

Osteoblast Adhesion and Proliferation

Osteoblast-like cell line MG63 was cultured on titanium surface for 7 days. Osteoblasts appeared well adhering and growing in monolayer on both Ti-untreated and Ti-treated samples (Figure 6a, 6b) after 24 hours from seeding. Cell proliferation was measured by WST1 test at 3 and 7 days. A significant higher proliferation was recorded for osteoblast grown on Ti-treated ($p<0.0001$) when compared to both Ti-untreated and CTR groups at 3 days (Figure 7a). CTR group significantly differed from other groups after 7 days ($p<0.05$ versus Ti-treated, $p<0.0001$ versus Ti-untreated).

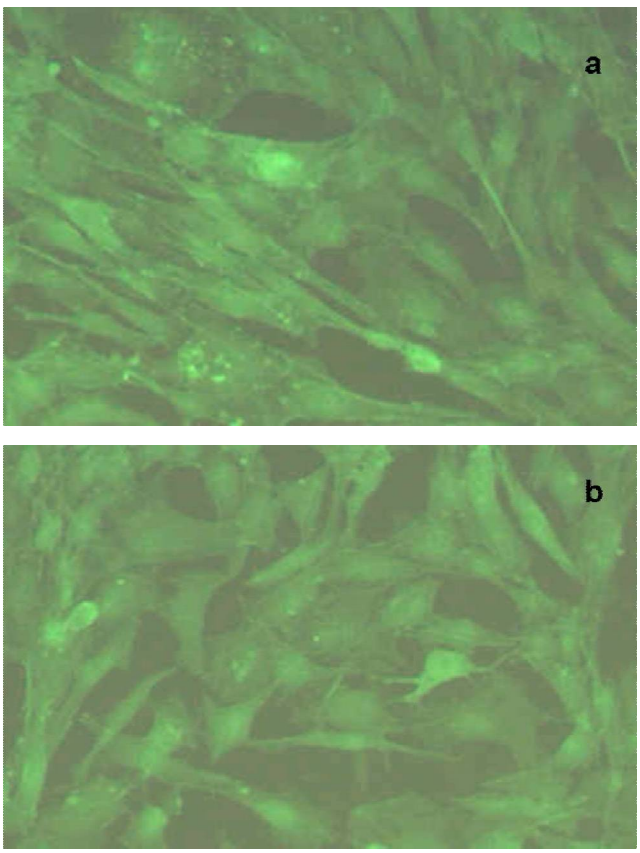

Figure 6. (a – b): Osteoblast adhesion after 24 hours from seeding. (a) Ti-untreated; (b) Ti-treated - Phalloidin staining - 10x.

Osteoblast Activity

ALP, CICP and OC were evaluated in order to assess cell activation and differentiation (Figure 7b, 7c, 7d). The results indicate that ALP activity was significantly higher in Ti-treated group both at 3 days ($p<0.05$ versus CTR) and at 7 days ($p<0.05$ versus Ti-untreated) when compared to other groups. CICP production was significantly higher in Ti-treated group, when compared to Ti-untreated ($p<0.05$) at 3 days. Both biomaterial showed higher values of CICP at seven days in comparison with CTR group ($p<0.01$ versus Ti-treated, Ti-

untreated). OC level was very low in all groups at 3 days, while the level at 7 days OC was significantly higher in Ti-treated group in comparison to CTR group ($p<0.05$).

LDH and IL-6 were measured in order to evaluate cytotoxicity of biomaterials (Figure 7e, f). LDH values showed no differences among all groups both at 3 and at 7 days. IL-6 level decreased from 3 to 7 days in all groups without statistical differences among them.

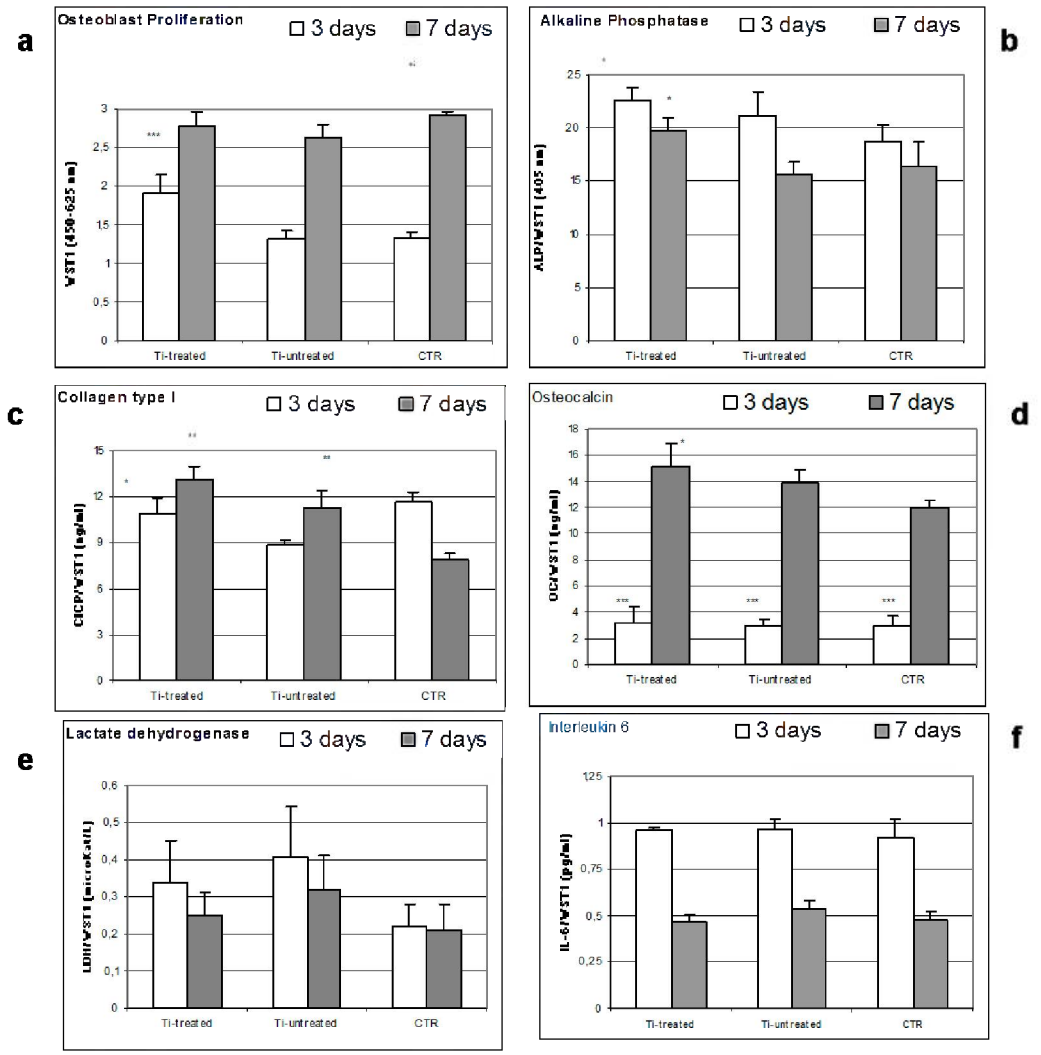

Figure 7. (a – f): Osteoblast proliferation, differentiation, and synthetic activity after 7 days of culture on discs of surface treated Ti-4Al-4V (Ti-Treated). Un-treated polished Ti-6Al-4V (Ti-untreated) was used as reference and polystyrene of culture plates was used as control (CTR). Mean, n = 6 triplicates. Scheffè post hoc multiple comparison test (* = $p<0.05$; ** = $p<0.005$; *** =$p<0.0001$): (a) Cell proliferation and viability. 3 days: *** Ti-treated versus Ti-untreated, CTR; 7 days: *Ti-treated versus CTR; *** Ti-untreated versus CTR. (b) ALP. 3 days: * Ti-treated versus CTR; 7 days: * Ti-treated versus Ti-untreated. (c) CICP. 3 days: * Ti-treated versus Ti ; 7 days: ** Ti-treated, Ti-untreated versus CTR. (d) OC. 7 days: * Ti-treated versus CTR; *** DMEM versus DMEM+D3 (e) LDH. 3 days : *ns*; 7 days : *ns*. (f) IL-6. 3 days : *ns*; 7 days : *ns*.

Osteoblast Morphology

SEM analysis of MG63 was performed in order to evaluate the morphology of cells grown on the different material surfaces after 3 and 7 days of culture. The osteoblasts were observed to attach and spread on both Ti-treated and Ti-untreated, showing few differences (Figure 8, a – d).

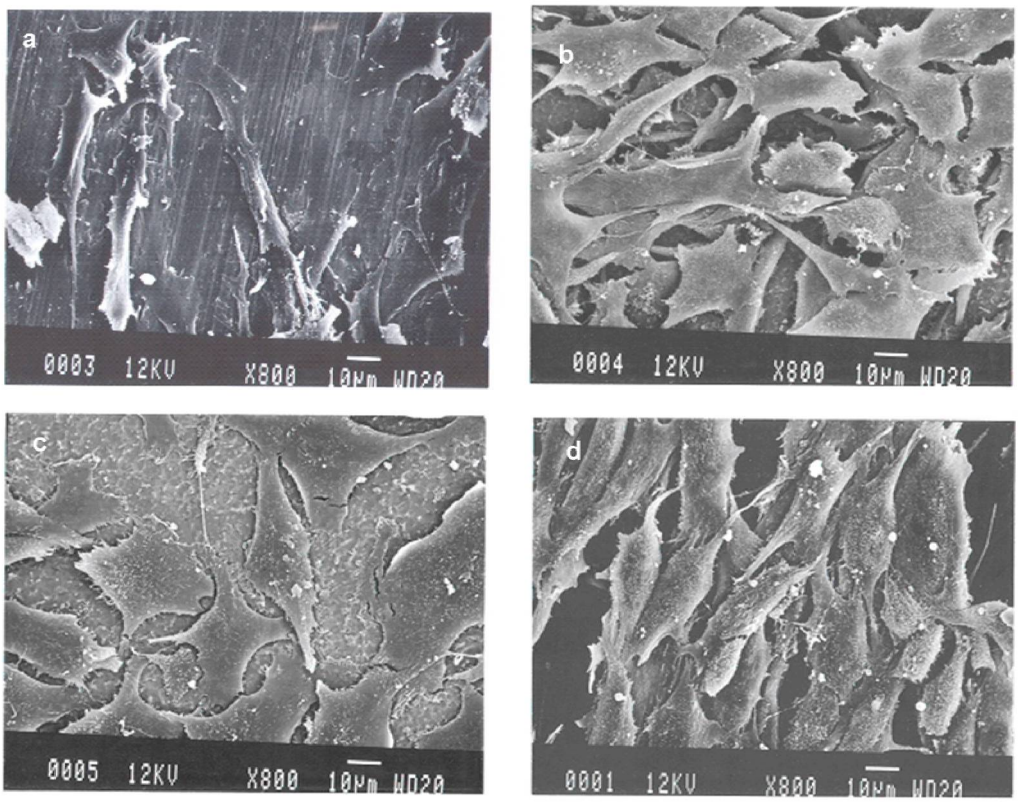

Figure 8. (a – d): SEM images of osteoblast-like MG63 on Ti-untreated (a, b) and Ti-Treated (c, d) samples after 3 (a – c) and 7 (b – d) days of culture.

In fact the cells colonized the surface of the samples exhibiting their phenotypic morphology: osteoblasts were flattened, with a polygonal configuration; they adhered securely to the surface and they frequently bridged the uneven surface by means of cellular processes. In particular, osteoblasts grown on Ti-treated appeared more spread, and presented more dorsal ruffles and numerous elongated filopodies than Ti-untreated reference.

Biochemical Functionalization

XPS survey analysis detects a significant increase in carbon and nitrogen on ALP grafted samples as shown in Table 1. Moreover the metallic substrate is hidden on these samples.

Table 1. Elemental composition (atomic %) from XPS survey analysis.

	% atomic			
	Ti-OH		Ti-ALP	
	mean	stdev	mean	stdev
O	47,55	0,070711	24,6	1,272792
Ti	12,45	0,070711	0	0
N	3,6	0,141421	8,2	0,989949
C	32,6	1,838478	62,15	2,616295

The detailed analysis of carbon region (Figure 9) underlines characteristic signals of the biomolecule. In fact signals of C-O and C-N bonds (286 eV), of C=O bonds (287,5 eV) and of aromatic rings flattened on the surface (292 eV) appears after functionalization, besides a peak (284 eV) attributable to organic contaminations, always present onto titanium.

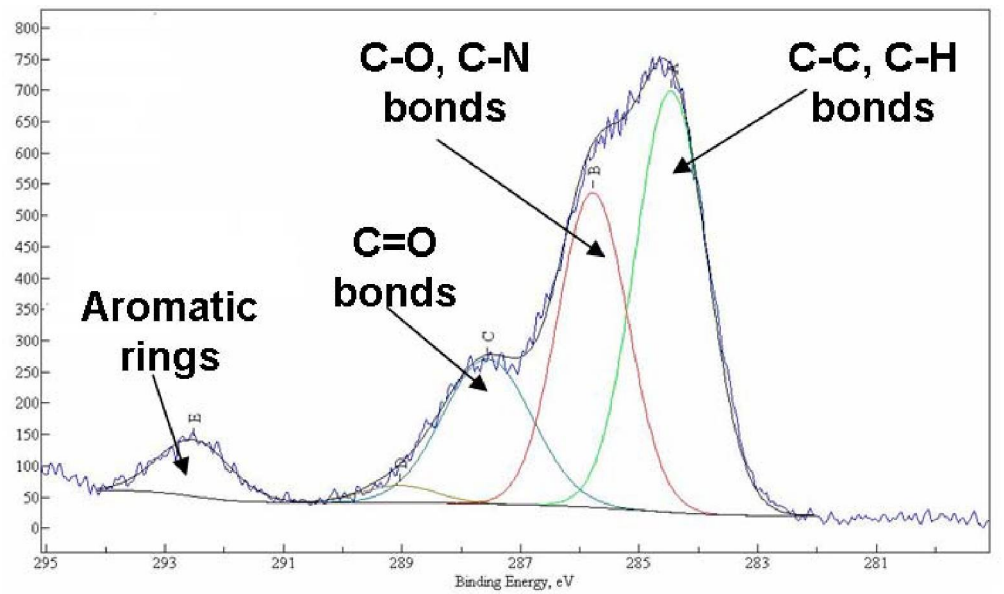

Figure 9. XPS detailed analysis of carbon region of a sample functionalized with ALP.

Enzymatic activity tests reveal that ALP maintains its activity after grafting. In fact an absorbance of 0,08±0,05 could be measured for functionalized samples. It corresponds to an ALP concentration comprised between 0,3 and 0,6 mg/ml, if compared with values of standard solution of ALP stored in the same conditions.

Discussion

The purpose of this research is the examination of the bioactive properties of an innovative surface modified titanium alloy. The surface modification consists in a thermo-chemical treatment performed by using H_2O_2. So it is a lower cost and environmental cleaner process, respect to other techniques proposed at this purpose, such as ion implantation [59],

alkaline etching [60], anodic or plasma oxidation [61, 62]. The parameters of the chemical treatments were optimized in order to obtain a moderate roughness, a low surface mechanical damage and good mechanical performances of the treated surface (fatigue and scratch resistance). The thermo-chemical oxidation involves the formation of a partially crystalline and nonstoichiometric oxide, presenting a negative surface charge and a high density of hydroxyl groups. It promotes selective Ca and P adsorption and bone-like apatite precipitation in SBF. Precipitated apatite is partially crystalline and it presents small size grains. The in-vitro examination of apatite formation in SBF solution is a useful method for predicting the in-vivo bone bioactivity of a material and as a first screening, avoiding a large number of animal tests [63]. An in-vivo physiochemical bioactive behaviour (apatite precipitation) of the implant surface is relevant for direct bone apposition and bone-bonding ability of the material. The proposed mechanism for this bioactive behaviour is related to the presence of hydroxyl groups on the surface [2] and it is in agreement with our results. It cannot be excluded that a synergistic effect among the topography, chemistry and crystallographic nature of the surface plays a role.

Multifunctional osteoinductive materials, presenting the ability of stimulate the growth of the biological and inorganic components of bone could be of great interest, so it is of interest the cell response to the treated surface. ALP, CICP and OC were chosen to evaluate osteoblast activation and differentiation. In fact they are the typical markers for osteoblast characterization. ALP activity is an early marker of osteoblast differentiation, and its increased expression is associated to the progressive differentiation of cultured osteoblasts [64, 65, 66]. Subsequently Type I collagen is produced (CICP), as one of the major component to form the extracellular matrix [67,,68, 69]. In the mean time begin to increase OC, marker of late osteoblast differentiation [70]. MG63 cultured on the Ti-treated surface, besides showing a very good rate of proliferation, exhibited significantly higher level of ALP, CICP at 3 and 7 days, and OC at 7 days, when compared to CTR. These results indicate that cells grown on the experimental material were active and well differentiated, in comparison to both CTR and standard reference (Ti-untreated).

LDH and IL-6 were measured in order to evaluate the possible cell damage after culture on treated substrates. LDH is released by cells in presence of membrane damage and it is used as an indicator of cytotoxicity. IL-6 has a major role in the mediation of the inflammatory response. The obtained values of LDH and IL-6, which did not differ among the analyzed groups, indicated that the surface modification treatment of Ti did not induce cytotoxicity.

Even if other in vitro and in vivo experiment will be performed for a complete characterization of the new surface treatment, the thermo-chemical oxidation seems to be a promising method for Ti clinical use in the dental and orthopaedic field.

Preliminary studies on biological functionalization of the modified titanium surface show that it is possible to covalently graft an enzyme (alkaline phosphatase) maintaining its activity. It has been shown [56] that ALP can improve bone formation and mineralization around implants, so its presence onto metal surface could accelerate and enhance its bone integration. Future experiments will investigate cellular response to functionalized materials and also possible synergies between inorganic and biological modifications.

Conclusion

Bioactivity and osseointegration ability of titanium is an open problem both in case of dental and orthopaedic implantable devices. Plasma sprayed multilayer and CaP electrodeposited coatings are available on the market nowadays. On the other hand a lot of techniques were tested in order to obtain in-vivo inorganic and biological bioactive behaviour, without applying thick coatings, but they are not enough cost-effective and performant. The transformation of a metallic device to a biological one involves also several complications for storage and preservation that should be considered.

In this chapter data about an innovative surface treatment that could be of interest at this regard are also reported. The treated surface shows a partially crystalline and nonstoichiometric oxide, presenting a negative surface charge and a high density of hydroxyl groups. It promotes bone-like apatite precipitation in SBF and in-vitro osteoblast differentiation. So it is of interest in order to promote in-vivo rapid osseointegration and new bone formation by stimulating both the growth of the inorganic and the biological component of it. The modified surface is suitable for further biological functionalization, in fact the enzyme alkaline phosphatase has been successfully grafted to it, with a direct covalent linking.

References

[1] Puleo, DA.; Nanci, A. (1999). Understanding and controlling the bone-implant interface. *Biomaterials*, **20**, 2311-2321

[2] Kokubo T; Kim HM; Kawashita M. (2003). Novel bioactive materials with different mechanical properties. *Biomaterials*, **24**, 2161–2175

[3] Rammelt S; Illert T; Bierbaum S; Scharnweber D; Zwipp H; Schneiders W. (2006). Coating of titanium implants with collagen, RGD peptide and chondroitin sulfate. *Biomaterials*, **27**, 5561-5571

[4] Xiao, S-J; Kenausis, G; Textor, M. Biochemical modification of titanium surfaces. In Springler, *Titanium in Medicine* – Chapter 13, Springler; 2001; 417-453

[5] De Jonge, L. T; Leeuwenburgh, S. C. G; Wolke, J. G. C; Jansen, J. A. Organic-Inorganic Surface Modifications for Titanium Implant Surfaces *Pharm Res*, 2008, 25,10, 2357-2369

[6] Rizzi, G; Scrivani, A; Fini, M; Giardino, R Biomedical coatings to improve the tissue-biomaterial interface. *Int J Artif Organs*, 2004, 27, 649-657

[7] Renghini, C; Girardin, E; Fomin, A.S; Manescu, A; Sabbioni, A; Barinov, S.M; Komlev, V.S; Albertini, G; Fiori, F Plasma sprayed hydroxyapatite coatings from nanostructured granules, *Mater Sci Eng B* **152** (2008) 86-90

[8] Lee, T.M; Chang, E; Wang, B.C; Yang, C.Y. Characteristics of plasma-sprayed bioactive glass coatings on Ti6Al4V alloy: an in vitro study. *Surf Coat Technol*, 1996, 79, 170-177

[9] Vernè, E; Bona, E; Angelini, E; Rosalbino, F; Appendino, P; Correlation between microstructure and properties of biocompatible coatings. *J Eur Ceram Soc*, 2002, 22, 2315-2323

[10] Miola, M; Ferraris, S; Di Nunzio, S; Robotti, P; Bianchi, G; Fucale, G; Maina, G; Cannas, M; Gatti, S; Masse, A; Vitale-Brovarone, C; Vernè, E; Surface Silver-doping of biocompatible glasses to induce antibacterial properties. Part II: plasma sprayed glass coatings, *J Mater Sci. Mater Med*, 2009, 20, 741-749

[11] Verné, E; Ferraris, S; Miola, M; Fucale, G; Maina, G; Robotti, P; Bianchi, G; Martinasso, G; Canuto, RA; Vitale Brovarone, C Synthesis and characterization of a bioactive and antibacterial glass-ceramic (II): Plasma Spray coatings on metallic substrates, *Adv Appl Cer*, 2008, 107, 1743-6753

[12] Szmukler-Moncler, S; Perrin, D; Piattelli, A; Scarano, A Evaluation of a soluble calcium phosphate coating obtained by electrochemical deposition: A pilot study in the pig maxillae. In *Biological Mechanism of Tooth Eruption, Resorption and Replacement by Implants, Z. Davidovitch and J. Mah*, 1998, 481-485

[13] Neumann, H-G; Beck, U; Drawe, M; Steinbach, J; Multilayers systems for corrosion protection of stainless steel implants. *Surf Coat Technol*, 1998, 98, 1157 – 1161

[14] Zeggel, P. Bioactive calcium phosphate coatings for dental implants. *International magazine of oral implantology*, 2000, 1, 52-57

[15] Szmukler-Moncler, S; Perrin, D; Ahossi, V; Pointaire, Ph Evaluation of BONIT®, a fully resorbable CaP coating obtained by electrochemical deposition, after 6 weeks of healing: a pilot study in the pig maxilla. *Key Eng Mater*, 2001, 192-195, 395-398

[16] Yang, Y; Kim, K-H; Ong, J.L. A review on calcium phosphate coatings produced using a sputtering process – an alternative to plasma sprayng. *Biomaterials*, 2005, 26,327-337

[17] Leeuwenburg, S.G.C; Heine, M.C; Wolke, J.C.G; Pratsinis, S.E; Schoonman, J; Jansen J.A Morphology of calcium phosphate coatings for biomedical applications deposited using Electrostatic Spray Deposition. *Thin Solid Films*, 2006, 503, 69-78

[18] Arias, J.L; Mayior, M.B; Pou, J; Leng, Y; Leon, B; Perez-Amor, M. Micro- and nano-testing of calcium phosphate coatings produced by pulsed laser deposition. *Biomaterials*, 2003, 24, 3403-3408

[19] Hashimoto, Y, Kawashima, M; Hatanaka, R; Kusunoki, M; Nishikawa, H; Hontsu, S; Nakamura, M. Cytocompatibility of calcium phosphate coatings deposited by an ArF pulsed laser. *J Mater Sci: Mater Med*, 2008, 19, 327-333

[20] Wang, D; Chen, C; He, T; Lei, T. Hydroxyapatite coating on Ti6Al4V alloy by a sol-gel method. *J Mater Sci: Mater Med,* 2008, 19, 2281-2286

[21] Stoch, A; Jastrzebski, W; Dlugon, E; Lejda, W; Trybalska, B; Stoch, G.J; Adamczyk, A. Sol-gel derived hydroxyapatite coatings on titanium and its alloy *Ti6Al4V. J Mol Struct*, 2005, 744-747, 633-640

[22] Wang, X.X; Yan, W; Hayakawa S;, Tsuru, K; Osaka, A. Apatite deposition on thermally and anodically oxidized titanium surfaces in a simulated body fluid. *Biomaterials*, 2003, 24 4631-4637

[23] Forsgren, J; Svahn, F; Jarmar, T; Engqvist, H. Formation and adhesion of biomimetic hydroxyapatite deposited on titanium substrates. *Acta Biomater*, 2007, 3, 980-984

[24] Mao, C; Li, H; Cui, F; Ma, C; Feng, Q Oriented growth of phosphates on polycrystalline titanium in a process mimickling biomineralization. *J Cryst Growth*, 1999, 206, 308-321.

[25] Lausmaa, J. *Mechanical, thermal, chemical and electrochemical surface treatment of titanium.* Springler, Titanium in Medicine – Chapter 8, Springler; 2001; 231-266

[26] Kokubo, T Formation of biologically active bone-like apatite on metals and polymers by a biomimetic process. *Thermochimica Acta* 280/281 (1996) 479-490

[27] Nishiguchi, S; Nakamura, T; Kobayashi, M; Kim, H-Min; Miyaji, F; Kokubo, T The effect of heat treatment on bone-bonding ability of alkali-treated titanium. *Biomaterials*, 1999, 20, 491-500

[28] Kokubo, T; Matsushita, T; Takadama, H Titania-based bioactive materials. *J Eur Ceram Soc*, 2007, 27, 1553-1558

[29] Kokubo, T. Apatite formation on surfaces of ceramics metals and polymers in body environment. *Acta Mater*, 1998, 46, 7, 2519-2527

[30] Fawzy, A.S; Amer, M.A. An in vitro and in vivo evaluation of bioactive titanium implants following sodium removal treatment. *Dent Mater*, 2009, 25, 48-57

[31] Spriano, S; Bosetti, M; .Bronzoni, M; Vernè, E; Maina, G; .Bergo, V; Cannas, M Surface properties and cell response of low metal ion release Ti-6Al-7Nb alloy after multi-step chemical and thermal treatments. *Biomaterials*, 2005, 26, 1219-1229

[32] Spriano, S; Bronzoni, M; Vernè, E; Maina, G; Bergo, V; Windler, M Characterization of surface modified Ti-6Al-7Nb alloy. *J Mater Sci Mat Med,* 2005, 16, 1-12

[33] Wang, X-X; Hayakawa, S; Tsuru, K; Osaka, *A* Bioactive titania gel layers formed by chemical treatment of Ti substrate with H2O2/HCl solution. *Biomaterials*, 2002, 23, 1353-1357

[34] Kaneko, S; Tsuru, K; Hayakawa, S; Takemoto, S; Ohtsuki, C; Ozaki, T; Inoue, H; Osaka, A. In vivo evaluation of bone-bonding of titanium metal chemically treated with hydrogen peroxide solution containing tantalum chloride. *Biomaterials*, 2001, 22, 875-881

[35] Xiao, F; Tsuru, K; Hayakawa, S; Osaka, A. Low temperature synthesis of bioactive TiO2 thin film by two step treatment. In *Bioceramics* 15 Trans. Tech. Publishers, 2002, 533-536

[36] K.Shibata, K.Tsuru, S.Hayakawa, A.Osaka Biomimetic apatite deposition on titanium substrates treated with low concentrations H2O2 solutions In *Bioceramics* 15 Trans. Tech. Publishers, 2002, 55-58

[37] Wu, J-M; Hayakawa, S; Tsuru, K; Osaka, A. Low temperature deposition of bioactive crystalline titania films: effects of tantalum. In *Bioceramics* 15 Trans. Tech. Publishers, 2002, 537-540

[38] Kawasaki, S; Tsuru, K; Hayakawa, S; Osaka, A. Control of morphology of titania film with high apatite forming ability derived from chemical treatments of titanium with hydrogen peroxide. In *Bioceramics* 16 Trans. Tech. Publishers, 2003, 443-446

[39] Wu, J-M; Hayakawa, S; Tsuru, K; Osaka, A. Porous titania films prepared from interactions of titanium with hydrogen peroxide solution. *Scripta Mater*, 2002, 46, 101-106

[40] Wang, X-X, Hayakawa, S; Tsuru, K; Osaka, A A comparative study of in vitro apatite deposition on heat, H2O2, and NaOH treated titanium surfaces. *J Biomed Mater Res*, 2001, 54, 172-178

[41] Wang, X-X; Hayakawa, S; Tsuru, K; Osaka, A Improvement of bioactivity of H2O2/TaCl5-treated titanium after subsequent heat treatments. *J Biomed Mater Res,* 2000, 52: 171-176

[42] Chiesa, R; Giavaresi, G; Fini, M; Mandrini, E; Giordano, C; Bianchi, A; Giardino, R In vitro and in vivo performance of a novel surface treatment to enhance osseointegration of endosseous implants. *Oral Surg Oral Med oral Pathos oral Endol* 2007, 103: 745-46

[43] Sandrini, E; Chiesa, R; Rondelli, G; Santin, M; Cigada, A A novel biomimetic treatment for a n improved osteointegration of titanium. *JABB* 2003, 1, 33-42

[44] Giordano, C; Sandrini, E; Del Curto, B; Signirelli, E; Rondelli, G; Di Silvio, L Titanium for osteointegration: Comparison between a novel biomimetic treatment and commercially exploited surfaces, *JABB* 2004, 2, 35-44

[45] Aita, H; Hori, N; Takeuchi, M; Yamada, M; Anpo, M; Ogawa, T The effect of ultraviolet functionalization of titanium on integration with bone. *Biomaterials*, 2009, 30, 1015-1025

[46] Hildebrand, H.F; Blanchemain, N; Mayer, G; Chai, F; Lefebvre, M; Boschin, F Surface coatings for biological activation and functionalization of medical devices. *Surf Coat Tech*, 2006, 200, 6318-6324

[47] Morra, M Biochemical modification of titanium surfaces: peptides and ECM proteins. *Eur Cell Mater*, 2006, 1, 12, 1-5

[48] Lee, S-H; Shin, H. Matrices and scaffolds for delivery of bioactive molecules in bone and tissue engineering. *Adv Drug Del Rev*, 2007, 59, 339-359

[49] Bagno, A; Piovan, A; Dettin, M; Chiarion, A; Brun, P; Gambaretto, R; Fontana, G; Di Bello, C; Palù, G; Castagliuolo, I. Human hosteoblas-like cell adhesion on titanium substrates covalently functionalized with synthetic peptides. *Bone* 2007; 40, 693-699

[50] Nanci, A; Wuest, J.D; Peru, L; Sharma, V; Zalzal, S; McKee, M.D. Chemical modification of titanium surfaces for covalent attachemnt of biological molecules *J Biomed Mater Res*, 1998, 40, 324-335

[51] Hayakawa, T; Yoshinari, M; Nemoto, K Direct attachment of fibronectin to tresyl chloride-activated titanium. *J Biomed Mater ResA*, 2003, 67, 684-688

[52] Hayakawa, T; Nagai, M; Yoshinari, M; Makimura, M; Nemoto, K. Cell-adhesive protein immobilization using tresyl chloride-activation technique for the enhancement of initial cell attachment. *J Oral Tissue Engin* 2004, 2, 14-24

[53] Morra, M; Cassinelli, C; Cascando, G; Cahalan, P; Cahalan, L; Fini, M; Giardino, R. Surface engineering of titanium by collagen immobilization. Surface characterization and in vitro and in vivo studies. *Biomaterials*, 2003, 24, 4639-4654

[54] Morra, M; Cassinelli, C; Carpi, A; Giardino, R; Fini, M. Effects of molecular weight and surface functionalization on surface composition and cell adhesion to hyaluronan coated titanium. *Biomed Pharmacother*, 2006, 60, 365-369

[55] De Jonge L.T; Leeuwenburg, S.C.G; van den Beuken, J.J.J.P; Wolke, J.G.C; Jansen, J.A. Electrosprayed enzyme coatings as bioinspired alternatives to bioceramic coatings for orthopaedic and dental implants. *Adv Func Mater* 2009, 79, 1-8

[56] Piattelli, A; Scarano, A; Corigliano, M; Piattelli, M. Effects of alcaline phosphatase on bone healing around plasma-sprayed titanium implants: a pilot study in rabbits. *Biomaterials*, 1996, 17, 1443-1449

[57] Spriano S; Vernè E; Ferraris S. *Multifunctional titanium surfaces for bone integration.* Patent Application TO2007A000719

[58] Ocal C; Ferrer S. Low temperature diffusion of Pt and Au atoms through thin TiO2 films on a Ti substrate. (1987). *Surface Science*, 191, 147-156

[59] Maitz MF; Poon RWY; Liu XY; Pham MT; Chu P K. (2005). Bioactivity of titanium following sodium plasma immersion ion implantation and deposition. *Biomaterials*, **26**, 5465-5473

[60] Kim HM; Miyaji F; Kokubo T; Nakamura T. (1996*)*. Preparation of bioactive Ti and its alloys via simple chemical surface treatment. *Journal of Biomedical Materials Research*, **32**, 409-417

[61] Sul YT; Johansson C; Byon E; Albrektsson T. (2005). The bone response of oxidized bioactive and non-bioactive titanium implants. *Biomaterials*, **26**, 6720–6730

[62] Silva MAM; Martinelli AE; Alves Jr C; Nascimento RM; Ta´vora MP; Vilar CD. (2006). Surface modification of Ti implants by plasma oxidation in hollow cathode discharge. *Surface Coating Technology*, 200, 2618– 2626

[63] Kokubo T; Takadama H. (2006). How useful is SBF in predicting in vivo bone bioactivity? *Biomaterials*, **27**, 2907–2915

[64] Aubin JE; Liu F; Malaval L; Gupta AK. (1995). Osteoblast and chondroblast differentiation. *Bone*, **17**, 77S–83S.

[65] Malaval L; Liu F; Roche P; Aubin JE. (1999*)*. Kinetics of osteoprogenitor proliferation and osteoblast differentiation in vitro. *Journal of Cell Biochemistry*, **74**, 616–27.

[66] Atsushi E; Korenori O; Satoshi I; Shigeyuki E; Takayoshi N; Yukichi U. (2003). Effects of -TCP and TetCP on MC3T3-E1 proliferation, differentiation and mineralization. *Biomaterials*, **24**, 831-836.

[67] Franceschi RT; Iyer BS. Relationship between collagen synthesis and expression of the osteoblast phenotype in MC3T3-E1 cells. (1992). *Journal of Bone and Mineral Research*, **7**, 235-246.

[68] Cowles EA; DeRome D; Pastizzo G; Brailey LL; Gronowicz GA. (1998). Mineralization and the expression of matrix proteins during in vivo bone development. *Calcified Tissue International*, **62**, 74-82.

[69] Fini M; Giardino R; Borsari V; Torricelli P; Rimondini L; Giavaresi G; Nicoli Aldini N. (2003). In vitro behaviour of osteoblasts cultured on orthopaedic biomaterials with different surface roughness, uncoated and fluorohydroxyapatite-coated, relative to the in vivo osteointegration rate. *International Journal of Artificial Organs,* **26**, 520-528.

[70] Mayr-Wohlfart U; Fiedler J; Gunther KP; Puhl W; Kessler S. (2001). Proliferation and differentiation rates of a human osteoblast-like cell line (SaOS-2) in contact with different bone substitute materials. *Journal of Biomedical Materials Research*, **57**, 132-139.

In: Titanium Alloys: Preparation, Properties and Applications ISBN: 978-1-60876-151-7
Editor: Pedro N. Sanchez, pp. 295-318

Chapter 6

ULTRASONIC MACHINING OF TITANIUM AND ITS ALLOYS

Rupinder Singh*

Production Engineering, Department of Production Engineering, Guru Nanak Dev Engineering College, Ludhiana-141006 (India)

Abstract

Ultrasonic machining (USM) is a mechanical material removal process used to erode holes and cavities in hard or brittle work pieces by using shaped tools, high frequency mechanical motion, and an abrasive slurry. Unlike other non-traditional processes such as laser beam, and electrical discharge machining, ultrasonic machining does not thermally damage the work piece or appear to introduce significant levels of residual stress, which is important for the survival of materials in service. The fundamental principles of stationary ultrasonic machining, the material removal mechanisms involved and the effect of operating parameters on material removal rate, tool wear rate, and work piece surface finish of titanium and its alloys are reviewed, for application in manufacturing industry.

Introduction

The human race has distinguished itself from all other forms of life by using tools and intelligence to create items that serve to make life easier and more enjoyable. Through the centuries, both the tools and the energy sources to power these tools have evolved to meet the increasing sophistication and complexity of mankind's needs. Initially, tools were powered by muscles; either human or animal. However as the power of water, wind, steam, and electricity were harnessed, mankind was able to further extend manufacturing capabilities with new machines, with greater accuracy, and faster rates.

With the development of technology, the scientists and technologists in the field of manufacturing face more and more challenges. The difficulty in adopting the traditional manufacturing processes can be attributed mainly to the following three basic sources:

* E-mail address: rupindersingh78@yahoo.com. Phone: +91 98722 57575.

a) New materials with low machinability.
b) Dimensional accuracy requirements.
c) Higher production rate and economy.

Many new materials and alloys that have been developed for specific uses possess a very low machinability. Producing complicated geometries in such materials becomes extremely difficult with the traditional methods. Also, sometimes the combination of the material properties and the job dimensions is such that it makes the use of traditional processes impossible. Examples of these types of jobs are, machining a complicated turbine blade made of super alloys, and producing holes and slots (both through and blind) in materials such as glass and semiconductors. So, drilling a non-circular hole or a micro hole becomes problematic (and sometimes impossible) if the traditional processes are used. Apart from the situations cited, higher production rate and economic requirements may demand the use of nontraditional (or unconventional) machining processes [1-2]. The basic objective of all machining operations is to remove the excess material to obtain the desired shape and size. Yet in the past 50 years, different nontraditional manufacturing processes have been invented and successfully implemented in production. The reason that there are such a large number of non-traditional processes is the same as there are such a large number of conventional processes; each process has its own characteristic attributes and limitations, hence no one process is the best for all manufacturing situations [2].

Ultrasonic machining (USM) is of particular interest for the machining of non-conductive, brittle work piece materials such as engineering ceramics. Because the process is non-chemical and non-thermal, materials are not altered either chemically or metallurgically [1-2]. The process is able to effectively machine all materials harder than HRC 40, whether or not the material is an electrical conductor or an insulator [2-8]. Holes as small as 76μm in diameter can be machined, however, the depth to diameter ratio is limited to about 3:1[4, 8]. The history of USM began with a paper by R.W. Wood and A.L. Loomis in 1927[9, 10] and the first patent was granted to American engineer Lewis Balamuth in 1945[3, 11, 12]. USM has been variously termed ultrasonic drilling; ultrasonic abrasive machining; ultrasonic cutting; ultrasonic dimensional machining and slurry drilling [13]. However, from early 1950s it was commonly known either as ultrasonic impact grinding or USM [4, 11, 14, 15]. Since its invention, USM has developed into a process that is relied upon to solve some of the manufacturing community's toughest problems [1].

The USM process begins with the conversion of low- frequency electrical energy to a high-frequency electrical signal, which is then fed to a transducer [1, 13-18]. The transducer converts high frequency electrical energy into mechanical vibrations, which are then transmitted through an energy-focusing device, i.e. horn/tool assembly [19-21]. This causes the tool to vibrate along its longitudinal axis at high frequency (usually $\geq$ 20 kHz) [1, 13]. The tool vibrates with a total excursion of only a few hundredths of a millimeter in a direction parallel to the axis of tool feed [1, 20, 21]. For efficient material removal to take place, the tool and tool holder must be designed with consideration given to mass and shape so that resonance can be achieved within frequency range capability of the USM machine. Typical power ratings range from 50-3000 W [22] and can reach 4 kW in some machines [13]. A controlled static load is applied to the tool and abrasive slurry (composing a mixture of abrasive material; e.g. silicon carbide, boron carbide, alumina, etc. suspended in oil or water) is pumped around the cutting zone [13]. The vibration of the tool causes the abrasive particles held in slurry between the tool and the work

piece, to impact the work piece surface causing material removal by micro chipping [23]. Figure 1 shows the basic elements of an USM set up using either a magnetostrictive or piezoelectric transducer with brazed and screwed tooling [24].

Variations on this basic configuration include: -

- A variation of USM, known as rotary ultrasonic machining (RUM), involves the use of rotating diamond-plated tools on drilling, milling, and threading operations [1,13]. The construction of RUM machines is nearly identical to USM machines except for the addition of a 0.37-0.56 kW (1/2-3/4 HP) rotary spindle motor capable of rotating up to 5000 rpm [13, 25]. The ultrasonic power required for the RUM process is considerably less than that used for USM; RUM machines typically are rated at 300 W or less [1]. Machining performance in the rotary mode is found to be much superior to the conventional mode [26].Recently the feasibility to machine ceramic matrix composites (CMC) using RUM has been investigated, which results into better MRR, and hole quality (in terms of chipping dimensions) [27].
- USM combined with electrical discharge machining (EDM) and abrasive flow machining (AFM) [17, 19, 21, 28, 29]. Now a day's ultrasonic vibration are used successfully to enhance machining capability of micro-EDM to handle titanium alloys [30]. It has been found in micro-hole machining of titanium plate, micro ultrasonic vibration lapping enhance the precision of micro-holes drilled by micro electro-discharge machining [31].
- Ultrasonic assisted conventional/ non-conventional machining. USM assisted turning is claimed to reduce machining time, work piece residual stresses and strain hardening, and improve work piece surface quality and tool life compared to conventional turning [8, 29, 32-33].
- There are also non-machining ultrasonic applications such as cleaning, plastic/metal welding, chemical processing, coating and metal forming [1, 13].

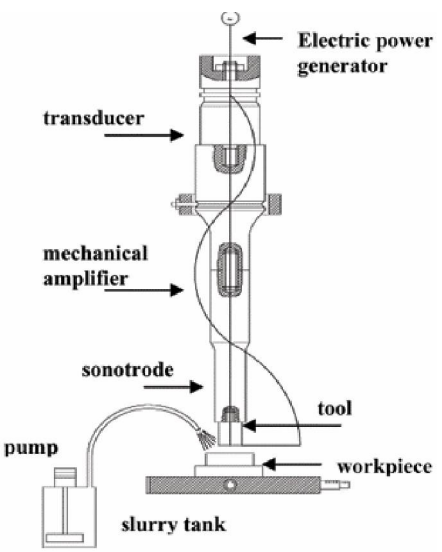

Figure 1. Basic elements of USM [24], schematic representation of the USM apparatus.

1.1. Tooling Considerations in USM

The tool made by silver brazing [34, 35] shaped conversely to the desired hole or cavity and positioned near, but not touching, the surface of the work piece [1]. Many USM applications are involved in drilling where a tool of either simple or complex cross section penetrates axially in to the work piece, to produce either a through or blind hole of the required dimensions [1, 13]. For three-dimensional cavity, a process analogous to die sinking is generally employed [3, 6, 10, 36-39] see figure 2. Although USM volumetric material removal rates are relatively low, the process remains economically competitive because of its ability, with a single pass of the tool, to generate complex cavities or multiple holes in work piece materials that are too hard or fragile to machine by alternate processes [1].

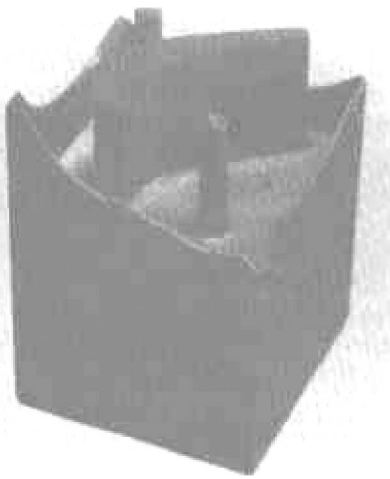

Figure 2. Silicon nitride turbine blade counter-sunk using USM [3].

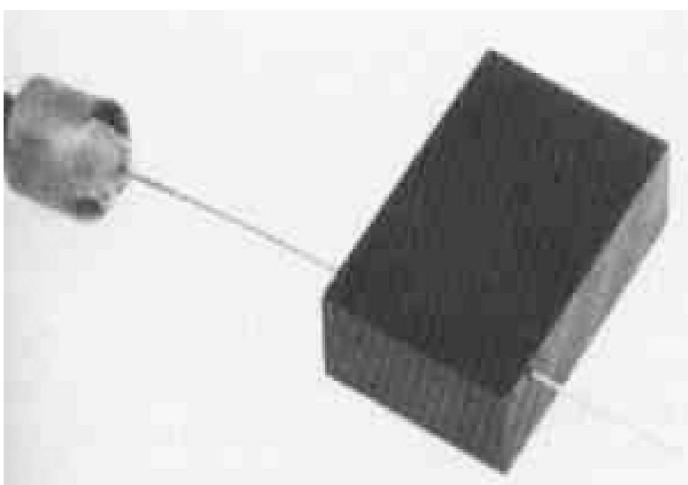

Figure 3. Silicon nitride machined by hypodermic needle using USM [45].

Using this technique graphite electrode for EDM has been shaped in 30 minutes instead of the 20 hours required by copy milling [40-43]. The problem with using tools of complex

form, however, is that they are not subject to same machining rate over the whole of their working surface and experience differential wear rate, both of which affect the product shape [13, 44]. In addition, there are also greater problems in tuning a complex tool to achieve maximum performance compared to more basic tool [13].

An alternative approach is to use a simple "pencil" tool and contour machine the complex shape with a CNC programme. Figure 3 shows hypodermic needle that was used to ultrasonically drill small holes through a silicon nitride (Si_3N_4) work piece [45]. Recently, the feasibility of using this technique has become of interest and has been investigated in a number of countries including the UK, France, Switzerland, Japan, etc. [13, 23]. A few CNC controlled path rotary USM systems are available commercially such as the SoneX300 from Extrude Hone Limited (France); and the Erosonic US400/US800 from Erosonic AG (Switzerland) [13].

1.2. Ultrasonic Machining of Titanium Alloys

Titanium has been recognized as an element (Symbol Ti; atomic number 22; and atomic weight 47.9) for at least 200 years. However, commercial production of titanium did not begin until the 1950's. At that time, titanium was recognized for its strategic importance as a unique lightweight, high strength alloyed structurally efficient metal for critical, high-performance aircraft, such as jet engine and airframe components [46]. Significant unused worldwide sponge, melting and processing capacity for titanium can accommodate continued growth in to new, high-volume applications. These alloys are branded as difficult to machine materials but have high utility in manufacturing sector [47]. Poor thermal conductivity of Titanium alloys retard the dissipation of heat generated, creating, instead a very high temperature at the tool work-piece interface and adversely affecting the tool life [48]. Titanium is chemically reactive at elevated temperature and therefore the tool material either rapidly dissolves or chemically reacts during the machining process resulting in chipping and pre mature tool failure [47]. Compounding of these characteristics is the low elastic modulus of Titanium, which permits greater deflection of the work piece and once again adds to the complexity of machining these alloys [47-49]. It is important to avoid having the drill ride on the titanium surface in conventional drilling operation since the resultant work hardening makes it difficult to re-establish the cut .So the conventional machining processes are unable to provide good machining characteristics on Titanium alloys [48]. Commercially these alloys are machined by non-conventional Electric Discharge Machining (EDM), which is giving good material removal rate however accuracy and surface finish are some problematic area [50-52]. The combined process of EDM with USM improved the machining efficiency and accuracy [53]. In Ultrasonic assisted cutting the chip, and work face are periodically separated leading to lower temperature/ forces there by increasing tool life [54]. The problem of length of unsupported section of drill has been solved easily using USM. Here the portion of drill is no longer and still allows the chips to flow unhampered out of the hole [55, 56]. This permits application of maximum cutting pressure, as well as rapid drill removal to clear chips and drill re-arrangement without breakage. It has been observed in experimentation using Alumina as slurry and TITAN 15 (ASTM Gr2) as work material [50]. This experimentation set up can be used for commercial use of machining titanium on USM [50, 57].

USM data on titanium alloys from work by Singh and Khamba is summarized in table 1.

Table 1. Data from titanium alloys ultrasonically machined using 5mmØ solid tool [50, 54-57].

Work piece material	Tool	Recommended abrasive	Surface Roughness (Ra) μm	MRR (gm/min)	TWR (gm/min)
TITAN 15 (ASTM Gr.2)	S.S	Al_2O_3	0.48	$5*10^{-3}$	$1.01*10^{-2}$
		SiC	0.31	$4.13*10^{-3}$	$9.20*10^{-3}$
		B_4C	046	$2.63*10^{-3}$	$7.13*10^{-3}$
TITAN 31 (ASTM Gr.5)	S.S	Al_2O_3	0.44	$3.71*10^{-3}$	$8.38*10^{-3}$
		SiC	0.46	$2.77*10^{-3}$	$5.55*10^{-3}$
		B_4C	0.56	$2.47*10^{-3}$	$6.63*10^{-3}$

The chemical composition of titanium alloys (TITAN 15, TITAN31) used is listed in table 2 and 3. The hardness of Ti15 work piece used was 201 HV and for Ti31 was 341 HV at 5 kg. Load.

Table 2. Chemical Analysis (%) TITAN 15 (UTS 491 MPa) ASTM Gr. 2 [50, 54-57].

C	H	N	O	Fe	Ti
0.006	0.0007	0.014	0.140	0.05	Balance

Table 3. Chemical Analysis (%) TITAN 31 (UTS 994 MPa) ASTM Gr. 5 [50, 54-57].

C	H	N	O	Al	V	Fe	Ti
0.019	0.0011	0.007	0.138	6.27	4.04	0.05	Balance

2. Basic Elements of an Ultrasonic Machine Tool

The machines for USM range from small, tabletop-sized units to large- capacity machine tools. In addition to the part-size capacity of a USM machine, suitability for a particular application is also determined by the power rating [1]. Figure 4 shows compact 500W USM machine for small, light- weight work piece [58].

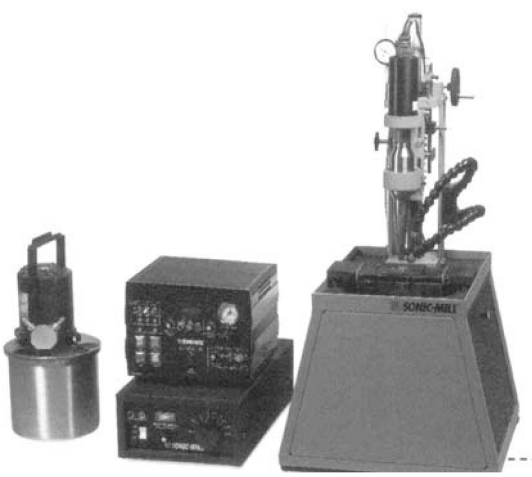

Figure 4. Compact 500W USM machine for small, light- weight work piece [58].

The material removal rate is directly related to power capability of the USM machine. All USM machines share common subsystems regardless of the physical size or power [1]. The most important of these subsystems are the power supply, transducer, tool holder, tool and abrasives [1, 13].

2.1. Ultrasonic Power Supply

The power supply for USM is more accurately characterized as a high power sine-wave generator that offers the user control over both the frequency and power of the generated signal [1]. It converts low-frequency (60Hz) electrical power to high-frequency (approximately 20 kHz). This electrical signal is supplied to the transducer for conversion in to mechanical motion [1, 13].

2.2. Ultrasonic Transducer

In the case of USM transducer, electrical energy is converted in to mechanical motion [1, 13, 56, 57]. With a conventional generator system, the tool and horn are set up and mechanically tuned by adjusting their dimensions to achieve resonance [13]. Recently however, resonance following generators has become available which automatically adjust the output high frequency to match the exact resonance of the horn/tool assembly [2]. They can also accommodate any small error in set up and tool wear, giving minimum acoustic energy loss and very small heat generation [20]. The power supply depends on the size of transducer [22]. Two types of transducers used for USM are based on two different principle of operation, piezoelectric and magnetostrictive [1]. Piezoelectric transducers used for USM generate mechanical motion through the piezoelectric effect by which certain materials, such as quartz or lead zirconate titanate [59-62, 63]. Piezoelectric transducers, by nature, exhibit extremely high electromechanical conversion efficiency (up to 96%) [1, 13, 32, 59, 60, 63, 64], which eliminates the need for the water-cooling of the transducer [1]. These transducers are available with power capabilities up to 900W. Figure 5 shows the converter for compact 500W USM machine [58]. Magnetostrictive transducers are usually constructed from a laminated stack of nickel or nickel alloy sheets. These types of transducers are rugged but have electromechanical conversion efficiencies ranging from only 20 to 35% [1].

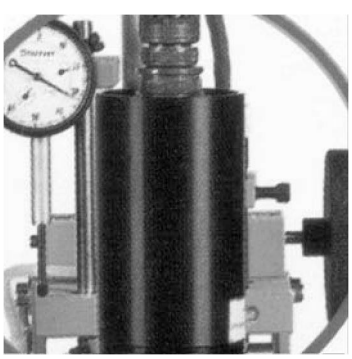

Figure 5. Converter for compact 500W USM machine [58].

2.3. Tool Holder

The function of tool holder is to attach and hold the tool to the transducer. Additionally, the tool holder also transmits the sonic energy to the tool, and in some applications, also amplifies the length of the stroke at the tool [1,]. Figure 6 shows the amplitude coupling for compact 500W USM machine [58]. Tool holders are attached to the transducer by means of a large, loose-fitting screw [1, 58].

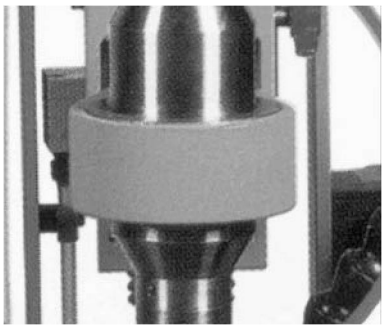

Figure 6. Amplitude coupling for compact 500W USM machine [58].

Half hard copper washers are used between the transducer and tool holder to dampen and cushion the interface, which further reduces the chances of unwanted ultrasonic welding [1]. Figure 7 shows the amplifying tool holders, and mechanically attached tools used for USM [58].

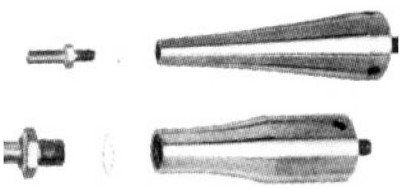

Figure 7. Amplifying tool holders, and mechanically attached tools used for USM [1, 58].

The horn is variously referred to as an acoustic coupler, velocity/mechanical transformer, tool holder, concentrator, stub or sonotrode. The oscillation amplitude at the face of the transducer is too small (0.001-0.1 μm) [63, 65, 66] in order to achieve any reasonable cutting rate; therefore, the horn is used as an amplification device [9, 67, 68]. Figure 8 shows different horn designs with and without additional tool heads [67].

Tool holders are available in two configurations: non- amplifying and amplifying. Non-amplifying tool holders are cylindrical and result in the same stroke amplitude at the output end as at the input end. Amplifying tool holders have a modified cross section, as shown in figure 7 and are designed to increase the amplitude of the tool stroke as much as 600% [1, 58]. The material used should have high wear resistance, good elastic and fatigue strength

properties, and have optimum values of toughness and hardness for the application [10, 63, 69]. Tungsten carbide, silver steel, and monel are commonly used tool materials [13]. Polycrystalline diamond (PCD) has recently been detailed for the machining of very hard work piece material such as hot iso-statically pressed silicon nitride [70]. Tool can be attached to the horn by either soldering or brazing, screw/taper fitting [13, 35]. Also, the actual tool configuration can be machined on to the end of the horn [1, 10, 13, 22, 41, 71-73]. Threaded joints are conventionally used because of quick and easy tool changing, however problems can occur such as self-loosening, loss of acoustic power, fatigue failure etc. [74].

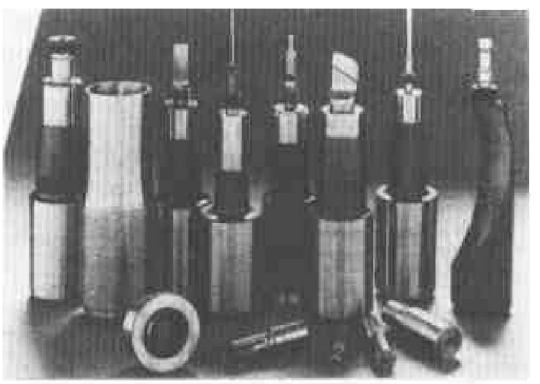

Figure 8. Different horn designs with and without additional tool heads [67].

2.4. Tools and Abrasives

To minimize tool wear, tools should be constructed from relatively ductile materials such as stainless steel, brass and mild steel [1,13]. Depending upon the abrasive used, the work-piece material, work-piece/tool wear ratio can range from 1:1 to 100:1 [1,56, 57]. The tool is normally held against the work piece by a static load exerted via a counter weight/ static weight, spring, pneumatic/hydraulic or solenoid feed system [10, 25, 66, 69, 75]. For optimum results, the system should maintain a uniform working force while machining and be sufficiently sensitive to overcome the resistance due to the cutting action [68, 72]. Static load values of about 0.1-30 N are typically used [13]. The force is particularly critical when drilling small holes less than 0.5 mm diameter as bending of the tool can occur under too high a load. The transport medium for the abrasive should possess low viscosity with a density approaching that of the abrasive, good wetting properties and, preferably, high thermal conductivity and specific heat for efficient cooling, water meets most of these requirements [9, 11, 68]. The abrasive material is mixed with water to form the slurry. The most common abrasive concentration is 50% by weight [1, 58]; however this can vary from 30-60%. Thinner mixtures are used to promote efficient flow when drilling deep holes or when forming complex cavities [1, 11, 66, 69, 76, 77]. Once abrasive has been selected and mixed with water, it is stored in a reservoir at the USM machine and pumped to the tool- work piece interface by re-circulating pumps at rate up to 26.5 L/min [1, 58].

3. Material Removal Mechanisms

Extensive work on the mechanism of material removal reported by Shaw [22], Miller [78], Cook [79], Rosenberg [3] and others [38, 65, 80, 81]. Most of work is on machining mechanism of hard and brittle material [51, 55-56]. These mechanisms are detailed in figure 9 and comprise: -

- Material abrasion by direct hammering of the abrasive particles against the work piece surface [6,21,22,32,36,43,66,72,78,82];
- Micro chipping by impact of the free moving abrasive particles [11,22,36,43,72,82,83];
- Cavitation effect from the abrasive slurry [6,11,22,37,43,83];
- Chemical action associated with the fluid employed [11, 22].

Markov [84] and others [10,22] considered that cavitation erosion and chemical effects were of secondary significance with the majority of work piece material acting essentially to weaken the work piece surface, assist the circulation of the abrasive and the removal of debris.

The individual or combined effect of the above mechanisms result in a work piece material removal by shear [29, 72, 77] by fracture (for hard or work hardened material) and displacement of material at the surface, without removal, by plastic deformation [29] which will occur simultaneously at the transient surface [13]. With porous materials like graphite as opposed to hardened steels and ceramics, cavitation erosion is a significant contributor to material removal [6, 11, 22, 36, 82].

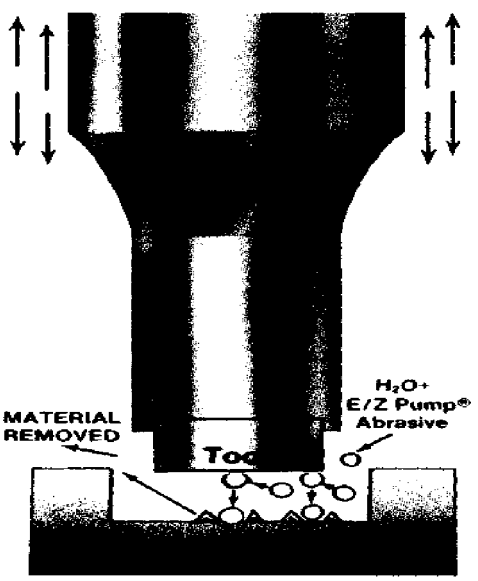

Figure 9. USM material removal mechanisms [58].

3.1. Process Parameters

The major USM process variables effecting material removal rate, accuracy, and surface finish are tool/ horn design, power, amplitude, abrasive size and frequency [1, 13].

Several authors have reviewed the theory and art of designing the tool/ horns, but it is not as yet fully understood [3, 85-92]. Detailed guidelines for tool design are described by Roberg et.al. [3]. Traditional methods of acoustic horn design are based upon differential equation which considers the equilibrium of an infinitesimal element under the action of elastic and inertia forces, which is then integrated over the horn length to achieve resonance [88, 89]. Typical design includes cylindrical, stepped, conical and exponential types [7, 89, 93]. Dam et.al. [94] claimed that a horn can be designed which converts the longitudinal ultrasonic action into a mixed lateral and longitudinal vibration mode. This lateral motion obviously aids contouring work [13, 94].Tuning is normally done from the transducer (screw thread end) where a tuning allowance of 10-15 mm should be made [71, 89, 95]. Recently, finite element modelling (FEM) has been used [7, 88, 89] to design axi-symmetric horn shapes. The analysis can take into consideration the weight of the tool [13]. FEM has also been used to access the working stress to ensure safe stress limits [87].

Power primarily determines the mass of the tool-tool holder combination that can be utilized for an application and also determines the frontal-cutting area of the tool. The more power available in a USM machine, the larger the frontal-cutting area that can be supported [1]. Figure 10 shows the Effect of Ultrasonic power on M.R.R on Ti15/Ti31 using alumina slurry of 320 grit-size with H.S.S. tool [55]. While drilling large size holes, the machine power requirements can be reduced by trepanning the shape with a hollow tool rather than by using a solid tool [96, 97]. Figure 11 shows effect of ultrasonic power on H.S.S. Tool wear [55] while machining Ti15/Ti31 with alumina slurry of 320 grit size on 500W ultrasonic drilling machine [58]. Goetze [98] reported that for tools with equal contact area, there is an increase in penetration rate for tools with larger perimeters; the effect mainly due to difficulty of adequately distributing the abrasive slurry over the machining zone [19, 68, 99-100].

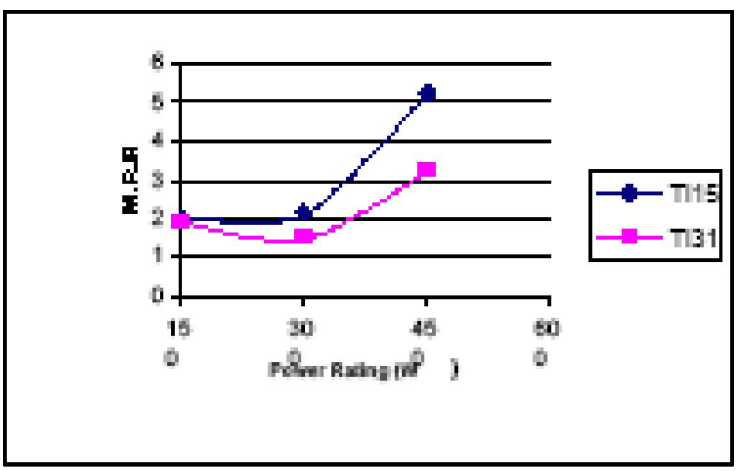

Figure 10. Effect of Ultrasonic power on M.R.R on Ti15/Ti31 using alumina slurry of 320 grit size and H.S.S tool [55].

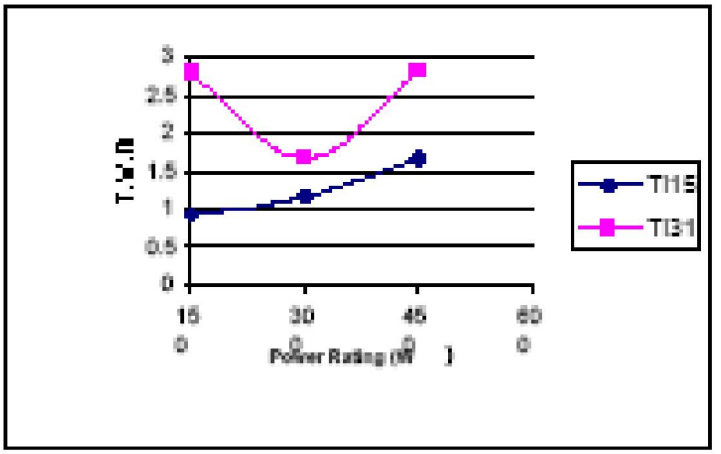

Figure 11. Effect of ultrasonic power on H.S.S. tool wear while machining Ti15/Ti31 [55].

Komaraiah et. al. [101] and others [100, 102] have shown that tool materials can be ranked in order of superiority as follows: Nimonic 80A> thoriated tungsten > silver steel > stainless steel > maraging steel > titanium > mild steel. Neppiras [10] using other tool materials gave the following ranking: tungsten carbide > brass > mild steel > silver steel > stainless steel > copper. Tool with diamond tips have been shown to have good material removal characteristics and extremely low wear rate [2]. Tool wear is an important variable in USM, affecting both MRR and hole accuracy [100,103,104]. The complex tool wear pattern in USM can be divided into longitudinal wear [73, 102,104] and lateral/side/diametral wear [98,105], some of which will occur as a result of cavitation or suction wear [105-108]. Adithan [73] and Venkatesh [109] reported that tool wear maximum at a particular static load, which may be considered optimum for the point of view of maximum MRR [13]. Tool wear affected by work piece hardness and can also be affected by the toughness of work piece [110]. If the hardness of the tool increases by work hardening, the penetration of the abrasive grains into the tool will decrease resulting in higher work piece MRR. In addition, material removal from the periphery of the work zone will be greater so that a convex surface will be formed in the work piece. This causes plastic deformation of the centre of the tool face, forming a dish [13]. It has been found that the degree of hardening is highest at the periphery and lowest at the centre for the tool material [101]. As a result, soft materials, e.g. copper and brass, are unsuitable as tools since they develop burrs at large oscillatory amplitudes [14, 68].

The amplitude (ξ) of the tool motion affects the removal rate and determines the maximum size of the abrasive particles that can be used [1, 13]. Ideally the amplitude should be equal to the mean diameter of the abrasive grit used in order to optimize cutting rate [2, 5, 6, 42]. Shaw [22] showed that MRR $\alpha\ \xi^{3/4}$ while other researchers [78, 84, 98] have advocated that MRR $\alpha\ \xi$, and yet other [3, 10, 11, 77] have suggested that Kops [111] indicated that the uses of a smaller that optimal value (based on MRR) for the static load is better for reducing abrasive wear and increasing tool life. Kazantsev [112] claimed that forced delivery of the slurry increased the output of USM five fold without the need to increase grit size or machine power. The abrasive particle size strongly influences the MRR and surface finish. MRR $\alpha\ \xi^{2}$ at constant frequency and static load. Rosenberg et. al. [3] and Kainth et al. [113] have shown that, in practice, an increase in static load from zero, with other parameters constant, yields an

approximately linear relationship between MRR and static load. As particle size increases; MRR increases proportionally and surface finish is decreased [1, 13, 114-116]. The temperature of slurry also affects the surface finish of the work piece obtained [88]. Figure 12 shows the Photomicrographs of ultrasonically machined surface of titanium at various slurry temperatures (Power rating: 150W, Magnification; 100x). The results shows that more uniform distribution of surface texture (non-directional) at low temperature (10°C) followed by high temperature (60°C) and then at room temperature (27°C) leading to better strength and improved mechanical properties.

Kennedy et al. [19] and Koval'chenko et al. [117] pointed out the difficulty of machining a flat at the bottom of a hole because of uneven slurry distribution across the machining face, resulting in fewer active grits at the tool centre. When the work piece is a hard material, a slightly better surface finish can be obtained than with a material of lower hardness, value as low as 0.4 micron are obtainable [2]. Dam et. al. [94] suggested that better surface finish is obtained when feed rates and depths of cut are decreased. A decrease in abrasive grain size during USM leads to lower Ra value [13]. In addition, the accuracy of the machined hole is improved [6, 10, 15, 77] and a better surface finish is obtained on the bottom face than on the walls of the cavity [2, 3,117].

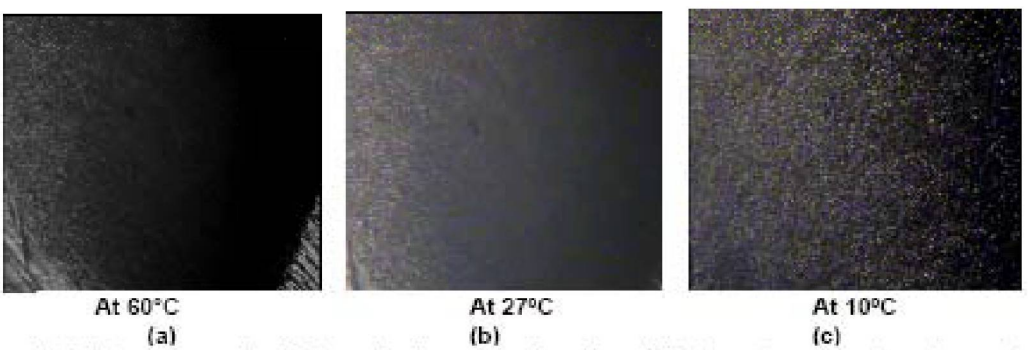

Figure 12. Photomicrographs of ultrasonically machined surface of titanium at various slurry temperatures (Power rating: 150W, Magnification; 100x).

Babitsky et. al. [118] highlighted ultrasonic assisted turning of aviation materials through simulation and experimental study. The suggested finite-element model provides numerical comparison between conventional and ultrasonic turning of inconel 718 in terms of stress/strain state, cutting forces and contact conditions at the work-piece/ tool interface.

Sharma et. al. [119] outlined a new longitudinal mode ultrasonic transducer with an eccentric horn for micro machining. The device can produce an angular vibration of the order of 40 kHz at the cutting tip attached to the end of the horn. The vibrating tip was to be used for precision machining of straight micro-grooves, which are difficult to achieve using existing precision machine tools. The appearance of the machined surface is excellent compared with the torn surface obtained in conventional groove machining.

Rutan [85] reported special USM tools used to simultaneously produce a multitude of holes in precise pattern. This gang-drilling technique significantly increases productivity without compromising quality, see figure 13. Surface finish is governed by the particle abrasive size [1, 13, 51, 58]. The best surface finish results when using 800-grit abrasives and

is on the order of 0.25 microns. As USM is a non-thermal material removal process, material properties remain essentially unaltered. Bellow et. al. has reported that the high cycle fatigue (HCF) properties of some material can be enhanced through the creation of compressive residual stresses on the USM-machined surfaces [86]. This is similar to the effect on HCF properties resulting from shot-peening operations. Figure 14 show the surface of an ultrasonically machined titanium sample exhibits a non-directional surface texture when compared with a conventionally machined (ground) surface [1].

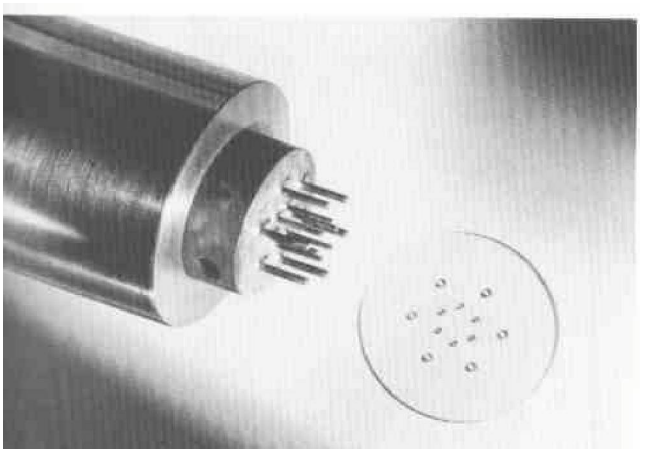

Figure 13. USM Gang drill tool for drilling 12 holes simultaneously [85].

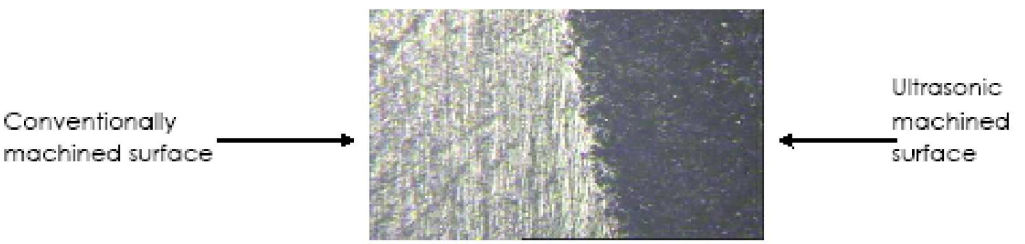

Figure 14. Photomicrograph of the machined surface showing comparison of the conventional machining and ultrasonic machining; Magnification; 100x [1].

The strength of conventionally ground surface was significantly depending upon the grinding action. However the difference between machining directions were statistically insignificant for the specimen prepared by USM. Also for USM specimen, a small difference in strength could be attributed to the abrasive particle size selected [1].The smaller particle size, and correspondingly finer surface finish, resulted in increased tensile strength [1, 13, 56]. The main advantages of the process are that USM is burr-less, distortion-less, having no thermal effects. It is single pass cavity sinking and can be economically used for non-conductive material machining. The main limitation of the process involves relative high tool wear than MRR, frequent tuning of machine, un-economical nature for soft materials machining [51, 55, 88, 90, 93, 95, 120-123] and more over this process does not compete with conventional material removal operations on the basis of stock removal [124- 126]. The results are in line with the observations made by other investigators [121-131].

3.2. Limitations of Study

The results are valid within the specified range of the process parameters. In the present reported work, 500W piezoelectric transducer based USM apparatus was used. The depth of cut was limited as excessive length of the tool was adding to tool weight, and tool weight more than 50mg was resulting in auto-cut for machine. Hence results are limited in present form to machine comparatively small sized work pieces.

The use of solid tool leads to the problem of flushing of slurry particles from the machined surface after a certain depth of cut. Because of this reason, the depth of cut was limited to 1.0 mm in the present work. Also the fabrication of hollow tool was a constraint especially for diamond tool.

Maintaining slurry temperature below 10°C at tool-work interface was a problem in the present set up. Experimentation below slurry temperature of 10°C was not done.

3.3. Future Scope

In the present work, only six process parameters viz. work piece, tool, slurry concentration, ultrasonic power rating, slurry grit size and slurry temperature were investigated. Study of other process parameters like frequency of vibration, static load, flow rate of slurry, depth of cut and type of horns can be done.

The further study can be focused on magnetized flow of abrasive slurry while machining with USM on titanium and its alloys. The magnetic field direction can be so adjusted to check effect of magnetic field on surface quality of work piece, in the same direction or counter direction of slurry flow.

Although effect of ultrasonic power rating has been established in this study in terms of machinability, it can be further investigated with different combinations of process parameters on high power machines.

The same study can be implemented on other tough/soft materials like aluminum, copper etc for their commercial application in manufacturing industry.

4. Conclusion

1) USM is a non-thermal process, which does not rely on a conductive work piece and is preferable for machining work pieces with low ductility and hardness above 40 HRC. It is possible to ultrasonically drill holes in titanium without causing excessive surface integrity damage; specifically cracking using ultrasonic assisted drilling. Higher surface finish is attained when machining on titanium alloy is undertaken by USM and it is not always necessary that if work piece with higher toughness value is machined, it will have less MRR rather it is combination effect of material composition (hardness of work piece) relative to the tool and work piece. In other words selection of operating parameter levels is critical in order to achieve acceptable productivity. No major fatigue problems were encountered with the high-speed steel tool, any chipping/ fracture generally being due to tool/ hole

misalignment during fabrication. Ultrasonic drilling caused no deformation of the work piece microstructure.

2) In general we can say that at low temperature (10oC) when machining is performed better surface finish is attained than at room temperature (27oC) and at high temperature (60oC) at all Power Rating values.
3) The design of tool and horn play an important role in providing a resonance state in USM to maximize the material removal rate.
4) The optimum static load for maximum machining rate has been found to be dependent on the tool configuration (e.g. cross sectional area and shape), the amplitude and mean grit size.
5) The hardness of slurry material should me more than the work piece, in general larger abrasive grit sizes and higher slurry concentrations results in to higher MRR.
6) USM is assumed to be stress and damage free process, so for contour machining it is recommended as it can automatically adjust the output high frequency to match exact resonant frequency of the tool assembly. This also accommodates any small errors in set up and tool wear, giving minimum acoustic energy loss and very small heat generation.
7) For complex shape machining a simple USM tool followed by CNC programming is preferred rather than die sinking using complex form tools.
8) As regards to tool material it should have high wear resistance, good elastic and fatigue strength properties, and have optimum values of toughness and hardness based upon the specific application.
9) Horn material should be corrosion resistant, strong enough to take screw attachment, have high toughness, good brazing characteristics, good acoustic transmission properties and high fatigue resistance at high working amplitude.
10) The tightening of screw attachment with tool horn should be optimum, higher tightening results in to permanent ultrasonic welding of screw with horn. Proper sized acoustic washer generally made up of copper or white metal should be used and replaced after every dismantling of tool/ horn assembly for optimum MRR/TWR.
11) The insert of the tool tip should be counter sunk in head of screw and for joint preparation silver brazing with filler rod which contains silver composition above 50% is preferred for greater joint strength and longer tool life.
12) The slurry acts as a coolant for the horn, tool and work piece, supplies fresh abrasive to the cutting zone and removes debris from the cutting area. The tool may crack from joint if inadequate supply of slurry is there. It also provides a good acoustic bond between the tool, abrasive and work piece, allowing efficient energy transfer.
13) The transport medium for the abrasive should possess low viscosity with a density approaching that of the abrasive, good wetting properties and, preferably, high thermal conductivity and specific heat for efficient cooling. Water is one of best option as regard to transport media for slurry.
14) During operation in USM slurry is splashed out from sump tank because of high vibrations of tool, so, proper care should be made for fixing the slurry concentration and slurry flow rate as it will have a serious effect on tool life and MRR.

Acknowledgements

The author would like to thank Dr. Jaimal Singh Khamba (Prof. Mechanical Engg. UCoE. Punjabi University, Patiala), Mr. Trilok Singh & Mr. Sukhdev Chand (Lab Superintendents Thapar University Patiala) and Dr. M. S. Saini (Principal, Guru Nanak Dev Engineering College, Ludhiana) for providing laboratory facilities.

References

[1] Benedict Gary F., *Book on Non Traditional Manufacturing Processes*, Chapter No.6, Marcel Dekker, Inc., New York, 1987, pp 67-86.

[2] Singh R., *Investigating the machining characteristics of titanium alloys using ultrasonic machining,* Ph.D. Thesis, Thapar University Patiala (2006), pp 2-12.

[3] Rozenberg L. D., Kazantsev V. F., *Ultrasonic cutting*, Consultants Bureau, New York, 1964.

[4] Kohls, J. B., Ultrasonic-manufacturing process: Ultrasonic machining (USM) and ultrasonic impact grinding (US1G), *The Carbide and Tool J.,* 1984, 16(5), pp12-15.

[5] Haslehurst M., *Manufacturing technology* (3rd edn.), 1981, pp 270-271.

[6] Soundararajan, V. and Radhakrishnan, V., An experimental investigation on the basic mechanisms involved in ultrasonic machining. *Int. J. MTDR*, (1986), Vol. 26, No. 3, pp 307-321.

[7] Satyanarayana, A. and Krishna Reddy, B. G., *Design of velocity transformers for ultrasonic machining, Electrical India*, 1984, 24(14), pp 11-20.

[8] Drozda T. J. and Wick C., Non-traditional machining - Book chapter 29: Tool and manufacturing engineers handbook (Desk Ed.), *Soc. Manuf Engrs*, Dearborn, MI, ISBN No. 0872633519, 1, 1983, pp 1-23.

[9] Nishimura, G., *Ultrasonic machining* - Part I. J. Fac. Engg. Tokyo Univ., 1954, 24(3), pp 65-100.

[10] Neppiras E. A., *Report on ultrasonic machining,* Metalworking Prod., (1956), 100, pp 1283-1288, 1333-1336, 1377-1382, 1420-1424, 1464-1468, 1554-1560, 1599-1604

[11] Weller, E. J., *Non-traditional machining processes (*2nd edn.), Soc. of Manuf. Engineers, 1984, pp 15-71.

[12] Fairer, J. O., *English Patent No. 602801 from 3.6.1948 - USM.*

[13] Thoe T. B., Aspinwall D. K. and Wise M. L. H., Review on Ultrasonic Machining, *International Journal of Machine Tools Manufacture*, (1998), Vol. 38, No. 4, pp. 239-255.

[14] Scab, K. H. W., Parametric studies of ultrasonic machining, *SME Tech. paper*, MR90-294, (1990), pp 11.

[15] Neppiras, E. A., Macrosonics in industry: *Ultrasonics*, (1972), Vol. 10, pp 9-13.

[16] Perkins J., An outline of power ultrasonics, *Technical Report by Kerry Ultrasonics,* (1972), pp 7.

[17] Farago, F. T., *Abrasive methods engineering.* Industrial Press, 1980, Vol. 2, pp 480-81.

[18] Balamuth, L., Ultrasonic vibrations assist cutting tools, *Metalworking Prod.*, (1964), Vol. 108, No. 24, pp 75-77.

[19] Kennedy, D. C. and Grieve, R. J., Ultrasonic machining - A review. *The Prod. Engineer*, (1975), Vol. 54, No. 9, pp 481-486.

[20] Kremer, D., New developments on ultrasonic machining, *SME Technical Paper*, MR91-522, 1991, pp 13.

[21] Clifton, D., Imal, Y. and Mc-Geough, J. A., Some ultrasonic effects on machining materials encountered in the offshore industries, *Proc. 30th Int. MATADOR Conf.*, (1993), pp 119-123.

[22] Shaw, M. C., *Ultrasonic grinding, Microtechnic,* (1956), Vol. 10, No. 6, pp 257-265.

[23] Moreland M. A., Ultrasonic machining — Book chapter: Ceramics and glasses, ASM International, *Engineering Material Handbook*, 4, ISBN 0871702827, Schneider and Samuel J., 1991, pp 359-362.

[24] Guzzo P. L., Shinohara A. H. and Raslan A. A., A comparative study on ultrasonic machining of hard and brittle materials, *Journal of Brazil Soc. of Mech. Sci. & Engg.*, (2004), Vol. 26, No. 1, pp 56-61.

[25] Komaraiah, M., Manan, M. A., Narasimha Reddy, P. and Victor, S., Investigation of surface roughness and accuracy in ultrasonic machining, *Precision Engg.* (1988), Vol. 10, No. 2, pp 59-65.

[26] M. Komaraiah and P. Narasimha Reddy, A study on the influence of workpiece properties in ultrasonic machining, *International Journal of Machine Tools and Manufacture,* (1993), Vol. 33, Issue 3 ,pp 495-505.

[27] Z. C. Li, Y. Jiao, T. W. Deines, Z. J. Pei and C. Treadwell, Rotary ultrasonic machining of ceramic matrix composites: feasibility study and designed experiments, *International Journal of Machine Tools and Manufacture, (2005),* Vol. 45, Issues 12-13 , pp 1402-1411.

[28] Seah, K. H. W., Wong, Y. S. and Lee, L. C., Design of tool holders for ultrasonic machining using FEM., *Journal of materials processing technology*, (1993), Vol. 37, No. 1-4, pp 801-816.

[29] Neppiras, E. A., Ultrasonic machining and forming. *Ultrasonics*, (1964), Vol. 2, pp 167-173.

[30] A Cheng Wang, Biing Hwa Yan, Xiang Tai Li and Fuang Yuan Huang, Use of micro ultrasonic vibration lapping to enhance the precision of microholes drilled by micro electro-discharge machining, *International Journal of Machine Tools and Manufacture, (2002),* Vol. 42, Issue 8 , pp 915-923.

[31] Z. C. Li, Y. Jiao, T. W. Deines, Z. J. Pei and C. Treadwell, Rotary ultrasonic machining of ceramic matrix composites: feasibility study and designed experiments, International *Journal of Machine Tools and Manufacture*, (2005), Vol. 45, Issues 12-13 , pp 1402-1411.

[32] Balamuth, L. A., Ultrasonic assistance to conventional metal removal. *Ultrasonics*, (1966), Vol. 4, pp125-130.

[33] Isaev, A. I., Learning with ultrasonically vibrated reamers. *Machines and Tooling,* (1962), Vol. 33, No. 6, pp 27-30.

[34] Singh Rupinder and Khamba J. S., *Silver brazing for tool preparation in USM process, Proceedings of National Workshop of Welding Technology in India-Present status and future trends,* SLIET Longowal (Pb.) INDIA. (2003) pp 61-63.

[35] Singh Rupinder and Khamba J.S, Tool Manufacturing Technique in Ultrasonic Drilling Machine, *Journal of Manufacturing Technology Today*, (2004), Vol-3, Issue-1, pp 05-07.

[36] Machining data handbook (3rd edn.), *Compiled by the Technical Staff' of the Machinability Data Centre,* Cincinnati Metcut Research Associates Inc., 1980, Vol. 2, pp 43-63.

[37] Halm, R. and Schulz, P., *Ultrasonic machining of complex ceramic components, Erosion AC Report,* DKG 70. No. 7, 1993, pp 6.

[38] Graff, K. F., Macrosonics in industry: 5. ultrasonic machining. *Ultrasonics*, (1975), Vol. 13, pp 103-109.

[39] Moreland, M. A., Ultrasonic advantages revealed in the hole story, *Cer. Appl. Manuf.*, (1988), Vol. 187, pp 156-162.

[40] Gilmore R., Ultrasonic machining and orbital abrasion techniques, *SME Technical Paper (Series) AIR*, NM89-419, 1989, pp 1-20.

[41] Moore D., Ultrasonic impact grinding, *Proc. Non-traditional Machining Con/,* Cincinnati, 1985, pp 137-139.

[42] Black, P., An ultrasonic impact grinding technique for electrode-forming and redressing, *Proc. Non-traditional Machining Conf.*, Cincinnati, Ohio, ASM, 1985, pp 129-136.

[43] Kremer, D., Bazine, G. and Moison, A., *Ultrasonic machining improves EDM technology, Electro machining, Proc. 7th Int. Symp.*, ed. by Prof. Crookall J. R., Birmingham, UK, 1983, pp 67-76.

[44] Ghabrial, S. R., Trends towards improving surfaces produced by modem processes, Paper *presented at the 3rd Int. Conf. on Metrol and Prop, of Eng'g Surf*, Teesside, Engl., 1986, pp 113-118.

[45] Robare, M. W. and Richerson, D. W., *Proceedings of ARPA/NAVSEA-Garrett/Ai Research Ceramic Gas Turbine Engine Demonstration Program Review at Rotor blade machining development,* Marine Maritime Academy, 1977.

[46] Singh Rupinder, Ultrasonic machining for tough materials and its application in mechanical industry, *Proc. of fourth national symposium of research scholars on metal and materials at IIT Madras* (INDIA), 2002, pp 31.

[47] D. R. S. V. Verma, B. G. Nanda Gopal, K. Srinivasulu and S. Sudhakar Reddy, Effect of Pre- Drilled holes on Tool life in Turning of Aerospace Titanium Alloys, AMS-03, *Proceedings of National Conference on Advances in Manufacturing System.* Prod. Engg. Dept. Jadavpur University. Kolkata {INDIA}, 2003, pp 42-47.

[48] D. A Dornfeld, J. S.Kim, H. Dechow, J. Hewsow and L. J. Chen, Drilling burr formation in Titanium alloy Ti-6Al-4V, *Annals of CIRP*. Vol. 48/1 (1999), pp 73-76.

[49] *Tool and Manufacturing Engineers hand- book Materials* (1985), SME Vol. 3.

[50] Khamba J.S and Singh Rupinder (2003), Effect of Alumina (White fused) Slurry in Ultrasonic Assisted Drilling of Titanium Alloys (TITAN 15), *Proceedings of National Conference on Materials and Related Technologies (NCMRT-2003)* at TIET Patiala (Pb.) India, pp 75-79.

[51] Singh Rupinder and Khamba J.S. (2003), A Frame work for modeling the machining characteristics of titanium alloys using USM, *Proc. of Int. Conf. Digital aided modeling and simulation at CIT*, Coimbatore, INDIA, pp 31.

[52] A. L Mantle and D. K. Aspinwall (1995), Single point turning of titanium aluminide intermetallic, Titanium 95- Proceedings of the eight world conference on Titanium. Vol. 1 , pp 248-255.

[53] Lin Yan Cherng, Yan, Bing, Hwa Chang and Yong Song, Machining characteristics of titanium alloys (Ti-6Al-4V) using a combination process of EDM and USM, *Journal of material processing technology*, (2000), Vol.104, No.3, pp 171-177.

[54] Singh Rupinder and Khamba J.S. and Grewal J.S, Machining Characteristics optimization using Taguchi Technique in Ultrasonic Drilling of Titanium Alloys, *Proceedings of International Conf. on emerging Technologies in Intelligent System and control (EISCO-2005),* Kumaraguru college of Technology, Coimbatore (Tamilnadu), India, Vol. 1, 5-7 Jan, 2005, pp 81-87.

[55] Singh Rupinder and Khamba J.S., Study of Machining characteristics of Titanium Alloys in Ultrasonic Machining, *Proceedings of the 21st AIMTDR Conf.*, at Vellore Institute of Tech. (Tamilnadu), India, Dec 20-22, 2004.

[56] Singh Rupinder and Khamba J.S., Machining Characteristics comparison of Titanium Alloys in Ultrasonic Assisted Drilling, *Proceedings of International Conf. on recent advances in composite materials (ICRACM2004),* Institute of Technology, B.H.U, India, Dec. 17-19, 2004, pp 438-442.

[57] Singh Rupinder and Khamba J. S., Comparison of Machining characteristics of Titanium Alloys: Effect of Slurry in Ultrasonic Machining Process, *Proceedings of Global congress on Manufacturing and Management*, *The international Conf. on Manufacturing and Management (GCMM-2004)*, at Vellore Institute of Tech. (Tamilnadu) India, Dec.8-10, 2004.

[58] *Instruction manual for stationary* SONIC- MILL 500 W Model 2002 (U.S.A).

[59] Gilmore, R, Ultrasonic machining, *SME Technical Paper*, EM89-123, 1989, pp l0.

[60] Legge, P., Machining without abrasive slurry. *Ultrasonics*, (1966), Vol.4, pp157-162.

[61] Ed. by L. D. Rozenberg, *Physical principles of ultrasonic technology* — Vol. 1 and 2, Plenum Press, N.Y. (1973).

[62] Frederick, J. R., *Ultrasonic engineering*, John Wiley and Sons Inc., New York, ISBN 0471277258 (1965).

[63] Kaczmarek, I., Impact Grinding (Ultrasonic machining) - Book chapter 21: *Principles of machining by cutting, abrasion and erosion*, Peter Peregrinus Ltd., Stevenage, ISBN 0901223662, 1976, pp 448-462.

[64] Jay, F., *IEEE standard dictionary of electrical and electronics terms*, 3rd edition, 1984, pp. 405 and 519.

[65] Kremer, D., The state of the art of ultrasonic machining. *Annals of the CIRP*, 1981, 30(1), pp 107-110.

[66] Mc-Geough, J. A., *Advanced methods of machining*, Chapman and Hall, ISBN 0412319705, 1988, pp 170-198.

[67] US400 - *Ultrasonic machining system*, Brochure from Erosonic AG (1994).

[68] Neppiras, E. A. and Foskett, R. D., Ultrasonic machining - II. Operating conditions and performance of ultrasonic drills. *Philips Tech. Rev.,* 1957, 18(12), pp 368-379.

[69] Kennedy D.C and Grieve R.J, Ultrasonic Machining: A Review, *Prod. Engg*, Vol. 54, (1975), pp 481-486.

[70] Thoe, T. B., Aspinwall, D. K. and Wise, M. L. H., The effect of operating parameters when ultrasonic contour machining, *Twelfth Annual Conference of the Irish Manufacturing Committee (IMC-12),* Cork, Ireland, September 1995, pp. 305-312.

[71] Prabhakar, D. and Haselkorn, M., An experimental investigation of material removal rates in rotary ultrasonic machining. *Trans. of NAMR1/SME*, (1992), 20, pp 211-218.

[72] Wojchiechowski, M. P. et al., Ultrasonic machining: Past, present and future, *SME Paper*, MR72-188, (1972), pp 12.

[73] Adithan, M., Tool wear studies in ultrasonic drilling, *Wear*, (1974), Vol.29, pp 81-93.

[74] Kumehara, H., Characteristics of threaded joints in ultrasonic vibrating system. *Bull, of JSME,* (1984), Vol.27, No. 223, pp 117-123.

[75] Adithan, M., Production accuracy of holes in ultrasonic drilling. *Wear*, (1976), Vol.40, No.3, pp 309-318.

[76] Kazantsev, V. F., Improving the output and accuracy of ultrasonic machining. *Machines and Tooling*, (1966), Vol.37, No.4, pp 33-39.

[77] Pentland, E. W. and Ektermanis, J. A., Improving ultrasonic machining rates - some feasibility studies. *J. Engg. for Ind., Trans. of the ASME*, (1965), 87(Series B), pp 39-46.

[78] Miller, G. E., Special theory of ultrasonic machining. *J. Appl. Phy.*, (1957), Vol. 28, No.2, pp 149-156.

[79] Cook N. H., *Manufacturing analysis*, Addison-Wesley, New York, 1966, pp 133-138.

[80] Kainth, G. S., Nandy Amitav and Singh Kuldeep, *On the mechanics of material removal in ultrasonic machining.* Int. J. MTDR, Pergamon Press, (1979), Vol.19, pp 33-41.

[81] Neppiras, E. A. and Foskett, R. D., Ultrasonic machining -I. Technique and equipment. *Philips Tech. Rev.*, (1957), Vol.18, No.11, pp 325-334.

[82] Khairy, A. B. E., Assessment of some dynamic parameters for the ultrasonic machining process. *Wear*, (1990), Vol.137, pp 187-198.

[83] Ghabriel, S. R., Saleh, S. M., Kohail, A. and Moisan, *A.,* Problems associated with electro-discharge machined electro-chemically machined and ultrasonically machined surfaces. *Wear*, (1982), Vol. 83, pp 275—283.

[84] Markov, A.I., *Kinematics of the dimensional ultrasonic machining method.* Machines and Tooling, (1959), Vol. 30, No.10, pp 28-31.

[85] Rutan, H.L., *Ultrasonic machining (Impact grinding), Proceedings of topical meetings on optical fabrication and test,* at U.S. Department of Energy, 1984.

[86] Bellows G. and Kohls J.B., Drilling without drills, *Am. Machinist, Special Rep.* No. 743, Mar, 1982, pp187.

[87] Amin, S. G., Ahmed, M. H. M. and Youssef, H. A., Optimum design charts of acoustic horns for ultrasonic machining. *Proc. Int. Conf on AMPT'93*, (1993), Vol. 1, pp 139-147.

[88] Pandey, P. C. and Shan, H. S., *Modern machining processes*, Tata McGraw-Hill, Chapter 2, 1980, pp 7-38.

[89] Amin, S. G., Ahmed, M. H. M. and Youssef, H. *A.,* Computer aided design of acoustic horns for ultrasonic machining using finite element analysis. *Proc. AMPT93 Conf.*, (1993), Vol. 2, pp 1455-1465.

[90] Jain V.K., *Advanced machining process*, Allied Publisher Pvt. Limited, India, 2002, pp. 28-56.

[91] *Ultrasonic assembly of thermoplastic mouldings and semi-finished product - Recommendations on methods, construction and applications.* Manual written by German Electrical Manufacturers Association ZVEI.

[92] Merkulov, L. G., Design of ultrasonic concentrations. *Akusticheskiy Zhurnal*, (1957), 3, pp 246-255.

[93] Adithan, M. and Venkatesh, V. C., Study of the performance characteristics of an ultrasonic drilling head, *Wear*, (1975), Vol. 33, pp 261-270.

[94] Dam, H. et.al. Surface characterization of ultrasonic machined ceramics with diamond impregnated sonotrode, *Proc. the Int. Conf. on Machining of Adv. Metals*, Gaithersburg, Maryland, July 1993, pp125-133.

[95] Hahn, R., Ultrasonic machining of glass and ceramics. *Am. Cer. Soc. Bull., (*1993), Vol. 72, No.8, pp 103-106.

[96] E.O. Ezugwa and Z. M. Wang, "Titanium alloys and their machinability - A review", *Journal of Material processing technology*, (1997), Vol. 68, pp 262-274.

[97] Bhattacharyya A., *Book on New Technology,* The institution of engineers (I), Calcutta, 1973.

[98] Goetze, D., Effect of vibration amplitude, frequency and composition of the abrasive slurry on the rate of ultrasonic machining in Ketos tool steel. *The J. Acoust. Soc. of Am.*, (1956), Vol.28, No.6, pp 1033-1037.

[99] Markov A.I., Ultrasonic drilling and milling of hard non-metallic materials with diamond tools, *Mach. Tooling*, (1977), Vol. 48, No.9, pp.45-47.

[100] Mc-Geough J.A, *Advanced methods of machining,* Chapman and Hall, London, 1988.

[101] Komaraiah, M and Narasimha Reddy, P, A study on the influence of work piece properties in ultrasonic machining, *Int. J. Mach. Tools Manuf*, (1993), Vol.33, No.3, pp 495-505.

[102] Smith, T. L., Parameter influence in ultrasonic machining, *Ultrasonics*, (1973), Vol.11, No.5, pp 196-198.

[103] Adithan, M., Tool wear characteristics in ultrasonic drilling. *Tribology* Int., (1981), Vol.14, No.6, pp 351-356.

[104] Markov A. I., *Ultrasonic machining of intractable materials* Iliffe Books Ltd., London (1966).

[105] Riddei, V., Cavitation erosion - A survey of the literature, 1940-1970, *Wear*, (1973), Vol. 23, pp133-136.

[106] Ultrasonic machining of glass at the N. P.L., *Machinery*, May 1964, pp1172-1176.

[107] Adithan, M., Abrasive wear in ultrasonic drilling, *Tribology International*, (1983), Vol.16, No.5, pp 253-255

[108] Adithan, M. and Venkatesh, V. C., Parameter influence on tool wear in ultrasonic drilling, *Tribology Int.*, (1974), Vol.7, No.6, pp 260-264

[109] Venkatesh, V. C., Machining of glass by impact processes, *J. Mech. Working Technology*, (1983), Vol.8, pp247-260.

[110] Iwanek, H., Grathwohl, G., Hamminger, R. and Brugger, N., Machining of ceramics by different methods, Cer. Mat'ls and Components for Engines, *Proc. 2nd Int. Symp.*, 1986, pp 417-423.

[111] Kops, L., *Investigation into the influence of the wear of the abrasive powder on the technological indices of ultrasonic machining. CIRP Annals*, Springer Verlag, Berlin, (1964), Vol.12, No.3, pp151-157.

[112] Kazantsev, V. F., The relationship between output and machining conditions in ultrasonic machining, *Machines and Tooling,* (1963), Vol.34, pp14-17.

[113] Kainth G.S., Nandy A. and Singh K., On the mechanics of material removal in ultrasonic machining, *Int. Jol. Mach. Tool Des. Res.,* (1979), Vol.19, pp 33-41.

[114] Kubota, M., Tamura, Y. and Shimamura, N., Ultrasonic machining with a diamond impregnated tool, *Bull. Japan. Soc. of Free. Engg*, (1977), Vol.11, No.3, pp127-132.

[115] Smith, T. L., *Parameter influence in ultrasonic machining*, BSc. (Hon) Diss., The Nottingham Trent Uni., 1971.

[116] Ghabrial, S. R., Saleh, S. M., Moisan, A. and Kremer D., Some aids towards improving performance in U.S.M. 1984 SME *Manuf Engg. Trans., 12th NAMRC Conf. Proc.,* 1984, pp. 227-232.

[117] Koval'chenko, M. S., Paustovskii, A. V. and Perevyazko, V. A., Influence of properties of abrasive materials on the effectiveness of ultrasonic machining of ceramics, *Sov. Powder Metallurgy and Metal Ceramic,* (1986), Vol. 25, No.7, pp560-562.

[118] Babitsky, V.I.; Mitrofanov, A.V.; Silberschmidt, V.V., Ultrasonically assisted turning of aviation materials: Simulations and experimental study, *Ultrasonics*, (2004), Vol. 42, No. 1-9, pp 81-86.

[119] Sharma, Anurag; Mishiro, Shoji; Suzuki, Kiyoshi; Imai, Tomoyasu; Uematsu, Tetsutaro; Iwai, Manabu, A new longitudinal mode ultrasonic transducer with an eccentric horn for micro machining, *Key Engineering Materials*, (2003), Vol. 238-239, pp 147-152.

[120] Gilmore R., Ultrasonic machining: a case study, *Journal of Materials Processing Technology*, (1991), Vol. 28, Issues 1-2, pp 139-148.

[121] Mishra P. K., *Book on Non conventional machining*, Chapter 3, Narosa publishing house, New Delhi, 2005, pp 22-43.

[122] Singh R. and Khamba J. S., Ultrasonic machining of titanium and its alloys: A review, *Journal of Material Processing Technology*, (2006), Vol. 173, Issue 2, pp 125-135.

[123] Singh R. and Khamba J. S., Investigations for ultrasonic machining of titanium and its alloys, *Journal of Material Processing Technology*, (2007), Vol. 183, Issue 2-3, pp 363-367.

[124] Kumar J. and Khamba J. S., An experimental study on ultrasonic machining of pure titanium using designed experiments, *Journal of Braz. Soc. of Mech. Sci. & Engg.,* (2008), Vol. XXX, No. 3, pp 231-238.

[125] Kumar J., Khamba J. S. and Mohapatra S. K., Investigating and modeling tool wear rate in the ultrasonic machining of titanium, *International Journal of Advanced Manufacturing Technology*, (2008), DOI 10.1007/s00170-008-1556-8.

[126] Singh R. and Khamba J. S., Taguchi approach for modeling material removal rate in ultrasonic machining of titanium, *Material Sci. & Engg.: A*, (2007), Vol. 460-461, pp 365-369.

[127] Singh R. and Khamba J. S., Macro-model for ultrasonic machining of titanium and its alloys: designed experiments, *Journal of Engineering Manufacture*, (2007), Issue B_2, pp 221-229.

[128] Singh R. and Khamba J. S., Comparison of slurry effect on machining characteristics of titanium in ultrasonic drilling, *Journal of Material Processing Technology*, (2008), Vol. 197, Issue 1-3, pp 200-205.

[129] Singh R. and Khamba J. S., Mathematical modeling of tool wear rate in ultrasonic machining of titanium, *The International Jol. of Advanced manufacturing technology*, (2008), DOI 10.1007/s00170-008-1729-5.

[130] Singh R., Experimental investigations on machining characteristics of titanium in ultrasonic impact grinding, *International Jol. of Nanomanufacturing*, (2009), In-press.

[131] Singh R. and Khamba J. S., Mathematical modeling of surface roughness in ultrasonic machining of titanium using Buckingham-∏ approach: A Review, *International Jol. of Abrasive Technology (IJAT)*, (2009), Vol. 2, No. 1, pp 3-24.

In: Titanium Alloys: Preparation, Properties and Applications ISBN: 978-1-60876-151-7
Editor: Pedro N. Sanchez, pp. 319-363

Chapter 7

MODE II FRACTURE BEHAVIOR OF TITANIUM ALLOY TC6 IN COMPARISON WITH STEEL AND ALUMINUM ALLOYS UNDER THERMAL/MECHANICAL LOADING: IN-PLANE SHEAR CASE

X.S. Tang[*]
School of Civil Engineering and Architecture, Changsha University of Science and Technology, Changsha, Hunan, 410114, China

Abstract

Fracture behaviors of titanium alloy TC6 under thermal/mechanical loading in the in-plane shear case are investigated and compared with steel and aluminum materials. A macroscopic crack would be diathermanous for heat. The heat flow would partly or completely pass the crack surface. The crack is then called as the uninsulating crack. An insulating crack implies that the heat flow cannot pass the crack surface completely. The proposed crack model includes both insulating and uninsulating crack cases. The problem of a line crack under the combination of remote uniform heat flow and mechanical shear loading is analytically solved by the complex function method. Obtained are the analytical solutions including the temperature distribution, thermal stress intensity factor, total stress field and strain energy density function. It is found that if the temperature gradient perpendicular to the crack line on the upper and lower crack surfaces remains constant, the mode II thermal stress intensity factor prevails while the mode I thermal stress intensity factor vanishes. It is a typical mode II crack problem. Moreover, the mode II thermal stress intensity factor only depends on the temperature gradient component perpendicular to the crack. The temperature gradient component parallel to the crack line has no influence on the thermal stresses. The diathermanous feature of the crack would affect the thermal stress field. Three materials, say titanium alloy TC6, steel alloy 38Cr2Mo2VA and aluminum alloy LY12, are selected to perform the numerical calculations. Their fracture behaviors under thermal and mechanical loading are discussed and compared by application of strain energy density theory. It is found

[*] E-mail address: tang_xuesong@sina.com (Xue-Song Tang); Fax: +86-731-85256006. (Corresponding author)

that for an insulating crack, the positive temperature gradient would partly kill the mechanical loading that would impede the crack growth. However, the uninsulating crack behaves quite different. For the uninsulating crack, the positive temperature gradient would enhance the mechanical loading or the crack growth. The temperature boundary condition plays an important role in the material failure behaviors. The results are useful for the safety assessment of structural members, especially in the pressurized vessels and pipes and nuclear power plants.

Keywords: thermoelasticity; complex function method; mode II crack; mechanical and thermal loading; crack growth enhancement and retardation; insulating and uninsulating crack; failure analysis; analytical solution; fracture resistance; strain energy density theory.

1. Introduction

Failure analysis and safety assessment of structural members under the combined applications of mechanical and thermal loadings are crucial for engineering problems. To this aim, several fracture criteria have been developed. The energy density criterion [1] has the ability to account for failure by crack initiation and propagation in a wide range of problems [2-7]. Moreover, the volume energy density theory have predicted (not preassumed) that a bifurcation damage pattern could prevail very close to the crack tip. The commonly known macrocrack growth accompanied by plastic enclaves to the side can still be predicted at distance away from the crack tip region. Both damage patterns are determinable from the same continuum mechanics formulation that is not restricted to any size scale if the prevailing physical constants are left undefined as demonstrated for macro/micro dual scaling fatigue analyses in [8, 9]. However, the negative values of energy release rate G and path-independent J-integral are predicted in the fracture analysis for piezoelectric materials [10-13]. This violates their physical definitions. Moreover, the maximum stress criterion encounters contradiction when a crack moves. The near tip maximum normal stress is found to be parallel rather than normal to the prospective crack path [14].

Some basic results were obtained for a crack under the heat flow in the early works [15-17]. The temperature field has no singularity at the crack tip like the displacement field. The temperature gradient field has a $1/r^{1/2}$ singularity similar to the strain field while the volume energy density field still shows a $1/r$ singularity. These basic characteristics should be satisfied in the formulation for thermal cracking problems. If the cracked plate contains the heat source, the problem can be solved by using the singular integral equations [18].

Recent investigations for the in-plane crack problem under mechanical/thermal loading can be found in the literature. For instance, a modified crack closure integral based computation of stress intensity factors for thermal loading through boundary element method (BEM) is presented in [19]. Interfacial crack growth analysis in a TBC/superalloy system due to oxide volume induced internal pressure and thermal loading is done in [20]. In [21], shear band formation and fracture are characterized during mode II loading for a Zr-based bulk metallic glass. In [22], a cracked orthotropic semi-infinite plate under thermal shock is investigated. Ref. [23] discusses the thermal stresses caused by a symmetric indentation of a line crack by an inclusion in an infinite isotropic elastic heat conducting solid. A plane problem for a thermally insulated interface crack with a contact zone in an isotropic

bimaterial under tension-shear mechanical loading and a temperature flux is considered [24]. Discussed in [25] is the fracture behavior of a cracked smart actuator on a substrate under thermal load. Thermoelastic problems for cracked bodies under some types of thermal loading are solved in [26]. The work in [27] is concerned with the application of the volume energy density criterion for predicting the crack trajectories as influenced by mechanical and thermal disturbance in an anisotropic material.

This work focuses on the in-plane shear crack subjected to mechanical/thermal loading. In solids, the predominant effect of heat transfer is due to heat conduction while convection is negligible small. The radiation need not be considered unless the environment calls for it. Moreover, if the temperature gradients are not sufficiently great to cause material transformation, then for all practical purposes the thermoelastic parameters may be assumed to be temperature independent. Coupling between the stress and temperature fields may also be disregarded. The conventional theory of linear thermoelastic theory can thus be applied such that the temperature field is determined independent of the stress or strain fields. More important are how the thermal effect influences the fracture behavior and in what cases the heat flow would enhance or retard the crack propagation.

2. Analytical Model and Temperature Field Solution

Consider an infinite plate with a central crack of length $2a$. The uniform shear stress τ^{∞} is applied at infinite. A uniform heat flow along any direction is also applied at infinite. The heat flow at infinite can be divided into to parts, respectively, along two coordinate axes, say x_1 and x_2 axes. Note that the heat flow is proportional to the negative temperature gradient. Two temperature gradient components along two coordinate axes at infinite are denoted by $\Theta_{,1}^{\infty}$ and $\Theta_{,2}^{\infty}$. The analytical model for the problem is depicted in Fig. 1.

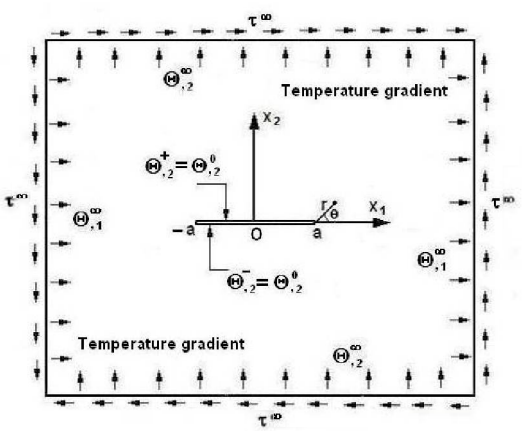

Figure 1. An infinite plate with a crack subjected to uniform heat flow and shear stress at infinite.

Let Θ denote the temperature variation, $\Theta=T-T_0$, in which T is the current temperature and T_0 is the reference temperature. For the pure heat conduction problem, the governing

differential equation is the Laplace equation, $\nabla^2\Theta=0$. The solution can be represented by an analytical function $F(z)$ as

$$\Theta=\frac{1}{2}[F(z)+\overline{F(z)}] \tag{1}$$

$$F'(z)=\Theta_{,1}-i\Theta_{,2} \tag{2}$$

$$F'(z)-\overline{F'(z)}=-2i\Theta_{,2} \tag{3}$$

where $\overline{F(z)}$ is a conjugate function to $F(z)$ and i is the unit imaginary. Let symbol "L" denote the crack line. Refer to Fig. 1, the temperature boundary condition on the crack surfaces can be written as

$$\begin{cases}[F'(t)-\overline{F}'(t)]^{+}+[F'(t)-\overline{F}'(t)]^{-}=-4i\Theta_{,2}^{0} \\ [F'(t)+\overline{F}'(t)]^{+}-[F'(t)+\overline{F}'(t)]=0\end{cases}, \text{ on L, } -a\le t\le a \tag{4}$$

where t is a real argument on L. a is the crack half length. $\Theta_{,2}^{0}$ is the temperature gradient on the upper and lower surfaces normal to the crack line. $\Theta_{,2}^{0}=0$ means that the crack is an insulating crack where any heat cannot pass the crack slit along the x_2 direction. $\Theta_{,2}^{0}$ can be positive or negative. $\Theta_{,2}^{0}\neq 0$ implies that the crack is an uninsulating crack where some heat can pass the crack slit along the x_2 direction.

The temperature boundary value problem described by Eqs. (4) is a Hilbert problem. The solution for Hilbert problem can be found in [28] such that

$$F'(z)=\frac{-2i\Theta_{,2}^{0}}{2\pi i\sqrt{z^2-a^2}}\int_{\mathrm{L}}\frac{\sqrt{t^2-a^2}}{t-z}dt+\frac{c_0+c_1z}{\sqrt{z^2-a^2}}+\Gamma \tag{5}$$

$$\overline{F}'(z)=\frac{2i\Theta_{0,2}}{2\pi i\sqrt{z^2-a^2}}\int_{\mathrm{L}}\frac{\sqrt{t^2-a^2}}{t-z}dt-\frac{c_0+c_1z}{\sqrt{z^2-a^2}}+\Gamma \tag{6}$$

in which c_0, c_1 and Γ are integral constants.

The integrand in Eqs. (5) and (6) has a simple pole at $t=z$. By using the residue theorem in complex function theory, there prevails

$$\frac{1}{2\pi i}\int_{L}\frac{\sqrt{t^2-a^2}}{t-z}dt=\sqrt{z^2-a^2} \tag{7}$$

Therefore, it can be obtained from Eqs. (5) and (6) that

$$F'(z) = -2i\Theta_{,2}^{0} + \frac{c_0 + c_1 z}{\sqrt{z^2 - a^2}} + \Gamma \tag{8}$$

$$\overline{F}'(z) = 2i\Theta_{,2}^{0} - \frac{c_0 + c_1 z}{\sqrt{z^2 - a^2}} + \Gamma \tag{9}$$

By a comparison between Eq. (8) and Eq. (9), it is known that $\Gamma = \overline{\Gamma}$ (real constant) and $c_0 = -\overline{c}_0$, $c_1 = -\overline{c}_1$ indicating Γ is a real constant while c_0 and c_1 are the pure imaginary constants. For a pure heat conduction problem without any heat source in the plane, the heats flow into and flow out any closed curve C should be the same, i.e., $\oint_C F'(z)dz = 0$. This requires that c_0=0. The thermal boundary condition at infinite gives the expression

$$-2i\Theta_{,2}^{0} + c_1 + \Gamma = \Theta_{,1}^{\infty} - i\Theta_{,2}^{\infty} \tag{10}$$

such that

$$c_1 = i\left(2\Theta_{,2}^{0} - \Theta_{,2}^{\infty}\right), \ \Gamma = \Theta_{,1}^{\infty} \tag{11}$$

Therefore, the expression of $F'(z)$ is known as

$$F'(z) = i\left(2\Theta_{,2}^{0} - \Theta_{,2}^{\infty}\right)\frac{z}{\sqrt{z^2 - a^2}} + \Theta_{,1}^{\infty} - 2i\Theta_{,2}^{0} \tag{12}$$

and

$$F(z) = \int F'(z)dz = i\left(2\Theta_{,2}^{0} - \Theta_{,2}^{\infty}\right)\sqrt{z^2 - a^2} + (\Theta_{,1}^{\infty} - 2i\Theta_{,2}^{0})z + A \tag{13}$$

where A is an integral constant.

Further assume that the temperature on x_1-axis for $|x_1| \geq a$ maintains a constant variation Θ_0 when $\Theta_{,1}^{\infty} = 0$. This gives $(A + \overline{A})/2 = \Theta_0$. Parameter A only affects the temperature field by a constant and has no influence on the thermal stress field. The constant A can then be taken as Θ_0, say $A = \overline{A} = \Theta_0$.

Finally, the full field temperature solution is written as

$$F(z) = i\left(2\Theta_{,2}^{0} - \Theta_{,2}^{\infty}\right)\sqrt{z^2 - a^2} + (\Theta_{,1}^{\infty} - 2i\Theta_{,2}^{0})z + \Theta_0 \tag{14}$$

$$\Theta = \frac{i}{2}(2\Theta^0_{,2} - \Theta^\infty_{,2})(\sqrt{z^2 - a^2} - \sqrt{\bar{z}^2 - a^2}) + \frac{1}{2}\Theta^\infty_{,1}(z + \bar{z}) - i\Theta^0_{,2}(z - \bar{z}) + \Theta_0 \quad (15)$$

Near the crack tip, the asymptotic solution of temperature field is

$$\Theta = (\Theta^\infty_{,2} - 2\Theta^0_{,2})\sqrt{2ar}\sin\frac{\theta}{2} + 2\Theta^\infty_{,2} r\sin\theta + a\Theta^\infty_{,1} + \Theta_0 \quad (16)$$

The result in [29] for an orthotropic plate can be simplified to the result for the isotropic case which is found to be identical to Eq. (15).

Take $\Theta^\infty_{,1} = \Theta^\infty_{,2} = 500$ K/m, Θ_0=100K, a=10mm, $\Theta^0_{,2}$=50K/m for an uninsulating crack. K is the absolute temperature. The temperature distribution in the crack region can be calculated. The result is plotted in Fig. 2. The ellipse in the central region indicates that the temperatures on the upper and lower are different. All curves have a zig shape. A pronounced characteristics exhibited in Fig. 2 is that the temperature is skew-asymmetrically discontinuous when cross the x_2-axis from left to right side that remains to be verified by the experimental investigation.

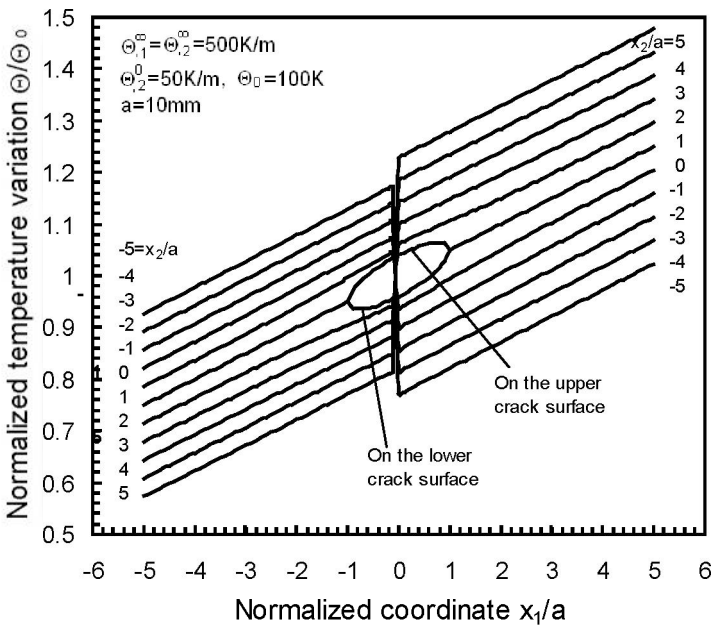

Figure 2. Temperature distribution in the crack region.

3. Thermal Stress Intensity Factor

In this section, only consider the thermal loading. It is well known that for an infinite plate with a crack subjected to in-plane loading, the solution can be written as

$$\sigma_{22}^{\Theta}+\sigma_{11}^{\Theta}=2[(z^2-a^2)^{-\frac{1}{2}}f(z)+g(z)+(\overline{z}^2-a^2)^{-\frac{1}{2}}\overline{f(z)}+\overline{g(z)}] \tag{17}$$

$$\sigma_{22}^{\Theta}-\sigma_{11}^{\Theta}+2i\sigma_{12}^{\Theta}=2\Big\{(z^2-a^2)^{-\frac{1}{2}}[\overline{f}(z)-f(z)]-[g(z)+\overline{g}(z)]- (z-\overline{z})[(\overline{z}^2-a^2)^{-\frac{1}{2}}f'(z)+g'(z)-(z^2-a^2)^{-\frac{3}{2}}zf(z)]\Big\} \tag{18}$$

where $f(z)$ and $g(z)$ are two continuous analytical functions in the plane. Superscript "Θ" means that the stresses produced only by thermal loading. The solution given by Eqs. (17) and (18) has satisfied the free-surface condition on the crack surfaces. The stresses at infinite vanish such that functions of $f(z)$ and $g(z)$ take the forms of

$$f(z)=F_0+F_1z,\ g(z)=G_0 \tag{19}$$

and

$$F_1=0,\ G_0+\overline{G_0}=0 \tag{20}$$

The constant G_0 is related to the rigid rotation of the body such that it can be taken as zero, G_0=0. Eqs. (17) and (18) become

$$\sigma_{22}^{\Theta}+\sigma_{11}^{\Theta}=2[(z^2-a^2)^{-\frac{1}{2}}F_0+(\overline{z}^2-a^2)^{-\frac{1}{2}}\overline{F}_0] \tag{21}$$

$$\sigma_{22}^{\Theta}-\sigma_{11}^{\Theta}+2i\sigma_{12}^{\Theta}=2\Big\{(z^2-a^2)^{-\frac{1}{2}}[\overline{F}_0-F_0]+(z-\overline{z})(z^2-a^2)^{-\frac{3}{2}}zF_0\Big\} \tag{22}$$

The constant F_0 can be determined from the single-valued condition of displacement. The thermal displacement solution is

$$2\mu(u_1^{\Theta}+iu_2^{\Theta})=\kappa F_0\alpha_0(z)-(z-\overline{z})\overline{F}_0\alpha_0'(z)-F_0\alpha_0(\overline{z})+\alpha E\int F(z)dz+\text{const.} \tag{23}$$

where α, E and μ are the linear expansion coefficient, Young's modulus and shear modulus. κ=3-4ν for plane strain and n is Poisson's ratio. Function $F(z)$ has been given by Eq. (14). Function $\alpha_0(z)$ is in the form of

$$\alpha_0(z)=\log[z+\sqrt{z^2-a^2}] \tag{24}$$

It is well known that function $\alpha_0(z)$ is a multi-valued function. The single-valued displacement requires the term $\alpha_0(z)$ should vanish in Eq. (24). The coefficient of the term $\alpha_0(z)$ in Eq. (23) must be zero. This gives

$$(\kappa+1)F_0 - i\alpha E(2\Theta_{,2}^0 - \Theta_{,2}^\infty)\frac{a^2}{2} = 0 \tag{25}$$

Constant F_0 is now known from Eq. (25) as

$$F_0 = \frac{ia^2\alpha E(2\Theta_{,2}^0 - \Theta_{,2}^\infty)}{2(\kappa+1)} \tag{26}$$

Finally, we obtain the asymptotic solution of thermal stresses and the expression of thermal stress intensity factor as follows.

$$\sigma_{11}^\Theta = \frac{-K_2^\Theta}{\sqrt{2\pi r}}\sin\frac{\theta}{2}(2+\cos\frac{\theta}{2}\cos\frac{3\theta}{2}) \tag{27}$$

$$\sigma_{22}^\Theta = \frac{K_2^\Theta}{\sqrt{2\pi r}}\sin\frac{\theta}{2}\cos\frac{\theta}{2}\cos\frac{3\theta}{2} \tag{28}$$

$$\sigma_{12}^\Theta = \frac{K_2^\Theta}{\sqrt{2\pi r}}\cos\frac{\theta}{2}(1-\sin\frac{\theta}{2}\sin\frac{3\theta}{2}) \tag{29}$$

$$K_1^\Theta = 0, \quad K_2^\Theta = 2iF_0\sqrt{\frac{\pi}{a}} = \frac{a\alpha E(\Theta_{,2}^0 - 2\Theta_{,2}^\infty)}{\kappa+1}\sqrt{\pi a} \tag{30}$$

K_1^Θ and K_2^Θ are mode I and mode II thermal stress intensity factors. It is seen that under the given temperature boundary conditions as shown in Fig. 1, the problem is a typical mode II crack problem. Mode II thermal stress intensity factor prevails while mode I thermal stress intensity factor vanishes. Note that temperature gradient component $\Theta_{,1}^\infty$ parallel to crack has no contribution to thermal stresses. Mode II thermal stress intensity factor depends on temperature gradient $\Theta_{,2}^\infty$ as well as $\Theta_{,2}^0$. Thermal stresses greatly depend on the conductivity of crack for heat. When $\Theta_{,2}^0 = 2\Theta_{,2}^\infty$, no thermal stress is produced. For the insulating crack case, $\Theta_{,2}^0 = 0$, thermal loading always produces thermal stresses.

4. Strain Energy Density Contours

Under the combined application of thermal and mechanical loading as shown in Fig. 1, the asymptotic solution of stress field is written as

$$\sigma_{11} = \frac{-K_2}{\sqrt{2\pi r}} \sin\frac{\theta}{2}\left(2 + \cos\frac{\theta}{2}\cos\frac{3\theta}{2}\right) \tag{31}$$

$$\sigma_{22} = \frac{K_2}{\sqrt{2\pi r}} \sin\frac{\theta}{2}\cos\frac{\theta}{2}\cos\frac{3\theta}{2} \tag{32}$$

$$\sigma_{12} = \frac{K_2}{\sqrt{2\pi r}} \cos\frac{\theta}{2}\left(1 - \sin\frac{\theta}{2}\sin\frac{3\theta}{2}\right) \tag{33}$$

$$\sigma_{33} = \nu(\sigma_{11} + \sigma_{22}) - \alpha E\Theta\,,\ \sigma_{13} = \sigma_{23} = 0 \tag{34}$$

$$K_2^{\tau} = \tau^{\infty}\sqrt{\pi a}\,,\ K_2^{\Theta} = \frac{a\alpha E(\Theta_{,2}^{0} - 2\Theta_{,2}^{\infty})}{\kappa + 1}\sqrt{\pi a}\,,\ K_2 = K_2^{\tau} + K_2^{\Theta} \tag{35}$$

The superscripts "τ" and "Θ" stand for the mechanical and thermal parts respectively. Note that the term of $\alpha E\Theta$ in Eq. (34) is a nonsingular term that can be eliminated since the temperature field is nonsingular.

The strain energy density for thermoelastic problem is expressed as

$$\frac{\mathrm{d}W}{\mathrm{d}V} = \frac{1}{2}\sigma_{ij}\varepsilon_{ij} - \frac{1}{2}\alpha\Theta\sigma_{kk} \tag{36}$$

By application of the constitutive relation of the linear thermoelasticity

$$\varepsilon_{ij} = \frac{1+\nu}{E}\sigma_{ij} - \frac{\nu}{E}\sigma_{kk}\delta_{ij} + \alpha\Theta\delta_{ij} \tag{37}$$

the strain ε_{ij} in Eq. (36) can be eliminated and Eq. (36) becomes

$$\begin{aligned}\frac{\mathrm{d}W}{\mathrm{d}V} &= \frac{1+\nu}{2E}\left(\sigma_{ij}\sigma_{ij} - \frac{\nu}{1+\nu}\sigma_{kk}^2\right) \\ &= \frac{1+\nu}{2E}\left[\sigma_{11}^2 + \sigma_{22}^2 + \sigma_{33}^2 - \frac{\nu}{1+\nu}(\sigma_{11} + \sigma_{22} + \sigma_{33})^2 + 2\sigma_{12}^2\right]\end{aligned} \tag{38}$$

Note that Eq. (38) is the same in the form as the isothermal problem. However, the thermal effect is implicit in Eq. (38).

Eq. (36) can also be rewritten as

$$\frac{\mathrm{d}W}{\mathrm{d}V} = \frac{3}{2}\sigma_m \varepsilon_m - \frac{1}{2}\alpha\Theta\sigma_{kk} + \frac{1}{2}s_{ij}e_{ij} \tag{39}$$

in which $\sigma_m = \sigma_{kk}/3$ and $\varepsilon_m = \varepsilon_{kk}/3$ are the hydrostatic stress and strain; s_{ij} and e_{ij} are the deviatoric stress and strain tensors. The dilatational and distortional parts of strain energy density are

$$\left(\frac{\mathrm{d}W}{\mathrm{d}V}\right)_{\mathrm{v}} = \frac{3}{2}\sigma_m \varepsilon_m - \frac{1}{2}\alpha\Theta\sigma_{kk} \tag{40}$$

$$\left(\frac{\mathrm{d}W}{\mathrm{d}V}\right)_{\mathrm{d}} = \frac{1}{2}s_{ij}e_{ij} \tag{41}$$

By application of Eq. (37) to eliminate the strain, Eqs. (40) and (41) take the form as

$$\left(\frac{\mathrm{d}W}{\mathrm{d}V}\right)_{\mathrm{v}} = \frac{1-2\nu}{6E}(\sigma_{11}+\sigma_{22}+\sigma_{33})^2 \tag{42}$$

$$\left(\frac{\mathrm{d}W}{\mathrm{d}V}\right)_{\mathrm{d}} = \frac{1+\nu}{6E}[(\sigma_{11}-\sigma_{22})^2 + (\sigma_{22}-\sigma_{33})^2 + (\sigma_{33}-\sigma_{11})^2 + 6\sigma_{12}^2] \tag{43}$$

The substitution of the first equation in Eq. (34) into Eqs. (38), (42) and (43) yields that

$$\frac{\mathrm{d}W}{\mathrm{d}V} = \frac{1+\nu}{2E}\left[\sigma_{11}^2 + \sigma_{22}^2 - \nu(\sigma_{11}+\sigma_{22})^2 + 2\sigma_{12}^2\right] \tag{44}$$

$$\left(\frac{\mathrm{d}W}{\mathrm{d}V}\right)_{\mathrm{v}} = \frac{(1-2\nu)(1+\nu)^2}{6E}(\sigma_{11}+\sigma_{22})^2 \tag{45}$$

$$\left(\frac{\mathrm{d}W}{\mathrm{d}V}\right)_{\mathrm{d}} = \frac{1+\nu}{3E}[\sigma_{11}^2 + \sigma_{22}^2 - \sigma_{11}\sigma_{22} - \nu(1-\nu)(\sigma_{11}+\sigma_{22})^2 + 3\sigma_{12}^2] \tag{46}$$

Then, by substituting Eqs. (31)~(33) into Eqs. (44)~(46), it is obtained that

$$\frac{dW}{dV} = \frac{(1+\nu)K_2^2}{8\pi E r}\left[4 + 4(1-2\nu)\sin^2\frac{\theta}{2} - 3\sin^2\theta\right] \tag{47}$$

$$\left(\frac{dW}{dV}\right)_v = \frac{(1+\nu)^2(1-2\nu)K_2^2}{3\pi Er}\sin^2\frac{\theta}{2} \tag{48}$$

$$\left(\frac{dW}{dV}\right)_d = \frac{(1+\nu)K_2^2}{24\pi Er}[12+4(1-2\nu)^2\sin^2\frac{\theta}{2}-9\sin^2\theta] \tag{49}$$

There are two basic ways in which a volume element absorbs energy: an element can store energy by "dilatation" and "distortion". The former is associated with the change in volume and the latter is associated with the change in shape. When an element of the material exceeds a certain threshold fracture could occur. The dilatational energy density $(dW/dV)_v$ is related to the material fracture. The distortional energy density $(dW/dV)_d$ is related to the material yielding.

Figs. 3(a), (b) and (c) are, respectively, the contours of strain energy density dW/dV, dilatational energy density $(dW/dV)_v$ and distortional energy density $(dW/dV)_d$ in the vicinity of the crack tip. The value of contour curve decreases from the inside to outside. Contour curves of dW/dV have the gourd shape. Contour curves of $(dW/dV)_v$ have the apple shape. Contour curves of $(dW/dV)_d$ look like a dumbbell.

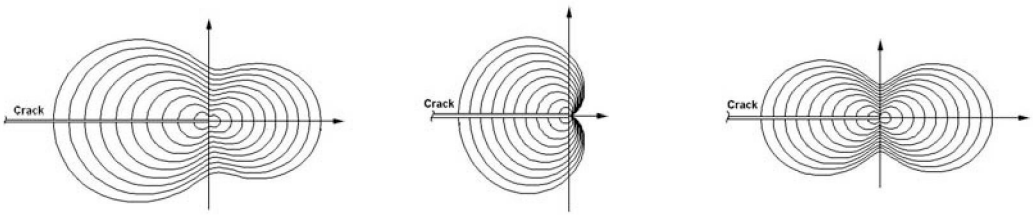

(a) dW/dV (b) $(dW/dV)_v$ (c) $(dW/dV)_d$

Figure 3. Contour curves of strain energy density in the vicinity of the crack tip: (a) dW/dV; (b) $(dW/dV)_v$; (c) $(dW/dV)_d$.

5. Failure Analysis for the Insulating Crack Case

Two cases will be studied, say the insulating and uninsulating cases. Insulating crack problem is analyzed in this section. Note that the case of $\Theta_{,2}^0 = 0$ indicates the crack is an insulating crack by contrast with the case of $\Theta_{,2}^0 \neq 0$ for which the heat flow normal to the crack line direction could pass the crack slit.

5.1. Strain Energy Density Factor

Consider the case of an insulating crack where the heat flow cannot pass the crack slit completely. By inserting Eq. (35) into Eq. (47) and using $\Theta_{,2}^0 = 0$, the strain energy density factor S can be written as

$$S = r\left(\frac{dW}{dV}\right) = B_{11}(\tau^{\infty})^2 + 2B_{12}\tau^{\infty}\Theta_{,2}^{\infty} + B_{22}(\Theta_{,2}^{\infty})^2 \tag{50}$$

where

$$B_{11} = \frac{(1+\nu)[4+4(1-2\nu)\sin^2\frac{\theta}{2} - 3\sin^2\theta]a}{8E} \tag{51}$$

$$B_{12} = -\frac{(1+\nu)[4+4(1-2\nu)\sin^2\frac{\theta}{2} - 3\sin^2\theta]\alpha a^2}{16(1-\nu)} \tag{52}$$

$$B_{22} = \frac{(1+\nu)[4+4(1-2\nu)\sin^2\frac{\theta}{2} - 3\sin^2\theta]\alpha^2 E a^3}{32(1-\nu)^2} \tag{53}$$

For the numerical computation, three materials are chosen. They are steel alloy 38Cr2Mo2Va, aluminum alloy LY12 and titanium alloy TC6. The mechanical parameters can be found in [30] and listed in Table 1. Note that Poisson's ratio of steel alloy 38Cr2Mo2Va cannot be found in [30]. It is assigned to a value of 0.3 in the numerical calculations. In addition, take $\Theta_{,2}^{0} = 0$ (insulating crack), a=10mm, τ^{∞}=10MPa. The temperature gradient $\Theta_{,2}^{\infty}$ at infinite along x_2 direction as a running parameter, $\Theta_{,2}^{\infty}$=-600, -400, -200, 0, 200, 400, 600 K/m. Values of strain energy density factor S with angle θ for three materials are calculated.

Table 1. Material parameters at room temperature [30].

Material Parameters	Titanium alloy TC6	Steel alloy 38Cr2Mo2VA	Aluminum alloy LY12
$\alpha \times 10^{-6}$ (1/°C)	9.2	12.94	21.4
E (GPa)	113	200	68
ν	0.3	Not found	0.33
K_{1c} (MN/m$^{3/2}$)	60.0	58.8	37

Figs. 4, 5 and 6 plot strain energy density factor S versus angle θ for steel, aluminum and titanium alloys respectively. All curves have a symmetrical W-shape. Fig. 2 shows that the magnitudes of strain energy density factor S curves decrease with temperature gradient $\Theta_{,2}^{\infty}$ from negative to positive while the curves become flat. The curve of $\Theta_{,2}^{\infty} = 600$ K/m overlaps into the x-axis which means that the thermal effect almost kills the mechanical loading completely. The positive temperature gradient counteracts the applied mechanical shear stress τ^{∞}. Three maximum values of S locate at θ=±180° and θ=0° respectively.

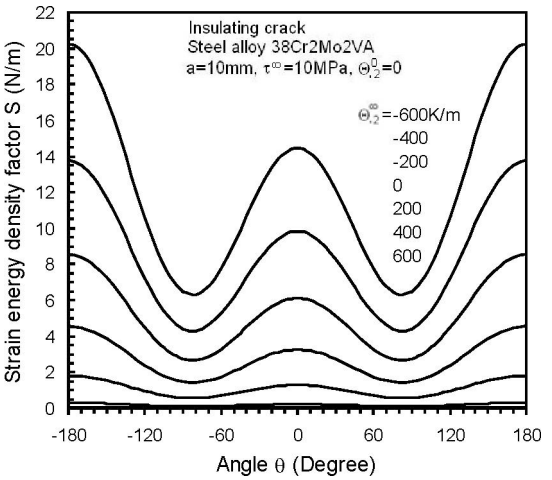

Figure 4. Strain energy density S versus angle θ curves: insulating crack, steel alloy 38Cr2Mo2VA.

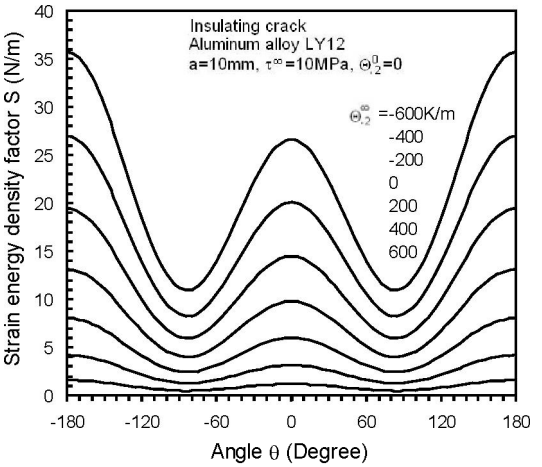

Figure 5. Strain energy density S versus angle θ curves: insulating crack, aluminum alloy LY12.

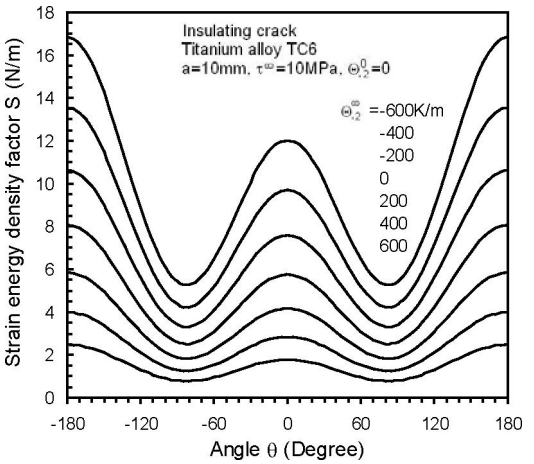

Figure 6. Strain energy density S versus angle θ curves: insulating crack, titanium alloy TC6.

Two minimum values occur at $\theta \approx \pm 83^{\circ}$ which indicate the potential crack initiation directions. The real crack initiation direction depends on the directions of heat flow and applied shear stress. Figs. 5 and 6 are strain energy density factor S versus angle θ curves for aluminum and titanium alloys. Two curves of $\Theta_{,2}^{\infty} = 600$ K/m in Figs. 5 and 6 do not overlap into the x-axis that differ from Fig. 4 for steel material. Comparatively, steel material is sensitive to thermal effect, then aluminum and titanium.

5.2. Failure Stress

The crack initiation angle θ_0 can be found from the direction of S_{min}

$$\frac{\partial S}{\partial \theta} = 0, \quad \frac{\partial^2 S}{\partial \theta^2} > 0 \tag{54}$$

It is obtained by substituting Eq. (50) into Eq. (54) that

$$\sin\theta\,[2(1-2\nu) - 6\cos\theta] = 0 \tag{55}$$

From $\sin\theta = 0$, it is obtained that $\theta = -180^{o}, 0^{\circ}, 180^{\circ}$ which correspond to three maximum values of S as shown in Figs. 4~6. From $2(1-2\nu) - 6\cos\theta = 0$, the crack initiation angle θ_0 which corresponds to the maximum of minimum S or $(dW/dV)_{mim}^{\max}$ can be determined. θ_0 depends on Poisson's ratio ν. The results are listed in Table 2.

Table 2. Values of crack initiation angle θ_0 for three materials.

	Titanium alloy TC6	Steel 38Cr2Mo2VA	Aluminum alloy LY12
ν	0.3	0.3	0.33
θ_0	$\pm 82.34^{\circ}$	$\pm 82.34^{\circ}$	$\pm 83.49^{\circ}$

It is seen that there are two possible directions of crack initiation since dW/dV is a positive definite function. The sign choice of θ_0 can be made on physical grounds that material on the side with the lower temperature is in tension while compression is on the hotter side. With reference to the temperature distribution near crack as shown in Fig. 2, θ_0 should be taken as the negative sign for the right crack tip under the positive temperature gradient $\Theta_{,2}^{\infty}$.

According to strain energy density criterion, there prevails

$$\left(\frac{dW}{dV}\right)_c = \frac{S}{r} \to \frac{S_c}{r_c} \tag{56}$$

$$S_c = \frac{(1+\nu)(1-2\nu)K_{1c}^2}{2\pi E} \tag{57}$$

Substituting Eqs. (50) and (57) into Eq. (56), it is obtained that

$$(\tau_f^\infty)^2 + 2\frac{B_{12}(\theta_0)}{B_{11}(\theta_0)}\Theta_{,2}^\infty \tau_f^\infty + \frac{B_{22}(\theta_0)}{B_{11}(\theta_0)}(\Theta_{,2}^\infty)^2 = \lambda\frac{(1+\nu)(1-2\nu)K_{1c}^2}{2\pi E B_{11}(\theta_0)} \tag{58}$$

Note that $\lambda=r/r_c\leq 1$ with r_c being the terminal ligament that triggers global instability. The failure stress τ_f^∞ for $\lambda=1$ (i.e. $r=r_c$) is the final failure stress which causes the global instability to break down. The cracking stress at different scale represented by parameter λ) is different. The failure stress τ_f^∞ can be solved from Eq. (58).

$$\tau_f^\infty = -\frac{B_{12}(\theta_0)}{B_{11}(\theta_0)}\Theta_{,2}^\infty + \sqrt{\lambda\frac{(1+\nu)(1-2\nu)K_{1c}^2}{2\pi E B_{11}(\theta_0)} + \left[\frac{B_{12}^2(\theta_0)}{B_{11}^2(\theta_0)} - \frac{B_{22}(\theta_0)}{B_{11}(\theta_0)}\right](\Theta_{,2}^\infty)^2} \tag{59}$$

Once the fracture toughness value K_{1c} is known for a given material, the mechanical failure stress τ_f^∞ with reference to a given scale λ can be predicted from Eq. (59) that depends on the crack half length a, thermal temperature gradient $\Theta_{,2}^\infty$ and mode I fracture toughness K_{1c}.

Fig. 7 to Fig. 24 (18 figures in total) depict failure stress curves for the insulating crack case (i.e., $\Theta_{,2}^0=0$) for three chosen materials. Figs. 7 to 15 (9 figures) show the failure stress τ_f^∞ versus temperature gradient $\Theta_{,2}^\infty$ curves with crack half length a as a running parameter, a=5, 10, 15, … , 50mm. Figs. 7, 8, 9 are for steel alloy 38Cr2Mo2VA. Figs. 10, 11, 12 are for aluminum alloy LY12. Figs. 13, 14, 15 are for titanium alloy TC6. Moreover, Figs. 16 to 24 (also 18 figures in total) describe the failure stress τ_f^∞ versus crack half length a with temperature gradient as a running parameter, $\Theta_{,2}^\infty$=500, 300, 100, 0, -100, -300, -500K/m. Failure stress τ_f^∞ at three different scales of $\lambda=r/r_c$=0.01, 0.1 and 1 are calculated. r_c is the critical ligament of crack growth to induce the global instability.

For the insulating crack case, $\Theta_{,2}^0=0$, Eqs. (35) show that the thermal stress intensity factor K_2^Θ is from positive to negative when temperature gradient $\Theta_{,2}^\infty$ changes from negative to positive while the mechanical stress intensity factor K_2^τ is always positive. Thermal loading always produces thermal stresses. Therefore, the positive temperature gradient $\Theta_{,2}^\infty$ decrease the total stress intensity factor K_2. The negative temperature gradient $\Theta_{,2}^\infty$ increases the total stress intensity factor.

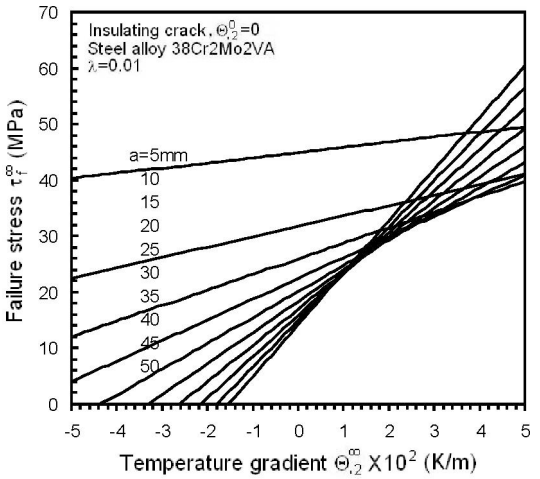

Figure 7. Failure stress τ_f^{∞} versus temperature gradient $\Theta_{,2}^{\infty}$ for different crack half length a: insulating crack, steel alloy 38Cr2Mo2VA, λ=0.01.

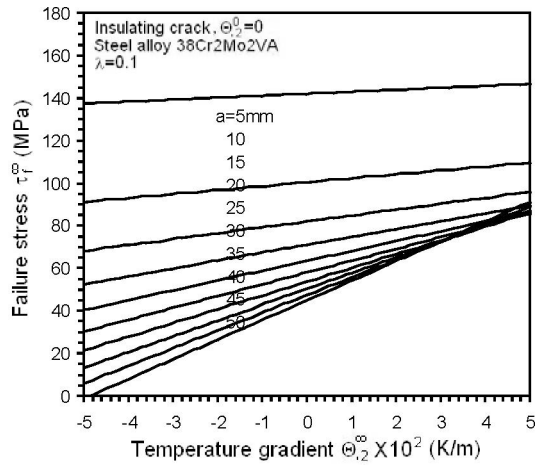

Figure 8. Failure stress τ_f^{∞} versus temperature gradient $\Theta_{,2}^{\infty}$ for different crack half length a: insulating crack, steel alloy 38Cr2Mo2VA, λ=0.1.

Figs. 7, 8 and 9 are τ_f^{∞} versus $\Theta_{,2}^{\infty}$ for steel material for different a with λ=0.01, 0.1 and 1. All curves in three figures are almost straight lines. The slope of curves increases with crack half length a. That is the curves rotates counter-clockwise with length a. In addition, the slope of curves decreases with the increment of scaling parameter λ from 0.01 to 1. Fig. 7 indicates that failure stress τ_f^{∞} increases with the increment of temperature gradient $\Theta_{,2}^{\infty}$ for the given values of α and λ. The curves cross one another in the right region. This phenomenon implies that the thermal effect would become dominant for large cracks at a small scale. Fig. 8 shows that the cross region decreases when the crack growth scale λ

increases from 0.01 to 0.1. Fig. 9 illustrates that the cross region disappears when the crack growth scale λ further increases to 1. Comparatively, the magnitudes of τ_f^{∞} pronouncedly increase with the increment of the scale of crack growth segment.

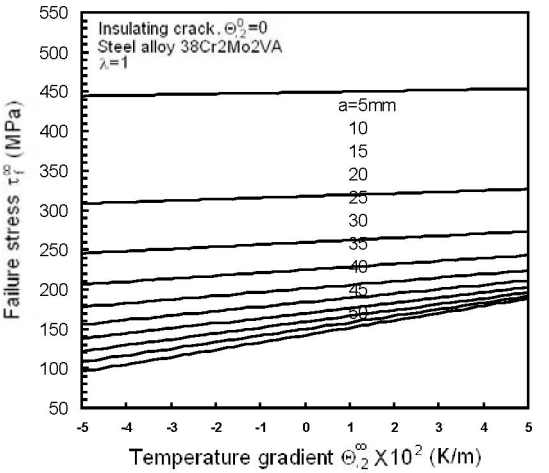

Figure 9. Failure stress τ_f^{∞} versus temperature gradient $\Theta_{,2}^{\infty}$ for different crack half length a: insulating crack, steel alloy 38Cr2Mo2VA, λ=1.

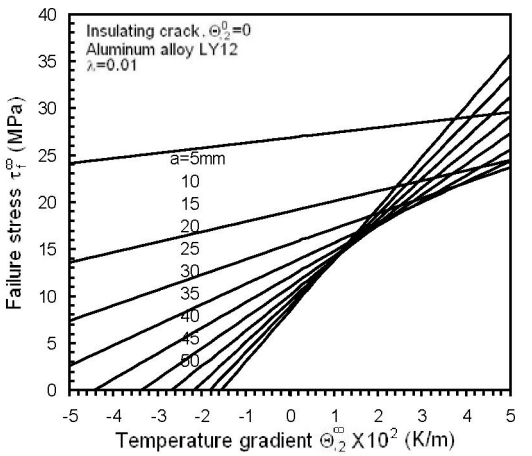

Figure 10. Failure stress τ_f^{∞} versus temperature gradient $\Theta_{,2}^{\infty}$ for different crack half length a: insulating crack, aluminum alloy LY12, λ=0.01.

Fig. 10, 11 and 12 are for aluminum material with λ=0.01, 0.1 and 1 respectively. Figs. 13, 14 and 15 are for titanium material with λ=0.01, 0.1 and 1 respectively. They have the similar features as steel material as shown in Figs. 7, 8, and 9. By comparison of Figs. 9, 12 and 15, the magnitude of τ_f^{∞} for titanium is greater than steel under the same conditions while steel is greater than aluminum. In general, there is little difference of fracture resistance

between titanium and steel under the combined application of mechanical and thermal loading. Comparatively, aluminum material has a bad performance.

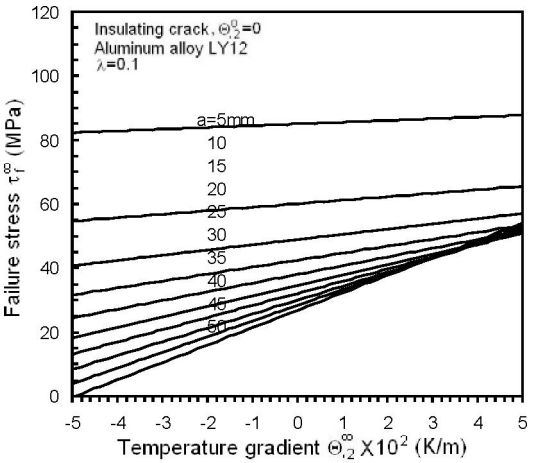

Figure 11. Failure stress τ_f^∞ versus temperature gradient $\Theta_{,2}^\infty$ for different crack half length a: insulating crack, aluminum alloy LY12, λ=0.1.

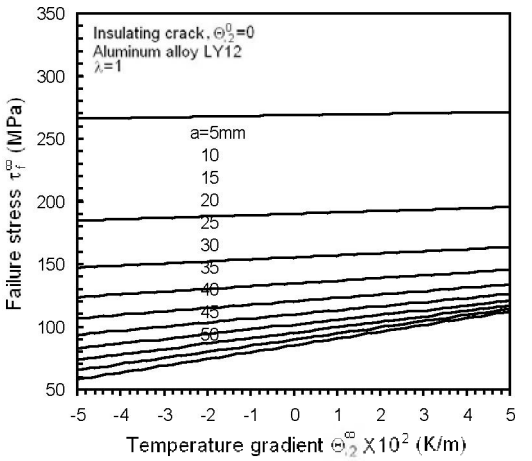

Figure 12. Failure stress τ_f^∞ versus temperature gradient $\Theta_{,2}^\infty$ for different crack half length a: insulating crack, aluminum alloy LY12, λ=1.

Now discuss Figs. 16 to 24 which are failure stress τ_f^∞ versus crack half length a for three materials at different scales (λ=0.01, 0.1 and 1) with the temperature gradient as a running parameter, $\Theta_{,2}^\infty$=500, 300, 100, 0, -100, -300, -500K/m. Fig. 16 is for steel alloy 38Cr2Mo2VA with λ=0.01. Fig. 16 shows that for a<5mm the curves are bundled together.

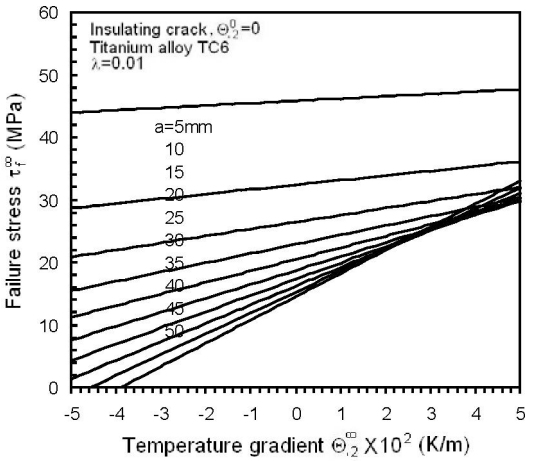

Figure 13. Failure stress τ_f^∞ versus temperature gradient $\Theta_{,2}^\infty$ for different crack half length a: insulating crack, titanium alloy TC6, λ=0.01.

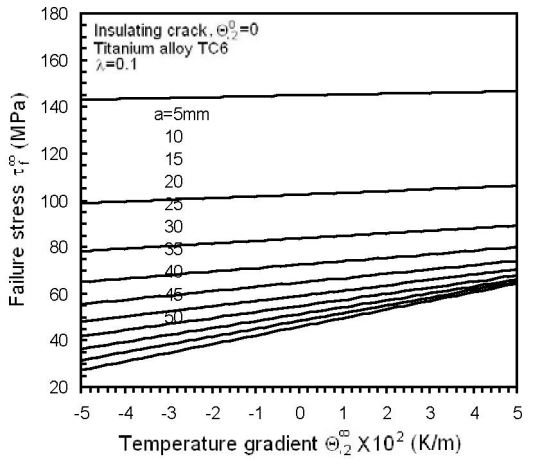

Figure 14. Failure stress τ_f^∞ versus temperature gradient $\Theta_{,2}^\infty$ for different crack half length a: insulating crack, titanium alloy TC6, λ=0.1.

Then the curves scatter with the increment of crack half length a. The magnitudes of τ_f^∞ decrease with the decrement of $\Theta_{,2}^\infty$ from positive to negative. For the negative temperature gradient, $\Theta_{,2}^\infty \leq 0$, the curves decrease monotonically which means the failure stress τ_f^∞ always decreases by the negative $\Theta_{,2}^\infty$. Two curves of $\Theta_{,2}^\infty$=-500, -300K/m drop to zero at a≈22.5, 32mm respectively. In this case, only thermal loading can trigger the crack extension by 1%r_c. With reference to two curves of $\Theta_{,2}^\infty$=300, 500K/m in Fig. 16, failure stress τ_f^∞ rapidly drops in the beginning for small values of length a.

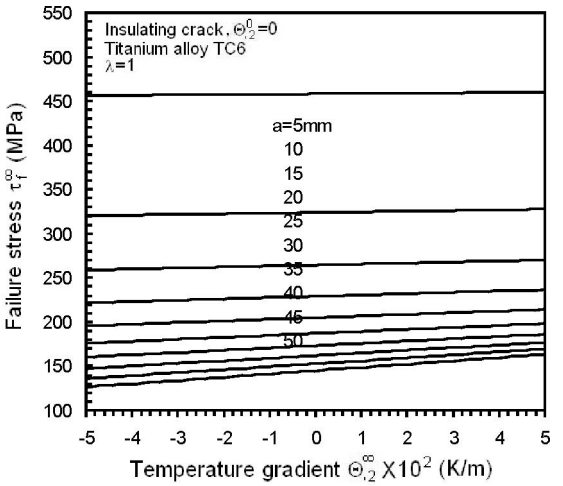

Figure 15. Failure stress τ_f^∞ versus temperature gradient $\Theta_{,2}^\infty$ for different crack half length a: insulating crack, titanium alloy TC6, λ=1.

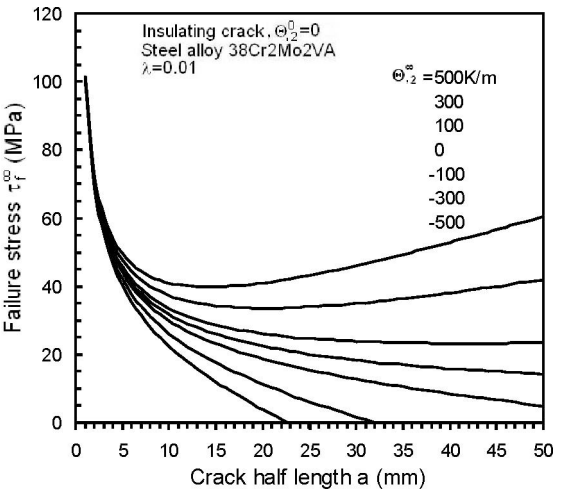

Figure 16. Failure stress τ_f^∞ versus crack half length a for different temperature gradient $\Theta_{,2}^\infty$: insulating crack, steel alloy 38Cr2Mo2VA, λ=0.01.

Then, two curves start to increase slowly after a>20mm that implies the failure stress τ_f^∞ slowly increases with crack half length a because the thermal loading becomes dominant and starts to play a role. Refer to Eq. (35). The thermal stress intensity factor K_2^Θ becomes negative for the positive temperature gradient $\Theta_{,2}^\infty$ for the insulating crack with $\Theta_{,2}^0$=0. The positive temperature gradient $\Theta_{,2}^\infty$ partly kills the mechanical loading. This counteraction effect would be enhanced by the increment of crack size such that the cracking stress

increases accordingly. This effect corresponds to the cross regions of the curves in Figs. 7 and 8. When the cracking scale λ increases from 0.01 to 0.1, this effect is weaken. The curve for $\Theta_{,2}^{\infty}$=500K/m in Fig. 17 becomes nearly horizontal after a=20mm with little increment. As illustrated in Fig. 18, all curves decrease monotonically with length a in the case of λ=1. Figs. 19, 20 and 21 are failure stress τ_f^{∞} versus crack half length a curves for aluminum alloy LY12 with λ=0.01, 0.1 and 1 respectively. Figs. 22, 23 and 24 are for titanium alloy TC6. Situations are similar to steel material. The discussion is omitted.

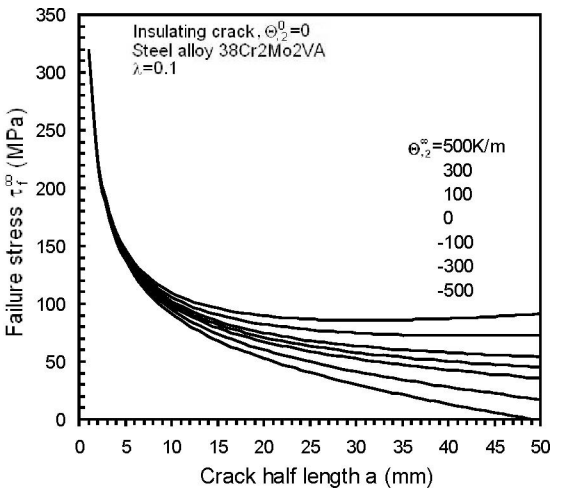

Figure 17. Failure stress τ_f^{∞} versus crack half length a for different temperature gradient $\Theta_{,2}^{\infty}$: insulating crack, steel alloy 38Cr2Mo2VA, λ=0.1.

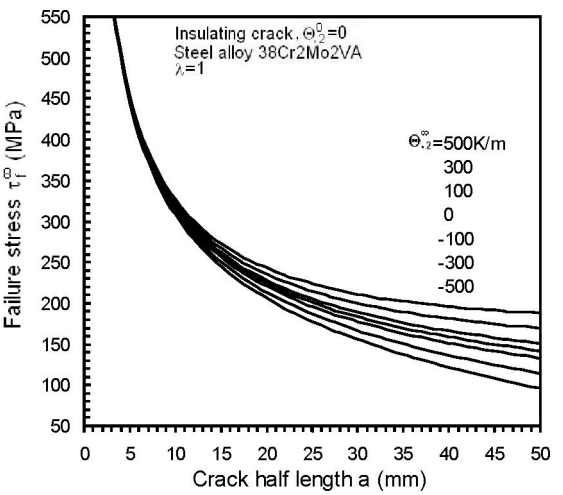

Figure 18. Failure stress τ_f^{∞} versus crack half length a for different temperature gradient $\Theta_{,2}^{\infty}$: insulating crack, steel alloy 38Cr2Mo2VA, λ=1.

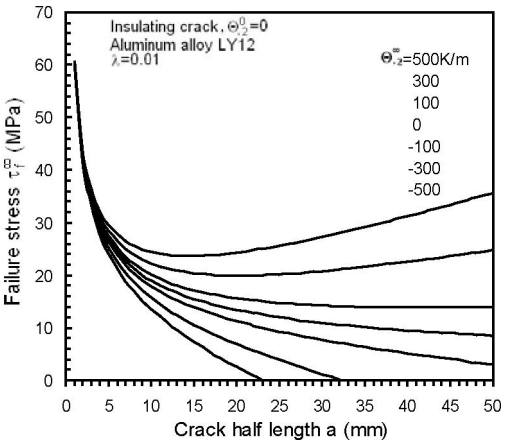

Figure 19. Failure stress τ_f^∞ versus crack half length a for different temperature gradient $\Theta_{,2}^\infty$: insulating crack, aluminum alloy LY12, λ=0.01.

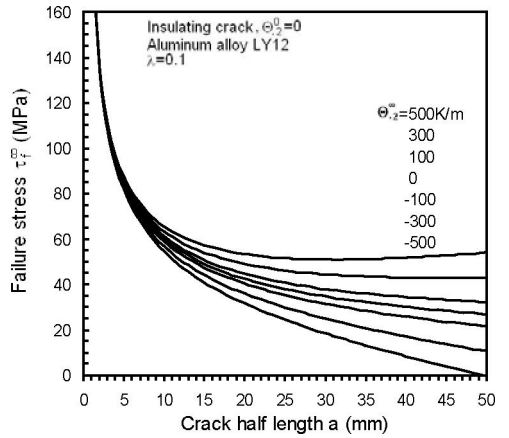

Figure 20. Failure stress τ_f^∞ versus crack half length a for different temperature gradient $\Theta_{,2}^\infty$: insulating crack, aluminum alloy LY12, λ=0.1.

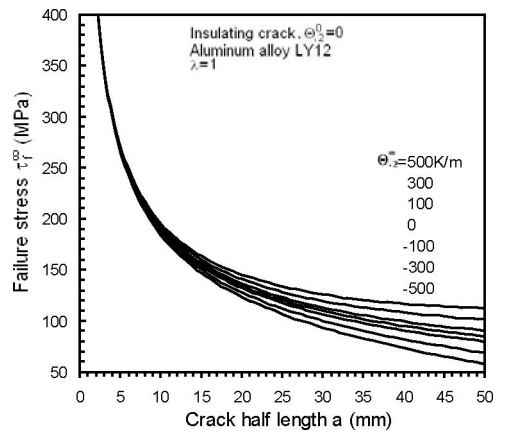

Figure 21. Failure stress τ_f^∞ versus crack half length a for different temperature gradient $\Theta_{,2}^\infty$: insulating crack, aluminum alloy LY12, λ=1.

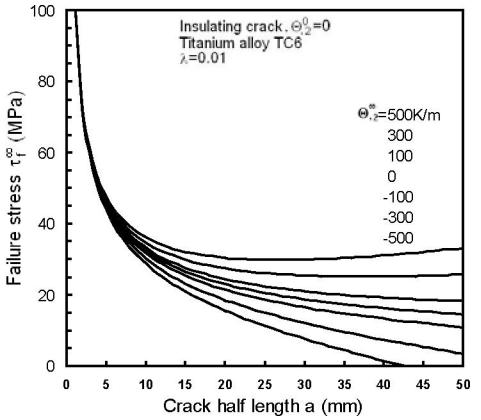

Figure 22. Failure stress τ_f^∞ versus crack half length a for different temperature gradient $\Theta_{,2}^\infty$: insulating crack, titanium alloy TC6, λ=0.01.

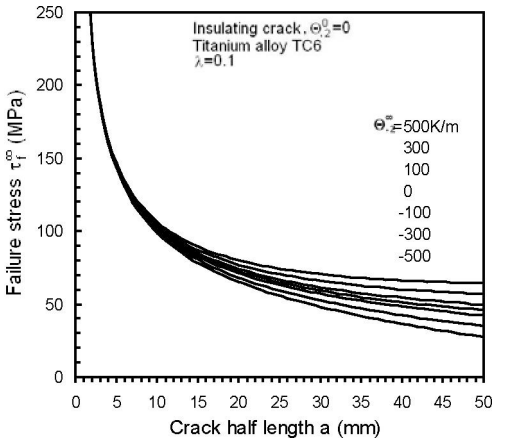

Figure 23. Failure stress τ_f^∞ versus crack half length a for different temperature gradient $\Theta_{,2}^\infty$: insulating crack, titanium alloy TC6, λ=0.1.

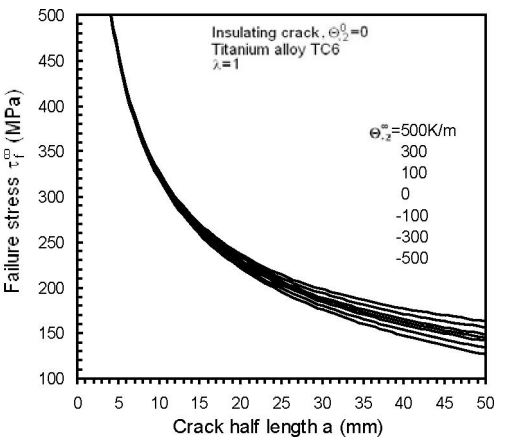

Figure 24. Failure stress τ_f^∞ versus crack half length a for different temperature gradient $\Theta_{,2}^\infty$: insulating crack, titanium alloy TC6, λ=1.

5.3. Enhancement and Retardation of Crack Growth by Thermal Effect

Refer to Eq. (50). The term $\tau^{\infty}\Theta_{,2}^{\infty}$ would affect the value of strain energy density factor S which depends on whether the temperature gradient $\Theta_{,2}^{\infty}$ is positive, zero or negative. When the direction of temperature gradient $\Theta_{,2}^{\infty}$ is changed, the crack growth behavior would be changed accordingly.

Let the superscripts −, 0, + denote, respectively, the situations for negative, zero and positive $\Theta_{,2}^{\infty}$. The corresponding crack growth segments are denoted by r^{-}, r^{0}, and r^{+}, while the strain energy density factors are noted by S^{-}, S^{0} and S^{+}. By application of the strain energy density theory, the first segment of crack growth r_1 for three cases can be written as

$$\left(\frac{dW}{dV}\right)_c = \frac{S_1^-}{r_1^-} = \frac{S_1^0}{r_1^0} = \frac{S_1^+}{r_1^+} = \cdots \tag{60}$$

In Table 3, the values of coefficients B_{11}, B_{12} and B_{22} in Eq. (50) for the insulating crack case are given. It is known that the values of B_{12} are negative such that the positive temperature gradient $\Theta_{,2}^{\infty}$ will reduce the magnitude of strain energy density factor S, i.e., $S_1^- > S_1^0 > S_1^+$. Therefore, we can know from Eq. (60) that

$$r_1^- > r_1^0 > r_1^+ \tag{61}$$

Table 3. Values of coefficients B_{11}, B_{12} and B_{22} in Eq. (50) for three materials with $\theta=\theta_0$ and a=10mm.

Bij (i, j=1, 2)	Material		
	Titanium alloy TC6	Steel 38Cr2Mo2VA	Aluminum alloy LY12
θ0	82.34o	82.34o	83.49o
B11(θ0)×10-14	2.51180	1.41917	4.01314
B12(θ0)×10-10	-1.86519	-2.62343	-4.35816
B22(θ0)×10-6	1.38504	4.84960	4.73283

Eq. (61) says that in the case of insulating crack, positive temperature gradient $\Theta_{,2}^{\infty}$ would impede the crack propagation. The negative $\Theta_{,2}^{\infty}$ would intensify the crack propagation. Minimum values of strain energy density factor S_{min} for three materials for different $\Theta_{,2}^{\infty}$ are listed in Table 4 where is the crack initiation direction with cracking angle θ_0. Values of S_{min} decrease with the increment of $\Theta_{,2}^{\infty}$. Table 5 shows the variations of the

first normalized crack growth segment $r_1^{\pm}/r_1^0$ with temperature gradient $\Theta_{,2}^{\infty}$. When $\Theta_{,2}^{\infty}>0$, $r_1^{\pm}/r_1^0<1$; when $\Theta_{,2}^{\infty}<0$, $r_1^{\pm}/r_1^0>1$. Fig. 25 describes the influence of thermal effect on the crack growth behavior. The numerical results in Tables 4 and 5 are also plotted in Figs. 26 and 27. It can be concluded that for the insulating crack case, positive temperature gradient $\Theta_{,2}^{\infty}$ impedes the crack propagation while the negative $\Theta_{,2}^{\infty}$ enhances the crack propagation.

Table 4. Minimum values of strain energy density S_{min} as a function of $\Theta_{,2}^{\infty}$ for three materials with $\theta=\theta_0$, a=10mm and τ^{∞}=10MPa.

Material	Minimum values of strain energy density factor S_{min} (N/m)										
	Temperature gradient $\Theta_{,2}^{\infty}$ (K/m)										
	-500	-400	-300	-200	-100	0	100	200	300	400	500
Titanium alloy TC6	4.723	4.226	3.756	3.313	2.899	2.512	2.153	1.821	1.517	1.241	0.993
Steel alloy 38Cr2Mo2VA	5.255	4.294	3.430	2.663	1.992	1.419	0.943	0.564	0.282	0.096	0.008
Aluminum alloy LY12	9.555	8.257	7.054	5.946	4.932	4.013	3.189	2.459	1.824	1.284	0.838

Table 5. Normalized first crack growth segments $r_1^{\pm}/r_1^0$ for three materials with $\theta=\theta_0$, a=10mm and τ^{∞}=10MPa.

Material	Normalized first crack growth segments $r_1^{\pm}/r_1^0$										
	Temperature gradient $\Theta_{,2}^{\infty}$ (K/m)										
	-500	**-400**	**-300**	**-200**	**-100**	**0**	**100**	**200**	**300**	**400**	**500**
Titanium alloy TC6	1.880	1.682	1.495	1.319	1.154	1	0.857	0.725	0.604	0.494	0.395
Steel alloy 38Cr2Mo2VA	3.703	3.026	2.417	1.876	1.404	1	0.664	0.397	0.198	0.068	0.397
Aluminum alloy LY12	2.381	2.057	1.758	1.482	1.229	1	0.795	0.613	0.455	0.320	0.209

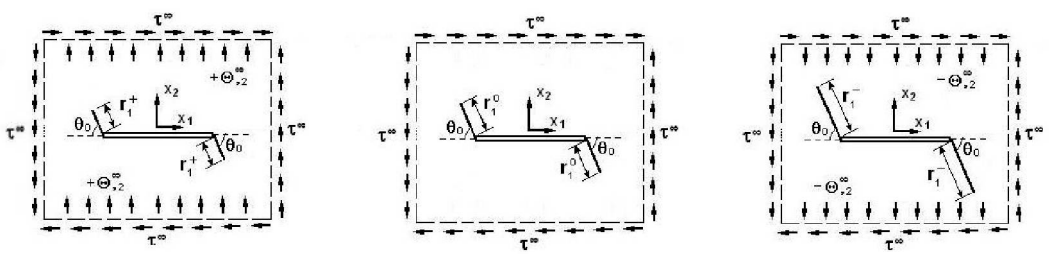

(a) positive $\Theta_{,2}^{\infty}$ (b) zero $\Theta_{,2}^{\infty}$ (c) negative $\Theta_{,2}^{\infty}$

Figure 25. Enhancement and retardation behavior of crack growth by thermal effect for the insulating crack: (a) positive $\Theta_{,2}^{\infty}$; (b) zero $\Theta_{,2}^{\infty}$; (c) negative $\Theta_{,2}^{\infty}$.

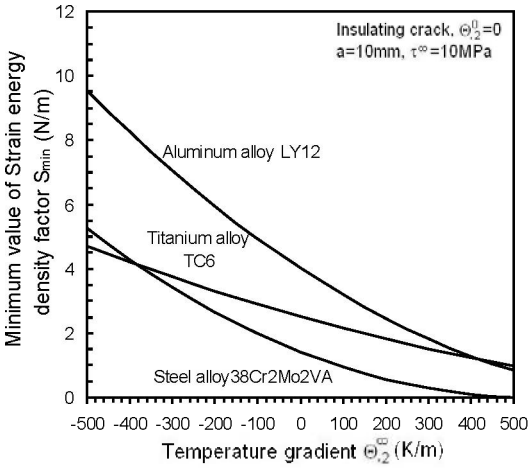

Figure 26. Minimum value of strain energy density factor S_{min} versus temperature gradient $\Theta_{,2}^{\infty}$ for three materials for the insulating crack.

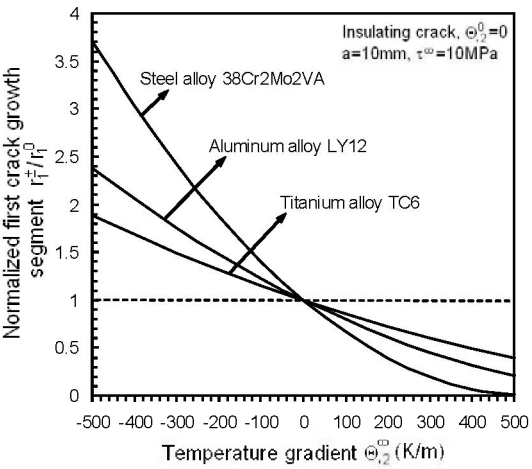

Figure 27. Normalized first crack growth segment r_1^+ / r_1^0 versus temperature gradient $\Theta_{,2}^{\infty}$ for three materials for the insulating crack.

5.4. Log-Log Plot for Strain Energy Density Dw/Dv versus Distance R

Expression of strain energy density (*dW/dV*) has been given by Eq. (47) where the total stress intensity factor K_2 has been known by Eq. (35). It is known from Eq. (47) that the product of *dW/dV* and distance *r* is a constant. The *dW/dV* versus *r* curve is a hyperbola in a rectangular coordinate system. It becomes a straight line in a bi-logarithm coordinate system. Figs. 28, 29 and 30 illustrate the strain energy density *dW/dV* versus distance *r* curves in a log-log plot for three materials respectively. Fig. 28 is for steel alloy 38Cr2Mo2VA while Fig. 29 for aluminum alloy LY12 and Fig. 30 for titanium alloy TC6. All curves are the parallel straight lines. Spacing of the straight lines decreases from Fig. 28 to 30 which implies the sensitivity to thermal effect for three materials is different.

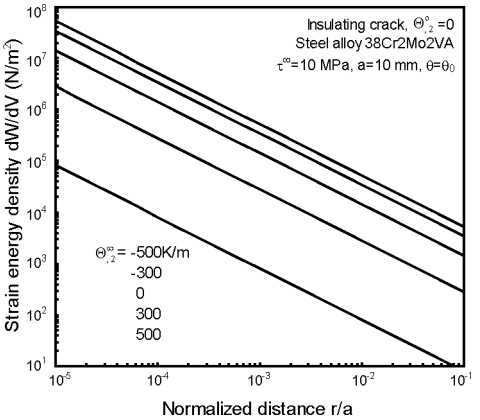

Figure 28. Log-log plot of strain energy density *dW/dV* versus normalized distance *r/a* for different temperature gradient $\Theta^{\infty}_{,2}$: insulating crack, steel alloy 38Cr2Mo2VA.

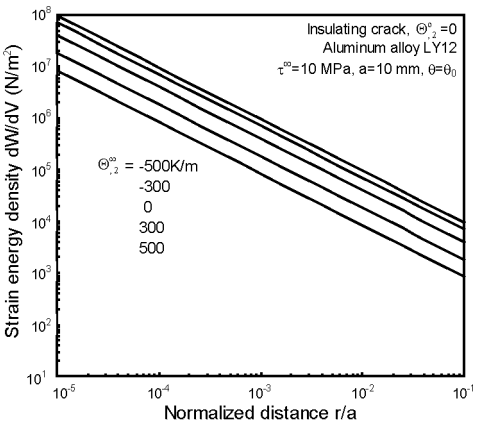

Figure 29. Log-log plot of strain energy density *dW/dV* versus normalized distance *r/a* for different temperature gradient $\Theta^{\infty}_{,2}$: insulating crack, aluminum alloy LY12.

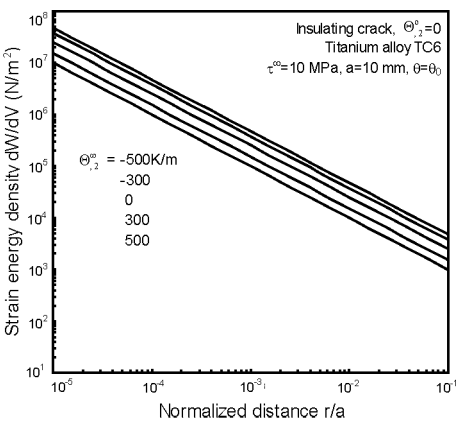

Figure 30. Log-log plot of strain energy density *dW/dV* versus normalized distance *r/a* for different temperature gradient $\Theta^{\infty}_{,2}$: insulating crack, titanium alloy TC6.

Accomplished in this section are the discussions for the insulating crack case with $\Theta_{,2}^{o} = 0$. In fact, the crack slit would be diathermanous for heat. The heat flow normal to the crack could pass the crack slit. In this case the fracture behavior of materials is quite different. The crack should by modeled by an uninsulating crack which will be treated in the next section.

6. Failure Analysis for the Uninsulating Crack Case

In this section, the case $\Theta_{,2}^{0} \neq 0$ will be considered, i.e., the heat flow perpendicular to the crack line can pass the crack slit. Without losing generality, it can be assumed that $\Theta_{,2}^{\infty} = 0$ while $\Theta_{,2}^{0} \neq 0$. Direction of the heat flow normal to the crack passing the crack slit is the negative direction of temperature gradient $\Theta_{,2}^{0}$ on the crack surfaces.

6.1. Strain Energy Density Factor

Refer to Eq. (35). In the case of uninsulating crack, $\Theta_{,2}^{0} \neq 0$, and take $\Theta_{,2}^{\infty} = 0$. The thermal stress intensity factor is written as

$$K_2^{\Theta} = \frac{a\alpha E\Theta_{,2}^{0}}{4(1-\nu)}\sqrt{\pi a} \tag{62}$$

In this case, the strain energy density factor S can be obtained from Eq. (47) that

$$S = r\left(\frac{dW}{dV}\right) = C_{11}(\tau^{\infty})^2 + 2C_{12}\tau^{\infty}\Theta_{,2}^{0} + C_{22}(\Theta_{,2}^{0})^2 \tag{63}$$

where

$$C_{11} = \frac{(1+\nu)[4+4(1-2\nu)\sin^2\frac{\theta}{2} - 3\sin^2\theta]a}{8E} \tag{64}$$

$$C_{12} = \frac{(1+\nu)[4+4(1-2\nu)\sin^2\frac{\theta}{2} - 3\sin^2\theta]\alpha a^2}{32(1-\nu)} \tag{65}$$

$$C_{22} = \frac{(1+\nu)[4+4(1-2\nu)\sin^2\frac{\theta}{2} - 3\sin^2\theta]\alpha^2 Ea^3}{128(1-\nu)^2} \tag{66}$$

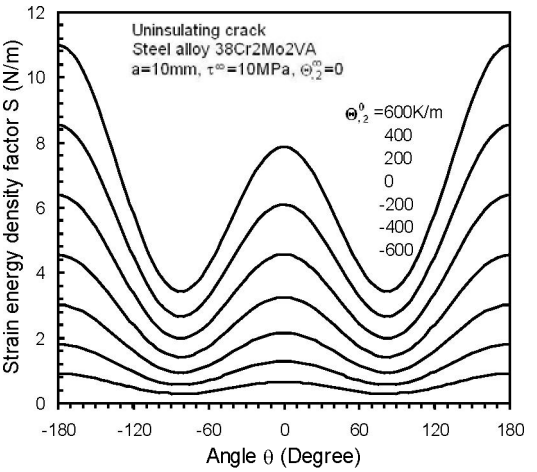

Figure 31. Strain energy density S versus angle θ curves: uninsulating crack, steel alloy 38Cr2Mo2VA.

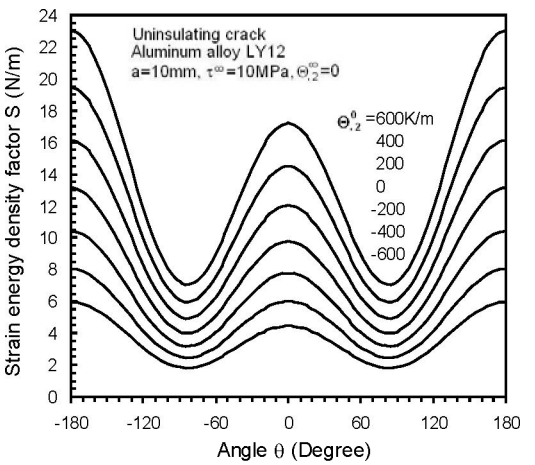

Figure 32. Strain energy density S versus angle θ curves: uninsulating crack, aluminum alloy LY12.

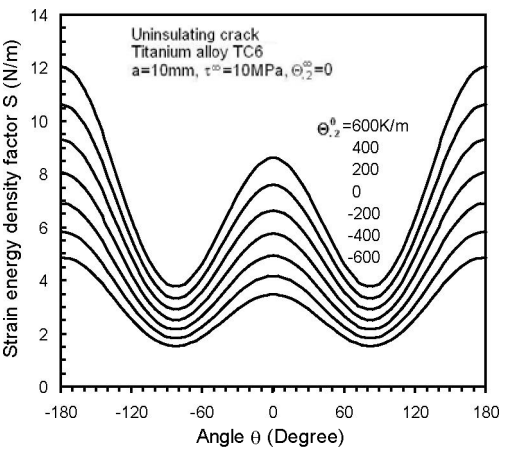

Figure 33. Strain energy density S versus angle θ curves: uninsulating crack, titanium alloy TC6.

Take a=10mm and $\tau^{\infty} = 10$ MPa. Now we can plot strain energy density factor S versus angle θ curves for three materials under different temperature gradient $\Theta_{,2}^{0}$. The results are illustrated in Figs. 31, 32 and 33 for steel, aluminum and titanium alloys respectively. All curves have a W-shape that is similar to those in Figs. 4, 5 and 6 for the insulating crack. However, in the case of uninsulating crack, strain energy density factor S increases with the increment of $\Theta_{,2}^{0}$ from negative to positive. This effect is different from the insulating crack.

6.2. Failure Stress

Figs. 31, 32 and 33 show that the crack initiation angle θ_0 corresponding to the minimum values of S is identical to those in Table 2 for the insulating crack. In the same way, the expression of failure stress τ_f^{∞} can be derived.

$$\tau_f^{\infty} = -\frac{C_{12}(\theta_0)}{C_{11}(\theta_0)}\Theta_{,2}^{0} + \sqrt{\lambda\frac{(1+\nu)(1-2\nu)K_{1c}^2}{2\pi E C_{11}(\theta_0)} + \left[\frac{C_{12}^2(\theta_0)}{C_{11}^2(\theta_0)} - \frac{C_{22}(\theta_0)}{C_{11}(\theta_0)}\right](\Theta_{,2}^{0})^2} \tag{67}$$

where the coefficients C_{11}, C_{12} and C_{22} have been given by Eqs. (64)~(66). Now we can calculate the values of failure stress τ_f^{∞} from Eq. (67) at different scale.

Figs. 34 to 51 with 18 figures in total are the failure stress τ_f^{∞} curves for the uninsulating crack where $\Theta_{,2}^{0} \neq 0$, and take $\Theta_{,2}^{\infty} = 0$. The former nine figures of Figs. 34 to 42 are failure stress τ_f^{∞} versus temperature gradient $\Theta_{,2}^{0}$ curves for different crack half length a for three materials. The latter nine figures of Figs. 43 to 51 are failure stress τ_f^{∞} versus crack half length a curves for different temperature gradient $\Theta_{,2}^{o}$ for three materials. Three cracking scales are calculated with λ=0.01, 0.1 and 1 respectively. Refer to Eq. (62). The thermal stress intensity factor K_2^{Θ} is positive for positive $\Theta_{,2}^{0}$, and negative for negative $\Theta_{,2}^{0}$. The negative temperature gradient $\Theta_{,2}^{0}$ on the crack line would partly kill the mechanical loading. This is different from the case of insulating crack. Recall that for the insulating crack, it is the positive temperature gradient $\Theta_{,2}^{\infty}$ at infinite would partly kill the mechanical effect.

Fig. 34 describes the variations of failure stress τ_f^{∞} with temperature gradient $\Theta_{,2}^{0}$ for steel alloy 38Cr2Mo2VA with a=5, 10, 15, … , 50mm. The corresponding crack growth segment scale is $\lambda = r/r_c$=0.01. All curves in Fig. 34 are nearly straight line. The curves monotonically decrease with the increment of $\Theta_{,2}^{0}$ from negative to positive. The slopes of curves increase with crack half length a. The curves rotate clockwise with length a. The curves overlap in the left zone for large values of length a. This phenomenon has been

explained early for the insulating crack case in section 5. The cross effect disappears in Figs. 35 and 36 where the crack growth scale λ increases from 0.01 to 0.1 and 1 respectively. This says the fracture behavior is more sensitive to thermal effect at small scale than at large scale. By comparing Figs. 34, 35 and 36, it is found that the slope of curves for the same length a decreases when the scaling parameter λ increases from 0.01 to 1. In Fig. 36 for λ=1, all curves almost become the horizontal lines with little difference of slopes. Figs. 37, 38 and 39 are for aluminum alloy LY12 with λ=0.01, 0.1 and 1 respectively. Figs. 40, 41 and 42 are for titanium alloy TC6. The situations are similar to steel material. No more discussion is needed. Note that the failure stress τ_f^{∞} for λ=1 corresponds to the ultimate failure stress that causes the global instability of structural members. A comparison of Figs. 36, 39 and 42 indicates that the value of τ_f^{∞} or the fracture resistance is great for titanium, medium for steel, small for aluminum. However, there is littler difference between titanium and steel. This coincides with the case of the insulating crack.

Fig. 43 depicts the variation of failure stress τ_f^{∞} with crack half length a for different temperature gradient $\Theta_{,2}^0$ on the crack surface for steel material with the scale λ=0.01. The curves in Fig. 43 correspond to the thermal loading of $\Theta_{,2}^0$=-500, -300, -100, 0, 100, 300, 500K/m respectively. All curves are bundled together at the start, then scattered with length a. The magnitude of curves decreases with the increment of the thermal loading $\Theta_{,2}^0$. When $\Theta_{,2}^0$>0, failure stress τ_f^{∞} drops rapidly and monotonically with length a. Then, the drop trend slows down or stops. Note that for the negative $\Theta_{,2}^0$ such as $\Theta_{,2}^0$=-500 and -300K/m in Fig. 43, the curves behave differently. When $\Theta_{,2}^0$=-300K/m, the values of τ_f^{∞} has little difference after a>20mm. The trend of the curve for $\Theta_{,2}^0$=-500K/m changes from decreasing to slightly increasing at a=20mm. This increasing segment in Fig. 43 corresponds to the overlap of curves in Figs. 34 and 37. This is because for the uninsulating crack the positive $\Theta_{,2}^0$ increases the total stress intensity while the negative $\Theta_{,2}^0$ decreases the total stress intensity factor. Therefore, when $\Theta_{,2}^0$=-500K/m for large a the thermal effect becomes pronounced such that it suffices to increase the failure stress. When the scale increases from 0.01 to 0.1 and 1 respectively, all curves monotonically drop with length a as shown in Figs. 44 and 45. Figs. 46, 47 and 48 are for aluminum alloy LY12 while Figs. 49, 50 and 51 for titanium alloy TC6. The situations are similar to those for steel. No more comment is needed.

In general, Figs. 34 to 51 for the uninsulating crack have an opposite effect compared to Figs. 7 to 24 for the insulating crack.

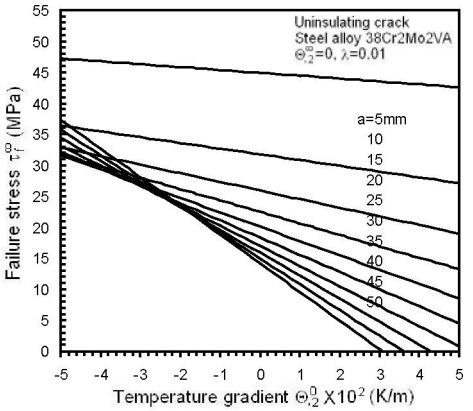

Figure 34. Failure stress τ_f^{∞} versus temperature gradient $\Theta_{,2}^{0}$ for different crack half length a: uninsulating crack, steel alloy 38Cr2Mo2VA, λ=0.01.

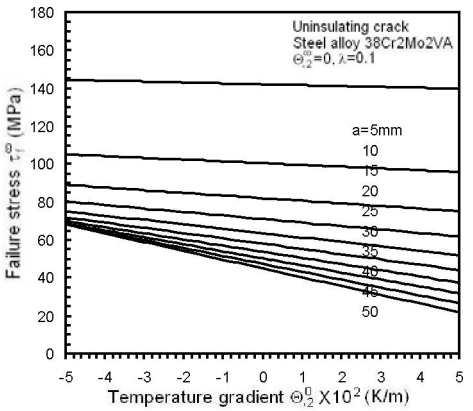

Figure 35. Failure stress τ_f^{∞} versus temperature gradient $\Theta_{,2}^{0}$ for different crack half length a: uninsulating crack, steel alloy 38Cr2Mo2VA, λ=0.1.

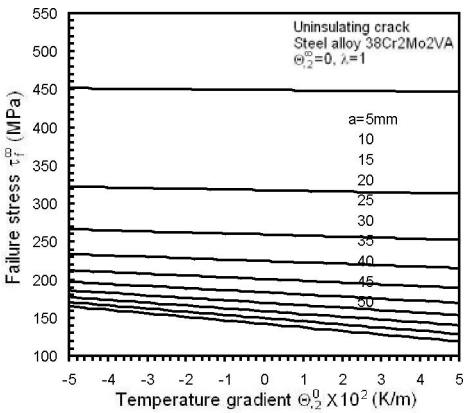

Figure 36. Failure stress τ_f^{∞} versus temperature gradient $\Theta_{,2}^{0}$ for different crack half length a: uninsulating crack, steel alloy 38Cr2Mo2VA, λ=1.

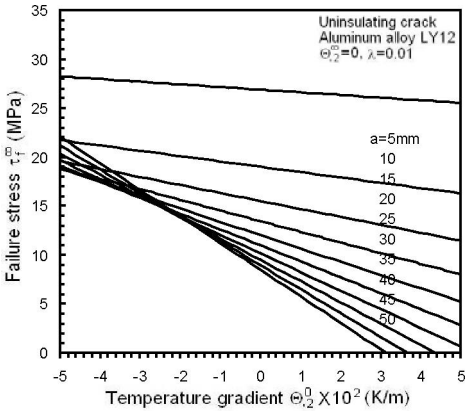

Figure 37. Failure stress τ_f^{∞} versus temperature gradient $\Theta_{,2}^{0}$ for different crack half length a: uninsulating crack, aluminum alloy LY12, λ=0.01.

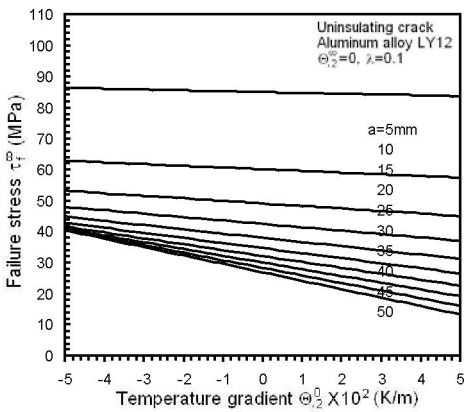

Figure 38. Failure stress τ_f^{∞} versus temperature gradient $\Theta_{,2}^{0}$ for different crack half length a: uninsulating crack, aluminum alloy LY12, λ=0.1.

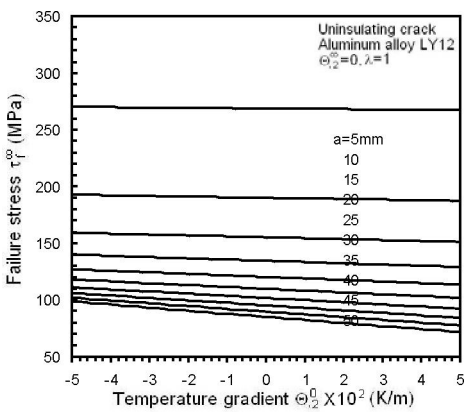

Figure 39. Failure stress τ_f^{∞} versus temperature gradient $\Theta_{,2}^{0}$ for different crack half length a: uninsulating crack, aluminum alloy LY12, λ=1.

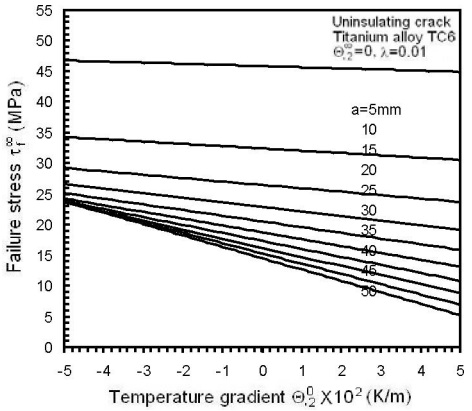

Figure 40. Failure stress τ_f^{∞} versus temperature gradient $\Theta_{,2}^{0}$ for different crack half length a: uninsulating crack, titanium alloy TC6, λ=0.01.

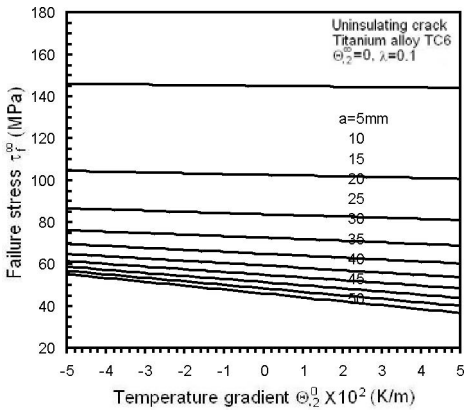

Figure 41. Failure stress τ_f^{∞} versus temperature gradient $\Theta_{,2}^{0}$ for different crack half length a: uninsulating crack, titanium alloy TC6, λ=0.1.

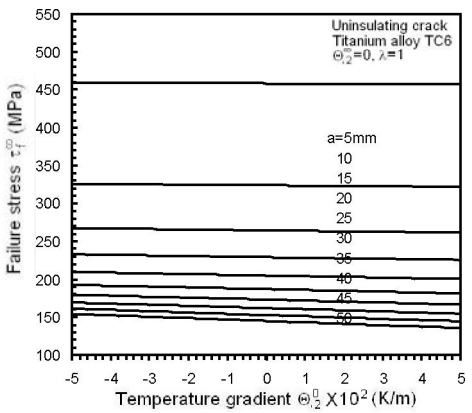

Figure 42. Failure stress τ_f^{∞} versus temperature gradient $\Theta_{,2}^{0}$ for different crack half length a: uninsulating crack, titanium alloy TC6, λ=1.

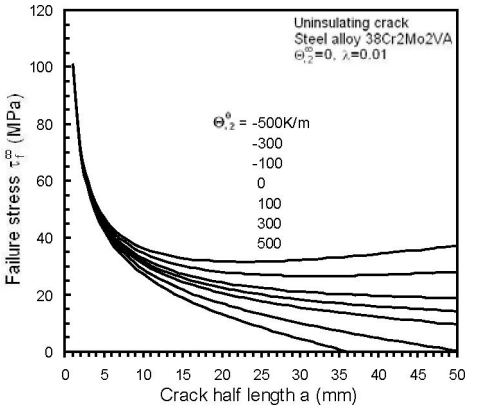

Figure 43. Failure stress τ_f^{∞} versus crack half length a for different temperature gradient $\Theta_{,2}^{0}$: uninsulating crack, steel alloy 38Cr2Mo2VA, λ=0.01.

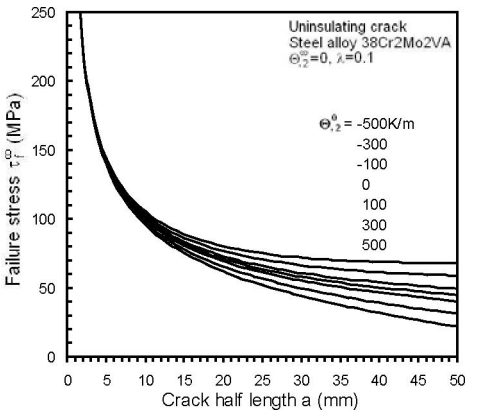

Figure 44. Failure stress τ_f^{∞} versus crack half length a for different temperature gradient $\Theta_{,2}^{0}$: uninsulating crack, steel alloy 38Cr2Mo2VA, λ=0.1.

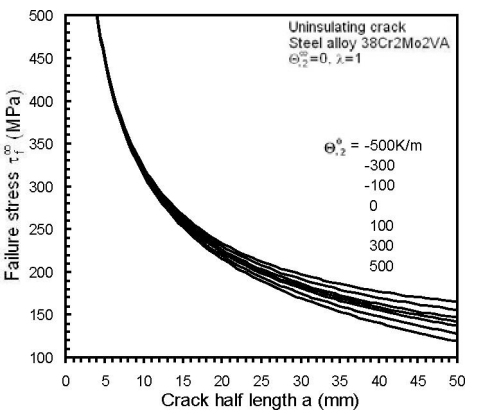

Figure 45. Failure stress τ_f^{∞} versus crack half length a for different temperature gradient $\Theta_{,2}^{0}$: uninsulating crack, steel alloy 38Cr2Mo2VA, λ=1.

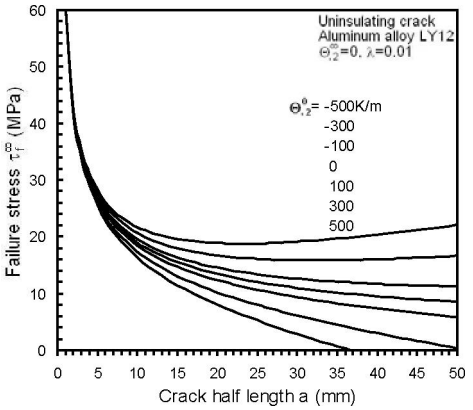

Figure 46. Failure stress τ_f^{∞} versus crack half length a for different temperature gradient $\Theta_{,2}^{0}$: uninsulating crack, aluminum alloy LY12, λ=0.01.

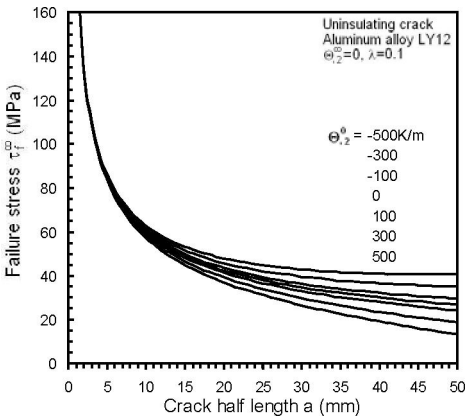

Figure 47. Failure stress τ_f^{∞} versus crack half length a for different temperature gradient $\Theta_{,2}^{0}$: uninsulating crack, aluminum alloy LY12, λ=0.1.

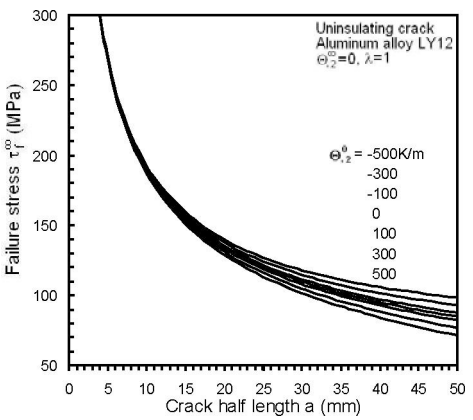

Figure 48. Failure stress τ_f^{∞} versus crack half length a for different temperature gradient $\Theta_{,2}^{0}$: uninsulating crack, aluminum alloy LY12, λ=1.

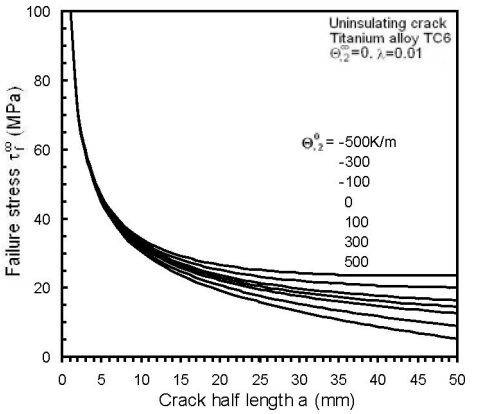

Figure 49. Failure stress τ_f^∞ versus crack half length a for different temperature gradient $\Theta_{,2}^0$: uninsulating crack, titanium alloy TC6, λ=0.01.

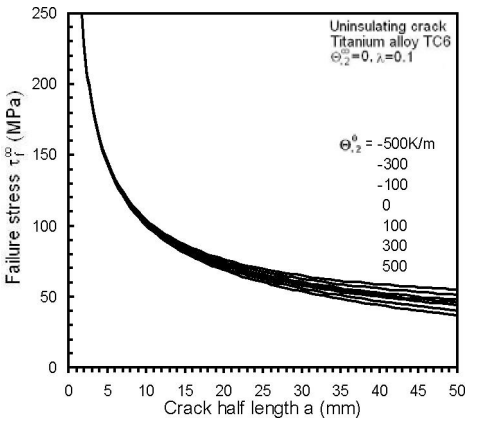

Figure 50. Failure stress τ_f^∞ versus crack half length a for different temperature gradient $\Theta_{,2}^0$: uninsulating crack, titanium alloy TC6, λ=0.1.

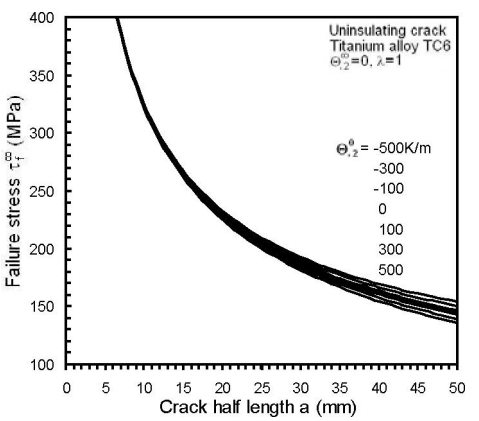

Figure 51. Failure stress τ_f^∞ versus crack half length a for different temperature gradient $\Theta_{,2}^0$: uninsulating crack, titanium alloy TC6, λ=1.

6.3. Enhancement and Retardation of Crack Growth by Thermal Effect

As shown in Eq. (63), the thermal loading would affect the magnitude of S depending on whether the temperature gradient $\Theta_{,2}^0$ on crack surface is positive, zero or negative. According to the strain energy density theory, this would affect the crack growth behavior as the direction of $\Theta_{,2}^0$ is altered.

Let the superscripts –, 0, + denote, respectively, the situations for negative, zero and positive $\Theta_{,2}^0$. The corresponding first segment of crack growth is denoted respectively by r_1^-, r_1^0, and r_1^+. The strain energy density factor is represented respectively by S_1^-, S_1^0 and S_1^+. By application of the strain energy density theory, there prevails

$$\left(\frac{dW}{dV}\right)_c = \frac{S_1^-}{r_1^-} = \frac{S_1^0}{r_1^0} = \frac{S_1^+}{r_1^+} = \cdots \tag{68}$$

Values of three coefficients C_{11}, C_{12} and C_{22} in Eq. (63) for three materials with a=10mm and $\theta=\theta_0$ are calculated and tabulated in Table 6. θ_0 is the cracking angle for mode II crack. Since coefficient C_{12} is positive, positive $\Theta_{,2}^0$ on the crack surface would increase the value of strain energy density factor S while negative $\Theta_{,2}^0$ would reduce the value of S, say $S_1^- < S_1^0 < S_1^+$. Therefore, it can be derived from Eq. (68) that

$$r_1^- < r_1^0 < r_1^+ \tag{69}$$

For the uninsulating crack, Eq. (69) indicates that the positive $\Theta_{,2}^0$ would intensify the crack growth while the negative $\Theta_{,2}^0$ would retard the crack growth. Minimum value of strain energy density factor S_{min} occurs along angle θ_0 where the crack growth initiates. Values of S_{min} with thermal loading $\Theta_{,2}^0$ for three materials are listed in Table 7. Normalized first crack growth segment $r_1^{\pm}/r_1^0$ with temperature gradient $\Theta_{,2}^0$ are tabulated in Table 8. It is shown that $r_1^+/r_1^o > 1$ for $\Theta_{,2}^o > 0$ and $r_1^-/r_1^o < 1$ for $\Theta_{,2}^o < 0$. Fig. 52 illustrates the influence of thermal loading on the crack growth behavior. Numerical results in Tables 7 and 8 are also depicted in Figs. 53 and 54 respectively. As shown in Figs. 52 and 54, the positive temperature gradient $\Theta_{,2}^0$ enhances the crack growth while negative $\Theta_{,2}^0$ impedes the crack growth which is different from the insulating crack case.

Table 6. Values of coefficients C_{11}, C_{12} and C_{22} in Eq. (63) for three materials with $\theta=\theta_0$ and a=10mm.

C_{ij} (i, j=1, 2)	Material		
	Titanium alloy TC6	Steel 38Cr2Mo2VA	Aluminum alloy LY12
θ_0	82.34°	82.34°	83.49°
$C_{11}(\theta_0)\times10^{-14}$	2.51180	1.41917	4.01314
$C_{12}(\theta_0)\times10^{-10}$	0.932595	1.31172	2.17908
$C_{22}(\theta_0)\times10^{-6}$	0.346259	1.21240	1.18321

Table 7. Minimum values S_{min} of strain energy density factor as a function of temperature gradient $\Theta_{,2}^0$ for three materials with $\theta=\theta_0$, a=10mm and τ^∞=10MPa.

Material	Minimum values of strain energy density factor S_{min} (N/m)										
	$\Theta_{,2}^0$ (K/m)										
	-500	-400	-300	-200	-100	0	100	200	300	400	500
Titanium alloy TC6	1.666	1.821	1.983	2.153	2.329	2.512	2.702	2.899	3.103	3.313	3.531
Steel alloy 38Cr2Mo2VA	0.411	0.564	0.741	0.943	1.169	1.419	1.694	1.992	2.315	2.663	3.034
Aluminum alloy LY12	2.130	2.459	2.812	3.189	3.589	4.013	4.461	4.932	5.427	5.946	6.488

Table 8. Normalized first crack growth segment $r_1^{\pm}/r_1^0$ versus temperature gradient $\Theta_{,2}^0$ three materials with $\theta=\theta_0$, a=10mm and τ^∞=10MPa.

Material	Normalized first crack growth segments $r_1^{\pm}/r_1^0$										
	$\Theta_{,2}^0$ (K/m)										
	-500	-400	-300	-200	-100	0	100	200	300	400	500
Titanium alloy TC6	0.663	0.725	0.790	0.857	0.927	1	1.076	1.154	1.235	1.319	1.406
Aluminum alloy LY12	0.531	0.613	0.701	0.795	0.894	1	1.112	1.229	1.352	1.482	1.617
Titanium alloy TC6	0.663	0.725	0.790	0.857	0.927	1	1.076	1.154	1.235	1.319	1.406

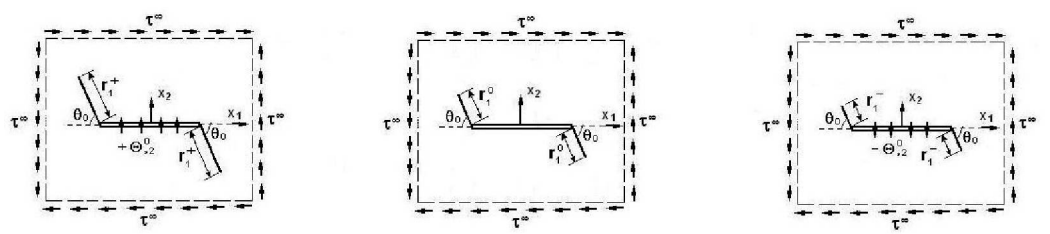

(a) positive $\Theta_{,2}^0$ (b) zero $\Theta_{,2}^0$ (c) negative $\Theta_{,2}^0$

Figure 52. Enhancement and retardation behavior of crack growth by thermal effect for the uninsulating crack: (a) positive $\Theta_{,2}^0$; (b) zero $\Theta_{,2}^0$; (c) negative $\Theta_{,2}^0$.

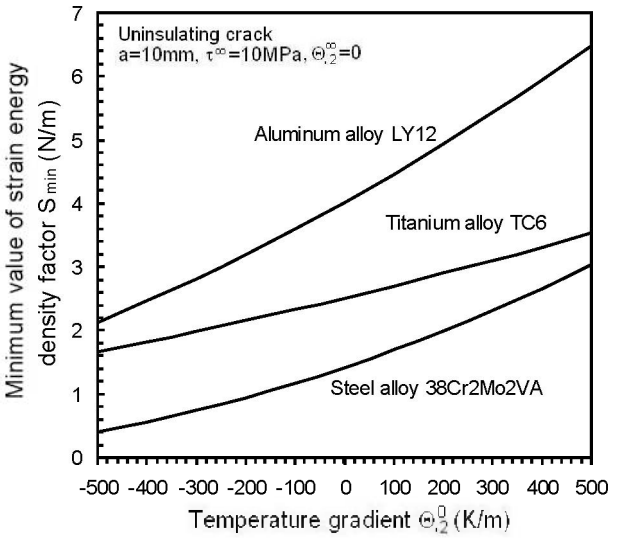

Figure 53. Minimum value of strain energy density factor S_{min} versus temperature gradient $\Theta_{,2}^{0}$ for three materials for the uninsulating crack.

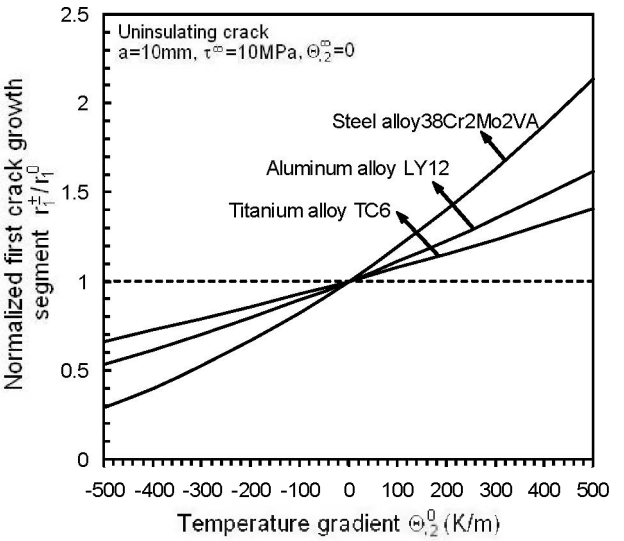

Figure 54. Normalized first crack growth segment $r_1^{\pm} / r_1^{0}$ versus temperature gradient $\Theta_{,2}^{0}$ for three materials for the uninsulating crack.

6.4. Log-Log Plot for Strain Energy Density Dw/Dv Versus Distance R

Strain energy density function dW/dV has been given by Eq. (47) in which $K_2 = K_2^{\tau} + K_2^{\Theta}$, $K_2^{\tau} = \tau^{\infty}\sqrt{\pi a}$ and K_2^{Θ} can be known from Eq. (62) for the uninsulating

crack. In the case of uninsulating crack model, $\Theta_{,2}^{0} \neq 0$, and take $\Theta_{,2}^{\infty} = 0$. The $dW/dV \sim r$ behavior is different from the insulating crack model. Log-log plots of dW/dV versus distance r for three materials are respectively depicted in Figs. 55, 56 and 57. Curves of strain energy density dW/dV increase with the increment of temperature gradient $\Theta_{,2}^{0}$ on the crack line from negative to positive by contrast to those in Figs. 28, 29 and 30. In addition, the spacing in Figs. 55, 56 and 57 is smaller than that in Figs. 28, 29 and 30.

This accomplishes the discussion for the uninsulating crack model.

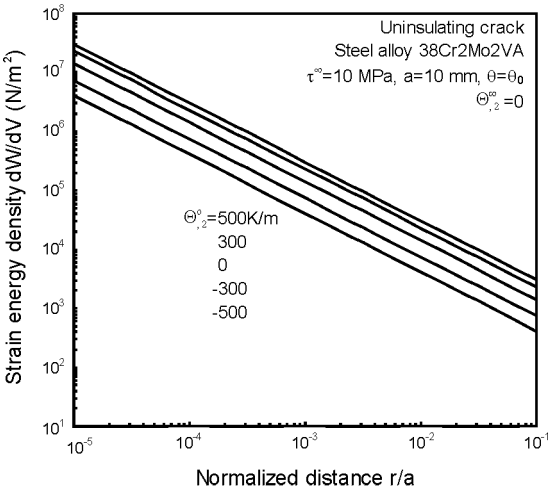

Figure 55. Log-log plot of strain energy density dW/dV versus normalized distance r/a for different temperature gradient $\Theta_{,2}^{0}$: uninsulating crack, steel alloy 38Cr2Mo2VA.

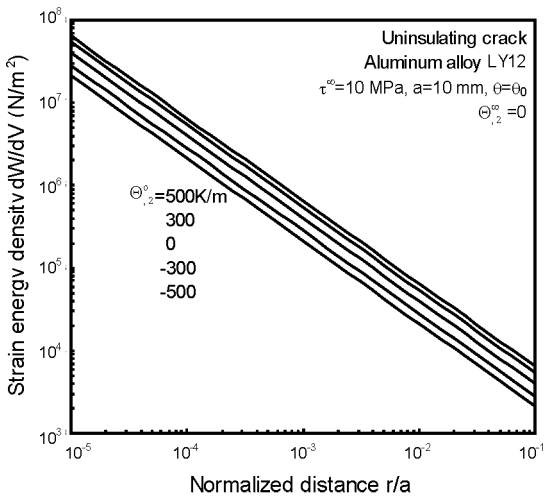

Figure 56. Log-log plot of strain energy density dW/dV versus normalized distance r/a for different temperature gradient $\Theta_{,2}^{0}$: uninsulating crack, aluminum alloy LY12.

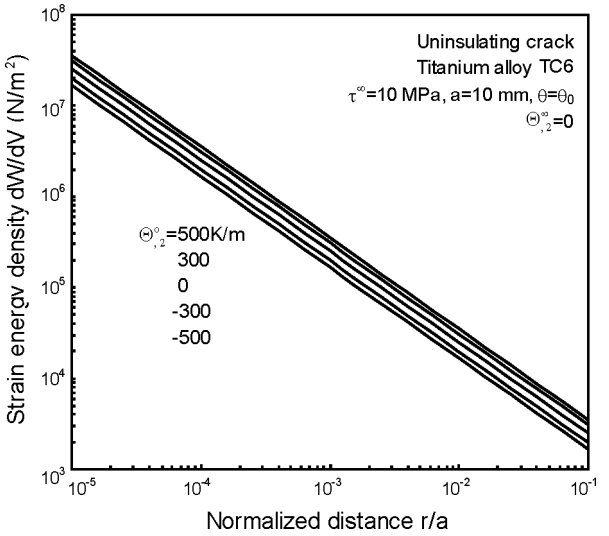

Figure 57. Log-log plot of strain energy density dW/dV versus normalized distance r/a for different temperature gradient $\Theta^0_{,2}$: uninsulating crack, titanium alloy TC6.

7. Conclusion

For the crack problem under the thermal condition, solution depends on the temperature boundary condition. For instance, an infinite plate with a central crack subjected to the uniform heat flows has been investigated in [31]. When the upper and lower crack surfaces retain a constant temperature, the mode I thermal stress intensity factor prevails while the mode II thermal stress intensity factor is zero. The temperature boundary condition on the crack surfaces would be dominant for the solution of thermal crack problem. When the temperature boundary condition is changed, the type of solution would be altered. Accomplished in this work is for the same problem as in [31]. However, the temperature boundary condition on the crack surfaces is changed. Assumed is that the temperature gradient $\Theta^0_{,2}$ on the upper and lower crack surfaces normal to the crack line remains constant. It was found that in this case the mode II thermal stress intensity factor prevails while the mode I thermal stress intensity factor is zero. The model involves both the insulating and uninsulating crack represented respectively by $\Theta^0_{,2}=0$ and $\Theta^0_{,2}\neq 0$. Obtained are analytical solutions including temperature distribution, thermal stress intensity factor, strain energy density function and strain energy density factor, etc. A unique characteristics was found that the mode II temperature field is skew-symmetrically discontinuous with respect to the x_2-axis. It is needed further to verify whether this phenomenon is necessary to produce a mode II thermal stress intensity factor or not.

Based on the analytical solutions derived in this work, the fracture behaviors of three materials of steel, aluminum and titanium alloys are discussed and compared under the interaction of thermal and mechanical loading by application of strain energy density theory. The failure stress is calculated at different scales. Both the insulating and uninsulating crack

models are considered. It was found that the diathermancy of the crack slit has a pronounced influence on the fracture behavior. More specifically, for an insulating crack, the positive temperature gradient $\Theta_{,2}^{\infty}$ at infinite perpendicular to the crack can partly or completely kill the mechanical loading depending on the magnitude of $\Theta_{,2}^{\infty}$. Alternatively, the negative $\Theta_{,2}^{\infty}$ intensifies the mechanical loading that enhances the crack growth. An uninsulating crack behaves differently. It is the positive temperature gradient $\Theta_{,2}^{0}$ on the crack surfaces that intensifies the crack growth while the negative $\Theta_{,2}^{0}$ impedes the crack propagation.

The recent works in [32-34] reveal that singularities have been known to represent the character of the stress fields around defects at different scales. The $r^{-1/2}$ stress singularity is particularly well known for a macroscopic line crack. It is indicative of the intensity of the local stress field over a circular region with a radius approximately 10^{-3}~10^{-1} cm such that the unaided eye can detect. If the distance r is made smaller and smaller, then the $r^{-1/2}$ description becomes less and less adequate because the solid can no longer be regarded as homogeneous and isotropic by taking the average of the bulk properties. No doubt, there prevails a distance r at which the $r^{-1/2}$ stress singularity would change to some other order that can be weaker or stronger. A real material would possess both macroscopic and microscopic features of the material. They appear to be different only when viewed far away and very close to the crack tip. Continuum mechanics theories, however, cannot reflect the multiscale character of the stress singularities in a single formulation. A more precise crack model can be developed by attaching a microscopic damage zone to the macro-crack tip based on this work to explore the macro/micro damage interaction by integrating with the thermal/mechanical application. This is a different proposition that will surely lead to very different results. It is no doubt one of the problems that need to be addressed in the future.

Acknowledgement

This work was jointly supported by Natural Science Foundation of Hunan Province of China under the contract No. 07JJ3004 and by Natural Science Foundation of University Doctoral Disciplines of China under the contract No. 200805360002.

References

[1] G.C. Sih. *Mechanics of Fracture Initiation and Propagation.* Kluwer Academic Publishers, Dordrecht, The Netherlands, 1991.

[2] G.C. Sih. A field model interpretation of crack initiation and growth behavior in ferroelectric ceramics: change of poling direction and boundary condition. *Theoretical and Applied Fracture Mechanics*, **38**(1) (2002) 1-14.

[3] G.C. Sih, J.Z. Zuo. Multiscale behavior of crack initiation and growth in piezoelectric ceramics. *Theoretical and Applied Fracture Mechanics*, **34**(2) (2000) 123-141.

[4] G.C. Sih, E.P. Chen. Dilatational and distortional behavior of cracks in megnetoelectroelastic materials. *Theoretical and Applied Fracture Mechanics*, **40**(1) (2003) 1-21.

[5] G.C. Sih, R. Jones, Z.F. Song. Piezomagnetic and piezoelectric poling effects on mode I and II crack initiation behavior of magnetoelectroelastic materials. *Theoretical and Applied Fracture Mechanics*, **40**(2) (2003) 161-186.

[6] D.Y. Tzou, G.C. Sih. Thermal/mechanical interaction of subcritical crack growth in tensile specimen. *Theoretical and Applied Fracture Mechanics*, 10(1) (1988) 59-72.

[7] J. Chen, Z. X. Liu, Z.Z. Zou. Crack initiation behavior of functionally graded piezoelectric material: prediction by the strain energy density criterion. *Theoretical and Applied Fracture Mechanics*, **41**(1-3) (1988) 63-82.

[8] G.C. Sih, X.S. Tang. Form-invariant representation of fatigue crack growth rate enabling linearization of multiscale data. *Theoretical and Applied Fracture Mechanics*, **47**(1) (2007) 1-14.

[9] G.C. Sih, X.S. Tang. Random property of micro/macro fatigue crack growth behavior predicted from energy density amplitude range. *Theoretical and Applied Fracture Mechanics*, **48**(2) (2007) 97-111.

[10] C. P. Spyropoulos. Energy release rate and path independent integral study for piezoelectric material with crack. *International Journal of Solids and Structures*, **41**(3-4) (2004) 907-921.

[11] Y.E. Pak. Crack extension force in a piezoelectric material. *Journal of Applied Mechanics,* **57**(3) (1990) 647-653.

[12] Z. Suo, C.M. Kuo, D.M. Barnett, J.R. Willis. Fracture mechanics for piezoelectric ceramics. *Journal of the Mechanics and Physics of Solids*, **40**(4) (1992) 739-765.

[13] T.Y. Zhang, C.F. Qian, P. Tong. Linear electro-elastic analysis of a cavity or a crack in a piezoelectric material. *International Journal of Solids and Structures*, **35**(17) (1998) 2121-2149.

[14] G.C. Sih. Dynamic crack problem – strain energy density fracture theory. In: G.C. Sih (Ed.), *Elastodynamic Crack Problems*, Noordhoff, Leiden, 1977, pp. 17-47.

[15] G.C. Sih. Heat conduction in the infinite medium with lines of discontinuities. *Journal of Heat Transfer*, **87**(2) (1965) 293-298.

[16] G.C. Sih. On the singular character of thermal stresses near a crack tip. *Journal of Applied Mechanics*, **29**(3) (1962) 587-589.

[17] A.L. Florence, J.N. Goodier. Thermal stresses due to disturbance of uniform heat flow by an insulated ovaloid hole. *Journal of Applied Mechanics*, **27**(6) (1960) 635-639.

[18] X. Z. Zhang, N. Hasebe. Basic singular thermoelastic solutions for a crack. *International Journal of Fracture*, **62**(1) (1993) 97-118.

[19] N.K. Mukhopadhyay, S.K. Maiti, A. Kakodkar. Modified crack closure integral based computation of stress intensity factors for 2-D thermoelastic problems through boundary element method. *Nuclear Engineering and Design*, **187**(3) (1999) 277-290.

[20] S.Q. Nusier, G.M. Newaz. Growth of interfacial cracks in a TBC/superalloy system due to oxide volume induced internal pressure and thermal loading. *International Journal of Solids and Structures*, **37**(15) (2000) 2151-2166.

[21] Katharine M. Flores, Reinhold H. Dauskardt. Mode II fracture behavior of a Zr-based bulk metallic glass. *Journal of the Mechanics and Physics of Solids*, **54**(11) (2006) 2418-2435.

[22] A.A. Rizk. Orthotropic semi-infinite medium with a crack under thermal shock. *Theoretical and Applied Fracture Mechanics*, **46**(3) (2006) (217-231).

[23] B.M. Singh, J. Rokne, R.S. Dhaliwal. Thermal stresses in a two-dimensional infinite medium containing a rigid inclusion embedded in a line crack. *Theoretical and Applied Fracture Mechanics*, **46**(2) (2006) 148-155.

[24] K.P. Herrmann, V.V. Loboda, I.V. Kharun. Interface crack with a contact zone in an isotropic bimaterial under thermomechanical loading. *Theoretical and Applied Fracture Mechanics*, **42**(3) (2004) 335-348.

[25] B.L. Wang, N. Noda. Thermally induced fracture of a smart functionally graded composite structure. *Theoretical and Applied Fracture Mechanics*, **35**(2) (2001) 93-109.

[26] N.N.V. Prasad, M.H. Aliabadi, D.P. Rooke. Effect of thermal singularities on stress intensity factors: edge crack in rectangular and circular plate. *Theoretical and Applied Fracture Mechanics*, **24**(3) (1996) 203-215.

[27] C.K. Chao, R.C. Chang. Crack trajectories influenced by mechanical and thermal disturbance in anisotropic material. *Theoretical and Applied Fracture Mechanics*, **17**(3) (1992) 177-187.

[28] N.I. Muskhelishivili. *Some Basic Problems of the Mathematical Theory of Elasticity*. P. Noordhoff Ltd., Groningen, The Netherlands, 1953.

[29] X.S. Tang. Analytical solutions of temperature fields for an orthotropic plate with a central crack under remote uniform heat flows. *Engineering Mechanics*, **24**(3) (2007) 28-33. (in Chinese)

[30] Editorial Board. *Practical Handbook of Engineering Materials*. Chinese Standard Press, Beijing, 1988, Vol. 1. (in Chinese)

[31] X.S. Tang. *Analytical solution of mode I crack problem under mechanical/thermal loading and comparison of fracture behaviors of steel, aluminum and titanium alloys.* Theoretical and Applied Fracture Mechanics, in press.

[32] X.S. Tang, G.C. Sih. Weak and strong singularities reflecting multiscale damage: micro-boundary conditions for free-free, fixed-fixed and free-fixed constraints. *Theoretical and Applied Fracture Mechanics*, **43**(1) (2005) 5-62.

[33] X.S. Tang, G.C. Sih. Kinetics of microcrack blunting ahead of macrocrack approaching shear wave speed. *Theoretical and applied fracture mechanics*, 2004, 42(2) (2004) 99-130.

[34] G.C. Sih, X.S. Tang. Scaling of volume energy density function reflecting damage by singularities at macro-, meso- and micro-scopic level. *Theoretical and Applied Fracture Mechanics*, **43**(2) (2005) 211-231.

In: Titanium Alloys: Preparation, Properties and Applications ISBN: 978-1-60876-151-7
Editor: Pedro N. Sanchez, pp. 365-384

Chapter 8

TI-MO CAST ALLOYS FOR BIOMEDICAL APPLICATIONS. ANODIC BEHAVIOR AND PASSIVE FILM PROPERTIES

N.T.C. Oliveira[1], A.C. Guastaldi[1], S. Piazza[2] and C. Sunseri[2]
[1]Grupo de Biomateriais, Dept. de Físico-Química, Instituto de Química/UNESP, Araraquara – SP, Brazil (Brazil)
[2]Dipartimento di Ingegneria Chimica dei Processi e dei Materiali, Università di Palermo, Viale delle Scienze, 90128 Palermo (Italy)

Abstract

Casting of Ti-Mo alloys having different Mo content (4 to 20 wt%) was performed by arc-melting of pure metals. These alloys present interesting features for potential biomedical applications, e.g., in artificial proteases, owing the favorable characteristics of Ti alloys: apart from mechanical properties and good osseointegration, the strong corrosion resistance in biological environment and the low toxicity of their corrosion products.

The corrosion and anodic behavior of the different alloys was investigated in different electrolytes, including neutral, acidic and chloride-containing solutions. A strong tendency to passivation was observed, caused by the oxygen affinity of the metallic material. However, partial Mo dissolution is likely to occur at very low pH.

Composition and solid-state properties of the passive films were studied by ex-situ XPS, in-situ photoelectrochemical and impedance experiments. Films were found to consist of a mixed oxide phase, mainly containing TiO_2 and bearing small concentrations of MoO_3. The latter depends on starting alloy composition and film thickness.

As a result, also the behavior of the passive films depends on these two factors. In fact thin films or films grown on alloys bearing a small Mo content display n-type semiconducting behavior, analogous to what reported for pure TiO_2. On the contrary, films grown on alloys with higher Mo content are more resistive and change their behavior from semiconducting to insulating with increasing thickness.

1. Introduction

Artificial implants in human body meet an increasing demand, owing to the increasing lifetime of population in most countries. This stimulates research on new materials having suitable characteristics, i.e., local and systemic biocompatibility, proper mechanical characteristics and noticeable corrosion resistance in biological fluids [1-3]. High mechanical strength is obviously required for artificial proteases; moreover, osseointegration (direct contact between implant and viable bone, without soft-tissue layer formation) is necessary [1]. Materials having low elasticity modulus favor a better osseointegration, by stimulating the natural bones [4, 5]. Corrosion resistance is a key issue for long term durability of implants: corrosion caused by biological fluids affects their fatigue life, leading to mechanical failure. Further, presence of corrosion particulate and wear products in the tissues surrounding the implant may result in bone damage [6].

Among the most promising metallic materials, titanium and its alloys are widely investigated for several biomedical applications, including bones and dental proteases, due to their favorable mechanical and physico-chemical properties [3, 5, 7]. In fact these alloys present high mechanical strength, low specific gravity and elasticity modulus, high corrosion resistance and excellent biocompatibility. The latter originates from the very low both metal release and toxicity of corrosion products of Ti, Zr, Nb, Ta and Mo, at variance with stainless steels and Co-Cr alloys [8-10]. Thus, even if stainless steels and Co-Cr alloys are still utilized, Ti alloys are mostly employed in medical surgery for artificial joints and bone plates fabrication [11].

Titanium presents two allotropic phases, because Hpc (α phase) and bcc (β phase) crystalline structures may exist; hence, Ti alloys belong three classes: α alloys, $\alpha+\beta$ alloys and β alloys. The latter can be stabilized by addition of β alloying elements. In fact, β titanium alloys present enhanced characteristics as biomaterials: a reduced elasticity modulus, an improved tissue response and higher corrosion resistance. This explains the effort to develop new β Ti alloys containing non-toxic elements, like Nb, Ta, Zr, Mo and Sn [5, 12].

In recent years, Ti-Mo alloys applied as biomaterials have been studied with an emphasis on their microstructure and mechanical properties; in [3, 4, 13-16] studies have been carried out on microstructure, stress release and mechanical properties of Ti-Mo alloys. Formation of stress-induced α martensite phase in a metastable β Ti–Mo alloy is reported in [17]. The same authors used high-resolution transmission electron microscopy and *in situ* X-ray diffraction analyses to elucidate the compositional sensitivity of the deformation behavior in two different Ti–Mo-based alloys [18].

However, only few studies have been dedicated to investigate the electrochemical behavior and the corrosion resistance of these materials [3, 7]. The corrosion resistance of a Ti–30 Mo alloy in 35% HCl was studied in [19] by electrochemical and open circuit analysis, and results show that this alloy is more resistant than pure Ti. The behavior of a new Ti–Mo–Ni–Pd alloy in different acid environments and at various temperatures was investigated in [20]: authors found that adding those alloying elements results in a positive shift of the open circuit potential, and leads to spontaneous passivation through formation of a compact, protective titanium dioxide layer. The structure of the anodic films was found affected by the incorporation of Mo species from the substrate, resulting in an amorphous mixed phase having a low defect density [21].

We have fabricated Ti-Mo cast alloys with different compositions using an arc-melting furnace under ultra-pure argon atmosphere. For all alloys, composition, investigated by XRF and EDX, was close to the nominal one, with a homogeneous Mo distribution. XRD analysis shows that alloy crystalline structure is sensitive to Mo content [3].

Corrosion resistance and anodic behavior of the alloys were studied in neutral and acidic inorganic aqueous electrolytes, as well as in a Ringer physiological solution. A spontaneous passivation of the alloys occurs in every solution, owing to the formation of an oxide surface layer; no pitting occurrence is observed in the Cl^--containing electrolyte up to 8 V. EIS studies suggest highly protective properties of the surface films, increasing with Mo content in the alloy and immersion time. The electrochemical results suggest that the Ti-15 Mo alloy is promising for application in orthopedic devices, since electrochemical stability is directly associated with biocompatibility [7].

The anodic behavior of the alloys with different Mo content was investigated in different solutions, and passive films were grown potentiodynamically up to different thicknesses; barrier-type surface oxides, evidencing interference colors, are formed on the alloys surface with a thickness increasing with the anodizing voltage. This reveals a valve-metal behavior of the Ti-Mo alloys; however, film growth kinetics is influenced by anodizing solution and Mo content in the alloy [22].

Properties and composition of the anodic oxides were studied by photoelectrochemical and XPS experiments. Surface films consist of a TiO_2 phase containing MoO_3 groups; XPS data at different film thicknesses indicate a progressive enrichment in Ti of the oxide films. This is reflected in their different solid-state properties: very thin films and thicker films grown on alloys with lower Mo contents show a semiconducting behavior, whilst thicker films grown on Mo-rich alloys show an insulating behavior, as revealed by both photoelectrochemical and impedance experiments. These findings indicate that MoO_3 groups into the mixed oxide tend to compensate oxygen deficiency, which is responsible for the n-type semiconducting behavior of TiO_2.

2. Alloys Casting and Structure

The Ti–Mo cast alloys with different compositions (4 to 20 Mo wt.%), were melted, starting from high-purity chemical elements, in an arc-melting furnace with a non-consumable W electrode and a water-cooled copper hearth under an ultra-pure argon atmosphere, following a well-known procedure described in the literature [5, 22]. Initially, a vacuum of 10^{-3} atm was created and then ultra-pure argon was injected. This procedure was repeated three times and a vacuum of 10^{-3} atm argon was maintained at the end of the process, ensuring removal of all gaseous oxygen. After, the different alloys were melted. In order to ensure homogeneity, samples were turned and melted 20 times more [5, 22].

All Ti–Mo alloys were studied in as-cast conditions, just after a mechanical polishing with emery paper and rinsing with distilled water.

Chemical composition of the alloys was assessed by X-ray fluorescence spectroscopy (XRF) [5], whilst surfaces were examined by Scanning Electron Microscopy (SEM) and Energy Dispersed Spectroscopy (EDS) [5, 22]. The chemical analyses of different areas (bulk and surface) revealed composition of the alloys close to the nominal value (see Table 1), with a slight difference only for the Ti–20 Mo alloy.

Table 1. Bulk compositions (determined by XRF) and surface compositions (determined by EDS in different points), of the investigated alloys.

Nominal composition	XRF: Mo wt.%	EDS: Mo wt.%
Ti-4 Mo	4.3	4.2
Ti-6 Mo	6.3	6.5 ± 0.3
Ti-10 Mo	10.1	10.1 ± 0.1
Ti-15 Mo	14.6	14.9 ± 0.2
Ti-20 Mo	18.2	17.8 ± 0.2

Moreover, alloys composition was homogeneous, with no appreciable differences between surface and bulk. We remark that compositions in Table 1 correspond to Mo content in the alloy ranging between about 2 and 10 at%.

X-ray diffraction patterns (Fig. 1) revealed that crystalline structure of the alloys is sensitive to their Mo concentration: in particular, α' (hexagonal) and α" (orthorhombic) phases are present for low Mo contents in the alloys, whilst β (bcc) phase predominates for higher Mo content (≥ 10 wt%) [5]. Ho et al. [4] found similar results on binary Ti-Mo alloys. β phase retention in Ti alloys with higher Mo concentrations is in agreement also with results presented in [23], whilst in [24] it was shown that a minimum of 10% Mo was required to stabilize the β phase at room temperature. Knowing microstructure of Ti alloys is very important, because the coexistence of hexagonal α Ti and bcc β Ti is an important factor controlling mechanical properties and corrosion resistance.

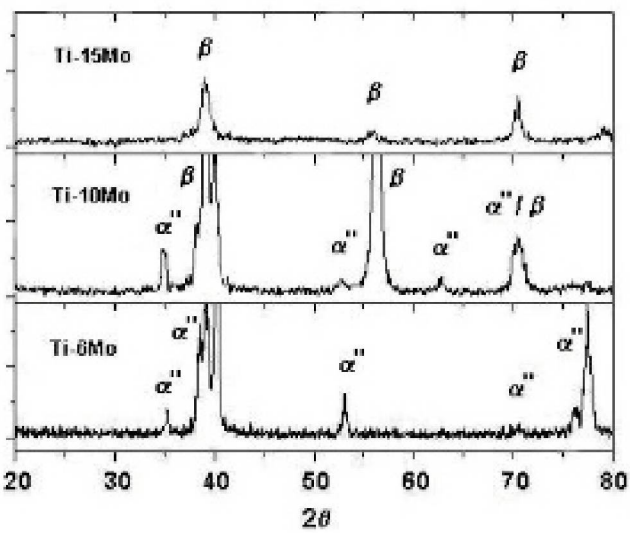

Figure 1. XRD diffractograms of Ti-Mo alloys from 6 to 15 Mo wt.%.

Moreover, elemental mapping showed a homogeneous Mo distribution for all alloys [5]. Such homogeneity suggests a complete miscibility of both elements in the solid state, according to the Hume-Rothery rules.

Before experiments, cylindrical ingots of samples were embedded into glass cylinders using an epoxy resin; the back electrical contact was ensured with a silver paste. The front surface was polished using silicon carbide papers (down to 1200 grade), rinsed ultrasonically twice in distilled water and dried under a nitrogen stream. No chemical etching was performed, in order to avoid modification of the alloys surface composition.

3. Corrosion Behavior

Soon after mechanical preparation, electrodes were immersed into the working solution at room temperature, and the variation of the open circuit potential (E_{oc}) with time was followed in neutral (Na_2SO_4) and acidic (H_2SO_4) aerated aqueous electrolytes, and also in a Cl^--containing environment (Ringer solution). The last one is a usual solution used to simulate physiological media [3, 5, 7, 25–28].

Time profiles obtained for all samples are qualitatively similar: in neutral solutions E_{oc} was initially quite negative and it shifted upwards for 30-60 minutes finally reaching an almost stationary value (Fig.2). The same trend was observed in H_2SO_4 electrolyte, but here initial variation of E_{oc} was lower and faster (about 10 minutes), and more negative stationary values were recorded. The positive shift of E_{oc} with immersion time indicates that, similarly to pure Ti, all alloys undergo spontaneous passivation in the examined solutions, owing to the formation of an oxide surface film on their surface.

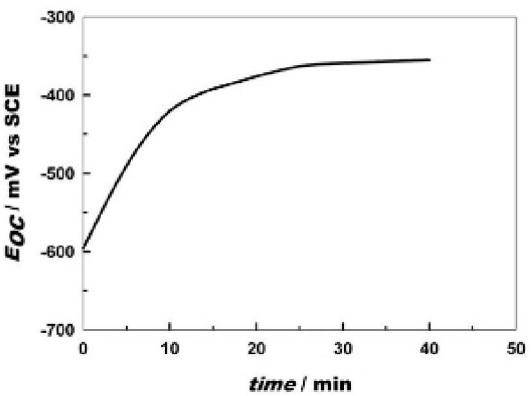

Figure 2. Open circuit potential (E_{oc}) vs. time for the Ti-10 Mo alloy in 0.15 mol L^{-1} Na_2SO_4 solution.

While initial E_{oc} values suffered a certain scatter (likely due to a scarce reproducibility of mechanically treated surfaces), stationary E_{oc} were well reproducible (within ± 30 mV over different identical experiments) and shifting towards slightly higher potentials with increasing the Mo content in the metallic alloy. Stationary E_{oc} values are reported in Table 2 for the different samples in each solution; they suggest that all samples passivates spontaneously, regardless of solution. However, less negative values in the chloride-free neutral solution indicate easier passive layer formation and/or better corrosion protection characteristics of the surface film formed in this electrolyte. On the contrary, in the acidic solution more negative values of the stationary open circuit potential could reveal a slow partial dissolution. This conclusion is supported also by long-term E_{oc} measurements carried out in the same aerated

solutions at 37°C: at this temperature values shifted for the first 70 – 100 h, afterwards they stabilize up to about 400 h of immersion. Again, changing electrolyte final E_{oc} values decrease in the same order (Na_2SO_4 > Ringer > H_2SO_4) as before. Analogous results were found in [25] for the Ti–13Nb–13Zr and Ti–50Zr alloys.

Table 2. Steady-state open circuit potentials (E_{oc}) recorded at room temperature in different aerated aqueous electrolytes for the investigated Ti-Mo alloys.

Sample	0.5 M H_2SO_4 E_{oc} [mV/SCE]	0.15 M Na_2SO_4 E_{oc} [mV/SCE]	Ringer sol. E_{oc} [mV/SCE]
Ti	-	- 350	- 428
Ti - 4 Mo	-	- 350	- 421
Ti - 6 Mo	- 515	- 352	- 414
Ti - 10 Mo	- 489	- 355	- 407
Ti - 15 Mo	- 457	- 345	- 405
Ti - 20 Mo	-	- 321	- 388

Resistance of the alloys to localized corrosion and pitting attack was checked performing voltammograms in a Ringer aerated solution (NaCl 8.61 g/L, CaCl2 0.49 g/L, KCl 0.30 g/L). Curves obtained scanning the electrode potential toward positive values at a scan rate of 50 mV/s are displayed in Fig.3: the absence of pitting initiation up to potentials of 8 V(SCE) can be noted. This testifies an extremely high stability of the oxide surface films even in the presence of a high concentration of Cl^- ions, arising from the strong oxygen affinity of titanium based materials [3, 7]. Similar results were obtained in [25] for the for the Ti–13Nb–13Zr alloy in the same Ringer solution: also in that case no pitting occurrence was noticed up to 8 V, at variance with the Ti-50 Zr alloy [26] In fact, Yu and Scully [29] reported that the Ti–13Nb–13Zr alloy presents a pitting potential greater than 22.8 V in the same solution. Comparison of previous results confirms a beneficial effect of Mo addition for improving resistance to localized corrosion of the alloy. Indeed, in [19] it is reported that a Ti-30 Mo alloy displays a corrosion resistance in 35% HCl much higher than pure Ti.

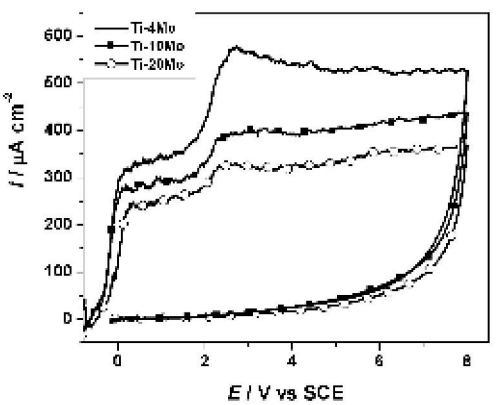

Figure 3. Cyclic voltammograms in Ringer solution at 100 mV/s for different Ti-Mo alloys.

Also SEM examination of samples surface confirms the absence of any localized attack after cycling the potential up to 8 V: surface appeared smooth and featureless, with no presence of pits. They were fully similar to those of samples anodized in Na_2SO_4 solution, and roughness reflects the initial surface preparation of the metallic material [22].

Thus, even in this solution the electrochemical behavior of the alloys resembles that of valve-metals, with the formation of barrier-type protective oxide films, whose thickness increases with the potential during the positive scan, whilst in the negative scan no appreciable oxide reduction occurs, so that oxide thickness can be assumed constant. This point will be discussed further in the next paragraph, with regard to the anodizing curves in chloride-free electrolytes.

4. Anodic Formation of Passive Films

It is well known that the corrosion resistance of most metallic materials is strictly related to the formation of compact (passivating) surface layers and to their chemical solid-state characteristics. In order to study systematically growth and properties of the passive films grown on the surface of the investigated Ti-Mo alloys in the different electrolytes, we performed constant rate anodizing at room temperature for the different metallic specimens in each solution. Hence, soon after reaching the stationary E_{oc}, a linear potential scan at different rates (10 – 200 mV/s) was applied, starting from E_{oc} up to different formation potentials (E_f), ranging between 1 and 8 V(MSE).

The potentiodynamic growth curves recorded for films formed up 8 V on different alloys in neutral solutions are shown in Fig.4, where the effect of both sweep rate (Fig.4a) and alloy composition (Fig.4b) are evidenced. After a fast current peak (below 0 V/MSE), current curves present a first plateau, followed by a second hump at electrode potentials close to 2 V(MSE), more evident for alloys with higher Mo content. Then circulating current decreases towards an almost constant value, more or less rapidly depending on both alloy composition and sweep rate. For the alloy with the lowest Mo content, a monotonic increase of circulating current occurs at high potentials (Fig.4b); this phenomenon is more evident at lower growth rates, and it is related to the parasitic reaction of oxygen evolution. Growth curves recorded in H_2SO_4 solution present similar features [22], but current values were different for each solution at corresponding alloy and growth rate.

The behavior depicted above reveals a valve-metal behavior of all the investigated alloys in the exploited electrolytes; in fact, it resembles that of pure Ti metal [30-32], which forms in the exploited solutions barrier-type oxide films, according to the high-field law:

$$dE_f/dt = (M/z\Im\rho)\, F\, j\, \eta_F \qquad (1)$$

where E_f is the formation potential, M and ρ are the molar mass and the density of the oxide, z the equivalence of the anodic reaction, $\Im$ the Faraday's constant, F the anodizing electric field within the growing film, j the total current density during anodization and η_F the efficiency of formation.

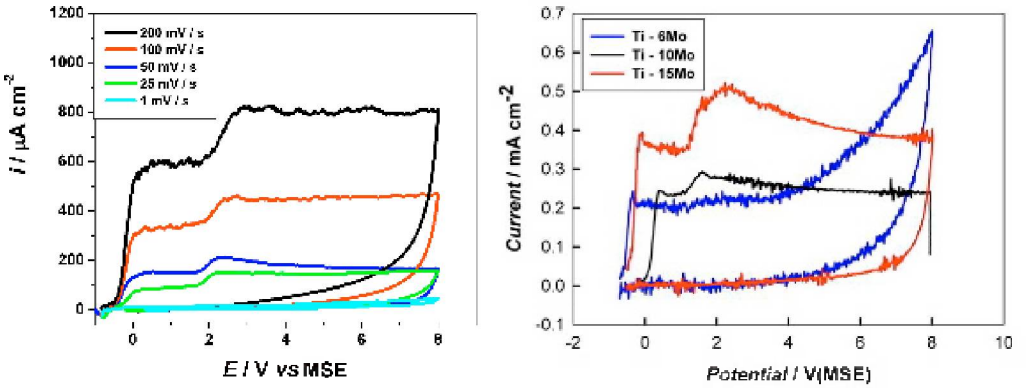

(a) (b)

Figure 4. Cyclic voltammograms (a) for the Ti–15 Mo alloy in 0.15 mol L^{-1} Na_2SO_4 solution at different scan rates and (b) for different Ti–Mo alloys in 0.1 mol L^{-1} ammonium pentaborate at 50 mV/s.

A confirmation comes from the finding that after anodization all passive films displayed interference colors (see Table 3), essentially depending on the formation voltage (i.e., the film thickness), with no sensible influence of other parameters.

Table 3. Interference colours of anodic films grown on Ti-Mo alloys.

E_f / V(MSE)	Stabil. 30 min	Colour
4-8	yes	blue
2	yes	gold
1	yes	metallic
4-8	no	yellow
2	no	pale yellow
1	no	metallic

The increase of the anodizing current with the growth rate (dE_f/dt) is almost linear [22], as expected.

Whilst the similar behavior observed in all the investigated solutions testifies that alloys passivate everywhere (including Cl^-- containing electrolytes), owing to the formation of compact, protecting surface oxide films, the different anodizing currents recorded in different electrolytes for the same alloy suggest that growth kinetics is influenced by solution composition, mainly through the formation efficiency, and possibly also through the value of anodizing electric field. For example, lower formation efficiency recorded in the acidic solution, can be connected with partial film dissolution during the growth. More importantly, Fig.4b can be interpreted in terms of a lowering of the anodizing field and/or formation efficiency with increasing Mo content in the alloy. In fact, eventual changes in film composition should lead to much smaller variations in the anodic current (through the $M/z\Im\rho$ factor), considering also the moderate atomic fraction of Mo in the investigated alloys (10.5 at% for the Ti–20 Mo alloy). Such a finding indicates that the presence of Mo(VI) groups into the

anodic TiO_2 films probably generates mobile defects and lowers the energy barrier for ions transport into the bulk of the films.

The presence of Mo species into the passive layers is confirmed by XPS measurements (see below), and reveals that films growth occurs by inwards migration of O^{2-} species and simultaneous outwards migration of both metallic cations (Ti^{4+} and Mo^{6+}) leading to the formation of a mixed Ti-Mo oxide, analogous to results pertaining passive films on other binary alloys [32-35].

5. Passive Films Characterization

In order to assess the influence of metallic alloy composition on both composition and solid-state properties of the anodic films on the investigated Ti-Mo alloys, we have performed XPS (X-ray Photoelectron Spectroscopy), photoelectrochemical and impedance experiments on films grown on the alloys in various solutions and up to different formation voltages (i.e., having different thicknesses). In the followings we will summarize the main results relative to each kind of characterization, for giving a comprehensive picture of passive films structure and electrical behavior.

5a. XPS Measurements

X-ray Photoelectron Spectroscopy experiments were initially performed on anodic films grown on different alloys at 100 mV/s in 0.15 M Na_2SO_4 solution up to 8 V(MSE). The estimated thickness of the film is around 16 nm, slightly depending on alloy composition (see previous paragraph). Measurements were performed under high-vacuum conditions (5 10^{-9} Torr) using a commercial spectrometer. The Mg Kα line was used ($h\nu$ = 1253.6 eV) and the analyzer pass energy was set to 10 eV. Binding energies of the spectra were corrected using the hydrocarbon component of adventitious carbon fixed at 285.0 eV. Spectra were fitted without placing constraints using multiple Voigt profiles; accuracy of the peak positions was ±0.1 eV.

The XPS spectrum (Fig.5a) relative to the passive film grown on the Ti-15Mo alloy shows the presence of peaks related to both Ti and Mo species, together with the O 1s peak (at 530 eV, corresponding to O^{2-} in oxides [33]). High resolution spectra relative to Ti and Mo peaks are shown in Figs.5 b,c: in both cases the spin-orbit components of each peak are deconvoluted by only one curve. In Fig.5b peaks are attributable to Ti^{4+} $2p_{3/2}$ (at 458 eV) and to Ti^{4+} $2p_{1/2}$, in agreement with those reported in the literature for both pure titania films [36, 37] and for mixed Ti-Zr oxides [33]. Analogous considerations hold for the peaks of Fig.5c, relative to Mo 3d. Because the oxidation states of the Mo 3d region overlap, the curve fitting becomes complicated. It is necessary to fix the area ratio between the Mo $3d_{5/2}$ and Mo $3d_{3/2}$ peaks to 0.67 and the energy split on 3.15 ± 0.05 eV [38]. According to what reported in [39], the binding energy at 232 eV can be assigned to electrons in Mo^{6+} species. Hence, spectra reported in Fig.5 indicate that a mixed Ti-Mo oxide phase is formed on the metallic surface, containing both TiO_2 and MoO_3 groups.

A semi-quantitative determination of the films surface composition was performed based on the relative peak areas, corrected for the relative sensitivity factors. Results for different

anodizing solutions and formation voltages are reported in Table 4, for three different alloys: quite similar surface compositions of the passive film were detected; oxide films consist mainly of TiO_2 oxide bearing small concentrations (< 1 at%) of MoO_3. Thus a strong enrichment in Ti occurs in the passive film with respect to the metallic alloy composition. This finding reveals a much faster transport of Ti^{4+} ions than Mo^{6+} ions within the growing oxide. Similar effect, even less pronounced, was found by us in thin anodic films on a Ti-Zr alloy [32, 33]; others have found also that often composition of passive films differs from that of the starting metallic alloy as for the cationic content [40].

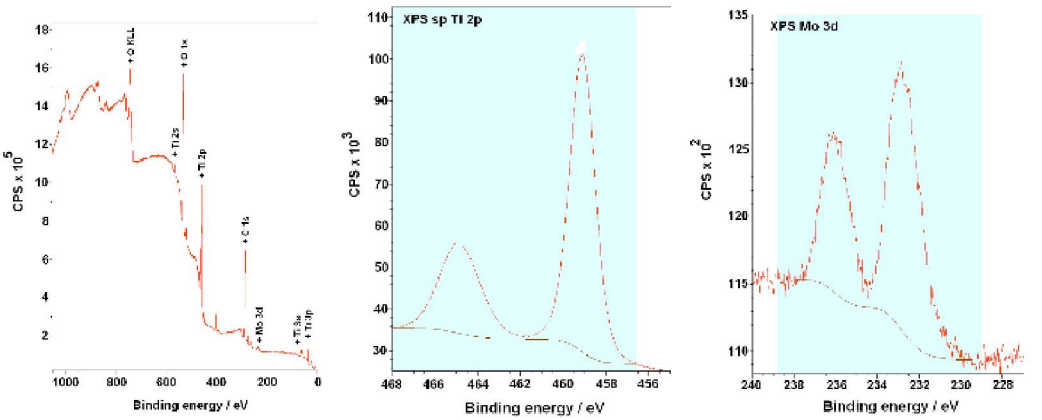

(a) (b) (c)

Figure 5. (a) XPS spectrum recorded after 30 min polarization at E_f for a film grown on the Ti-15Mo alloy in 0.15 M Na_2SO_4 solution at 100 mV/s up to 8V(SCE). (b) High-resolution spectra in the Ti 2p and (c) Mo 3d regions.

However, inspection of data reported in Table 4 indicates that concentration of MoO_3 groups into the anodic films increases less than linearly with the Mo content in the metallic material. Thus, ion transport into the anodic film is also influenced by the alloy composition, likely through the different anodizing electric field; in fact, in this solution the formation efficiency is expected to be very high, close to unity, differently than in other electrolytes [22]. An XPS experiment carried out on the Ti-15 Mo alloy after simple immersion in the same solution (without anodizing) reveals a sensibly higher Mo content (almost 2 at%) in the thin surface passive layer, formed owing to the spontaneous passivation of the material. This confirms the slower transport of Mo^{6+} ions through the bulk oxide film. Moreover, XPS data taken after different immersion times in various electrolytes reveal a Mo depletion on film surface after prolonged immersion in acidic solution, confirming the much stronger tendency to a selective dissolution of Mo in sulfuric acid electrolyte, compared to the neutral sulfate or the Ringer solutions.

Taking into account previous results we can finally state that anodic films grown on the different Ti-Mo alloys consist of a homogeneous mixed oxide phase, having the structure of anodic TiO_2 films doped with variable quantities (depending on starting alloy composition, thickness and anodizing solution) of MoO_3 groups.

Table 4. Composition of anodic films grown on Ti-Mo alloys in 0.15 M Na_2SO_4 solution up to 8 V(MSE), as estimated by XPS measurements.

Alloy	Ti / at.%	Mo / at.%	O / at%
Ti-6Mo	33,0	0,37	66,6
Ti-10Mo	32,4	0,53	67,1
Ti-15Mo	31,1	0,64	68,3

5b. Photoelectrochemical Experiments

A photoelectrochemical investigation was carried out on anodic films grown in different experimental conditions and having variable thickness. In order to avoid thickness changes during characterization and to achieve a good blocking character of the oxide/electrolyte interface, normally these experiments were performed after stabilization for 30 min at E_f.

Samples surface was irradiated with a monochromatic beam through the flat quartz windows of the cell: the monochromatic irradiation was achieved by means of a 150 W xenon lamp (Spectral Energy) connected with a UV-VIS monochromator (Bausch & Lomb). The exit beam was focused onto the surface under investigation by quartz focusing lenses. The photocurrent response was detected by a lock-in amplifier, coupled to a mechanical chopper (frequency: 10 Hz), acquired by a desk computer through an analogic interface, managed through a home-made LABVIEW 7™ program, and corrected for the photon emission of the light source. The latter was detected previously with a calibrated thermopile, and referred to the wavelength of 400 nm. Thus photocurrent action spectra reported below represent the quantum yield in arbitrary units.

Independent of anodizing solution, film thickness and alloy composition, when irradiated all passive film displayed anodic photocurrent already at the open circuit potential. A photocurrent spectrum recorded for a film grown on the Ti-10 Mo alloy up to 8.0 V(MSE) in 0.15M Na_2SO_4 solution is displayed in Fig.6; its shape is characteristic of anodic films, with a maximum photocurrent response at around 250 nm (photon energy of about 5 eV). For longer wavelengths (lower photon energies) photocurrent decreases parallel to the film absorption coefficient, becoming almost zero at the band gap value, whilst for shorter wavelengths (higher photon energies) surface recombination is responsible of the photoresponse decay [41].

Assuming a direct proportionality between quantum efficiency and absorption coefficient near the absorption edge, from this spectrum the indirect band gap of the film was derived using the formula:

$$(i_{ph}\, h\nu)^{0.5} \propto (h\nu - E_g) \qquad (2)$$

where i_{ph} is the quantum efficiency (in arbitrary units), $h\nu$ is the photon energy and E_g the band gap. We remark that eq.(2) holds for crystalline materials, but it can be applied also to disordered materials for non-direct optical transitions [41]; in the latter case the measured value is rather an optical gap.

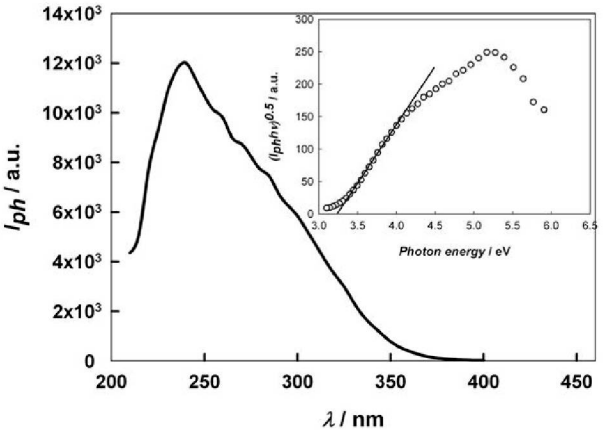

Figure 6. Photocurrent action spectrum of a film grown on the Ti-10 Mo alloy in 0.15 M Na_2SO_4 solution at 50 mV/s up to 8 V(MSE). Electrode potential: 2 V(MSE).

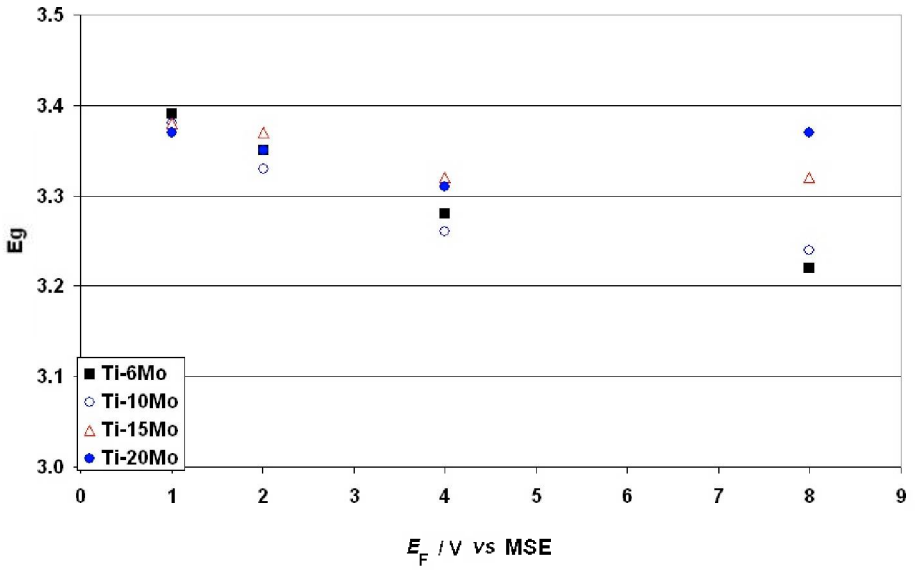

Figure 7. Optical gap vs. E_f for passive films grown on different Ti-Mo alloys in Na_2SO_4 solution.

The elaboration of the spectrum according to eq.(2) is shown in the inset of Fig.6: for this film an indirect gap of (3.24 ± 0.03 eV) was derived from measurements at changing electrode potential in the positive domain. However, an effect of film thickness and metallic alloy composition was observed on the band gap (see Fig.7): in particular, under anodic polarization very thin films (E_f = 1 V/MSE) display gap values close to 3.4 eV, independent of starting alloy, whilst for thicker films gaps are slightly lower and shifting downwards with decreasing Mo wt%. The latter effect is more evident with films grown up to 8 V. The E_g values of Fig.7 are compatible with the film compositions derived from XPS experiments: in fact, anodic oxide films on pure Ti present band gap values of 3.0 eV (rutile phase), 3.2 eV (anatase) or 3.35 – 3.4 eV (amorphous TiO_2) [41-48]. Similar gaps are reported also for MoO_3

thin films [41, 49-51], but the scarce quantity of these groups detected by XPS (see previous paragraphs) suggests these groups act more as dopant of titanium oxide, that constitutes the passive film band structure. Taking into account that anodic films on pure Ti metal present a disordered structure when they are very thin, and tend to crystallize at higher thicknesses [48], we can postulate that a higher content of Mo species into the passive film increases the tendency to retain an amorphous structure, thus delaying the amorphous-to-crystalline transition with respect to pure titania films [21, 52].

Another difference in the photoelectrochemical behaviour stems from the photocurrent values; in Fig.8 we have plotted the maximum photocurrent, derived from the spectra, for films grown on the alloys at corresponding thickness and polarization. It is evident that maximum photocurrent intensity is sensibly higher for the lowest Mo content in the alloy; this could be interpreted in term of a decrease of the semiconducting properties of the films having higher concentration of MoO_3 groups with respect to pure titania. This hypothesis agrees with the more disordered structure of these films and it is also confirmed by the photocurrent vs. electrode potential curves (photocharacteristics), recorded in neutral solutions for the various films at constant thickness under monochromatic irradiation with different wavelengths; such curves present dissimilar features depending on metallic alloy composition, as shown in Figs.9 a,b for passive films grown up to 8 V on different alloys. For the film grown on the alloy with a low Mo content (Fig.9a) the photocurrent decreases monotonously on going in negative direction, revealing a n-type semiconducting behavior; for the alloy with higher Mo content (Fig.9b) a minimum occurs in photocurrent intensity, followed by an increase of photocurrent at more negative potentials. This last shape suggests strongly the occurrence of a photocurrent sign inversion (from anodic to cathodic) in the negative potential region, typical of insulating films. Moreover, a stronger hysteresis is observed between forward and reverse scan in this latter case.

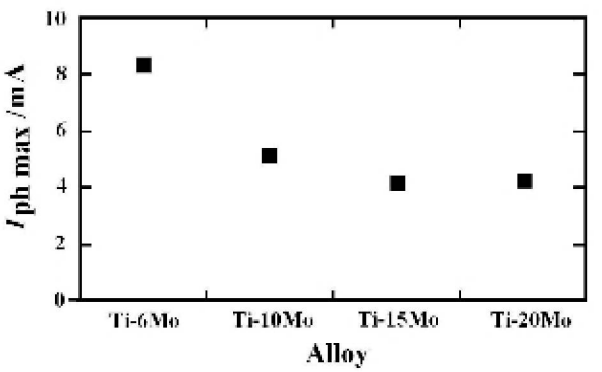

Figure 8. Maximum photocurrent values measured at 2 (MSE) for films grown in 0.15 mol L^{-1} Na_2SO_4 solution at 50 mV/s up to E_f=8 V (MSE) on different alloys.

The photocurrent sign inversion was confirmed by the current-time transients recorded by chopping manually light on and off at different potentials and irradiating light wavelengths [22], and it was observed in neutral electrolytes with anodic oxides not very thin ($E_f \geq 4$ V/MSE) grown on alloys having higher Mo content, whilst passive films grown on the Ti-6 Mo alloy never display cathodic photocurrent. Also very thin films ($E_f \leq 2$ V/MSE) do not

show photocurrent sign inversion. Where inversion occurred, cathodic photocurrent spectra were recorded under negative polarizations, and their elaboration gave optical thresholds very close to those derived from the anodic spectra (see Table 5). This suggests that cathodic photocurrent can hardly be ascribed to photoemission phenomena, but it likely originates from band-to-band excitation in an insulating material with reversed electric field.

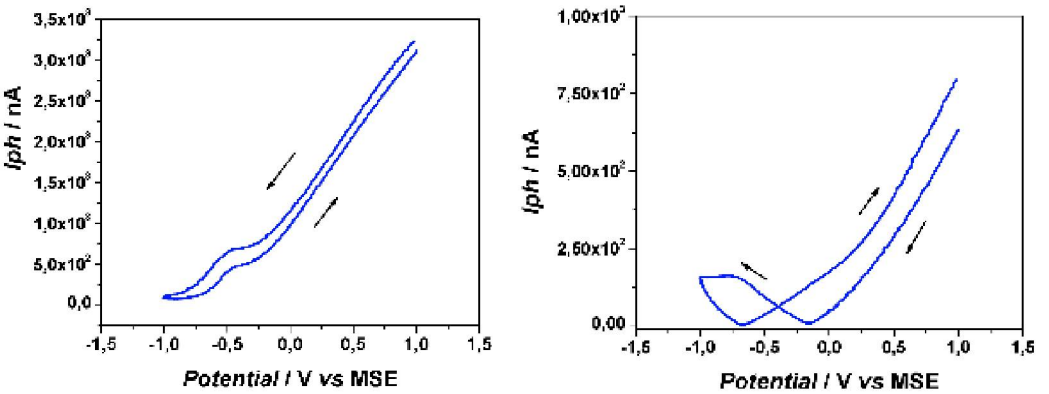

Figure 9. Photocurrent vs. potential curves at λ=290 nm for films grown in 0.15 mol L^{-1} Na_2SO_4 solution at 50 mV/s up to E_f=8 V(MSE) on the Ti-6Mo alloy (a) and on the Ti-15 Mo alloy (b). Sweep rate: 10 mV/s.

Table 5. Optical absorption thresholds derived from cathodic photocurrent spectra of films grown in neutral sulfate solution on different Ti-Mo alloys. Measuring electrode potential: -0.5 or -0.75 V(MSE).

Alloy	Formation potential [V/MSE]	Absorption Threshold [eV]
Ti-10Mo	8	3.33
Ti-15Mo	8	3.37
Ti-15Mo	4	3.37
Ti-20Mo	8	3.50

In conclusion, photoelectrochemical experiments evidence a n-type semiconducting behavior for thin ($E_f \leq 2$ V/MSE) anodic films grown on all the investigated alloys, as well as for thicker films grown on alloys with low Mo content; on the contrary, films grown on alloys with Mo content ≥ 10 wt% change to an insulating behavior with increasing thickness. This finding has been further confirmed by the impedance experiments reported in the next paragraph.

5c. Impedance Measurements

The solid-state properties of films grown anodically on the different Ti-Mo alloys up to various thicknesses were also investigated by EIS (Electrochemical Impedance Spectroscopy) and film capacitance measurements.

In the former case, films were grown in 0.15 M Na_2SO_4 up to 8 V (MSE) on the different alloys, and their impedance dispersion was measured after 30 min of polarization at the formation potential, using a Frequency Response Analyzer (FRA, Solartron, mod.1260) in the range 0.01 Hz – 100 kHz. Fig.10 displays the Nyquist plots for the different films, having almost equal thicknesses; it appears evident that film becomes more resistive as the Mo content in the starting alloy increases. This result is confirmed by the fitting of the dispersion, performed assuming a simple R(RQ) circuit, consisting of a (solution) resistance in series with the film impedance, having the bulk resistance and a constant phase element (Q), which takes into account the non-ideal capacitive behavior of the film. This fitting was validated by low standard deviations of parameters (never higher than 2%) and by an equal solution resistance value across all experiments (110 Ω cm^{-2}, with standard deviations less than 1%), and it gave always values close to 1 for the exponent α of the CPE element (almost ideal capacitor behavior). Fitting parameters are reported in Table 6.

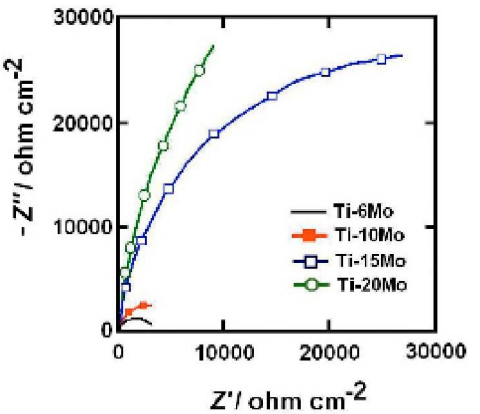

Figure 10. Nyquist plots recorded at 8 V(MSE) for films grown in 0.15 mol L^{-1} Na_2SO_4 solution at 50 mV/s up to E_f=8 V(MSE) on different Ti-Mo alloys. Impedance dispersions were measured after 30 min polarization at E_f.

Table 6. Values of the circuital parameters derived from the fitting of the impedance dispersion, measured after 30 minutes stabilization at E_f, for passive films grown on different Ti-Mo alloys in Na_2SO_4 solution up to 8 V(MSE).

Solution	R_s Ω cm^2	|Q| S s^{α} cm^{-2}	α	R_p Ω cm^2
Ti-6Mo	110.4	$2.1\ 10^{-6}$	0.907	$3.3\ 10^{3}$
Ti-10Mo	110	$1.3\ 10^{-6}$	0.945	$5.3\ 10^{3}$
Ti-15Mo	110.6	$9.9\ 10^{-7}$	0.973	$5.4\ 10^{4}$
Ti-20Mo	108	$1.2\ 10^{-6}$	0.965	$1.1\ 10^{5}$

The almost ideal capacitor behavior (impedance phase angle not far from -90°, in a large frequency interval), pushed us to verify the semiconducting or insulating character of the films recording directly the film capacitance vs. applied potential using the lock-in technique. At this aim, films were grown up to various formation potentials (E_f), and stabilized for 30

min at E_f. Afterwards, potential was scanned slowly (10 mV/s) in the negative direction while interface capacitance at constant thickness was recorded by the lock-in, superimposing a small (5 mV peak-to-peak) ac perturbation. Results are summarized in Figs.11-12. The first figure (Fig.11) evidences the effect of thickness on the properties of anodic films grown on the same alloy having a high Mo content (Ti-15 Mo); for low E_f values curves, recorded at f=10 Hz, display a capacitance variation with the electrode potential typical of a n-type semiconductor, whilst with increasing E_f (i.e., film thickness) curves flatten and capacity becomes independent of potential, revealing an insulating character of the films. This confirms the conclusion of the photoelectrochemical investigation, that films grown on alloys with high Mo content behave as n-type SCs or as insulators at low and higher thicknesses, respectively. Moreover, the systematic frequency dispersion of the measured capacitance (not shown here) points out to an amorphous structure of the films. This change in the behavior does not occur with films grown on alloys having a low Mo content. This is shown in Fig.12, where the capacitance – potential curves are reported for to films grown up to 8 V(MSE) on two different alloys: it is evident that for the Ti-6 Mo alloy, anodic films retain always their semiconducting behavior, even at the highest thickness investigated.

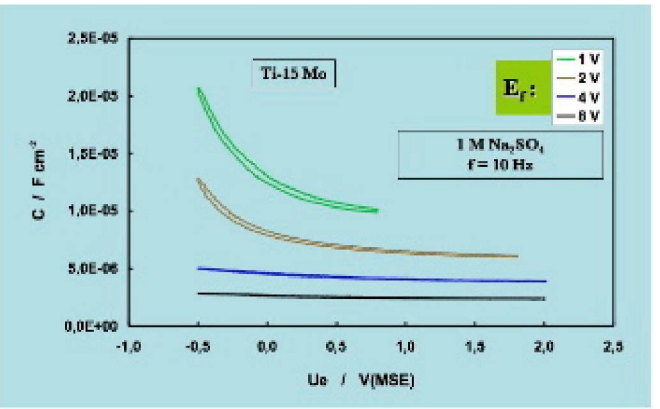

Figure 11. Capacitance vs. potential curves for anodic films grown and stabilized up to different formation potentials on the Ti-15Mo alloy in 1.0 mol L^{-1} Na_2SO_4 solution. Measuring frequency: 10 Hz.

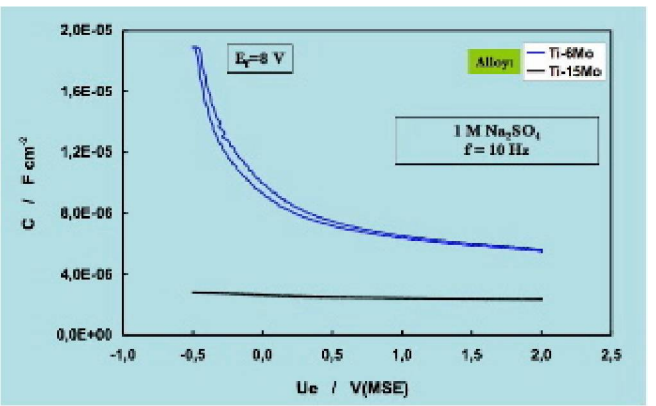

Figure 12. Capacitance vs. potential curves for anodic films grown and stabilized at 8.0 V (MSE) on the Ti-6Mo and the Ti-15Mo alloys in 1.0 mol L^{-1} Na_2SO_4 solution. Measuring frequency: 10 Hz.

6. Conclusions

- Ti-Mo cast alloys, having different Mo content (4 to 20 wt%) were fabricated by arc melting in a furnace under argon atmosphere. For all samples, chemical analyses (XRF and SEM) showed a uniform alloy composition, both in the bulk and on surface, with an even distribution of Mo, as revealed by Mo elemental mapping.
- The crystalline structure of the alloys, investigated by X-ray analysis, was found sensitive to Mo concentration, with the presence of α' (hexagonal) and α" (orthorhombic) phases for low Mo contents, and increasing presence of β (bcc) phase at higher Mo content.
- Corrosion behavior of the alloys was studied by immersion in acidic, neutral and physiological solutions. Regardless of alloy composition, open circuit potential values indicated a tendency to spontaneous passivation in all environments. However, results suggest easier passive layer formation and/or better corrosion protection characteristics of the surface film formed in neutral chloride-free electrolyte, and possible partial film dissolution in acidic environment.
- These cast Ti-Mo alloys displayed an excellent resistance to pitting attack: in fact voltammograms recorded in the Ringer solution reveal no traces of pitting occurrence up to 8 V(MSE). From this point of view, these alloys display a better behavior than other Ti alloys, previously investigated.
- The good corrosion resistance of the Ti-Mo alloys is related to the strong oxygen affinity of the metallic material. In fact the alloys display a valve-metal behavior both in neutral and acidic aqueous electrolytes, owing to the formation of barrier-type surface oxide films according to the high-field law. Analogous to other anodic oxides on metals and alloys, film growth occurs by inward migration of O^{2-} species and simultaneous outward movement of both metallic cations (Ti^{4+} and Mo^{6+}). However, passive films growth kinetics is influenced by the anodizing solution (mainly through the formation efficiency) and Mo content in the starting alloy. This second parameter affects the value of anodizing electric field, likely because the presence of Mo(VI) groups generates mobile defects and lowers the energy barrier for ions transport into the bulk of the films.
- Anodic films composition was investigated by ex-situ XPS experiments. As expected, they revealed the presence of both Ti and Mo oxides in all cases, confirming the hypothesized growth mechanism. However, Mo content in the external part of the films, estimated from the peaks area, is always much lower than that in the metallic material, and decreasing with increasing film thickness. This leads to surface compositions very enriched in Ti for thick films, whose upper layer can be described as TiO_2 doped with increasing amounts of MoO_3 for increasing Mo content in the alloy (0.37 to 0.64 at%), and indicates a much slower transport of Mo^{6+} species across the oxide.
- Thus, surface films on these alloys consist of a mixed TiO_2 - MoO_3 phase, having a large excess of titanium and a strong tendency to present a disordered structure. The presence of Mo delays the amorphous-to-crystalline transition, occurring in pure anodic titanium films. However, composition of the anodic films seems not uniform

along thickness, due to different migration rates of Ti^{4+} and Mo^{6+} species; analogous finding is reported for Ti-Zr alloys [33].

- Regardless of the alloy composition, formation potential and electrolyte, all passive films show anodic photocurrent. From the anodic photocurrent spectra, optical gaps ranging between 3.2 and 3.4 eV were derived. For thick films, gap values are slightly influenced by the starting alloy composition. The measured gaps are compatible with the film structure revealed by XPS, taking into account the values reported for both amorphous and crystalline TiO_2.
- A more interesting result concerns the semiconducting or insulating behavior of the oxides grown in neutral electrolytes. Films on alloys with low Mo content display always SC behavior, independent of thickness, as revealed by the photocurrent – potential curves, analogous to those relative to pure anodic TiO_2 films. On the contrary, for higher Mo wt% in the alloy films change from a semiconducting to an insulating behavior with increasing thickness. This finding is disclosed by the photocurrent – potential curves, current transients under manually chopped illumination, and cathodic photocurrent spectra, but also confirmed by impedance measurements. These last indicate that increasing Mo content in the alloy, films having corresponding thickness become more resistive. Moreover, their capacitance – potential curves flatten, whereas the same curves relative to thinner films, or to films grown on alloys with low Mo content, display the typical shape of n-type semiconducting materials.
- The fact that increasing Mo content into the films their behavior switch from semiconducting to insulating, suggests that MoO_3 groups into the mixed oxide tend to compensate oxygen deficiency, which is responsible for the n-SC behavior of TiO_2. Hence, the Fermi level, which is located 0.2-0.4 eV below the conduction band edge in pure titania films [48, 53, 54], shifts downwards in the forbidden (mobility) gap with increasing the concentration of MoO_3 groups within the oxide film; XPS data reported in Table 4 advise that electrical compensation of defects should occur for MoO_3 concentration exceeding 0.5 at%. However, more data on depth profile compositions of films having different thicknesses are necessary before reaching a less qualitative correlation between Mo content in the alloy, MoO_3 concentration into the passive film, and their semiconducting or insulating behavior.

Acknowledgements

This work is supported financially by Università di Palermo (ex 60% funds). Authors are grateful to FAPESP (Brazil) for providing a post-doc fellowship to N.T.C. Oliveira for his stay at the University of Palermo.

References

[1] Branemark, P.I.; Hansson B.; Adell R.; Breune U.; Lindstron J.; Halen O.; Ohman, A. *Osseointegrated implants in the treatment of the edentulous law*, Almqvist Swikssell, Stockolm, 1997.

[2] Cai, Z.; Shafer, T.; Watanabe, I.; Nunn, M.E.; Okabe, T. *Biomaterials* 2003, 24, 213-218.
[3] Oliveira, N.T.C.; Guastaldi, A.C. *Corros Sci* 2008, 50, 938-945.
[4] Ho, W.F.; Ju, C.P.; Chern Lin, J.H. *Biomaterials* 1999, 20, 2115-2122.
[5] Oliveira, N.T.C.; Aleixo, G.; Caram, R.; Guastaldi, A.C. *Mater Sci Eng A* 2007, 452-453, 727-731.
[6] Geetha, M.; Kamachi Mudali, U.; Gogia, A.K.; Asokamani, R.; Baldev, R. *Corros Sci* 2004, 46, 877-92.
[7] Oliveira, N.T.C.; Guastaldi, A.C. *Acta Biomater* 2009, 5, 399-405.
[8] Okazaki, Y.; Gotoh, E.; Manabe, T.; Kobayashi, K. *Biomaterials* 2004, 25, 5913-5920.
[9] Okazaki, Y.; Gotoh, E. *Biomaterials* 2005, 26, 11-21.
[10] Zhou, Y.L.; Niinomi, M.; Akahori, T.; Fukui, H.; Toda, H. *Mater Sci Eng A* 2005, 398, 28-36.
[11] Kobayashi, E.; Matsumoto, S.; Yoneyama, T.; Hamanaka, H. *J Biomed Mater Res* 1995, 29, 943–950.
[12] Niinomi, M.; Kuroda, D.; Fukunaga, K.; Morinaga, M.; Kato, Y.; Yashiro, T.; Suzuki, A. *Mater Sci Eng A* 1999, 263, 193–199.
[13] Sugano, M.; Tsuchida, Y.; Satake, T.; Ikeda, M. *Mater Sci Eng A* 1998, 243, 163-168.
[14] Guo, H.; Enomoto, M. *Scripta Mater* 2006, 54, 1409-1413.
[15] Sukedai, E.; Yoshimitsu, D.; Matsumoto, H.; Hashimoto, H.; Kiritani, X. *Mater Sci Eng A* 2003, 350, 133-138.
[16] Liu, Y.; Wei, W.F.; Zhou, K.C.; Chenl, F.; Tang, H.P. *J Central South Univ Technol* 2003, 2, 81-86.
[17] Zhang, L.C.; Zhou, T.; Aindow, M.; Alpay, S.P.; Blackbur, M.J.; Wu, M.H. *J Mater Sci* 2005, 40, 2833–2836.
[18] Zhang, L.C.; Zhou, T.; Alpay, S.P.; Aindow, M.; Wu, M.H. *Appl Phys Lett* 2005, 87, 241909.1–241909.3.
[19] Sakaguchi, S.; Nakahara, K.; Hayashi, Y. *Met Mater Int* 1999, 2, 193–195.
[20] Popa, M.V.; Vasilescu, E.; Drob, P.; Vasilescu, C. *Rev Chim* 2005, 56, 908 –912.
[21] Habazaki, H.; Uozumi, M.; Konno, H.; Nagata, S.; Shimizu, K. *Surf Coat Technol* 2003, 169-170, 151-154.
[22] Oliveira, N.T.C.; Guastaldi, A.C.; Piazza, S.; Sunseri, C. *Electrochim Acta* 2009, 54, 1395-1402.
[23] Davis, R.; Flower, H.M.; West, D.R.F. *J Mater Sci* 1979, 14, 712-722.
[24] Bania, P.J. in: *Titanium Alloys in the 1990's*; Eylon, D.; Boyer, R.; Koss, D. (Eds.), Beta TMS, Warrendale, PA, 1993.
[25] Oliveira, N.T.C.; Ferreira, E.A.; Duarte, L.T.; Biaggio, S.R.; Rocha-Filho, R.C.; Bocchi, N. *Electrochim Acta* 2006, 51, 2068-2075.
[26] Oliveira, N.T.C.; Biaggio, S.R.; Rocha-Filho, R.C.; Bocchi, N. *J Biomed Mat Res A* 2005, 74A, 397-407.
[27] González, J.E.G.; Mirza-Rosca, J.C. *J Electroanal Chem* 1999, 471, 109-115.
[28] Schmidt, H.; Konetschny, C.; Fink, U. *Mat Sci Tech* 1998, 14, 592-598.
[29] Yu, S.Y.; Scully, J.R. *Corrosion* 1997, 53, 965-976.
[30] Young, L. *Anodic Oxide Films*, Academic Press, London, 1961.
[31] Blackwood, D.J.; Greef, R.; Peter, L.M. *Electrochim Acta* 1989, 34, 875-879.

[32] Oliveira, N.T.C.; Biaggio, S.R.; Piazza, S.; Sunseri, C.; Di Quarto, F. *Electrochim Acta* 2004, 49, 4563-4576.
[33] Oliveira, N.T.C.; Biaggio, S.R.; Nascente, P.A.P.; Piazza, S.; Sunseri, C.; Di Quarto, F. *Electrochim Acta* 2006, 51, 3506-3515.
[34] Habazaki, H.; Skeldon, P.; Thompson, G.E.; Wood, G.C. *Philos Mag B* 1995, 71, 81-90; idem *Philos Mag B* 1996, 73, 297-308.
[35] Milosev, I.; Metikos-Hukovic, M.; Strehblow, H.-H. *Biomaterials* 2000, 21, 2103-2113.
[36] Babelon, P.; Dequiedt, A.S.; Mostéfa-Sba, H.; Bourgeois, S.; Sibillot, P.; Sacilotti, M. *Thin Solid Films* 1998, 322, 63-67.
[37] Marino, C.E.B.; Nascente, P.A.P.; Biaggio, S.R.; Rocha-Filho, R.C.; Bocchi, N. *Thin Solid Films* 2004, 468, 109-112.
[38] Olsson, C.O.A.; Mathieu, H.J.; Landolt, D. *Surf Interface Anal* 2002, 34, 130–134.
[39] Park, P.Y.; Akiyama, E.; Habazaki, H.; Kawashima, A.; Asami, K.; Hashimoto, K. *Corrosion Sci* 1996, 38, 1649-1667.
[40] Habazaki, H.; Uozumi, M.; Konno, H.; Shimizu, K.; Nagata, S.; Asami, K.; Matsumoto, K.; Takayama, K.; Oda, Y.; Skeldon, P.; Thompson, *G.E. Electrochim Acta* 2003, 48, 3257-3266.
[41] Di Quarto, F.; Piazza, S.; Santamaria, M.; Sunseri, C. in: *Handbook of Thin Film Materials*, Nalwa, H.S. (Ed.), Vol. **2**, chap. 8, p.373, Academic Press, 2002.
[42] Laser, D.; Yaniv, M.; Gottesfeld, S. *J Electrochem Soc* 1978, 125, 358-365.
[43] Koffyberg, P.; Dwight, K.; Wold, A. *Solid State Commun* 1979, 30, 433-437.
[44] Leitner, K.; Schultze, J.W.; Stimming, U. *J Electrochem Soc* 1986, 133, 1561-1568.
[45] Peraldo Bicelli, L.; Pedeferri, P.; Razzini, G. *Int J Hydrogen Energy* 1986, 11, 647-651.
[46] Kozlowski, M.R.; Tyler, P.S.; Smyrl, W.H.; Atanasoski, R.T. *Surf Sci* 1988, 194, 505-530.
[47] Di Quarto, F.; Piazza, S.; Sunseri, C. *Electrochim Acta* 1993, 38, 29-35.
[48] Piazza, S.; Calà, L.; Sunseri, C.; Di Quarto, F. *Ber Bunsenges Phys Chem* 1997, 101, 932-942.
[49] Deb, S.R. *Proc Royal Soc Ser A* 1968, 304, 211-220.
[50] Granqvist, C.G. *Handbook of Inorganic Electrochromic Materials*, Elsevier, Amsterdam,1995.
[51] Bojinov, M.; Betova, I.; Raicheff, R. *J Electroanal Chem* 1996, 411, 37-42.
[52] Habazaki, H.; Uozumi, M.; Konno, H.; Shimizu, K.; Nagata, S.; Asami, K.; Skeldon, P.; Thompson, G.E. *Electrochim Acta* 2002, 47, 3837-3845.
[53] Schultze, J.W.; Stimming, U.; Weise, J. *Ber Bunsenges Phys Chem* 1982, 86, 276-282.
[54] Piazza, S.; Sunseri, C.; Di Quarto, F. *AIChe J* 1992, 38, 219-226.

In: Titanium Alloys: Preparation, Properties and Applications ISBN: 978-1-60876-151-7
Editor: Pedro N. Sanchez, pp. 385-403

Chapter 9

MICROSTRUCTURAL EVOLUTION DURING FRICTION STIR WELDING OF TI-6AL-4V ALLOY

S. Mironov, Y. Zhang, Y.S. Sato and H. Kokawa
Department of Materials Processing, Graduate School of Engineering, Tohoku University, 6-6-02 Aramaki-aza-Aoba, Sendai 980-8579, Japan

Abstract

The successful application of the Ti-6Al-4V alloy relies heavily on the availability of welding process producing superior quality joints. Fusion welding technologies, which are conventionally used to join titanium alloys, generally enable to produce high-quality welds with a relatively high productivity. However, the fusion welding is usually associated with solidification problems which may significantly deteriorate service properties of the titanium weldments.

In this regard, friction stir welding, being an innovative "solid-state" joining technology, may potentially be attractive for Ti-6Al-4V. Basically, FSW involves plunging a specially designed tool rotating at high speeds into abutted edges of sheet workpieces to be welded and then translating the tool along the weld seam. The rotating tool produces frictional heat which softens the material so it can be readily extruded around the tool to fill the cavity to the rear of the tool and to form a joint in a solid state. As a solid-state process, FSW avoids (or limits) solidification problems and thus provides defect-free welds having excellent mechanical properties.

In order to improve the basic physical understanding of FSW of Ti-6Al-4V, the present contribution is focused on microstructural evolution during the welding process. The microstructural development is found to be a complex process involving α-to-β phase transformation during heating stage, deformation in the high-temperature β-phase field during stirring stage and β-to-α phase transformation upon cooling stage of FSW. The α-to-β phase transformation is shown to be governed by epitaxial growth of the pre-existing β phase consuming the α phase. Reconstruction of the β-grain structure and orientation measurements in the retained β phase have demonstrated that microstructural evolution in the high-temperature β phase field is a complex process involving grain growth, geometrical effects of strain, transverse grain subdivision and discontinuous recrystallization stimulated by local grain boundary migration; material flow may be described in the term of simple shear deformation arising from {110}<111> slip. The β-to-α phase transformation after FSW is established to be governed by Burgers orientation relationship which dictated the final weld crystallography.

Keywords: Friction stir welding; Ti-6Al-4V alloy; Phase transformation

1. Introduction

The two-phase α-β titanium alloy Ti-6Al-4V is featured by a very promising balance of properties including low density, superior specific strength, high stiffness, excellent fracture toughness and good corrosion resistance. As a result, this material is commonly considered to be a "workhorse" titanium alloy in various industrial, domestic, and medical applications, such as turbine engine parts, chemical reactors, bicycle frames, orthopedic implants, etc.

The successful application of the Ti-6Al-4V relies heavily on the availability of welding process producing superior quality joints. Fusion welding technologies, which are conventionally used to join the titanium alloys, include gas tungsten arc welding, plasma arc welding, and electron beam welding. These techniques generally enable to produce high-quality welds with a relatively high productivity. However, the fusion welding is usually complicated by the problems associated with high reactivity of the titanium alloys (especially in a liquid phase), inert gas bubble porosity, residual stress, significant coarsening of the microstructure in a fusion zone as well as with the formation of martensite structure at the weld center. The undesirable solidification structure may significantly deteriorate some service properties of the weldments, especially ductility and fatigue performance.

Friction stir welding (FSW), an innovative "solid-state" joining technology [1], might be potentially attractive for Ti-6Al-4V. The basic concept of FSW is very simple, as shown in Figure 1 [2]. A specially designed tool rotating with a high rotational speed is plunged into workpieces to be joined and then is traversed along the weld seam. The rotating tool produces frictional heat which softens the material so that it is readily extruded around the tool. The simultaneous rotational and translation motion of the tool forces the material to flow around the tool filling a cavity at the rear of the tool and thus creating a solid-state joint. As a solid-state process, FSW avoids (or limits) solidification problems associated with conventional fusion welding and thus provides defect-free welds having good properties even in materials that are not generally considered for welding applications.

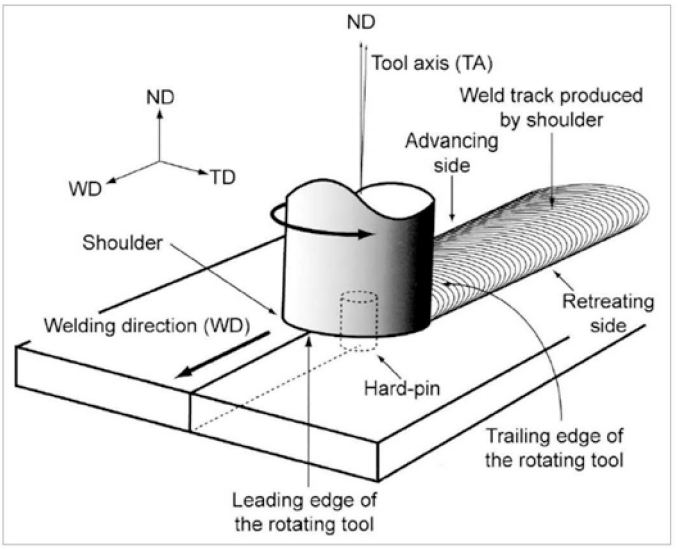

Figure 1. Schematic illustration of FSW process (after Park et al [2])

Given potential advantages of FSW, several research efforts have been made recently to evaluate effect of FSW on structure and properties of the Ti-6Al-4V [3-9]. The first studies in this field have shown that FSW can produce defect-free welds in the Ti-6Al-4V [3, 5, 9]. The obtained joints typically demonstrate very high joint efficiency with respect to both yield and tensile strength (85-100%) and only minor loss of ductility has been found [3, 9]; limited experimental data evidences excellent fatigue properties of friction-stir-processed material [8]. These encouraging results necessitated the development of a more fundamental understanding of the FSW process with the aim to precisely control weld properties through the structure-properties relationship.

The research studies carried out over recent years have shown that the microstructure evolution during FSW of Ti-6Al-4V presumably goes through the following sequence of events. As the welding tool approaches the point of interest near a weld line, temperature begins to rise [3]. Fraction of β-phase starts to increase at the expense of α-phase [3-5, 8, 9] and the process intensifies rapidly near the tool [3]. At the periphery of the deformation zone around the tool, deformation begins to concurrent with the phase transformation [3-5, 7]. Survived α-phase tends to globularize forming equiaxed primary α [3-5, 7, 9]. Near the tool, temperature would exceed the β-transus temperature and α-phase completely transforms into β-phase [3-5, 9]. β-grains observed within the stir zone (SZ) are sheared in a direction of material flow thus reflecting deformation of the β-phase [3]. However, deformation mechanisms operating in the β phase field are almost completely unknown. Mean size of the β-grains formed in the stir zone (SZ) is typically relatively small (10-30 μm) [3-5, 9], despite of well-known very rapid grain growth in a β-phase field. This indicates a possible microstructure refinement of the β-phase during FSW but actual mechanism of this process is unclear.

Upon cooling down to ambient temperature after FSW, microstructural development is largely dictated by the β-to-α phase transformation [3-5, 9]. Measured cooling rate is too low for martensite transformation, and thus the phase transformation occurs via diffusion mechanism [3]. Within the framework of this process, grain boundary α first nucleates at prior-β grain boundaries and then acicular α grows from the α-layer into interior of the prior-β grains [3-5, 9]. The β-to-α phase transformation in Ti-6Al-4V is known to follow a well-established the Burgers orientation relationship, viz.: $\{110\}_\beta // \{0001\}_\alpha$, $<111>_\beta // <11\bar{2}0>_\alpha$. However, experimental evidences of the Burgers orientation relationship in the friction-stirred materials are fairly limited to a few examples [4] and it is difficult to know whether they are isolated cases, or representative results.

The above-mentioned research efforts have provided a contribution insight into microstructural development during FSW of Ti-6Al-4V resulting in a general framework of the structural response. However, relatively little attention has been paid to the *actual* mechanisms governing this process and, thereby, many important aspects of the physical phenomena involved remain unclear. Obviously, more research efforts should be directed to this field.

The current work is focused on more fundamental issues of the microstructural development. For this purpose, electron back-scatter diffraction (EBSD) technique in conjunction with field emission gun scanning electron microscopy (FE-SEM) has been

employed in an attempt to provide a comprehensive overview of microstructural evolution during FSW of Ti-6Al-4V.

2. Experimental

The material used in present investigation was a commercial Ti-6Al-4V alloy having a chemical composition (wt. %) of Al 6.09, V 4.02, C 0.011, Fe 0.14, N 0.008, H 0.0023 and balance Ti. The material was received as 3-mm thick sheets 250 mm long and 60 mm wide.

The received sheets were butt-welded along longitudinal direction on an FSW machine fitted with an automated control system. Welding tool was fabricated from a Mo-based alloy, and consisted of a convex shoulder having a diameter of 15 mm and a pin, tapered from 5.1 mm at the shoulder to 3 mm at the pin tip. FSW was performed at a tool rotation speed of 500 rpm and a travel speed of 60 mm/min. The FSW machine operated under depth control with the plunge depth maintained at ~ 2 mm. To minimize surface oxidation, argon shielding was employed around the tool during FSW. In this paper, the reference directions in FSW geometry are denoted by the conventional FSW terminology, i.e. WD, welding direction; ND, normal direction; TD, transversal direction.

Following FSW, the obtained welds were cross-sectioned perpendicular to the WD for the microstructure examinations. For optical microscopy (OM) and scanning electron microscopy (SEM) observations, the samples were ground with water abrasive paper, mechanically polished with a final polishing step comprising of colloidal silica, and then etched in Kroll's reagent (2 vol% HF, 4 vol% HNO_3 and 94 vol% H_2O). A suitable surface finish for EBSD was obtained by applying a mechanical polishing in a similar fashion followed by electro-polishing in a 30-ml acetic acid + 50-ml perchloric acid solution at ambient temperature with an applied potential of 25 V.

All microstructural observations were made on the transversal (i.e. ND-TD) plane. The OM studies were carried out using Nikon Optiphot-100 optical microscope. SEM observations and high resolution EBSD analysis were performed with a Hitachi S-4300SE field emission gun SEM FE-SEM equipped with TSL OIM^{TM} EBSD system. Orientation mapping involving automatic beam scanning was performed using a triangular scanning grid. On each pattern, nine Kikuchi bands were used for indexing, minimizing the possibility of misindexing error. EBSD maps of ~50,000-500,000 pixels with step (pixel) sizes of 0.05–1 μm were obtained. Pattern solving efficiency was in the range of 99-100% and average confidential index (CI) for each EBSD map ranged from 0.15 to 0.52. By comparison, experiments on face-centered cubic (FCC) materials have shown that the fraction of correctly indexed patterns with CI's greater than 0.1 is 95% [10]. In order to ensure the reliability of the EBSD data, all small grains including less than 5 pixels were cleaned using the function of grain dilation provided in the TSL software. In order to eliminate spurious boundaries caused by orientation noise, a lower limit boundary misorientation cut-off of 2° was used. All misorientation angles quoted are relative to the rotation axis with the minimum misorientation and a 15° criterion was used to define low-angle boundaries (LABs) versus high-angle boundaries (HABs). All OM, SEM and EBSD micrographs were taken in the ND-TD plane and are presented such that the TD is horizontal, and the ND is vertical.

3. Results and Discussion

3.1. Base Material

Characteristic microstructural features of the as-received (base) material are summarized in Fig. 2. Typical SEM image of the microstructure is shown in Fig. 2a; in this and other SEM micrographs, hexagonal close-packed (HCP) α is the darker phase and body-centered cubic (BCC) β-phase is the lighter constituent. The base material (BM) exhibits an elongated α phase separated by thin β streaks (~ 0.1 μm thick); prior-β grains and colony α structure are not well defined. Volume fraction of the β phase measured by point count method is 8.6%.

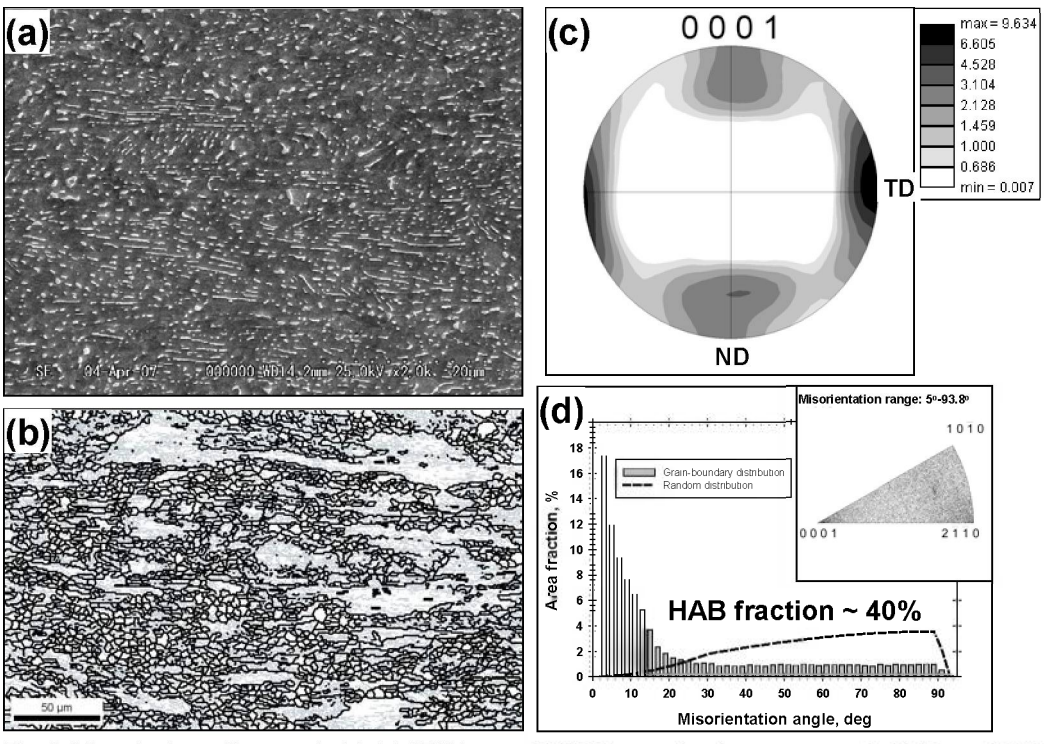

Figure 2. Microstructure of base material: (a) SEM image, (b) EBSD map showing arrangement of LABs and HABs (grey and black lines, respectively), (c) (0002) pole figure, (d) misorientation distribution (misorientation-axis distribution is shown in the top right corner). See text for details.

EBSD map, showing arrangement of low- and high-angle boundaries (grey and black lines, respectively) in the α phase, is presented in Fig. 2b. The EBSD map demonstrates that the α phase has a partially recrystallized (globularized) microstructure. The microstructure consists of the very coarse elongated grains containing dense sub-structure blended with the bands of much finer equiaxial grains. The α phase has a two-component texture with <0001> direction tending to align either with the ND (weaker component) or with the TD (stronger component), as shown in Fig. 2c. Misorientation-angle distribution in the α phase is dominated by LABs whereas misorientation axes show nearly random distribution (Fig. 2d).

3.2. Low Magnification Overview

A low magnification overview of transverse cross section of the friction stir weld is shown in Fig. 3. Three distinct zones may be seen: base material, stir zone and a narrow (~ 500 μm width) transition region. The SZ exhibits a basin-like shape significantly widening towards the upper surface. The SZ is approximately symmetric about the centerline and shows relatively homogeneous contrast; no welding defects or evident features are seen.

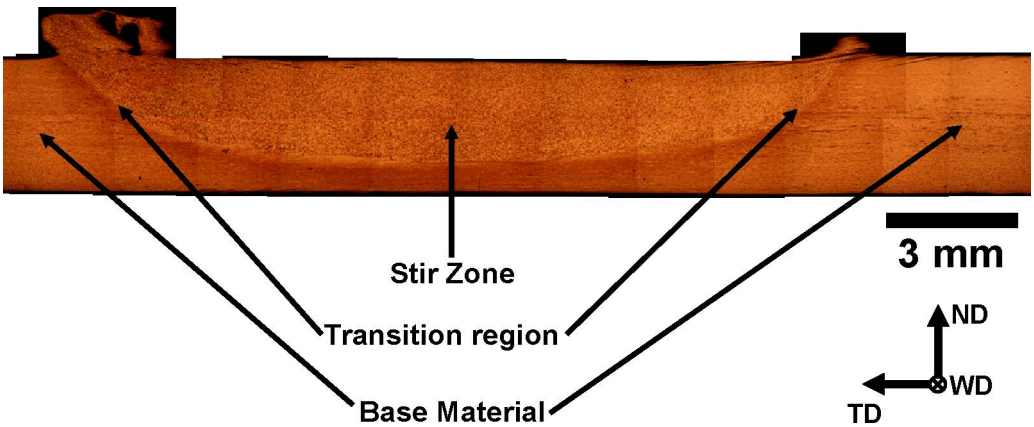

Figure 3. Low magnification overview of transversal cross section of friction stir weld. WD, TD and ND correspond to welding, transversal and normal directions, respectively.See text for details.

3.3. Transition Region

SEM images of the microstructures developed at different distances away from the SZ are shown in Fig. 4. Variation of the volume fraction of the β phase (or β-transformed structure) with the distance towards the SZ is summarized in Table 1. Near outer edge of the transition region (~550 μm from the SZ), the β-phase begins to grow epitaxially from the pre-existing β phase, consuming the α phase (Fig. 4a, Table 1). At the distance of ~ 150 μm from the SZ, a bimodal (or duplex) microstructure develops which consists of primary α phase mixed with transformed β structure; the transformed β structure may be described in terms of very small prior-β grains containing secondary α platelets (Fig. 4b). The β phase volume fraction in this region during FSW might be estimated as high as ~70% (Table 1). Closer to the tool, it increases rapidly achieving ~95% directly near the SZ (Fig. 4c, Table 1). Formation of the bimodal microstructure evidences that the temperature in the transition region did not exceed the β-transus temperature (~1000°C) and the material experienced partial α-to-β phase transformation during heating stage and β-to-α transformation upon cooling. Therefore, microstructural evolution in the transition region appears to be dominated by the phase transformation rather than deformation.

Table 1. Variation of volume fraction of β-phase (or β-transformed structure) across transition region.

	Distance from SZ, μm					
	550	400	150	90	60	Directly adjacent
Fraction of β-phase (or β-transformed structure), vol.%	19	31	71	78	87	95

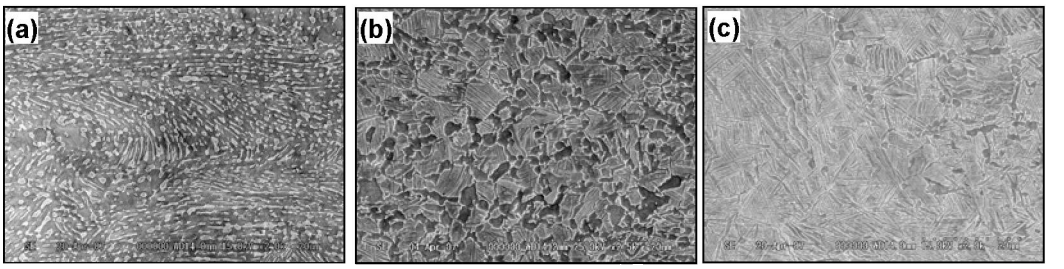

Figure 4. SEM observations of the microstructures developed at the different distances from SZ: 550 μm (a), 150 μm (b), and directly adjacent to SZ (c). See text for details.

3.4. Stir Zone

3.4.1. Transformed β Structure

Typical SEM image of the SZ microstructure is shown in Fig. 5. The microstructure corresponds to a classical transformed β structure consisting of prior-β grains which are delineated by a thin α-layer and contain sandwiched α and β laths. The structure morphology evidences that the peak temperature in the SZ exceeded the β-transus temperature and that the final structure was produced via decomposition of the high-temperature β phase to α phase and a small fraction of retained β phase during cooling following FSW.

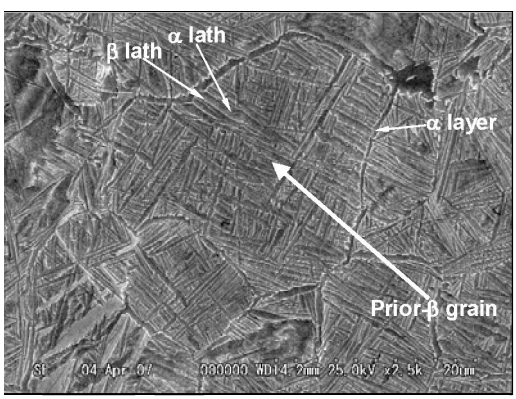

Figure 5. Typical microstructure in SZ. See text for details.

The β-to-α phase transformation in titanium alloys is well known to follow the Burgers orientation relationship (OR) between the phases where close packed planes $\{0001\}\alpha/\{110\}\beta$ and close packed directions $<11\bar{2}0>\alpha/<111>\beta$ are parallel. In order to examine the Burgers OR between the phases in the present study, high-resolution EBSD map was obtained from the central part of the SZ, as shown in Fig. 6a. To evaluate the orientation relationship between the α and β phases, local crystallographic orientations of both phases were compared with each other in many different locations within the map. A typical example of the analyzed region is shown in Fig. 6b; α grains whose orientations were compared with those of the β particle are numbered 1 to 7. The obtained orientation data are summarized in Fig. 6c as $\{110\}$ and $\{111\}$ pole figures for the β phase and as $\{0002\}$ and $\{11\bar{2}0\}$ pole figures for the α phase. For simplicity, crystallographic directions in the α phase which are close to those in the β phase are encircled. It is seen that the $<0001>$ and $<11\bar{2}0>$ directions of the α grains numbered 1 to 6 are nearly parallel to the $<110>$ and $<111>$ directions of the β phase, respectively. This indicates that these α grains and β phase nearly satisfy the Burgers OR. On the other hand, there is no the Burgers OR between the β phase and the α grain # 7 (Fig. 6c). In total, 32 pairs of β particle–α grain were compared in the present study in a manner described above and lack of the Burgers OR was found in 7 cases.

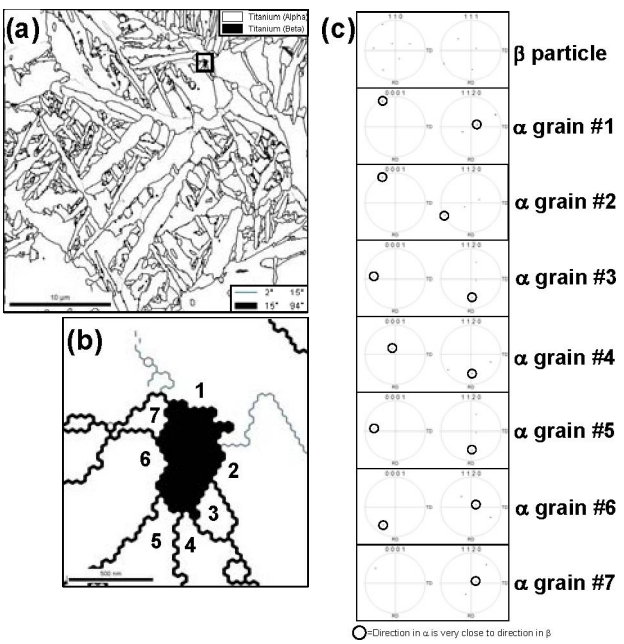

Figure 6. (a) EBSD phase map with selected area shown at higher magnification in (b) and (c) orientation of b particle and a grains numbered 1 to 7 in (b). (after Mironov et al [11]).

It should be stressed however that the β laths are very thin (~0.1 μm) and are usually featured by very diffuse Kikuchi-patterns. As a result, it is difficult to know whether the few examples given in Fig. 6 show representative trend or not. To provide a thorough

investigation, more statistically reliable evidences are required. Grain boundaries between α colonies may be used for this purpose. Due to crystal symmetry of the α and β phases, there are 12 possible α orientations (each satisfying the Burgers OR) that can transform from a single parent β grain (i.e., there are 12 α variants) in transformed β microstructure. Misorientations between the α variants (also known to as α colonies) inherited from the same parent β grain are very specific, as shown in Table 2. Therefore, original nature of these boundaries may serve as an additional indicator for the Burgers OR.

Table 2. Specific misorientations between α variants inherited from the same parent β grain [12-16].

Misorientation (angle - axis pair)	Fraction assuming no variant selection, %	Symbol	Location of misorientation axis on stereographic triangle
$60^\circ < 11\bar{2}0 >$	18.2	●	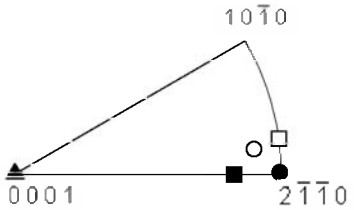
$60.83^\circ < \overline{1.377};\bar{1};2.377;0.359 >$	36.4	○	
$63.26^\circ < \bar{1}0;5;5;\bar{3} >$	18.2	■	
$90^\circ < 1;\overline{2.38};1.38;0 >$	18.2	□	
$10.53^\circ < 0001 >$	9.0	▲	

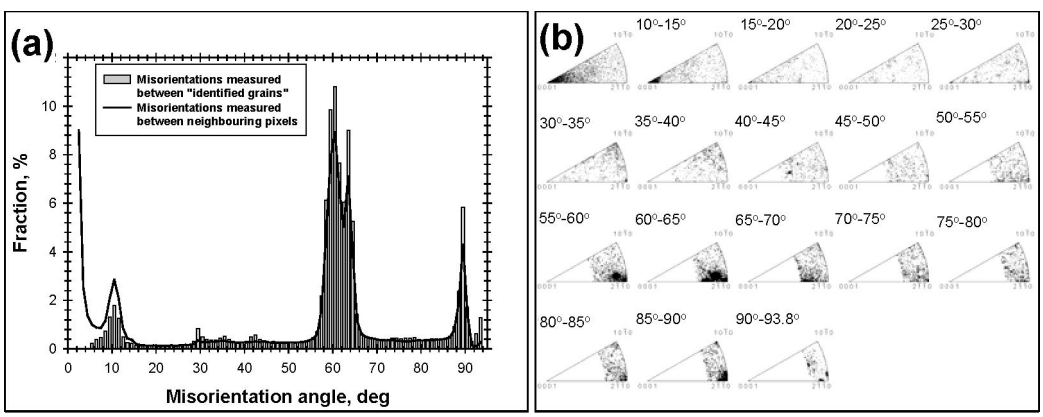

Figure 7. Misorientation data taken from the α phase: (a) misorientation-angle distribution and (b) misorientation axis distribution (after Mironov et al [11]). See text for details.

Misorientation distribution of the α phase derived from a large (~60,000 α laths) EBSD map (not shown) is given in Fig. 7. Two types of misorientation-angle distribution are shown in Fig. 7a. Misorientations measured between neighboring pixels are illustrated by a solid line. In this type of representation, boundary segments are weighted by their respective length and the relative frequencies are proportional to the boundary area fraction. Misorientation

data measured between neighboring α "grains" (which are identified as regions completely surrounded by a boundary with misorientation higher than 5°), are shown as a vertical bar chart. In this material, this type of the misorientation distribution has an advantage that it may convey some information about variant selection occurring during the β-to-α phase transformation. If no variant selection occurs, proportion of the boundaries between the α variants should be close to those shown in Table 2.

Both misorientation-angle distributions have a very complex shape exhibiting three sharp peaks: near 10°, 90° and a split peak in the vicinity of 60°; the distribution for neighboring pixels is additionally featured by a strong low-angle maximum. Misorientation axes (Fig. 7b) are not oriented randomly but form one cluster around the $<0001>$ pole and four clusters near the $<2\bar{1}\bar{1}0>$ pole. The cluster near the $<0001>$ is composed primarily of boundaries with misorientation angles ranging from 5° to 15°, whereas the clusters near the $<2\bar{1}\bar{1}0>$ pole are mainly produced by the boundaries in the angular ranges of 55-65° and 80-90°.

Comparison between the measured misorientations (Fig. 7) and those predicted for the Burgers OR (Table 2) shows very close agreement. The measured fraction of the boundaries between the α-variants (within 5-degree tolerance) achieves ~55-60% of the total grain boundary area in the α phase. Therefore, the misorientation distribution for the α-phase additionally confirms that crystallography of the α and β phases in the SZ is related via the Burgers OR. It is noteworthy that the relative proportion of the boundaries between the α variants is slightly different from those assuming no variant selection (Table 2) and this indirectly indicates a limited variant selection occurring during the β-to-α phase transformation.

It should be noted that there is some angular spread around the misorientation peaks in the real misorientation-angle and misorientation axis distributions (Figs. 7a and b, respectively). Though relatively small, the spread exceeds the angular inaccuracy of the EBSD technique which is usually considered to be ~2°. This phenomenon is already described in the literature and is usually attributed to small deviations from exact Burgers relation during diffusional transformations [e.g. 12].

3.4.2. Microstructural Evolution in High-Temperature β Phase Field

Microstructural observations presented in the previous section provided insight into phase transformation occurring *after* FSW upon cooling down to ambient temperature. However, these results virtually do not convey vital information about microstructural development *during* FSW. This is primarily because material flow in the SZ occurred in the high-temperature β-phase field and, therefore, β-to-α phase transformation taking place during FSW cooling cycle, significantly complicated the final microstructure by the phase transformation products. As a result, dynamic features of the *friction-stirred* β structure cannot be observed directly.

In the following sections we attempt to overcome this problem by adopting of β-grain reconstruction technique as well as by direct crystallographic measurements in the retained β-phase.

3.4.2.1. Reconstruction of β Grain Structure

In the present study, morphology of the β-grain structure existing before β-to-α phase transformation was reconstructed by using an approach developed by Gey and Humbert [13]. This method is simplest among the methods currently employed for the grain reconstruction [e.g. 12, 13] and is based on the idea that the α variants inherited from the same parent β grain are characterized by very specific misorientations linked to the Burgers OR (Table 2). Therefore, grain boundaries between these variants can be readily discriminated from all other boundaries. The remaining boundaries are believed to separate α-variants originating from different parent β-grains, i.e., they represent β grain boundaries. In this way contours of prior-β grains might be identified in the structure. Practically, the experimental misorientations between neighboring pixels in the EBSD maps for the α-phase were automatically compared to the theoretical misorientations given in Table 2. When the experimental misorientation between two pixels was close to one of the theoretical misorientations (within five-degrees tolerance), both pixels were assumed to belong to the same β-grain and the boundary segment between the pixels was automatically "removed" from the reconstructed EBSD map. On the contrary, when the experimental misorientation differs from those listed in Table 2 more than five degrees, the pixels were considered to belong to the different parent β-grains and the boundary segment between the pixels was assumed to be a former β/β grain boundary; in this case the boundary segment remained in the reconstructed EBSD map.

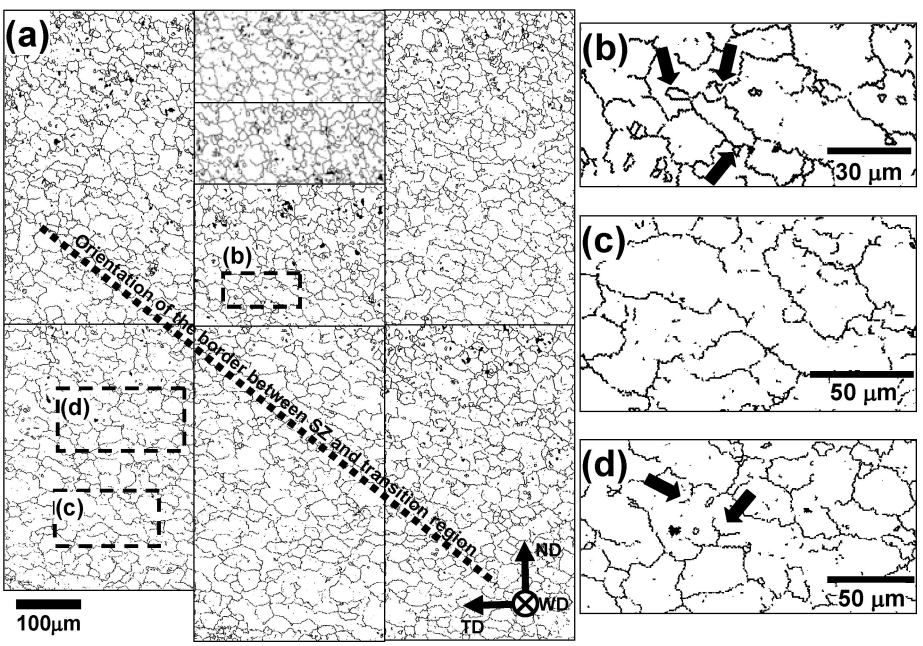

Figure 8. Reconstructed β-grain structure in the SZ (a) with selected areas shown at higher magnification in (b), (c) and (d). Note: black clusters correspond to retained β-phase (after Mironov et al [17]). See text for details.

Additionally, all LABs have been also removed from the reconstructed map because these boundaries are attributable to small deviations from the Burgers orientation relationship during β-to-α phase transformation (as noted above) and thus they may do not exist in the high-temperature β-phase. In this way boundary traces of the prior-β grains were reconstructed in the EBSD maps for the α-phase.

A reconstructed EBSD map showing arrangement of the boundary traces of the prior-β grains in the SZ is given in Fig. 8a; some selected areas are shown at higher magnifications in Figs. 8b-d. Black clusters in the map correspond to the retained β-phase. It is seen that the boundary traces are arranged as an evident grain structure; this supports reliability of the approach used for the β-grain reconstruction.

The dotted line in Fig. 8a illustrates the orientation of the border between the SZ and the transition region. It is seen that the reconstructed β-grains tend to be aligned approximately parallel to this border. Directionality of the transformed β structure in the SZ has also been reported by Lienert [3]. This observation indirectly indicates that the β grains were deformed (sheared) during FSW.

In order to quantify the reconstructed β-grain structure, mean β-grain size was measured by linear intercept method in different locations within the SZ and the obtained results are summarized in Table 3. The mean β grain size ranges ~ from 30 to 40 μm. This is notably larger than the initial size of the β grains nucleated in the transition region (Fig. 4b). In other words, the material in the SZ experienced substantial grain growth. The observed β-grain coarsening is not surprising because the β-grain structure is well known to be prone to a very rapid grain growth in the β-phase field.

Table 3. Mean grain intercept of reconstructed β-grain structure in different locations within SZ.

	Location within SZ		
	Retreated side	**Center**	**Advancing side**
Mean β-grain intercept in TD/ND, μm	37/36	36/31	37/32

The high-magnification images in Figs. 8b-d demonstrate that the boundary traces of the reconstructed β-grains are not straight over a long distance and exhibit some bulges. Of particular interest is the observation that some of the bulges tend to form fine grains (some examples are arrowed in Fig. 8b). It should be noted that these grains are significantly larger than the pixels size (0.5 μm) and, therefore, are unlikely to be a result of misindexing error during EBSD mapping. On the other hand, they also have not been able to be introduced by the β grain reconstruction technique because the approach employed in the preset study only involves removal of grain boundaries between α variants from the EBSD map. Therefore, the fine grains are thought to reflect the real microstructure and the observed phenomenon may be interpreted as evidence of discontinuous recrystallization stimulated by local grain boundary migration. However, the fraction of the fine grains in the microstructure is obviously low and, therefore, contribution of this mechanism, if any, to the microstructural evolution is probably minor.

The principal microstructural feature of the reconstructed β-grain structure is a relative low-aspect ratio of the β-grains (Fig. 8a, Table 3). However, closer inspection of the EBSD map reveals that some β-grains are very highly elongated, as exemplified in Figs. 8c and d. In some cases, these high-aspect ratio β-grains contain transverse subboundaries, which tend to subdivide them into several nearly equiaxed grains (some examples are arrowed in Fig. 8d). Careful examination of the microstructure within the SZ showed that these highly elongated and partially subdivided grains are typical features of the reconstructed β-grain structure. Based on this observation, it may be hypothesized that the low-aspect ratio grains dominating in the reconstructed β-grain structure resulted from preliminary severe elongation (shearing) and subsequent transverse subdivision of the β-grains. It seems likely that this mechanism is one of the main contributors to the microstructure development in the β-phase field in the present study.

Thus the analysis of the reconstructed β-grain structure indicates that the microstructural evolution in the high-temperature β phase field is a complex process presumably driven by the dynamical balance between the grain growth, grain elongation (shearing) and transverse grain subdivision but might also involve some limited discontinuous recrystallization stimulated by the local grain boundary migration.

3.4.2.2. Texture Evaluations

The approach used in the present study for β-grain structure reconstruction does not enable recovery of the orientation of the β-grains. As a result, texture and misorientation distribution developed in the β-phase during FSW cannot be derived from the reconstructed EBSD maps. Attempting to overcome this problem (partially, at least), crystallographic measurements have been performed in the retained β-phase and the obtained results are presented in the following two sections.

Table 4. Main ideal orientations in simple shear deformation of BCC metals (after Li et al. [21]).

Notation	{*hkl*}<*uvw*>	Euler angles, deg		
		φ_1	ϕ	φ_2
D_1	$(\bar{1}\,\bar{1}\,2)[111]$	54.74/234.74	45	0/90
		144.74	90	45
D_2	$(11\bar{2})[111]$	125.26	45	0/90
		35.26/215.26	90	45
E	$(110)[1\,\bar{1}\,1]$	90	35.26	45
$\bar{E}$	$(\bar{1}\,\bar{1}\,0)[\bar{1}\,11]$	270	35.26	45
J	$(110)[1\,\bar{1}\,2]$	90/210	54.74	45
$\bar{J}$	$(\bar{1}\,\bar{1}\,0)[\bar{1}\,1\bar{2}]$	30/150/270	54.74	45
F	$\{110\}<001>$	0/180	45	0/90
		90/270	90	45

Before considering texture developed in the β-phase, it is necessary to discuss briefly straining state and geometry of straining during FSW. Although material flow during FSW appears to be very complicated, the predominant deformation mode is expected to be simple shear [18-20]. Shear textures are conventionally defined in terms of the crystallographic plane {*hkl*} and direction <*uvw*>, aligned with the shear plane and shear direction, respectively. In BCC metals (including β-titanium), the simple shear deformation usually forms the fiber textures of {*hkl*}<111> and {110}<*uvw*> types. Ideal simple shear orientations for BCC metals are summarized in Table 4 and Fig. 9a (after Li et al. [21]); in Fig. 9a, SD is shear direction and SPN is shear plane normal.

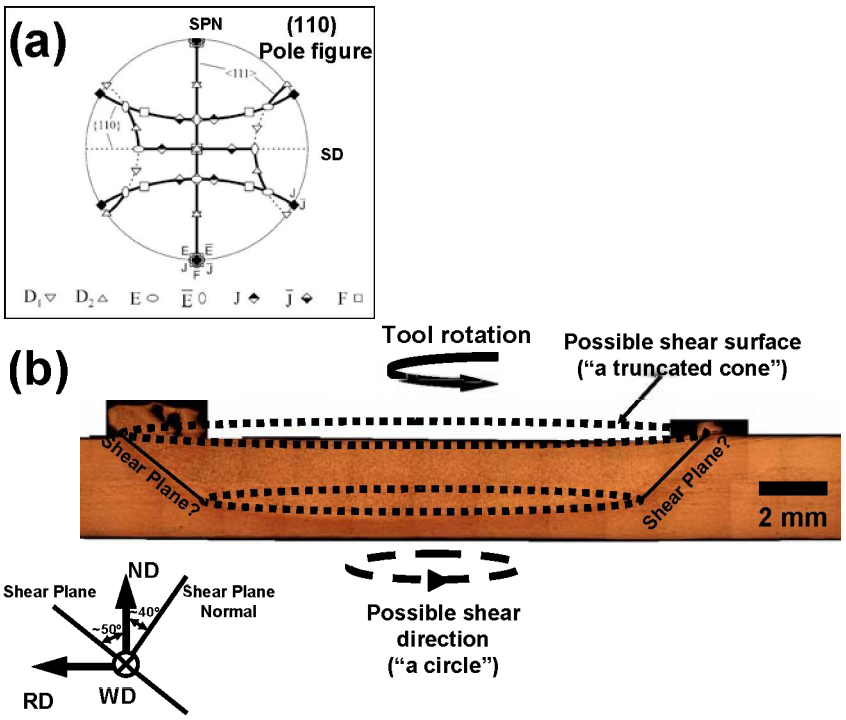

Figure 9. (110) pole figure showing the main ideal orientations and fiber textures associated with simple shear deformation of BCC materials (after Li et al. [21]) (a) and schematic representation of orientations of the shear plane and the shear direction within the SZ (b).

During FSW, the shear plane and direction are not simply related to the sample geometry, but might be expected to be approximately parallel to either the pin column surface [2] or flow lines [18, 20]. If so, the shear direction/plane should not be constant within the SZ but follow a curved line/surface across the SZ because of rotation of the tool. The geometrical arrangement of possible shear directions within the SZ appears to be a circle with the shear direction approximately parallel to TD in the central part of the SZ, as illustrated in Fig. 9b. Orientation of the shear plane is not so evident in a general case but the alignment of the reconstructed β-grains approximately parallel to the border between the SZ and the transition region (Fig. 8a) indirectly indicates that the shear plane may be nearly parallel to this border in the present study. In this case, the shear surface can be roughly described as a truncated

cone having a diameter close to the tool shoulder diameter in the top part of the SZ and to the pin diameter in the bottom part of the SZ and with the angle between the cone surface and the ND of about 50°, as shown in Fig. 9b. This idea is in agreement with the recent investigations of the texture developed during FSW of β-titanium alloy [20].

Orientation data obtained from the retained β-phase in the central part of the SZ are arranged as {110} pole figure in Fig. 10a; the pole figure has the orientation with the ND in vertical and the TD in horizontal. In order to transform the orientation data into a conventional reference frame for simple shear (SD is horizontal and SPN is vertical), the pole figure was tilted by +40° around the TD to align the assumed SPN vertical (see scheme in Fig. 9b). The rotated pole figure is shown in Fig. 10b. The pole figure may be roughly described in the terms of nine textural peaks (poles) whose positions match reasonably well the projections of the $\bar{J}$ $(\bar{1}\,\bar{1}\,0)[\bar{1}\,1\bar{2}]$ ideal simple shear texture component (marked as diamonds on the pole figure), according to the adopted convention (Fig. 9a and Table 4).

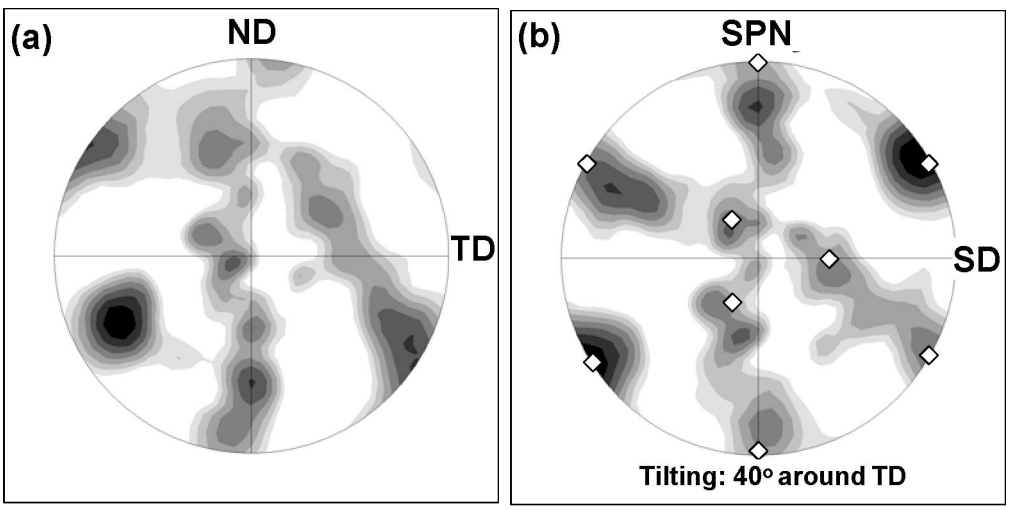

Figure 10. Orientation data obtained from retained β-phase and arranged as {110} pole figures. In (a) the pole figure have the orientation with the normal direction vertical and the transversal direction horizontal. In (b) the pole figure was tilted by 40° around TD in order to align the assumed shear direction (SD) horizontal (see text for details). The diamonds superimposed on the pole figures are the positions of ideal simple shear texture component.

It should be pointed out that the experimental peaks deviate from their ideal positions and the real pole figure exhibits some additional peaks which cannot be explained in the terms of the simple shear texture. Taking into account that the textural data were obtained from the very limited number of orientation measurements, it is difficult to be sure that the identified simple-shear texture is indeed representative for the bulk high-temperature β phase. To provide a thorough investigation, more statistically reliable measurements are required.

Again, the more statistically reliable information may be derived from the α phase. Assuming that the material flow in the β-phase was mainly governed by the simple shear deformation, there is no need to reconstruct entire orientation distribution in the β-phase to

evaluate the simple shear texture and only {110} pole figure is enough for this, as shown in Fig. 9a. On the other hand, crystallography of the α and β phases in the SZ are related through the Burgers OR, as shown above, and thus {110}β should be nearly parallel to {0002}α. In other words, the {0002}α pole figure may be employed to estimate shear texture developed in β phase during FSW. In addition to the direct orientation measurements in the retained β phase, this approach appears to be a very simple and effective method to roughly estimate the bulk β texture: the retained β phase provides direct information about the texture, whereas the {0002}α pole figure ensures its statistical reliability.

The orientation data for the α and β phases were derived from a large (~1x1 mm^2 in size) EBSD map taken from the central part of the SZ (not shown) and were arranged as $\{0002\}$ pole figure for the α phase and as $\{110\}$ pole figure for the β phase, as shown in Fig. 11. The pole figures have the reference directions as the simple-shear geometry (i.e., SD is horizontal and SPN is vertical). For convenience, the projections of $\bar{J}$ and D_2 ideal simple shear components are superimposed on the pole figures according to the adopted convention (Fig. 9a).

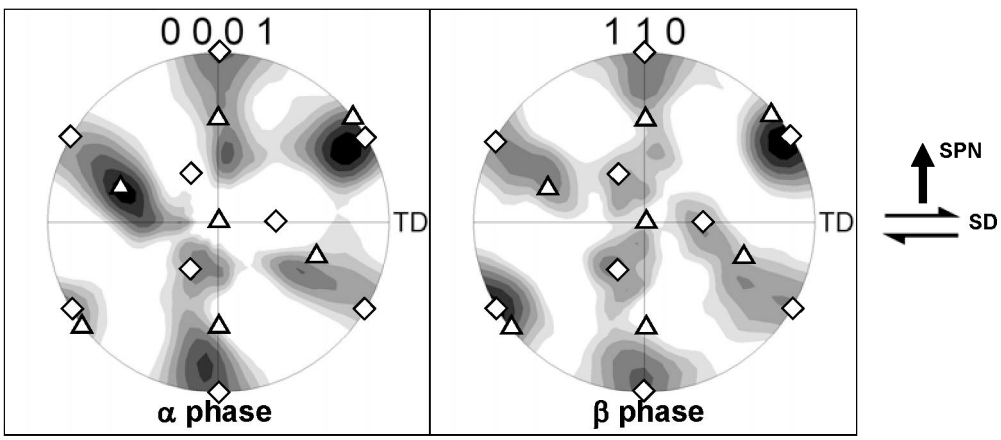

Figure 11. {0001}α and {110}β pole figures in the reference frame for simple shear taken from the central part of the SZ. The diamonds and triangles superimposed on the pole figures are the positions of the –J and D_2 ideal simple shear texture component, respectively. See text for details.

The pole figures in Fig. 11 are not absolutely identical but agreement appears to be reasonable. This additionally confirms the Burgers orientation relationship (OR) between the α and β phases in the SZ. To a first approximation, the distributions of orientation peaks in the {110}β and {0002}α pole figures may be described in terms of a mixture of the $\bar{J}$ and D_2 ideal simple shear components for BCC metals (Fig. 9b), where the $\bar{J}$ component appears to be more evident. It should be stressed that orientation data for the α phase were extracted from an EBSD-map comprising of ~ 1,000 parent β grains (~60,000 α laths). In other words, the good correspondence between the {110}β and {0002}α pole figures ensures reliability of the textural measurements in the retained β-phase. Thus, bulk texture developed

in the high-temperature β phase during FSW may be roughly estimated as a mixture of $\bar{J}$ and D_2 components of the simple shear texture. This presumably means that the material flow in the high-temperature β-phase resulted from a simple-shear deformation and arose mainly from {110}<111> slip (Table 4).

3.4.2.3. Estimation of Misorientation Distribution

Misorientation distributions measured in the retained β-phase in different locations of the SZ are summarized in Fig. 12; misorientation-axis distributions are shown as inserts in top right corners. It may be seen that all the misorientation distributions contain two common features. In all cases, the distributions are dominated by LABs and they always contain some fraction of 60°<111> misorientations. It should be emphasized that extremely limited number of grain boundary segments was measured, as shown in Fig. 12. It is unlikely, therefore, that they are statistically representative for the high-temperature β-phase in general. Nevertheless, the repeatability of the significant proportion of the LABs together with 60°<111> misorientations in each distribution may be associated with some crystallographic preference of these boundaries. It is worthy therefore to give them some consideration.

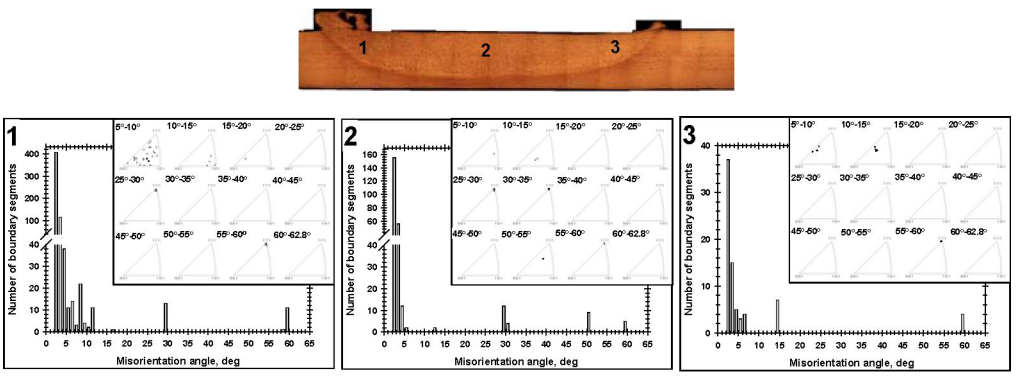

Figure 12. Misorientation distribution measured in the retained β-phase in different locations of SZ; misorientation-axis distributions are shown in the top right corner of the figures. See text for details.

The LABs presence in the β-phase is a quite expectable result because the material in the SZ should experience deformation during FSW. Virtually, the LABs in the retained β phase support our hypothesis about subdivision of the β-grains in the SZ proposed above. In contrast, the possible crystallographic preference of the 60°<111> misorientations is not clear. In materials with BCC crystal structure, these boundaries may be associated with twins. However, number of slip systems in the BCC materials is high enough to accommodate an arbitrary plastic strain (as required by the Taylor criterion) and, thereby, there is no evident need for mechanical twinning in the β-titanium. On the other hand, the BCC materials are generally believed to be not prone to annealing twinning. Thus, the 60°<111> misorientations in the retained β phase is a very surprising results requiring thorough experimental verification.

4. Conclusion

The present study examined microstructural evolution of the Ti-6Al-4V during FSW. The microstructural development was found to be a complex process involving α-to-β phase transformation during heating stage, deformation in the high-temperature β phase field during stirring and β-to-α phase transformation upon cooling down to ambient temperature after FSW.

The α-to-β phase transformation is shown to be governed by epitaxial growth of the pre-existing β phase consuming the α phase. Reconstruction of the β-grain structure have demonstrated that microstructural evolution in the high-temperature β phase field is a complex process involving grain growth, geometrical effects of strain, transverse grain subdivision and discontinuous recrystallization stimulated by local grain boundary migration. Local orientation measurements in the retained β phase have shown that the material flow resulted from a simple-shear deformation and arose mainly from {110}<111> slip. The β-to-α phase transformation after FSW is established to be governed by Burgers orientation relationship which dictated the final weld crystallography.

Aknowledgements

The authors wish to thank Hitachi Ltd. for supplying the test material. One of the authors (S.M.) also would like to express his hearty thanks to the Japan Society for the Promotion of Science and Tohoku University for providing scientific fellowship. Financial support from the Japanese Ministry of Education, Science, Sports and Culture with a Grant-in-Aid from the Global COE program in Materials Integration International Center of Education and Research at Tohoku University is also gratefully acknowledged.

References

[1] Thomas W.M.: *Friction stir butt welding*, Int. Patent № PCT/GB92/02203 (1991).

[2] S.H.C. Park, Y.S. Sato, H. Kokawa. Basal plane texture and flow pattern in friction stir weld of a magnesium alloy. *Met. Mater Trans A,* 2003 (34) 987-994.

[3] T.J. Lienert, Microstructure and mechanical properties of friction stir welded titanium alloy, Friction Stir Welding and Processing, ed. R.S. Mishra, M.W. Mahoney, *ASM International*, 2007, pp. 123-154.

[4] A.J. Ramirez and M.C. Juhas. Microstructural evolution in Ti-6Al-4V friction stir welds. *Mater. Sci. Forum*, 2003 (426-432) 2999-3004.

[5] A.L. Pilchak, Z.T. Li, J.J. Fisher, A.P. Reynolds, M.C. Juhas, J.C. Williams, The relationship between friction stir process (FSP) parameters and microstructure in investment cast Ti-6Al-4V, *Friction Stir Welding and Processing IV*, TMS, Warrendale, PA, 2007, pp. 419-427.

[6] A.L. Pilchak, M.C. Juhas, and J.C. Williams, Observations of tool-workpiece interactions during friction stir processing of Ti-6Al-4V, *Met. Mat. Trans. A* 2007 (38) 435-437.

[7] A.L. Pilchak, M.C. Juhas, J.C. Williams, Microstructural changes due to friction stir processing of investment-cast Ti-6Al-4V, *Met. and Mat. Trans. A* 2007 (38) 401-408.

[8] A.L. Pilchak, D.M. Norfleet, M.C. Juhas, J.C. Williams, Friction stir processing of investment-cast Ti-6Al-4V: microstructure and properties, *Met. and Mat. Trans. A* 2008 (39) 1519-1524

[9] Y. Zhang, Y.S. Sato, H. Kokawa, S.H.C. Park, S. Hirano, Microstructural characteristics and mechanical properties of Ti-6Al-4V welds, *Mat. Sci. and Eng. A* 2008 (485) 448-455

[10] TSL (2001) OIM Version 3.0. *On-line help.* TSL, Draper, UT. U.S.A

[11] S. Mironov, Y. Zhang, Y.S. Sato, H. Kokawa H., Crystallography of transformed β microstructure in friction stir welded Ti-6Al-4V alloy, *Scripta Mater.* **59** (2008) 511-514.

[12] N. Gey, M. Humbert, Charactirization of the variant selection occurring during the α-β-α phase transformation of a cold rolled titanium sheet, *Acta Materialia* **50** (2002) 277-287.

[13] N. Gey, M. Humbert, Specific analysis of EBSD data to study the texture inheritance due to the β-α phase transformation, *Journal of Materials Science* **38** (2003) 1287-1294.

[14] L. Germain, N. Gey, M. Humbert, *Reliability of reconstructed β-orientation maps in titanium alloys,* Ultramicroscopy 107 (2007) 1129-1135.

[15] T. Karthikeyan, S. Saroja and M. Vijayalakshmi, Evaluation of misorientation angle axis set between variants during transformation of bcc to hcp phase obeying Burgers orientation relation, *Scripta Mater.* **55** (2006) 771-774.

[16] S.C. Wang, M. Aindow, M.J. Starink, Effect of self accommodation on α/α boundary populations in pure titanium, *Acta Materialia* **51** (2003) 2485-2503.

[17] S. Mironov, Y. Zhang, Y.S. Sato, H. Kokawa H., Development of grain structure in β-phase field during friction stir welding of Ti-6Al-4V alloy, *Scripta Mater.* **59** (2008) 27-30.

[18] P.B. Prangnell, C.P. Heason, Grain structure formation during friction stir welding observed by the "stop action technique", *Acta Materialia* **53** (2005) 3179-3192.

[19] Fonda R.W., Bingert J.F., Colligan K.J., Development of grain structure during friction stir welding, *Scripta Mater* **51** (2004) 243-248.

[20] A.P. Reynolds, E. Hood, W. Tang, Texture in friction stir welds of Timetal 21S, *Scripta Mater.* **52** (2005) 491-494.

[21] S. Li, I.J. Beyerlein, M.A.M. Bourke, Texture formation during equal channel angular extrusion of fcc and bcc materials: comparison with simple shear, *Mater. Sci. Eng.* **A394** (2005) 66-77.

In: Titanium Alloys: Preparation, Properties and Applications ISBN: 978-1-60876-151-7
Editor: Pedro N. Sanchez, pp. 405-422

Chapter 10

MICROSTRUCTURE AND MECHANICAL PROPERTIES OF INVESTMENT CAST TI-6AL-4V AND γ- TIAL ALLOYS

Milan T. Jovanović [*] ***and Ivana Cvijović-Alagić***
Department of Materials Science, Institute of Nuclear Sciences, „Vinča", Mike Petrovića Alasa 12-14, 11001 Belgrade, Serbia

Abstract

The effects of preheat and pouring temperatures, as well as annealing temperatures and cooling rates, on microstructure and mechanical properties of γ-TiAl and Ti-6Al-4V (wt.%) investment castings have been studied performing X-ray diffraction (XRD) analysis, light microscopy (LM) and scanning electron microscopy (SEM), quantitative metallography, hardness and room temperature tensile tests. Annealing of Ti-6Al-4V above and below the β phase transus temperature produces different combinations of strength and elongation, but a compromise may be achieved applying temperature just below the β phase transus of Ti-6Al-4V alloy. Higher values of tensile strength together with lower ductility than reported in the literature cannot be only ascribed to the presence of α' martensite in the microstructure of Ti-6Al-4V alloy. Yttria coating of graphite crucible must be considered as insufficient in preventing the chemical reaction between aggressive titanium melt and carbon. The processing technology of a "self-supporting" ceramic shell mold was successfully verified during precision casting of both tensile-test samples of Ti-6Al-4V and the prototype of the turbocharger wheel made of γ-TiAl. According to experimental results, a processing window for investment casting of the prototype of a turbocharger wheel was established. The results of this paper also show that besides annealing treatment parameters, melting and casting practice together with ceramic mold technology strongly influence the properties Ti-6Al-4V and γ-TiAl castings.

Keywords: investment casting, "self-supporting" ceramic mold, annealing, phase transformations, strength and elongation, turbocharger wheel

[*] E-mail address: miljov@vin.bg.ac.rs

1. Introduction

The most widely used titanium alloy nowadays is Ti-6Al-4V (wt.%). This alloy possesses an excellent combination of strength, toughness and good corrosion resistance and finds application in aerospace, pressure vessels, aircraft compressor blades and discs, surgical implants *etc*. Aluminum stabilizes the hexagonal close-packed (hcp) α phase, and vanadium, being body-centered cubic (bcc), stabilizes the β phase. Because of high melting point and excessive reactivity of the melt with crucibles, melting and pouring of titanium alloys have to be performed under vacuum. Due to the high cost of titanium, the use of net-shape or near-net-shape technologies receive an increasing interest considering the large cost saving potential of this technology in manufacturing parts of complex shapes. Investment (precision) casting is by far the most fully developed net-shape technology compared to powder metallurgy, superplastic forming and precision forging. Production of investment castings of titanium alloys was considerably increased during last years due to significant cost savings compared with complicated process of machining.

When Ti-6Al-4V is slowly cooled from the β region, α begins to form below the β transus temperature that is about 980 °C [1]. The kinetics of $\beta \rightarrow \alpha$ transformation upon cooling strongly influences properties of this alloy. Contrary to wrought material, however, the possibilities to optimize the properties *via* the microstructural control are limited for cast parts to purely heat treatments. For many alloys mechanical properties of castings are inherently lower than those of wrought alloys. Nevertheless, heat treatment of titanium castings yields mechanical properties comparable, and often superior, to those of wrought products.

Compared with Ti-6Al-4V, which is usually used in the temperature range of 300-550 °C, the γ-TiAl aluminides ("γ alloys") exhibits a higher oxidation resistance and a lower tendency to hydrogen embrittlement. These alloys with two-phase structure consisting of the major γ phase (ordered TiAl face-centred-tetragonal with $L1_0$ crystal structure) and the minor α_2 phase (ordered Ti_3Al close-packed-hexagonal with DO_{19} structure) were intensively studied within the last decade. They are nearly equal to Ni-based superalloys for turbine blades (Inconel 713C) in specific tensile strength (tensile strength *vs.* density) and specific creep strength (creep strength *vs.* density) over temperatures from 20 to 1000 °C, but are slightly inferior to superalloys in oxidation resistance above 700 °C. However, TiAl alloys do not show appreciable room temperature elongation with a maximum 3% for cast alloys [2-5]. There were some efforts to introduce TiAl castings for the 4th stage compressor turbine blade in jet engines, but further development was called off due to insufficient reliability resulting from low temperature elongation, in spite of other good attributes [3]. In contrast to the tremendously critical requirements for jet engines, it would be far easier to concentrate efforts on technology and application of TiAl aluminides to passanger cars. TiAl aluminides have a high potential to become a new class of structural material to be used mostly in automobile engine construction in the temperature range 500-800 °C.

Advantages to be obtained through the application of TiAl turbocharger rotor to a passanger car are as follows [6]:

- specific power increase which improves wehicle performance
- improves fuel economy
- broad engine application range.

The main difficulties in production high quality titanium and titanium alloy castings are: the high melting point, the extremely high reactivity of melt with solids, liquids and gases at high temperatures. For these reasons, traditional casting techniques and materials cannot be used for both melting and molding operations. In addition, melting and pouring have to be performed under vacuum or inert gas. Different crucibles for melting of titanium alloys have been evaluated, *e.g.* graphite and ceramic crucibles, sometimes inside coated with chemically stable or slightly reactive compounds with the melt, in order to decrease probability of melt – crucible interaction to occur. The production of investment molds for titanium casting is similar to the production of investment molds for ferrous and superalloys castings [7] except for some very important differences. The major difference is in the investment slurry formulation. Due to a very high reactivity of molten titanium a special attention must be paid to the chemical composition of ceramic molds. For these reasons the conventional ceramic molds of silica and zirconia (zirconium silicate), or alumina/silica are not suitable. Molds made of such refractories result in titanium castings having unacceptable surface finish and gross porosity. To avoid these problems, investment molds for titanium castings must be made of special high-stable refractories such as zirconia, thoria and yttria.

The effects of preheat and pouring temperatures as well as annealing temperatures and cooling rates on microstructure and mechanical properties of TiAl and Ti-6Al-4V investment castings have been studied performing X-ray diffraction (XRD) analysis, quantitative microscopy, light microscopy (LM) and scanning electron microscopy (SEM), hardness and room temperature tensile tests.

2. Experimental

2.1. Shell Mold Preparation, Melting and Casting Procedure

In the present work a "lost wax" procedure was performed to fabricate a "self supporting" ceramic mold [8]. Actually, this procedure represents a modified technology previously successfully applied for production of molds for investment casting of superalloys [9]. The process consists of alternate dipping of a wax pattern (samples for tensile tests) into a colloidal suspension (in which, except for zirconia powder, some quantity of yttria powder was also added) and subsequent pouring with ZrO_2 powder (particle size about 200 μm). A "primary coating" (consisting of, at least, three layers) formed by this process must be smooth, chemically stable and with sufficient strength to sustain the pressure of chemically very aggressive melt. In the next step, five to seven layers of the "secondary coating" were produced by pouring mullite (a compound $3Al_2O_3 \cdot 2SiO_2$) with particle size ranging between 200 and 500 μm. "Secondary coating" should enable the strength of the shell mold. The mold was first dried, then de-waxed and fired at 900 °C for 1h to enable the sufficient strength for handling and the following process of casting. Figure 1a shows the "self-supporting" ceramic mold after firing of tensile test specimens. The porosity of these molds was between 20 and 25%. The same procedure was performed for turbocharger wheel shell molds (Figure 1b). The cross-section of a mold showing wax pattern inside the mold together with "primary" and "secondary coatings" is presented in Figure 1c. The final thickness of a mold was between 5 and 7 mm. The main difference between developed "self supporting" mold and the mold proposed by other

manufacturers is that the "self supporting" mold is at least five times lighter offering high chemical stability, high strength and thermal shock resistance at the same time.

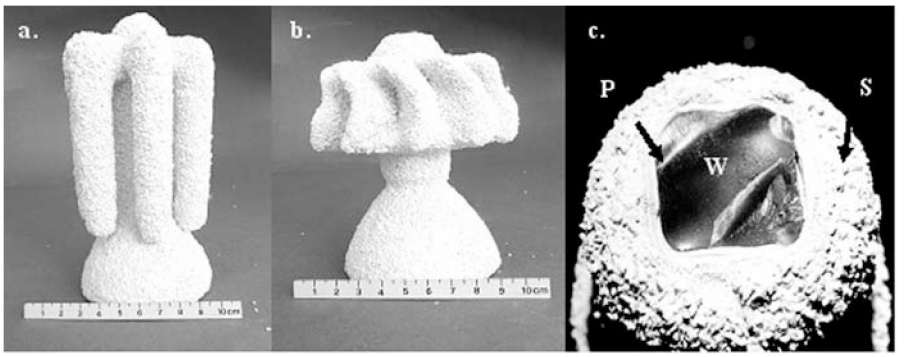

Figure 1. "Self-supporting" ceramic shell mold. (a) Tensile test specimens; (b) turbocharger wheel; (c) cross-section of ceramic mold P-primary coatings, S-secondary coatings, W-wax.

The rods of a commercial Ti-6Al-4V alloy (with the chemical composition 6.4 wt.% Al, 3.9 wt.% V, 0.35 wt.% Fe, less than 0.05 wt.% C, the rest was Ti) were melted in a vacuum induction centrifugal furnace "Linn". Graphite crucibles, which inside surface were coated by plasma sprayed yttria, were used for melting. Conditions during melting and casting were as follows: pouring temperature – 1700 °C, preheated temperature of the ceramic shell mold – 600 °C, vacuum during melting and casting – 1 Pa, speed of mold rotation – 200 rpm. As soon as the charge was melted, argon was released into the chamber. In order to prevent the possible chemical reaction with crucible, melt was poured into the mold after 2 min of holding in the crucible.

To prepare TiAl alloy a "master alloy" in the shape of small ingots (buttons of 50 g) was manufactured by vacuum arc-melting of high-purity aluminum (99.5 wt.%) and a commercial Ti-6Al-4V alloy To ensure homogeneous chemical composition buttons were remelted for several times in an argon protective atmosphere. The chemical composition (note: chemical compositions concerning TiAl are given in at.%) of buttons was: 48 at.% Al, 1 at.% V, balance Ti. The amount of oxygen was approximately 0.2. The charged stock of "master alloy" was remelted in a "Linn" vacuum centrifugal furnace, whereas the same sort of graphite crucibles and a "self supporting" mold was used as in the case of melting of Ti-6Al-4V alloy. Vacuum pumps were switched off before pouring and the entire system was filled with high purity (99.99%) argon up to 1 kPa pressure and the melt was poured into a previously preheated ceramic mold. Conditions during melting and casting were as follows: pouring temperature was varied in the range between 1550 and 1650 °C, preheated temperature of ceramic shell mold was varied between 400 and 800 °C, speed of mold rotation – 200 rpm, vacuum during processing – 1 Pa. Intermetallic compound with the nominal chemical composition Ti-48Al-1V will be referred as TiAl in further text. Approximately the same melting and casting procedure was performed for the processing of turbocharger wheels and specimens for tensile tests. "Self-supporting" ceramic molds demonstrated excellent chemical stability, very good thermal shock resistance coupled with strength to sustain pressure of the melt during solidification. In the same time, it was possible to break molds quite easily without imposing any damage to castings.

2.2. Annealing Treatment of Ti-6Al-4V Alloy

There are some commonly used annealing treatments for the commercial Ti-6Al-4V alloy. For each of these, the following descriptions are typical of temperatures and times applied, but the actual practice varies with alloy producer and user. According to the literature data [10] a typical procedure involves solutionising at 100 °C above the β transus followed by a cooling and aging in the α + β region. However, other sources [1] suggest solutionising below the β transus which might be followed by aging.

In this study the heat treatment procedure of samples for LM and tensile tests was as follows:

- annealing at 800, 850, 900, 950, 1000, 1050 and 1100 °C for 1h
- three cooling rates were applied for each annealing temperature, *i.e.* furnace-cooling, air-cooling and water-quenching.

The heat treatment was performed in the electro-resistance furnace under the protection of flowing argon.

2.3. Characterization of Microstructure and Mechanical Properties

XRD analysis with CuK_α irradiation, LM and quantitative microscopy utilizing the software "VIDAS" program (for the evaluation of the volume fraction of phases in TiAl alloy) and SEM were used for microstructural characterization. Specimens for these examinations were cut out from the central sprue. Kroll's reagent (a mixture of 10 ml HF, 5 ml HNO_3 and 85 ml H_2O) was used for both alloys as an etchant for LM. The same specimens were used for Vickers hardness tests with applied load of 10 kg. To avoid the possible influence of alpha case (a brittle and relatively deep layer which might be formed on the surface of casting) all hardness measurements were performed in the middle part (core) of the specimens. Screw-type samples for tensile tests produced by investment casting (Figure 2) were 4 mm in diameter and 20 mm in gauge length. Uniaxial tensile tests were carried out at room temperature at a strain rate $\dot{e} = 1.3x10^{-3}\ s^{-1}$.

Figure 2. Assembly of precision cast samples for tensile tests.

3. Results and Discussion

3.1. The Effect of Melting and Casting Parameters on the Quality of Castings

As far as Ti-6Al-4V alloy was concerned castings of a good quality (smooth surface, without external porosity and misrun) were obtained. The density of castings was 98% of theoretical density.

However, quite the different situation was encountered in the case of TiAl alloy. The turbine turbocharger wheel casting with 75mm in diameter has a rather complicated configuration consisting of 10 twisted blades with thin (~1 mm) leading edges. Therefore, the precision casting with ceramic investment mold was as a near net-shape processing technique. Some attempts were made with conventional gravity vacuum induction casting, but the quality of castings were unacceptable because they suffered from defects such as misrun, small surface cracks and macroporosity. The most promising technique was found to be centrifugal vacuum casting.

In addition to mold material, primary interest for the successful casting of TiAl alloy requires careful attention to casting parameters, such as pouring temperature and mold preheat temperature, since mold preheat temperature is one of the most important casting parameters. Higher preheat not only improve fill and feeding, but also reduces thermal gradient and cooling rates. However, higher preheating may lead to severe mold/metal reaction and may increase the propensity for surface-connected porosity. Slower cooling rates may induce coarser grain size and inferior mechanical properties. Therefore, between these parameters a balance must be found in order to achieve properties according to design requirements.

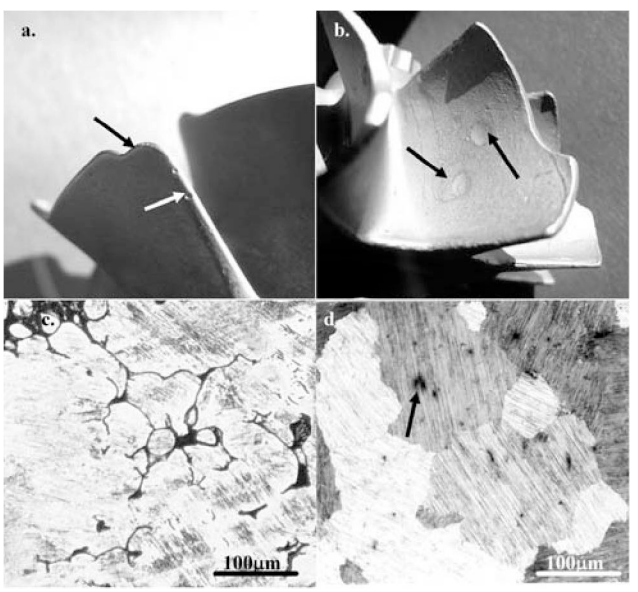

Figure 3. Macro and micro defects in TiAl alloy caused by inadequate mold preheat or melt pouringtemperature. (a) Misrun and small macropores; (b) rough surface and large macropores; (c) interdendritic porosity; (d) micropores.

It should be noted that the first castings showed defects such as a misrun and macropores (denoted with arrows in Figure 3a) when the preheat temperature of molds was below 500 °C. In the case when the preheating was too high (above 800 °C) rough surface and a pronounced macroporosity occurred (Figure 3b). Pouring temperature above 1600 °C causes a significant extent of interdentritic porosity (Figure 3c) and microporosity (Figure 3d).

Applying higher preheat temperature (between 750 and 800 °C) many of these defects were successfully eliminated and a smooth surface together with thin and sharp blade edges were obtained (Figures 4a and b). The same conditions enabled a good quality of samples for tensile testing.

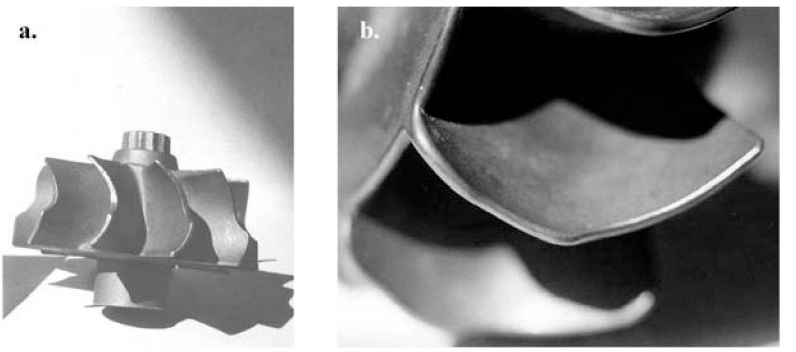

Figure 4. Correctly cast turbochargel wheel. (a) General look of the turbocharger wheel; (b) detail showing blade edge.

3.2. XRD Analysis

3.2.1. Ti-6Al-4V Alloy

XRD patterns of as-cast Ti-6Al-4V alloy sample and samples annealed at different temperatures then furnace-cooled, air-cooled and water-quenched are shown in Figures 5a-c, respectively. Reflections of α and β phase as well as reflections of the face-centered cubic (fcc) phase were detected in diffraction patterns of as-cast and all furnace-cooled samples (Figure 5a). It should be noted that β reflections are rather weak, suggesting a relatively low volume fraction of the β phase. Diffractograms corresponding to air-cooling (Figure 5b) are similar to previous regarding α, β and fcc phases except that reflections of the α′ metastable martensitic phase appear after cooling from β-region above 1000 °C. The broaden α reflections having the fullwidth at half maximum (FWHM) higher than 0.2° 2θ are the evidence for the presence of the supersaturated martensitic phase with hcp structure. Considerable appearance of martensite may be seen in patterns of samples water-quenched from 1000, 1050 and 1100 °C (Figure 5c). In those patterns FWHM of α reflections rise up to 0.8° 2θ due to the martensitic transformation and the formation of hcp diffusionless martensite structure closely related to the hcp structure of the α phase originated from diffusional transformation of a fraction of the β phase. Intensity of α′ reflections decreases as the annealing temperature decreases indicating the decrease of the α′ fraction. Cooling from the α+β region (800 and 900 °C) produces a large fraction of the primary α phase with FWHM less than 0.2° 2θ. No traces of the β phase are visible in the patterns of

water-quenched samples except from 1050 °C, whereas the fcc phase was observed in all diffractograms.

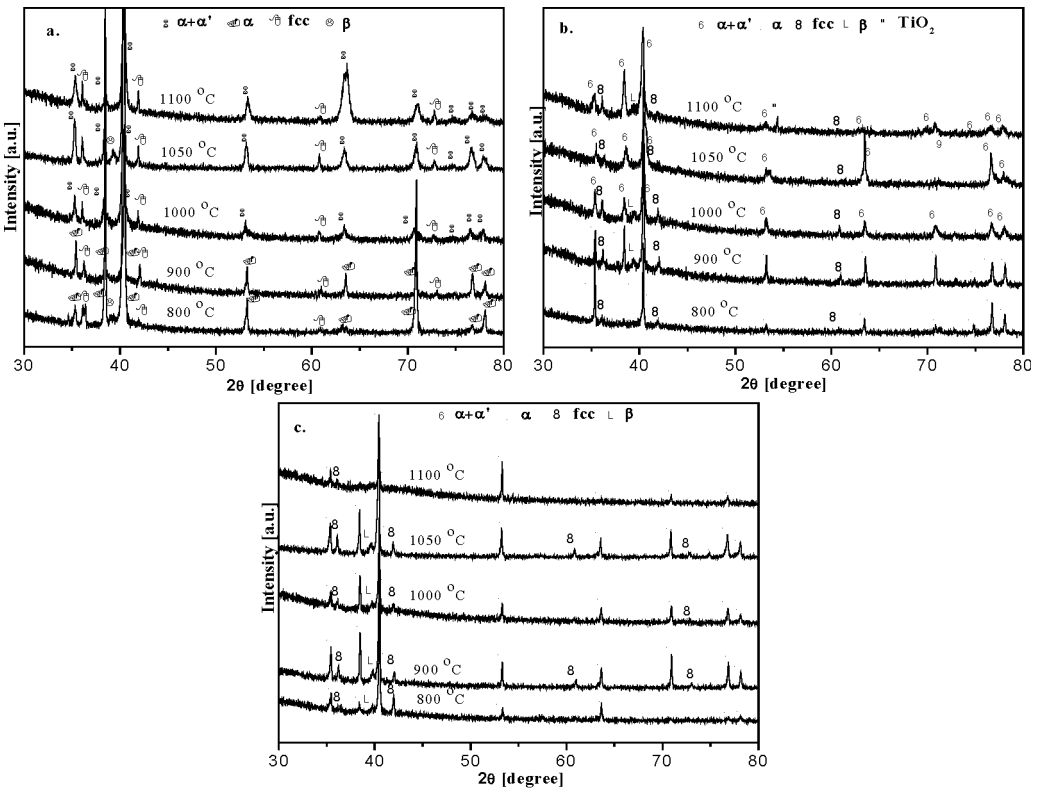

Figure 5. XRD patterns of as-cast Ti-6Al-4V alloy sample and samples annealed at different temperatures then (a) furnace-cooled; (b) air-cooled and (c) water-quenched.

There is no agreement between authors on the crystal structure of martensite that forms from the β phase. According to some authors [11] two different types of the martensitic phase may form depending on the quenching temperature. These phases are designated as α′, which is fcc or face-centered tetragonal, and the α″ hcp phase. Other authors [12] claim that α″ is orthorhombic, but Malinov *et al.* [13] very recently have suggested that orthorhombic α″ precipitates only upon aging of the supersaturated hcp α′ phase. Since in our paper only a phase having hcp structure was detected upon air-cooling and water-quenching from above 1000°C, the martensitic transformation was designated as β→α′. The presence of some small amount of the β phase in the diffractograms upon quenching from the above the β transus is due to the fact that the martensite finish temperature, M_f, is below 25 °C for this alloy [1]. Thus, upon quenching not all β is converted to martensitic α′ phase. On the other side, reflections of the fcc phase that may be seen in all diffractograms, including that of as-cast sample, correspond to TiC, TiOC or TiCN according to the fcc lattice parameter of 0.430 nm. It is quite possible that TiC originates from the process of melting (the presence of TiC is the result of the reaction between aggressive Ti-based melt and carbon from crucible) in spite of the fact that inside of crucible was protected by yttrria layer.

3.2.2. TiAl Alloy

XRD analysis of as-cast TiAl alloy (Figure 6) proved the existence of α_2 ordered Ti_3Al phase with close-packed-hexagonal lattice (a = 0.5753 nm and c = 0.4644 nm) and γ ordered TiAl phase with tetragonal lattice (a = 0.4016 nm and c = 0.4073 nm) with c/a ratio of 1.014. This ratio is close to 1.02 which corresponds to the equiatomic TiAl composition, whereas tetragonality increases up to c/a = 1.03 with increasing aluminum concentration [5]. A few peaks of retained ordered β (B2) phase, which crystallizes in the CsCl structure, have also been detected. Contrary to castings of Ti-6Al-4V alloy when a peak of TiC and/or TiCN was detected due to reaction of melt and carbon crucible, no presence of carbon in castings was detected in this case.

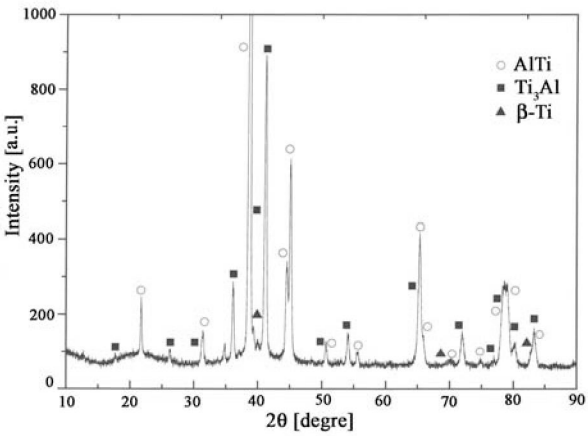

Figure 6. XRD pattern of as-cast TiAl alloy.

3.3. Microstructure

3.3.1. Ti-6Al-4V Alloy

Microstructure of as-cast Ti-6Al-4V sample is shown in Figure 7.

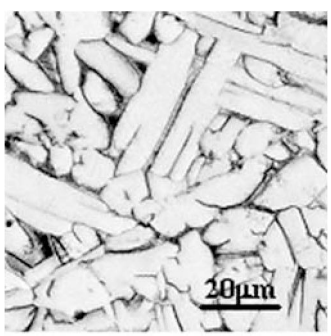

Figure 7. LM micrograph of as-cast Ti-6Al-4V alloy microstructure.

As the alloy is slowly cooled from the β region, the α phase begins to appear in the shape of plates below the β transus, with the crystallographic relationship to the β phase in which it forms. The white plates correspond to the α phase, forming a typical Widmansttäten structure, whereas thin dark regions between α plates are the β phase. Some characteristic microstructures after different heat-treatment are shown in Figures 8-10.

Water-quenching from all annealing temperatures leads to the formation of the α' martensite structure which volume fraction decreases with decreasing temperature. After quenching from 1100 °C α' martensite prevails in the microstructure (Figure 8a), whereas water-quenching from 950 °C produces a mixture of α and β structures with α plates formed inside and at prior β grain boundaries. A fraction of α' martensite is present inside the β phase (Figure 8b). Similar microstructure is obtained upon water-quenching from 900 °C except that the volume fraction of the α phase is higher (Figure 8c).

Figure 8. LM micrographs of Ti-6Al-4V alloy microstructure upon water-quenching from: (a) 1100 °C; (b) 950 °C; (c) 900 °C.

Air-cooling, i.e. slower cooling rate, leads to the formation of somewhat different type and morphology of microconstituents compared to water-quenching. Upon air-cooling from 1100 °C acicular α_{AC} (transformed β) [14] appear in the β matrix (Figure 9a). Note that the square or rectangular-like particles are also present in the same microstructure. Morphology of these plates (in the center of some particles very small globule may be seen) is very similar to TiC and TiCN which may be found in some superalloys [15]. This result is also in accordance with the results of XRD analysis, supporting the idea that the source for carbides is probably carbon from the graphite crucibles. Titanium carbon nitride $TiC_{0.7}N_{0.3}$ was detected in the Ti-6Al-4V alloy as-cast microstructure when graphite crucible was used [16].

It is obvious that some β (dark matrix) is transformed to fine acicular α_{AC} upon air-cooling from 1050 °C (Figure 9b). Primary α plates at boundaries of prior β grains may be also seen. Air-cooling from 950 °C produces structure with higher amount of the α phase at the expense of α_{AC} and β mixture (Figure 9c).

Plates of the primary α phase with some retained intergranular β are present in samples furnace-cooled from all annealing temperatures (Figures 10a-c). Thickness of α plates is higher as annealing temperature is higher, being ~15 μm at 1100 °C (Figure 10a), ~10 μm at 950 °C (Figure 10b) and ~8 μm at 800 °C (Figure 10c). Also, furnace-cooling produces thicker α plates than air-cooling from the same annealing temperature.

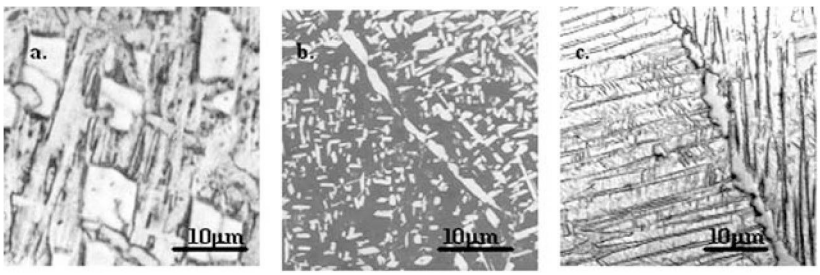

Figure 9. LM micrographs of Ti-6Al-4V alloy. Microstructure upon air-cooling from: (a) 1100 °C; (b) 1050 °C; (c) 950 °C.

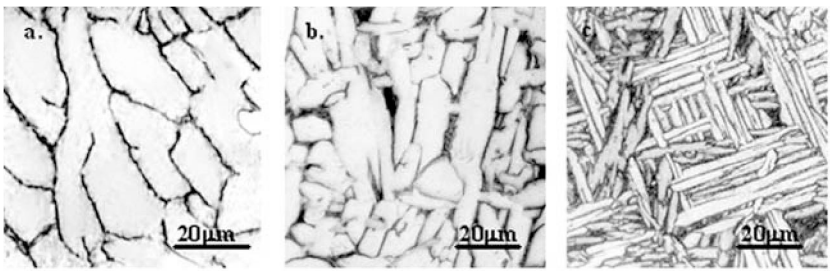

Figure 10. LM micrographs of Ti-6Al-4V alloy microstructure upon furnace-cooling from: (a) 1100 °C; (b) 950 °C; (c) 800 °C.

The results of quantitative microscopy showing the volume fraction of phases present in Ti-6Al-4V alloy after different annealing temperatures and cooling rates are illustrated in Table 1.

Table 1. Volume fraction (%) of present phases in Ti-6Al-4V alloy upon different annealing temperatures and cooling rates.

T, °C	Water-quenching	Air-cooling	Furnace-cooling
1100	***1.3** (β) α'=98.7	**14.7** (α) β+α_{AC}=85.3	**95** (α) β=rest
1050	**5** (β) α'=95	**34.5** (α) β+α_{AC}=65.5	**97** (α) β=rest
1000	**7.8** (β) α' =92.2	**50.9** (α) β+α_{AC} =49.1	**90** (α) β=rest
950	**42.2** (α) α' ~ 50-57.8 β ~ 8	**72.2** (α) β+α_{AC} =28.8	**95** (α) β=rest
900	**63.1** (α) α' ~ 26.9 β ~ 10	**81.3** (α) β+α_{AC} =18.7	**95** (α) β=rest
850	**80** (α) α' ~ 10 β ~ 10	**84.5** (α) β+α_{AC} =15.5	**95** (α) β=rest

* bold values correspond to the measured volume fraction

Taking into account that the measured volume fraction represents only one microconstituent, then the volume fraction of other microconstituents might only be a rough estimate which equals to the supplement to 100%. According to this approximation, together with the literature data that the volume fraction of the β phase upon water-quenching from 900 and 950 °C is between 5 and 10 vol.% [1], it was possible to calculate the volume fraction of previously identified and remaining phases. The results from Table 1 may be summarized as follows: (a) upon water-quenching the volume fraction of α' martensite decreases with decreasing annealing temperature, whereas the opposite case is with the primary α phase; the amount of β also increases, although not so significantly; (b) the similar situation is experienced upon air-cooling, *i.e.* the sum of volume fractions of acicular α_{AC} and β decreases and the presence of the primary α is increased with decrease in temperature; (c) the volume fraction of the primary α phase that is only present in the microstructure upon furnace-cooling remains practically unchanged and is around 95 vol.% (the rest is β) irrespective of annealing temperature. The similar result for the amount of the β phase upon furnace-cooling from β and α + β regions was obtained by other authors [17].

3.3.2. TiAl Alloy

When TiAl alloy of composition corresponding to the solid vertical line C is cast from the temperature T_M (around 1600 °C in Figure 11a) the resulting microstructure consists of grains ranging between 50 and 200 μm (Figure 11b).

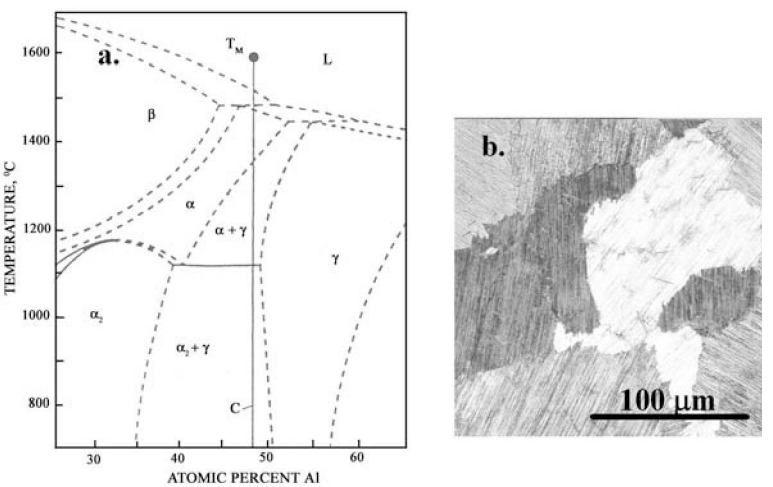

Figure 11. (a) The central part of the equilibrium Ti-Al phase diagram with C composition line corresponding to Ti-48Al alloy [18]. (b) LM micrograph of differently sized grains in the as-cast microstructure of TiAl alloy.

In addition to cooling rate the as-cast microstructre of TiAl alloy depends on the chemical composition. Some literature data show that grains are becoming smaller with decreasing aluminum content and with small additions of vanadium, manganese and chromium [19,20]. However, in the case of this work the cooling rate during solidification was a predominant factor influencing the grain size. Higher cooling rate (mold was preheated

at 500 °C) yielded grains between 100 and 300 μm in size (Figure 12a), whereas lower cooling rate (mold temperature was around 800 °C) produced rather coarse (between 300 and 600 μm) grains (Figure 12b). Higher magnification clearly reveals that coarse grains possess the fully lamellar microstructure where the lamellae are mostly γ intermixed with dark lamellae of the α_2 phase (Figure 12c). Individual rod-like particles and particles at grain boundaries (having light contrast) of the β (B2) phase may be also seen in the same micrograph. A similar morphology of this phase was reported in ingots of Ti-47Al-4(Cr,Nb,Mo,B) [21].

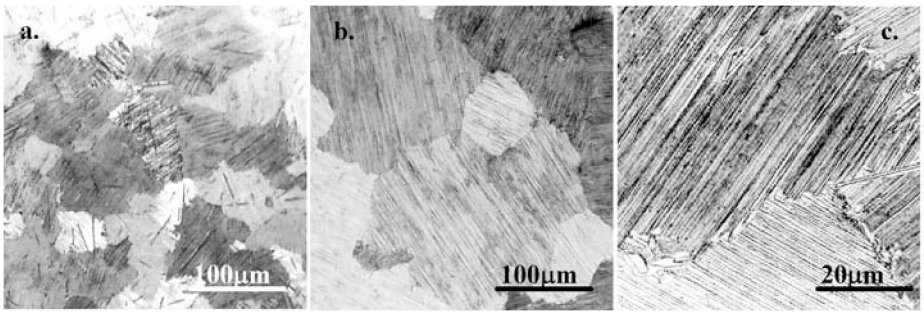

Figure 12. LM micrographs of as-cast TiAl alloy microstructure. (a) Mold preheated at 500 °C; (b) mold preheated at 800 °C; (c) higher magnification of specimen shown in b illustrating lamellar structure (light contrast corresponds to the β (B2) phase).

Although a number of experiments was performed applying variations of pouring temperature and preheating temperature of the ceramic shell, the appearance of some porosity could not be avoided. To preserve this lamellar structure that might be lost during hot-isostatic pressing (HIP) [22], no experimets with HIP have been performed in order to eliminate microporosity. In general, lamellar structure could result in low ductility (even less than 1%) [23], but with regard to creep properties a fully lamellar structure is desirable [24, 25]. Lamellar spacing was found to depend on cooling rate (Figures 13a and b), *i.e.* in coarse grains (slower cooling rate, Figure 13a) this spacing was somewhat larger than in smaller grains (higher cooling rate, Figure 13b). This is in accordance with the results of Kim [26] who reported the effect of cooling rate on α_2/γ spacing.

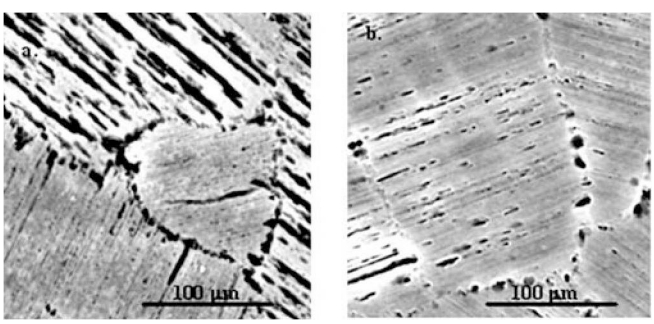

Figure 13. SEM micrographs showing the effect of preheat mold temperature (cooling rate) on α_2/γ lamellar spacing of TiAl alloy. (a) Slower cooling rate; (b) higher cooling rate.

3.4. Mechanical Properties

3.4.1. Ti-6Al-4V Alloy

Mechanical properties of Ti-6Al-4V alloy as a function of annealing temperatures and cooling rates are illustrated in Table 2.

Table 2. The effect of different annealing temperatures and cooling rates on mechanical properties of Ti-6Al-4V alloy.

Temperature, °C	Water-quenched		Air-cooled		Furnace-cooled	
	Tensile strength, MPa	Elongation, %	Tensile strength, MPa	Elongation, %	Tensile strength, MPa	Elongation, %
1100	1385	1.5	1350	1.8	1230	2.6
1050	1390	1.5	1350	1.8	1290	2.5
950	1310	1.8	1290	2.4	1230	2.9
900	1250	2.0	1190	2.8	1150	3.5
800	1200	2.5	1165	3.0	1120	4.0

In general, tensile strength increases with increase in annealing temperature being highest upon water-quenching, whereas upon furnace-cooling the lowest strength values were registered. A saturation of strength was reached after 1050 °C and the plateau was formed between 1050 and 1100 °C. On the other hand, elongation decreases with increasing both annealing temperature and cooling rate. In addition, values of strength and ductility of as-cast samples are lower than those after heat treatment. The highest values of strength, although accompanied with the lowest elongation, are obtained when the martensitic α' phase is produced upon water-quenching irrespective of annealing temperature, indicating that caution should be exercised if applying this annealing treatment. According to the results of XRD analysis, LM and tensile tests, a compromise between adequate values of strength and elongation may be achieved with the annealing temperature just below the β transus, *i.e.* between 900 and 950 °C, and applying air-cooling as a moderate cooling rate. Some improvement in elongation could be achieved with the finer thickness of the primary α plates.

The data on values on mechanical properties of heat-treated Ti-6Al-4V alloy castings are rather limited. Comparing the results of this paper with the literature data (tensile strength: 980-1150 MPa; elongation: 8-10%, although the parameters of heat treatment were not specified) [27-29] it is obvious that the values of tensile strength from Table 1 are higher, but elongation is rather lower. To account for these values, although the effect of α' martensite on tensile strength and elongation cannot be neglected, the process of melting of Ti-6Al-Al should be analyzed in view of some important details. Namely, although the graphite crucible was coated with yttria coating it is quite possible that during melting this coating was damaged and some amount of carbon diffused into the melt forming carbides with titanium and vanadium. The presence of TiC was documented by XRD analysis in as-cast and all annealed samples. This type of carbide was also identified by LM (Figure 9a). Considering that even a small amount of carbon significantly increases strength (*e.g.* increase of carbon from 0.1 to 0.2 wt.% raises tensile strength between 60 and 80 MPa and deteriorates ductility

for about 5% [30]) it is quite possible that the higher level of strength and unexpectedly low values of elongation are the result of increase of carbon content in the alloy due to its absorption during melting [31]. From this point of view it is obvious that coating protection of graphite crucible by yttria proved to be ineffective. Evidently, according to the results of this paper the utmost care must be paid to the protective coating of graphite crucibles, but the quality of the crucible itself (density of graphite, type of binder) must not be neglected. Also, parameters of melting practice such as time of holding the melt in the crucible, intensity of induction field, interrelation between the height of charge and the height of induction coil affect the quality of castings. For melting of high quality titanium alloys, apart from expensive skull melting with the cold crucible which enables contamination-free castings, a very recent literature report suggests the application of less expensive standard casting practice, but with ceramic crucibles made of yttria and calcia [32].

3.4.2. TiAl Alloy

Room temperature mechanical properties of TiAl-based alloys (with a chemical composition similar to alloy of this work) are compared in Table 3.

Table 3. Room temperature mechanical properties of some TiAl-based alloys.

Alloy, at.%	Strength, MPa		Elongation, %	Hardness, HV_{10}	Reference
	Yield Strength	Ultimate Tensile Strength			
Ti-48Al-1V* (100÷200 μm)	430	500	1.2	360	33
Ti-48Al-1V* (300÷500 μm)	400	475	1.8	330	33
Ti-48Al*	390	483	0.-2.1	250	3
Ti-48Al-1V	400	507	2.3	-	3
Ti-44Al-1V	754	-	0.6	-	34
Ti-48Al-(1-3)V	520	-	1.5-3.5	-	3
Ti-48Al-2Nb-2Mn (as-cast+HIPed)	392	460	0.9	-	35
Ti-47Al-5Nb*	480	510	0.5	-	36
Ti-47Al-2Cr-2Nb*	560	659	1.6	300	37

*as-cast

Concerning the results of mechanical properties the results of this paper represent the average value of four tests. The effect of smaller grain size on mechanical properties on TiAl-based alloys is evident, *i.e.* higher strength and hardness, but lower elongation showed

samples solidified under higher cooling rate. Although in most alloys the previous "thermal history" was not specified, it is obvious that the results [33] agree quite well with the literature data. Considering the results of mechanical testing presented in this paper one should be cautious since these values refer not to the turbocharger wheel itself, but to tensile specimens solidified under the conditions intended to be similar during solidification of casting with different geometry.

Based on inspection of casting, microstructural analysis and mechanical properties, a processing window for precision casting of a prototype of the turbocharger wheel made of TiAl alloy may be established, *i.e.* pouring temperature between 1580 and 1600 °C; shell mold preheating temperature between 750 and 800 °C; speed of mold rotation - 200 rpm; vacuum during melting - 1 Pa. Although with mold preheat temperature at 500 °C smaller grains and higher strength were achieved, higher preheat temperature was chosen due to better quality of surface castings. Applying these parameters, the prototype of the TiAl turbocharger wheel having yield strength of 400 MPa, ultimate tensile strength of 475 MPa, elongation of 1.8%, hardness of 330 HV and grain size between 300 and 500 μm was produced.

4. Conclusions

The effects of preheat and pouring temperatures as well as annealing temperatures and cooling rates on microstructure and mechanical properties of of γ-TiAl alloy (with the nominal chemical composition Ti-48Al-1V) and Ti-6Al-4V castings have been studied performing XRD analysis, LM and SEM, hardness and room temperature tensile tests.

Annealing of Ti-6Al-4V above and below the β phase transus temperature produces different combinations of strength and elongation, but a compromise may be achieved applying temperature just below the β phase transus. Higher values of tensile strength together with lower ductility than reported in the literature cannot be only ascribed to the presence of α' martensite in the microstructure. Yttria coating of graphite crucible must be considered as insufficient in preventing the chemical reaction between aggressive titanium melt and carbon.

The processing technology of a "self-supporting" ceramic shell molds was successfully verified during investment casting of both tensile-test samples of Ti-6Al-4V and the prototype of the turbocharger wheel made of γ-TiAl alloy. "Self-supporting" ceramic shell molds demonstrated excellent chemical stability together with strength to sustain pressure during solidification.

According to experimental results, a processing window for precision casting of the prototype of a turbocharger wheel was established. The results of this paper also show that besides annealing treatment parameters, melting and casting practice together with ceramic mold technology strongly influence the properties Ti-6Al-4V and γ-TiAl alloy castings.

Acknowledgement

The work was financially supported by the Ministry of Science and Technological Development of the Republic of Serbia through projects Nos. 1966 and 142027.

References

[1] Brooks, C.R. *Heat Treatment, Structure and Properties of Non Ferrous alloys;* ASM International: Metals Park, OH.; 1982; pp. 315-320.

[2] Kim, Y.W. *J. Metals* 1994, 46, 30-39.

[3] Kim, Y.W. *J. Metals* 1989, 4, 24-30.

[4] Ramanujan, R.V. *Int. Mat. Rev.* 2000, 45, 217-240.

[5] Klemens, H; Kestler, H. *Adv. Eng. Mat.* 2000, 2, 551-570.

[6] Nishiyama, Y.; Miyashita T.; Isobe, S.; Noda, T. In: *High Temperature Aluminides and Intermetalics;* Eds. Wang, S.H.; Liu, C.T.; Pope, D.P.; Stiegler J.O.; TMS: Indianapolis, IN, 1990; pp. 557-570.

[7] Jovanović, M.T.; Lukić, B. ; Mišković, Z.; Bobić, I.; Cvijović, I.; Dimčić, B. *J. Metall. – MJoM*, 2007, 13, 91-106.

[8] Bobić, I.; Tadić, S.; Jovanović, M.T; Đurić, I.; Pantović, M. *A Self-Supporting Ceramic Shell Mold for Investment Casting of Titanium Alloys;* JUS Patent 2003; No. 449/03, (patent pending).

[9] Mišković, Z.; Jovanović, M.T.; Gligić, M.; Lukić, B. *Vacuum* 1992, 43, 709-711.

[10] Noort, RV. *J. Mat. Sci.* 1987, 22, 3801-3811.

[11] Hammond, C.; Nutting, *J. Met. Sci.* 1977, 10, 474-489.

[12] *Handbook Titanium Alloys;* Eds. Boyer, R.; Welsh, G.; Collings, E.W.; ASM International: Materials Park, OH; 1994; pp. 325-335.

[13] Malinov, S.; Sha, W.; Guo, Z.; Tang, C.C.; Long, A.E. *Mat. Charact.* 2001, 48, 279-295.

[14] Metals Handbook 10th ed.; *Metallography and Microstructures*; ASM International: Materials Park, OH; 1986; Vol. 9, pp. 346-349.

[15] Jovanović, M.T.; Mišković, Z.; Lukić, B. *Mat. Charact.* 1998, 40, 261-268.

[16] Žitňanský, M.; Čaplovič, L. *J. Mat. Proc. Techn.* 2004, 157-158, 782-787.

[17] Malinov, S.; Guo, Z.; Sha, W.; Wilson, W. *Metall. Mater. Trans. A* 2001, 32, 879-87.

[18] McCullough, C.; Valencia, J.J.; Mateos, H.; Levi, C.G.; Mehrabian, R.;. Rhyne, K.A. *Scripta Met.* 1988, 22, 1131-1137.

[19] Tetsui, T.; Miura, Y. *Mitsubishi Heavy Industries Technical Review*, 2002, 39, 592-615.

[20] Clemens, H.; Lorich, A.; Eberhardt, N.; Glatz, W.; Knabl, W.; Kestler, H. Z. Metallkde 1999, 90, 569-580.

[21] Clemens, H.; Jeglitsch, F. Prakt. Metall. 2000, 37, 194-217.

[22] Tetsui, T. *Mat. Sci. Eng. A* 2002, 329-331, 582-588.

[23] Kim, Y.W.; Dimiduk, D.M. In: *Structural Intermetallics*; Eds. Nathal, M.V.; Darolia, R.; Liu, C.T.; Martin, P.L.; Miracle, D.B.; Wagner, R.; Yamaguchi, M.; The Minerals , Metals and Materials Society: Warrendale; 1997; pp. 531-543.

[24] McQuay, P.A.; Sikka, V.K. In: *Intermetallic Compounds, Principles and practice*; Eds. Westbrook, J.H.; Fleischer, R.L.; John Willey and Sons: New York, Vol. 3, 2000, pp. 592-615.

[25] Dimiduk, D.M.; Miracle, D.B.; Kim, Y.W.; Mendiratta, M.G. *ISIJ Int.* 1991, 31, 1223-1234.

[26] Kim, Y.W. *Mat. Sci. Eng. A* 1995, 192-193, 519-533.

[27] ASTM Standard F 1108-02; *Standard Specification for Titanium-6Aluminum-4Vanadium Surgical Implants*; (UNS 54406).
[28] Ruckle, D.L.; Millan, P.P. *Method for Heat Treating Cast Titanium Articles to Improve Their Mechanical Properties*; U.S. Patent 1986; No. 4.631.092.
[29] Eylon, D.; Barice, W.J.;.Froes, F.H. *SAMPE* 1985, 17, 585-595.
[30] Jaffee, R.I. In: *Progress in metal physics*; Eds. Chalmers, B; King, R.; Pergamon Press: New York, 1958; Vol. 7, pp. 646-655.
[31] Jovanović, M.T.; Tadić, S; Zec, S; Mišković Z.; Bobić, I. *Mat. Design* 2006, 27, 192-199.
[32] Barbosa, J; Ribeiro, C.S.; Monteiro, C. *Intermetallics* 2007, 15, 945-955.
[33] Jovanović, M.T; Dimčić, B; Bobić, I.; Zec, S.; Maksimović, V. *J. Mat. Proc. Techn.* 2005, 167, 14-21.
[34] Lipsitt, H.A. *Titanium Aluminides - an Overview*; *Mat. Res. Soc. Symp*; Proc. 39, MRS; Pittsburgh, PN; 1985, pp. 351-360.
[35] Kuang, J.P.; Harding, R.A.; Campbell, J. *Mat. Sci. Eng. A* 2002, 329-331, 31-37.
[36] Yang, R.; Cui, Y.Y.; Dong, L.M;. Jia, Q. *J. Mat. Proc. Techn.* 2003, 135, 178-188.
[37] Chouen, W.; Peiquan, G.; Liying, Y. *J. Mat. Proc. Techn.* 2008, 204, 492-497.

In: Titanium Alloys: Preparation, Properties and Applications ISBN: 978-1-60876-151-7
Editor: Pedro N. Sanchez, pp. 423-439

Chapter 11

THERMAL FORMABILITY OF TITANIUM TAILOR-WELDED BLANKS

C.P. Lai[*], *L.C. Chan*[**] *and T.C. Lee*[***]
Department of Industrial & Systems Engineering, The Hong Kong Polytechnic University, Hung Hom, Kowloon, Hong Kong

Abstract

Due to the shift of market trends and increasing awareness of the need to be environmentally friendly, the most important task facing manufacturers is to reduce the part weight significantly without impinging on its function. Use of the light-weight alloys is becoming important in the material selection stage. One of the most common light alloys is titanium alloys. The applications of titanium alloy are not widespread, however, owing to its high cost. To minimize the weight and cost of products and maximize the efficiency and functions of the material usage, tailor-welded blank technology can be combined with the light-weight alloy and applied during the production stage. However, the forming capability of a light-weight alloy and its tailor-welded blanks are relatively limited. In order to counter these disadvantages, one solution is to use temperature as the process parameters during the forming operation. This can increase the ductility significantly and reduce the yield strengths, forces and pressures during the forming process. This chapter will give an overview of he research activities examination titanium tailor-welded blanks under thermal forming condition.

Keywords: Titanium, Tailor-welded Blanks, Thermal, Forming

Introduction

Production of light-in-weight, high strength and fuel-saving products is the trend of modern industry. One of the approaches is the use of light materials, such as titanium alloys,

[*] E-mail address: ise.cplai@polyu.edu.hk. (Corresponding author)
[**] E-mail address: mflcchan@inet.polyu.edu.hk.
[***] E-mail address: mftclee@inet.polyu.edu.hk.

instead of conventional steels. Light-weight alloys are being used widely in different kinds of industries for automobiles, aerospace and domestic use. Compared to other light metals such as aluminum alloys and magnesium alloys, titanium alloys do have advantages, such as high strength, high working temperatures, extraordinary corrosion resistance and competitive light weight [1], although, the high cost of titanium alloy prevents it from being used widely in automotive applications [2].

In order to meet the approaches of fuel saving and cost-effectiveness, tailor-welded blanks (TWBs) technology was developed in the 1980s [3-4]. Combining the advantages of both titanium alloys and the tailor-welded blanks technology, titanium tailor-welded blanks (Ti-TWBs) have great potential for use in other industries, such as in the aircraft, space, marine and military industries [5-6]. Although there has been a number of studies published on TWBs, most have only concentrated on steel blanks. Thus, there is a great need for a better and more thorough understanding of the formability of Ti-TWBs.

It is well acknowledged that titanium alloy sheets and their TWBs will normally characterize a low ductility and yield a very poor formability in process operations under room temperature [7]. In recent years, products are becoming increasingly complicated in order to meet customer expectations. Superplastic forming (SPF) seemed to be a unique solution for producing complex titanium alloys products in the past [8]. However, this technique is inefficient in meeting the requirements of high production rate and low price. The warm forming of titanium tailor-welded blanks is being developed to circumvent the aforementioned shortcomings.

In this chapter the thermal forming condition of Ti-TWBs was simulated with a specially designed forming device and temperature controller [9]. Different forming temperatures can be chosen to investigate the forming behaviors of Ti-TWBs. Using a combination of experimental and theoretical analysis, the optimum formability of forming Ti-TWBs can be identified. This research studied the accuracy and characteristics of the structural deformation and mechanical behaviors of Ti-TWBs under the thermal forming process at different elevated temperatures. It is vital for designers and engineers to understand the process fully and to characterize it accurately so that engineers and designers can fabricate high-quality heterogeneously structured components successfully and economically.

Mechanical Properties of Titanium Tailor-Welded Blanks

Titanium, one of the world's metallic elements, constitutes 0.6% of the earth's crust. It is a light, lustrous, corrosion-resistance metal of a silvery metallic color. Its density is 60% and its weight is 43% lighter than steel [10]. One of the most commonly used titanium alloys is an alpha-beta alloy containing 6% Al and 4% V. It is usually referred to as Ti-6Al-4V, and exhibits an excellent combination of corrosion resistance, strength and toughness [7]. Ti-6Al-4V is used widely in aircraft, military, spacecraft and consumer products [11]. Some basic mechanical properties of Ti-6Al-4V [12] are listed as follows:

Table 1. The general mechanical properties of Ti-6Al-4V (Annealed, Grade 5).

Mechanical Properties	Metric value
Density	4.43kg/m^3
Poisson ratio (@20°C)	0.342
Ultimate tensile strength (@20°C)	950MPa
Yield strength (@20°C)	880MPa
Elongation at break (@20°C)	14 – 15%
Shear Modulus	44.0GPa
Shear Strength	550 MPa
Melting point	1600 – 1650 °C

Welding Methods of Ti-Twbs

The tailor-welded blank (TWB) technology has matured since the 1990s. The recent developments in welding technology and considerations of material cost, dimensional accuracy and weight, have forced automakers and appliance manufacturers to use tailor-welded blanks in the stamping operations. The main advantage of using tailor-welded blanks is reduction of the amount of scrap due to the odd shapes of the blanks. Smaller pieces of metals which form oddly shaped blanks can be nested easily for better utilization [13]. Tailor-welded blanks present the opportunity to manufacture steel components with the minimum quantity of material, thus reducing overall weight. The continuous weld-line and thickness differential in TWBs can often result in difficulty in stamping. The marketing advantages and legislation associated with the demand for reduced fuel consumption and reduced emissions of TWBs have been addressed.

TWB is considered to be one of the structural products which combines different materials, thicknesses and mechanical properties [2]. It can be joined by different welding processes, such as tungsten inert gas (TIG) welding [14-15], resistance welding, electron beam welding [16], and laser welding [17-20]. Some potential applications of high power laser have been purposed [11] for welding different types of metal sheets, like carbon steel, aluminum alloys, magnesium alloys and titanium alloys. Nowadays, the laser welding is recommended for fabricating light-weight structures, especially joining titanium alloy because of low distortion, small HAZ, narrow weld bead and high consistency [5, 21]. It can also be achieved without undercut and porosity [24]. In addition, the laser welding can afford a high aspect-ratio bead, low distortion and excellent mechanical properties, which make it possible to create well-designed, advance-performance, light-weight structures [12, 18, 21]. Combinings the advantages of both titanium alloy and TWB technology, Ti-TWBs exhibits its excellent mechanical properties.

Laser Welding Technique of Ti-Twbs

In fact, the weldability of titanium alloy is fair-to-good compared with other light-weight alloys [22]. Some engineers or manufacturers consider that titanium and its alloy are difficult to weld due to serious weld cracking problems. In order to investigate the thermal formability

study of Ti-TWBs, high quality Ti-TWBs should be prepared in advance. The well-planned preparation before welding is a necessity. The edges of the specimen were cut and ground by a milling process to ensure all are as smooth as possible and have regular profiles. The oxide layer and machining contamination on the specimen surface can be removed by chemical pickling. One typical pickling solution is 27% HNO_3, 3% HF and the balance is water [23].

A special welding fixture [24] has been designed and developed for alignment and fit up during the laser welding process. Optimal welding parameters can be obtained by fine-adjusting the laser power, welding speed, focal length and shielding gas flow so as to fabricate the qualified Ti-TWBs. Visual assessment can be used as the initial inspection of the weld quality. The color change of weldment surface is an indicator to determine the shielding arrangement and the oxidizing potential during the process. The satisfactory color is silver or light straw; on the contrary, grey or white colors mean unacceptable levels of heavy contamination at the weldment. The sample of qualified Ti-TWBs is shown in Figure 1. Further destructive inspections, metallographic examination, uniaxial tensile test, and microhardness test, were carried out to examine the weld quality in accordance with titanium welding handbook [5] and ISO standards 15612-11:2002 [25].

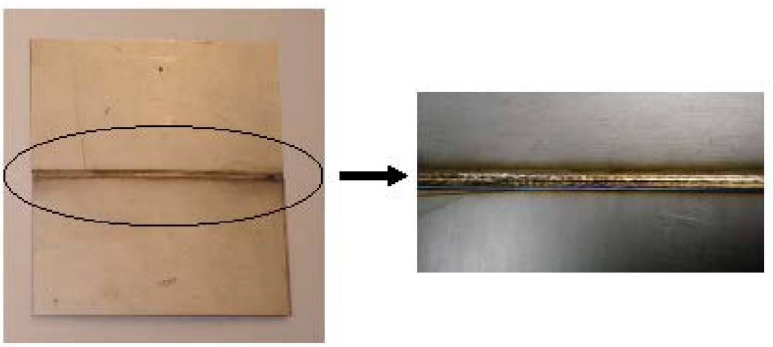

Figure 1. Visual inspection of Ti-TWB.

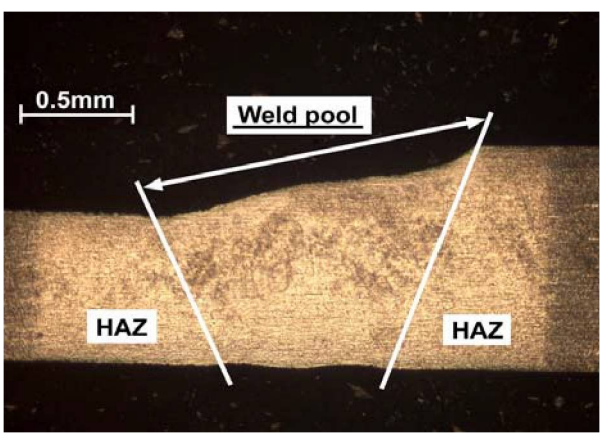

Figure 2. The cross-sectional weld profile of weldment obtained from an acceptable Ti-TWB (0.7mm/1.0mm) [24].

Intrinsic Examination of Ti-Twbs

Macroscopic examination is another approach for inspecting weld profile [26-27]. The microstructure of the weldzone is very complex, showing the phase transformation during the laser welding process, as shown in Figure 2. It shows the full penetration and without porosity inside the weld. As well, the enlarged photo shows that the microstructure transits rapidly from the weldment to the parent metal via the heat affected zone (HAZ). It can be observed that,

- Weldment: The consist of a mixture of martensitic (α"), acicular (α') and primary (α)
- HAZ: The primary alpha (α) structure to the mixture of short martensitic and acicular (α"+α')

The microhardness and strength distributions at the weldment should be improved compared with the parent metal. The hardness and ultimate strength of HAZ and weldment is higher than that of the parent metal. The optimum case is when the hardness of weldment is 10-15% more than the parent metal; otherwise, brittleness should occur. Some researchers have also found that the acicular matensite (α') presents the highest hardness at the weldment [28] then improves the strength as well.

In addition, the mechanical properties of the weldment in Ti-TWBs have been investigated under various temperatures [27-29]. All regions (i.e. parent metal, HAZ and weldment) show poor ductility at temperature below 450ºC with relatively high ultimate tensile strength. The special dual-image image capturing system [28] device is employed to determine the deformation during the processing. The system was applied to other laser welded blanks and investigated successfully with high accuracy. The results reveal that the strength was higher than the parent metal but the ductility decreased accordingly.

Thermal Forming of Titanium Tailor-Welded Blanks

As we known, light-weight construction leads to TWBs associated with the poor formability. Forming light-weight products, at room temperature, particular titanium alloys, can lead to problems including poor workability, potential embitterment, notch sensitivity and high cost of supplying [30-45]. In the past, superplastic forming (SPF) seemed to be the best solution for forming titanium alloy parts [46-51] in order to prevent these problems. This process can be used to produce very complex shapes and integrated structures. However, the production rate is very slow due to the slow strain rates and the high cost of equipment with protective atmosphere (i.e. argon and helium). Some findings have demonstrated that the optimum superplastic forming condition is the temperature within 750ºC – 950ºC and the strain rate is approximately 2×10^{-2} s^{-1}[52]. Indeed, some studies have been concerned chiefly with the formability of traditional steel TWB [53-59]. The formability of other light-weight alloy TWBs under room temperature or superplastic forming (SPF forming) [60-66] has been investigated. It appears that studies of the warm forming of Ti-TWBs have been relatively limited, especially those which have taken into account the effects of the tooling temperature.

Tooling for Thermal Forming of Ti-Twbs

In order to carry out the formability study of Ti-TWBs at elevated temperatures, a newly developed tooling device with heating control function has been fabricated and employed for this purpose [9]. This concept has been demonstrated by some researchers in the USA [64, 67] since the 1990s with different sheet materials. The sheet metal testing device – HILLE 20/40 Ton Swift forming tester was selected and modified for this study. Most of the machine configuration was re-designed and modified to satisfy the thermal condition. The temperature control/monitoring device was accompanied by the re-constructed tooling system, in order to control the temperature variation of the die and the blank holder from RT to 600ºC [9]. The temperature variation of the whole system could be ascertained within ±10ºC. The consistent formability of Ti-TWBs could thus be obtained by properly adjusting the temperature control device properly. In addition, heat insulators were installed into the tooling to reduce the heat loss to the surroundings. The schematic diagram of the tooling system with built-in heating elements is shown below:

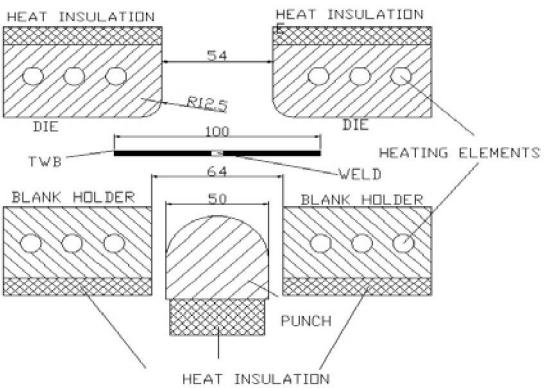

Figure 3. The schematic diagram of the tooling with built-in heating element [9].

Forming Behaviours of Ti-Twbs

Traditional methods of evaluating sheet metal formability were applied directly on the Ti-TWBs. In this section, the limit dome height (LDH) and forming limit diagram (FLD) will be discussed.

The drawability of Ti-TWBs with tooling effect was determined. Specimens in asymmetrical shapes and different widths were produced according to the ASTM standard [68] or other related studies [9, 28]. Specimens in different widths (i.e. 25mm, 90mm and 110mm) and different temperature combinations (i.e. RT, 300C and 550C) were selected and inspected. The results revealed that the LDH values increased approximately twofold increase at 550ºC and showed at least 60% improvement at 300ºC. The results also demonstrated that all Ti-TWBs were preformed even much better at the temperature of 550ºC. Cracks were observed to initiate at the location near the radius of die set and to propagate perpendicular to the major stretching direction. The temperature of the die's corner was higher than that of the surface, whereas the radius section was heat concentrated. The LDH values of Ti-TWBs

produced at the elevated tooling temperature were compared with the base metal [24] and Ti-TWBs without heated tooling. It is clear that the heating control device of the tooling system is an essential installation for stabilizing the temperature of the major components, such as the die, blank holder and punch, through the whole system. It can be concluded that the tooling temperature is one of the major factors affecting the values of LDH [9].

Forming Limit Diagram is another way to determine the formability of sheet metal as well as TWB. It is the most realistic and efficient way to estimate the possibilities of producing a metal part and to avoid unsuccessful design. The FLD indicates the limiting strains that sheet metals can sustain within the range of the major-to-minor strain. To measure the strain displacement relationship, strain analysis by different grid patterns is an efficient method. Many types of grid patterns were used, such as a circle grids pattern, square grids pattern and combination pattern [41, 68-74]. The circle grid size of 2.5mm diameter is recommended to measure the large strains deformation. The square grid is used to measure the strains of non-homogenous deformation [70, 75]. Although, this method is quite time-consuming [76], it can be adapted to measure the sharp strain gradients which are found close to the crack region. Nevertheless, only a few previous publications have been mentioned the grid marking techniques. A reliable and practical technique for TWBs formability analysis is called for.

Electrochemical etching [77], photochemical technique [78] and a combine of these two methods have been studied. The photochemical technique can produce accurate grids but is time-consuming and results in poor adhesion [79]. This technique is used widely for the sheet metal forming process under room temperature. However, the pattern is easily rubbed off due to the friction during the operation. Another method is electrochemical etching, but with this method the accuracy of the grid pattern is not high. The laser marking/engraving method is being developed to overcome these limitations of electrochemical etching and the photochemical technique. A grid pattern marked by laser engraving provides high accuracy and tolerance, and does not damage the material or physical properties of the work-pieces. This method has been used widely in electronic products, metal products and printed circuit boards. In addition, the pattern is accurate for strain analysis [76, 79]. The FLD of Ti-TWBs at 550°C, using laser marked grids is plotted and shown in Figure 4.

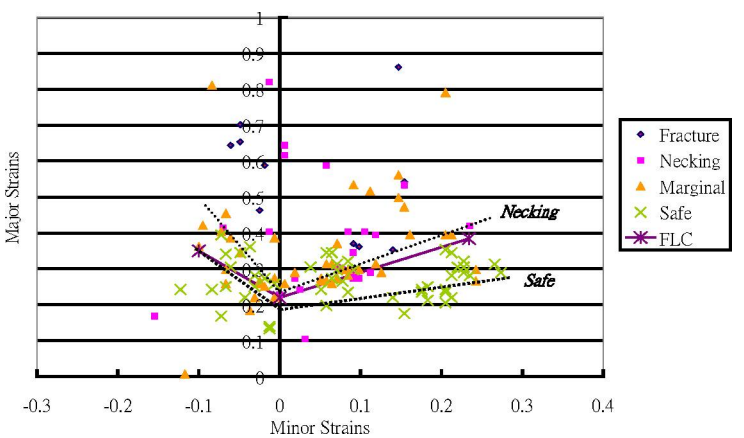

Figure 4. FLD of Ti-TWBs at tooling temperature of 550C [83].

In fact, stress should occur after machining or welding. Most researchers have so far focused on the forming behaviours and material characterization of titanium alloys forming at temperatures below 450°C. There seems to have been no effective way identified to evaluate the effects of residual stresses on the forming capability of the Ti-TWBs. Stress relieving [81] is the solution to this problem. Heat treatment after machining or processing is able to relieve at least 70% of undesirable residual stress of the component. As well, it could not induce any microstructual changes that from non-uniform forging, cold forming, welding and asymmetric machining [82]. It can maintain the shape stability and eliminate unfavorable conditions, such as Bauschinger effect. According to the handbook [82], the Ti-TWBs were heat-treated up to 600°C for about one hour and air-cooled in a normal atmosphere. The mechanical properties of the Ti-TWBs, such as ductility and strength, should not be affected by this stress-relieving process. Both LDH values of treated and non-treated were compared accordingly. The formability of Ti-TWBs was enhanced at least 50% after SR at 300°C and even doubled at 550°C [81].

Finite Element Analysis of Forming Ti-Twbs

Nowadays, the market is facing most significant challenges: overcapacity, international competition, technology improvements, decreasing demand and increasing pressure from customers for low-pricing. Traditional trial-and-error methods used to evaluate the formability of materials and possibility of design is time consuming and expensive. Numerical simulation is being developed to meet the market demand. The software allows engineers to minimize the rework cost during the actual production stage. Also, it has proven to be efficient to check all possible defects at the design stage [84-98]. The troubleshooting and optimizing processes through the computer simulation rather than through extensive shop trials have been realized. Forming simulation of TWBs, both traditional steels and light-weight alloys, are already being used in the automobile industries [89]. Some of them are used to predict the performance of complicated components [70]. The finite element analysis of the forming process with temperature effect has not yet been extended to Ti-TWBs.

To determine the formability of light-weight alloys and their TWBs, the first priority is to consider numerical simulation of temperature effects, combined with the basic forming phenomena under room temperature. The process parameters and material properties, such as thermal expansion, heat transfer, friction heat and temperature change during the deformation are also need to be taken into account. In addition, selection of the most suitable finite element codes is important for specific sheet metal forming process simulation. Some common types of finite element code have been developed and addressed [90]. In this chapter, one of the common industrial software packages PAM-STAMP™ [91] has been selected for discussion.

PAM-STAMP™ is a general-purpose finite element software package to simulate the entire industrial production. To simulate the warm forming condition of Ti-TWBs, add-on modules with explicit and implicit methods are imported. Some common plasticity criteria are available in this software, such as HILL 48's Material Law with isotropic hardening law, HILL's 48 Material law with isotropic and kinematic hardening law and HILL's 90 criterion.

As in other commercial packages, the forming conditions are user-defined to enhance the accuracy and reliability of the simulated results, including material mechanical properties, forming conditions and tooling geometry. Users can define the tooling geometry in the same way as the actual forming condition. The blanks can be defined as tailor-welded blanks with different thickness combinations or a plain sheet.

The meshing system of this program was refined automatically. One-level refinement was preformed by the system before processing, and then all elements were cut into a number of pieces based on the refinement level which was set by the user. The refinement level ranged from 1-10 and the symmetric diagram of the refinement scheme is illustrated in Figure 5.

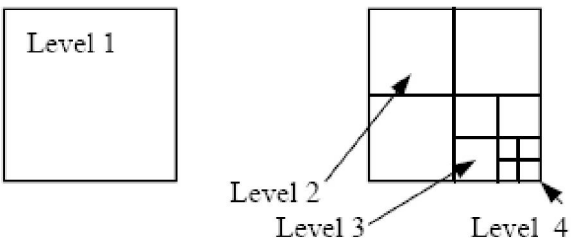

Figure 5. The diagram which illustrated the refinement method of PAM-STAMP [97].

Various stamping results can be obtained such as stress and strain distributions, thickness change in X, Y and Z-axis, failure location of the blanks, thinning of the blank in %, and the time of the deformation process etc. Through these results, the initial crack region and displacement along the z-axis were determined and compared with the experimental results. In fact, the discrepancy between the numerical and experimental results was around 10%. This can be attributed to the isothermal conditions assumed in the simulation and over expectation of the actual heat loss to the surrounding. On the other hand, the initial failure location can be determined obliquely by change of thickness, stress and strain as well the forming limits. According to simulative results, the failure occurring initially at the corner accounts for the stress concentration on both sides of the cylindrical punch rather than the top of the punch surface. Some typical results [92-93] are shown in Figures 6 - 10.

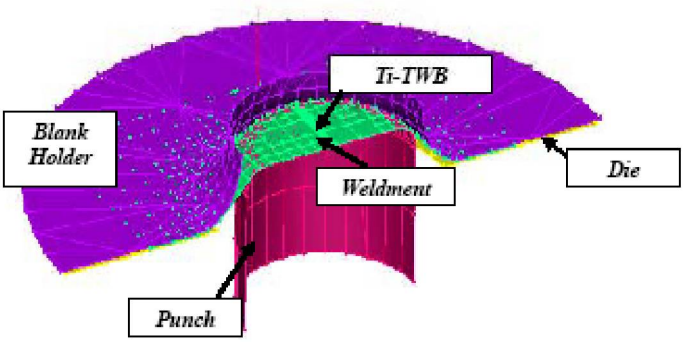

Figure 6. Geometry model in simulation [98].

Figure 7. Specimen of 25mm width Ti-TWB after forming test at 550ºC.

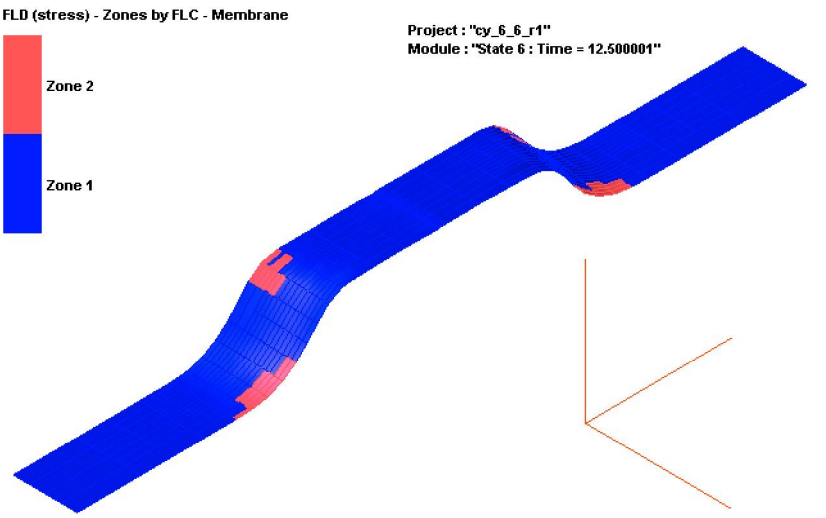

Figure 8. The stress distribution of 25mm width Ti-TWBs after forming test at 550ºC.

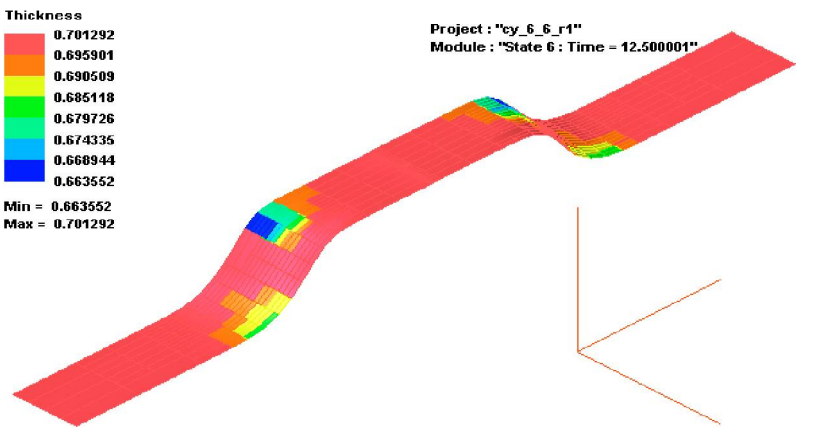

Figure 9. The change of thickness of 25mm width Ti-TWBs after forming test at 550ºC.

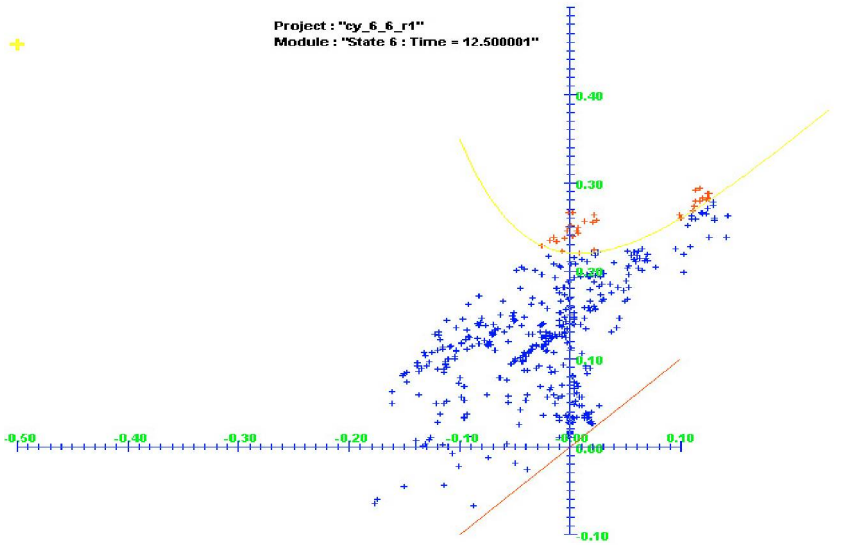

Figure 10. The FLD of stress distribution of 25mm width Ti-TWBs after forming test at 550°C.

Conclusions

This chapter has described an integrative approach to investigating the thermal forming of titanium tailor-welded blanks (Ti-TWBs) has been attempted through quantitative and qualitative analysis.

Ti-TWBs have the advantages of both laser welding and titanium alloy which is used widely in different industries: automobile, aircraft, military and domestic applications. To produce quality Ti-TWBs that are defect free for further experiment, well-planned preparation and examinations should be carried out. Those inspections are in accordance with the titanium welding handbook, metal handbook and international standards. In addition, some destructive testing can be applied to check the metallurgical bond.

Forming Ti-TWBs at room temperature is problematic due to their specific mechanical properties. Superplastic forming (SPF) seems to be a unique solution to forming Ti-TWBs that has been used in the last two decades. With the aid of the modified sheet metal forming device and temperature controller, Ti-TWBs can be formed under a warm forming condition. The ductility of Ti-TWBs is improved at tooling temperature of around 550°C with a low strain rate (i.e. below $1x10^{-2}$/s). In addition, the plasticity of Ti-TWBs can be improved by stress relieving.

Forming Limit Diagram (FLD) and Limit Dome Height (LDH) are the common ways of measuring the forming behaviours of Ti-TWBs. However, the traditional grid marking method is not suitable for Ti-TWBs due to the printing fade-out under high temperature. Laser marking/engraving is the best way to tackle the aforementioned problem with more accurate and a high tolerance.

The finite element analysis package is a reliable and economic method for predicting the failure of the forming process of Ti-TWBs at elevated temperatures. The forming criteria, tooling design and material properties can be defined manually with the package's explicit

model. The predicted results have been found to agree well with those obtained from the experiments. This analysis can be applied readily to the design and manufacture TWB components or structures so as to satisfy the needs and demands of the market.

Acknowledgments

The work described is partially supported by grants from the Research Grants Council of the Hong Kong Special Administrative Region, China (Project No. PolyU 5255/04E) and the Research Committee of the Hong Kong Polytechnic University (Project No. RGDF).

References

[1] Chan S. M., Chan L. C. and Lee T. C., (2003), Tailor-welded blanks of different thickness ratios effects on forming limit diagram, *Journal of Materials Processing Technology,* Vol. 132, pages 95 – 101

[2] Waddell W. and Davies G. M. (1995), Laser welded tailored blanks in the automotive industry, *Welding and Metal Fabrication*, Vol. 63, No. 3, pages 104 – 108

[3] Milian J. L. and Adonyi Y., (1992), Formability of tailored blanks for automotive applications, *Mechanical Working and Steel Processing Conference Proceedings*, Vol. 30, pages 83 – 91

[4] Selige A. and Prange W., (1990), *Laser-welded steel sheet - A new design material,* Stahl und Eisen, September, pages 152 – 153

[5] Smith L. S., Gittos M. F. and Threadgill P. L., (1999), *Welding titanium: a designers and users handbook,* Titanium Information Group

[6] Pallett R. J. and Lark R. J., (2001), The use of tailored blanks in the manufacture of construction components, *Journal of Materials Processing Technology*, Vol. 117, No. 1-2, pages 249 – 254

[7] Lutjering G. and Williams James. C., *Titanium,* Springer (2003)

[8] ASM Handbook; *Forming and Forging*, Vol. 14B.

[9] Lai C. P., Chan L. C. and Chow C. L., (2007), Effects of Tooling Temperatures on Formability of Titanium TWBs at Elevated Temperatures, *Journal of Materials Processing Technology*, Vol. 191, pages 157 – 160

[10] Trogolo J. M. and Dieffenbach J. R., (1998), *SAE Paper* 980446

[11] Donachie M. J., (2000), *Titanium – A Technical Guide,* ASM International

[12] http://www.maweb.com

[13] Geiger M., Hoffmann P. and Hutfless J., (1993), Laser technology in synergy with forming technology, *Blech Rohre Profile*, Vol. 40(4), pages 324 – 330

[14] Choi B. H. and Choi B. K., (2008), The Effect of Welding Conditions according to Mechanical Properties of pure Titanium, *Journal of Materials Processing Technology,* Vol. 201, n 1-3, pages 526 – 530

[15] Feige N. G. and Mitchell D. R., (1967), Welding of Alpha-Beta Titanium Alloys in One Inch Plate, *Welding Journal*, Vol. 46, pages 193 – 202

[16] Yunlian Q., Ju D., Quan H. and Liying Z., (2000), Electron beam welding. *Material Science and Engineering A,* Vol. 280, pages 177 – 181

[17] Liu Q. S., Mahdavian S. M., Aswin D. and Ding S. (2009), Experimental study of temperature and clamping force during Nd:YAG Laser butt welding, *Optics & Laser Technology*, Vol. 41 (6), pages 794 – 799

[18] Akman E., Demir A., Canel T., Sınmazçelik T. (2009), Laser welding of Ti6Al4V titanium alloys, *Journal of Materials Processing Technology*, Vol. 209 (8), pages 3705 –3713

[19] *http://www.Key-to-Metals.com*

[20] Li Z., Gobbi S. L., Norris I., Zolotovsky S. and Richter K. H., (1997), Laser welding techniques for titanium alloy sheet, *Journal of Materials Processing Technology,* Vol. 65, pages 203 – 208

[21] Hideki Fujii, Kazuhiro Takahashi and Yoshito Yamashita, (2003), Application of Titanium and Its alloy for Automobile Parts, *Nippon Steel Technical Report*, No. 88, pages 70 –75

[22] Gao Y., He S. Y., Yang D. Z. and Geng H. B., (2002), Effect of low temperature on tensile properties of aged TC4 alloy, *Materials Science and Technology (Chinese),* Vol. 10, No. 4, pages 352 – 356

[23] ASM Handbook, *Surface Cleaning*, Vol. 5

[24] Cheng C. H., Chan L. C., Lai C. P. and Chow C. L., (2006), Formability of Ti-TWBs at elevated temperatures, *SAE Transactions – Journal of Materials and Manufacturing,* pages 327 – 335

[25] British Standard. (2002). Specification and qualification of welding procedures for metallic materials – *Welding procedure test - Part 11: electron and laser beam welding,* EN ISO 15614-11.

[26] Smith W. F., *Structure and Properties of Engineering Alloys*, 2nd Ed. McGraw-Hill, 1993, pages 433 – 484

[27] Wang S. H., Wei M. D. and Tsay L. W., (2003), Tensile Properties of LBW welds in Ti-6Al-4V alloy at elevated temperatures below 450°C, *Materials Letters*, Vol. 57, pages 1815 – 1823

[28] Chan L. C., Lai C. P., Chow C. L. and Cheng C. H., (2009), Experimental Approach on Stress-strain Analysis of Weldment in Ti-TWBs at Elevated Temperatures, *International Journal of Advanced Manufacturing Technology*, Vol. 40, n5-6, pages 470-477

[29] Cheng C. H., Chan L. C., Tang C. Y and Chow C. L., (2005), Determination of True Stress-Strain Curve for the Weldment of Aluminum Laser-welded Blanks, *Journal of Laser Applications*, Vol. 17 (30), Pages 159 – 170

[30] Doege E. and Droeder K., (2001), Sheet metal forming of magnesium wrought alloys – formability and process technology, *Journal of Materials Processing Technology*, Vol. 115, pages 14 – 19

[31] Yin D. L., Zhang K. F., Wang G. F. and Han W. B., (2005), Warm deformation behavior of hot-rolled AZ31 Mg alloy, *Materials Science and Engineering A,* Vol. 392A, pages 320 – 325

[32] Quan G. F., (2005), Yield and plastic deformation of Mg-alloy AZ31 at elevated temperatures, *Material Science Forum*, Vol. 488-489, pages 623 – 628

[33] Chen Fuh-Kuo and Huang Tyng-Bin, (2003*),* Formability of stamping magnesium-alloy AZ31 sheets, *Journal of Materials Processing Technology*, Vol. 142, pages 643-647

[34] Zhang K. F., Yin D. L. and Wu D.Z., (2006), Formability of AZ31 magnesium alloy sheets at warm working condition, *International Journal of Tools and Manufacture*, Vol. 146, pages 1276 – 1280

[35] Odenberger Eva-Lis, Pederson Robert, Oldenburg Mats, (2008), Thermo-mechanical material response and hot sheet forming Ti-6242, *Materials Science and Engineering*: A, Vol. 489, Issues 1-2, pages 158 – 168

[36] Neugebauer R., Altan T., Geiger M., Kleiner M., Sterzing A., (2006), Sheet Metal Forming at Elevated Temperatures, *CIRP Annals - Manufacturing Technology*, Vol. 55, Issue 2, Pages 793 – 816

[37] Thomas J. F., Oh S. I. and Gegel H. L.,(1980), Sheet Forming of Titanium Alloys, *Proceedings of the World Conference of Titanium*, pages 81 – 100

[38] Bachelet E. and Honnorat Y., (1984), Recent Development Trends in the Forming Techniques of Titanium Alloys, *Proceedings of the World Conference of Titanium*, pages 453 – 460

[39] Lee Y. H., Lee C. S., Shim, T. JU. Hwang S. M. and Shim I. O., (2004), High temperature forming of Ti6Al4V alloy considering microstructural evolution, *Key Engineering Materials* Vol. 274 – 276, pages 117 – 122

[40] Suzuki H. G., Fujii H. and Takano N., (1988), Hot Workability of Titanium Alloys investigated using hot tensile testing machine, *Industrial Heating*, pages 18 – 20, 25

[41] Chen Fuh-Kuo and Chiu Kuan-Hua, (2005), Stamping formability of pure titanium sheets, *Journal of Materials Processing Technology*, Vol. 170, pages 181 – 186

[42] Jones P., Hutchison W. B., (1981), Stress-state dependence of slip in titanium-6Al-4V and other HCP metals, *Acta Metallurgica*, Vol. 29, pages 951 – 968

[43] Vanderhasten M., Rabet L., and Verlinden B., (2008), Ti-6Al-4V: Deformation map and modelisation of tensile behaviour, *Materials & Design*, Vol. 29, pages 1090 – 1098

[44] Stevenson R., (1981), *The low temperature deformation behavior of 5182-O and 2036-T4 aluminum,* Report GMR-3865, General Motor Research laboratories (Warren, MI)

[45] Shehata F., Painter M. J. and Pearce R., (1978), Warm forming of aluminum/magnesium alloy sheet, *Journal of Mechanical Working Technology*, Vol. 2, pages 279 – 290

[46] Wenhai Ji, Zhenguo Wang and Feiling Song, (1990), Development of SPF amd SPF/DB techniques of Ti and Al Alloys and their applications, *Proceeding of the International Conference of Superplasticity in Metals, ceramics and intermetallics symposium*, pages 173 – 180

[47] Paton N. E. and Hamilton C. H., (1984), Superplasticity in Titanium Alloys, *Proceedings of the Fifth International Conference on Titanium Congress*, Vol. 2, pages 649 – 672

[48] Wisbey A. and Goodwin P. S., (1997), Superplasticity in advanced titanium base materials, *Materials Science Forum*, Vol. 243 – 245, pages 537 – 546

[49] Swale W. and Broughton R., (2004), Applying superplastic forming principles to titanium sheet metal forming problems, *Materials Science Forum,* Vol. 447 – 448, pages 239 – 246

[50] Dutta A., Birla N. C. and Gupta A. K.,(1983), Some aspects in superplastic behaviour of Ti-6Al-4V Alloy, *Transactions of the Indian Institute of Metals*, Vol. 36 (3), pages 169 – 180

[51] Dunne F. P. E. and Kim T. Q., (1982), *Inhomogeneous deformation and failure in Superplasticity,* Proceedings of the Royal Society of London, Series A, Vol. 455, pages 719 – 735

[52] Arieli A. and Rosen A., (1977), *Superplastic Deformation of Ti-6Al-4V,* Metallurgical Transactions A, Vol. 8, pages 1591 – 1596

[53] Azama K., Ikemoto K., Arima K., Sugiura H. and Takasago T., (1988), *Sheet Metals in Forming processes, Proceedings of the 16th biennial congress,* ASM International, pages 205 – 215

[54] Nakagawa N., Ikura S. and Natsumi F., (1993), *SAE Papers* 930522

[55] Iwata, N., Matsui, M., Nakagawa, N. & Ikura, S. (1993). *NUMISHEET* 93, Proceedings of the 2nd International Conference of Numerical Simulation 3D Sheet Metal Forming Processes, pages 303 – 312

[56] Radlmayr K. M. and Szinyur J., (1991), *Proceeding of IDDRG Working groups meeting,* Association of Italian Metallurgy, Milano, Vol. 2

[57] Shi M. F., Pickett K. M. and Bhatt K. K., (1993), *SAE paper* 930278

[58] Wang B. Y., Shim M. F., Sadrina H. and Lin F., (1995*), SAE paper* 950376

[59] Saunders F. I. and Wagoner R. H., (1996), Forming of Tailor-welded Blanks, *Metallurgical and Materials Transactions A*, Vol. 27A, pages 2605 – 2616

[60] Bravar, M., Kinsey, B. and Krishnan, N., (2005), Comparison of Analytical Model to Experimental Results and Numerical Simulations for Tailor Welded Blank Forming, *Proceedings of the ASME Applied Mechanics Division* 2004, pages 13-19

[61] Sastry, S. M. L., Lederich, R.J., Mackay, T. L. and Kerr, W. R.,(1983), Superplastic Forming Characterization of Titanium Alloys, *Journal of Metals*, Vol. 35 (1), pages 48 – 52

[62] http://www.kobelco.co.jp/english/titan/2.1

[63] http://www.deutschetitan.de/

[64] Hirata T., Oguri T., Hagino H., Tanaka T., Wook C. S. and Tsujikawa M., (2007), Formability of Friction Stir Welded and Arc Welded 5083 Aluminum Alloy Sheets, *Key Engineering Material*, Vol. 340 – 341, pages 1473 – 1478

[65] Miles M. P., Melton D. W. and Nelson T. W., (2005), Formability of Friction-Stir-welded Dissimilar Aluminum-alloy sheets, *Metallurgical and Materials Transactions A,* Vol. 36 pages 3335 – 3342

[66] Bayley C. J., Pilkey A. K., (2006), A Bifurcation Criterion for Predicting Weld-line Failures in AA5754 Alloy Tailor-welded Blanks, *Materials Science and Engineering: A,* Volumes 435 – 436, Pages 62 – 70

[67] Leighmen D. E. and Lee D., (1994), The Effect of Tooling Temperature on the Formability of Sheet Steel, *Journal of Materials Processing Technology*, Vol. 45, pages 577 –582

[68] ASTM E2218-2002, *Standard Test method for Determining Forming Limit Curves*

[69] Leung Y. C., Chan L. C., Tang C. Y. and Lee T. C.,(2004), An Effective Process of Strain Measurement for Severe and Localized Plastic Deformation, *International Journal of Machine Tools & Manufacture*, Vol. 44, pages 669 – 676

[70] Dally J. W., (1991), *Experimental Stress Analysis*, McGraw-Hill, New York

[71] Lee W. B. and Wen X. Y., (2000), A Dislocation-model of Limit Strain Prediction in Aluminum Sheet Metals under Biaxial Deformation, *International Journal of Damage Mechanics*, Vol. 9, pages 286 – 301

[72] Chan L. C., Cheng C. H., Jie M. and Chow C. L., (2005), Damage-based Formability Analysis for TWBs, *International Journal of Damage Mechanics*, Vol. 14, pages 83 – 96

[73] Wang C. C., Lee J., Chen L. W. and Lai H. Y., (2002), A New Method for Circular Grid Analysis in the Sheet Metal Forming Test, *Experimental Mechanics*, Vol. 40, pages 190 – 196

[74] Lai C. P., Chan L. C. and Chow C. L., (2007), *Grids* Reformation for Effective Strain Measurement of Forming Titanium Tailor-welded Blanks at Elevated Temperatures, Experimental Analysis of Nano and Engineering Materials and Structures*: Proceedings of the 13th International Conference on Experimental Mechanics*, pages 459 – 460

[75] Marciniak Z., Duncan J. L. and Hu S. J., (2002), *Mechanics of Sheet Metal Forming*, Butterworth Heinemann

[76] Nibeberlein V. A., (1980), Thermal Marking, Proceeding of American Society of Mechanical Engineers and American Institute of Chemical Engineers, *Joint National Heat Transfer Conference*, Orlando, Fla.

[77] Keeler S. P., (1971), *Sheet Metal Industries*

[78] Keeler S. P., (1968), *Machinery*

[79] Richard L. Stevenson, (1984), Laser engraving for microelectronic packaging marking, *Proceedings of the Technical Conference* – IEPS, *Fourth Annual International Electronics Packaging Conference*, pages 383 – 391

[80] McClean W., McCandless A. J. and Bahrani A. S., (1978), A Strain-Measurement System for Sheet-metal Forming, *Sheet Metal Industries*, July, pages 653 – 658

[81] Lai Chiping, Chan Luenchow and Chow Chiloong, (2006*),Effect of Stress Relieving on Limit Dome Height of Titanium Tailor-welded Blanks at Elevated Temperatures, Materials Science Forum*, Vol. 522-523, pages 977 – 980

[82] *ASM Handbook, Heat Treating, Vol. 4*

[83] Lai C. P. and Chan L. C., (2007), Comparative Study of Forming Titanium Tailor-welded Blanks under Single and Multi-stage Forming Process at Elevated Temperatures, *Proceedings of the 11th World Conference on Titanium* (Ti-2007), Vol. II, pages 1013-1016

[84] Piela A., Kocanda A. and Zimniak Z., (2001), FEM Simulation of Drawing of Tailor-welded Blanks, *Simulation of Materials Processing*: *Theory, Methods and Applications*, pages 795 – 800

[85] Frewin M. R. and Scott D. A., (1992), Finite Element Simulation of Welding of Large Structures, *Journal of Engineering for Industry*, Vol. 114(11), pages 441 – 451

[86] Meinders T., A. van den Berg, Huétink J., (2000), Deep drawing simulations of tailored blanks and experimental verification, *Journal of Materials Processing Technology*, Vol. 103, pages 65-73

[87] Kinsey B., Liu Z., Cao J., (2000), A novel forming technology for tailor welded blanks, *Journal of Materials Processing Technology*, Vol. 99, pages 145 – 153

[88] Tisza M., (1998), Application of FEM Simulation in Process Planning of Deep-drawing, *Proceedings of the First ESAFORM Conference*, pages 169 – 178

[89] Thomas W. and Altan T., (1998), Application of Computer Modeling in Manufacturing of Automotive stampings. *Steel Research*, Vol. 69 (4/5), pages 181 – 187

[90] Makinouchi A., (1996), Sheet Metal Forming Simulation in Industry, *Journal of Material Processing Technology*, Vol. 60, pages 19 – 26

[91] *PAM-STAMP Manual*

[92] Lai C. P., Chan L. C. and Chow C. L., (2007), Warm Forming Simulation of Titanium Tailor-welded Blanks with Experimental Verification, *Materials Processing and Design -- Proceeding of the 9th International Conference on Numerical Methods in Industrial Forming Processes*, pages 1621 – 1626

[93] Cheng Chi-Ho and Chan Luen-chow, (2006), Forming Simulation of Ti-TWBs at Different Elevated Temperatures, *Materials Science Forum*, Vol. 532 – 533, pages 981 – 984

In: Titanium Alloys: Preparation, Properties and Applications ISBN: 978-1-60876-151-7
Editor: Pedro N. Sanchez, pp. 441-471

Chapter 12

MODE I FRACTURE BEHAVIOR OF TITANIUM ALLOY TC6 IN COMPARISON WITH STEEL AND ALUMINUM ALLOYS UNDER THERMAL/MECHANICAL LOADING: IN-PLANE TENSION CASE

X.S. Tang [*]
School of Civil Engineering and Architecture, Changsha University of Science and Technology, Changsha, Hunan, 410114, China

Abstract

Fracture behaviors of titanium alloy TC6 under thermal/mechanical and mode I condition are discussed and compared with steel and aluminum materials. Considered is a line crack in an infinite plate subjected to the combined mechanical and thermal loading. The problem is solved in the framework of thermoelastic theory by integrating with the complex function method. An analytical solution is obtained under the boundary condition that the constant temperature is retained on the crack surfaces while the remote uniform heat flow is imposed. In this case, thermal loading only induces the mode I stress intensity factor and at the same time the mode II thermal stress intensity factor vanishes. Moreover, the heat flow component along the normal direction to the crack line has no influence on the thermal stress intensity factor which only depends on the heat flow component parallel to the crack line. The problem is a typical mode I crack problem. Fracture behaviors of three materials, say TC6 titanium, 38Cr2Mo2VA steel and LY12 aluminum alloys, are analyzed under the combination of mechanical and thermal loading by application of strain energy density factor theory. The applied failure stresses at different scales are numerically calculated. By comparison, the fracture resistances of three materials are different. It is found that the thermal loading would enhance the crack propagation. If the direction of heat flow is changed to an opposite direction, the thermal effect would impede the crack growth. That is the thermal effect has the positive or negative effect which depends on the direction of heat flow.

Keywords: thermoelasticity; complex function method; mode I crack; mechanical and thermal loading; crack growth; failure analysis; analytical solution; fracture resistance; strain energy density factor theory.

[*] E-mail address: tang_xuesong@sina.com (Xue-Song Tang); Fax: +86-731-85256006. (Corresponding author)

1. Introduction

The safety assessment is a vital problem for pressurized vessels and pipes, aircrafts and structural members when a crack prevails. An overview for this subject can be found in [1]. The failure behavior of solids is affected not only by mechanical loads but also by the change of temperature. These external disturbances can interact and their influence on the structural integrity can be reflected by the energy stored in a unit volume of material. Determination of the volume energy density will involve mechanical deformation in addition to changes in temperature [2]. In solids, the predominant effect of heat transfer is due to heat conduction while convection is negligible small and radiation need not be considered unless the environment calls for it. Moreover, if the temperature gradients are not sufficiently great to cause material transformation, then for all practical purposes the thermoelastic parameters may be assumed to be temperature independent. Coupling between the stress and temperature fields may also be disregarded. The conventional theory of linear thermoelastic theory can thus be applied such that the temperature field is determined independent of the stress or strain fields [3, 4].

Some early investigations for the crack problem subjected to heat flow can be found in [5-7] which revealed that the temperature field has no singularity at the crack tip like the displacement field. The temperature gradient was found to increase unboundedly as a function of $1/\sqrt{r}$ as $r\to 0$, where r is the distance measured from the crack tip. This singular character is preserved in the thermoelastic stress field in the vicinity of the crack tip. The corresponding strain energy density function dW/dV possesses the singularity of $1/r$. Unlike the stresses whose singular behavior depends on the constitutive relation, the $1/r$ singularity of dW/dV field remains unchanged not only for all constitutive relations, but also for all shapes of planes of discontinuities. This conclusion has been further proved by using a molecular dynamics approach [8].

The thermal/mechanical coupling effect for a cracking structural member has been a concern in recent years. Some of these works are listed here. Three new analytical/experimental groups of methods are developed including isodyne methods, strain gradient methods and thermoelastic methods in [9]. Crack opening and closure under the action of mechanical and thermal loads is discussed in [10]. Thermoelastic solutions for cracked bodies under some types of thermal loading are obtained in [11]. A plane problem for a thermally insulated interface crack with a contact zone in an isotropic bimaterial under tension–shear mechanical loading and a temperature flux is solved in [12]. An interaction integral to account for non-uniform temperatures is derived in [13]. The algorithm is then implemented in conjunction with commercial finite element software to calculate the stress intensity factors. Crack arrest analyses for the cracked conducting plates by Joule heating are addressed in [14, 15]. In addition, the piezothermoelastic problems are also interested in the researches [16-19].

It should be emphasized that there are two basic ways in which a volume element absorbs energy: an element can store energy by "dilatation" and "distortion". The former is associated with the change in volume and the latter is associated with the change in shape. When an element of the material exceeds a certain threshold fracture could occur. The tradition of mechanics is to treat the surface properties as a separate entity from those in the bulk. It becomes troublesome when dealing with the behavior of objects whose volume-to-surface

ratios can change from the very small to the very large. Thus, the isoenergy density theory has been developed by accounting for volume to surface ratio effect [20]. Hysteresis loop effect for polycrystals under mechanical/thermal condition is predicted by application of isoenergy density theory [21, 22]. The mutually interacting thermal/mechanical effects are accounted for by retaining the rate of change of volume with surface dV/dA, in the surface/volume energy density theory [23].

This work focuses on the fracture behavior of titanium alloy under the combination of mechanical and thermal loading. It is found that the temperature boundary condition plays an important role for the failure process of a material.

2. Analytical Model and Temperature Field

Now consider an infinite plate with a central crack of length $2a$. The uniform tensile stress σ^{∞} is applied at infinite. A uniform heat flow is also applied at infinite. There is an angle between two directions of heat flow and crack line. The heat flow can be divided into to parts, respectively, along two coordinate axes. Note that the heat flow is proportional to the negative temperature gradient. Two temperature gradient components along two coordinate axes at infinite are denoted by $\Theta_{,1}^{\infty}$ and $\Theta_{,2}^{\infty}$. The analytical model for the problem is depicted in Fig. 1.

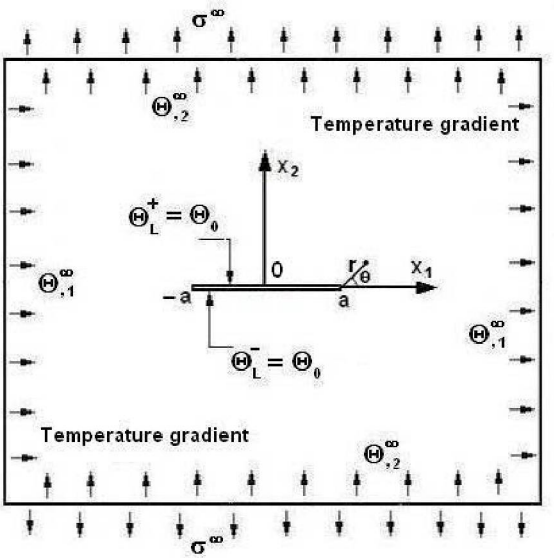

Figure 1. A schematic of the analytical model.

There is no heat source in the plate. It is a typical heat conduction problem. The governing differential equation is the Laplace equation, say $\nabla^2\Theta = 0$. The solution of Laplace equation can be written as

$$\Theta = \frac{1}{2}[F(z) + \overline{F(z)}] \tag{1}$$

where Θ stands for the temperature difference to the reference temperature. $F(z)$ is an analytical function which should be determined from the thermal boundary conditions. It can be derived from Eq. (1) that

$$F'(z) = \Theta_{,1} - i\Theta_{,2} \tag{2}$$

and

$$F'(z) + \overline{F'(z)} = 2\Theta_{,1} \tag{3}$$

Assume that the temperature on the upper and lower surfaces of the crack keeps constant, i.e.,

$$\Theta_{\mathrm{L}}^{+} = \Theta_{\mathrm{L}}^{-} = \Theta_0, \text{ on L} \tag{4}$$

The symbol "L" denotes the crack line. "+" and "–" stand for, respectively, the upper and lower crack surfaces. Θ_0 is the constant temperature on the upper and lower crack surfaces. Eq. (4) is identical to

$$\Theta_{,1}^{+} = \Theta_{,1}^{-} = 0, \text{ on L} \tag{5}$$

It can be derived from Eq. (5) that

$$\begin{cases} [F'(t) + \overline{F}'(t)]^{+} + [F'(t) + \overline{F}'(t)]^{-} = 0 \\ [F'(t) - \overline{F}'(t)]^{+} - [F'(t) - \overline{F}'(t)]^{-} = 0 \end{cases}, \text{ on L}, \ -a \le t \le a \tag{6}$$

where t is a real argument.

Eq. (6) describes a typical Hilbert problem. The solution for the Hilbert problem can be found in [24]. The solution of Eq. (6) is

$$F'(z) + \overline{F}'(z) = \frac{2(c_0 + c_1 z)}{\sqrt{z^2 - a^2}} \tag{7}$$

$$F'(z) - \overline{F}'(z) = -2\Gamma \tag{8}$$

Eqs. (7) and (8) give the expression of $F(z)$ as

$$F'(z) = \frac{c_0 + c_1 z}{\sqrt{z^2 - a^2}} - \Gamma \tag{9}$$

$$\overline{F}'(z) = \frac{c_0 + c_1 z}{\sqrt{z^2 - a^2}} + \Gamma \tag{10}$$

A comparison between Eqs. (9) and (10) shows that c_0 and c_1 are the real constants while Γ is a pure imaginary. According to the boundary condition of temperature gradients at infinite, it is found that

$$c_1 = \Theta_{,1}^{\infty}, \ \Gamma = i\Theta_{,2}^{\infty} \tag{11}$$

such that

$$F'(z) = \frac{c_0 + \Theta_{,1}^{\infty} z}{\sqrt{z^2 - a^2}} - i\Theta_{,2}^{\infty} \tag{12}$$

By integrating Eq. (12), it is obtained that

$$F(z) = c_0 \log[z + \sqrt{z^2 - a^2}] + \Theta_{,1}^{\infty}\sqrt{z^2 - a^2} - i\Theta_{,2}^{\infty} z + A \tag{13}$$

and

$$\begin{aligned}\Theta = \frac{c_0}{2}[\log(z + \sqrt{z^2 - a^2}) + \log(\overline{z} + \sqrt{\overline{z}^2 - a^2})] + \\ \frac{\Theta_{,1}^{\infty}}{2}(\sqrt{z^2 - a^2} + \sqrt{\overline{z}^2 - a^2}) - \frac{i}{2}\Theta_{,2}^{\infty}(z - \overline{z}) + \frac{A + \overline{A}}{2}\end{aligned} \tag{14}$$

It is seen that the temperature solution Eq. (14) satisfies the single-valued condition of the temperature. For a pure heat conduction problem without any heat source in the plate, the heats flow into and flow out any closed curve C should be the same, i.e., $\oint_C F'(z)dz = 0$. This gives c_0=0. The constant A can be determined from the temperature boundary condition on the crack surfaces. Eq. (14) can be substituted into Eq. (4) to yield

$$\Theta_{\mathrm{L}}^{+} = \frac{A + \overline{A}}{2} = \Theta_0, \text{ on } \mathrm{L}^{+}; \ \Theta_{\mathrm{L}}^{-} = \frac{A + \overline{A}}{2} = \Theta_0, \text{ on } \mathrm{L}^{-} \tag{15}$$

Hence, the constant A can be taken as

$$A = \overline{A} = \Theta_0 \tag{16}$$

Finally, the full field temperature solution is given by

$$F(z) = \Theta_{,1}^{\infty}\sqrt{z^2 - a^2} - i\Theta_{,2}^{\infty} z + \Theta_0 \tag{17}$$

$$\Theta = \frac{1}{2}\Theta_{,1}^{\infty}(\sqrt{z^2 - a^2} + \sqrt{\bar{z}^2 - a^2}) - \frac{i}{2}\Theta_{,2}^{\infty}(z - \bar{z}) + \Theta_0 \tag{18}$$

The asymptotic solution of the temperature near the crack tip is expressed as

$$\Theta = \Theta_{,1}^{\infty}\sqrt{2ar}\cos\frac{\theta}{2} + \Theta_{,2}^{\infty} r\sin\theta + \Theta_0 \tag{19}$$

where r is the distance from the crack tip.

The analytical solution of temperature field for an orthotropic plate with a central crack under the same thermal boundary condition has been obtained in [25], which can be reduced to the isotropic case. The result is the same as Eqs. (18) and (19). Take a=10 mm, Θ_0=100 K, $\Theta_{,1}^{\infty} = \Theta_{,2}^{\infty} = 100$ K/m. The temperature distribution in the crack region is illustrated in Fig. 2. The curves are symmetrical to the x_2-axis with the V-shape. The straight line segment in the center corresponds to the temperature condition on the upper and lower crack surfaces given by Eq. (4).

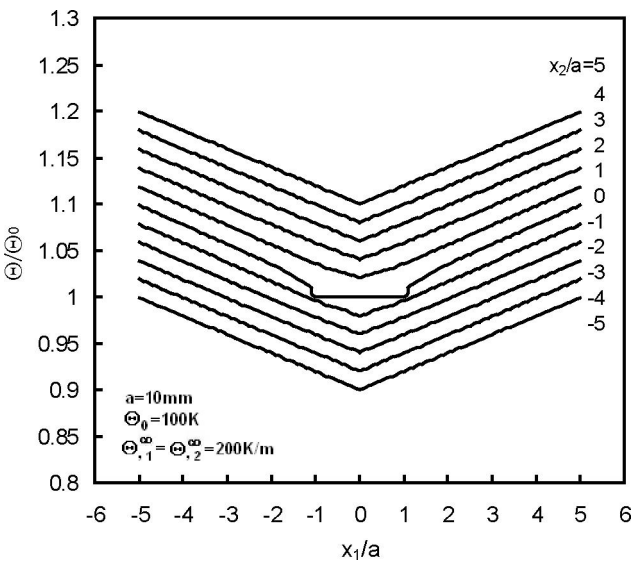

Figure 2. Temperature distribution near the crack.

3. Thermal Stresses

The general solution of the thermal stresses for an infinite plane with a centered crack is expressed as

$$\sigma_{22}^{\Theta} + \sigma_{11}^{\Theta} = 2[(z^2 - a^2)^{-\frac{1}{2}} f(z) + g(z) + (\bar{z}^2 - a^2)^{-\frac{1}{2}}\overline{f(z)} + \overline{g(z)}] \tag{20}$$

$$\sigma_{22}^{\Theta}-\sigma_{11}^{\Theta}+2i\sigma_{12}^{\Theta}=2\Big\{(z^2-a^2)^{-\frac{1}{2}}[\bar{f}(z)-f(z)]-[g(z)+\bar{g}(z)]- (z-\bar{z})[(\bar{z}^2-a^2)^{-\frac{1}{2}}f'(z)+g'(z)-(z^2-a^2)^{-\frac{3}{2}}zf(z)]\Big\} \tag{21}$$

where $f(z)$ and $g(z)$ are two continuous analytical functions in the plane. The superscript "Θ" denotes the thermal effect. Eqs. (20) and (21) have satisfied the free-free condition on the upper and lower crack surfaces. According to the stress boundary condition at infinite, the functions $f(z)$ and $g(z)$ should be of the form

$$f(z)=F_0+F_1z,\ g(z)=G_0 \tag{22}$$

The thermal stresses should vanish at infinite. This requires that

$$F_1=0,\ G_0+\overline{G}_0=0 \tag{23}$$

The constant G_0 represents the rigid rotation of the body such that it can be taken as zero, G_0=0. Eqs. (20) and (21) become

$$\sigma_{22}^{\Theta}+\sigma_{11}^{\Theta}=2[(z^2-a^2)^{-\frac{1}{2}}F_0+(\bar{z}^2-a^2)^{-\frac{1}{2}}\overline{F}_0] \tag{24}$$

$$\sigma_{22}^{\Theta}-\sigma_{11}^{\Theta}+2i\sigma_{12}^{\Theta}=2\Big\{(z^2-a^2)^{-\frac{1}{2}}[\overline{F}_0-F_0]+z(z-\bar{z})(z^2-a^2)^{-\frac{3}{2}}F_0\Big\} \tag{25}$$

The constant F_0 can be determined from the single-valued displacement condition. The displacement solution is written as

$$2\mu(u_1^{\Theta}+iu_2^{\Theta})=\kappa F_0\alpha_0(z)-(z-\bar{z})\overline{F}_0\alpha_0'(z)-F_0\alpha_0(\bar{z})+\alpha E\int F(z)dz+\text{const.} \tag{26}$$

where α, E and μ are the linear expansion coefficient, Young's modulus and shear modulus. ν is the Poisson's ratio and $\kappa=3-4\nu$ for plane strain. Function $F(z)$ has been given by Eq. (17). Function $\alpha_0(z)$ is in the form of

$$\alpha_0(z)=\log[z+\sqrt{z^2-a^2}] \tag{27}$$

It is well known that function $\alpha_0(z)$ is multi-valued such that the coefficient of $\alpha_0(z)$ in Eq. (26) should vanish. This requires that

$$(\kappa+1)F_0-\frac{1}{2}\alpha Ea^2\Theta_{,1}^{\infty}=0 \tag{28}$$

$$F_0=\frac{\alpha Ea^2\Theta_{,1}^{\infty}}{2(\kappa+1)} \tag{29}$$

Finally, we obtain the asymptotic solution of the thermal stresses and the expression of the stress intensity factor as

$$\sigma_{11}^{\Theta}=\frac{K_1^{\Theta}}{\sqrt{2\pi r}}\cos\frac{\theta}{2}\left(1-\sin\frac{\theta}{2}\sin\frac{3\theta}{2}\right) \tag{30}$$

$$\sigma_{22}^{\Theta}=\frac{K_1^{\Theta}}{\sqrt{2\pi r}}\cos\frac{\theta}{2}\left(1+\sin\frac{\theta}{2}\sin\frac{3\theta}{2}\right) \tag{31}$$

$$\sigma_{12}^{\Theta}=\frac{K_1^{\Theta}}{\sqrt{2\pi r}}\sin\frac{\theta}{2}\cos\frac{\theta}{2}\cos\frac{3\theta}{2} \tag{32}$$

where

$$K_1^{\Theta}=\frac{\alpha Ea\Theta_{,1}^{\infty}}{\kappa+1}\sqrt{\pi a}\ ,\ K_2^{\Theta}=0 \tag{33}$$

It is clear that only the mode I thermal stress intensity factor prevails while the mode II thermal stress intensity factor vanishes. It is a typical crack problem of mode I. The stress intensity factor is only related to the heat flow along x_1-direction. The heat flow along x_2-direction does not produce thermal stresses.

4. Strain Energy Density Contours under Mechanical and Thermal Loading

Under the combination of thermal and mechanical loading, the asymptotic solution of the total stress field in the vicinity of crack tip are written as [2]

$$\sigma_{11}=\frac{K_1}{\sqrt{2\pi r}}\cos\frac{\theta}{2}\left(1-\sin\frac{\theta}{2}\sin\frac{3\theta}{2}\right) \tag{34}$$

$$\sigma_{22}=\frac{K_1}{\sqrt{2\pi r}}\cos\frac{\theta}{2}\left(1+\sin\frac{\theta}{2}\sin\frac{3\theta}{2}\right) \tag{35}$$

$$\sigma_{12} = \frac{K_1}{\sqrt{2\pi r}} \sin\frac{\theta}{2}\cos\frac{\theta}{2}\cos\frac{3\theta}{2} \tag{36}$$

$$\sigma_{33} = \nu(\sigma_{11} + \sigma_{22}) - \alpha E\Theta\,,\ \sigma_{13} = \sigma_{23} = 0 \tag{37}$$

where r and θ are the local polar coordinates measured from the crack tip as shown in Fig. 1. The term $\alpha E\Theta$ in Eq. (37) is nonsingular since the temperature field is nonsingular at the crack tip in view of Eq. (18) or (19). It can be omitted. The total stress intensity factor K_1 is a sum of the mechanical and thermal parts.

$$K_1 = K_1^{\sigma} + K_1^{\Theta} \tag{38}$$

The mechanical and thermal stress intensity factors K_1^{σ} and K_1^{Θ} have been known as

$$K_1^{\sigma} = \sigma^{\infty}\sqrt{\pi a}\,,\ K_1^{\Theta} = \frac{\alpha E a \Theta_{,1}^{\infty}}{\kappa + 1}\sqrt{\pi a}\,,\ K_1 = (\sigma^{\infty} + \frac{\alpha E a \Theta_{,1}^{\infty}}{\kappa + 1})\sqrt{\pi a} \tag{39}$$

Eqs. (39) indicate that the temperature gradient $\Theta_{,1}^{\infty}$ can be regarded as an equivalently applied stress at infinite denoted by σ_{Θ}^{∞} which is written as

$$\sigma_{\Theta}^{\infty} = \frac{\alpha E a \Theta_{,1}^{\infty}}{\kappa + 1} \tag{40}$$

Therefore, the total applied stress at infinite is equal to

$$\sigma = \sigma^{\infty} + \sigma_{\Theta}^{\infty} \tag{41}$$

where σ^{∞} is the mechanical part and σ_{Θ}^{∞} is the thermal part.

The strain energy density for the thermoelastic problem is expressed as

$$\frac{\mathrm{d}W}{\mathrm{d}V} = \frac{1}{2}\sigma_{ij}\varepsilon_{ij} - \frac{1}{2}\alpha\Theta\sigma_{kk} \tag{42}$$

By application of the constitutive relation of linear thermoelasticity

$$\varepsilon_{ij} = \frac{1+\nu}{E}\sigma_{ij} - \frac{\nu}{E}\sigma_{kk}\delta_{ij} + \alpha\Theta\delta_{ij} \tag{43}$$

The strain ε_{ij} in Eq. (42) can be eliminated and Eq. (43) becomes

$$\frac{dW}{dV} = \frac{1+\nu}{2E}\left(\sigma_{ij}\sigma_{ij} - \frac{\nu}{1+\nu}\sigma_{kk}^2\right)$$
$$= \frac{1+\nu}{2E}\left[\sigma_{11}^2 + \sigma_{22}^2 + \sigma_{33}^2 - \frac{\nu}{1+\nu}(\sigma_{11}+\sigma_{22}+\sigma_{33})^2 + 2\sigma_{12}^2\right] \quad (44)$$

where dW/dV is the strain energy density function per unit volume. Note that Eq. (44) has the same form as the isothermal problem. However, the thermal effect is implicit in Eq. (44). Removing the term σ_{33} by using Eq. (37), Eq. (44) takes the form for plane strain

$$\frac{dW}{dV} = \frac{1+\nu}{2E}\left[\sigma_{11}^2 + \sigma_{22}^2 - \nu(\sigma_{11}+\sigma_{22})^2 + 2\sigma_{12}^2\right] \quad (45)$$

Eq. (44) can also be written as

$$\frac{dW}{dV} = \frac{3}{2}\sigma_m\varepsilon_m - \frac{1}{2}\alpha\Theta\sigma_{kk} + \frac{1}{2}s_{ij}e_{ij} \quad (46)$$

in which $\sigma_m = \sigma_{kk}/3$ and $\varepsilon_m = \varepsilon_{kk}/3$ are the hydrostatic stress and strain; s_{ij} and e_{ij} are the deviatoric stress and strain. The dilatational part $(dW/dV)_v$ and distortional part $(dW/dV)_d$ of strain energy density are

$$\left(\frac{dW}{dV}\right)_v = \frac{3}{2}\sigma_m\varepsilon_m - \frac{1}{2}\alpha\Theta\sigma_{kk} \quad (47)$$

$$\left(\frac{dW}{dV}\right)_d = \frac{1}{2}s_{ij}e_{ij} \quad (48)$$

By application of Eq. (43) to eliminate the strain, Eqs. (47) and (48) become

$$\left(\frac{dW}{dV}\right)_v = \frac{1-2\nu}{6E}(\sigma_{11}+\sigma_{22}+\sigma_{33})^2 = \frac{(1-2\nu)(1+\nu)^2}{6E}(\sigma_{11}+\sigma_{22})^2 \quad (49)$$

$$\left(\frac{dW}{dV}\right)_d = \frac{1+\nu}{6E}[(\sigma_{11}-\sigma_{22})^2 + (\sigma_{22}-\sigma_{33})^2 + (\sigma_{33}-\sigma_{11})^2 + 6\sigma_{12}^2]$$
$$= \frac{1+\nu}{3E}[\sigma_{11}^2 + \sigma_{22}^2 - \sigma_{11}\sigma_{22} - \nu(1-\nu)(\sigma_{11}+\sigma_{22})^2 + 3\sigma_{12}^2] \quad (50)$$

The substitutions of Eqs. (34)~(36) into Eqs. (45), (49) and (50) yield

$$\frac{\mathrm{d}W}{\mathrm{d}V}=\frac{(1+\nu)(1+\cos\theta)(3-4\nu-\cos\theta)}{8\pi Er}K_1^2 \tag{51}$$

$$\left(\frac{\mathrm{d}W}{\mathrm{d}V}\right)_{\mathrm{v}}=\frac{(1-2\nu)(1+\nu)^2(1+\cos\theta)}{6\pi Er}K_1^2 \tag{52}$$

$$\left(\frac{\mathrm{d}W}{\mathrm{d}V}\right)_{\mathrm{d}}=\frac{(1+\nu)(1+\cos\theta)[2(1-2\nu)^2+3(1-\cos\theta)]}{24\pi Er}K_1^2 \tag{53}$$

Eqs. (51)~(53) show that the constant contours of dW/dV, $(dW/dV)_v$ and $(dW/dV)_d$ are not affected by the thermal effect. That is they have the same form as the isothermal case [2]. The contours look like the ear, apple and dumbbell, respectively for dW/dV, $(dW/dV)_v$ and $(dW/dV)_d$ as shown in Figs. 3.

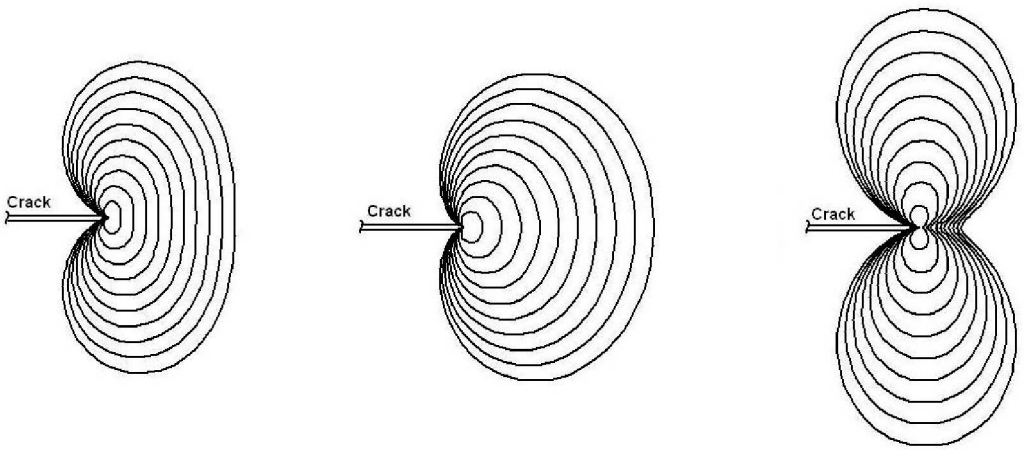

(a) Contours of dW/dV (b) Contours of $(dW/dV)_v$ (c) Contours of $(dW/dV)_d$

Figure 3. Contours of dW/dV, $(dW/dV)_v$ and $(dW/dV)_d$ near the crack tip.

5. Strain Energy Density Factor

In the linear elastic fracture mechanics theory, the strain energy density factor S is defined as $dW/dV=S/r$ [2]. By substituting Eqs. (34), (35), (36) and (39) into Eq. (49), the strain energy density factor S is in the form of

$$S=A_{11}(\sigma^{\infty})^2+2A_{12}\sigma^{\infty}\Theta_{,1}^{\infty}+A_{22}(\Theta_{,1}^{\infty})^2 \tag{54}$$

where

$$A_{11}=\frac{(1+\nu)(1+\cos\theta)(3-4\nu-\cos\theta)a}{8E} \tag{55}$$

$$A_{12} = \frac{(1+\nu)(1+\cos\theta)(3-4\nu-\cos\theta)\alpha a^2}{32(1-\nu)} \tag{56}$$

$$A_{22} = \frac{(1+\nu)(1+\cos\theta)(3-4\nu-\cos\theta)]\alpha^2 Ea^3}{128(1-\nu)^2} \tag{57}$$

Three materials are chosen to perform the numerical calculations. They are steel alloy 38Cr2Mo2Va, aluminum alloy LY12 and titanium alloy TC6. The material parameters for three materials can be found in [26] and are given in Table 1. Note that Poisson's ratio of steel alloy 38Cr2Mo2Va cannot be found in [26] and is assigned to a value of 0.3 in the numerical calculations.

Table 1. Material parameters at room temperature [26].

Material Parameters	Titanium alloy TC6	Steel alloy 38Cr2Mo2VA	Aluminum alloy LY12
$\alpha \times 10^{-6}$ (1/°C)	9.2	12.94	21.4
E (GPa)	113	200	68
ν	0.3	Not found	0.33
K_{1c} (MN/m$^{3/2}$)	60.0	58.8	37

The thermal effect can be positive or negative depending on the direction of temperature gradient. Refer to the third expression of Eqs. (39). When the temperature gradient $\Theta_{,1}^{\infty}$ reaches a critical value

$$(\Theta_{,1}^{\infty})^c = -\frac{4(1-\nu)}{\alpha Ea}\sigma^{\infty} \tag{58}$$

the thermal effect can counteract the mechanical loading completely. Take a=10mm and $\sigma^{\infty} = 10\text{MPa}$. For three different materials, the values of $(\Theta_{,1}^{\infty})^c$ are

$$(\Theta_{,1}^{\infty})_{ti}^{c} = -2693\text{K/m}\,,\ (\Theta_{,1}^{\infty})_{st}^{c} = -1082\text{K/m}\,,\ (\Theta_{,1}^{\infty})_{al}^{c} = -1842\text{K/m}\,. \tag{59}$$

Figs. 4, 5 and 6 illustrate the strain energy density factor S versus angle θ curves for three materials, say titanium alloy TC6, steel alloy 38Cr2Mo2Va and aluminum alloy LY12. The curves are symmetric since the problem is mode I. The minimum values of S occur at θ=0 that indicates the crack propagation for mode I is self-similar.

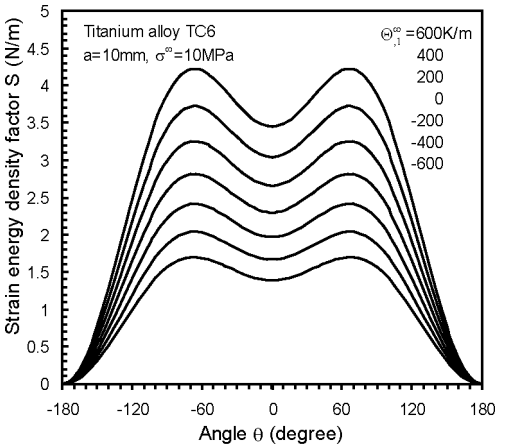

Figure 4. Strain energy density factor S versus angle θ curves for titanium alloy TC6.

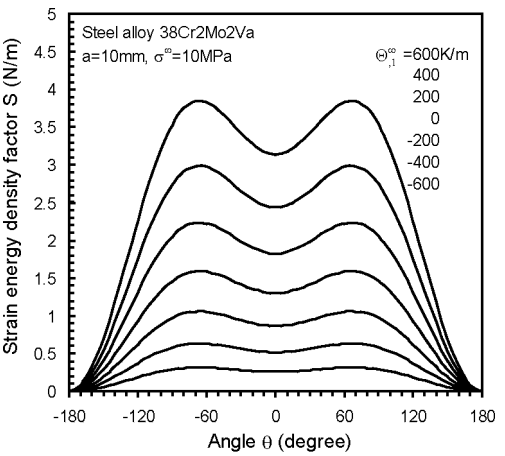

Figure 5. Strain energy density factor S versus angle θ curves for steel alloy 38Cr2Mo2Va.

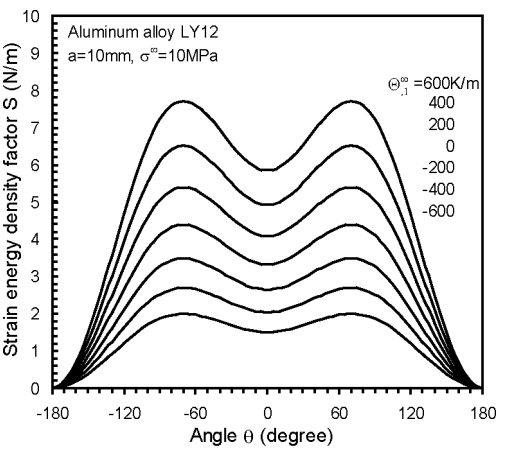

Figure 6. Strain energy density factor S versus angle θ curves for aluminum alloy LY12.

6. Strain Energy Density Factor Criterion

In the linear elastic fracture mechanics, the mode I fracture toughness K_{1c} and the critical strain energy density factor S_c for the plane strain problem are related by the expression [2]

$$S_c = \frac{(1+\nu)(1-2\nu)K_{1c}^2}{2\pi E} \tag{60}$$

The strain energy density factor criterion is plotted in Fig. 7. Crack growth is assumed to initiate when the maximum of the local minimum of dW/dV or $(dW/dV)_{mim}^{\max}$ reaches a critical value $(dW/dV)_c$. At the micro-, meso- and macro-scale, the orders of magnitudes of r/a are 10^{-4}, 10^{-2}~10^{-3} and 10^{-1} respectively. It is seen that the critical values of dW/dV at the different scale levels are different. The order of magnitude of $(dW/dV)_{\text{macro}}$ might be MPa while $(dW/dV)_{\text{micro}}$ might be GPa. The areas below the lines $(dW/dV)_{\text{micro}}$, $(dW/dV)_{\text{meso}}$ and $(dW/dV)_{\text{macro}}$ are the relative critical values of the strain energy density factors, say S_{micro}, S_{meso} and S_{macro}.

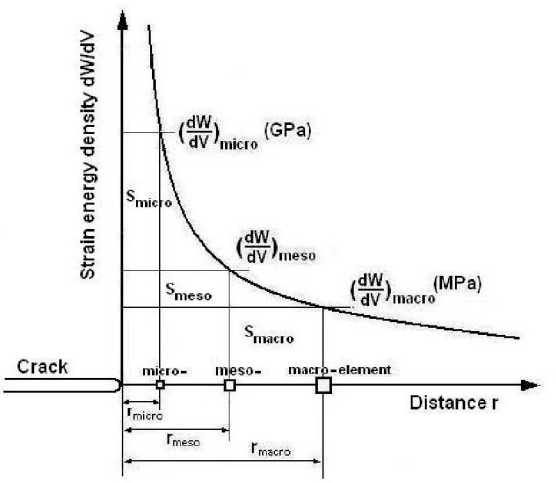

Figure 7. Fracture criterion at different scale levels.

Fracture is a process that necessarily involves crack initiation, growth and rapid propagation. These three stages are in fact one of the same process and should be assessed accordingly in order to avoid inconsistencies. The energy density criterion can satisfy the aforementioned requirement and be in terms of three hypotheses:

1) The location of fracture initiation is assumed to coincide with the maximum of minimum of dW/dV or $(dW/dV)_{mim}^{\max}$.
2) Failure by crack initiation and growth is assumed to occur when $(dW/dV)_{mim}^{\max}$ reaches a critical value $(dW/dV)_c$ being characteristics of the material.
3) Stable crack growth increments r_1, r_2, etc., are assumed to be governed by

$$\left(\frac{dW}{dV}\right)_c = \frac{S_1}{r_1} = \frac{S_2}{r_2} = \cdots = \frac{S_j}{r_j} = \cdots = \frac{S_c}{r_c} = \text{const.} \tag{61}$$

Unstable fracture is assumed to take place when

$$\left(\frac{dW}{dV}\right)_c = \frac{S_c}{r_c} \tag{62}$$

where r_c is the critical ligament ahead of a crack.

Eqs. (61) and (62) show that crack growth consists of a sequence of nucleation processes involving the burst of isolated energy pockets over the discrete ligaments r_1, r_2, etc. For monotonically increasing loads, each succeeding segment would increase in size:

$$r_1 < r_2 < \cdots < r_j < \cdots < r_c \tag{63}$$

This is plotted in Fig. 8. A relative increase in the energy density intensity factors takes place:

$$S_1 < S_2 < \cdots < S_j < \cdots < S_c \tag{64}$$

A terminal segment r_c would eventually be reached to trigger global instability. Such a threshold in energy release quantified by S_c has been referred to in fracture mechanics as the "fracture toughness" that is characteristics of the material's resistance to fracture at the macroscale level. The critical ligament should be sufficiently large such that homogeneity could be invoked to swear out the discreteness of the material microstructure while sufficiently large amount of energy could also be packed in the ligament to trigger global instability.

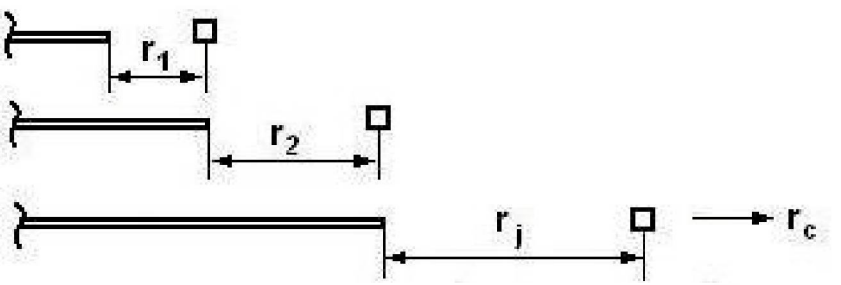

Figure 8. Increasing crack growth segments leading to instability.

In situations where the loads transmitted to the crack tip decrease monotonically, then the inequalities in Eqs. (63) and (64) are reversed as

$$r_1 > r_2 > \cdots > r_j > \cdots > r_a \tag{65}$$

$$S_1 > S_2 > \cdots > S_j > \cdots > S_a \tag{66}$$

This would result in crack arrest as in the indentation tests [22, 23]. In general, the load may fluctuate and the description of crack growth will correspond to a combination of Eqs. (63) and (65) as dictated by the load spectrum.

7. Failure Stress Analysis

By application of the strain energy density criterion, it is needed to determine the angle θ_0 of crack initiation. For a fixed distance r from the crack tip, the minimum of dW/dV is equivalent to minimum of S which can be found from the conditions

$$\frac{\partial S}{\partial \theta} = 0, \quad \frac{\partial^2 S}{\partial \theta^2} > 0 \tag{67}$$

Substituting Eq. (54) into Eq. (67), it can be found that

$$\sin\theta\,[\cos\theta - (1-2\nu)] = 0 \tag{68}$$

It is shown from Eq. (68) and in Figs. 4~6 that there are three minima of S or $(dW/dV)_{\min}$ at the points $\theta = -180^o, 0^o, 180^o$. The maximum of minimum S or $(dW/dV)_{mim}^{\max}$ occurs at the point $\theta = 0^o$. The maximum point of S or $(dW/dV)_{\max}$ can be determined from $\cos\theta = (1-2\nu)$. The maximum point is located in the angle range -70^o to -65^o and 65^o to 70^o as shown in Figs. 4~6. It is clear that the crack would initiate along the angle θ_0=0° direction for mode I problem.

Let σ_f^{∞} represents the critical remotely applied stress that sets off cracking when the thermal loading is applied. $K_{1c} = \sigma_c\sqrt{\pi a}$ corresponds to the onset of rapid fracture with no thermal loading applied. Note that the thermal loading has the positive or negative effect on the applied failure stress depending on the direction of the thermal loading. Along the crack initiation direction $\theta_0 = 0^o$, Eqs. (54)~(57) become

$$S = A_{11}(\sigma^{\infty})^2 + 2A_{12}\sigma^{\infty}\Theta_{,1}^{\infty} + A_{22}(\Theta_{,1}^{\infty})^2 \tag{69}$$

$$A_{11} = \frac{(1+\nu)(1-2\nu)a}{2E} \tag{70}$$

$$A_{12} = \frac{(1+\nu)(1-2\nu)\alpha a^2}{8(1-\nu)} \tag{71}$$

$$A_{22} = \frac{(1+\nu)(1-2\nu)\alpha^2 E a^3}{32(1-\nu)^2} \tag{72}$$

According to the energy density criterion

$$\left(\frac{dW}{dV}\right)_c = \frac{S}{r} \to \frac{S_c}{r_c} \tag{73}$$

The substitutions of Eqs. (69)~(72) into Eq. (73) produces

$$(\sigma_f^\infty)^2 + 2\frac{A_{12}}{A_{11}}\sigma_f^\infty \Theta_{,1}^\infty + \frac{A_{22}}{A_{11}}(\Theta_{,1}^\infty)^2 = \lambda \frac{K_{1c}^2}{\pi a} \tag{74}$$

This gives a relation between σ_f^∞ and $\Theta_{,1}^\infty$ as

$$\sigma_f^\infty = -\frac{A_{12}}{A_{11}}\Theta_{,1}^\infty + \sqrt{\lambda \frac{K_{1c}^2}{\pi a} + \left[\left(\frac{A_{12}}{A_{11}}\right)^2 - \frac{A_{22}}{A_{11}}\right](\Theta_{,1}^\infty)^2} \tag{75}$$

The parameter λ is a scaling factor. A necessary condition is that $\lambda = r/r_c \le 1$ with r_c being the terminal ligament that triggers global instability. When λ=1, i.e., r=r_c, σ_f^∞ given by Eq. (75) is the ultimate failure stress that causes the crack instable growth.

Once the fracture toughness value K_{1c} is known for a given material, the mechanical failure stress σ_f^∞ can be predicted from Eq. (75) for the given crack size a, thermal loading $\Theta_{,1}^\infty$ and scale level λ. Three materials are studied.

Figs. 9, 10, 11 show the failure stress σ_f^∞ versus temperature gradient $\Theta_{,1}^\infty$ curves of steel alloy 38Cr2Mo2VA for scaling parameter λ=0.01, 0.1 and 1, respectively. There is a set of curves in each figure for half crack length a=5, 10, 15,…, 50mm. Fig. 9 indicates that the failure stress σ_f^∞ decreases with the temperature gradient $\Theta_{,1}^\infty$ and the half crack length a. The slope of curves increase with length a that implies the large cracks are more sensitive to thermal effect than the small ones. The curves with large slopes for large cracks are overlapped because the large negative temperature gradient $\Theta_{,1}^\infty$ can pronouncedly increase the failure stress. This effect disappears in Figs. 10 and 11 when the scaling parameter λ is changed from 0.01 to 0.1 and 1. A comparison of Figs. 9, 10 and 11 indicates that the magnitudes of failure stress σ_f^∞ with the increment of λ from 0.01 to 0.1, then to 1, while the curves become flat. Figs. 12, 13 and 14 are the σ_f^∞ versus $\Theta_{,1}^\infty$ curves for aluminum alloy LY12 with λ= 0.01, 0.1, 1, respectively. Figs. 15, 16 and 17 are the curves for titanium alloy LC6 with λ= 0.01, 0.1, 1. They have the similar shapes as those for steel alloy.

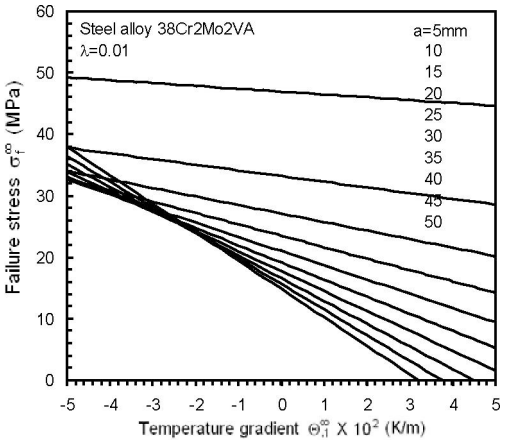

Figure 9. Failure stress versus temperature gradient curves for different crack sizes: λ=0.01, steel alloy 38Cr2Mo2VA.

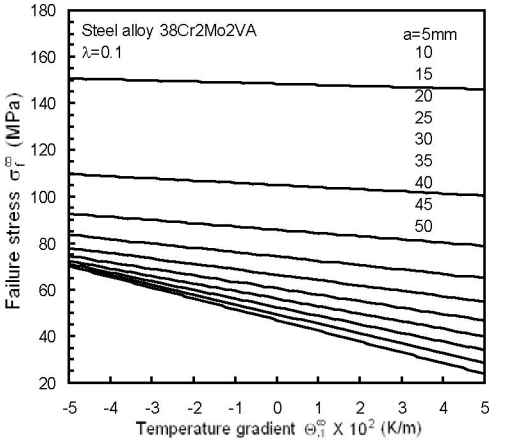

Figure 10. Failure stress versus temperature gradient curves for different crack sizes: λ=0.1, steel alloy 38Cr2Mo2VA.

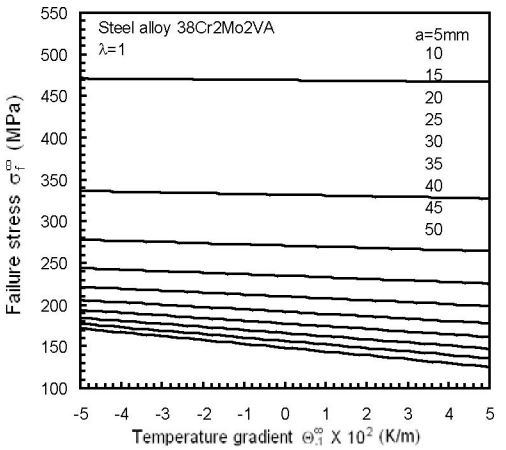

Figure 11. Failure stress versus temperature gradient curves for different crack sizes: λ=1, steel alloy 38Cr2Mo2VA.

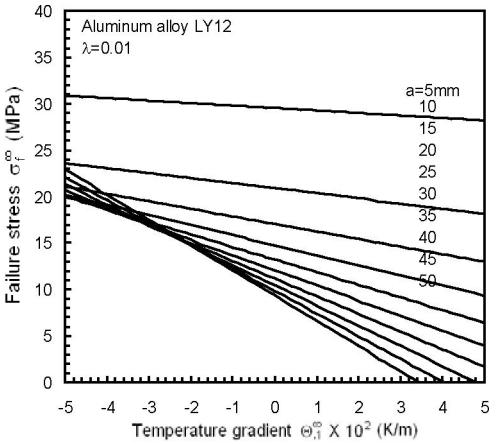

Figure 12. Failure stress versus temperature gradient curves for different crack sizes: λ=0.01, aluminum alloy LY12.

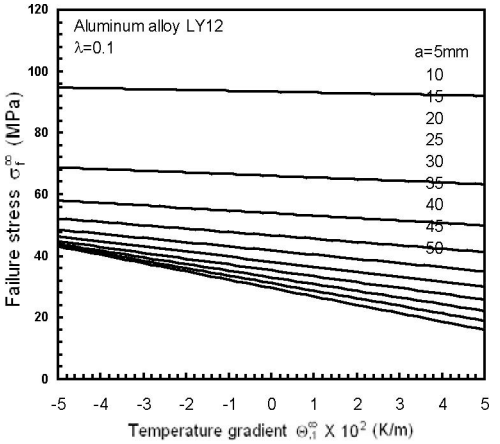

Figure 13. Failure stress versus temperature gradient curves for different crack sizes: λ=0.1, aluminum alloy LY12.

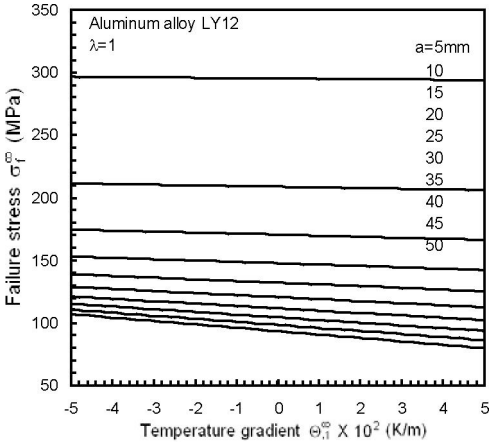

Figure 14. Failure stress versus temperature gradient curves for different crack sizes: λ=1, aluminum alloy LY12.

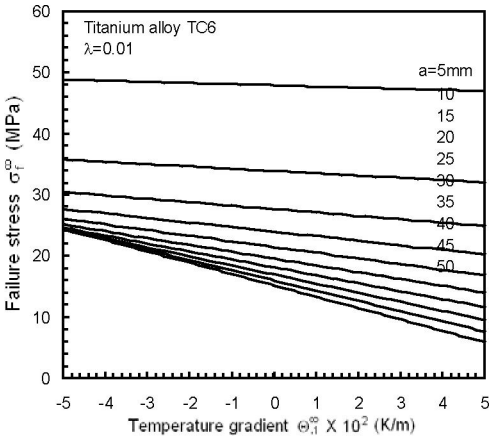

Figure 15. Failure stress versus temperature gradient curves for different crack sizes: λ=0.01, titanium alloy TC6.

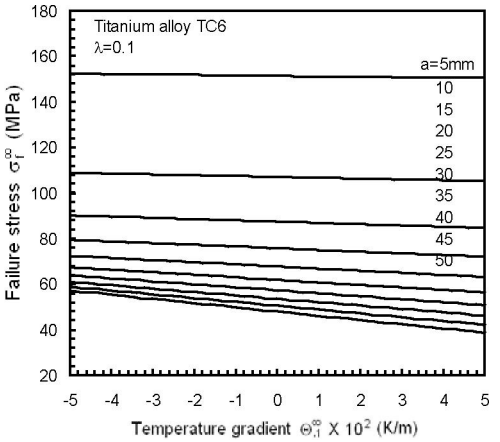

Figure 16. Failure stress versus temperature gradient curves for different crack sizes: λ=0.1, titanium alloy TC6.

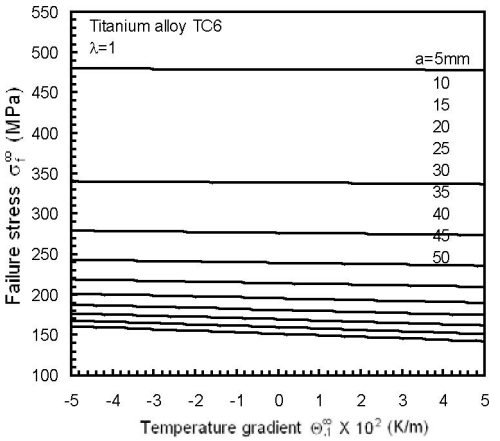

Figure 17. Failure stress versus temperature gradient curves for different crack sizes: λ=1, titanium alloy TC6.

By using the data in Figs. 9 to 17, another set of σ_f^{∞} versus a curves for different $\Theta_{,1}^{\infty}$ can be plotted. Figs. 18, 19 and 20 depict the failure stress σ_f^{∞} versus half crack length a curves for steel alloy 38Cr2Mo2VA with λ=0.01, 0.1 and 1 respectively. In each plot, the curves are bundled at the beginning, then scattered, and decrease with the crack size a. The space of the curves decreases with the increment of scaling parameter λ from 0.01 to 1. For the $\Theta_{,1}^{\infty}$=500K/m curve in Fig. 18, the failure stress σ_f^{∞} vanishes at a=37mm that means only the thermal loading can lead to the crack growth. Figs. 21 to 23, and 24 to 26 are, respectively, for aluminum alloy LY12 and titanium alloy TC6. They exhibit the similar characteristics as steel alloy as shown in Figs. 18 to 20. Note that two curves of $\Theta_{,1}^{\infty}$=-500K/m in Figs. 18 and 21 slightly increase with crack half length a after a>20mm. This effect corresponds to the overlap of curves for large negative temperature gradient $\Theta_{,1}^{\infty}$ in Figs. 9 and 12. With reference to Eq. (39), for the negative temperature gradient the thermal loading would counteract the mechanical loading. In other cases, the failure stress monotonically decreases with the increment of length a.

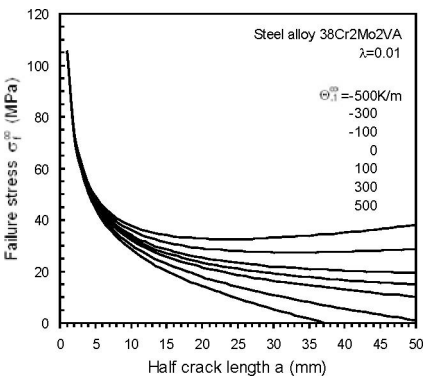

Figure 18. Failure stress versus half crack length curves for different temperature gradient: λ=0.01, steel alloy 38Cr2Mo2VA.

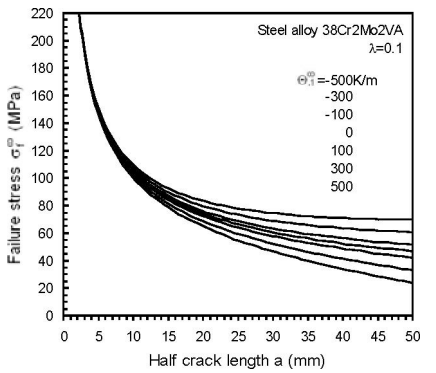

Figure 19. Failure stress versus half crack length curves for different temperature gradient: λ=0.1, steel alloy 38Cr2Mo2VA.

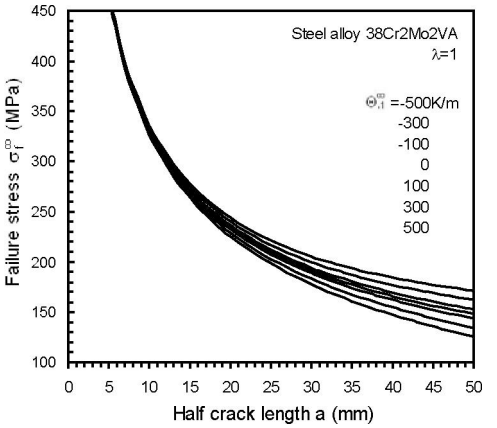

Figure 20. Failure stress versus half crack length curves for different temperature gradient: λ=1, steel alloy 38Cr2Mo2VA.

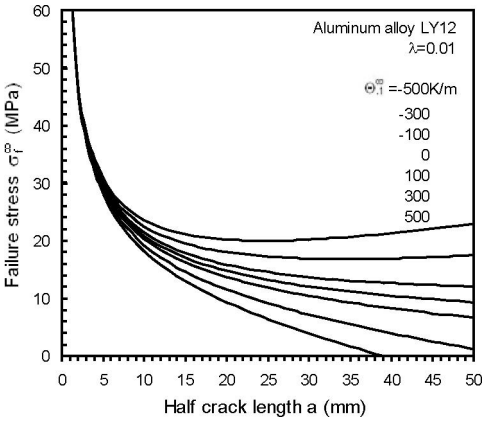

Figure 21. Failure stress versus half crack length curves for different temperature gradient: λ=0.01, aluminum alloy LY12.

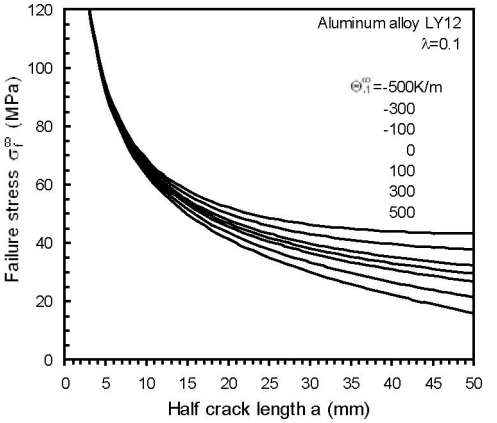

Figure 22. Failure stress versus half crack length curves for different temperature gradient: λ=0.1, aluminum alloy LY12.

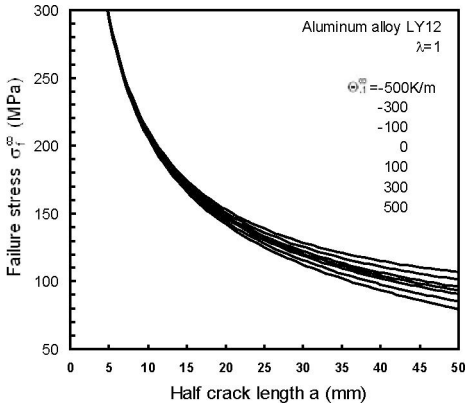

Figure 23. Failure stress versus half crack length curves for different temperature gradient: λ=1, aluminum alloy LY12.

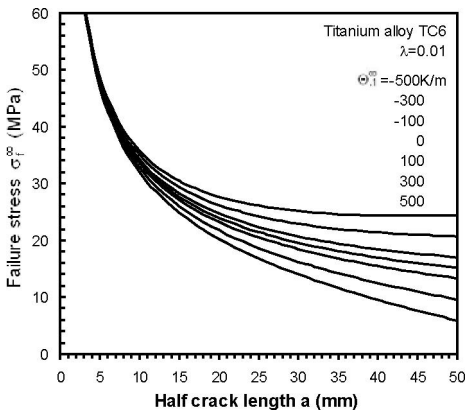

Figure 24. Failure stress versus half crack length curves for different temperature gradient: λ=0.01, titanium alloy TC6.

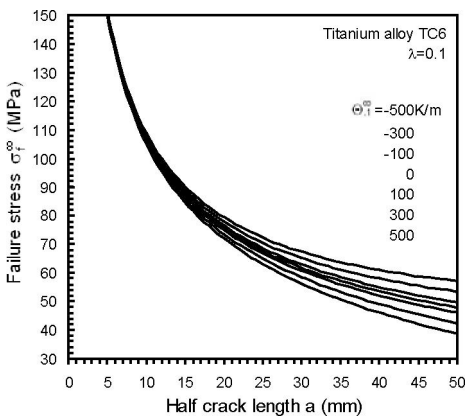

Figure 25. Failure stress versus half crack length curves for different temperature gradient: λ=0.1, titanium alloy TC6.

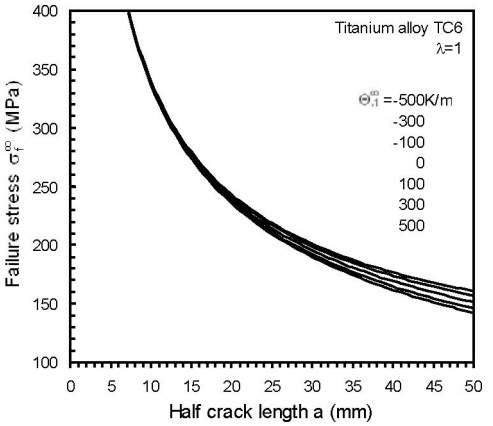

Figure 26. Failure stress versus half crack length curves for different temperature gradient: λ=1, titanium alloy TC6.

8. Crack Growth Enhancement and Retardation by Thermal Effect

It is known from Eq. (54) that the term $\sigma^{\infty}\Theta_{,1}^{\infty}$ would affect the value of strain energy density factor S depending on whether the temperature gradient $\Theta_{,1}^{\infty}$ is positive, zero or negative. In view of the third hypothesis of strain energy density theory presented by Eq. (61), the crack growth behavior would depend on the direction of temperature gradient $\Theta_{,1}^{\infty}$.

Let the superscripts –, 0, + denote, respectively, the situations of negative, zero and positive $\Theta_{,1}^{\infty}$. The corresponding crack growth segments are denoted by r_1^-, r_2^-, …, r_1^0, r_2^0, …, and r_1^+, r_2^+, …, while the strain energy density factors are denoted by S_1^-, S_2^-, …, S_1^0, S_2^0, …, and S_1^+, S_2^+, …. etc. Application of Eq. (61) yields

$$\left(\frac{dW}{dV}\right)_c = \frac{S_1^-}{r_1^-} = \frac{S_2^-}{r_2^-} = \cdots = \frac{S_1^0}{r_1^0} = \frac{S_2^0}{r_2^0} = \cdots = \frac{S_1^+}{r_1^+} = \frac{S_2^+}{r_2^+} = \cdots = \text{const.} \tag{76}$$

It follows that for the j-th segment of crack growth there prevails the relationship

$$\frac{S_j^-}{r_j^-} = \frac{S_j^0}{r_j^0} = \frac{S_j^+}{r_j^+}, j=1, 2, \ldots \tag{77}$$

or

$$\frac{S_j^-}{S_j^0} = \frac{r_j^-}{r_j^0} \text{ and } \frac{S_j^+}{S_j^0} = \frac{r_j^+}{r_j^0}, j=1, 2, \ldots \tag{78}$$

The coefficients of A_{11}, A_{12} and A_{22} in Eq. (69) are calculated for three materials. The result is given in Table 2. The values of strain energy density factor S for different temperature $\Theta_{,1}^{\infty}$ are also tabulated in Table 3. The result in Table 3 indicates that

$$S_j^- < S_j^0 \text{ and } S_j^0 < S_j^+ \tag{79}$$

Eqs. (78) and (79) can be further applied to show that

$$r_j^- < r_j^0 \text{ and } r_j^0 < r_j^+ \tag{80}$$

Table 2. Values of coefficients A_{11}, A_{12} and A_{22} for three materials with θ_0=0° and a=10mm.

A_{ij}	Titanium alloy TC6	Steel 38Cr2Mo2VA	Aluminum alloy LY12
$A_{11}\times10^{-14}$	2.301	1.300	3.325
$A_{12}\times10^{-10}$	0.854	1.202	1.805
$A_{22}\times10^{-6}$	0.317	1.111	0.980

Table 3. Values of strain energy density factor S for different $\Theta_{,1}^{\infty}$ for three materials with θ_0=0°, a=10mm and σ^{∞}=10MPa.

Material	Strain energy density factor S (N/m)										
	$\Theta_{,1}^{\infty}$ (K/m)										
	-500	-400	-300	-200	-100	0	100	200	300	400	500
Titanium alloy TC6	1.526	1.668	1.817	1.972	2.133	2.301	2.475	2.655	2.842	3.035	3.234
Steel 38Cr2Mo2VA	0.376	0.516	0.679	0.864	1.071	1.300	1.551	1.825	2.121	2.439	2.779
Aluminum alloy LY12	1.765	2.038	2.330	2.642	2.974	3.325	3.696	4.086	4.496	4.926	5.376

By using the crack growth segment r_j^0 as a reference of comparison, crack growth is enhanced ($r_j^0 < r_j^+$) when $\Theta_{,1}^{\infty}$ along the positive direction of x_1-axis. Alternatively, the crack growth is retarded ($r_j^- < r_j^0$) when $\Theta_{,1}^{\infty}$ is opposite to the direction of x_1-axis. This is shown in Fig. 27.

Table 4 shows the numerical result of normalized crack growth segment $r_j^{\pm}/r_j^o$ versus temperature $\Theta_{,1}^{\infty}$. In Table 4, values greater than one means that the thermal loading enhances the crack growth. Values smaller than one imply that the thermal loading impedes the crack growth. The numerical results in tables 3 and 4 are also illustrated in Figs. 28 and 29. Fig. 28 depicts the variation of strain energy density factor S with temperature loading $\Theta_{,1}^{\infty}$ for three

materials. Fig. 29 plots the curves of normalized crack growth segment versus temperature loading $\Theta_{,1}^{\infty}$ for three materials.

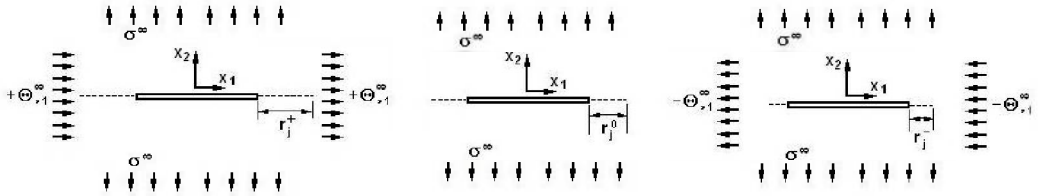

(a) positive $\Theta_{,1}^{\infty}$ (2) Zero $\Theta_{,1}^{\infty}$ (c) negative $\Theta_{,1}^{\infty}$

Figure 27. Schematic of crack growth enhancement and retardation behavior: (a) positive $\Theta_{,1}^{\infty}$; (2) Zero $\Theta_{,1}^{\infty}$; (c) negative $\Theta_{,1}^{\infty}$.

Table 4. Normalized *j*-th crack growth segment $r_j^{\pm}/r_j^0$ for positive and negative temperature gradient for three materials with θ_0=0°, a=10mm and σ^{∞}=10MPa.

Material	Normalized *j*-th crack growth segments $r_j^{\pm}/r_j^0$										
	$\Theta_{,1}^{\infty}$ (K/m)										
	-500	-400	-300	-200	-100	0	100	200	300	400	500
Titanium alloy TC6	0.663	0.725	0.790	0.857	0.927	1	1.076	1.154	1.235	1.319	1.406
Steel 38Cr2Mo2VA	0.289	0.397	0.522	0.664	0.824	1	1.193	1.404	1.631	1.876	2.138
Aluminum alloy LY12	0.531	0.613	0.701	0.795	0.894	1	1.112	1.229	1.352	1.482	1.617

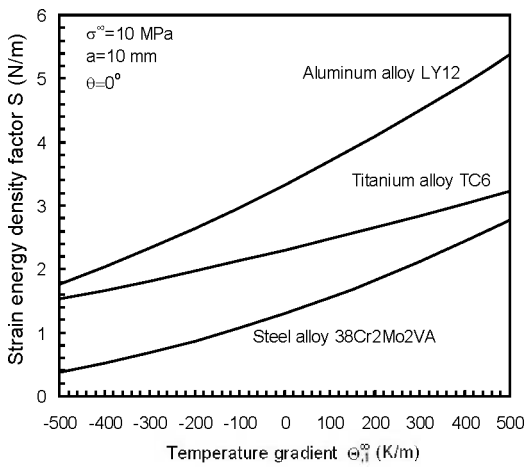

Figure 28. Strain energy density factor versus temperature gradient for three materials.

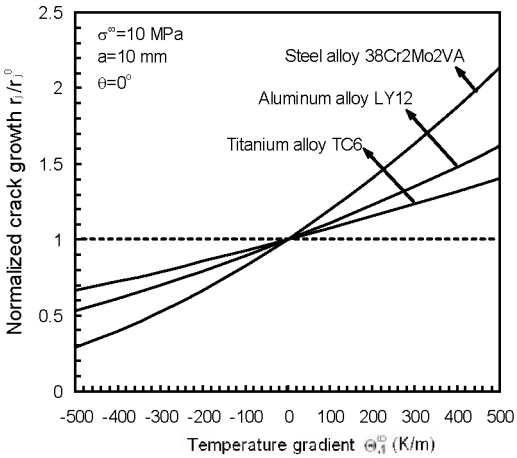

Figure 29. Normalized crack growth segment versus temperature gradient for three materials.

9. Strain Energy Density Function Affected by Thermal Loading

Refer to Eq. (51). The strain energy density field possesses a $1/r$ singularity. The relation between dW/dV and distance r is a standard hyperbola. The product of dW/dV and distance r is a constant for the same dW/dV versus r curve. In the log-log plot, the dW/dV versus r curve is a straight line. These features are not changed by the thermal effect. Plotted in Figs. 30, 31 and 32 are dW/dV versus distance r for different temperature gradient for steel, aluminum and titanium alloys respectively. They are three sets of parallel straight lines in log-log coordinates. The distance of straight lines is large for steel alloy, then for aluminum alloy, small for titanium alloy. This implies that the steel material is sensitive to temperature, then aluminum. The titanium material is not sensitive to temperature compared to steel and aluminum.

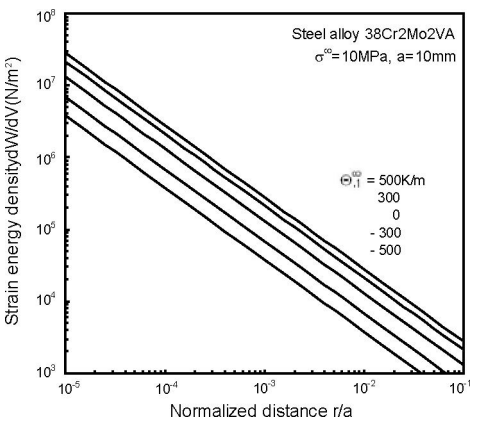

Figure 30. Log-log plot of strain energy density versus distance for different temperature gradient for steel alloy 38Cr2Mo2VA.

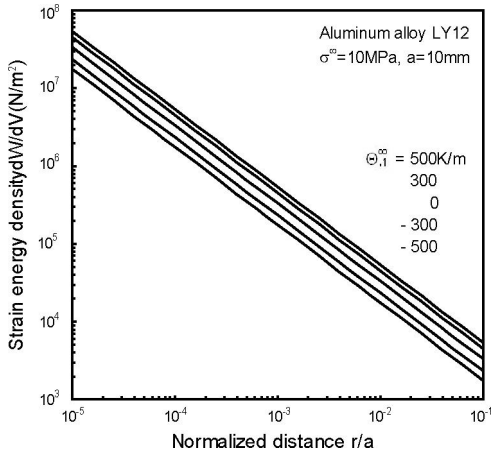

Figure 31. Log-log plot of strain energy density versus distance for different temperature gradient for aluminum alloy LY12.

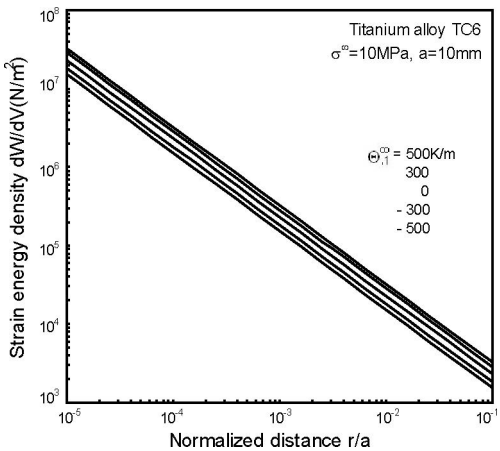

Figure 32. Log-log plot of strain energy density versus distance for different temperature gradient for titanium alloy TC6.

10. Concluding Remarks

The problem for an infinite plate with a central crack subjected to the remote uniform heat flow along any direction has been solved by the complex function method. Under the temperature boundary condition of the constant temperature variation on the upper and lower crack surfaces, the thermal boundary value problem can be transfer to a typical Hilbert problem. Obtained are the analytical solutions including the full field temperature field, asymptotic thermal stress field and thermal stress intensity factor. Under the given condition, it is found that the heat flow vertical to the crack line has no influence on the solution. Only mode I thermal stress intensity factor prevails. By the combination of mechanical and thermal loading, the fracture behaviors of three materials of steel, aluminum and titanium alloys are discussed and compared by application of strain energy density theory. Failure analysis is

performed. It is found that the thermal effect does not affect the shapes of the strain energy density contours ahead of the crack tip compared to the isothermal case. The thermal effect can enhance or impede the crack propagation depending on the direction of temperature gradient. In addition, steel material is more sensitive to the thermal loading than aluminum and titanium materials. The thermal effect has a small influence on titanium compared to aluminum and steel.

Bodies with large volume to surface ratio dissipate more energy by dilatation in contrast to distortion [20-23]. The dominance of dilatation tends to exhibit brittle behavior. As the volume to surface ratio is decreased, energy dissipation via distortion would overtake that of dilatation and a unit volume of the same material become more ductile. The ductile-brittle transition depends on the material microstructure, specimen shape and size, temperature and rate of deformation. Regardless of nonlinearity, the proportion of energy expanded by dilatation and distortion can be assessed from the stationary values of the energy density function. Dominance by dilatation or distortion is a concept that remains to be validated for analyzing size from macro to micro [27]. Recent developments with reference to multiscaling damage theories based on the restraining stress zone for both static and dynamic cracks can be found in [28, 29]. The current work can be extended to the multiscaling damage problem provided that a microscopic damage zone is attached to the macro-crack tip. This is valuable to do in the future work.

Acknowledgement

This work was jointly supported by Natural Science Foundation of Hunan Province of China under the contract No. 07JJ3004 and by Natural Science Foundation of University Doctoral Disciplines of China under the contract No. 200805360002.

References

[1] B.R. Bass, C.E. Pugh, J. Sievers, H. Schulz. Overview of the International Comparative Assessment Study of Pressurized Thermal-Shock in Reactor Pressure *Vessels. International Journal of Pressure Vessels and Piping*, **78**(2-3) (2001) 197-211.

[2] G.C. Sih. *Mechanics of Fracture Initiation and Propagation*. Kluwer Academic Publishers, Dordrecht, The Netherlands, 1991.

[3] B.A. Boley and J.H. Weiner. *Theory of Thermal Stresses*. Wiley, New York, 1960.

[4] G.C. Sih, J. Michopoulos, S.C. Chou. *Hygrothermoelasticity*. Martinus Nijhoff Publishing, The Netherlands, 1986.

[5] G.C. Sih. Heat conduction in the infinite medium with lines of discontinuities. *J. Heat Transfer*, **87**(2) (1965) 293-298.

[6] G.C. Sih. On the singular character of thermal stresses near a crack tip. *Journal of Applied Mechanics*, **29**(3) (1962) 587-589.

[7] A.L. Florence, J.N. Goodier. Thermal stresses due to disturbance of uniform heat flow by an insulated ovaloid hole. *J. of Applied Mechanics*, **27**(6) (1960) 635-639.

[8] D.Y. Tzou. Strain energy density – a molecular appraisal. *Journal of the Chinese Institute of Engineers,* 2004, 27(6): 919-926.

[9] J.T. Pindera. Local effects in plates - theoretical and practical consequences. *Theoretical and Applied Fracture Mechanics*, **10**(1) (1988) 1-18.

[10] M. Matczynski, M. Sokolowski. Crack opening and closure under the action of mechanical and thermal loads. *Theoretical and Applied Fracture Mechanics*, **11**(3) (1989) 187-198.

[11] N.N.V. Prasad, M.H. Aliabadi, D.P. Rooke. Effect of thermal singularities on stress intensity factors: edge crack in rectangular and circular plate. *Theoretical and Applied Fracture Mechanics*, **24**(3) (1996) 203-215.

[12] K.P. Herrmann, V.V. Loboda, I.V. Kharun. Interface crack with a contact zone in an isotropic bimaterial under thermomechanical loading. Theoretical and Applied Fracture Mechanics, **42**(3) (2004) 335-348.

[13] Janine Johnson, Jianmin Qu. An interaction integral method for computing mixed mode stress intensity factors for curved bimaterial interface cracks in non-uniform temperature fields. *Engineering Fracture Mechanics*, **74**(14) (2007) 2282-2291.

[14] X.S. Tang. Healing of a crack in a thin metal plate by application of electrothermal effect. In: G.C. Sih, S.T. Tu and Z.D. Wang (eds.), FM2003 - Structural Integrity and Materials Aging: *Fracture Mechanics and Application*, East China University of Science and Technology Press, Shanghai, (2003) 287-296.

[15] T.J.C. Liu. Thermo-electro-structural coupled analyses of crack arrest by Joule heating. *Theoretical and Applied Fracture Mechanics*, 2008, 49(2): 171-184.

[16] F. Shang, Z. Wang, Z. Li. Thermal stress analysis of a three-dimensional crack in a piezothermoelastic solid. *Engineering Fracture Mechanics*, **55**(5) (1996) 737-750.

[17] P. Lu, M.J. Tan, K.M. Liew. Piezothermoelastic analysis of a piezoelectric material with an elliptic cavity under uniform heat flow. *Archive of Applied Mechanics*, **68**(10) (1998) 719-733.

[18] Q.H. Qin. Thermoelectroelastic Green's function for thermal load inside or on the boundary of an elliptic inclusion. *Mechanics of Materials*, **31**(10) (1999) 611-626.

[19] Q.H. Qin. General solutions for thermopiezoelectrics with various holes under thermal loading. *International Journal of Solids and Structures*, **37**(39) (2000) 5561-5578.

[20] G.C. Sih. Thermomechanics of solids: nonequilibrium and irreversibility. *Theoretical and Applied Fracture Mechanics*, **9** (3) (1988) 175–198.

[21] G.C. Sih, D.Y. Jeong. Hysteresis loops predicted by isoenergy density theory for polycrystals, Part I: fundamentals of non-equilibrium thermal–mechanical coupling effects. *Theoretical and Applied Fracture Mechanics*, **41**(1-3) (2004) 233-266.

[22] G.C. Sih and D.Y. Jeong. Hysteresis loops predicted by isoenergy density theory for polycrystals, Part II: cyclic heating and cooling effects predicted from non-equilibrium theory for 6061-T6 aluminum, SAE 4340 steel and Ti–8Al–1Mo–1V titanium cylindrical bars. Theoretical and Applied Fracture Mechanics, **41**(1-3) (2004) 267-289.

[23] D.Y. Tzou, G.C. Sih. Thermal/mechanical interaction of subcritical crack growth in tensile specimen. *Theoretical and Applied Fracture Mechanics*, **10**(1) (1988) 59-72.

[24] N.I. Muskhelishivili. *Some Basic Problems of the Mathematical Theory of Elasticity.* P. Noordhoff Ltd., Groningen, The Netherlands, 1953.

[25] X.S. Tang. Analytical solutions of temperature fields for an orthotropic plate with a central crack under remote uniform heat flows. *Engineering Mechanics*, **24**(3) (2007) 28-33. (in Chinese)

[26] Editorial Board. *Practical Handbook of Engineering Materials*. Chinese Standard Press, Beijing, 1988, Vol. 1. (in Chinese)

[27] G.C. Sih, X.S. Tang. Scaling of volume energy density function reflecting damage by singularities at macro-, meso- and micro-scopic level. *Theoretical and Applied Fracture Mechanics*, **43**(2) (2005) 211-231.

[28] X.S. Tang, G.C. Sih. Weak and strong singularities reflecting multiscale damage: micro-boundary conditions for free-free, fixed-fixed and free-fixed constraints. *Theoretical and Applied Fracture Mechanics*, **43**(1) (2005) 5-62.

[29] X.S. Tang, G.C. Sih. Kinetics of microcrack blunting ahead of macrocrack approaching shear wave speed. *Theoretical and applied fracture mechanics*, **42**(2) (2004) 99-130.

In: Titanium Alloys: Preparation, Properties and Applications ISBN 978-1-60876-151-7
Editor: Pedro N. Sanchez, pp. 473-484

Chapter 13

TITANIUM-BASE NANO-/ULTRAFINE EUTECTIC AND COMPOSITES

Jayanta Das*
Department of Metallurgical and Materials Engineering,
Indian Institute of Technology, Kharagpur 721 302,
West Bengal, India

Abstract

This article reviews the recent work on the synthesis of multiphase composites in titanium base alloys to develop high strength and light weight materials with metastable phases. The strategies for alloy development, processing methods, evolution of different phase in the microstructure, elastic-plastic behavior are discussed for Ti-Fe-base eutectic and near-eutectic alloy compositions. It is revealed that modification of the eutectic microstructure by 'a non-uniform grain size distribution' *i.e.*, by introducing relatively larger grains in a eutectic matrix, or using multiple phases, is an effective way for improving the plasticity of nanostructured alloys. The influence of alloy compositions, intrinsic structure of the nano-/ultrafine phases and their elastic properties are crucial for developing nano-heterostructured composites.

Introduction

Nanostructured matrix-dendrite composites [9,19,25] have become central to the development of advanced composites [21], and have overtaken to bulk metallic glasses (BMGs) [10,41] and nanocrystalline materials in importance [39] due to their attractive mechanical properties. Typically, the high-strength nanostructured matrix is toughened by incorporating ductile micrometer-size dendritic/spherical particles, either body-centered cubic (bcc) phase precipitates in Ti- [19], Zr- [9], Cu- [2], Fe- [38] and Mg-base [31] multicomponent alloys or alternatively a hexagonal α-Zr solid solution phase [37], respectively, borrowing the strategy typically used to synthesize BMG composites [16]. Among them, Ti-base alloys are superior in comparison to other alloys due to their high corrosion resistance [33]

*E-mail address: j.das@metal.iitkgp.ernet.in

and low density of the main constituent element (4.5 g/cm^3). Recently, the composite microstructure formation and their effect on the mechanical properties has been investigated by manipulating the glass forming alloy compositions in a series of Ti-Cu-Ni/Fe-Sn-X (X=Ta, Nb, Mo or Zr) alloys [11]. The fabrication, evolution of the microstructure, deformation mechanism and mechanical properties of bcc β-Ti phase - nanostructured/glassy matrix composites in Ti-base alloys is recently reviewed [11]. While studying the solidification mechanism of the Ti-Cu-Ni-Sn-Ta/Nb multicomponent alloys, it was revealed that after the formation of micrometer size β-Ti dendrites, the residual melt undergoes metastable "binary" eutectic reaction, which finally solidifies to alternating layers of bcc β-Ti and either NiTi or $CuTi_2$ colonies with 100-200 nm interlamellar spacing. It is well known that BMGs are usually obtained near deep (stable / metastable) eutectic in multicomponent systems. However, for the available eutectic reactions in any alloy system, most of them may not be sufficiently deep to allow bulk glass formation at relatively low cooling rates (100-500 K/sec) by casting in metallic molds. In such a situation an eutectic reaction is expected to occur in the melt.

In this review, processing and microstructure of Ti-Fe-base eutectic and hyper-/ hypoeutectic alloys to achieve high strength together with enhanced plasticity and the intrinsic structure related deformation of such nano-/ultrafine eutectic and their composites are discussed.

Processing, Microstructure and Mechanical Properties

Since it is reported [11, 19] that the nanostructured matrix in Ti-Cu-Ni/Fe-Sn-X (X=Ta, Nb, Mo or Zr) composites exhibit two phase eutectic microstructure [40], therefore, $Ti_{70.5}Fe_{29.5}$ eutectic [32] was chosen as a model system and a large number of eutectic and hyper-/hypoeutectic composites were prepared, in binary Ti-Fe [6, 27], ternary Ti-Fe-Sn [3, 6–8, 13, 14, 42], Ti-Fe-Co [26, 28], Ti-Fe-Ta [43], and quaternary Ti-Fe-Co-X (V, Ni, Cu, Sn, B) alloys [24]. These alloys were prepared under high purity Ar-atmosphere either in the shape of rods of 3-6 mm diameter (ϕ) by cold crucible/Cu-mold casting or in the shape of button shape ingots by arc-melting as shown in Fig. 1. The density (ρ) of these alloys was estimated to vary in between 5.58-6.0 g/cm^3.

According to the morphology and the presence of different metastable phases, the as-solidified microstructures are classified as follows: (i) fully eutectic, and (ii) eutectic matrix composites. In the former case, the colonies are solidified through the following eutectic reaction: (a) L$\rightarrow$ $\beta-$Ti (Im$\bar{3}$m) + FeTi (Pm$\bar{3}$m) [6] or (b) class II-type eutectic reaction with four phases in equilibrium, *i.e.* L + Ti_3Sn (P63/mmc) $\rightarrow$ $\beta-$Ti (Im$\bar{3}$m) and FeTi (Pm$\bar{3}$m) [13, 14]. A typical microstructure of cold crucible cast $(Ti_{0.705}Fe_{0.295})_{96}Sn_4$ with homogeneous eutectic consisting of $\beta-$Ti and FeTi nano-lamellar phases are presented in Fig. 2(a). The interlamellar spacing (λ) was estimated to be smaller (λ = 100-150 nm) than that of $Ti_{70.5}Fe_{29.5}$ (λ = 200-400 nm). TEM bright field image of cold crucible cast $Ti_{70.5}Fe_{29.5}$ is presented in the inset of Fig. 2(a) showing the presence alternating lamellar of FeTi (darker phase) with dislocations and brighter $\beta-$Ti phases. The colony boundaries exhibit features of remelting and presence of coarse particles. The lattice parameter of the $\beta-$Ti ($a_{\beta-Ti}$) in $(Ti_{0.705}Fe_{0.295})_{100-x}Sn_x$ ($0 \leq x \leq 6$) increase from $a_{\beta-Ti}$ = 0.3165 nm for x = 0 to a value $a_{\beta-Ti}$ = 0.3255 nm for x = 3.85-4 then remain constant upon

Figure 1. Outer shape of a Ti-Fe-Sn ingot solidified at a cooling rate of ~10 K/s.

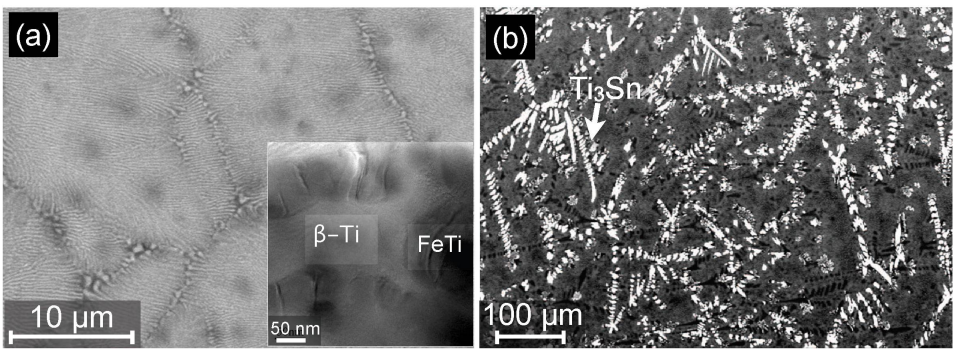

Figure 2. Typical microstructural features of the Ti-base nano-/ultrafine eutectic and their composites. SEM back-scattered electron image of $(Ti_{0.705}Fe_{0.295})_{100-x}Sn_x$: (a) x = 4 (6 mmϕ rod), and (b) x = 6 (ingot). Inset to (a) : TEM bright field image of $Ti_{70.5}Fe_{29.5}$ revealing the eutectic phases ($\beta-$Ti and FeTi).

further addition of Sn. Whereas, the lattice parameter of the FeTi phase (a_{FeTi}) was found to be constant (a_{FeTi} = 0.298 $\pm$ 0.001 nm) for all the Ti-Fe-Sn / Ti-Fe-Ta / Ti-Fe-Co-(X) alloys as mentioned above. The composition of the $\beta-$Ti phase in $Ti_{70.5}Fe_{29.5}$ and in $Ti_{67.79}Fe_{28.36}Sn_{3.85}$ was reported to be $Ti_{77.7}Fe_{22.3}$ and $Ti_{82.3}Fe_{9.2}Sn_{8.5}$, respectively [6]. However, the maximum solubility of Sn in FeTi intermetallic was estimated to be $\leq$0.7 at.%.

The eutectic matrix composites are composed of 20-50 μm size proeutectic $\beta-$Ti, FeTi or Ti_3Sn phase(s) with spherical or dendritic morphology. These composite microstructures are similar to that of the nanostructured matrix-$\beta-$Ti dendritic composites in as-cast (3 mmϕ) $Ti_{60}Cu_{14}Ni_{12}Sn_4Ta_{10}$ [19]. Figure 2(b) shows the microstructure of $(Ti_{0.705}Fe_{0.295})_{94}Sn_6$ ingot exhibiting the presence of proeutectic Ti_3Sn (white) dendrites embeded in an ultrafine eutectic matrix (λ = 400-600 nm). It is worth to note that the eutectic matrix in the above mentioned alloys is composed of ultrafine $\beta-$Ti and FeTi/ Ti(Fe,Co) phases. It is further reported by Han *et al.* [13, 14] that two different eutectic colony as "bimodal-eutectic" comprising of $\beta-$Ti + FeTi and $\beta-$Ti + Ti_3Sn lamelle coexist with 40-50 vol.% of Ti_3Sn dendrites in $(Ti_{0.705}Fe_{0.295})_{91}Sn_9$. Synthesis of eutectic matrix com-

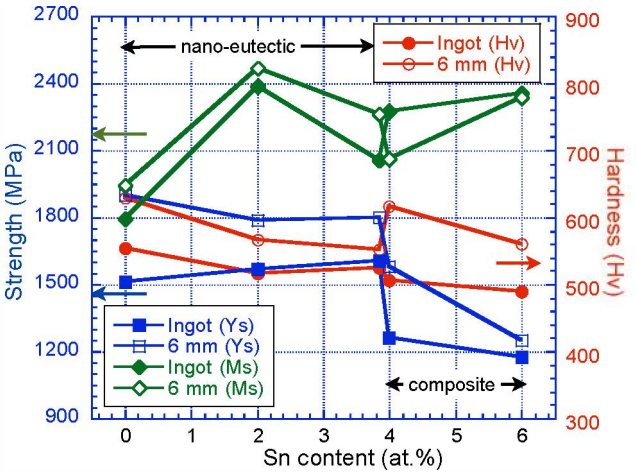

Figure 3. The variation of yield stress (Ys), maximum stress (Ms) and Vicker's hardness (Hv) of a series of nano-/ultrafine eutectic (β-Ti+FeTi), and eutectic matrix$-Ti_3Sn$ dendrite composites in $(Ti_{0.705}Fe_{0.295})_{100-x}Sn_x$ $(0 \leq x \leq 6)$ ingots and cold crucible cast rods (6 mm ϕ).

posites have been also reported in hypereutectic Ti-Fe [27] or Ti-Fe-Co-(X) (X=V, Ni, Cu, Sn, B) [26, 28] with proeutectic FeTi or Ti(Fe,Co) phases, respectively. The solubility of Co in FeTi phase was found to be 25 at.%. The lattice parameter of the proeutectic and eutectic FeTi / Ti(Fe,Co) was estimated to vary in between 0.299-0.300 nm only, whereas, the lattice parameter of the $\beta-$Ti solid solution ($a_{\beta-Ti}$) was estimated to vary in between $a_{\beta-Ti}$ = 0.316 nm ($Ti_{76}Fe_{12}Co_{12}$) and $a_{\beta-Ti}$ = 0.320 nm for ($Ti_{70}Fe_{15}Co_{15}$). However, addition of Sn increases the $a_{\beta-Ti}$ to 0.326 nm in $Ti_{67}Fe_{14}Co_{14}Sn_5$ [24]. Therefore, $a_{\beta-Ti}$ increases with increase of Sn, Co and decrease of Fe in the $\beta-$Ti phase.

The mechanical properties of nano-/ultrafine eutectic and eutectic matrix composites were evaluated by hardness measurement under 100 g and compression test at a strain rate of 10^{-4}/s. The strength (Ys) and compressive plasticity (up to 25%) of the composites are much superior compared to not only bulk metallic glasses, glass matrix composites but also nanostructure-dendrite composites. The variation of hardness, yield strength and maximum strength of $(Ti_{0.705}Fe_{0.295})_{100-x}Sn_x$ $(0 \leq x \leq 6)$ ingots and cold crucible cast rods (6 mm ϕ) are shown in Fig. 3. The homogeneous Ti-Fe/Ti-Fe-Sn nanoeutectic shows similar yield strength values (Ys_{ingot} = 1500-1600 MPa, and $Ys_{6\ mm\phi}$ = 1800-1900 MPa) but a large range of stress for work-hardening (from Ys = 1500 MPa to Ms = 2400 MPa) have been noticed upon addition of 2 at.% Sn to $Ti_{70.5}Fe_{29.5}$. The volume fraction of the $\beta-$Ti phase decreases from 71 vol.% ($Ti_{70.5}Fe_{29.5}$) to 64 vol. % ($Ti_{67.79}Fe_{28.36}Sn_{3.85}$), and therefore, hardening becomes weaker in the specimens containing 3.85 at.% Sn. The yield strength of all the ingot specimens exhibit lower values than that of the cold crucible cast specimens due to coarser interlamellar spacing. On the other hand, $(Ti_{0.705}Fe_{0.295})_{94}Sn_6$ composites with Ti_3Fe dendrites exhibit much lower yield strength ($\sim$1200 MPa) and hardness values (500-550 Hv) than that of the homogeneous eutectic microstructure (Fig. 3), as also reported by Han et al. [13, 14]. Very similar results has been reported in hypereutectic

Table 1. Elastic properties of homogeneous eutectic and single-phase polycrystalline alloys with different chemical composition: Young's modulus E, Poisson's ratio ν, shear modulus G, bulk modulus K.

Alloy composition/Phase(s)	E (GPa)	ν	G (GPa)	K (GPa)
$Ti_{70.5}Fe_{29.5}$ ($\beta-$Ti, FeTi)	153	0.319	58	141
$Ti_{80}Fe_{20}$ ($\beta-$Ti)	136	0.314	52	122
$Ti_{51.5}Fe_{48.5}$ (FeTi)	222	0.277	87	166
$Ti_{67.79}Fe_{28.36}Sn_{3.85}$ ($\beta-$Ti, FeTi)	137	0.339	51	142
$Ti_{82}Fe_{10}Sn_{8}$ ($\beta-$Ti)	100	0.323	38	94
$Ti_{51.5}Fe_{48}Sn_{0.5}$ (FeTi)	218	0.268	86	156

Ti-Fe-Co alloys with proeutectic Ti(Fe,Co) reinforced eutectic matrix composites by varying Ti (60-70 at.%), Fe (12-27 at.%), and Co (5-20 at. %). $Ti_{70}Fe_{20}Co_{10}$ and $Ti_{60}Fe_{20}Co_{20}$ reported to be two extreme types of hypereutectic alloys with significantly different volume fractions of the primary cP2 Ti(Fe,Co) phase, $i.e.$, 25% and 70% respectively. The hardness (Hv), yield strength (Ys), maximum strength (Ms) and plasticity (ϵ_p) in these alloys were reported to be Hv = 560-550, Ys = 1770-1510 MPa, Ms = 1890-2100 MPa, ϵ_p = 8.1-15 %, respectively. The compressive plasticity was reported to improve significantly (ϵ_p = 25 %) in $Ti_{67}Fe_{14}Co_{14}Sn_5$ [24]. On the other hand, Ti-Fe-Ta eutectic matrix-FeTi dendrite composites [43] exhibit yield strength about 2300 MPa, which is much higher than that of Ti-base bulk metallic glasses (2000 MPa) [44] and Ti–Cu–Ni–Sn–Ta/Nb/Mo nanostructured composites (1800 MPa) reported so far [11, 19].

In order to investigate the elastic properties of the different phases in the homogeneous eutectic/composites, single-phase polycrystalline samples have been prepared after identifying the individual phase composition in the binary and ternary Ti–Fe–(Sn) alloys [6]. The elastic constants obtained from ultrasonic sound wave velocity measurements are given in Table 1. The decrease in the shear/bulk modulus ratio G/K for the $\beta-$Ti phase from 0.423 to 0.402 and for the homogeneous eutectic from 0.408 to 0.359 upon addition of 3.85 at.% Sn to $Ti_{70.5}Fe_{29.5}$ points to an increase in the intrinsic toughness of $\beta-$Ti phase and the eutectic specimens [5]. However, the change in the elastic properties of FeTi upon addition of Sn is very less.

Deformation and Fracture Mechanism

It is reported that nanostructure-dendrite composite deform by shear banding similar to the mechanism of plastic deformation process in bulk metallic glasses and in glass matrix composites [35]. Recently, systematic microstructural studies at different stages of compressive deformation revealed that plastic deformation proceeds with the early yielding of the composite due to dislocation slip in the bcc $\beta-$Ti dendrites and subsequent shear band formation in the dendrites as well as in the nanostructured matrix. However in case homogeneous eutectic and eutectic matrix composites, three different mechanisms have been proposed as reported in the literatures : (a) dislocation based slip [4, 6, 8], (b) shear banding

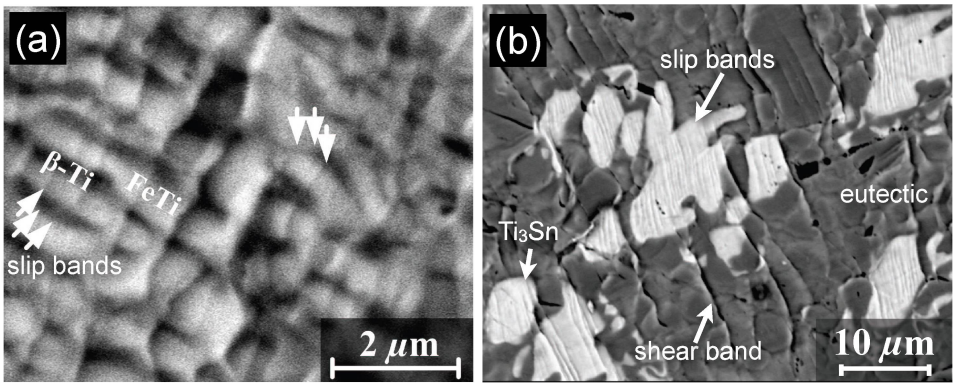

Figure 4. Typical fractographic features of Ti-Fe-(Sn) nano-/ultrafine eutectic specimens. (a) BSE image showing the slip transfer across the $\beta-$Ti/FeTi interface.

and rotational deformation [6, 13, 14], and (c) phase transformation [29].

In case of homogeneous eutectic microstructure in Ti-Fe-Sn, profuse slip traces have been found in the nanolamellar phases after deformation, as reported by Das et al. [6]. The evolution of such slip transfer accross the interface of $\beta-$Ti/FeTi in $(Ti_{0.705}Fe_{0.295})_{98}Sn_2$ ingot after 11% compressive strain is shown in Fig. 4(a) as marked by arrows. Whereas in case of brittle $Ti_{70.5}Fe_{29.5}$, cleave fracture preferably occurs along the (100) plane without showing any slip traces. Smooth cleave planes in $\beta-$Ti phase with protrusions of rod shape FeTi phase has been observed on the fracture surface without any crack-bridging. This confirms that the FeTi intermetallic compound is harder than the $\beta-$Ti phase [8]. On the other hand, the eutectic matrix composites with either micrometer-size Ti_3Sn or Ti(Fe,Co) show dislocation slip is the dominant deformation mechanism in the proeutectic Ti_3Sn phases as well as in $\beta-$Ti phase in the ultrafine eutectic matrix as investigated through SEM (Fig. 4(b)) and TEM in the case of $(Ti_{0.705}Fe_{0.295})_{94}Sn_6$ [5] and $Ti_{60}Fe_{20}Co_{20}$ [30], respectively. Therefore, dislocation slip must be responsible for the strong work-hardening of the composites. It has already been reported that hexagonal Ti_3Sn ($D0_{19}$) polycrystalline samples are brittle at room temperature and exhibit a yield strength about 600-800 MPa for polycrystalline specimens [15]. Therefore, early yielding of the composite is related to the slip in this soft Ti_3Fe phase through either prismatic $(\bar{1}100)[\bar{1}\bar{1}20]$ or pyramidal $(1\bar{1}\bar{2}1)[\bar{1}\bar{1}26]$ slip systems [15]. However, the antiphase domain boundary energy for these slip systems is lower (0-200 mJ/m^2) [22] compared to other $D0_{19}$ compounds (Ti_3Al, 100-400 mJ/m^2 [23]), which indicates the possibility for dissociation of the superdislocations and thus the interaction of superdislocations and antiphase domains can contribute to the hardening.

It is reported [29] that the large compressive plasticity (15-20%) in Ti-Fe-Co alloys is due to the presence of micrometer size Ti(Fe,Co) (cP2) phase, which undergoes deformation induced martensitic phase transition from cP2 $\rightarrow$ NiTi-type mP4 phase and local amorphization in the shear band. TEM investigation of partly deformed sample revealed [30] that the β-Ti solid solution phase deform by dislocation-slip, whereas no dislocations rather shear bands were found in the cP2 Ti(Fe,Co) phase. However, it is worth to note that composites containing micrometer size 70 vol.% of Ti(Fe,Co) phase in $Ti_{60}Fe_{20}Co_{20}$ and 80

vol.% of Ti(Fe,Co) phase $Ti_{54}Fe_{23}Co_{23}$ exhibit 15% and 0.5% plastic strain, respectively, as reported by Louzguine et al. [28]. The authors have suggested that such phase transition has a minor contribution on enhancing the plasticity of the composites.

Since stress concentration occurs around the deformed grains, therefore, preferential deformation of grains within the affected zone of the large grains is considered to behave like a soft region to result in heterogeneous deformation in the specimen, as observed in formation of the Lüders bands [12]. In case of the eutectic matrix composites similar mechanism has been found to be operative. At the initial stage of deformation, macroscopic investigation revealed that the slip spacings in the outer regions of the individual Ti-Fe-Sn eutectic colonies are coarser, whereas, the inner portion of the colonies displays refinement in both microstructure and slip traces [8, 13]. Further deformation ($\epsilon_p > 10\%$) induces heterogeneous deformation/strain localization and nucleation of the shear bands, which propagates through the nanoeutectic matrix and are arrested by the proeutetic phases as illustrated in Fig. 4(b). The wavy propagation of the shear bands occurs along the interfaces of the bimodal eutectic structure, i.e., along the boundaries between the coarse and fine eutectic areas, causing a rotation of the eutectic colonies and fracture [6, 13].

Role of Nanolamellar $\beta-$Ti Phase on Plasticity

Even though it was suggested that a nanoeutectic matrix can be easily toughened by incorporating a ductile dendritic phase, it is interesting to notice that some of these micrometer-size β-Ti phase reinforced nanostructured-matrix composites show extended plastic deformability [11, 19] and others do not [17, 18]. It should be noted that the lattice parameter of β-Ti phase in Ti-Fe-base eutectic and near eutectic alloys changes upon alloying with Co, Sn, or V, whereas the lattice parameter of FeTi is unaltered for different alloy system. Therefore, the role of the $\beta-$Ti phase on the mechanical properties of nano-/ultrafine eutectic should be considered.

In order to understand the enhancement of plasticity of the homogeneous eutectic microstructure upon addition of 2-3.85 at.% Sn to $Ti_{70.5}Fe_{29.5}$, a detailed structural investigations was carried out by high resolution transmission electron microscopy (HRTEM), selected area electron diffraction pattern (SAED) analysis and electron energy loss spectroscopy [4]. Besides the same orientation relationship of the eutectic phases, *i.e.*, $[110]_{\beta-Ti} \parallel [110]_{FeTi}$ and $[200]_{\beta-Ti} \parallel [200]_{FeTi}$ in both $Ti_{70.5}Fe_{29.5}$ and $Ti_{67.79}Fe_{28.36}Sn_{3.85}$, a diffuse scattering from the $\beta-$Ti phase appears around the (100) reflection of the FeTi phase for $Ti_{70.5}Fe_{29.5}$, as presented in the inset of Fig. 5. Such a feature was not observed for $Ti_{67.79}Fe_{28.36}Sn_{3.85}$. Apparently, these reflections are linked with the formation of an ω-like short-range order (SRO) in the nanolamellar $\beta-$Ti phase, which involves stacking fauls in the bcc lattice i.e., a displacement of $(222)_\beta$ planes along their normals, accompanied by the insertion of additional $(222)_\beta$ plane segments. The HRTEM image of the eutectic $\beta-$Ti and FeTi phases in $Ti_{67.79}Fe_{28.36}Sn_{3.85}$ shows clear lattice fringes. Whereas, the lattice of the $\beta-$-Ti phase is severely distorted as shown in Fig. 5. The overall structure consists of very fine-scale twins with 3-4 atomic layers and a size of only 2 nm. It was found that the nano-euetctic phases are chemically homogeneous but the addition of Sn releases the local lattice strain, modifies the structural SRO and prevents the formation of stacking faults in the bcc $\beta-$Ti phase resulting in improved plastic deformability.

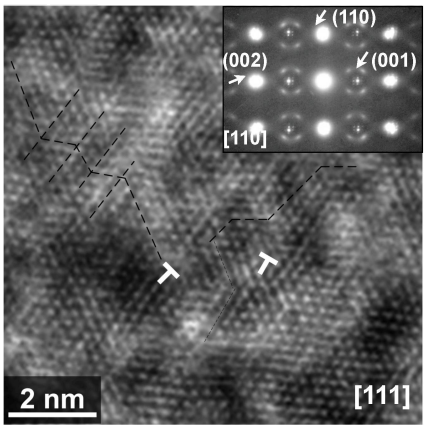

Figure 5. HRTEM image of $Ti_{70.5}Fe_{29.5}$ showing lattice distortion, 2-3 nm size twins (marked by the dashed lines) and stacking faults in the bcc lattice terminated with a dislocation. The structural short-range order of the $\beta-$Ti phase coexisting with the '$\omega-$like' structure is confirmed through the diffuse scattering around the $(001)_{FeTi}$ reflections as revealed in the SAED pattern (inset).

In order to investigate the influence of lattice strain in $\beta-$Ti phase on the deformation behavior, the values of lattice parameter of the $\beta-$Ti phase ($a_{\beta-Ti}$) versus plasticity under compression or tension for various Ti-base alloys as reported in the literature with wide range of microstructures and grain sizes are plotted as shown in Fig. 6. In the case of Ti-Fe-Sn [3], the microstructure consists of either nanalamellar $\beta-$Ti and FeTi phases (Fig. 2(a)) or with micrometer-sized Ti_3Sn dendrites (Fig. 2(b)) as described above. Similarlly, micrometer size Ti(Fe,Co) dendrites coexist with ultrafine $\beta-$Ti and (Co,Fe)Ti eutectic matrix in case of Ti-Fe-Co [28]/Ti-Fe-Co-X (X=V, Ni, Cu, Sn, B) [24]. Whereas, 20-40 volume fraction of microcrystalline plate shaped $\beta-$Ti coexists with Widmastätten/superfine α phase in the as-cast Ti-6Al-4V and Ti-6Al-7Nb. Even though the average composition of these as-cast Ti-Al-Nb/V remain same after various secondary processing, but the lattice parameter of the $\beta-$Ti phase changes after thermomechanical processing with a post-heat treatment from $a_{\beta-Ti}$ = 0.317 to $a_{\beta-Ti}$ = 0.327 nm due to different degree of supersaturation and dissolve H_2 in the $\beta-$Ti phase [1]. Figure 6 clearly shows that the plasticity of nano-/ultrafine eutectic, their composites and microcrystalline $\alpha + \beta$ alloys increases with increase of $a_{\beta-Ti}$. However, these lattice parameter values are smaller than the lattice constant of pure $\beta-$Ti ($a_{\beta-Ti}$ = 0.3311 nm) [34]. It is proposed that the β phase become unstable with increase of $a_{\beta-Ti}$ and thus plastic deformability improves [1,36]. In addition, an increase of dislocation width due to the increase of the lattice parameter, can reduce the effective Pierls stress for slip [20]. Whereas, the presence of high lattice strain (with low values of $a_{\beta-Ti}$), local distortion of the lattice and stacking faults can easily increase the pile-up stress and decrease the intrinsic cleavage strength of the material [4].

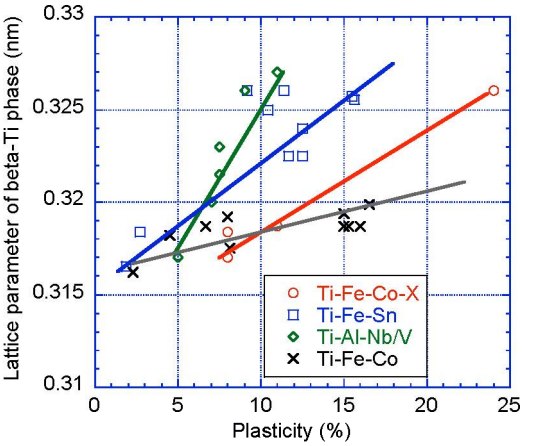

Figure 6. Plot showing the macro-plasticity is strongly influenced by the lattice parameter of β-Ti phase in microcrystalline Ti-Al-Nb/V [1], and nano-/ultrafine Ti-Fe-Co-X (X=V, Ni, Cu, Sn, B) [24, 28] and Ti-Fe-Sn [3] eutectic and eutectic matrix composites.

Conclusions

A new class of high strength nano-/ultrafine eutectic composites have been developed in Ti-Fe-base alloys by suitable choice of alloying elements by simple in-situ processing methods. The evolution of such non-equilibrium nano-/ultrafine eutectic is realized by inexpensive processing at low cooling rates (10 K/sec). The combination of appreciable ductility (up to 25%) and strength (>1800 MPa) for these alloys is believed to be promising for several engineering applications such as high-performance springs, microgears, medical devices, sports equipment etc. Synthesizing such a composite microstructure has paved the way to develop advanced composites by manipulating the microstructures as a function of both composition and intrinsic structure. Designing new ultrafine alloys with biocompatible elements (Sn, Co, Ta and Fe) that combine both high strength and low elastic modulus (100 GPa) is promising for a wide range of biomedical applications. It is also anticipated that nano-/ultrafine composites with/without micrometer-sized intermetallic phases can be widely used to toughen other Al-, Mg-, La-, Pd-, Fe- and Cu-base eutectic alloys.

Acknowledgements

The author is grateful to F. Ettingshausen, J. Eckert, A. Gebert, K. B. Kim, M. H. Lee, W. Löser, R. Mitra, S. Pauly, S. K. Roy, L. Schultz, S. Scudino, M. Stoica, R. Theissmann, S. Venkataraman, T. G. Woodcock, W. Xu, and Z. F. Zhang for stimulating discussions. Financial support provided by EU within the framework of the research and training networks on Ductile BMG Composites (MRTN-CT-2003-504692) as well as by the Deutscher Akademischer Austauschdienst (DAAD) and Defense Research Development Organization of India (New Delhi) are gratefully acknowledged.

References

[1] Akahori, T.; Niinomi, M.; Suzuki, A. *Metall. Mater. Trans. A* 2002; 33, 503–510.

[2] Bian, Z.; Kato, H.; Qin, C. L.; Zhang, W.; Inoue, A. *Acta Mater.* 2005, 53, 2037–2048.

[3] Das, J., *Heterostructured copper- and titanium-base ultrafine and glassy alloys*; Ph.D. Thesis, TU Dresden, Germany 2008.

[4] Das, J.; Eckert, J.; Theissmann, R. *Appl. Phys. Lett.* 2006, 89, 261917.

[5] Das, J.; Ettingshausen, F.; Eckert, J. *Scr. Mater.* 2008, 58, 631–634.

[6] Das, J.; Kim, K. B.; Baier, F.; Löser, W.; Eckert, J. *Appl. Phys. Lett.* 2005, 87, 161907.

[7] Das, J.; Kim, K. B.; Baier, F.; Löser, W.; Gebert, A.; Eckert, J. *J. Alloys Comp.* 2007, 434–435, 28–31.

[8] Das, J.; Kim, K. B.; Xu, W.; Löser, W.; Eckert, J. *Mater. Sci. Eng. A* 2007, 449–451, 737–740.

[9] Das, J.; Löser, W.; Kühn, U.; Eckert, J.; Roy, S. K.; Schultz, L. *Appl. Phys. Lett.* 2003, 82, 4690–4692 .

[10] Das, J.; Tang, M. B.; Kim, K. B.; Theissmann, R.; Baier, F.; Wang, W. H.; Eckert, J. *Phys. Rev. Lett.* 2005, 94, 205501.

[11] Eckert, J.; Das, J.; Kim, K. B. *The Dekker Encyclopedia of Nanoscience and Nanotechnology*; Marcel Dekker, 2006; chap. Nanostructured composites: Ti-base alloys, pp. 1–40.

[12] Fujita, H.; Fujita, N. *Radiation effects and defects in solids* 2002; 157, 85–100.

[13] Han, J. H.; Kim, K. B.; Yi, S.; Park, J. M.; Kim, D. H.; Pauly, S.; Eckert, J. *Appl. Phys. Lett.* 2008, 93, 201906.

[14] Han, J. H.; Kim, K. B.; Yi, S.; Park, J. M.; Sohn, S. W.; Kim, T. E.; Kim, D. H.; Das, J.; Eckert, J. *Appl. Phys Lett.* 2008, 93, 141901.

[15] Hashimoto, T.; Nakamura, M.; Takeuchi, S. *Mater. Trans. JIM* 1990; 31, 195–199.

[16] Hays, C. C.; Kim, C. P.; Johnson, W. L. *Phys. Rev. Lett.* 2000, 84, 2901–2904.

[17] He, G.; Eckert, J.; Hagiwara, M. *Metall. Mater. Trans. A* 2004, 35, 3605–3612.

[18] He, G.; Eckert, J.; Hagiwara, M. *Mater. Lett.* 2006, 60, 656–661.

[19] He, G.; Eckert, J.; Löser, W.; Schultz, L. *Nature Mater.* 2003, 2, 33–37.

[20] Hobart, R. *J. Appl. Phys.* 1965, 36, 1944–1948.

[21] Hofmann, D.; Suh, J.; Wiest, A.; Duan, G.; Lind, M.; Demetriou, M.; Johnson, W. *Nature* 2008, 451, 1085–1089.

[22] Jones, P.; Edington, J. *Phil. Mag.* 1973, 27, 393–404.

[23] Koizumi, Y.; Ogata, S.; Minamino, Y.; Tsuji, N. *Phil. Mag.* 2006, 86, 1243–1259.

[24] Louzguina, L. V.; Louzguine, D. V.; Inoue, A. *Intermetallics* 2006; 14, 255–259.

[25] Louzguine, D. V.; Kato, H.; Inoue, A. *J. Alloys Comp.* 2004, 375, 171–174.

[26] Louzguine, D. V.; Kato, H.; Inoue, A. *Phil. Mag. Lett.* 2004, 84, 359–364.

[27] Louzguine, D. V.; Kato, H.; Louzguina, L. V.; Inoue, A. *J. Mater. Res.* 2004, 19, 3600–3606.

[28] Louzguine, D. V.; Louzguina, L. V.; Kato, H.; Inoue, A. *Acta Mater.* 2005, 53, 2009–2017.

[29] Louzguine, D. V.; Louzguina, L. V.; Polkin, V. I.; Inoue, A. *Scripta Mater.* 2007, 57, 445–448.

[30] Louzguine-Luzgin, D.; Louzguina-Luzgina, L.; Kato, H.; Inoue, A. *J. Alloys Comp.* 2007, 434, 32–35.

[31] Ma, H.; Xu, J.; Ma, E. *Appl. Phys. Lett.* 2003, 83, 2793–2795.

[32] Massalski, T. B.; Okamoto, H.; Subramanian, P. R.; Kacprzak, L., *Binary alloy phase diagrams*; ASM International, Materials Park, OH, 1990; 2nd ed. Vol. 1.

[33] Parlapanska, S.; Parlapanski, D. *Corros. Sci.* 1997, 39, 1321.

[34] PCPDFWIN, Version 2.2; JCPDS-International Centre for Diffraction Data 2001.

[35] Pekarskaya, E.; Kim, C. P.; Johnson, W. L. *J. Mater. Res.* 2001, 16, 2513–2518.

[36] Sakaguchi, N.; Niinomi, M.; Akahori, T.; Takeda, J.; Toda, H. *Mater. Sci. Eng. C* 2005, 25, 370–376.

[37] Scudino, S.; Das, J.; Stoica, M.; Kim, K. B.; Kusy, M.; Eckert, J. *Appl. Phys. Lett.* 2006, 88, 201920.

[38] Shen, B. L.; Men, H.; Inoue, A. *Appl. Phys. Lett.* 2006, 89 101915.

[39] Wei, Q.; Jia, D.; Ramesh, K.; Ma, E. *Appl. Phys. Lett.* 2002, 81, 1240–1242.

[40] Woodcock, T. G.; Kusy, M.; Mato, S.; Alcala, G.; Thomas, J.; Löser, W.; Gebert, A.; Eckert, J.; Schultz, L., *Acta Mater.* 2005, 53, 5141–5149.

[41] Xing, L. Q.; Li, Y.; Ramesh, K. T.; Li, J.; Hufnagel, T. C. *Phys. Rev. B* 2001, 64, 180201.

[42] Zhang, L. C.; Das, J.; Lu, H. B.; Duhamel, C.; Calin, M.; Eckert, J. *Scripta Mater.* 2007, 57, 101–104.

[43] Zhang, L. C.; Lu, H. B.; Mickel, C.; Eckert, J. *Appl. Phys. Lett.* 2007, 91, 051906.

[44] Zhang, T.; Inoue, A. *Mater. Trans. JIM* 1998, 39, 1001–1006.

INDEX

A

B

C

D

E

F

G

H

I

J

K

L

M

N

O

P

Q

R

S

T

U

V

W

X

Y

Z